VDE VERLAG

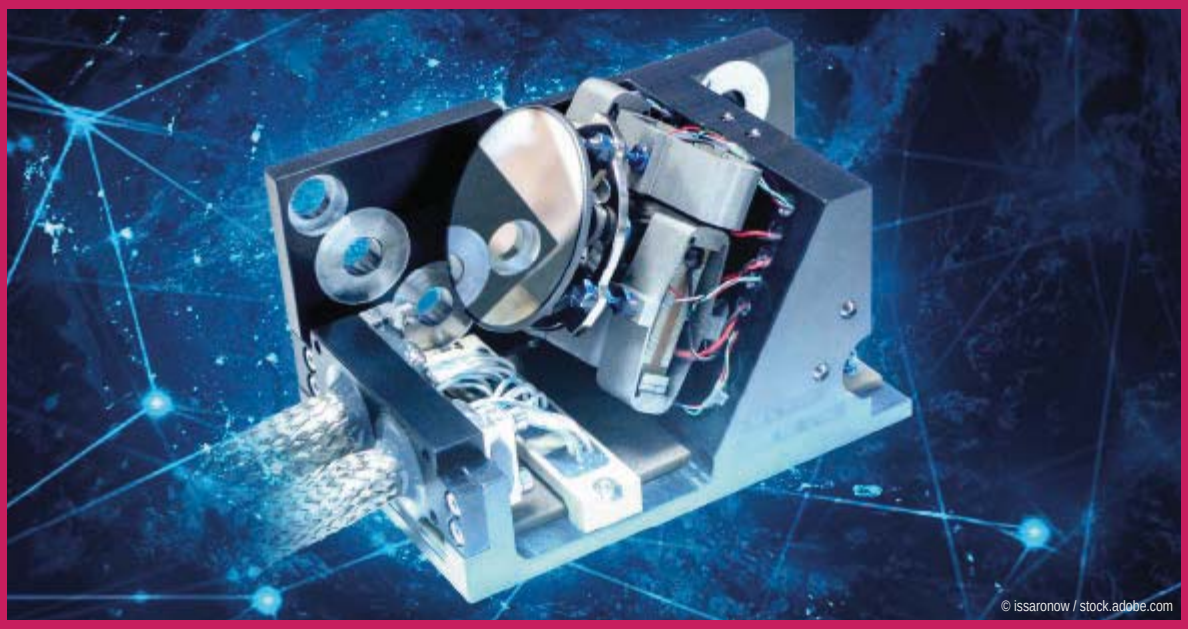
GMM-Fachbericht 115

ACTUATOR 2026

International Conference and Exhibition on New Actuator Systems and Applications

ACTUATOR 26

GMM Conference
June 30 – July 1, 2026 in Wiesbaden



VDE VDI GMM

Sponsors and Exhibitors

















GMM-Fachbericht **115**

ACTUATOR 2026

International Conference and Exhibition on New Actuator Systems and Applications

GMM Conference
June 30 – July 01, Wiesbaden

Chairman:
Prof. Dr. Manfred Kohl, Karlsruhe Institute of Technology, Germany

Organizer:
VDE VDI-Society Microelectronics, Microsystems and Precision Engineering (GMM)

VDE VERLAG GMBH



Cover picture: © Michael Gareis, TU Berlin – Olena/stock.adobe.com

Bibliographic Information of the German National Library
The German National Library lists this publication in the National Bibliography;
detailed bibliographic data are available on the Internet at **https://portal.dnb.de/**.

ISBN 978-3-8007-6743-4 (CD-ROM)
ISBN 978-3-8007-6744-1 (E-Book)
ISSN 1432-3419

© 2026 VDE VERLAG GMBH · Berlin · Offenbach, Bismarckstraße 33, 10625 Berlin
www.vde-verlag.de

All rights reserved. Any utilization in breach of the strict limits of copyright law, without the prior approval of the publisher, is prohibited. Reproductions of common names, brand names, trademarks etc. in this publication are not subject to the acceptance that these names could be regarded as free or could be used by anyone, even without particular marking, in the sense of the trademark and brand protection legislation. Publication does not imply that the solutions described are not protected by intellectual property rights (e.g. patents and utility models). The publisher assumes no liability for the correctness and practicability of the programs, circuits, and any other arrangements and instructions published, nor for the correctness of the technical content of this publication. The up-to-date valid versions of the relevant statutory and official regulations and technical regulations (e.g. VDE body of regulations) have to be respected.

CD Production: DMS – Disk Media Service, Berlin
Produced in Germany

Welcome to the new ACTUATOR Conference 2026

The ACTUATOR Conference 2026 – may we inform you ...
ACTUATOR is a major biennial event bringing together leading experts, suppliers and users in the field of new actuators from all over the world. The invitation to attend ACTUATOR is aimed at executives and researchers from industrial companies as well as institutes, colleges and universities who are interested in the transfer of R&D results into innovative actuator applications and drive technologies.

ACTUATOR 2026 – together with you on an international stage
With about 200 participants from more than 20 countries, the International Conference on New Actuator Systems and Applications has been the most important place to meet leading international specialists, to share their expertise and to start business co-operations in the field of new actuator technologies.

ACTUATOR – the key forum for actuators
based on smart materials and micro technologies as well as their applications in all areas of engineering for thirty years now. Over the years, a huge variety of excellent ideas and results have been reported. A lot of them have been raised from vision to mass product. Among the success stories you will find established applications of new actuators, in their use in fuel injection, adaptive shock absorbers, nanopositioning, precision engineering like camera lenses and other applications of miniaturized drives. New product generations

In this way, ACTUATOR has launched the realization of new product generations with outstanding compactness and high performance properties which so far have not been achieved in conventional technologies.

The Exhibition
The exhibition will present components, system approaches and applications of smart actuators and low-power electromagnetic drives based on conventional (electromagnetic) and innovative working principles (new actuators), and associated subjects. The range of topics also includes measurement techniques, control concepts and circuits, driver components and units, system integration, layout and simulation tools etc.

ACTUATOR 2026 Steering Committee
Manfred Kohl, Jürgen Maas, Salvador Pané i Vidal,
Emmanuel Vander Poorten,
Ulrike Wallrabe, Yoko Yamanishi

Program Committee

Steering Committee Members

Kohl, Manfred, Karlsruher Institut für Technologie, Germany
Maas, Jürgen, Technische Universität Berlin, Germany
Vander Poorten, Emmanuel, Katholieke Universiteit Leuven, Heverlee, Belgium
Wallrabe, Ulrike, University of Freiburg, Department of Microsystems Engineering – IMTEK, Germany
Yamanishi, Yoko, Kyushu University, Japan

Program Committee Members

Biedermann, Miriam, Bürkert Werke GmbH & Co. KG, Karlsruhe, Germany
Chikhaoui, M. Taha, Université Grenobles-Alpes, France
Choi, Seung-Bok, The State University of New York, Korea (SUNY Korea), Incheon, South Korea
Claeyssen, Frank, CEDRAT Technologies S.A., Meylan, France
Goldasz, Janusz, BWI Beijing West Industries Technical Center Kraków, Poland
Jager, Edwin, Linköping University, Sweden
Kanda, Takefumi, Okayama University, Japan
Kohl, Manfred, Karlsruher Institut für Technologie, Germany
Lötters, Joost, Bronkhorst High-Tech B.V., Ruurlo, Netherlands
Maas, Jürgen, Technische Universität Berlin, Germany
Manfredi, Luigi, University of Dundee, Great Britain
Marienfeld, Peter, ContiTech Deutschland GmbH, Hannover
Merlo, Sabina, University of Pavia, Italy
Milana, Edoardo, University of Freiburg, Department of Microsystems Engineering (IMTEK)
Monner, Hans Peter, German Aerospace Center (DLR), Braunschweig, Germany
Morishima, Keisuke, Osaka University, Yamadaoka, Japan
Morita, Takeshi, The University of Tokyo, Japan
Müller, Bert, University of Basel, Switzerland
Nienhaus, Matthias, Universität des Saarlandes, Saarbrücken, Germany
Pagounis, Emmanouel, ETO MAGNETIC GmbH, Stockach, Germany
Pané i Vidal, Salvador, Swiss Federal Institute of Technology (ETH) Zurich, Switzerland
Pott, Peter, University of Stuttgart, Germany
Price, Aaron, The University of Western Ontario, Canada
Renaud, Pierre, Institut National des Sciences Appliquées Strasbourg INSA, Strasbourg, France
Schubert, Franz, PI Ceramic GmbH, Lederhose, Germany
Seelecke, Stefan, Universität des Saarlandes, Saarbrücken, Germany
Spomer, Waldemar, Physik Instrumente (PI) GmbH & Co. KG, Karlsruhe, Germany
Takasaki, Masaya, Saitama University, Japan
Uchino, Kenji, The Pennsylvania State University, USA
Ugurlu, Barkan, Ozyegin University, Çekmeköy - Istanbul, Turkey
Vander Poorten, Emmanuel, Katholieke Universiteit Leuven, Heverlee, Belgium
Vergani, Giorgio, SAES Getters S.p.A., Lainate, Italy
Vorrath, Markus, Technische Universität Dresden, Germany
Wallrabe, Ulrike, University of Freiburg, Department of Microsystems Engineering – IMTEK, Germany
Wapler, Matthias, Otto-von-Guericke University Magdeburg, Germany
Yamanishi, Yoko, Kyushu University, Japan

Content

Mechanisms of hygromorphic actuation: from analysis to tuning of biomimetic actuators for adaptive facades 1
Eleonora Galli, Mohamed Abdelrasoul, Jürgen Rühe
(University of Freiburg, Germany)

An AlN piezoelectric thermomagnetic generator for waste heat recovery 4
Maxim Wischnewski, Erik Mackensen, Dirk Meyners, Manfred Kohl
Karlsuhe Institute of Technology (KIT), Germany
Christian-Albrechts-Universität (CAU), Kiel, Germany

Piezoelectric Fine Steering Mirrors and electronics for Optical Inter-Satellite Links 10
Xavier De Lépine, Jocelyn Rebufa, David Ferris, Aurore Loubet, Frank Claeyssen, Sylvain Chardon, Arnaud Gilson, Thomas Maillard, Pascal Mexe, Francis Bortolaso
CEDRAT TECHNOLOGIES S.A.S, France
MICROTEC S.A.S, France

A miniature-scale thermomagnetic actuator driven by low-grade heat 18
Athira Kattiparambil Sivaprasad, Joel Joseph, Amir-Abbas Haghighirad, Manfred Kohl, Jingyuan Xu
Institute of Microstructure Technology (IMT), Karlsruhe Institute of Technology (KIT), Germany
Institute for Quantum Materials and Technologies (IQMT), Karlsruhe Institute of Technology (KIT), Germany

Magnetic Fast Steering Mirrors for Tracking and Optical Communication for Defense and Aerospace Industries 22
Xavier De Lépine, Timotéo Payre, Clément Joseph Galteau, Nabil Bencheikh, Patrick Meneroud, Florian Bonnet, Hugo Grardel, Pierre Personnat, Clément Cote, Guillaume Mansuy, Arnaud Gilson, Frank Claeyssen
Cedrat Technologies, France

Shape Memory Alloy drives for micro-electronical actuator systems 28
Andreas Erben, Daniel Hoffmann, Kenny Pagel,Sven Spieth, Alexander Jähnigen, Welf-Guntram Drossel, Alfons Dehé
Fraunhofer Institute for Machine Tools and Forming Technology IWU, Dresden, Germany
Hahn-Schickard Gesellschaft, Villingen-Schwenningen, Germany

Tailoring the spatial thickness distribution of a membrane using 3D printing for enhanced operation as a dielectric elastomer actuator 30
Andreas Hubrachta, Bingzhi Wanga, Chen Jiaob, Ashwani Sharan Tripathib, Uwe Marschnerb, Andreas Richterb, E.-F., Markus Vorrath, Jürgen Maas
Mechatronic Systems Lab, Technische Universität Berlin,
Institute of Semiconductors and Microsystems, Technische Universität Dresden

Robust and Efficient Finite Element Modeling of an Electrostatic Microactuator Relying on the Pull-In Effect 36
Arwed Schütz, Dwarakesh Sudhahar, Martin Hoffmann,, Tamara Bechtold
Jade University of Applied Sciences, Wilhelmshaven, Germany
Microsystems Technology, Ruhr University Bochum, Germany

Electrostatic MEMS actuator for controlled Quasi-Static spherical Rotation 41
Dwarakesh Sudhahar, Arwed Schütz, Martin Hoffmann, Tamara Bechtold
Microsystems Technology, Ruhr University Bochum, Germany
Jade University of Applied Sciences, Wilhelmshaven, Germany

Highly Conductive Metallic Thin Films on Flexible Substrates 44
Benjamin R. Zemlin, Jonas Hubertus, Dirk Göttel, Alberto Priuli, Saveria Addario, Gianluca Rizzelo, Stefan Seelecke, Günter Schultes, John Heppe
University of Applied Sciences of Saarland, Saarbruecken, Germany
Saarland University, Saarbruecken, Germany

Towards scaling Cooperative Dielectric Elastomer Actuator Systems 47
Alberto Priuli, Saverio Addario, Benjamin Zemlin, John Heppe, Gianluca Rizzello
Saarland University, Department of Systems Engineering, Saarbrücken, Germany
University of Applied Sciences, Department of Sensors and Thin Films, Saarbrücken, Germany.

Response Surface Modeling and Multi-Response Optimization of PVDF/BaTiO3/CNT Films for Flexible Actuator Applications 51
Ahmed Attaoui, Ayda Bouhamed,Chokri Bouraoui, Olfa Kanoun
Professorship of Measurement and Sensor Technology (MST), Chemnitz University of Technology, Chemnitz, Germany Laboratory of Mechanics of Sousse (LMS), National Engineering School of Sousse (ENISo), University of Sousse, Technopole de Sousse, Sousse, Tunisia Faculty of Sciences of Gafsa (FSGF), University of Gafsa, Gafsa, Tunisia Laboratory of Electromechanical Systems (LASEM), National Engineering School of Sfax, University of Sfax, Sfax, Tunisia

Energy efficient electro-mechanical wing ice protection system for future aircrafts 63
Denis Becker, Thorsten Koch, Christopher Davies, Valerian Palanque, Matthias Schmidt, Valentin Mees, Michael Matthias
Fraunhofer LBF, Darmstadt, Germany
Parker Meggitt, Shepshed, Loughborough, United Kingdom
Airbus, Toulouse, France

Giving voice to flat plastic panels with piezoceramic actuators: vibrational analyses with feedback interferometry 65
Elisabetta Bodo, Carlo Anelli, Valentina Bello, Sabina Merlo
Eindhoven University of Technology, The Netherlands
University of Pavia, Italy

High-resolution rotating piezo motors for LISA large interferometer space antenna 67
Nicolas Bourgeot, Jocelyn Rebufa, Alexis Gierczak, Clément Cote, Olivia Stadler, François Barillot, Frank Claeyssen
(CEDRAT TECHNOLOGIES S.A.S, France)

Improving the reliability of piezoelectric actuators and motors subjected to significant self-heating and several billion actuation cycles or severe environments 73
Nicolas Bourgeot, Frank Claeyssen, Boris Laluc, Rasmus Lou-Møller, François Barrot, Iman Mehdipour, Yves Ruffieux, Guillaume Mansuy
CEDRAT TECHNOLOGIES S.A.S, France
CTS Corporation, Denmark
CSEM, Switzerland

Adaptive surface actuation via magnetoactive elastomer membranes 79
Ina Bregu, Jürgen Maas
(TU Berlin, Germany)

Electrostatically Actuated Liquid Lenses for an Anamorphotic Zoom 85
Debatri Das, Martin Hoffmann
(Microsystems Technology, Ruhr University Bochum, Germany)

Lead free 4-layered piezoelectric motor 90
Bülent Delibas, Burhanettin Koc
Physik Instrumente GmbH & Co. KG, Germany

Electromagnetic characterization of Magnetorheological Dampers Gabriel Dias Mendes 94
Cracow, *University of Technology, Poland*

Piezo actuated jet for stealth aircraft applications 98
David Ferris, Guillaume Mansuy, Boris Laluc, Jan Rohac
CEDRAT TECHNOLOGIES S.A.S, France
ESC Defence, Czech Republic

Soft robotic artificial muscles for end-stage heart failure management 103
Javad Foroughi, Arjang Ruhparwar
School of Mechanical and Manufacturing Engineering, University of New South Wales, Sydney, Australia; Department of Cardiothoracic Transplantation and Vascular Surgery Hannover Medical School, Germany

Antagonistic bistable actuator based on shape memory alloy beams 105
Yasmina Frey, Zeliha Arabul, Ulrike Wallrabe
(University of Freiburg, Germany)

Soft and monolithic variable Stiffness Clutches to enhance Serial Elastic Actuators 108
Johannes Frey, Mohsen Jafarpour, Hugo Oliveira, Edoardo Milana
Department of Microsystems Engineering - IMTEK, Cluster of Excellence livMatS, University of Freiburg, Germany

Metamaterial for a localized simulated button-click 112
Mondher Ouari, Frédéric Giraud, Charles Croënne, Jean-Luc Bruyelle, Christophe.giraud-Audine
UMR - IEMN, Univ. Polytec hnique Hauts-de-France, CNRS, Univ. Lille, Valenciennes, France
Univ. Lille, Arts et Metiers Institute of Technology, Centrale Lille, Junia, France

Assembly-oriented redesign of a shape memory alloy driven bistable gripper 114
Tom Gorges, Fabian Adler, Sarah Zimmer, Sophie Nalbach, Paul Motzki
Depart. Smart Material Systems, ZeMA – Center for Mechatronics and Automation Technology, Saarbruecken, Germany
Depart. Systems Engineering, Saarland University, Saarbruecken, Germany
Depart. Assembly Systems, ZeMA – Center for Mechatronics and Automation Technology, Saarbruecken, Germany

Multilayered electrohydraulic soft actuators for safe-to-touch wearables and underwater systems 119
Chinmay Gupta, Krishnaprasad Rajagopalan, Gaurav Khandelwal, Ajay Giri Prakash Kottapalli
Department of Bioinspired MEMS and Biomedical Devices (BMBD), Engineering and Technology Institute (ENTEG), University of Groningen, Netherlands
Department of Engineering Science, University of Oxford, United Kingdom Motivation

Three-phase SMA model with optimized fit for both strain and resistance 124
Max Hauber, Arif Kazi
Hochschule Aalen, Germany

Pneumatic cylinder speed control system using particle-excitation flow control valve 128
Daisueke Hirooka, Naomichi Furushiro, Tomomi Yamaguti
Kansai University, Japan

A steerable concentric push–pull suction device for single-port surgery 130
Finn Hoffmann, Bob Lathrop, Mouloud Ourak, Wouter Everaerts,
Emmanuel Vander Poorten, Paul Breedveld
Department of Mechanical Engineering, KU Leuven, Belgium
Department of Mechanical Engineering, TU Delft, The Netherlands
Department of Urology, University Hospitals Gasthuisberg, Katholieke Universiteit Leuven, Belgium

Lumped modelling of loss mechanisms in piezoelectric transducers 135
Jan Holterman, Bas Jansen, Henry Schmidt
VIRO, The Netherlands
ASML, The Netherlands

Piezoelectric ultrasonic mirror tip tilt stage 139
Jan Homberg, Alexej Wischnewski, Bülent Delibas
Physik Instrumente GmbH & Co. KG, Germany

Change in stress-strain-characteristics of MSM-alloys
in weak magnetic fields for a daptive interfaces..... 142
Marco Hutter, Lukas Fuchs, Peter Schmid, Thomas Maier, Bernd Gundelsweiler
Institute of Design and Production in Precision Engineering, University of Stuttgart, Germany
Institute for Technical Design and Industrial Design, University of Stuttgart, Germany

Experimental setup for piezo relations validation..... 147
Bas Jansen, Ivan Staykov, Paul Vrancken, Hans Butler, Siep Weiland
ASML, The Netherlands
TU/e, Eindhoven, The Netherlands

Development of a highly dynamic and precise actuator
with magnetic weight compensation for 3D-wafer scanning..... 151
Maik Kadias, Heiko Knoll, Matthias Böhle, Dr. Rolf Slatter
ITK Precisioning GmbH, Germany
ELSOMA GmbH, Germany

Experiencing Coupled Resonance Dynamics when Designing with Vibrotactile Actuators..... 155
Prof. Dr. Thorsten A. Kerna, Dr. Mohammad Sadeghia, Dr. Ornella Tortoricia, Maximilian Beckera, Juliana Lüera, Ali Elnwegya,
Institute for Mechatronics in Mechanics, Hamburg University of Technology, Hamburg, Germany
ligeti center, Hamburg, Germany

Creep modeling and stability of PNZT shape memory piezoelectric actuators..... 161
Jurrien Keulen, Mireny Ugalde Reygadas, Bayu Jayawardhana, Monica Acuautla Meneses
University of Groningen, The Netherlands

Reliability and drift behaviour of CNT-modified grippers for soft robotics applications..... 165
Ivica Kolaric, Rolf Nothelfer-Richter, Takushi Sugino, Hirosato Monobe
Fraunhofer IPA, Germany
National Institute of Advanced Industrial Science and Technology (AIST), Japan

Theoretical and experimental investigations regarding small electric drive systems overload potentials in short-term operation **171**
Ulrike Kurz, Andreas Wagener, Bernd Gundelsweiler
Institute of Design and Production in Precision Engineering, University of Stuttgart, Germany
Dr. Fritz Faulhaber GmbH & Co. KG, Germany

Multi-DOF steerable endoscope for robot-surgeon collaborative control **177**
Robert Lathrop, Mouloud Ourak, Emmanuel Poorten
KU Leuven, Belgium

Finite Element Analysis of Asymmetric Inflatable Snapping Actuators **182**
Xin Li, Edoardo Milana
Department of Microsystems Engineering - IMTEK, University of Freiburg, Freiburg, Germany

Dual-Chevron Optothermal Rotary Microactuator for High Force and Large Displacement Actuation **186**
Yanze Li1, Alex J Thompson, Alfredo Fantetti, Belal Ahmad
Department of Surgery and Cancer, Imperial College London, United Kingdom
Department of Mechanical Engineering, Imperial College London, United Kingdom

Dual-Joint Cable-Driven Soft actuator for Miniaturized Flexible Endoscopy **190**
Zijian Liu, Luigi Manfredi
University of Dundee, United Kingdom

Enhancing the reliability of piezoelectric actuators and motors under severe self-Heating, high-cycle operation, and harsh environmental conditions **194**
Rasmus Lou-Møller, Iman Mehdipour, Charles Mangeot, Nicolas Bourgeot, Frank Claeyssen, Boris Laluc
CTS Denmark, Denmark, Cedrat Technologies, France

3D nano-printed optical MEMS with closed-loop control **199**
Florian Lux, Elijah Ditchendorf, Çağlar Ataman
(University of Freiburg, Germany)

Magnetoelectric cantilever beam with reduced bending mitigates power nulls in Wireless Power Transfer systems **203**
Hidelberto Macedo Zamudio, Pascal M. Weber, Tobias Gräf, Ulrike Wallrabe
University of Freiburg, IMTEK – Department of Microsystems Engineering, Laboratory for Microactuators, Germany

Compact piezo-driven inchworm rotary mechanism with high rotational accuracy for LISA Space mission **207**
Narendra Mahavar, Shashwat Kushwaha, Dominiek Reynaerts
KU Leuven, Belgium, Member Flanders Make, Belgium

Piezoelectric transducer for high intensity reversible acoustic rotational field generation 213
Piotr Vasiljev, Dalius Mažeika, Andrius Čeponis, Regimantas Bareikis, Sergejus Borodinas, Vilnius Gediminas
Technical University, Lithuania
Vytautas Magnus University, Lithuania

Compact piezoelectrically driven inchworm motor with large forces and strokes using advanced control 217
Ulrich Mescheder, Sonja Müller, Jahangir Khosravi, Bahman Azarhoushang
Hochschule Furtwangen, Germany, Universität Freiburg, Germany

Design methodology for electromechanical functional interfaces 223
Tom Migliaccio, François Pigache, Thomas Huguet
Laplace, France

Dual-mode electrosurgical device for selective tissue perforation via electrically-induced bubbles and discharge 227
Shigeaki Miura, Yuudai Aokusa, Mayu Nakahigashi, Nobutoshi Ota, Yoko Yamanishi
Kyushu University, Japan

Optimizing laser-induced graphene microstructure to enhance ion diffusion and actuation performance in PI-LIG-Ppy ionic actuators 230
David Morales, Alejandro Vega, Sergio Gabriel Flores
(CIMAV, Mexico)

Non-contact micro-mechanical stimulation of Arabidopsis root cap using ultrasonic standing waves for mechanotransduction analysis 233
Keisuke Morishima, Koki Ogawa
The University of Osaka, Japan

Thermal Impact on the Dynamic Model of a Magnetorheological Elastomer: Analysis and Experiments 238
Paweł Orkisz, Janusz Goldasz, Bogdan Sapiński
AGH University of Science and Technology, Poland
Cracow University of Technology, Poland

Plasmid delivery to suspension cells through electromechanical poration induced by a microbubble generator 242
Nobutoshi Ota, Kei Tateishi, Shigeo Sugano, Niko Kimura, Shinya Sakuma, Yoko Yamanishi
Kyushu University, Japan
National Institute of Advanced Industrial Science and Technology, Japan
Tokyo University of Agriculture and Technology, Japan

Bistable Piezoelectric Energy harvester with embedded power management electronics for railway monitoring 245
Timoteo Payre, Boris Laluc, Nicolas Decroix, Quentin Demouron, Celestin Metral, Romane Anseaume, Guillaume Mansuy
CEDRAT TECHNOLOGIES S.A.S, France
USMB, France, VOSSLOH, France

Closed-loop cooperative control of dielectric elastomer actuator arrays 248
Alberto Priuli, Saverio Addario, Benjamin Zemlin, John Heppe, Gianluca Rizzello
Saarland University, Department of Systems Engineering, Saarbrücken, Germany
University of Applied Sciences, Department of Sensors and Thin Films, Saarbrücken, Germany.

Engineering liquid crystal elastomer fibers for the next generation of soft robotics: A comparative analysis of fabrication techniques.....253
Manuel Reis Carneiro, Rafael Molter, Aníbal T. de Almeida, Mahmoud Tavakoli
Soft Machines Lab, Department of Mechanical Engineering, Carnegie Mellon University, Pittsburgh, USA
Institute of Systems and Robotics, Department of Electrical and Computer Engineering, University of Coimbra, Portugal;
Biomedical and Mobile Health Technology Lab, Department of Health Sciences and Technology, ETH Zürich, Switzerland

urface-dominated drying and crystalli ation effects in micropumps.....259
Martin Richter , Mohammadhossein Sheikhsarraf
Fraunhofer EMFT, Germany

Conceptual desi gn of a Tunable Magnet-based Reluctance Actuator 263
Endre Peder Ronaes, Andres Hunt, Ron van Ostayen, Hassan Hossein Nia
(Delft Univeristy of Technology, The Netherlands)

Design and characterization of a tactile multi-element dielectric elastomer actuator 266
Lukas Moritz Roth, Sebastian Gratz-Kelly, Daniel Bruch, Sophie Nalbach, Paul Motzki,
Saarland University, Germany
Center for Mechatronics and Automation Technology – ZeMA gGmbH, Germany

Design and control of motion stage driven by nonlinear reluctance actuator 272
Mohammad Saaideh, Natheer Alatawneh, Mohammad Al Janaideh
University of Guelph
Fraunhofer Institute for Applied Optics and Precision Engineering, Germany and University of Toronto

Displacement control for Piezo-based Deformable Mirrors with Unmodelled Hysteresis and Actuator Coupling.....278
Mohammad Saaideh, Matthias Goy, Mohammad Al Janaideh
University of Guelph
Fraunhofer Institute for Applied Optics and Precision Engineering, Germany
Fraunhofer Institute for Applied Optics and Precision Engineering, Germany & University of Toronto

Integration of sensors and trajectory control for the autonomous navigation of 3D-printed miniature robots driven by piezoelectric actuators 284
Byron Ricardo Zapata Chancusig, Jaime Rolando Heredia Velastegui,
Víctor Ruiz-Díez and José Luis Sánchez-Rojas.
Mechatronic Department, Universidad Politécnica Salesiana, Ecuador.
Microsystems, Actuators and Sensors Group, INAMOL-Universidad de Castilla-La Mancha, Spain

Investigation of the influence of dynamic magnetic excitation during drag finishing using abrasive magnetorheological fluids 289
Fabian Sordon, Jürgen Maas
(Mechatronic Systems Lab, Technische Universität Berlin, Germany)

Amplified Piezo Actuators with embedded Eddy Current Sensor for cryo space De-SPIN mechanism 295
Olivia Stadler, Jocelyn Rebufa, Alexis Gierczak, Clément Cote, David Ferris, François Barillot, Frank Claeyssen, Boris Laluc, Guillaume Mansuy
CEDRAT TECHNOLOGIES S.A.S, France

Engineered shape memory behavior in Nb-doped lead zirconate titanate piezoelectric actuators 299
M. Ugalde-Reygadas, M. Acuautla
Engineering and Technology Institute Groningen, University of Groningen, The Netherlands

SUPERPOSITION-BASED FORCE MODELING OF A MULTI-STABLE MAGNETIC LIFT ACTUATOR 303
Pascal M. Weber, Michael Olbrich, Yannik T. Rüde1, Christoph Ament, Ulrike Wallrabe
Laboratory for Microactuators, IMTEK – Department of Microsystems Engineering, University Freiburg, Germany
Chair of Control Engineering, Faculty of Applied Computer Science, University of Augsburg, Germany

Impact of Actuator Pretension and Heat Treatment on the Performance of Piezoelectric Micromembrane Pumps 305
Nora Weigel, Martin Wackerle, Daniel Anheuer, Gabriele Schrag, Martin Richter
Fraunhofer Research Institution for Microsystems and Solid-State Technologies EMFT, Munich, Germany, Technical University of Munich, Germany

Prototype of a camera focusing mechanism driven by a polyimide bimorph thin-film actuator 311
Daisuke Yamaguchi, Saki Takamura, Shuichi Wakimoto, Takefumi Kanda
(Okayama University, Japan)

Interlocking-based multistable actuators as fluidic memristors 313
Ayberk Yüksek, Mohsen Jafarpour, Edoardo Milana,2
Freiburg Center for Interactive Materials and Bioinspired Technologies, Germany
Department of Microsystems Engineering (IMTEK), University of Freiburg, Germany

Investigation of a pressure-driven dielectric elastomer multi-actuatorsystem 317
Bingzhi Wanga, Andreas Hubrachta, Abdelkarim Masouda, Chen Jiaob, Ashwani Sharan Tripathib, Uwe Marschnerb, Andreas Richterb, E. F. Markus Vorrathb, and Jürgen Maasa
Mechatronic Systems Lab, Technische Universität Berlin, Germany
Institute of Semiconductors and Microsystems, Technische Universität Dresden, Germany

Investigation of bistable mechanisms for energy-free holding using shape memory alloys for 3D-printed valves 323
Andreas Erben, Kenny Pagel, Christoph Nitschke, Niklas Brömme, Welf-Guntram Drossel
Fraunhofer Institute for Machine Tools and Forming Technology IWU, Dresden, Germany

 DOI: 10.30420/456743001

Mechanisms of Hygromorphic Actuation: From Analysis to Tuning of Biomimetic Actuators for Adaptive Facades

Galli Eleonora, Mohamed Abdelrasoul, Jürgen Rühe

Department of Microsystems Engineering (IMTEK) University of Freiburg, Georges-Köhler-Allee 103, 79110 Freiburg, Germany;
Cluster of Excellence livMatS @ FIT – Freiburg Center for Interactive Materials and Bioinspired Technologies, Georges-Köhler-Allee 105, 79110 Freiburg, Germany

E-mail address: eleonora.galli@imtek.uni-freiburg.de

Abstract

This study presents a semi-empirical model to predict and control the curvature of hygromorphic bilayer actuators for climate-responsive building facades. Based on an adaptation of Timoshenko's bimetallic strip theory, the model incorporates hygroscopic swelling and elastic properties to describe actuation driven by temperature while independently tuning the response via absolute humidity. Using minimal material characterization data, the approach enables efficient design and optimization of adaptive systems, addressing key limitations of passive biomimetic architectures by introducing user-controlled actuation thresholds.

1 Introduction

With increasing demands for sustainable solutions in architecture, the integration of smart, self-regulating systems into building design has become a crucial advancement in enhancing energy efficiency. Within the context of climate-responsive architecture, biomimetic systems offer a particularly elegant and efficient solution, drawing from nature's inherent ability to passively adapt to environmental changes[1,2] . Despite the many advantages offered by such passive systems, there are challenges that hinder their actual implementation and commercial distribution. Not only the user does not have any control over the passive actuation, but also the proper functioning of the system under extreme climate conditions is significantly hindered. These are the challenges this study addresses. In particular, this work focuses on the study of hygromorphic bilayer polymer actuators systems for adaptive facades that autonomously respond to the thermal stimulus (T), while immersed in an enclosed environment with controlled absolute humidity (AH) (i.e. total number of water molecules present in the system). By allowing the user to manually control the absolute humidity in the actuator's environment the critical temperature of actuation is arbitrarily tuned. This control is achieved by developing a semi-empirical model to describe the physical principles underlying the actuation of hygromorphic bilayers and the influence of uncoupled environmental parameters (T and AH). We offer a description of the radius of curvature of bilayers made of an active hygroscopic polymer network and an almost fully inert thermoplastic material functioning as passive layer (**Figure 1**). The model is based on Timoshenko's bimetallic strip theory[3–6], which is appropriately adapted to describe the curvature $k = 1/R$ of hygromorphic bilayers by writing the mismatch strain ϵ_m due to the difference in expansion coefficient between the two materials, in terms of

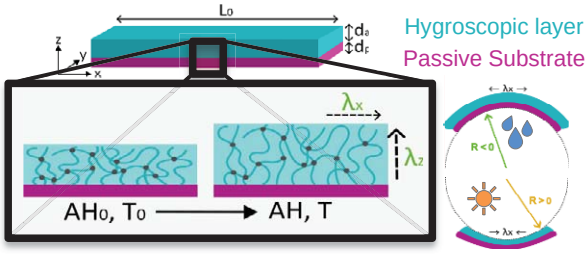


Figure 1 Scheme of hygromorphic bilayer actuators. The active polymer network swells anisotropically upon water uptake. However, the actuation is driven by the swelling/shrinking in the in-plane direction (x-direction). Due to the different swelling behavior of the two layers, a curvature takes place depending on the environmental conditions. In particular, the curvature is positive when moisture leaves the active layer, while it is negative upon moisture absorption.

hygroscopic coefficient difference $\Delta\beta$ and change in water uptake ΔM:

$$k = \frac{1}{R} = \epsilon_m \frac{f}{d_a + d_p} = (\Delta\beta\Delta M)\frac{f}{d_a + d_p}$$

where the factor f is a function of Young's moduli and thicknesses of the two layers:

$$f(m,n) = \frac{6(1+m)^2}{3(1+m)^2 + (1+mn)(m^2 + 1/(mn))}$$

$$n = E_p(T)/E_a(AH,T)$$

$$m = d_p/d_a(AH,\ T)$$

The model developed in this study is able to predict the curvature of rectangular hygroscopic bilayers given a small set of experimental measurements of hygroscopic and elastic properties of the materials involved.

 DOI: 10.30420/456743001

2 Results and discussion

2.1 Modeling the hygroscopic properties

A-priori calculations of hygroscopicity can be challenging, as they usually require the knowledge of hard to determine parameters, e.g. Flory-Huggins parameter χ(T) [7], or rely on computational effort intense simulation methods. In this study we opt for a semi-empirical approach based on the Guggenheim-Anderson-de Boer (GAB) model [8], a widely used equation to describe how material absorb or desorb moisture based on water activity $\alpha_w = \mathrm{RH}/100$. The GAB model defines the water uptake M as follows:

$$M = \frac{h_m c f \alpha_w}{(1 - f\alpha_w)(1 + cf\alpha_w - f\alpha_w)}$$

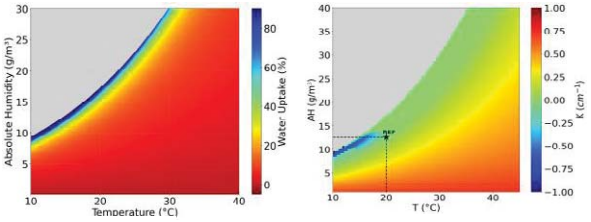
where the three parameters are the monolayer moisture content h_m, the Guggenheim constant c, which is related to the interaction energy of the monolayer with additional layers, and the multilayer adsorption constant f, which takes into account the interaction energy of additional layers beyond the first. The water uptake M of a given hygroscopic polymer network at given environmental conditions (relative humidity RH and temperature T) is measured via gravimetric analysis. The water uptake is measured for the same sample at equilibrium with a fixed temperature T across various humidity levels (at least four values of RH). The resulting isotherm can be fitted using the GAB model to determine the three parameters, which characterize the hygroscopic behavior of the material at the examined temperature. The three parameters' dependency on temperature is an exponential in the following form:

$$h_m = A_h exp(\Delta H/RT);$$
$$c = A_c exp(\Delta H_1/RT);$$
$$f = A_f exp(\Delta H_2/RT);$$

where R is the ideal gas constant and ΔH, ΔH_1, and ΔH_2 are the enthalpy change due to the interaction of the various moisture content layers. Thus, in order to determine the water uptake of the given material at any humidity and temperature condition, the measurement and fit are repeated for multiple temperatures (at least four values of T): the resulting data points of each GAB parameter are fitted with an exponential function in the shape above, so that for the constants A_h, A_c, A_f, as well as the enthalpy changes ΔH, ΔH_1, ΔH_2 are determined. These constants and enthalpy changes are characteristic of the material and its interaction with the water in its environment. Hence, the GAB model can be used to predict the water uptake of the given material at any operational condition. To decouple the effect of moisture content and temperature of the closed environment the hygromorphic actuators are designed to work in, instead of using temperature and water activity (or relative humidity) as environmental variables, the latter is expressed in terms of absolute humidity AH. Hence, for a given material we can draw a two-dimensional map of the water uptake $\mathrm{M(AH, T)}$ as shown in **Figure 2a**

2.2 Calculating the anisotropic swelling

The anisotropic swelling behavior of surface attached polymer network is a crucial aspect in the understanding of hygromorphic actuators. In general, the swelling ratio in the out-of-plane direction is larger than the swelling ratio in the in-plane directions $\lambda_z \geq \lambda_x = \lambda_y$. Determining the direction specific swelling ratios is essential to predict the curvature of the actuator as they indirectly appear in the Timoshenko's bilayer equation with various functional dependencies: $\Delta\beta = \Delta\beta(\lambda_x)$ and $d_a = d_a(\lambda_z)$. We determine the swelling ratios by solving a constrained optimization problem with the elastic strain potential energy stored in the bent bilayer as objective function. The applied constrains include the volume conservation $\lambda_x\lambda_y\lambda_z = \mathrm{V(M(AH,T))/V_0}$, and the anisotropy condition described above. By determining the swelling ratio for the surface attached rectangular hygroscopic network, characterized by the water uptake discussed in the previous paragraph, and measuring the Young's moduli of the two materials, the curvature can be calculated. Hence, for a given rectangular hygromorphic bilayer we can produce a two-dimensional map of the curvature as function of the environmental variables AH and T, like the one shown in **Figure 2b**.



(a) (b)

Figure 2 a) Map of water uptake as function of absolute humidity AH and temperature T of an hygroscopic polymer network made of PDMAA-20%MAz: N,N-dimethylacrylamide (DMMA) copolymerized with 20%wt. of 1-(4-(methacryloyloxy)butyl)-3-methyl-2-diazomalonat (MAz). The map is based on the gravimetric analysis data upon drying (i.e. the weight of the sample is measured at fixed temperature and decreasing humidity). The gray corner in the map, corresponds to the non-physical combinations of AH and T, i.e. combinations corresponding to RH > 99%. **b)** Map of curvature as function of AH and T of a 7cm x1cm hygromorphic bilayer made of a 100µm thick commercial PET sheet as passive layer, and a 500µm thick PDMAA-20%MAz active layer. The black star highlights the preparation condition, that is the condition at which the active layers polymer chains are relaxed.

3 Conclusion

This study developed a method to predict the curvature of hygromorphic bilayers starting from a small set of material characterization data (gravimetric analysis of the active material and Young's modulus of active and passive material as function of the environmental variables). The model allows not only for rapid exploration and optimization of system's material and geometry, but it also for the decoupling of the two environmental variables. Thus, the temperature can autonomously drive the actuation, while the absolute humidity can be modified to tune the actuation according to the specific needs of the user or to the location where the system is applied.

ISBN: 978-3-8007-6743-4 @ VDE VERLAG GMBH · Berlin · Offenbach

 DOI: 10.30420/456743001

4 Literature

[1] C. Dingler, H. Müller, M. Wieland, D. Fauser, H. Steeb, S. Ludwigs, *Adv. Mater.* **2021**, *33*, 2007982.

[2] R. El-Dabaa, S. Abdelmohsen, *Wood Sci. Technol.* **2023**, *57*, 557.

[3] S. Timoshenko, *JOSA* **1925**, *11*, 233.

[4] J. Zang, F. Liu, *Appl. Phys. Lett.* **2008**, *92*, 021905.

[5] S. Khoshtinat, V. Carvelli, C. Marano, *Cellulose* **2023**, *30*, 7779.

[6] A. Le Duigou, V. Keryvin, J. Beaugrand, M. Pernes, F. Scarpa, M. Castro, *Compos. Part Appl. Sci. Manuf.* **2019**, *116*, 36.

[7] P. Nardinocchi, M. Pezzulla, L. Teresi, *Soft Matter* **2015**, *11*, 1492.

[8] L. Tavares, L. R. Sousa, S. Magalhães da Silva, P. S. Lima, J. M. Oliveira, *Polymers* **2023**, *15*, 1634.

ISBN: 978-3-8007-6743-4 @ VDE VERLAG GMBH · Berlin · Offenbach

 DOI: 10.30420/456743002

An AlN Piezoelectric Thermomagnetic Generator for Waste Heat Recovery

Maxim Wischnewski[1], Erik Mackensen[2], Dirk Meyners[2] and Manfred Kohl[1]*
[1]Karlsruhe Institute of Technology (KIT), Institute of Microstructure Technology, Karlsruhe, Germany
[2]Kiel University, Department of Materials Science, Inorganic Functional Materials, Germany

Abstract

We present a miniature cantilever-type piezoelectric thermomagnetic (P-TM) generator for conversion of low-grade waste heat (<200 °C) into electrical power. The P-TM generator exploits the sharp magnetization transition of a Ni-Mn-Ga film at its Curie temperature to drive resonant self-actuation of the cantilever. The resulting mechanical oscillations are converted into electricity by a sputter-deposited AlN piezoelectric layer, yielding a rectified DC output of 2.6 V at a power density of 6.6 µW cm^{-2}. This work demonstrates a pathway toward autonomous powering of low-power sensors and IoT nodes from abundant low-temperature heat sources in industrial and civil environments.

1 Introduction

Low-grade heat below 200°C is a widely available source of energy that is created in industrial processes, in residential areas and in natural sources such as geothermal energy and solar radiation [1–4]. Energy harvesting systems capable of harnessing low-grade thermal energy reservoirs to generate electrical energy could potentially power wireless sensor nodes or other low-power applications to operate autonomously without supervision or maintenance [5,6]. The conventional approach for thermal-to-electrical conversion relies on thermoelectric generators (TEGs), exploiting the Seebeck effect in conductors or semiconductors. TEGs require large temperature gradients for efficient operation, typically demanding active cooling or bulky heat sinks [1,7], both of which are incompatible with the compact design goals of modern wireless sensor systems [6,7]. At low temperature differences between hot and cold side, thermoelectric materials suffer from a reduced figure of merit [8] and often generate only millivolt-level voltages, necessitating complex cascaded arrangements to achieve usable voltage levels [9–11].

An alternative are thermomagnetic (TM) generators that leverage the large, reversible change of magnetization in TM materials at their Curie temperature (T_C). This approach has gained increasing attention recently due to the availability of materials exhibiting a large magnetization change in a small temperature interval. Their conversion efficiency at small temperature differences can surpass the efficiency of thermoelectric materials at substantially lower material costs [12]. In previous work, a new class of miniature-scale TM generators was introduced, making use of large surface-to-volume ratios to enable the efficient conversion of low-temperature waste heat through the resonant self-actuation of a freely movable cantilever [13]. Being heat driven and self-oscillating devices, TM generators convert thermal into mechanical energy without the need for additional power supply. Forced convection is used as an additional effective cooling mechanism to foster heat transfer and, thus, conversion efficiency. In a subsequent step, the mechanical energy is converted to electrical energy, either by induction via an integrated pick-up coil or by converting the bending stress into electricity via an integrated piezoelectric layer.

Induction-based TM generators using Ni-Mn-Ga films oscillate at frequencies above 100 Hz and reach power densities of 50 µW/cm² [14]. However, they suffer from output voltages below 0.1 V. To enable power generation at usable voltage levels, the piezoelectric (P) TM generator was demonstrated [15], which generates DC outputs of up to 2 V at 105°C. Nevertheless, the achievable power density is constrained by its large device footprint and significant structural damping inherent to ceramic PZT materials.

This paper presents the design, fabrication and characterization of a P-TM generator using a sputter deposited, 3 µm thick and c-axis oriented Aluminium nitride (AlN) film for piezoelectric energy conversion, which is investigated under resonant self-actuation conditions.

2 Materials Properties

2.1 Thermomagnetic Material

TM actuation relies on a temperature-dependent reversible change of magnetization in soft-magnetic materials to modulate the magnetic attraction force F_{mag} of a nearby magnet. A prominent material is the Heusler alloy Ni-Mn-Ga, exhibiting a second-order ferromagnetic transition at T_C resulting in a sharp and hysteresis free drop in magnetization. Ni-Mn-Ga films of 10 µm thickness are deposited at room temperature on a polyvinyl substrate by RF magnetron sputtering at a power of 200 W using a $Ni_{52}Mn_{24}Ga_{24}$ target. As-deposited films are amorphous and, thus, require heat treatment, which is performed at 800 °C for 3600 ks (1 h). XRD of films with chemical composition $Ni_{53.5}Mn_{23.8}Ga_{22.7}$ determined by the inductive plasma method analysis suggests a 14M martensite crystal structure [16]. Fig. 1(a) shows the temperature-dependent magnetization of a Ni-Mn-Ga film of 10 µm thickness at an external magnetic field of 50 mT. The magnetization transitions sharply at T_C close to 84°C. Differential scanning calorimetry (DSC), Fig. 1(b), reveals a first-order martensitic transformation with austenite start and finish temperatures A_s and A_f on heating of 62°C and 81°C, and martensite start and finish temperatures on cooling M_s and M_f of 71°C and 54°C, respectively. The offset of roughly 10°C between the two peaks reflects the thermal hysteresis inherent to the first-order transformation. By cycling the

 DOI: 10.30420/456743002

temperature near T_C above M_s, the magnetization changes free of hysteresis.

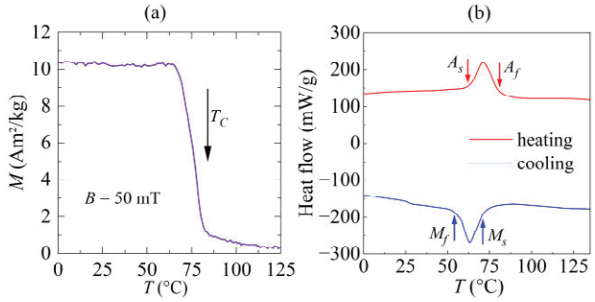


Figure 1: (a) Temperature-dependent magnetization of a $Ni_{53.5}Mn_{23.8}Ga_{22.7}$ film of 10 µm thickness at an external magnetic field of 50 mT showing a sharp second-order transition at T_C. (b) DSC measurement of the $Ni_{53.5}Mn_{23.8}Ga_{22.7}$ film revealing the first-order martensitic transformation, as indicated by the latent heat peaks on heating and cooling.

2.2 Piezoelectric Material

Piezoelectric aluminum nitride (AlN) is used for the conversion of mechanical to electrical energy. A c-axis textured AlN layer is deposited on a seed layer and bottom electrode consisting of a DC-sputtered Ta (10 nm) / Pt (100 nm) stack. The substrate is a 4-inch silicon (Si) wafer with a 3 µm thick titanium (Ti) layer deposited via sputtering onto a carbon release layer, enabling subsequent release and fabrication of the energy harvester (see Section 4). The deposition process is adapted from a method developed for bare Si wafers [17]. AlN is grown using reactive pulsed DC sputtering at 3000 W, a pure nitrogen plasma, and a pressure of 1.1 × 10^{-3} mbar, employing a 10-inch aluminum target with 5 N purity. The resulting AlN layer features a thickness of 3000 ± 10 nm and an average stress of 156 MPa over the 4-inch Wafer. The stress is measured optically along 8 lines over the full substrate. The top electrode is formed by a DC-sputtered Cr (10 nm) / Au (100 nm) bilayer. Both the AlN layer and the top electrode are patterned via wet-chemical etching to form a capacitor structure for electrical energy harvesting, with a size of 2 mm in width and 10 mm in length.

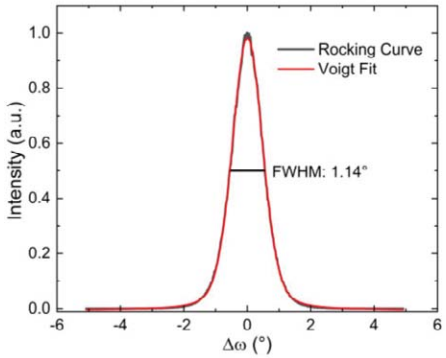


Figure 2: A rocking curve measurement of the featured material stack deposited on a bare Si wafer at a 2θ angle of 36.0°. The ω measurement shows a FWHM angle of 1.14°, which indicates a highly textured growth.

The piezoelectric properties and crystalline quality are characterized on a reference stack deposited on a Si wafer. The piezoelectric coefficient $d_{33,f}$ is measured using a double-beam laser interferometer, yielding a value of 6.0 pm/V. X-ray rocking curve analysis shown in Fig. 2 confirms high c-axis orientation, with a full width at half maximum (FWHM) of 1.14° at a 2θ angle of 36.0°. The relative permittivity (ε_r) of the AlN film is determined to be 10.5 ± 0.1, consistent with high-quality highly textured AlN.

3 Device Layout

3.1 Thermomagnetic actuation

Fig. 3 presents a schematic diagram of the P-TM generator, which includes two active material layers designed for energy conversion, namely the soft-magnetic Heusler alloy Ni-Mn-Ga (TM film) and a piezoelectric AlN layer. Above the TM film, a heated magnet is placed, acting simultaneously as a source of magnetic field and low-grade thermal energy. Initially, when the TM film is below T_C, it becomes magnetized by the field of the permanent magnet and is consequently attracted to it. Upon contact with the magnet, the TM film heats up, leading to a sharp reduction in magnetization and attraction force F_{mag} near T_C. Once the elastic force of the cantilever dominates, the TM film loses contact to the magnet and the cantilever resets to its neutral position. The TM film dissipates the stored thermal energy mainly via conduction to the cantilever [14,18], making the cantilever the TM film's primary heat sink. When the TM film's temperature decreases enough to re-magnetize, the cycle repeats, giving rise to self-actuated oscillatory motion. The generated mechanical energy is then converted to electrical energy via the P-layer [13].

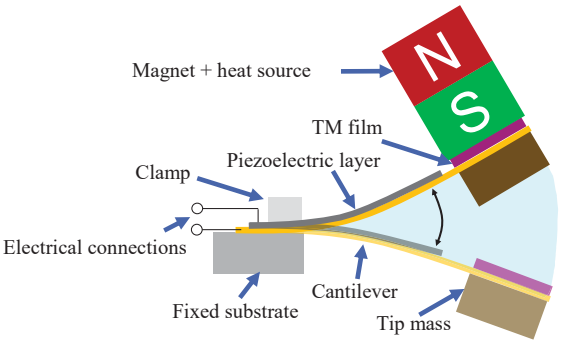


Figure 3: Schematic of the P-TM generator illustrating the oscillatory motion of the cantilever.

In general, the described actuation cycle yields a discontinuous oscillation characterized by magnetic attraction, which is followed by a decay phase until the TM film has cooled enough to be attracted again. In the case of resonant self-actuation, the device oscillates continuously without interruption, yielding a substantial boost in the average power output. This mode of operation is achieved by matching the thermal duty cycle with the mechanical cycle. Frequencies above 200 Hz can be reached [19].

 DOI: 10.30420/456743002

3.2 Device design

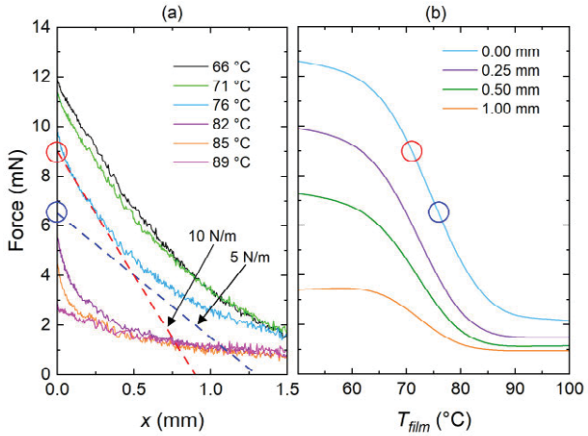


Figure 4: (a) Magnetic force between a Ni-Mn-Ga sample and a SmCo permanent magnet as a function of their distance x and for different sample temperatures T_{film}. Additionally, the reset forces of two different spring configurations are shown. (b) Magnetic force as a function of sample temperature T_{film} for different magnet positions. The respective spring forces at $x = 0$ are highlighted. A temperature-induced magnetic force reduction occurs near 80 °C.

A tensile testing machine equipped with a load cell is used to measure the magnetic force between a stationary Ni-Mn-Ga sample, consisting of two 10 µm thick films with a total area of 2 x 2 mm² placed on a heating platform, and a SmCo permanent magnet (3 x 3 x 8 mm³), which is mounted on the moving crosshead of the machine. The force is recorded as a function of distance x between permanent magnet and Ni-Mn-Ga sample for various film temperatures T_{film}. Fig. 4(a) presents the corresponding magnetic force characteristics as a function of x. The magnetic force decreases nonlinearly with increasing distance x and reduces with rising temperature T_{film}. Close to the magnet surface at $x = 0$, the magnetic force drops sharply when T_{film} reaches T_C, while the initial slope of the force-distance curve becomes steeper. Fig. 4(b) shows the magnetic force characteristics as a function of T_{film} for various distances x highlighting the force reduction close to T_C. For resetting, the stiffness of the cantilever has to be adjusted with respect to the magnetic attraction force. The effect of an elastic reset force is illustrated in Fig. 4 by the dashed blue and red lines representing the elastic force characteristics of a linear spring with stiffnesses of 5 and 10 N/m. Their respective neutral positions are located at the x-axis intercepts. Fig. 4(b) displays the spring forces only at $x = 0$. The spring with stiffness of 10 N/m yields a release force of 9 mN at the magnet surface ($x = 0$) and a theoretical release temperature of approximately 72 °C given by the force equilibrium as highlighted in Fig. 4b. However, at this temperature, the magnetic and spring forces decrease at comparable rates, which is unfavorable for TM actuation. For effective resetting, the temperature-induced decline in magnetic force must be substantially steeper than that of the spring force. This ensures that the restoring spring force exceeds the magnetic force over a substantial portion of distances, allowing for effective resetting at maximal stroke. For these reasons, a target spring stiffness of 5 N/m is selected in the design process. With a neutral position at $x = 1.3$ mm, this configuration yields a workable combination of a sufficiently large stroke, a release force of approximately 6.5 mN and a release temperature of about 76 °C. At this operating point, the rate of temperature-induced force reduction is more favourable for actuation.

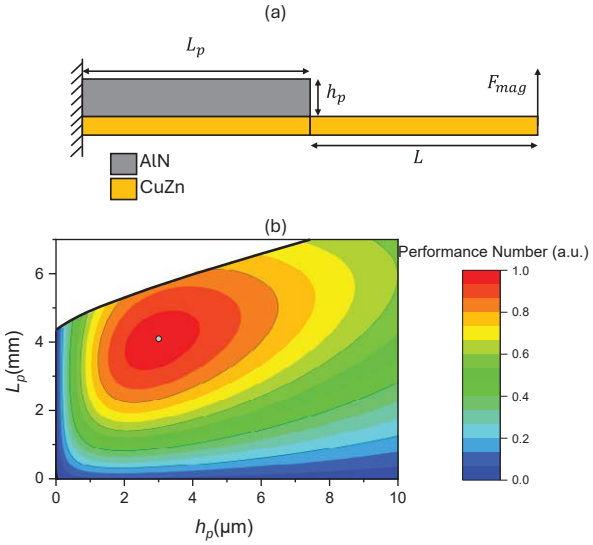


Figure 5: (a) Schematic of the composite cantilever beam model comprising a two-layer section of CuZn and AlN at the fixed end and a single-layer CuZn section at the free end. (b) Performance number given by the power per footprint area of the cantilever divided by stroke squared and frequency as a function of AlN layer length L_p and thickness h_p. The coloured region indicates the design space where the target stiffness of 5 N/m can be achieved.

To determine a suitable cantilever design, a modelling approach based on Bernoulli beam theory is used [20]. As shown in Fig. 5(a), the cantilever is modelled as a composite beam comprising two sections. A first section of length L_p near the fixed-end consists of a 20 µm thick carrier layer of CuZn and a piezoelectric layer of AlN of thickness h_p. A second section of length L is located at the front end consisting of only the CuZn layer resulting in a higher compliance. The total effective bending stiffness is calculated from the individual layer contributions. The used material parameters are summarized in Table 1. The cantilever width is set to 2 mm.

The strain distribution in the AlN layer caused by the magnetic attraction force F_{mag} is used to calculate the short-circuit current and open-circuit voltage due to the piezoelectric effect. Normalization of these values to actuation stroke and frequency as well as cantilever footprint area results in the normalized power density shown in Fig. 5(b). Varying h_p and L_p alters the bending stiffness of the two-layer section. Therefore, the length of the second section L needs to be adjusted to maintain the target total stiffness of 5 N/m. For large h_p, the two-layer section becomes increasingly stiff, forcing the increase of L and the corresponding footprint area. The resulting reduced deformation

 DOI: 10.30420/456743002

of the piezoelectric two-layer section and increased footprint area reduces the power density. On the other hand, for small h_p, less piezoelectric material is available for energy conversion. These competing effects yield an optimal h_p. At fixed h_p, increasing L_p requires L to decrease to preserve the target stiffness until L reaches zero. This limit is indicated by the white region in Fig. 5(b). Within the valid design space, an optimum in L_p arises from the trade-off between absolute power output and cantilever footprint area. The optimal configuration is obtained for h_p of 3 µm and L_p of 4 mm, resulting in a total cantilever length of 6.1 mm.

Table 1: Material parameters used in the modelling approach. Legend: $\boldsymbol{E}$ – elastic modulus; $\boldsymbol{s_{11}}$ – mechanical compliance; $\boldsymbol{d_{31}}$ – piezoelectric coefficient; $\boldsymbol{\varepsilon_{33}}$ – relative permeability.

Parameter	Value	Source
E of CuZn layer	$1.1 \cdot 10^{11}$ N·m^{-2}	[21]
s_{11} of AlN film	$3.44 \cdot 10^{-12}$ Pa^{-1}	[22]
d_{31} of AlN film	$-2 \cdot 10^{-12}$ C·N^{-1}	[22]
ε_{33} of AlN film	8.5	[22]

4 Fabrication

The cantilevers are fabricated from 20 µm cold rolled CuZn sheets. Due to the average surface roughness of 1.5 µm, which has been determined by confocal microscopy, direct sputtering of 3 µm thick AlN layers is not feasible. Instead, freestanding AlN samples are produced separately. A silicon wafer is first coated with a carbon release layer, followed by a 3 µm thick titanium layer, which serves as the growth substrate for the subsequent AlN deposition. The carbon layer prevents adhesion of the titanium to the wafer, enabling subsequent lift-off. AlN is then sputter-deposited onto the titanium and patterned by wet etching into strips of 2 mm width and 10 mm length. The stripes are subsequently cut out manually using a scalpel along the exposed titanium gaps and released from the wafer. Finally, the AlN–Ti stripes are bonded to the CuZn cantilever using a thin layer of epoxy.
Two 10 µm thick Ni-Mn-Ga pieces are bonded to the cantilever tip, along with a tip mass of 5 mg. The cantilever is mounted onto an aluminium substrate by mechanical clamping, and electrical contacts to the AlN layer are established.

5 Results

The AlN-based P-TM generator is characterized using an automated test setup. A heated SmCo magnet is positioned relative to the cantilever by motorized stages. Electrical power is dissipated across a variable load resistor, adjustable from 0 to 8.4 MΩ in 62.5 kΩ steps. Current and voltage are measured using a precision current pre-amplifier (SR570, Stanford Research Systems) and a high-impedance operational amplifier (OPA130, Texas Instruments), respectively. The mechanical oscillation of the cantilever is monitored by a laser displacement sensor. All data are recorded at a sampling rate of 5 kHz.
The spectrogram of the displacement signal, Fig. 6(a), shows oscillation onset near 100 °C, frequency increasing to 130 Hz between 150 and 165 °C. Above 165 °C, oscillations cease due to overheating effects [18]. Fig. 6(b) presents the power output as a function of source temperature and load resistance. The device operates over a temperature range of 140–165 °C, achieving a maximum AC power output of 1.2 µW.

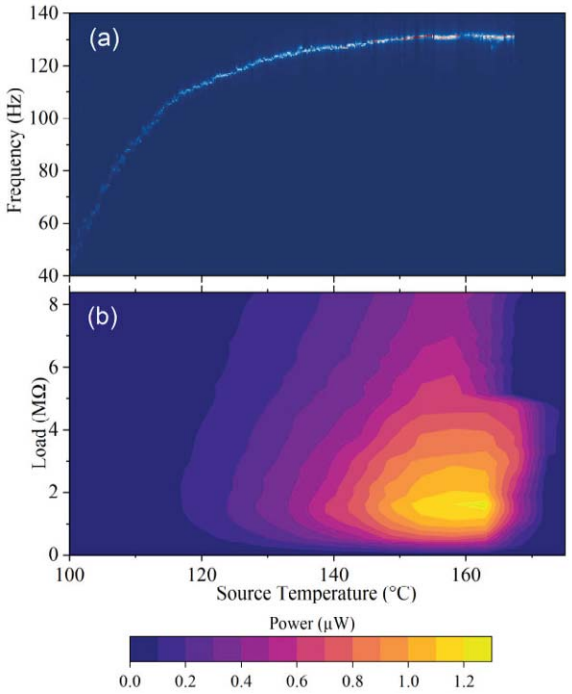


Figure 6: (a) Spectrogram of the stroke signal of a P-TM generator showing the oscillation frequency and cantilever stroke as a function of source temperature. (b) Corresponding AC power output as a function of source temperature and load resistance.

In resonant self-actuation mode, the P-TM generator oscillates harmonically, producing sinusoidal AC voltage and current signals. Since low-power microelectronics typically requires DC supply voltages of 1.8 V, the AC output must be rectified. Fig. 7(a) shows a rectification circuit comprising two small-signal diodes and two 10 µF ceramic capacitors. In this configuration, positive half-waves charge capacitor C_1 while negative half-waves charge capacitor C_2. The output voltage is the sum of voltages across both capacitors, effectively doubling the generated voltage. Fig. 7(b) shows the unrectified and rectified outputs across a load resistance of 8.4 MΩ. Without rectification, the generator produces a harmonic AC voltage of 3 V. After rectification, the circuit delivers 2.6 V and 0.3 µA DC across the same load. In open-circuit condition, the DC voltage reaches 5.4 V.

DOI: 10.30420/456743002

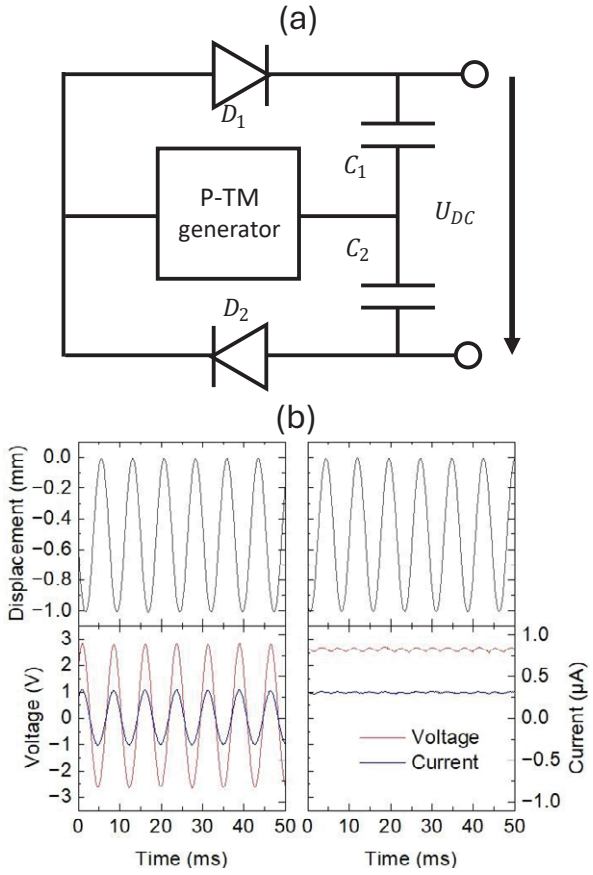


Figure 7: (a) Circuit diagram of the P-TM generator embedded into the rectification circuit comprising diodes D_1 and D_2 (1N4148) and capacitors C_1 and C_2 of 10 µF each. (b) Time-domain signals of the P-TM generator under resonant self-actuation at 160 °C. Left: Displacement and unrectified AC output of 3 V and 1 µA across an 8.4 MΩ load. Right: rectified DC output of 2.6 V and 0.3 µA across the same load.

Fig. 8 shows the measured rectified DC power output as a function of source temperature and load resistance, reaching 0.8 µW at load resistance of approximately 8 MΩ, which coincides with the upper measurement limit.
To verify that the true optimum lies within this range, the P-TM generator and rectification circuit are simulated using an electrical equivalent circuit model. The generator is represented by a sinusoidal current source in parallel with a capacitance, as depicted in Fig. 9. The current amplitude is 1.85 µA at 130 Hz, which corresponds to the short-circuit current at 160 °C. The capacitance of 770 pF is determined by fitting the simulated AC output voltage to the measured characteristics of Fig. 7(b). This source-capacitor model represents the electrically equivalent P-TM generator operating at 160 °C, with the corresponding simulated AC power output shown as the blue curve in Fig. 9. Incorporating the model into the rectification circuit of Fig. 7(a) yields the simulated DC power output, shown as the red curve in Fig. 9. Both curves are in good agreement with the experimental results, confirming that the optimal load resistance and maximum rectified power output are approximately 8 MΩ and 0.8 µW, respectively.

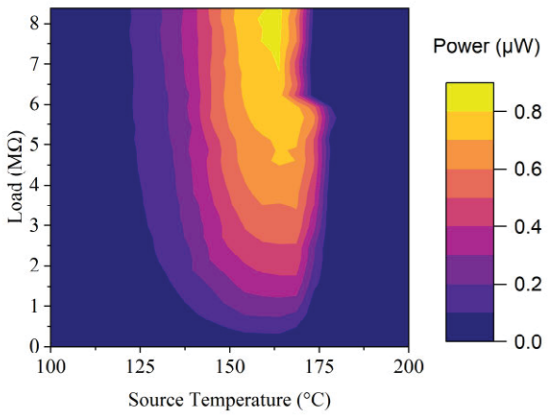


Figure 8: Rectified DC power output of the same device under identical conditions, reaching a maximum of 0.8 µW at 8 MΩ.

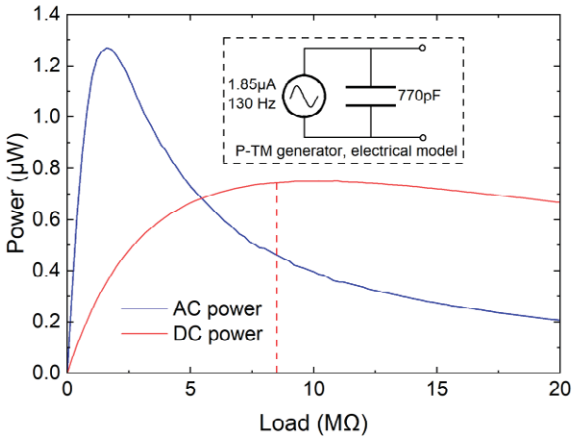


Figure 9: Electrical simulation of AC and DC output power of the P-TM generator operating at 160 °C using the equivalent circuit shown in the inset. The P-TM generator is modeled as a sinusoidal current source of 1.85 µA amplitude at 130 Hz in parallel with a 770 pF capacitor.

6 Conclusion

A cantilever-type P-TM generator based on thermomagnetic Ni-Mn-Ga and piezoelectric AlN has been designed, fabricated, and characterized. The device operates through resonant self-actuation by exploiting a sharp temperature induced magnetization change in the Ni-Mn-Ga film to drive harmonic mechanical oscillations of the cantilever, while the AlN film is used for mechanical-to-electrical power conversion.
The fabricated demonstrator achieves a maximum AC output power of 1.2 µW at a source temperature of 160 °C and an optimal load resistance near 1.6 MΩ, with oscillation frequencies reaching 130 Hz. After rectification, a DC output of 0.8 µW is obtained, corresponding to an AC-to-DC conversion efficiency of 67 %. The corresponding DC power density is 6.6 µW/cm². The rectified open-circuit voltage of 5.4 V and voltage of 2.6 V DC at the maximum power point are sufficient to operate modern microelectronics at 1.8 or 3.6 V. An electrical circuit model confirms

the measured results and provides a basis for further circuit optimization.

The results demonstrate that the P-TM generator is a viable approach for powering low power off-grid electronics from low grade waste heat sources. The rectified output enables parallelization of multiple P-TM generators, allowing their DC power contributions to be accumulated.

7 Literature

1. Hur, S.; Kim, S.; Kim, H.-S.; Kumar, A.; Kwon, C.; Shin, J.; Kang, H.; Sung, T.H.; Ryu, J.; Baik, J.M.; et al. Low-Grade Waste Heat Recovery Scenarios: Pyroelectric, Thermomagnetic, and Thermogalvanic Thermal Energy Harvesting. *Nano Energy* **2023**, *114*, 108596, doi:10.1016/j.nanoen.2023.108596.
2. Forman, C.; Muritala, I.K.; Pardemann, R.; Meyer, B. Estimating the Global Waste Heat Potential. *Renew. Sustain. Energy Rev.* **2016**, *57*, 1568–1579, doi:10.1016/j.rser.2015.12.192.
3. Luberti, M.; Gowans, R.; Finn, P.; Santori, G. An Estimate of the Ultralow Waste Heat Available in the European Union. *Energy* **2022**, *238*, 121967, doi:10.1016/j.energy.2021.121967.
4. Kishore, R.A.; Priya, S. A Review on Low-Grade Thermal Energy Harvesting: Materials, Methods and Devices. *Materials* **2018**, *11*, 1433, doi:10.3390/ma11081433.
5. Vullers, R.; Schaijk, R.; Visser, H.; Penders, J.; Hoof, C. Energy Harvesting for Autonomous Wireless Sensor Networks. *IEEE Solid-State Circuits Magazine* **2010**, *2*, 29–38, doi:10.1109/MSSC.2010.936667.
6. Citroni, R.; Mangini, F.; Frezza, F. Efficient Integration of Ultra-Low Power Techniques and Energy Harvesting in Self-Sufficient Devices: A Comprehensive Overview of Current Progress and Future Directions. *Sensors* **2024**, *24*, 4471, doi:10.3390/s24144471.
7. Steingart, D. Power Sources for Wireless Sensor Networks. In *Energy Harvesting Technologies*; Springer US: Boston, MA; pp. 267–286, doi:10.1007/978-0-387-76464-1_9.
8. Champier, D. Thermoelectric Generators: A Review of Applications. *Energy Convers. Manag.* **2017**, *140*, 167–181, doi:10.1016/j.enconman.2017.02.070.
9. Ayachi, S.; He, X.; Yoon, H.J. Solar Thermoelectricity for Power Generation. *Adv. Energy Mater.* **2023**, *13*, doi:10.1002/aenm.202300937.
10. Carmo, J.P.; Antunes, J.; Silva, M.F.; Ribeiro, J.F.; Goncalves, L.M.; Correia, J.H. Characterization of Thermoelectric Generators by Measuring the Load-Dependence Behavior. *Measurement* **2011**, *44*, 2194–2199, doi:10.1016/j.measurement.2011.07.015.
11. Wang, T.; Luan, W.; Wang, W.; Tu, S.-T. Waste Heat Recovery through Plate Heat Exchanger Based Thermoelectric Generator System. *Appl. Energy* **2014**, *136*, 860–865, doi:10.1016/j.apenergy.2014.07.083.
12. Dzekan, D.; Waske, A.; Nielsch, K.; Fähler, S. Efficient and Affordable Thermomagnetic Materials for Harvesting Low Grade Waste Heat. *APL Mater.* **2021**, *9*, 011105, doi:10.1063/5.0033970.
13. Gueltig, M.; Wendler, F.; Ossmer, H.; Ohtsuka, M.; Miki, H.; Takagi, T.; Kohl, M. High-performance Thermomagnetic Generators Based on Heusler Alloy Films. *Adv. Energy Mater.* **2017**, *7*, 1601879, doi:10.1002/aenm.201601879.
14. Joseph, J.; Ohtsuka, M.; Miki, H.; Kohl, M. Upscaling of Thermomagnetic Generators Based on Heusler Alloy Films. *Joule* **2020**, *4*, 2718–2732, doi:10.1016/j.joule.2020.10.019.
15. Wischnewski, M.; Joseph, J.; Ohtsuka, M.; Miki, H.; Kohl, M. Piezoelectric Conversion of Thermomagnetic Energy from Waste Heat. In MikroSystemTechnik Kongress Proceedings; pp. 425–429, doi:10.30420/456614032, https://ieeexplore.ieee.org/document/11440184
16. Chernenko, V.A.; Ohtsuka, M.; Kohl, M.; Khovailo, V. V; Takagi, T. Transformation Behavior of Ni–Mn–Ga Thin Films. *Smart Mater. Struct.* **2005**, *14*, S245–S252, doi:10.1088/0964-1726/14/5/012.
17. Yarar, E.; Hrkac, V.; Zamponi, C.; Piorra, A.; Kienle, L.; Quandt, E. Low Temperature Aluminum Nitride Thin Films for Sensory Applications. *AIP Adv.* **2016**, *6*, doi:10.1063/1.4959895.
18. Joseph, J.; Ohtsuka, M.; Miki, H.; Kohl, M. Thermal Processes of Miniature Thermomagnetic Generators in Resonant Self-Actuation Mode. *iScience* **2022**, *25*, 104569, doi:10.1016/j.isci.2022.104569.
19. Gueltig, M.; Ossmer, H.; Ohtsuka, M.; Miki, H.; Tsuchiya, K.; Takagi, T.; Kohl, M. High Frequency Thermal Energy Harvesting Using Magnetic Shape Memory Films. *Adv. Energy Mater.* **2014**, *4*, 1400751, doi:10.1002/aenm.201400751.
20. Brissaud, M.; Ledren, S.; Gonnard, P. Modelling of a Cantilever Non-Symmetric Piezoelectric Bimorph. *Journal of Micromechanics and Microengineering* **2003**, *13*, 832–844, doi:10.1088/0960-1317/13/6/306.
21. Joseph, J.; Ohtsuka, M.; Miki, H.; Kohl, M. Lumped Element Model for Thermomagnetic Generators Based on Magnetic SMA Films. *Materials* **2021**, *14*, 1234, doi:10.3390/ma14051234.
22. Wilson, S.A.; Jourdain, R.P.J.; Zhang, Q.; Dorey, R.A.; Bowen, C.R.; Willander, M.; Wahab, Q.U.; Willander, M.; Al-hilli, S.M.; Nur, O.; et al. New Materials for Micro-Scale Sensors and Actuators. *Materials Science and Engineering: R: Reports* **2007**, *56*, 1–129, doi:10.1016/j.mser.2007.03.001.

 DOI: 10.30420/456743003

Piezoelectric Fine Steering Mirrors and electronics for Optical Inter-Satellite Links

Frank Claeyssen[(1)], David Ferris[(1)], Arnaud Gilson[(1)], Xavier De Lepine[(1)], Jocelyn Rebufa[(1)], Aurore Loubet[(1)], Lucas Vermorel[(1)], Thomas Maillard[(1)], Pascal Mexe[(2)], Francis Bortolaso[(2)]

[(1)] *CEDRAT TECHNOLOGIES SAS, 59 Ch. du vieux Chêne, 38 240 Meylan, F., actuator@cedrat-tec.com*
[(2)] *MICROTEC SAS, 2 Rue Hermès, 31520 Ramonville-Saint-Agne, France*

ABSTRACT

Inter-sat optical links appear as promising technology named Free-Space Optical Communication (FSO) allowing fast communication between satellites in constellations, operating either in LEO, MEO and/or GEO orbits. Each satellite embeds several optical communication terminals (OCT), each one needing two Fast Steering Mirrors (FSM) for laser beam fine and fast steering. Thus, for some giant constellations, the total number of FSM can reach up to 100 000 FSM. This New Space market induces not only technical challenges, such as good SWaP, but also industrial challenges, in particular reproducibility, cost-effectiveness and low cost of ownership vs Orbit segment. To address these various FSM needs, CEDRAT TECHNOLOGIES is coordinating the CONECS project, aiming at developing piezo FSM and electronics as New Space COTS for constellations. Its existing products have been used as a starting point, exploiting their heritage: The DTT35XS, the P-FSM150S and the CCBu20 piezo controller. From these products, the project has achieved significant improvements as introduced below.

1. INTRODUCTION

Free-Space Optical Communication (FSO) is expanding in space with giant satcom constellations and optical inter-sat links (OISL) operating between LEO, MEO and GEO orbits (Figure 1). Each satellite embeds several optical communication terminals (OCT), each requiring two Fast Steering Mirrors (FSM) for laser beam fine and fast steering. Thus, for some LEO constellations, the total number of FSM can reach up to 100 000 units. This New Space market induces not only technical challenges, such as stringent SWaP requirements, but also industrial challenges, as reproducibility, cost-effectiveness and low cost of ownership vs Orbit segment.

CEDRAT TECHNOLOGIES (CTEC) specializes in high performance mechatronic devices. CTEC has a long track record on space mechanisms for satellites and other embedded applications, including Fine or Fast Steering Mirrors (FSM) for optical applications (**Figure 2**). Among CTEC flying mechanisms for traditional space missions [1-9], examples of are ROSETTA MIDAS XY stage for ESA in 2001, PHARAO delivered to CNES in 2003, ATLID BSA for ADS in 2015, MTG SCA for SENER in 2018, PAM30 for NASA PSYCHE in 2021 (**Figure 3**) and CNES IASI-NG BSMA for ADS in 2023. According to the stroke needs, the CTEC mechanisms are based either on piezo or magnetic actuators.

To address the needs of FSM for New Space markets, as OISL for constellation, CTEC is coordinating the CONECS project [10], aiming at developing piezoelectric FSM and associated space-grade electronics. CTEC existing products have been used as the starting point, exploiting their prover heritage: The DTT35XS, the P-FSM150S and the CCBu20 piezo controller [11,12]. CONECS project has achieved significant improvements presented in the paper.

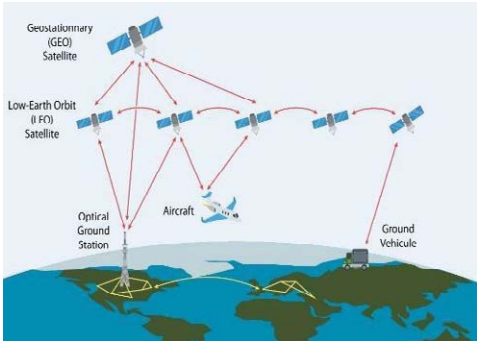


Figure 1 FSO Communication links



Figure 2 Various FSM products from CTEC



Figure 3 PAM30 for NASA PSYCHE [6]

DOI: 10.30420/456743003

2. DTT35XS & P-FSM35XS

The first DTT35XS piezoelectric Dynamic Tip Tilt mechanism (Fig.3.a) was developed with ECSS norms for the PHARAO ACES space atomic clock mission from CNES [1]. This is the first Cesium cold-atom clock ever to orbit Earth, operating outside the International Space Station. This successful mission has validated the DTT35XS for space, as this FSM is still working well in space.

This DTT35XS has inspired NASA JPL leading to the PAM30 (Figure3), flying in PSYCHE [6], for Deep Space Optical Communication (DSOC), presently operating an optical link on 2 AU.

This DTT35XS aims to perform small angular motion Rx and Ry of its platform along x and y axis. It can welcome different mirrors with diameters ranging from 5 to 50mm. It is based on 4 APA35XS Amplified Piezo Actuators ®.

The APA35XS actuator produces a 52µm stroke when supplied by a voltage varying between -20V and 150V. Its stiffness is 0.5N/µm. Each APA35XS is based on a 2x5x10 mm3 piezo multilayer actuator (MLA) with a 0.25µF capacitance. The MLA are equipped with strain gages (SG) acting as sensors for position control. This MLA offers a free stroke of 10µm and a blocked force of 360N. The MLA is in a shell ensuring both the MLA prestress and the stroke amplification, by a factor 5. The prestress is required to avoid tensile force in the MLA as the tensile limit is very low, while the compression limit is high. By this technique, the APA® can withstand vibrations and shocks occurring during launching. The metallic shell is designed to ensure the stress generated by prestress, actuations and external forces stays below material stress limits accounting for ECSS space margins. The advantage of the proposed mechanical amplification is high compactness and low power consumption per micron stroke, both meeting SWaP objectives.

To create a tilt motion, opposite APAs operate in push-pull mode. These APAs transmit their linear motion via elastic pivots to the mirror generating the Rx and Ry tilts. As the mechanism is frictionless and operates in deformation, its resolution is limited only by the electronic amplifier noise.

Several versions of the DTT35XS (Figure 4) have been defined to customize the product according to the need. Upon request CTEC can equip the DTT35XS with a mirror. On Fig. 3f and 6, the DTT35XS are equipped with SiO2 gold-coated mirror. Glued SiO2 mirrors are presently the cheapest mirror technology.

Then as the product becomes a P-FSM35XS, additional manufacturing and tests activities are performed in link with the mirror (for example mirror wave front error measurement).

While the standard version of DTT35XS is commercialized for ground optical instrumentation, a new version of the mechanism, named DTT35XS-NS has been developed for New Space markets. It is based on same piezo ceramics, also placed in an APA shell. It also uses 4 APAs to move the platform via pivots. But, as shown in table 1, the DTT35XS-NS offers a 27% larger angular stroke, reaching 6.1 mrad. Note that this value is experimentally achieved with a standard deviation of 2% on a set of few tens of products.

This larger stroke produces benefits for the customers: It increases its optical angular field of view which makes laser communication stabilization easier. It also permits a decrease in power consumption per millirad by 27%, which is good to reduce electric power demand to the satellite power supply.

This stroke improvement leads, in turn, to a reduction in resonant frequency of approximately 13%. The maximum theoretical bandwidth is reduced but this is not a problem in practice for satellite FSO: The maximum required operational bandwidth in FSO is limited to 500Hz, which can be achieved by DTT35XS-NS. The last risk is about the resistance to shock and vibration. This has been managed by stress analysis in the design and checked by tests, allowing CTEC to commit to satisfactory values.

Another difference with the DTT35XS-NS is a larger casing increasing weight but offering mechanical interfaces close to the mirror. This makes optical integration easier for the customer. The back side of the DTT contains a compartment for proximity electronics. This manages strain gain sensors offset. Having this offset management on the mechanism rather than in the electronics is also an advantage for the customer. It avoids the pairing with the electronic driver. This interchangeability simplifies the products management in OCTs.

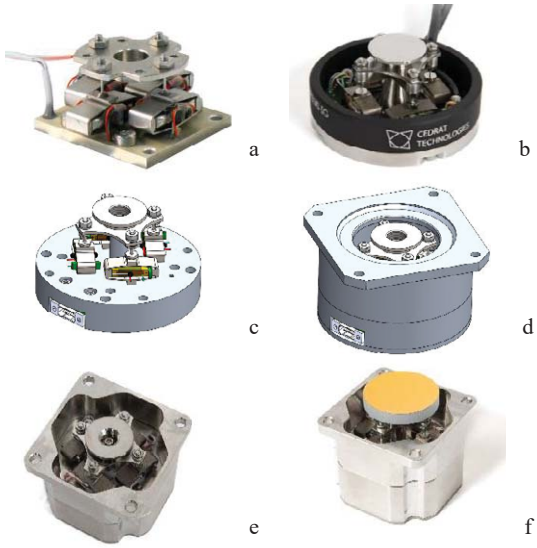


Figure 4 Versions of the DTT35XS from PHARAO (a), COTS lab (b), COTS for FSO (c-e) and P-FSM35XS-NS (f)

		DTT35XS	DTT35XS-NS
Mech. Stroke (open loop)	mrad	4.8	6.1
Mech Stroke (close loop)	mrad	4.5	5.5
Resonance Freq.	Hz	2450	2150
Capacitance per port	µF	0.7	0.7
Height	mm	22	32.45
Section	mm²	D45	40x40
Mass	gr	65	80
Random Vibration	G rms	-	35
SG Sensor type		full bridge	half bridge

Table 1 Performances of DTT35XS and DTT35XS-NS

 DOI: 10.30420/456743003

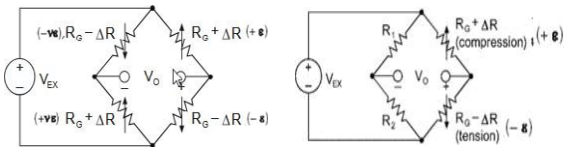
Another difference between DTT35XS and DTT35XS-NS comes from the SG sensors. The DTT35XS SG are in a full bridge configuration using the Poisson coefficient of the MLA, while the DTT35XS-SG MLA are in a half bridge (**Figure 5**).

In theory the resolution of half bridge is a bit reduced, by the factor $(1 + \nu)/2$, as sensitivities for ~~the~~ 2 ~~conf~~igurations are given in the next formulae:

Half Bridge $$\frac{Vo}{Vex} = \frac{GF.\varepsilon}{2}$$

Full bridge with Poisson: $$\frac{Vo}{Vex} = \frac{GF.\varepsilon}{(1+\nu)}$$

Where ε is the strain in the MLA and ν the transverse coefficient (the Poisson coefficient for a uniform material).



a - SG in full bridge *b - SG in half bridge*

Figure 5 SG configurations, where GF is typically 2, ΔR/R=GF.ε for axial stain gage, ΔR/R=GF.ε.(1+ν) for transverse strain gage

As the mechanism is in a Push-Pull mechanical configuration, such a simplified topology works well to address the minimization of the thermal effect if the R1, R2 dummy resistors are selected with low drift Temperature Coefficients.

However, from tests, the expected reduced sensitivity of half bridge is not observed.

The advantage of half bridge is a reduction of the number of wires to manage from 12 to 8 per mechanism; Both first benefits for New Space markets are a reduced manufacturing time and higher reliability, as wires are known in space as a source of failure.

Additionally, the non-linearity even improves, which may be explained by the fact that the transverse strain, measured in full bridge but not in half bridge, has a complex effect in an MLA. MLA is a non-isotropic material composed of buried electrodes and ceramics, with d33 and d31 effects, etc.

In DTT35XS-NS electronic compartment, a compensating network is also added to the Wheatstone bridge to address the residual offset. Offset is adverse for the resolution impacting the dynamic of the instrument conditioner. Measured offset after strain gages integration onto MLA could often cover the full stroke which reduces by twice the dynamic of the analogue to digital conversion.

The proposed solution is to modify directly onto one arm of the bridge the potential to balance the differential voltage Vo. This circuit (Figure 6) located on the electronic compartment allows compensation of the offset automatically during the MAI sequence without lot of work and keeping overall accuracy. This operation necessitates two measurements, the first one without compensation to establish the compensating network value and a second one to valid the resulting offset.

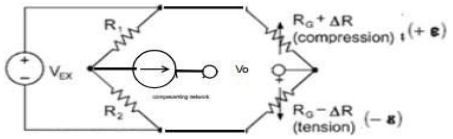


Figure 6 Principle of compensation network

All the presented improvements regarding design and process versus initial Pharao DTT35XS, allow both to benefit from a space heritage and to offer a cost-effective COTS FSM product for New Space series (**Figure 7**).



Figure 7 P-FSM35XS-NS batch for FSO constellation

3. P-FSM150S

The P-FSM150S (**Figure 8**) is a new-generation piezoelectric double-tilt mechanism, larger than the DTT35XS, equipped with a SiC mirror, and already selected in several space projects. Although it inherits from EARTHCARE ATLID Beam Steering Actuator [4,5], the P-FSM150S was designed and patented with structural changes to meet reduced series costs for FSO constellations. The P-FSM150S is composed of the following parts:

- 4 APA® Amplified Piezo Actuators provide the required displacement and are fixed to the baseplate and to the mirror support. The APA® are equipped with SG sensors.
- A baseplate where the APA® are screwed.
- An innovative flexible mirror support.
- A Silicon Carbide (SiC) substrate-based mirror from Mersen OptoSiC® screwed on the mirror flexible support.
- A guiding blade soldered onto the central cylinder that stiffens the assembly.

 DOI: 10.30420/456743003



Figure 8 P-FSM150S with SiC mirror [7]

The APA® used in the P-FSM150S are new APA150S deriving from CTEC standard APA120S. The existing CTEC actuators were either slightly too short in stroke or not stiff enough to ensure the mechanism survival during the launch. Therefore, the APA150S has been specifically designed for the application needs. It offers a stroke of 188 µm from

-20V to 150V in average on its first batch of 25 units, with a standard deviation of 0.9µm. As in DTT, they are operated by pair in push-pull mode to create a tilt motion. Thanks to these 4 APA150S, the P-FSM150S provides a mechanical stroke of 18mrad.

The initial mirror is a SiC mirror with 4 feet allowing the mirror to be fixed with screws. This solution offers more guarantees than glue: Resistance to shocks and vibrations can be justified by design, as well as lifetime in space; At the opposite, effects of radiation on glue is not so easy to guarantee for long lifetime in space. This choice of screwed SiC mirror technology is fully validated by PAM30 [6], flying on PSYCHE in deep space for few years.

The SiC mirror can be proposed with silver coating, gold coating or dielectric coating, according to the laser wavelength & power.

The flexible mirror support performs two functions. It transmits the APA® displacements to the mirror, replacing the 4 elastic pivots with one single flat part. This reduces integration time and leads to more compact in height mechanism. The second function is to solve hyper statism of the 4 mirror feet. The flexible mirror support, manufacturing process of which has been improved in CONECS, accommodates the few microns differences between feet without inducing additional wave front error (WFE) to the initial WFE found on the naked mirror [6]. Thus, this flexible support allows for a reduction in the mirror's manufacturing cost.

A large qualification test campaign of the P-FSM150S (HiRel), has given results [13] including:

- Functional Performance:
  - Open Loop Stroke: 18mrad
  - Resolution: < 20µrad
  - Resonance frequency > 700Hz
- WFE mirror analysis
- Lifetime test for more than 10^9 cycles
- Random vibrations at 0,65g²/hz
- 1000g SRS shock

Since 2023, several end-users have selected this product for various optical communication links from LEO, MEO, ground stations, and provides both feedback and proof-of-concept.

For example, [14] explains that the key applications of a steering mirror in a communications satellite are to correct for the platform jitter, keeping the incoming beam continuously centered on the receiving detector. To simulate this scenario on an optical bench, developed a set-up using silver coated P-FSM150S. The set-up shows a 5-fold improvement in concentration thanks to the P-FSM150S [14] compared to the uncorrected case, where the point track spreads over an angular extent of approximately 3400 µrad.

From December 2025, the P-FSM150S is proposed in 3 variants as presented in **table 2**.

Variant	**HI-REL**	**VAC**	**COTS**
Main application	Old space From LEO to Deep Space	New space LEO, MEO & GEO	Lab & New Space Low LEO
Lifetime	10 - 15 years	5 – 7 years	1-3 years
Quality standards & MAIT environ.t	ECSS ISO5-7	ISO9001 ISO 8	ISO9001
Wires Manufacturing	Lead solder	Lead-free solder	Lead-free solder
Parts Manufacturing	Passivation & coating	-	-
Mirror technology	Screw-fixed SiC	Screw-fixed SiC	SiO2 glued on support
Final cleaning	Bake-out	-	-

Table 2 P-FSM150S versions [11]

For New Space applications, the P-FSM150S COTS takes benefit of several changes to reduce its cost. The main rationale is two folds: The required lifetime which is often up to 15 years in orbit for old space, while it is generally less than 5 years for new space. The requested reliability is very high on old space while in new space, the application supports higher risks and a rate of failure in low LEO.

The main difference is the use of a cost-effective Fused silica SiO2 mirror with 15mm diameter instead of a SiC 17 mm diameter mirror. As the SiO2 mirror cannot be screwed on the flexible mirror support, the SiO2 mirror is glued to an aluminum mirror interface offering the same external interface as the SiC mirror (**Figure 9**).

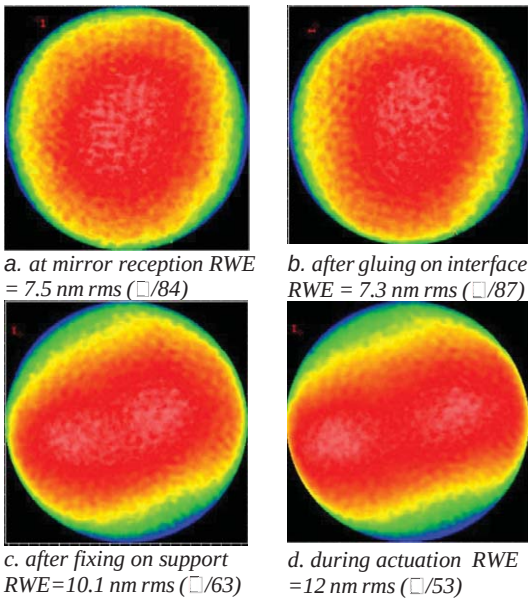


Figure 9 SiC mirror versus SiO2 mirror on interface

 DOI: 10.30420/456743003

As consequence, the process leading to the final flatness performance of a SiO2 needs one step more than a SiC mirror. This flatness is characterized by the Reflective WFE (RWE) measured with a Zygo interferometer at the end of different steps (Figure 10 & Table 3). The first step, which is gluing at the mirror on the interface, does not induce an RWE degradation (b. vs a.) if done carefully, i.e. by polymerization in oven at low temperature.
The second step which is the screwing of the mirror interface on the flexible support induces a small WFE degradation (c. vs b.).

The third step is achieved when the mechanism is actuated with a maximal Rx angular stroke. This also adds a Delta-RWE.
Compared with SiC RWE [13], the results at this stage on SiO2 are deemed encouraging. It should be noted that functional performance (strokes, resonance frequency, …) are the same between all 3 versions of the P-FSM150S.



a. at mirror reception RWE = 7.5 nm rms (□/84)
b. after gluing on interface RWE = 7.3 nm rms (□/87)
c. after fixing on support RWE=10.1 nm rms (□/63)
d. during actuation RWE =12 nm rms (□/53)

Figure 10 WFE of P-FSM150S SiO2 mirror vs steps

RWE (nm rms)	P-FSM150S HiRel	P-FSM150S COTS
Miror type	SIC	SiO2
RWE before integ.	14.2	7.5
RWE after integ.	17.5	10.1

Table 3 RWE of SiO2 vs SiC P-FSM150S mirrors

4. CCBu20 PIEZO CONTROLLERS

The CCBu20 is a compact dual-channel controller designed for driving and controlling piezoelectric mechanisms such as CTEC DTT, FSM and XY stages operated in push-pull mode (Figure 11). It is used in embedded and ground electro-optic imaging & laser systems. It is also used as a GSE or Bread Board Model (BBM) and sometimes Engineering Model (EM) for New Space applications.

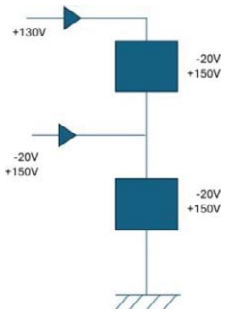


Figure 11 CCBu20 push-pull electronic drive

The CCBu20-NS is a space-grade version of the CCBu20 for New Space (Figure 12). It is also a dual-channel controller. In both CCBu20 and CCBu20-NS, the electronics power amplifiers for piezo are based on discrete components, rather on Operational Amplifiers chips which are not so reliable and have no space equivalence.

In these products, both channels of the piezo drivers can provide the [-20; +150V] range required to supply the piezo actuators in push-pull mode.

Table 4 compares features of CCBu20 to CCBu20-NS, allowing to see additional features of the NS version to provide a solution for New Space market.



Figure 12 CCBu20-NS and CCBu20 [12]

While the CCBu20 makes use of a standard push-pull driving, a new driving strategy invented by CTEC has been implemented in the CCBu20-NS to limit voltages on components below 100V, which is beneficial for electronic price.

The output currents are 35mA rms continuous. Driven with this continuous output current, the DTT35XS and P-FSM35XS can achieve a full stroke open loop bandwidth above 100Hz. The P-FSM150S can reach up to 30Hz.

CCBu20 drivers offer a higher peak current capacity which is limited by heating but can perform typically more than 1s. The CCBu20 can produce a 200mA peak current while the CCUBu20-NS is limited to 150mA because of rad-hard selected transistors (with lower SOA performance). This higher peak current than rms continuous one is useful for dynamic responses to steps or short time order signals, equivalent to 6 times more bandwidth.

 DOI: 10.30420/456743003

	CCBu20	CCBu20-NS	Unit
GENERAL			
Function	All-in-one piezo driver & controller	All-in-one piezo driver & controller	
Number of control channels	2	2	
Integrated sensor conditioning	Strain Gages	Strain Gages	
Digital communication	RS422	RS422 SPI	
PIEZO DRIVER			
Number of channels	2	2	
Delivered voltage range	-20 ... +150	-20 ... +150	V
Max output current	0.200	0.150 Typ. 0.174 @Tmin; 0.134 @Tmax	A
Permanent output current	0.035	0.035	Arms
Small signals bandwidth (-6 dB)	32	11 @-3db	kHz
STRAIN GAGES (SG) CONDITIONER			
Number of channels	2	2	
Reference output voltage	5	2,5	Vdc
Max. reference output current	30	2x15 (2x30 in option)	mA
Typical bridge impedance	350	350	Ohm
Real gain	546,45	1000	V/V
Small signals bandwidth	34 @-3 dB	5.1 @-6dB	kHz
DIGITAL CONTROL			
Control strategy	Tunable PID + Stabilizing filters	Tunable PID + Stabilizing filters	
Stabilising filters	Tunable lowpass & notch	Tunable lowpass & notch	
Sampling rate	20	20	kSps
Digital resolution	16	16	bits
POWER SUPPLY			
Recommended supply voltage	+28	20…30	Vdc
Supply voltage range	+24 … +28	20…30	Vdc
Supply current	0.2 … 1	0,2…4	Arms
MISCELLANEOUS			
Mass	0.25	0.715 +/-2%	kg
Dimensions	91 × 80 × 35.5	150 × 100 × 50 (other sizing on request)	mm
Cooling	Natural convection + Heat-sinking surface	Conduction to the base plate	
Operating temperature range	-40 … +70	-15 … +60	°C
Storage temperature range	-40 … +85	-40 … +85	°C
Warm up time	15	15	min
Protections	OV for HV, Thermal protection,	Driver Thermal protection; OCP,OVP,UVP for primary side; OVP/OCP/ UVP for HV - periodic monitoring by processor @ 1Hz	
Built in test	NA	Initiated Built In Test; Power Up Built In Test; Continuous Built In Test	
Discrete TC	Enable	SHUTDOWN_N: Inhibition CCBU-20-NS	
Discrete TM	Fault	ON-OFF_STATUS: Auxiliary Supply operating and SHUDDOWN-N inactive OPERATING: CCBU-20-NS is operating - Not insulated	
Digital TC/ TM	ORDER #1,2 SENSOR #1,2	ORDER #1,2 SENSOR #1,2; MODE1 OPEN LOOP, MODE2 CLOSED LOOP	
RADIATIONS			
SEL	NA	No latch-up events @LET ≤ 43MeV.cm2/mg	
SEE	NA	No critical effect	
TID	NA	10 to 30 k rad	
MECHANICAL STRESS			
Sine vibration	Industrial level	5g @ 70Hz 2.5g@ 110Hz	
Quasi-static loads	Industrial level	17.7g @ 20Hz	
Random vibration	Industrial level	13.6	gRMS
Shock	Industrial level	50g @100Hz 1500g @2000Hz	

Table 4 Comparison between piezo controllers CCBu20 and CCBu20-NS (New Space grade) [12]

 DOI: 10.30420/456743003

The bandwidth of CCBu20-NS driver is limited to 5kHz, but this is enough for operation in space where required operation bandwidth is generally 500Hz (for micro vibrations control).

Both CCBs include a strain gauges sensor conditioner for positioning feedback signals.

The close loop positioning control is performed with a 16bits digital controller. The control law is a PID associated with various possible stabilizing filters configurations:

- No filter
- 2nd order lowpass filter
- 2nd order notch filter
- 2 × 2nd order notch filters
- 4th order notch filter

In terms of functions, the CCBu20-NS integrates additional functions: SPI communication and a Telemetry (TM) and Telecommand data Communication (TC) which are required in space. The CCBu20-NS has been designed to support 5g static load, 13.6g rms random vibration and a 1500g SRC shock.

A last, a key advantage of the CCBu20-NS is its resistance to radiation. This is obtained thanks to selected space-grade components and thicker housing, leading to a larger mass than the CCBu20. A radiation resistance for total ionizing dose (TID) of 10 krad (design dose @ EEE level (die) is obtained with standard mechanical housing. With additional shielding at satellite level by customizing housing, the max TID can reach up to 30 krad.

The CCBu20-NS [4] is available in several versions. The Engineering Model (EM) has the same interfaces and functions as the Flight Models (FM) but instead of the FM space grade components, it is realized with equivalent non-space grade components. The EM allows the user to test its systems at a lower price. Tests can be done on the ground or in In-Orbit-Demo (IOD), provided with a few additional cares. The Flight Models 3 versions (V0, V1, V2) are built with polyimide PCB, Rad-tolerant space grade components and additional shielding, for LEO. Functional and mechanical acceptance tests are performed. The V0 offers a guaranteed lifetime between 1 and 3 years. The V1 offers a guaranteed lifetime up to 5 years. It includes LAT/PAD on components, and MIP & DRB manufacturing reviews as well as data packs.

The V2 is designed to ensure a guaranteed lifetime larger than 5 years. It respects ECSS-Q-ST-70-60C and ECSS-Q-ST-70-61C ESA space norms.

5. P-FSM SYSTEM

The P-FSM system studied hereafter is formed by the P-FSM150S with its SG sensors and the CCBu20-NS controller (Figure 13). The objective of the design is to define the Sensor Gains, the PID and the notches, to get a stable system offering the largest bandwidth and the shortest response time. Both CCBu20 and CCBu20-NS are based on the same control technique (Figure 14), relying on a PID and a double notch.



Figure 13 P-FSM150S connected to the CCBu20-NS

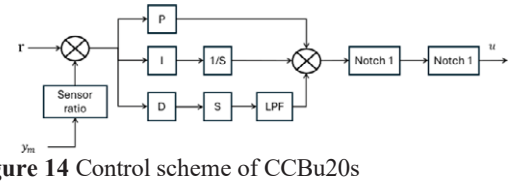


Figure 14 Control scheme of CCBu20s

By analysis of both sub-systems performances, the required Sensor Gain is 7.6 mrad/V, which has been checked adequate by open loop test, supplying an 18 mrad full stroke low frequency sine.

Using the 16bits numerical command of CCBu20-NS, a mechanical stroke of 16 mrad is achieved as with CCBu20, being compliant with product datasheet [11].

Open loop response (**Figure 15**) shows that both first resonances occur at 720Hz and at 1250 Hz.

So, both controller notches have been exploited to cancel these first resonance frequencies, they are destabilizing the close loop.

Thanks to these settings, the close loop bandwidth is larger than 250Hz (**Figure 16**).

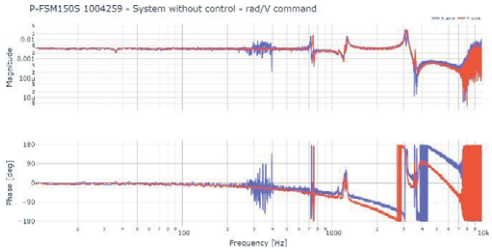


Figure 15 Open Loop Stroke per Volt Bode diagram

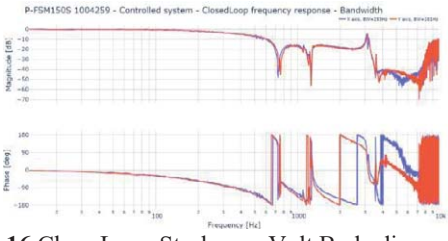


Figure 16 Close Loop Stroke per Volt Bode diagram

Another result of the close loop control is the rapid stabilization of the position when the system is submitted to a step order. As shown on **figure 17**, on a large step of 8 mrad, the rise time (from 10% to 90% stroke) is 1.5ms while the settling time is 4ms. The limiting factor in this case is the available maximum current, which explains the overshot. On a small step (**Figure 18**), the rise time is 1.1 ms, being shorter as the current limit does not occur the same way.

ISBN: 978-3-8007-6743-4 @ VDE VERLAG GMBH · Berlin · Offenbach

 DOI: 10.30420/456743003

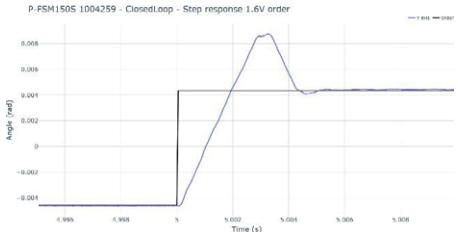


Figure 17 P-FSM150S step response in Close Loop

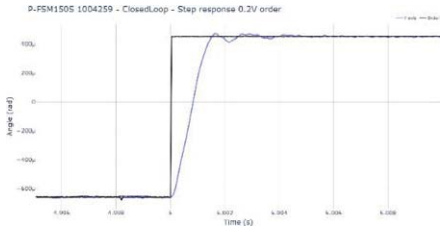


Figure 18 P-FSM150S small step resp. in Close Loop

Some solutions are implemented on the CCBu20-NS controller that might further improve the performance on the step response of the system. One of those solutions is the use of a slew rate limiter on the order of the closed loop (r in Figure 14) so that the order is never faster than the system at current saturation. This method has not been tested on CCBu20-NS controller with P-FSM150S, but on other CTEC mechanisms with great success, such as on a M-FSM45 Magnetic FSM [15] (**Figure 19**).

Further work is in progress to test more system performance and product combinations.

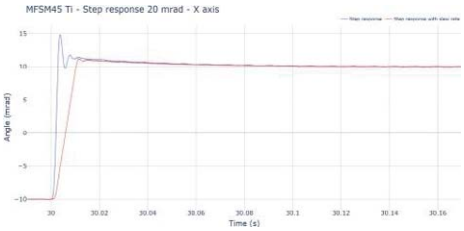


Figure 19 Effect of the slew rate limiter on the order on the step response of a system

6. CONCLUSION

Thanks to the CONECS project, CTEC P-FSM products portfolio has been extended to offer a coherent suite of FSM products for optical communication links in LEO. This suite includes:

- The DTT35XS and P-FSM35XS with SiO2 mirror, offering strokes up to 5mrad.
- The P-FSM150S with SiC or SiO2 mirrors, and various coating (Silver, Gold, Dielectric), offering strokes up to 18mrad.
- The CCBu20, as an industrial COTS and as a New Space COTS with various grades, for controlling DTT35XS, P-FSM35XS and P-FSM150S.

These products can be proposed with Hi-Rel space versions as well as space COTS. These COTS have been cost-optimized while retaining most of the performance, qualification and flight heritage of the original space products.

7. ACKNOWLEGDEMENT

The authors are grateful to BPI France for the financial support and CNES for the technical support, both provided within the CONECS project. This project was funded by the French State as part of the France 2030 program.

8. REFERENCES

1. R. Le Letty, Miniature Piezo Mechanisms for Optical and Space applications Proc ACTUATOR 2004 Conf, Ed. Messe Bremen (G), pp 177-180, June 2004
2. C. Allegranza, Actuators for Space Applications: State of the Art and New Technologies. In Proceedings of the 14th Inte. Conf. on New Actuators, Bremen, Germany, June 2014
3. N. Bencheikh, Voice coil actuators for two MTG instruments, Proc. Conf ESMATS 2015
4. E. Prevost, Beam steering mechanism for Earthcare atmospheric lidar instrument Atlid – an ultra-stable piezoelectric tip tilt mechanism, ICSO, Biarritz, 2016
5. F. Claeyssen, Beam Steering Mirrors from space applications to optronic solutions, Proc. OPTRO Conf, Paris, Feb. 2018
6. A. Guignabert, Point Ahead Mechanism for Deep Space Optical Communication – Development of a new Piezo-Optical Tip-tilt mechanism, AMS 45th, Houston Texas USA, 13-15 May 2020
7. F. Claeyssen, P-FSM & M-FSM Piezoelectric & Magnetic Fast Steering Mirrors, Proc. 7th Int Symp of Space Optical Instruments and Applications: ISSOIA 2022, 21-23 Oct, Beijing, China. Pub. Springer Proc. in Physics, 2023
8. F. Barillot, Tough precision piezoelectric motors for space applications, AMS, Virginia B.,2024
9. CTEC space heritage https://cedrat-technologies.com/wp-content/uploads/downloads/aerospace_heritage.pdf
10. CONECS Project, supported by France2030 https://cedrat-technologies.com/complete-pointing-systems-for-spatial-optical-communication/
11. DTT35XS & P-FSM150S piezo FSM products https://cedrat-technologies.com/fr/fine-and-fast-steering-mirrors/
12. CCBu20 controllers for piezo mechanisms https://cedrat-technologies.com/categorie-produit/oem-amplifiers-piezo-controllers/
13. G. Aigouy, Piezoelectric and Magnetic Fast Steering Mirrors for Space Optical Communication - Conference ICSO 2022, Croatia Dubrovnik, Oct. 2022
14. C. Graham, Steering Mirror System with Closed-Loop Feedback for Free-Space Optical Communication Terminals, Aerospace, *11*(5), 330, 2024
15. X. De Lepine, Magnetic Fast Steering Mirrors for Tracking and Optical Communication for Defense and Aerospace Industries, 159. Proc. Actuator 2026.

 DOI: 10.30420/456743004

A Miniature Thermomagnetic Actuator Driven by Low-Grade Heat

Athira Kattiparambil Sivaprasad[1], Joel Joseph[1], Amir-Abbas Haghighirad[2], Robert Kruk[3], Manfred Kohl[1], Jingyuan Xu[1]

[1]Institute of Microstructure Technology, Karlsruhe Institute of Technology, Karlsruhe, Germany
[2]Institute for Quantum Materials and Technologies, Karlsruhe Institute of Technology, Kaiserstraße 12, 76131 Karlsruhe, Germany
[3]Institute of Nanotechnology, Karlsruhe Institute of Technology, Karlsruhe, Germany

Abstract

We present the design, fabrication, and characterization of a miniature thermomagnetic (TM) actuator employing a La–Fe–Si thermomagnetic material plate to harness low-grade heat below 333 K. The actuation mechanism is based on the intrinsic temperature-dependent change in magnetization of the TM material under an applied magnetic field. A NdFeB permanent magnet simultaneously serves as the heat source and magnetic field source, enabling compact device integration. The fabricated actuator operates at an exceptionally low heat-source temperature of 305 K and achieves a displacement of 200 µm at an actuation frequency of 2.1 Hz in self-sustained operation mode. Surface engineering of the La–Fe–Si plate through copper electroplating and polishing significantly improves thermal contact. These results demonstrate the feasibility of miniature thermally driven actuators powered by near-room-temperature heat sources for compact and precisely controlled motion systems.

1 Introduction

A large fraction of unrecovered waste heat exists in the low-temperature range (<100 °C) [1], with a substantial portion available close to room temperature, where conventional energy-conversion technologies exhibit limited efficiency [2]. Recovering such low-grade thermal energy is of considerable interest due to its widespread availability and potential for sustainable energy utilization [3]. Thermomagnetic (TM) actuators utilize temperature-dependent changes in magnetization to directly convert thermal energy into controlled mechanical motion. Unlike conventional electrically driven actuators, TM actuators can operate through thermal triggering alone, enabling self-sustained actuation cycles suitable for autonomous and remote systems. In this work, a miniature TM actuator operating at a heat-source temperature slightly above room temperature is presented.

2 Operation Principle

The performance of the TM actuator strongly depends on the thermomagnetic material and magnitude of its temperature-dependent magnetization change near the magnetic phase transition. In this work, a La–Fe–Si-based alloy is selected due to its high magnetization, transition temperature (T_c) close to room temperature, sharp magnetization changes (dM/dT) within a narrow temperature interval [2], and small hysteresis. These characteristics are particularly advantageous for achieving efficient actuation under low-grade heat sources near room temperature. The La–Fe–Si used in this work showed a T_c of approximately 303 K during heating and 304 K during cooling at 400 mT, with a maximum dM/dT values of -13.3 $Am^2kg^{-1}K^{-1}$ and -14.2 $Am^2kg^{-1}K^{-1}$ during the heating and cooling cycles, respectively. **Figure 1** shows the temperature-dependent magnetization behaviour of the La–Fe–Si plate measured under three different magnetic fields.

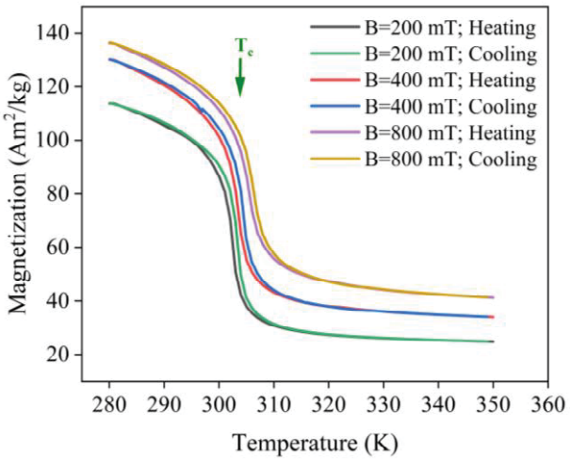


Figure 1. Magnetization–temperature curve of the La–Fe–Si plate.

The operating principle of the TM actuator is illustrated in **Figure 2**. The device consists of a La–Fe–Si plate coupled to a restoring spring that provides the mechanical restoring force, while a NdFeB permanent magnet serves simultaneously as the magnetic field source and heat source. Below the transition temperature T_c, the La–Fe–Si material is in a ferromagnetic state and is strongly attracted toward the magnet (State I in **Figure 2**). Upon contact with the heated magnet, the temperature of the TM material increases (State II in **Figure 2**). Heating above T_c transforms the material into a paramagnetic state, significantly reducing the magnetic attraction force and allowing the restoring spring force to return the material to its initial position (State III in **Figure 2**). During cooling below T_c, the material recovers its ferromagnetic state, re-establishing magnetic attraction and initiating the next actuation cycle. A heat sink maintained at ambient temperature is integrated into the system to accelerate cooling and support self-sustained actuation.

ISBN: 978-3-8007-6743-4 @ VDE VERLAG GMBH · Berlin · Offenbach

DOI: 10.30420/456743004

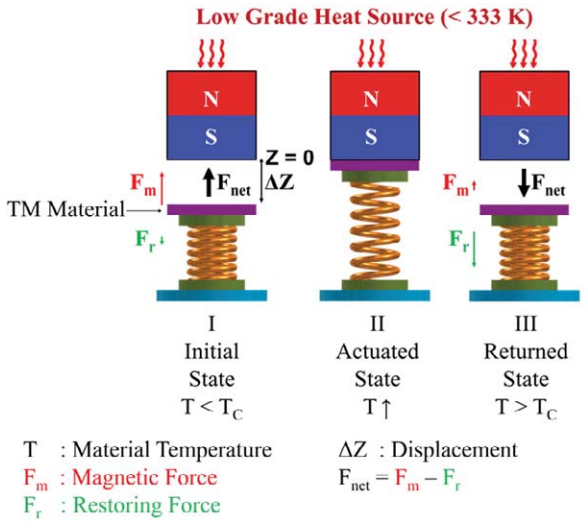


Figure 2. TM actuator architecture consisting of a La–Fe–Si plate, restoring spring, and heated NdFeB permanent magnet, illustrating the three actuation states.

3 Fabrication and Assembly

3.1 Material characterization

The 180 µm-thick La–Fe–Si plates were structured into 4 × 4 mm^2 samples using electrical discharge machining (EDM). Exposure of the material to the aqueous environment during EDM processing resulted in surface oxidation, as visible in **Figure 3(a)**. Although the investigated TM material exhibits a sharp magnetization change with temperature, a low rate of temperature change within the material (dT/dt) can limit the actuation frequency by increasing the heating and cooling times [4]. Therefore, efficient thermal contact with both the heat source and heat sink is essential for achieving high-frequency actuation.

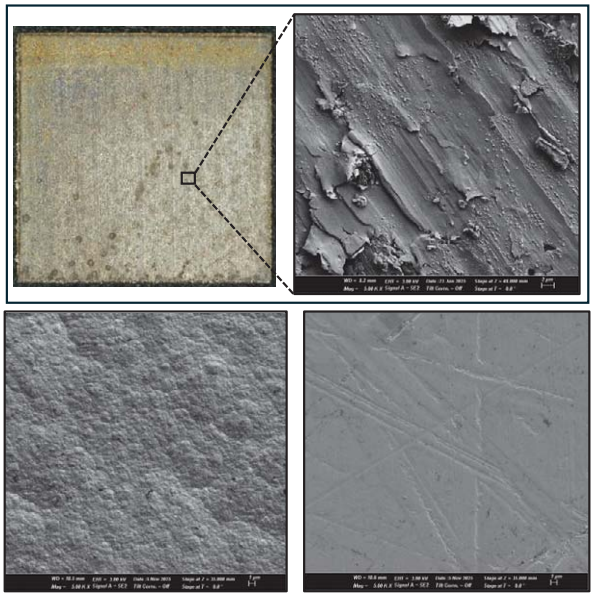


Figure 3. (a) Surface of the La–Fe–Si plate after EDM cutting, showing visible surface oxidation. Scanning electron microscope (SEM) image of the initial surface before electroplating indicating a rough and porous morphology is shown in the inset. (b) SEM image of the surface after electroplating. (c) SEM image of the polished material surface after electroplating.

As shown in the SEM image in **Figure 3(a),** the untreated La–Fe–Si surface exhibits a rough and porous morphology, which limits thermal contact and heat-transfer efficiency. To improve the thermal interface, the TM material was copper-electroplated and subsequently polished. Copper electroplating was performed using an alkaline electrolyte based on phosphonates (CHEMOPUR CUPA SANCY HE 4) with a pH value of 10, followed by the application of an anti-tarnishing coating layer. The deposited copper fills most surface pores and significantly reduces surface roughness, as illustrated in **Figure 3(b)**. In addition to improving thermal contact, the electroplated copper layer enhances the mechanical stability of the brittle La–Fe–Si plates. The polished surface shown in **Figure 3(c)** demonstrates a substantially smoother morphology, which is beneficial for efficient heat transfer during actuator operation.

3.2 Device design

Figure 4(a) presents the experimental setup of the TM actuator based on the operating principle described in Section 2. A fabricated prototype actuator with overall dimensions of 14.4 × 14.4 × 9.5 mm^3 is shown in **Figure 4(b)**. The NdFeB permanent magnet (4 × 4 × 16 mm^3) provides the magnetic attraction force and is heated using integrated resistive heaters. Two restoring springs with a combined spring constant of 1.3 N/mm provide the restoring force required for cyclic actuation. A laser displacement sensor is used to measure the actuator displacement, while the magnet temperature is monitored using a thermocouple positioned near the magnet tip.

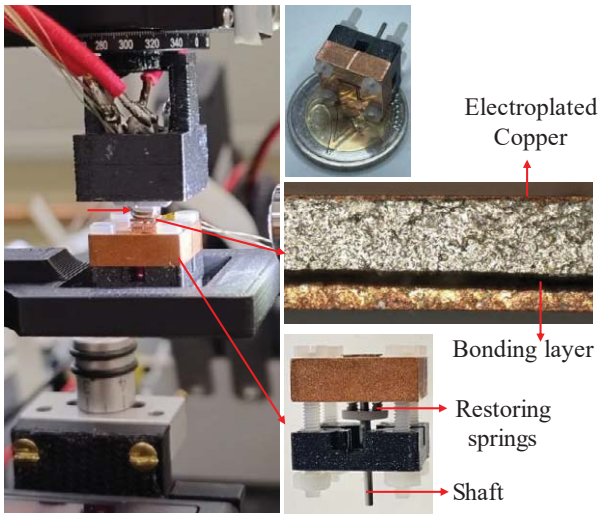


Figure 4. Experimental setup for investigating the actuator prototype. (a) test setup, (b) fabricated TM actuator prototype, (c) close-up view of the oscillating La–Fe–Si plate assembly, (d) exploded view of the heat sink showing the restoring spring elements.

ISBN: 978-3-8007-6743-4

@ VDE VERLAG GMBH · Berlin · Offenbach

 DOI: 10.30420/456743004

The TM material is bonded to a 100 µm-thick copper plate using a thermally insulating adhesive layer to improve mechanical stability, prevent fracture under contact loading, and enhance heat dissipation during contact with the heat sink, as illustrated in **Figure 4(c)**. **Figure 4(d)** presents an exploded view of the heat-sink and restoring-spring assembly. Tensile-force measurements of the investigated TM material–magnet combination indicate a maximum magnetic force of approximately 1 N near room temperature, as shown in **Figure 5**.

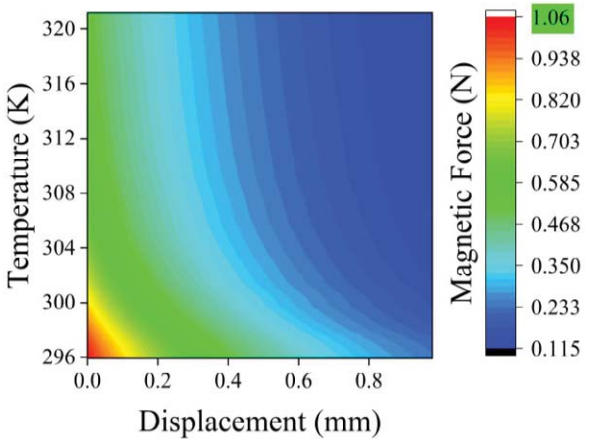


Figure 5. Magnetic force between the NdFeB magnet and La–Fe–Si, measured as a function of their separation distance at different TM material temperatures.

4 Results and Discussion

Figure 6 presents the experimentally determined force balance between the magnetic attraction force and the restoring spring force. Below the transition temperature T_c, the magnetic force dominates, causing the TM material to move toward the magnet (State I–II in **Figure 6**). Upon heating above T_c (State II–III in **Figure 6**), the magnetic attraction force decreases significantly as the material transitions into a paramagnetic state, allowing the restoring spring force to return the plate to its initial position (State III–IV in **Figure 6**). During subsequent cooling below T_c, (State IV–I in **Figure 6**) the material regains its ferromagnetic state and magnetic attraction force, thereby completing a self-sustained actuation cycle.

The dynamic performance of the fabricated actuator prototype is presented in **Figure 7**. The TM actuator operates at a heat-source temperature of 305 K and achieves a displacement amplitude of 200 µm with a self-sustained actuation frequency of 2.1 Hz. Due to the remanent magnetization of the TM material (**Figure 6**), contact with the heat sink is limited to approximately 90 ms, during which the material recovers sufficient magnetization to overcome the restoring spring force and move toward the magnet. Temporary equilibrium positions are observed during the transition process, likely resulting from a transient balance between the magnetic attraction force and restoring force. During the forward motion (State I–II in **Figure 6**), the two forces become nearly equal, requiring additional convective cooling before the magnetic attraction force exceeds the restoring force, after which the TM material rapidly accelerates toward the magnet.

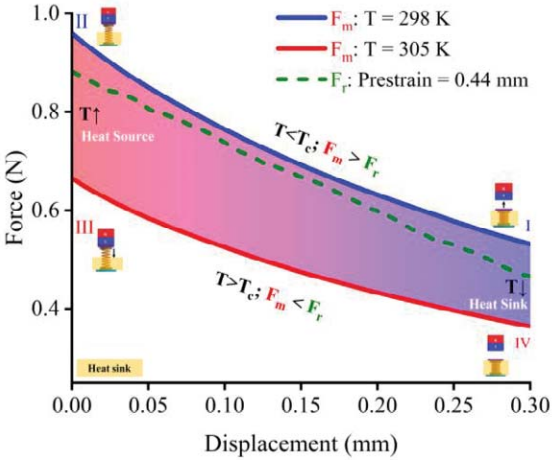


Figure 6. Experimental force-displacement characteristics of TM actuator and restoring spring. The region of temperature-induced force change is highlighted. Legend: F_m (magnetic attraction force), F_r (restoring spring force), T (TM material temperature).

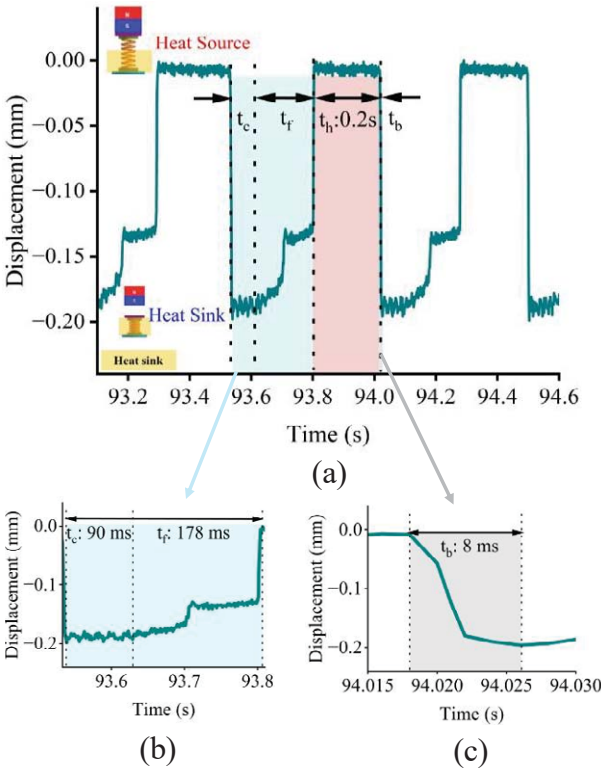


Figure 7. Experimental displacement versus time characteristics of the TM actuator operating in self-sustained actuation mode at the room temperature. The heat source temperature is 305 K. (a) overview, (b) forward motion, (c) backward motion. Legend: t_c (cooling time), t_f (forward-motion time), t_h (heating time), t_b (return time).

 DOI: 10.30420/456743004

A temperature sweep performed on the fabricated TM actuator reveals self-sustained operation within a narrow heat-source temperature interval between 305 K and 309 K, as shown in **Figure 8**. Within this temperature range, the actuation frequency remains nearly constant. At lower heat-source temperatures, longer heating times are required to raise the TM material above the transition temperature T_c, whereas at higher temperatures, increased heat dissipation times are needed during cooling. Beyond 309 K, the TM material stabilizes at a lower equilibrium position, likely due to trapped hot air between the magnet and the TM material, which inhibits sufficient cooling and prevents recovery of the magnetic attraction force required to overcome the restoring spring force.

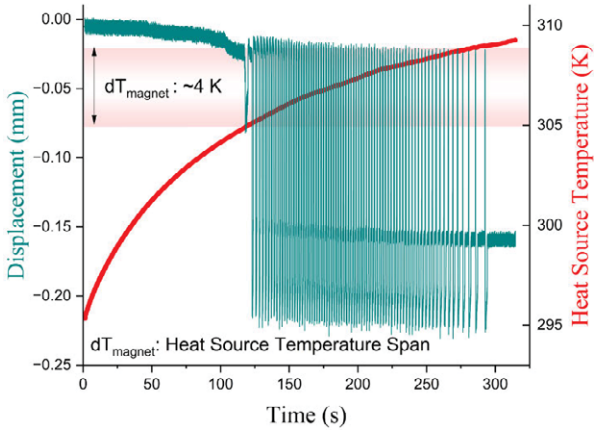


Figure 8 Experimental displacement versus time characteristic of the TM actuator at room temperature recorded during a temperature sweep from 295 K to 309 K indicating the regime of heat source temperature for self-sustained actuation.

The thermal resistance of the bonding layer between the La–Fe–Si plate and the copper support plays a critical role in the heat-transfer dynamics of the actuator and can be adjusted by varying the bonding-layer thickness. This interfacial layer governs the heat flow within the system and therefore strongly influences the thermal response of the TM material. An optimized bonding-layer thickness enables a sufficient temperature change ΔT with minimal heat input during contact with the heat source, while simultaneously promoting efficient heat dissipation during contact with the heat sink [5]. Consequently, tuning the bonding-layer thickness provides an effective approach for adjusting the operating temperature window and dynamic response of the actuator.

5 Conclusion

This work demonstrates the design, fabrication, and experimental characterization of a miniature thermomagnetic actuator capable of self-sustained operation using low-grade heat slightly above room temperature. The actuator utilizes thermally induced magnetization changes in a La–Fe–Si thermomagnetic material combined with a permanent magnetic field to generate cyclic mechanical motion without continuous electrical actuation. Copper electroplating and subsequent surface polishing significantly improved the thermal contact, heat-transfer performance, and mechanical stability of the brittle La–Fe–Si plates. The fabricated actuator prototype achieved stable self-sustained operation at a heat-source temperature of 305 K, generating a displacement amplitude of 200 µm at an actuation frequency of 2.1 Hz.

6 Acknowledgement

The authors gratefully acknowledge the funding provided by the Hector Fellow Academy.

7 Literature

[1] C. Forman, I. Muritala, R. Pardemann, and B. Meyer, “Estimating the global waste heat potential,” *Renewable and Sustainable Energy Reviews*, vol. 57, pp. 1568–1579, May 2016, doi: 10.1016/j.rser.2015.12.192.

[2] D. Dzekan, A. Waske, K. Nielsch, and S. Fähler, “Efficient and affordable thermomagnetic materials for harvesting low grade waste heat,” *APL Mater.*, vol. 9, no. 1, p. 011105, Jan. 2021, doi: 10.1063/5.0033970.

[3] J. Joseph, M. Ohtsuka, H. Miki, and M. Kohl, “Upscaling of Thermomagnetic Generators Based on Heusler Alloy Films,” *Joule*, vol. 4, no. 12, pp. 2718–2732, Dec. 2020, doi: 10.1016/j.joule.2020.10.019.

[4] H. Chen *et al.*, “Enhanced Heat Transfer for Thermomagnetic Generation in Low-grade Waste Heat Harvesting,” *Advanced Materials*, vol. 37, no. 21, p. 2500544, 2025, doi: 10.1002/adma.202500544.

[5] J. Joseph, M. Ohtsuka, H. Miki, and M. Kohl, “Thermal processes of miniature thermomagnetic generators in resonant self-actuation mode,” *iScience*, vol. 25, no. 7, p. 104569, Jul. 2022, doi: 10.1016/j.isci.2022.104569.

 DOI: 10.30420/456743005

Magnetic Fast Steering Mirrors for Tracking and Optical Communication for Defense and Aerospace Industries

Xavier De Lépine, Timotéo Payre, Clément Joseph Galteau, Nabil Bencheikh, Patrick Meneroud, Florian Bonnet, Hugo Grardel, Pierre Personnat, Clément Cote, Guillaume Mansuy, Arnaud Gilson, Frank Claeyssen

Cedrat Technologies, 59 Chemin du Vieux Chêne, 38240 Meylan (France)
Email: xavier.de.lepine@cedrat-tec.com

Abstract

Defense tracking or Space Communication applications rely on energy efficient and high precision control solutions where compactness, integration, reliability and robustness in severe conditions are critical. In order to cope with performances of Fine & Fast Pointing and Point Ahead Mechanism requirements for Defense or Space applications, CEDRAT TECHNOLOGIES (CTEC) is continuously improving its Magnetic Fast Steering Mirror products (M-FSM45 and M-FSM62) [1-3], based on proprietary MICA™ flexure bearing magnetic actuators mechanism (Moving Iron Controllable Actuator), with embedded eddy current sensors (ECS) for high controllability capacity. Thanks to its heritage and many years of experience in Magnetic Fast Steering Mirror (M-FSM) technologies, CTEC has developed new versions of the M-FSM62 and M-FSM45 through several Defense and Space R&D projects. These include a Defense project focused on InfraRed Search and Track (IRST) functions embedded on aircraft, as well as the Spanish QKD GEO project (demonstration of a Quantum Key Distribution system embarked on a geostationary satellite) and the SOLIS project (secured optical communications services relying on geostationary satellites). These new developments achieve higher performances than current products available on the market.

1 State of the art

High-performance M-FSM technology from CEDRAT TECHNOLOGIES (CTEC) is primarily based on variable reluctance magnetic circuits with magnetic preload obtained using permanent magnets (**Figure 1**). This approach allows for intense magnetic forces while maintaining a large overall stroke and linearity between the magnetic force and the driving current.



Figure 1 M-FSM concept

These actuators are powered with the MCLA18, which are current amplifiers, able to drive both axes simultaneously with the on-board controller (**Figure 2**). These amplifiers are capable of processing signals from the acquisition chain, which consists of the position sensor probes embedded in the mechanism (ECP) and the signal conditioner (ECS25). For improved resolution, a pre-conditioner, either integrated or external, can be added.
The control strategies applied to these systems are mainly based on state feedback in order to control the first natural mode of the mechanism and thus achieve high bandwidth for tracking control (**Figure 3**). Initial M-FSMs have been developed to cover needs for space optical communication



links, especially feeder links [1-3]. Presently, this application has reached high TRL and other application fields are emerging thanks to improvements.

Figure 2 M-FSM with electronics from CTEC

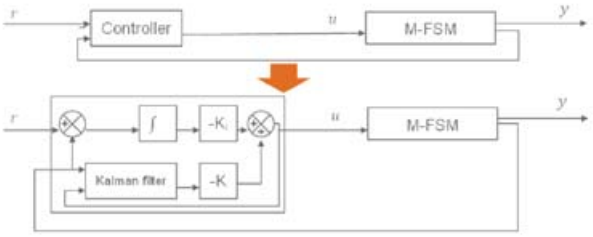


Figure 3 M-FSM state feedback control

These new fields include other space applications, such as intersatellite links (OISL), and Defense, such IRST.
These applications have generated recent developments presented in this paper, to incorporate additional features

 DOI: 10.30420/456743005

such as: robustness to demanding vibrational environments, infinite service life, redundancy in the power supply of the mechanism, improved integrated position sensors, and thermal draining between the mirror and the "thermal sink".

2 M-FSM for Defense

2.1 Application & challenges

The Infrared Search and Track (IRST) system passively scans wide areas to detect and track objects that emit infrared radiation. To achieve a large field of view, some imaging systems use tilting mirrors to sweep the scene. However, mirror motion during image acquisition can generate a blurred image and cause loss of information while the sensor transfers data to the control system. By implementing a CTEC back scanning solution based on a secondary piezoelectric or magnetic fine and fast steering mirror (M-FSM), the system compensates for the primary mirror motion, ensuring a stable image on the detector and continuous scene coverage for high-quality imaging (**Figure 4**).

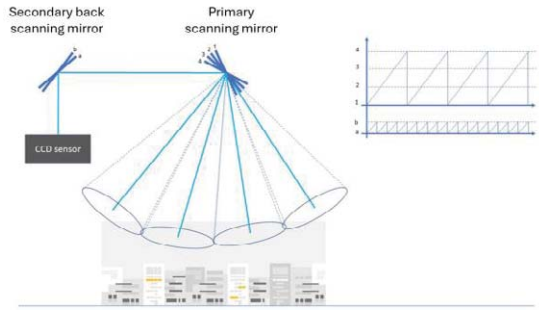


Figure 4 Working principle of an IRST

The back scanning mirror (M-FSM) will move continuously during an image acquisition, to make sure a fixed image is reaching the sensor. After the acquisition and the image transfer, the mirror will move to the next position, to ensure the continuity of the combined image (**Figure 5**).
The function of the M-FSM lies in its ability to precisely compensate for the scanning speed of the first mirror, thereby ensuring a stationary image in front of the sensor. The acquisition time is typically few milliseconds. Reducing the timing difference between these two mirrors has a direct impact on image sharpness.

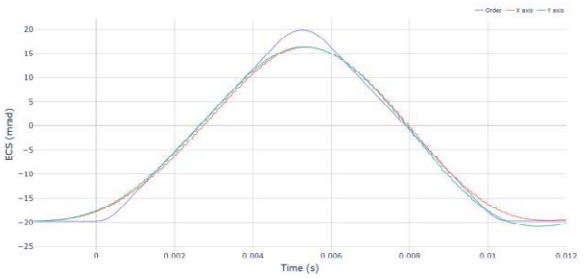


Figure 5 Triangle reference tracking

2.2 M-FSM62 design improvements

The M-FSM62 has benefited of improvements in 4 key areas: sensors, vibration resistance, stroke and mirror.

1. Position sensors are proprietary Eddy Current Sensor (ECS) for CTEC. This technology relies on the phenomenon of eddy currents, which develop in conductive materials when subjected to a time-varying magnetic field. The measurement principle is based on the variation in inductance due to the changing distance between the source and the target. In the M-FSM, the sources are PCB-based Eddy Current Probes, fixed on to the structure. The targets are Aluminum parts fixed on the mirror support, and so they are moving like the mirror.
In former configuration, the sensor conditioning was done in a distant electronic conditioner (**Figure 6**).

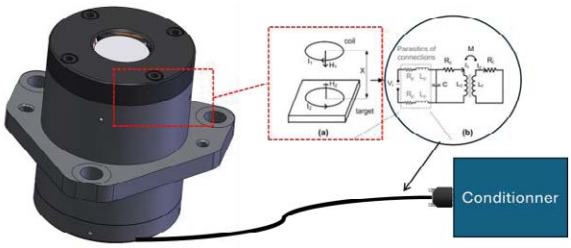


Figure 6 M-FSM Solution without prox

However, the cable carrying the signal also has varying inductance (and capacitance) as well as a sensitivity to external EM perturbations; Both these effects can interfere with the measurement. Therefore, it becomes desirable to add a device that isolates the probe (ECP) from the cable, thus eliminating the cable's influence on the measured signal.
This device is called proximity sensor electronics, or simply "prox". It can be mounted externally or integrated into the mechanism (**Figure 7**).
For the M-FSM62, such an integrated solution was developed, laboratory-tested, and delivered to a customer in defense.

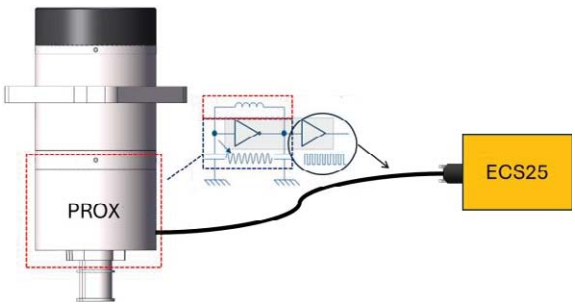


Figure 7 M-FSM Solution with prox

2. Stiffness in magnetic systems is lower compared to piezoelectric solutions. Therefore, it is necessary to have a system that ensures the mechanism's survival during rocket

DOI: 10.30420/456743005

launch. A mechanism stop system similar to the one developed for the M-FSM45 within the COOP space project has been integrated into the M-FSM62. This system has also been mechanically improved to facilitate its integration and reduce recurrent cost.

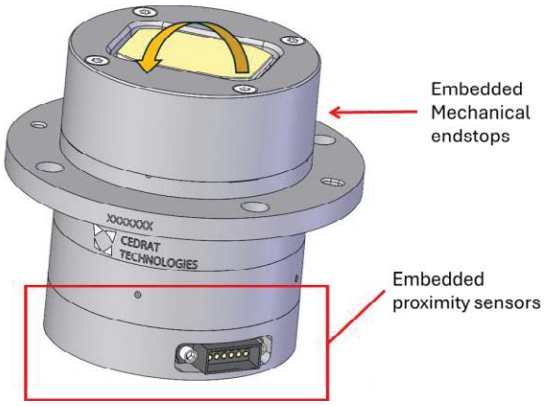


Figure 8 Main features of M-FSM62S model

3. Furthermore, the magnetic circuit was optimized to increase the overall stroke of the moving part at an equivalent level of consumption. Finally, open loop mechanical angular strokes as large as ~120mrad ie ~ 7° pk-pk are achieved (**Figure 9**) on both axis with currents below 1A.

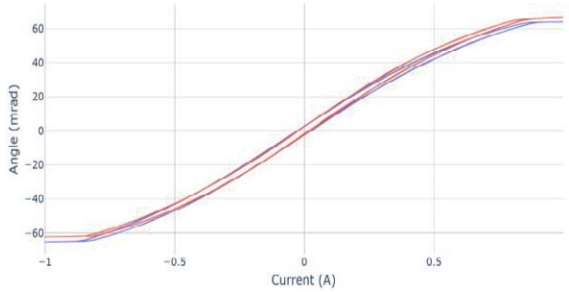


Figure 9 Strokes of M-FSM62 both axis (7° pk-pk)

4. At last, a mirror dedicated to the IRST application has been integrated, implying design changes in the mirror support. This mirror is a high-reflectivity gold-coated mirror with a 35x25mm² rectangular shape (**Figure 10**). Its flatness is λ/50rms.

2.3 Specific driving electronic development

To meet the compactness requirements inherent in defence applications, a specific version of the electronic equipment was developed for the M-FSM62.
The coil power supply function (MCLA18) was merged with the sensor conditioning function (ECS25) into a common package called the MLC72 (Magnetic Linear Controller 72W).
This new power supply package was optimized for triangular profile tracking applications, typically associated with scanning.
Furthermore, to best meet defence requirements, this enclosure includes:
- Amphenol TV07RW-XX type MIL-grade connectors.
- a waterproof housing, IP66/67 rated
- mechanical and electronic design sized to remain functional in demanding vibration environments

Final performance of the electronics is given in **Table 1**.



Figure 10 M-FSM62 + MLC72 system for IRST

Parameter	MLC72
Standalone drive electronics	Power board, sensor conditioners, and control board all in one single box
Dimensions	≤300 x 120 x 55 mm including connectors
Sealing	IP66/67
EMI/EMC Sealing	Yes
Sealed connectors	ML-38999 connector type
Power Supply	24 VDC
Interfaces	I. Interface for configuration: RS422 /RS232 II. Interface for command: Digital
Motion Pattern of the FSM	Triangle
Cable length	≥ 0.5 m

Table 1 MLC72 electronics performance

2.4 Control improvement

Eddy current sensor technology relies on measuring the inductance between the target and the excitation coil. However, the function relating these two quantities is not linear. To ensure control of the mechanism, it is necessary to identify an interpolation function that linearizes the actual travel of the moving part of the mechanism and the signal used by the controller.
In the case of mechanisms with a very large angular travel, such as that of the M-FSM62, the accuracy achievable with this method is limited. Indeed, the method of linking the angular travel to the output signal of sensor pairs does not allow for isolating the portion of the movement related to the pumping motion of the mirror (**Figure 11**).

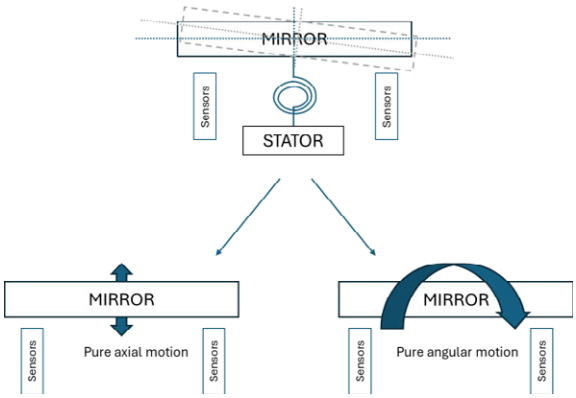


Figure 11 Decomposition of mirror motion

 DOI: 10.30420/456743005

Therefore, a specific processing method was developed to decouple the angular and axial movements of the mirror, thus improving accuracy by a factor of about 6.

While the initial average angular error was in the range of 1mrad, the final average angular error after processing is about 0.15mrad, so about 0.1% FS (**Figure 12)**. This improvement has an immediate effect on the quality of the associated control, particularly for triangular tracking.

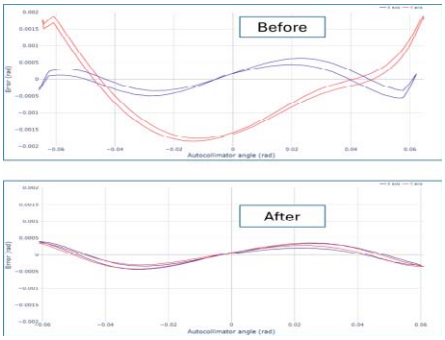


Figure 12 Angular error before and after processing

2.5 Synthesis of performances

The comparative performance between the different M-FSM models for CTEC is presented in **Table 2**.

Property/Device	M-FSM45S	M-FSM45D-SE	M-FSM62S-SE
Mecha. Stroke [mrad]	±26	±40	±60
Resonance Freq [Hz]	100	70 to 97	85
Vibration end stops	No	Yes	Yes
Mirror power drain	No	Yes	No
Size [mm^3] w/o flange	Ø45x40	Ø45x58	Ø62x75
Weight [g]	195	380	650
Inductance [mH]	20	30	35
Resistance [Ohm]	8	10	16
Redundancy	No	Yes (actuation coils)	No
Control Bandwidth [Hz]	150	100	120
Accuracy [%FS]	0.05	0.03	0.02
Resolution [urad]	0.05%FS	0.03%FS	0.01%FS
Voltage Range [V]	±28	±36	±36
Current Range [A]	±1	±1	±1
Sensor	No prox	No prox	Prox embedded
Driver	MCLA18	MCLA18	MLC72
Mirror Outer Diameter [mm]	Ø17 mm	Ø16.2mm	35mm x 25mm (rect.)

Table 2 Performance of M-FSM45S, M-FSM45D-SE and M-FSM62-SE

In this table, the ***-SE** stands for Severe Environment, it means that the associated models are designed to withstand challenging environmental conditions, such as vibrations, large temperature span, and so on. The mirror power drain stands for the feature of the mechanism that allows the power from laser to be extracted from the mirror surface to prevent overheat.

3 M-FSM for Space Satcom

3.1 Application & challenges

Fast steering mirrors are a critical enabling technology in space optical communications, where they provide high-bandwidth, fine angular correction to maintain precise beam alignment over long distances. They are widely used in OISL inter-satellite links (LEO constellation), ground-to-space optical feeder links (GEO sat) (**Figure 13**) and even deep-space communication terminals as done by CTEC for PSYCHE [4], supporting the growing demand for high-data-rate, low-latency connectivity.

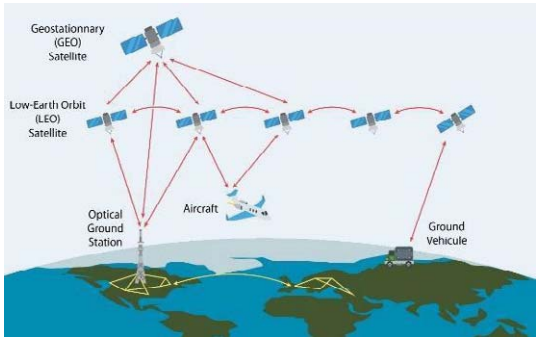


Figure 13 Optical communication links implying satellites

However, their deployment presents several challenges: achieving sub-microradian accuracy under strict size, weight, and power (SWaP) constraints; ensuring robustness against launch loads and long-term space environment effects (thermal cycling, radiation); maintaining high bandwidth to mitigate platform jitters and atmospheric disturbances.
Additionally, the integration of FSMs within complex Pointing, Acquisition, and Tracking (PAT) systems requires advanced control strategies and precise opto-mechanical design to balance speed, stability and reliability.
To address these needs, CTEC has developed piezoelectric FSM. Series of Flight Models (FM) of DTT35XS and P-FSM150S have been delivered for OISL constellations [5]. Such products are mature. But their mechanical stroke limited to 20mrad is not enough for several markets.

To cover needs of FSM requiring larger strokes, CTEC has developed M-FSM45 [1-3]. CTEC M-FSM45 are today selected for both beam stabilization and point ahead control for Quantum Key Distribution, for feeder links from space to earth communications, or for optical communication between satellites (OISL).
For example, M-FSM45D Flight Models (FM) are manufactured (**Figure 14)** for Spanish QKD GEO optical link developed by Thales Alenia Space [6,7]. This hosted payload onboard a GEO sat aims to demonstrate of a Quantum Key Distribution between two ground stations using a GEO satellite.

 DOI: 10.30420/456743005

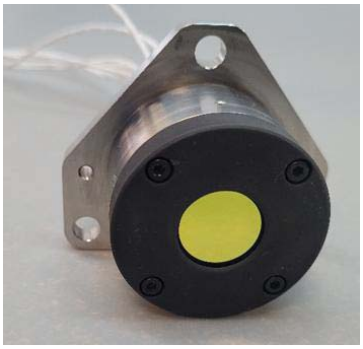


Figure 14 M-FSM45D delivered to Thales Alenia Space

M-FSM45 is also selected for the SOLiS space project led by Thales Alenia Space [8] (**Figure 15**) under CNES contract. SOLIS stands for *Service Optique de Liaisons Spatiales Sécurisées* (Secure optical space link service). Such a service is designed to make intercontinental networks more resilient at a time. Geostationary satellites offer an effective solution for ultra-secure transfers of large amounts with very high data rates of up to one terabit per second.
SOLiS payload will be flown on the Hellas Sat 5 geostationary communications satellite, while the pilot ground station will be set up at the operator's teleport in Cyprus. This station will communicate with CNES's FROGS station already operating at the Côte d'Azur Observatory on the Mediterranean coast.



Figure 15 SOLiS © Thales Alenia Space

3.2 Technical improvements

SOLiS optical terminal requires 2 M-FSM45: one Fast Steering Mirror for the beam stabilisation and one Fine Steering Mirror, for the PAM (Point Head Mechanism) function. Since the COOP M-FSM45 version, significant improvements have been made to address SOLiS needs, leading to a new product definition (**Figure 15**):

- Mirror integration in the final stage of FSM assembly.

Efforts have been made to allow mirror integration in the last stages of assembly. This approach provides better protection for the mirror, which is the most expensive part of the device, and also allows for delayed differentiation based on the application. This new version of the mechanism offers a more industrial solution, better suited to customer needs.

- Improved ECS sensor

A key element of the ECS position sensor is the magnetic surface shared between the ECP (that generates the alternate magnetic field) and the target, which is fixed to the moving part. This has a direct impact on the quality of the detection function, as it directly affects the accuracy of the mechanism's pointing during operation. The larger the target, the better the resolution.

Although considered yet as an option, a Prox condition electronics is also considered. This would lead to a higher resolution especially useful for PAM. This option will exploit experience gained by CTEC in ECS sensors and electronics for LISA BAM space piezoelectric motors [9]. The target is a resolution below ±6µrad (0.01%FS).

- Optical wavefront error (WFE)

The optical quality of the mechanism is closely linked to the mirror's deformation during the whole product life (ground tests, launching, in-orbit use). Indeed, excessive mirror deformation induces distortion of the optical signal to be oriented. CTEC's proposal combines a screw-mounted mirror adapted to space applications with mechanical isolation of the mirror from the magnetic moving part. This solution ensures minimal deformation throughout the entire stroke and over wide temperature ranges. The target was a WFE < 20nm on 16.2mm Clear Aperture for a power laser > 100W.

- Parallelism between mirror and FSM interface

CTEC has developed an assembly and fine-tuning methodology that ensures optimized parallelism of the mirror with the zero-current mounting interface. This approach minimizes the alignment efforts required when installing the mechanism on the customer's optical bench. This method guarantees that the angular error between the mirror and the interface shall be below 0.5mrad.

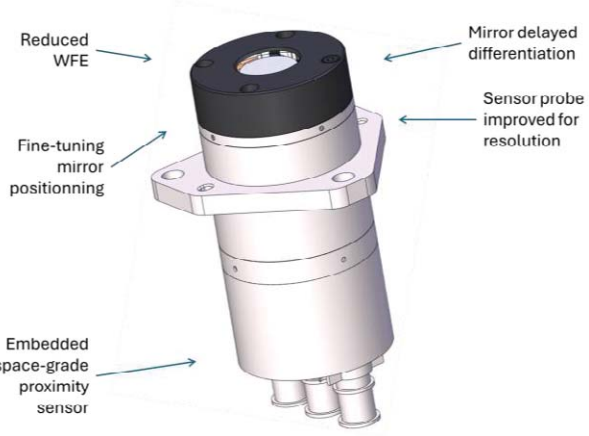


Figure 16 SOLiS M-FSM45-HPL new features

 DOI: 10.30420/456743005

3.3 New space applications

In the context of New Space and the rapid expansion of OISL on LEO constellations, fast steering mirrors must evolve toward highly compact, low-SWaP architectures while maintaining the precision and bandwidth required for stable optical links. These systems enable high-throughput inter-satellite communications across dense networks, where terminals must be replicated at scale and operate with stringent cost and power constraints. Key challenges include achieving sub-microradian pointing performance with miniaturized actuators and control electronics, ensuring low power consumption without sacrificing dynamic response, and designing manufacturability and scalability in high-volume production.

For cases where stroke of Piezo FSM [5] is not enough, Magnetic FSM should be considered. This is the case for example in IRIS² EU constellation, involving 300 satellites on multiple orbits (**Figure 16**).

In this context, CTEC is currently assessing a cost-optimized M-FSM45 solution with a lifetime tailored to LEO constellation requirements, designed for production at significantly higher volumes than those of traditional space-grade systems.

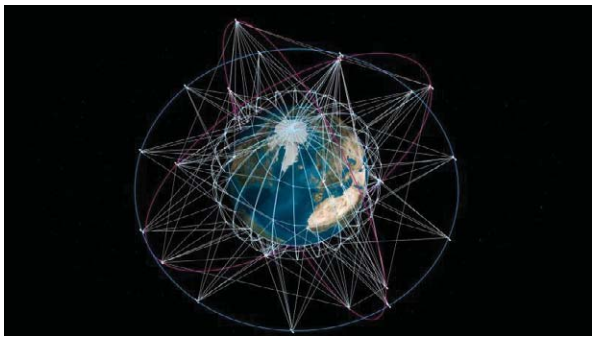


Figure 16 EU constellation IRIS² © Thales Alenia Space

4 Conclusion

Recent developments in the M-FSM mechanisms by CEDRAT TECHNOLOGIES demonstrate the ability of magnetic solutions to meet the growing demands of defense and space applications. The M-FSM62 significantly improves the performance of IRST systems, and the M-FSM45 has established itself as a key solution for high-speed optical communications in space (Quantum Key Distribution, Optical Feeder link & OISL).

Thanks to significant improvements in sensors, control electronics, mechanical robustness, and dynamic performance, these systems now offer an optimal balance between accuracy, bandwidth, compactness, low power and reliability in harsh environments.

5 Acknowledgment

The authors are grateful for the support of THALES ALENIA SPACE, CNES and the French state in France 2030. Initial works on M-FSM for defense have been funded by BPI France in CLEOPATRE project.

Last works on M-FSM for space have been funded by France2030 in SOLiS project.

The Spanish GEO QKD Project is an initiative of the State Secretariat for Telecommunications and Digital Infrastructure of Spain, managed by the CDTI (Center for Technological Development and Innovation), and financed with EU recovery funds through the PERTE Aeroespacial.

6 Literature

[1] F. Claeyssen, et al, Large-Stroke Fast Steering Mirror for Space Free-Space Optical communication, Proc Conf. OPTRO 2020, Paris France, 28-30 January 2020

[2] G. Aigouy, Piezoelectric and Magnetic Fast Steering Mirrors for Space Optical Communication, Proc. ICSO 2022

[3] E. Betsch, Magnetic Fast Steering Mirror for Inter-satellites and Feeder Link Optical Communication, Proc. ACTUATOR 2024

[4] A. Guignabert, et al, Point Ahead Mechanism for Deep Space Optical Communication – Development of a new Piezo-Optical Tip-tilt mechanism, AMS 45th, Houston Texas USA, 13-15 May 2020

[5] F. Claeyssen, et al, Piezoelectric Fine Steering Mirrors and electronics for Optical Inter-Satellite Links, #151 Proc ACTUATOR 2026

[6] A. Alvaro et al, GARBO QKD GEO: challenges and architecture, ICSO 2024, Antibes Juan-les-Pins, France, SPIE Conf Proc. 2025

[7] https://www.thalesaleniaspace.com/en/press-releases/thales-alenia-space-and-hispasat-start-development-worlds-first-quantum-key

[8] https://www.thalesaleniaspace.com/en/press-releases/thales-alenia-space-develop-solis-very-high-throughput-laser-communications

[9] J. Rebufa, et al High-resolution Rotating Piezo Motors for LISA Large Interferometer Space Antenna, #144 Proc ACTUATOR 2026

 DOI: 10.30420/456743006

Shape Memory Alloy drives for micro-electronical actuator systems

Andreas Erben[1], Daniel Hoffmann[2], Kenny Pagel[1],Sven Spieth[2], Alexander Jähnigen[2], Welf-Guntram Drossel[1], Alfons Dehé[2]
[1] Fraunhofer Institute for Machine Tools and Forming Technology IWU, Dresden, Germany
[2] Hahn-Schickard Gesellschaft, Villingen-Schwenningen, Germany
Andreas.Erben@iwu.fraunhofer.de

Abstract

This publication presents the results of the development of a micro-electro-mechanical systems (MEMS) based actuator system driven by shape memory wire. The drive concept is used to switch on a mechanical cycle counter when a target counting temperature is exceeded. The actuator systems were examined regarding the design of the actuator spring system, the reproducibility of the travel, the degradation behaviour, and the reliability of the counting function. For this purpose, test structures with different spring geometries were examined in combination with different semi-finished wire products. In addition, actuator spring systems were cyclically heated on heating plates and examined. The results show that the integration of standard wire components into MEMS structures is possible and offers great potential for high-performance actuators with high travel in MEMS.

1 Introduction

Drive concepts for silicon-based microelectromechanical systems (MEMS) have so far been based mainly on piezo-resistive and capacitive motion systems. However, these types of motion systems are not freely scalable and require high electrical voltages and large installation space with short travel distances. In contrast, shape memory alloy (SMA) wires are known and valued in applications such as smartphone camera adjustment and valves [1] due to the low electrical voltage required (< 3 V) and the high travel distances and forces at wire diameters below < 100 µm. Initial fundamental research into embedding SMA wires in MEMS was conducted in the AuSter project and indicates the high potential of heterogeneous integration [2,3].
The research activity forms the basis for the use of form-fit embedded SMA actuators in etched silicon structures. The focus of the investigation was on 76 µm wires from different manufacturers and one 100 µm alloy for comparison. To characterize the SMA-actuators, different silicon structures were manufactured and then characterized. Finally, complete actuator systems with counting structures were set up to investigate their reliability in the application.

2 Experimental

The design of SMA actuators is based on the stress-strain diagram for tension-loaded actuators. However, multi-axial stresses occur in bending actuators, meaning that the existing stress-strain diagrams can only be used to a very limited extent for the design. Against this background, a systematic investigation was carried out with a large number of test chips, which were manufactured by the Hahn Schickard Institute in Villingen-Schwenningen. The spring stiffness was varied from 400 to 1000 N/m. Furthermore, the length of the movable shuttles was varied in order to provide the bend-formed FGL actuators with different preloads.
The 76 µm and 100 µm Smart Flex wire and the 76 mm CleanMelt wire from SEAS Getters were examined, as well as the 76 µm NiTi#6 wire from FortWayne.

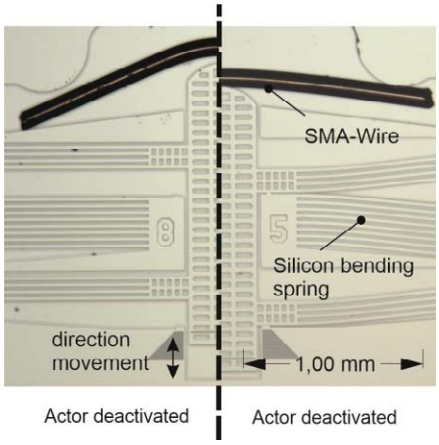


Figure 1: Test spring structure with SMA-wire

3 Results and Discussion

3.1 Stroke as a function of spring stiffness

The measurement curves for the two wire materials CleanMelt and SmartFlex 76 µm are shown in Figure 2. On the one hand, the curves show that the silicon springs are unable to return the CleanMelt wire completely to the zero position, with the position changing as the stiffness increases, while the SmartFlex wire reaches the zero position regardless of the spring stiffness. This results from the intrinsic two-way effect, which is particularly pronounced in SmartFlex wire and causes the wire to lie powerless in the recess in the shuttle after cooling, whereas in CleanMelt wire, the actuator spring system remains under preload. The resulting travel distances also differ depending on the alloy.

 DOI: 10.30420/456743006

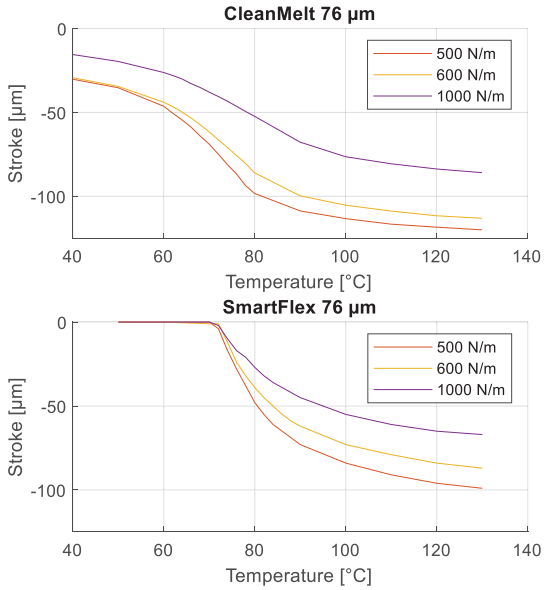


Figure 2: Measurement of SMA actuators against different springs

3.2 Measurement of the silicon Springs

To fully characterize the actuator system, test spring structures were also measured. The tensile-compression module from Kammrath und Weiss was used for this purpose. The measurements (Figure 3) show a systematic deviation of the measured stiffness in relation to the calculated stiffness. These deviations may result from the different etching speeds between transverse and deep etching, so that the bending springs do not have a rectangular cross-section but a trapezoidal cross-section.

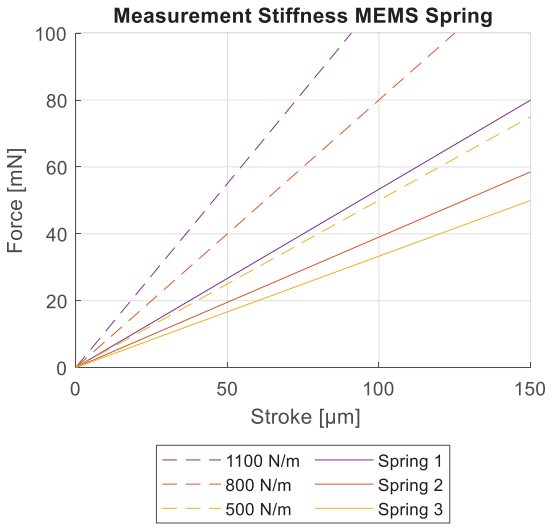


Figure 3: Measurement of the Spring-Stiffness

3.3 Design of the overall system

Based on the results of the characterization of the wire spring systems, the silicon counter and the SMA drive were combined at the end. The counter consists of two gears, one with 100 teeth and one with 99 teeth, enabling it to count up to 9900 cycles. The cycle counter is shown with a parallel design, whereby each gear is driven individually by the shuttle. This Test-MEMS was successfully tested for up to 1000 cycles, with the counter miscounting by 2 cycles. Possible causes for counting errors include tolerances and the bearing play of the gears, which changes during a revolution.

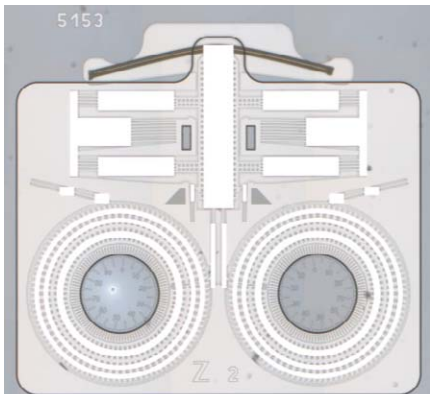


Figure 4: Cycle Counter with SMA-Wire

4 Summary

The investigations show that the high actuator potential of SMA actuators can also be applied at the MEMS level. Cost-effective semi-finished wire products can be used for this purpose, but direct design of the actuator systems based on classic stress-strain diagrams without prior investigations is only possible to a limited extent.

Acknowledgement

The described results were discovered in the project 23003 BG “Prozesstechnologien für die heterogene Integration von Formgedächtnislegierungen am Beispiel eines autonomen Sterilisationszyklenzählers (ProAuSter) " - supported via the German Federation of Industrial Research Associations (AiF) within the program for promoting the Industrial Collective Research (IGF) of the German Ministry of Economic Affairs and Energy (BMWE) based on a resolution of the German Parliament.

5 Literature

[1] https://www.actuatorsolutions.de/products/pneumatics-and-fluidics/3-3-module-as8p/ (14.02.2024)

[2] Daniel Hoffmann et al., Hybrid Integration of A Shape Memory Alloy Actuator For Micro Thermal Mechanical Systems, https://doi.org/10.1109/MEMS51670.2022.9699649

[3] K. Pagel; Daniel Hoffmann et al., “Development of a shape memory alloy actuator for a micromechanical sterilization cycle counter”, SMASIS2020. http://dx.doi.org/10.1115/SMASIS2020-2242

 DOI: 10.30420/456743007

Tailoring the spatial thickness distribution of a membrane using 3D printing for enhanced operation as a dielectric elastomer actuator

Andreas Hubracht[a], Bingzhi Wang[a], Chen Jiao[b], Ashwani Sharan Tripathi[b], Uwe Marschner[b], Andreas Richter[b], E.-F. Markus Vorrath[b], and Jürgen Maas[a]
[a]Mechatronic Systems Lab, Technische Universität Berlin, Hardenbergstraße 36, D-10623 Berlin
[b]Institute of Semiconductors and Microsystems, Technische Universität Dresden, Nöthnitzer Str. 64, D-01062 Dresden

Abstract

Dielectric elastomer transducers (DET) consist of a flexible dielectric sandwiched between two compliant conductive electrodes. When electrical voltage is applied electrostatic attraction compresses the dielectric. In addition to a number of advantages compared to conventional actuators, the manufacturing remains an ongoing challenge. Besides the possibility of using prefabricated elastomer films it is also possible to use liquid polymers as raw material and process them using a 3D printing system. The elastomer layers can be produced in variable shapes and thicknesses, which increases flexibility but poses particular challenges due to the µm-scale. This contribution presents a model-based approach for designing balloon-shaped dielectric elastomer membranes with a spatially varying initial layer thickness. The objective is to obtain a constant thickness in a defined deformed operating state. Based on a membrane model, an iterative procedure is used to calculate the required initial thickness profile to achieve a prescribed target thickness. The resulting profile is then realized by a 3D printing system, where the local material deposition is controlled through the strand space of an adapted spiral printing path. The results demonstrate the potential of 3D printing a DET membrane with spatially varying thickness for improved actuator performance, which can be used to realize multi-actuator configurations in the DFG project CALMAR.

1 Introduction

Dielectric elastomer transducers (DETs) are investigated in a wide variety of shapes, sizes, and applications. They simply consist of a soft dielectric layer sandwiched between two stretchable electrodes. The charge separation caused by applying electrical voltage generates electrostatic pressure. The dielectric is compressed, and this electromechanical coupling enables DETs to operate as actuators, sensors, or generators. [1]

In addition to their comparatively simple structure, there are further advantages, such as low weight and the intrinsic self-sensing property. This leads to a variety of configurations, including multilayer stacked transducers, foldable or rolled DETs, and minimum-energy structures. The applications are manifold, ranging from various types of grippers, to walking, flying, or swimming robots, and even human-machine interactions such as tactile displays. [2]

Large displacements have been generated using pneumatically inflated membranes, which in some cases even exhibited so-called snap-through behavior [3]. This type of deformation (see Figure 1 a) has already been described in detail analytically [3], but has been further developed thereafter [4] and in recent years [5]. This demonstrates that this type of DE transducer remains relevant, even though no snap-through behavior was observed for silicone materials [6]. One challenge with DET is still the handling of very thin layers in the low micrometer range, particularly during manufacturing. An idea is to take advantage of the benefits offered by certain manufacturing processes. The 3D printing technology for example has the ability to produce layers of varying thicknesses [7]. The idea of adjusting the DE structure using e.g., pre-stretch, or stiffeners is not entirely new [8]. Other examples of optimizing a configuration are using a spring-roll DE actuator or a com-

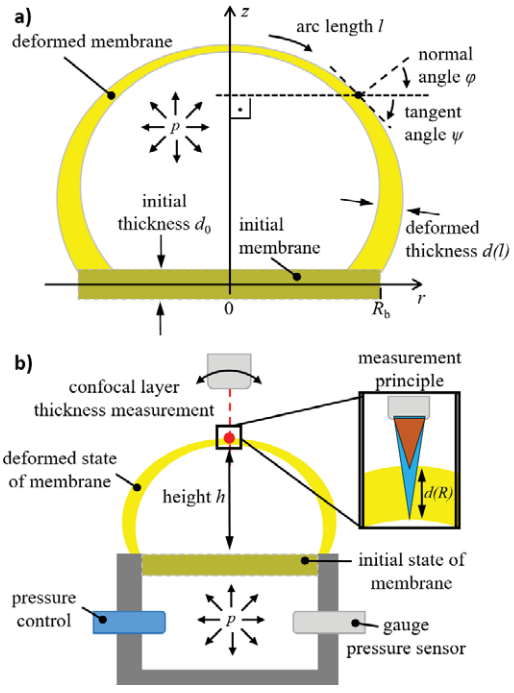


Figure 1 Schematic and measurement principle for balloon-shaped DET: a) geometrical variables and b) measurement setup and operation principle.

 DOI: 10.30420/456743007

pressed polymer core to enhance actuation [9, 10].
Since no uniform decrease in thickness is observed across the membrane during deformation (see Figure 2 c), this paper proposes a new approach based on varying the initial layer thickness. The goal is to achieve a constant thickness in the deformed state. A major advantage of this approach is the resulting electric field, which remains constant across the entire deformed surface.
The paper is divided into three parts. Section 2 describes the model of the deformation and a a design approach to find the initial thickness with a varying thickness profile based on a prescribed constant thickness in the deformed state. Section 3 presents the manufacturing process of a membrane using a 3D printer and the approach for getting a spatially varying layer thickness. Section 4 analyzes the layer thickness measurements of the fabricated membrane and uses simulation-based methods to motivate the potential of an adaptive initial layer thickness.

2 Modeling and design approach

In order to determine the initial film thickness required to achieve the target thickness in the deformed state, a model of the membrane is needed. Before deriving the model, the configuration of the DE-membrane is introduced.

2.1 DE balloon configuration

Figure 1 b) schematically shows the membrane clamped at its circular edge in the initial state (dark yellow) and in the deformed state (light yellow). In addition to pressure controller and sensor, the figure specifically illustrates the operating principle of the optical sensor used for measuring the film thickness. This sensor measures the thickness of a transparent film by detecting the reflections from the front and back surfaces and converting them into a thickness using the material's refractive index. The pressure p refers to the gauge pressure relative to atmospheric pressure. Due to the pressure p, the membrane bulges by a height h at its center (apex). Since this paper focuses primarily on the design of the DE membrane, the electrodes are not depicted.

2.2 Modeling of balloon-shaped DEA membrane

A wide range of models is available for DET membranes. One approach suitable for membranes was presented by Li et al. (2013). For commonly used models, a deformation assumption such as equibiaxial or planar must be made. This is not the case for the model of Li et al. (2013), which makes it particularly interesting for the large deformations occurring in the given configuration. Here, the focus is on necessary modifications due to the no longer constant initial layer thickness (for details, refer to [3]).
The deformation of the membrane can be described by the following state variables:

$$\mathbf{y}(R) = \left[r(R),\ z(R),\ \psi(R),\ \lambda_\theta(R)\right]^{\mathrm{T}}, \tag{1}$$

where $r(R)$ and $z(R)$ are the positions in the deformed state, ψ is the tangent angle, and λ_θ is the meridional stretch.

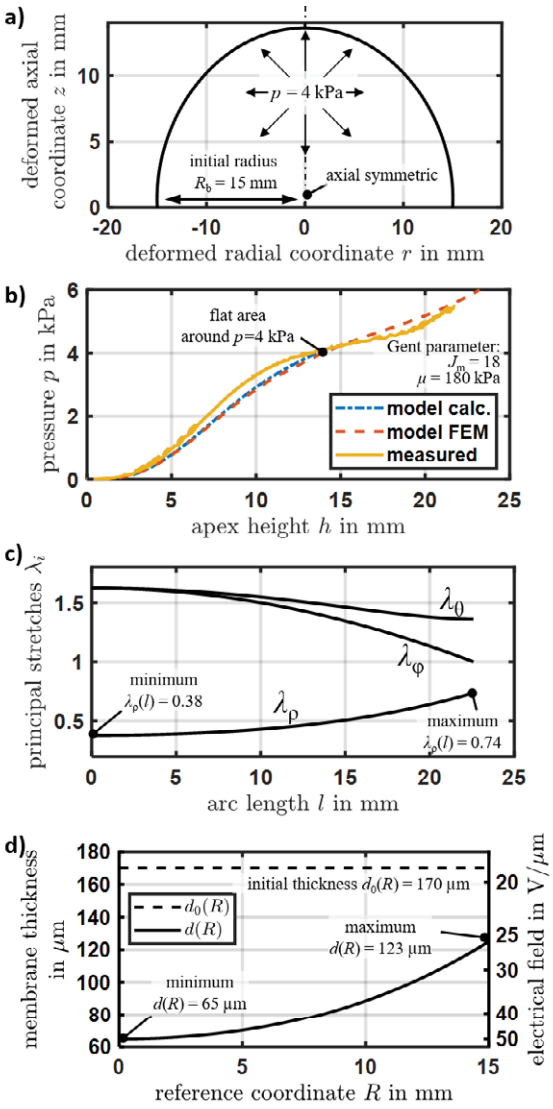


Figure 2 Deformation of an elastomer membrane with constant initial layer thickness: a) deformed membrane, b) measured vs. calculated pressure-displacement behavior, c) stretches, and d) layer thickness in deformed state.

The other two principal stretches are the circumference stretch λ_ϕ and the stretch in the thickness direction λ_ρ:

$$\lambda_\phi(R) = \frac{r(R)}{R}, \qquad \lambda_\rho(R) = \frac{1}{\lambda_\theta(R)\lambda_\phi(R)}. \tag{2}$$

Because of large strains the Gent model [11] is used. It is described by two parameters: the ground-state shear modulus μ and the extension limit parameter J_m.
The membrane stress resultants in the meridional and circumferential directions are:

$$N_\theta = d(R)\,\frac{\mu}{Q}\left(\lambda_\theta^2\lambda_\phi - \frac{1}{\lambda_\theta^2\lambda_\phi}\right), \tag{3}$$

$$N_\phi = d(R)\,\frac{\mu}{Q}\left(\lambda_\theta\lambda_\phi^2 - \frac{1}{\lambda_\theta\lambda_\phi^2}\right), \tag{4}$$

 DOI: 10.30420/456743007

$$\text{with} \quad Q = 1 - \frac{1}{J_m}\left(\lambda_\theta^2 + \lambda_\phi^2 + \frac{1}{\lambda_\theta^2\lambda_\phi^2} - 3\right). \tag{5}$$

As already mentioned, no assumptions (except incompressibility $\lambda_\theta\lambda_\phi\lambda_\rho = 1$) are made regarding the deformation. Using this notation with $d(R)$ as thickness in the deformed state, three cases can occur:

1. constant initial layer thickness: $d(R) = \frac{d_0}{\lambda_\theta\lambda_\phi}$,
2. constant target thickness: $d(R) = \tilde{d}$, and
3. general case: $d(R) = \frac{d_0(R)}{\lambda_\theta\lambda_\phi}$.

The first case corresponds to the usual formulation with constant initial thickness also used in Li et al. (2013). The second case is used in the present work and prescribes a constant thickness in the deformed state. The third case represents the more general formulation with a prescribed, spatially varying initial thickness.
The kinematic relations of the membrane implies:

$$r' = \lambda_\theta \cos\psi,\ z' = \lambda_\theta \sin\psi,\ \lambda_\phi' = \frac{\lambda_\theta\cos\psi - \lambda_\phi}{R}, \tag{6}$$

where $z' = \frac{dz}{dR}$, $r' = \frac{dr}{dR}$, and $\lambda_\phi' = \frac{d\lambda_\phi}{dR}$.

Using the equilibrium in normal direction, consisting of the change of the tangent angle ψ' balancing the pressure p and the circumferential force N_ϕ, it holds:

$$\psi' = \frac{p\,r\,\lambda_\theta - N_\phi \sin\psi}{R N_\theta}. \tag{7}$$

From the tangential equilibrium, the meridional stretch λ_θ can be derived using the membrane force $N_\theta(R, \lambda_\theta, \lambda_\phi)$:

$$\lambda_\theta' = \frac{\frac{N_\phi\cos\psi - N_\theta}{R} - \frac{\partial N_\theta}{\partial \lambda_\phi}\frac{\lambda_\theta\cos\psi - \lambda_\phi}{R} - \frac{\partial N_\theta}{\partial R}}{\frac{\partial N_\theta}{\partial \lambda_\theta}}. \tag{8}$$

Figure 2 represents the first case of the model to illustrate the negative effect of spatial film thinning in the deformed state. Figure 2 a) shows the deformed state of a membrane with an initial radius $R_\mathrm{b} = 15\,\mathrm{mm}$ and a pressure of $p = 4\,\mathrm{kPa}$. The Gent parameters ($J_\mathrm{m} = 18$ and $\mu = 180\,\mathrm{kPa}$) are calculated according to [6]. The initial thickness was set to a constant value of $d_0 = 170\ \mu\mathrm{m}$, which results in a profile with a minimum of 65 µm (at the apex) and 123 µm at the edge in the deformed state. If the deformed thickness varies spatially, the thinnest region determines the maximum allowed voltage due to the electrical breakdown limit. Consequently, thicker regions are operated below their actuation potential, and the membrane is poorly utilized. Since this effect is quadratic and the electric field is inversely proportional to the thickness, this underlines the advantage of a constant thickness in the deformed state.

2.3 Iterative approach for calculating the initial layer thickness

The target is to find an initial layer thickness $d_0(R)$, that the membrane has a prescribed constant thickness $\tilde{d}$ in the deformed state (case two from above):

$$d(R) = \tilde{d} = \text{const.} \quad \Longrightarrow \quad d_0(R) = \tilde{d}\,\lambda_\theta(R)\lambda_\phi(R). \tag{9}$$

Both stretches (λ_ϕ and λ_θ) depend on the solution of the overall system, and thus depend also on the initial layer thickness $d_0(R)$. Since $d_0(R)$ is controlled during manufacturing, it can be formulated as a fixed-point problem. For a given profile $d_0^{(k)}(R)$, the initial thickness is updated according to:

$$d_0^{(k+1)}(R) = \tilde{d}\,\lambda_\theta^{(k)}(R)\lambda_\phi^{(k)}(R). \tag{10}$$

The iterative solution should be continued until it satisfies:

$$\max_{R\in[0,R_b]}\left|\frac{d^{(k)}(R) - \tilde{d}}{\tilde{d}}\right| \le \varepsilon, \tag{11}$$

where ε is the allowed relative deviation in thickness.
Figure 5 b) shows the comparison of a membrane with initial constant thickness and an adapted thickness to achieve a constant thickness in the deformed state. Here, the prescribed layer thickness in the deformed state was set to $\tilde{d} = 75\ \mu\mathrm{m}$ (blue dotted). It is evident that the resulting layer in the deformed case varies by only a few micrometers. The corresponding initial thickness profile $d_0(R)$ has a thickness of 185 µm at the center, decreasing to 119 µm at the edge (blue dashed).

3 3D printing of membranes with spatially varying layer thickness

To print the membrane with the desired initial layer thickness $d_0(R)$, a 3D printing system was used [7]. This system consists of a two-component printer capable of printing liquid silicone rubber (ELASTOSIL RT 625, Wacker Chemie AG, Germany). Various methods can be used to spatially adjust the layer thickness, such as modifying the feed rate or adjusting the print path. As the latter can be specified simply via G-code, this approach was selected.
To ensure, that the film thickness can be measured in its stretched state later on, it should not be too thin (limitation is caused by the confocal sensor). The target film thickness is therefore set to 75 µm, even though this does not reflect the current state of the art for DE applications, which typically specifies $20 - 50$ µm. Using the approach described in Section 2.3, the required initial layer thickness $d_0(R)$ can be calculated. The profile has a thickness of 119 µm at the edge and increases parabolically to 185 µm towards the center (see Figure 3 a). It can be described with

$$d_0(R) = a + b\left(1 - \left(\frac{R}{R_\mathrm{b}}\right)^c\right), \tag{12}$$

where $a = 119\,\mu\mathrm{m}$ is the thickness on the clamped edge, $b = 66\,\mu\mathrm{m}$, and $c = 2$. To vary the layer thickness spatially, the strand space $s(R)$ is controlled via the G-code (see Figure 3 c). This is based on the inverse proportionality between the layer thickness and the space between the strands $d_0(R) \propto 1/s(R)$. At the edge $R = R_\mathrm{b}$, the printing

 DOI: 10.30420/456743007

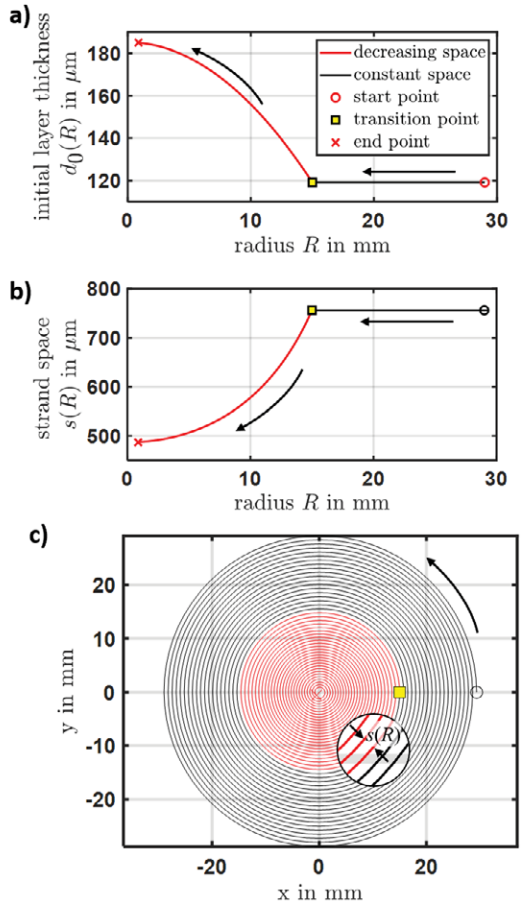


Figure 3 Adapted Archimedean spiral as printing path for membrane with varying layer thickness: a) targeted layer thickness over radius, b) corresponding strand space to reach targeted layer thickness, and c) plot of printing path showing decreasing space towards center.

parameters, including the strand spacing s_b, are selected such, that the layer thickness corresponds to the targeted 119 µm. The variation in the strand space is then calculated relative to (see Figure 3 b):

$$s(R) = s_b \frac{d_0(R_b)}{d_0(R)}. \tag{13}$$

The spiral with variable strand space can be parameterized:

$$x(\beta) = R(\beta)\cos\beta, \qquad y(\beta) = R(\beta)\sin\beta, \tag{14}$$

where β is the angle relative to the x-axis. The changing strand space can be defined with:

$$\frac{dR}{d\beta} = -\frac{s(R)}{2\pi}. \tag{15}$$

Combining Equations (12), (13), and (15) we get:

$$\frac{dR}{d\beta} = -\frac{s_b}{2\pi}\frac{a}{a+b\left(1-\left(\frac{R}{R_b}\right)^c\right)}. \tag{16}$$

The final printing path (solution of (15)) is depicted in Figure 3 c). It can be observed that the strands are more closely spaced towards the center to increase the layer thickness. To avoid a blob at the end, an area with a radius of 1 mm was left clear right in the center.

For validation, two samples were produced using the 3D printing process. One sample with a constant layer thickness (referred to as "initial const.") and another sample with the calculated initial layer profile (referred to as "adapted"). The constant initial layer thickness of 170 µm was selected, to obtain a comparable deformation at pressure $p = 4$ kPa (see Figure 6 a).

4 Results and discussion

The thickness of the printed membranes is measured during the printing process, representing the initial layer thickness $d_0(R)$. Then, the thickness is measured in the deformed state at $p = 4$ kPa (see Figure 1 b). In the end, an FEM-based analysis is used to determine the effect of the adapted layer thickness under electromechanical operation.

4.1 Measurement of initial layer thickness

Using a confocal laser sensor (CL-P015G, Keyence, Japan) the initial thickness $d_0(R)$ was measured during printing. The result is shown in Figure 4 a) with initial constant and b) with adapted layer thickness. The printed thickness is 165 µm, which is close to the targeted 170 µm. The center of the membrane is at the measured coordinate $R = 30$ mm. 15 mm in both directions form the membrane and the rest is used for clamping.

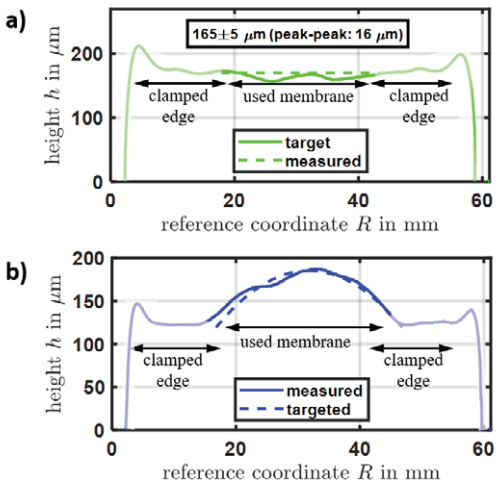


Figure 4 Thickness profile of two exemplarily printed membranes: a) constant layer thickness and b) adapted layer thickness for constant thickness in deformed state.

4.2 Measurement in deformed state

Figure 5 a) shows the setup for measuring the layer thickness in the deformed state. Therefore, discrete points in a 15-degree grid were measured, from 90° (apex) to

 DOI: 10.30420/456743007

0° (edge). The pressure was kept constant at $p = 4\,\text{kPa}$. The result of the measured layer thickness in the deformed state can be seen in Figure 5 b). The dashed lines represent the initial layer thickness $d_0(R)$. In the initial state, the arc length l is equivalent to the reference coordinate R. The dotted lines show the corresponding results in the deformed state from the model at 4 kPa (see Section 2). The measured points are marked with a diamond and are connected with a solid line. The sample with the initial constant layer thickness is shown in green and the sample with the adapted layer thickness is shown in blue.

The sample with the initial constant thickness has a higher thickness at the edge of $d = 114\,\mu\text{m}$ and at arc length $l = 12.5\,\text{mm}$ a thickness of $d = 52\,\mu\text{m}$. More towards the center, the thickness is too small to be measured. The thickness of the sample with the adapted thickness lies between $d = 78\,\mu\text{m}$ and $d = 86\,\mu\text{m}$. The goal of reaching a relatively constant layer thickness in the deformed state was thus achieved. The models show acceptable accuracy, although the values of the sample with initial constant thickness slightly differ. This may be due to inaccurate material parameters and will be examined in the future.

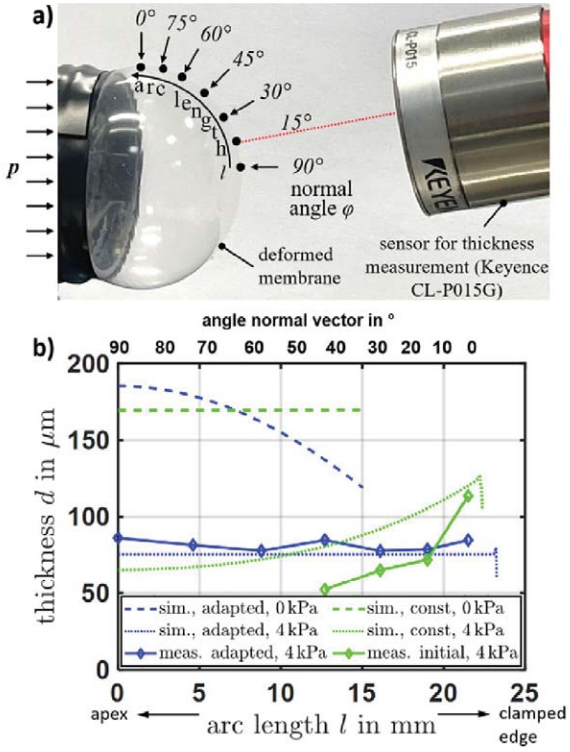


Figure 5 Comparison of measured and modeled layer thickness $d(R)$: a) measurement setup and geometry and b) measured and simulated results.

4.3 Simulation based analysis of the actuation performance

The purpose of the non-constant initial film thickness profile is to achieve a constant film thickness under stretched conditions. In this way, a larger displacement can be achieved with the same electric field, resulting in better, more uniform utilization of the material. However, achieving a constant layer thickness applies only to a specific operating point. The layer thickness with a constant initial layer thickness ($d_0 = 170\,\mu\text{m}$) was chosen such that the operating points at $p = 4\,\text{kPa}$ are roughly comparable. Figure 6 a) shows the model results of the pressure-strain behavior and the operating point at approximately $h = 14\,\text{mm}$. To determine the maximum

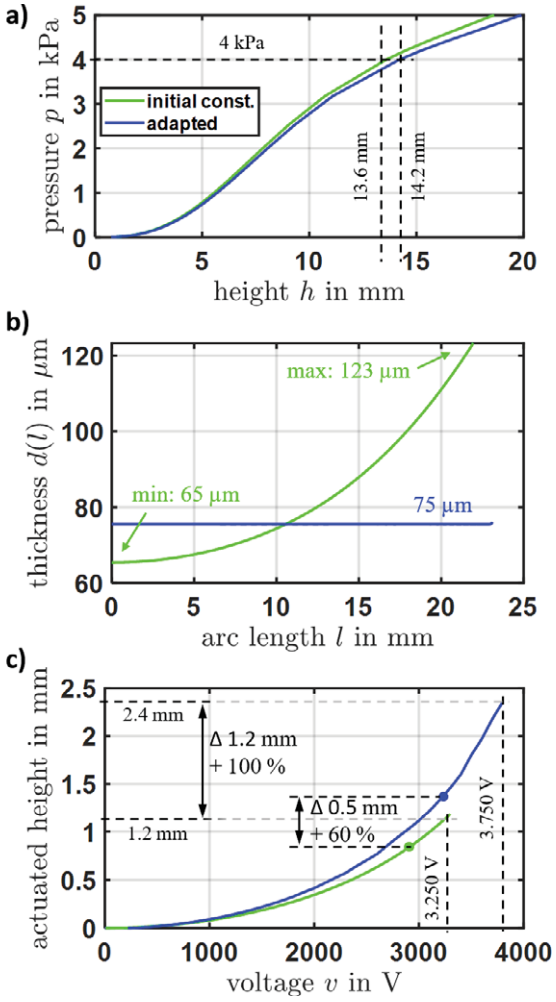


Figure 6 Simulation results comparing a constant initial thickness and the adapted thickness profile: a) operating point pressure vs. height, b) layer thickness in deformed state, and c) displacement when activated with voltage.

allowed voltage, the electrical breakdown field strength is set to a commonly used value of $50\,\text{V}/\mu\text{m}$. For the sample with the initial constant layer, the minimum thickness in the deformed state is at the apex with $d(l) = 65\,\mu\text{m}$ (see Figure 6 b). This results in a maximum electrical voltage of $v = 3250\,\text{V}$. For the adapted sample, the thickness remains constant at $d(l) = 75\,\mu\text{m}$ in the stretched state, allowing for a maximum voltage of $v = 3750\,\text{V}$.

The main finding is shown in the simulation results in Figure 6 c). Here, it is assumed that both sides of each sample are electrically conductive but without taking into account the mechanical influence [6]. The displacement change caused by the applied voltage is calculated relative to the height at the operating point. The usual sample with a constant initial layer thickness achieves a displacement of 1.2 mm. The adapted sample, in contrast, achieves a displacement of 2.4 mm, which is an increase of 100 %.
The Maxwell pressure induces an additional thinning of the membrane which locally increases the actual electric field. By taking into account the reduction of the film thickness due to Maxwell pressure and limiting it to 50 V/µm, the minimum film thickness is reduced to $d(l) = 58\,\mu\text{m}$ for the sample with an initial constant film thickness and to $d(l) = 64\,\mu\text{m}$ for the sample with an adapted film thickness. This results in new upper limits for the voltage of 2900 V and 3200 V, respectively. The displacements change to 0.83 mm (green bullet) and 1.33 mm (blue bullet), which is an increase of still 60 %. A further optimization could involve modeling and calculating the layer thickness to include the Maxwell pressure, so that a constant layer thickness is achieved in the actuated state and thus using the sample more optimally. Nevertheless, the substantial increase in displacement demonstrates the potential of the proposed method, even if it is somewhat reduced by the aforementioned effects in reality.

5 Conclusion

This work presents a model-based and manufacturing-oriented approach for realizing balloon-shaped dielectric elastomer membranes with a spatially varying initial thickness. The aim is to compensate the non-uniform thickness in the deformed state. An initial thickness profile for a target thickness of 75 µm was calculated and manufactured with a 3D printing system by adapting the strand space of the printing path.
The measurements confirm the basic feasibility of this approach. While the reference membrane with constant initial thickness showed a thickness variation in the deformed state, the adapted membrane reached a more homogeneous thickness. The simulation-based actuation analysis shows a displacement increase of 100 % in the ideal case and about 60 % when thinning due to Maxwell-pressure is considered too.
Future work should include the stiffness of the printed electrodes, electromechanical thickness reduction already during the design step, and experimental validation under electrical actuation.

Acknowledgement

This contribution was created as part of the joint project *CALMAR* - German Research Foundation (512586089). We thank Wacker Chemie AG for providing material.

Literature

[1] F. Carpi et al. *Dielectric Elastomers as Electromechanical Transducers*. Elsevier, 2008. DOI: 10.1016/B978-0-08-047488-5.00032-0.

[2] Yaguang Guo et al. “Review of Dielectric Elastomer Actuators and Their Applications in Soft Robots”. In: *Advanced Intelligent Systems* 3.10 (2021), p. 2000282. DOI: https://doi.org/10.1002/aisy.202000282.

[3] Tiefeng Li et al. “Giant voltage-induced deformation in dielectric elastomers near the verge of snap-through instability”. In: *Journal of the Mechanics and Physics of Solids* 61.2 (2013), pp. 611–628. DOI: 10.1016/j.jmps.2012.09.006.

[4] Amit Patil and Anirvan DasGupta. “Finite inflation of an initially stretched hyperelastic circular membrane”. In: *European Journal of Mechanics - A/Solids* 41 (2013), pp. 28–36. DOI: 10.1016/j.euromechsol.2013.02.007.

[5] Alberto Di Matteo, Gianmarco Nuzzo, and Francesco Paolo Pinnola. “Nonlinear response of circular hyperelastic dielectric membranes subject to inflation”. In: *International Journal of Non-Linear Mechanics* 181 (2026). DOI: 10.1016/j.ijnonlinmec.2025.105288.

[6] Andreas Hubracht et al. “Combination of dielectric elastomer membrane actuators with dielectric elastomer switches to create an autonomous elastomer-based platform”. In: vol. 13945. SPIE, 2026, p. 1394505. DOI: 10.1117/12.3091823.

[7] Andreas Hubracht, Ozan Cabuk, and Jürgen Maas. “3D printing of elastomer layers for dielectric elastomer transducers”. In: *Electroactive Polymer Actuators and Devices XXIV*. Vol. 12042. SPIE, 2022. DOI: 10.1117/12.2614828.

[8] Xuanhe Zhao and Zhigang Suo. “Method to analyze programmable deformation of dielectric elastomer layers”. In: *Applied Physics Letters* 93.25 (Dec. 2008), p. 251902. ISSN: 0003-6951. DOI: 10.1063/1.3054159.

[9] Mickael Moscardo et al. “On designing dielectric elastomer actuators”. In: *Journal of Applied Physics* 104.9 (Nov. 2008), p. 093503. ISSN: 0021-8979. DOI: 10.1063/1.3000440.

[10] Thorben Hoffstadt, Christian Graf, and Jürgen Maas. “Modeling of roll-actuators based on electroactive polymers”. In: ed. by Yoseph Bar-Cohen. Vol. 8687. International Society for Optics and Photonics. SPIE, 2013, 86871F. DOI: 10.1117/12.2010093.

[11] A. N. Gent. “A New Constitutive Relation for Rubber”. In: *Rubber Chemistry and Technology* 69.1 (Mar. 1996), pp. 59–61. ISSN: 0035-9475. DOI: 10.5254/1.3538357.

 DOI: 10.30420/456743008

Robust and Efficient Finite Element Modeling of an Electrostatic Microactuator Relying on the Pull-In Effect

Arwed Schütz[1], Dwarakesh Sudhahar[2], Martin Hoffmann[2], Tamara Bechtold[1,*]
[1] Jade University of Applied Sciences, Wilhelmshaven, Germany
[2] Microsystems Technology, Ruhr University Bochum, Bochum, Germany
[*] Correspondence: tamara.bechtold[at]jade-hs.de

Abstract

This contribution presents several best practices for finite element modeling of electrostatic microactuators to obtain a robust, accurate, and efficient model. These practices include electromechanical transducer elements to model electrostatic forces and mechanical contact, effective material data for perforation, and the use of beam and shell elements. A model that implements these practices offers better convergence and faster evaluation while maintaining high accuracy. Therefore, it can serve as a basis for optimizing actuation or design optimization. All these techniques are demonstrated for an electrostatic microactuator that relies on the highly nonlinear pull-in effect.

1 Introduction

Microactuators commonly rely on electrostatic actuation due to its numerous advantages, including favorable scaling effects and compatibility with established fabrication technologies. Consequently, electrostatic actuation has been adopted in a wide range of applications, each with its own unique requirements that require careful engineering. Due to the complexity of fabrication processes and time-consuming measurements, numerical simulation often plays a crucial role in the design phase. Once calibrated, simulations provide high accuracy, predict behavior under various scenarios, and offer detailed information. Furthermore, they enable efficient and parallelizable parameter studies and design optimization.

However, some actuators depend on strongly nonlinear effects such as electrostatic pull-in [1], which can impose substantial computational demands and lead to convergence issues. To address this challenge, specific techniques can be applied to create efficient and robust finite element (FE) models. This contribution presents such approaches and illustrates them with a numerical case study of an electrostatic microactuator [2]. This design exploits the pull-in effect and incorporates unconventional components such as a glued-in glass sphere.

The remainder of this contribution is structured as follows: Section 2 introduces the electrostatic microactuator and the system of which it is a part. Section 3 describes techniques for efficient FE modeling, including general guidelines, converting perforation into effective material data, representing electrostatic interaction by distributed one-dimensional transducer elements, and using beam instead of solid elements for the meander spring. On that basis, Section 4 implements all these techniques to study the electrostatic actuator's sequential pull-in behavior in three setups. Finally, Section 5 provides a summary and suggests directions for future work.

All FE studies use Ansys Mechanical 2022 R2.

2 The Actuator

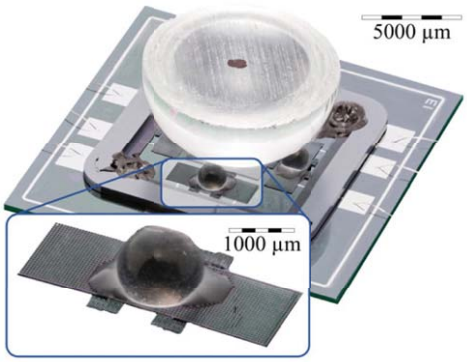


Figure 1 Tilt actuator system for incremental rotation of the central hemisphere. The inset highlights one of the four electrostatic actuators with glued-in glass sphere. Microscope image courtesy of Dwarakesh Sudhahar.

The electrostatic microactuator considered in this work is part of the microsystem shown in Figure 1 [2], which acts as a quasistatic micromirror. A large central hemisphere rests upon four smaller spheres, each of which is attached to an electrostatic actuator. Each of the four electrostatic actuators is suspended to four meander springs and features two electrodes below with a more detailed description available in the original work [2]. The corresponding actuation sequence rotates the actuator and moves it out of contact into pull-in. Therefore, the four electrostatic actuators cooperate to incrementally rotate the large central hemisphere into the desired orientation. In contrast to typical designs [3], structural links to the mirror are omitted, enabling a wide range of multistable orientations. Related work employs different techniques to rotate the large central sphere, i.e., periodic contact to an oscillating stage [4] or kick actuators for a free flight phase [5, 6]. Control concepts for optimized performance are available [7, 8].

ISBN: 978-3-8007-6743-4 @ VDE VERLAG GMBH · Berlin · Offenbach

 DOI: 10.30420/456743008

3 Techniques for Efficient Models

Several techniques can help create a robust, accurate, and efficient FE model. These include general guidelines and techniques such as effective material data, efficient modeling of electrostatic interaction and mechanical contact, and efficient element types, i.e., for the meander spring. The following subsections describe these approaches in more detail before Section 4 combines them to analyze the pull-in behavior of the electrostatic actuator.

3.1 General Guidelines

General guidelines for efficient FE models include using symmetry, correct element types, and rigid bodies, where appropriate. Exploiting symmetry not only reduces the computational load, but can also aid convergence as more unknowns are prescribed. Therefore, it should be utilized wherever possible. Employing beam and shell elements instead of three-dimensional elements can also bring significant improvements. Beam elements are tailored to long and thin structures and shell elements to thin structures. Compared to solid elements, they reduce the model's dimensionality, and allow for coarser discretization, further decreasing the computational load. Rigid bodies provide an efficient option to model components of much higher stiffness compared to other parts of the structure, i.e., the glued-in glass sphere in Figure 1. Such components can be efficiently represented as points associated with mass and inertia, which are rigidly attached to the contact interface via constraints. As a result, the model becomes significantly more efficient.

3.2 Effective Material Data

Detailed geometric patterns, such as perforation, can be efficiently modeled via effective material data [9]. These can be obtained by simulating a unit cell, as shown in Figure 2. As a result, geometric details can be replaced by homogeneous geometry, significantly reducing the model size. Table 1 provides material data for the original material, i.e., orthotropic silicon [10] used in standard wafers, and the effective values that consider perforation.

3.3 Electrostatic Interaction

Electrostatic effects for micro-electromechanical systems are typically modeled either via including the full dielectric geometry or via transducer elements. The first approach, i.e., including the dielectric geometry, provides more accurate results but is associated with a significantly larger model dimension. Furthermore, the pull-in effect poses a significant challenge for this approach because air elements could be compressed to negative volumes, causing divergence. A favorable alternative is to use distributed one-dimensional transducer elements [11]. These highly robust elements incorporate mechanical contact and electrostatic interaction as a parallel plate capacitor. If required, more detailed capacitance characteristics can be included. Figure 3 compares the capacitance characteristics of two parallel plate capacitors and a simulated unit cell.

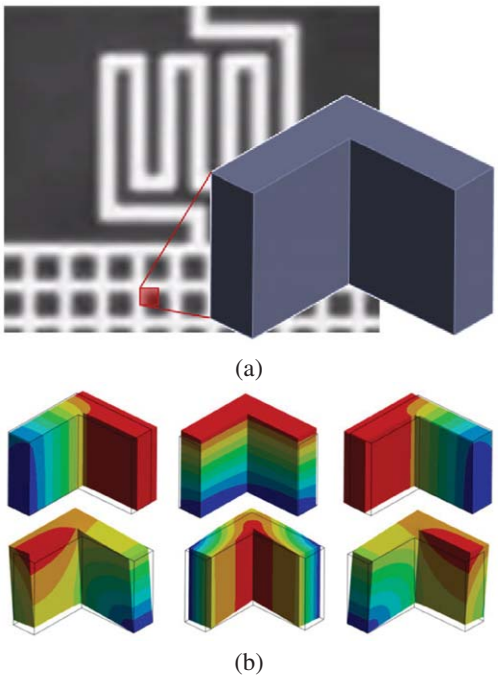


Figure 2 Deriving effective mechanical material data [9] by analyzing unit cell (a) of the perforation in six dedicated load cases (b). The unit cell exploits symmetry and gives parameters for linear elastic orthotropic behavior. Microscope image courtesy of Dwarakesh Sudhahar.

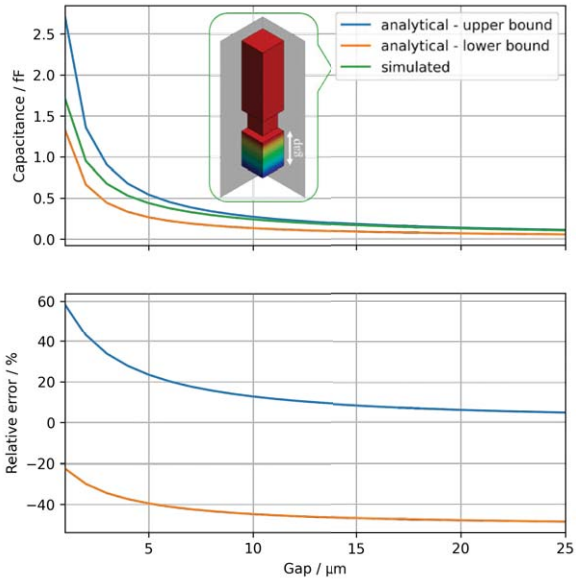


Figure 3 Capacitance vs. gap for a unit cell of the perforation computed by a dedicated FE model and two analytical approaches. The FE model contains the air domain and exploits symmetry. The two analytically computed capacitance characteristics assume a parallel plate capacitor. These two differ in whether they consider the area with or without perforation, giving a lower or upper bound, respectively. Their relative errors indicate valid operating ranges.

 DOI: 10.30420/456743008

3.4 Meander Spring Modeling

Meander springs are frequently used in microsystems to suspend moving components. Due to their thin geometry, they can often be modeled employing beam elements instead of solid elements. Figure 4 illustrates the corresponding geometries and FE meshes. For this example, the mesh featuring beam elements uses 80 % fewer degrees of freedom, which improves computational efficiency.

As with all simplifications, a preliminary study should compare it with a reference solution to assess its error and scope. For this purpose, both modeling approaches for meander springs, i.e., via beam elements and solid elements, are compared in a designated FE study. In each analysis, the meander spring is fixed at one end, while the other end is vertically displaced by negative 25 µm, i.e., the gap size. The analysis uses 25 steps and considers geometric nonlinearities. Figure 5 presents the restoring forces and effective stiffnesses for both modeling approaches. Especially for the first half, the deviation is small. The error slightly increases in the second half, which, however, is less relevant as the actuator is already in pull-in at this point.

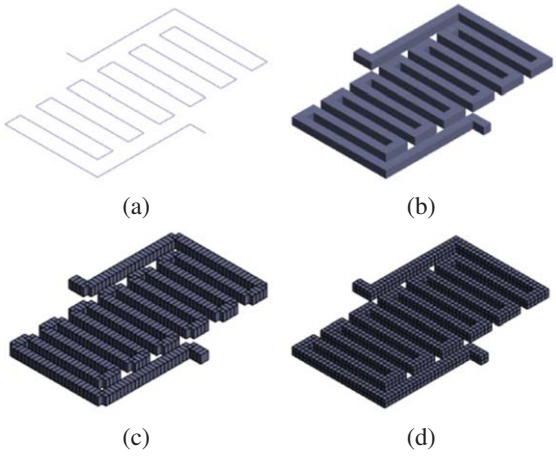


Figure 4 Two modeling approaches for a meander spring. A line geometry (a) is be meshed with efficient beam elements (c), while a volume (b) is meshed with solid elements (d) that constitute the reference solution.

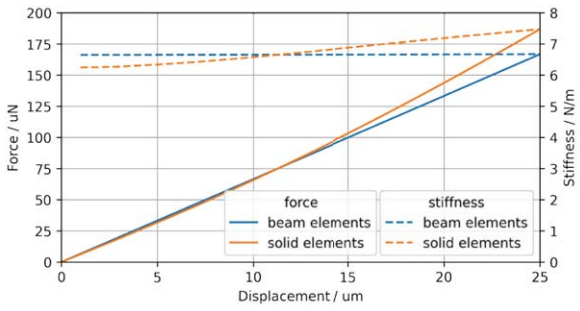


Figure 5 Restoring forces and stiffnesses of the two modeling approaches for meander springs shown in Figure 4 for varying vertical displacement.

4 Electrostatic Pull-In Study

This section studies the highly nonlinear sequential pull-in behavior of the electrostatic actuator shown in Figure 1. Analogously to experimental work, a single actuator is studied in three versions: a base version as manufactured, a version with the glued-in glass sphere, and a version representing the final microsystem. The following subsections describe the setup, detail the FE modeling, and present the results.

4.1 Setup

The actuator to be studied is one of the four electrostatic actuators of the microsystem shown in Figure 1. Figure 6 presents the setup, introducing coordinates and naming conventions. According to their position in the Z-direction, the two electrodes and endpoints for monitoring vertical displacement are labeled $z+$ or $z-$. The general actuation is sequential pull-in with linearly ramped voltages.

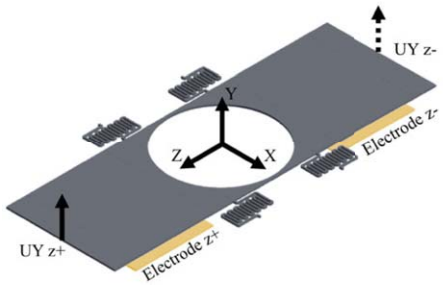


Figure 6 Basic modeling setup of a single electrostatic actuator. In later studies, the two electrodes are actuated sequentially. Vertical displacement is measured at the two endpoints. Labels are based on position in the Z-direction.

This basic setup is studied in three versions that correspond to successive manufacturing stages and measurement setups. These versions include a single electrostatic actuator, its combination with a glued-in glass sphere, and a version with both the small sphere and the large hemisphere. Figure 7 illustrates these versions in colors consistent with later result plots.

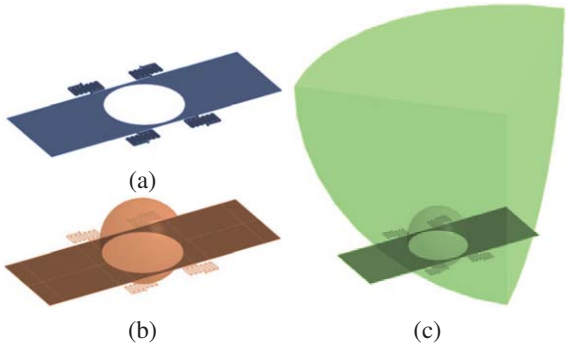


Figure 7 Three versions of the basic setup in Figure 6: the electrostatic actuator by itself (a), with glued-in sphere (b), and with both glued-in sphere and large hemisphere (c).

 DOI: 10.30420/456743008

4.2 Finite Element Model

The FE model aims for efficiency and employs the techniques described in Section 3. Hence, symmetry is exploited for the first two setup versions shown in Figure 7. The glued-in sphere is modeled as a node at its center of gravity with the corresponding mass and moments of inertia. This node is attached to the circular interface, i.e., the edge of the hole, via multipoint constraints that enforce a rigid behavior. The perforation is converted into effective material data which is given in Table 1 in the appendix. On that basis, shell and beam elements are utilized due to the homogenized geometry's aspect ratios. Electrostatic interaction and mechanical contact are modeled via electromechanical transducer elements for efficiency and robustness, especially due to the pull-in effect.

For each of the three setup versions shown in Figure 7, the free ends of the meander springs are fixed. Mechanical contact is implemented through electromechanical transducer elements. Loads include gravity and sequential pull-in with linearly ramped voltages as specified in Figure 8.

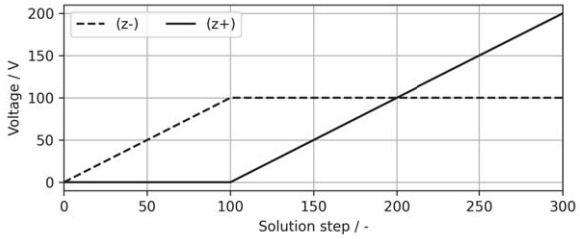


Figure 8 Voltages applied to the two electrodes.

The solver uses automatic step control, the full Newton Raphson procedure with convergence criteria for displacement and force. Geometric nonlinearities are considered, and the transducer elements employ the augmented stiffness method to aid convergence.

4.3 Results

Figure 9 presents the corresponding results for displacement in vertical direction. These are extracted at the two endpoints as illustrated in Figure 6. On that basis, the pull-in voltages are extracted. For the three setup versions, the first pull-in occurs at 62 V, 71 V, and 33 V. For the second pull-in, voltages of 114 V, 42 V, and 62 V are required.

A notable effect is the significant additional stiffness associated with the glued-in sphere. In the first setup version without it, the center acts as a hinge, which leverages the other side, thus increasing the voltage required for the second pull-in. In contrast, the second setup version with the glued-in sphere features a significantly lower second pull-in voltage. This difference in stiffness also affects behavior during the first pull-in: while the first setup version leverages the non-actuated side to large positive displacements, the second setup version tilts initially but is displaced as a whole upon the first pull-in. Another observation is the initial displacement of the third setup version due to the weight of the large hemisphere. As a result, the gap is reduced, and the first pull-in occurs at a lower voltage.

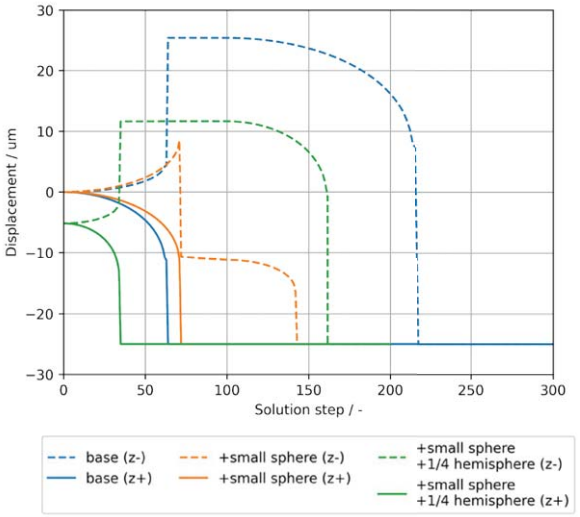


Figure 9 Vertical displacements for the two endpoints as illustrated in Figure 6 for the three load cases in Figure 7. Colors are consistent with the three load cases in Figure 7 and line styles with the arrows in Figure 6.

Note that experimental measurements of the pull-in voltage of the version with glued-in sphere are available [2]. The measured value of 75 V aligns well with the 71 V computed in this work, indicating good accuracy.

5 Conclusions and Outlook

This work has successfully demonstrated a FE modeling workflow for electrostatic microactuators that rely on the strongly nonlinear pull-in effect. In detail, several guidelines have been described to improve efficiency and robustness. They have been demonstrated for the case study of an electrostatic actuator, providing plausible results in all setups and agreeing well with experimental measurements.

A straightforward directions for future work is more experimental measurements to assess and calibrate the FE model. Another option is an alternative FE simulation that models the dielectric geometry instead of transducer elements to incorporate electrostatic interaction. This electrostatic modeling approach provides more accurate results and can be used to assess and calibrate the current model as well. However, note that this approach significantly increases computational costs and is not suited for the pull-in effect, especially when studying subsequent steps such as sequential pull-in or pull-out behavior.

6 Acknowledgements

This research is part of the project *ADOPT - Adaptive Optics for THz* within the priority program *KOMMMA - Cooperative Multistage Multistable Microactuator Systems* and was funded by Deutsche Forschungsgemeinschaft (German Research Foundation) grant number 424616052.

Appendix

Table 1 Orthotropic material data for silicon of a standard wafer [10] and effective data capturing the influence of perforation [9]. The latter results from numerical studies of a perforated unit cell as illustrated in Figure 2. To obtain orthotropic material properties, the effective values have been averaged.

Constant	Reference value	Effective value
E_x	169 GPa	51.8 GPa
E_y	169 GPa	51.8 GPa
E_z	130 GPa	63.7 GPa
G_{xy}	50.9 GPa	2.37 GPa
G_{yz}	79.6 GPa	24.5 GPa
G_{zx}	79.6 GPa	24.5 GPa
μ_{xy}	0.064	0.025
μ_{yz}	0.36	0.225
μ_{zx}	0.28	0.195

7 Literature

[1] Wen-Ming Zhang, Han Yan, Zhi-Ke Peng, and Guang Meng. Electrostatic pull-in instability in mems/nems: A review. 214:187–218, 2014. ISSN 09244247. doi: 10.1016/j.sna.2014.04.025. PII: S0924424714002088.

[2] Dwarakesh Sudhahar and Martin Hoffmann. Design, Simulation, and Fabrication of a MEMS-Based Electrostatic Microactuator for Precise Spherical Rotation. In *MikroSystemTechnik Kongress*, pages 288–290. VDE Verlag GmbH, Duisburg, 2025. ISBN 978-3-8007-6615-4. doi: 10.30420/456614135.

[3] Stefan Weinberger, Tran Trung Nguyen, Christoph Ament, and Martin Hoffmann. Quasi-static micromirror with enlarged deflection based on aluminum nitride thin film springs. *Sensors and Actuators A: Physical*, 210:165–174, 2014.

[4] Frank Bunge, Steffen Leopold, Sebastian Bohm, and Martin Hoffmann. Scanning micromirror for large, quasi-static 2D-deflections based on electrostatic driven rotation of a hemisphere. *Sensors and Actuators A: Physical*, 243:159–166, 2016.

[5] Mario Farny and Martin Hoffmann. Kick & Catch: elektrostatisches Rotieren einer Kugel. In *MikroSystemTechnik Kongress*, pages 274–277. VDE Verlag GmbH, Stuttgart-Ludwigsburg, 2021. ISBN 978-3-8007-5656-8.

[6] Mario Farny, Michael Olbrich, Christoph Ament, and Martin Hoffmann. Kick & Catch: Coaction of an electrostatic kick and magnetic catch system for the rotation of a sphere. In *ACTUATOR 2022*, GMM-Fachbericht. VDE VERLAG, Berlin and Offenbach, 2022. ISBN 978-3-8007-5894-4.

[7] Michael Olbrich, Mario Farny, Martin Hoffmann, and Christoph Ament. Modeling and Control Design of a Contact-Based, Electrostatically Actuated Rotating Sphere. *Actuators*, 11(3):90, 2022.

[8] Michael Olbrich, Christopher Mueller, Joshua Laun, and Christoph Ament. Motion Primitive Based Predictive Control of a Rotational Actuator Driven by Contact and Friction. In *MikroSystemTechnik Kongress*, pages 491–494. VDE Verlag GmbH, Duisburg, 2025. ISBN 978-3-8007-6615-4. doi: 10.30420/456614054.

[9] D. C. Webb, K. Kormi, and S.T.S. Al-Hassani. Use of FEM in performance assessment of perforated plates subject to general loading conditions. *International Journal of Pressure Vessels and Piping*, 64(2):137–152, 1995.

[10] Matthew A. Hopcroft, William D. Nix, and Thomas W. Kenny. What is the Young's Modulus of Silicon? *Journal of Microelectromechanical Systems*, 19(2):229–238, 2010.

[11] M. Gyimesi and D. Ostergaard. Electro-mechanical transducer for mems analysis in ansys. In *International Conference on Modeling and Simulation of Microsystems*, pages 270–273. IEEE Electron Devices Society, Computational Publ, 1999. ISBN 0-9666135-4-6.

 DOI: 10.30420/456743009

Electrostatic MEMS actuator for controlled Quasi-Static spherical Rotation

Dwarakesh Sudhahar[1,*], Arwed Schütz[2], Martin Hoffmann[1], Tamara Bechtold[2]
1 Microsystems Technology, Ruhr University Bochum, Bochum, Germany,
2 Jade University of Applied Sciences, Wilhelmshaven, Germany
* Correspondence: dwarakesh.sudhahar@ruhr-uni-bochum.de

Abstract

This work introduces a novel actuation strategy based on controlled stick–non-slip dynamics to enable continuous and accurate rotational manipulation of a central hemispherical element. The system comprises a primary hemisphere supported by four smaller, independently actuated hemispheres with segmented electrodes for directional control. Sequential electrode activation generates alternating stick and non-slip phases, producing incremental and repeatable tilt of the central element. The proposed model predicts the tilt per cycle and the number of cycles required to achieve a 1° rotation. These predictions are validated through simulations and experiments, demonstrating improved smoothness, precision, and controllability compared to conventional approaches.

1 Introduction

Microactuators typically exhibit lower energy efficiency compared to their macroscale counterparts, primarily due to scaling constraints that limit the implementation of conventional kinematic architectures. At microscale dimensions, traditional mechanical configurations become impractical or infeasible. However, these same geometric constraints reduce the magnitude of operational loads and displacements, thereby relaxing material performance requirements. As a result, micromechanical systems can utilize materials with lower strength and stiffness characteristics without compromising functional integrity [1,2]. Electrostatic actuation is the most widely utilized mechanism in MEMS (Micro-electromechanical Systems) and NEMS (Nano-electromechanical Systems) devices, owing to its inherent advantages such as low power consumption, fast response, and ease of integration with microfabrication processes [3]. Electrostatic actuators can be systematically classified into parallel-plate, comb-drive, scratch-drive, and cantilever-type based on their underlying operational mechanisms and structural design configurations [4,5,6].
This paper presents the design, modeling, and operational characterization of an electrostatic actuator capable of dual-mode operation, namely parallel-plate and torsional actuation. The integration of these actuation mechanisms enables controlled multi-axis motion, facilitating precise spherical rotation of a hemispherical element supported on the actuator array.

2 Design and fabrication

2.1 Design

In this study, the actuator is designed to operate in two distinct modes: tilting and parallel-plate actuation. Accordingly, the suspension spring is required to exhibit relatively high translational stiffness to support the weight of the spheres, while maintaining low rotational stiffness to enable efficient tilting motion. To meet these requirements, a specialized spring configuration, referred to as a rotated serpentine spring, is developed and symmetrically positioned at 400 µm from the center on both sides of the movable electrode.

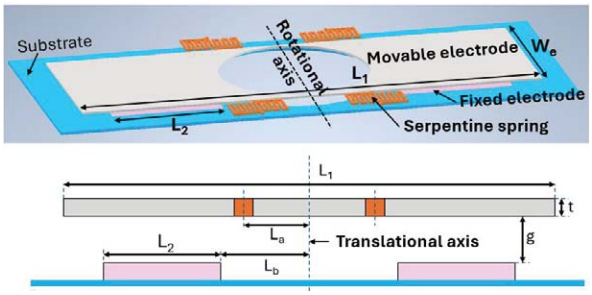


Figure 1 Structural representation of a single electrostatic actuator: 3D layout view (top left) and corresponding cross-sectional view (bottom left).

The geometrical dimensions of the structures are summarized in table 1.

Table 1 Dimensions of the Single actuator element

Dimensions	Values
L_1	3100 µm
L_2	750 µm
t	15 µm
L_a	400 µm
L_b	600 µm
W_e	1050 µm
g	25 µm

 DOI: 10.30420/456743009

To prevent electrical shorting during operation, the movable electrode is designed to satisfy the constraint $L_2 + L_b < L_1/2$. The upper electrode has a hole of 1 mm in the centre. The complete design consists of four actuators placed as illustrated in figure 3(b).

2.2 Fabrication

The fabrication process is implemented through three principal microfabrication stages: patterning and formation of (1) the movable electrode on a silicon-on-insulator (SOI) substrate featuring a 15 µm-thick device layer; (2) the fixed electrode on a 300 µm-thick silicon wafer; and (3) precise alignment and bonding of the movable and fixed electrode structures using conductive glue to complete the device assembly. Spheres with a nominal diameter of 1 mm (tolerance ± 0.02 mm) are positioned within the designated cavities of the movable electrode and secured using a thermally cured adhesive. Subsequently, the fabricated actuators are mounted onto a printed circuit board (PCB) to facilitate electrical interfacing and characterization. Finally, a hemisphere with a diameter of 7 mm is positioned inside the four actuators such that it is mechanically supported by the small spheres of the movable electrodes of each actuator.

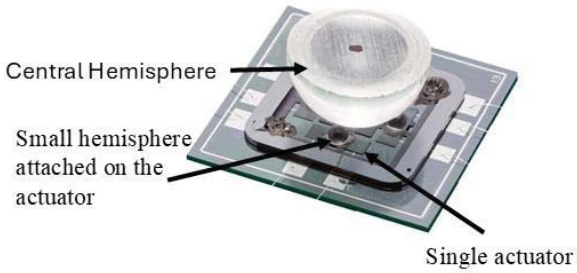


Figure 2 Fabricated setup with central hemisphere on four spherical actuators

3 Working principle

The mechanism consists of a primary hemisphere supported by four smaller hemispheres (**See figure 3**) that each driven by an independent actuator. Fixed electrodes beneath each actuator are divided into two spatially separated segments that facilitate directional control. When a single selected electrode is energized, the corresponding actuator tilts, producing a stick-phase rotation of the central hemisphere (Fig 3, step 2). Subsequent activation of the remaining electrodes enforces a non-slip interaction between the hemispheres, causing the central sphere to rest on the central stage settling into a tilted configuration (Fig 3, step 3). Deactivation of the electrodes then lifts the central hemisphere without turning thus preserving its tilt, thereby completing a single stick–non-slip cycle (Fig3, step 4). Repetition of this cycle yields incremental, precisely controlled increases in tilt angle. The selection of the tilted electrodes in the first phase distinguish the direction of sphere rotation.

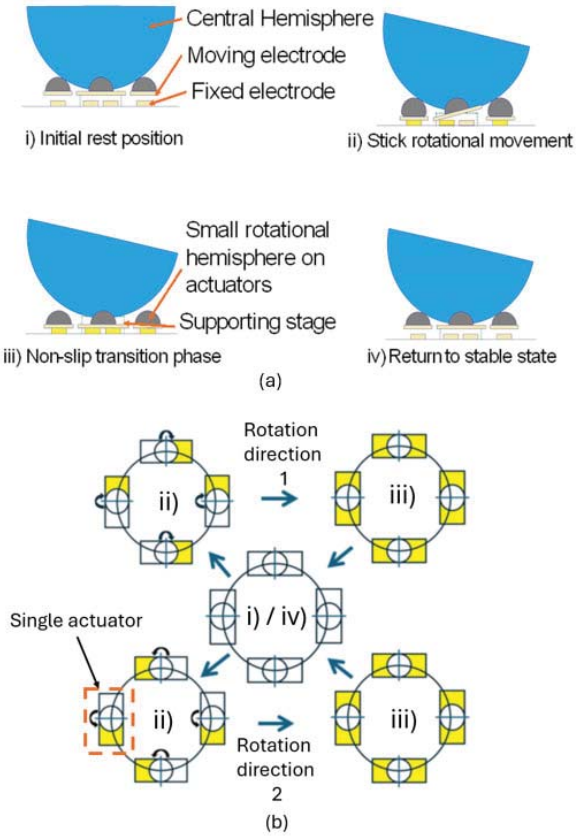


Figure 3 Schematic illustration of the operating principle: (a) front view depicting the central sphere supported by four micro spherical elements; (b) top view showing two of the four actuation sequences, where the activated electrodes are highlighted in yellow.

4 Experiments and Results

When a smaller hemisphere undergoes a rotation of angle θ_1, the corresponding rotation of the central hemisphere is ideally given by $\theta_2 = \theta_1/7$. However, accounting for the inclined actuation of the smaller hemispheres and the precise location of the contact interface, the effective transmission ratio is reduced to 0.101. Consequently, the resulting rotation of the central hemisphere can be expressed as $\theta_2 = 0.101\,\theta_1$.

In the initial configuration of the device, the electrode gap is 25 µm. Based on geometric constraints, upper bounds for the rotational displacements of both the smaller and central hemispheres can be derived. Specifically, during a single actuation cycle, the rotation of a smaller hemisphere is limited to $\leq 0.924°$, which corresponds to a maximum rotation of the central hemisphere of $\leq 0.093°$. It should be noted that this estimation neglects any initial deflection induced by gravitational effects.

According to mathematical calculation, the central hemisphere undergoes an incremental tilt of approximately 0.093° per actuation cycle; thus, achieving a net rotation of 1° requires on the order of 11 actuation cycles.
The fabricated device was experimentally characterized under an optical microscope. A controlled bias voltage was selectively applied to a designated set of fixed electrodes, as illustrated in Fig. 3(b) (step–ii), to induce directional rotation of the central hemisphere. As the actuation voltage is progressively increased, the movable electrode exhibits a continuous angular deflection. Upon reaching a critical threshold, the electrostatically generated torque surpasses the mechanical restoring torque of the suspension system, triggering pull-in instability and resulting in contact between the movable and fixed electrodes. This electro-mechanical interaction produces a discrete and repeatable angular displacement of the central hemisphere in the intended direction. The entire actuation sequence was recorded, and the resulting angular displacement was quantitatively evaluated using dedicated online measurement software.

The experiments were conducted across multiple fabricated chips to ensure statistical reliability, and the reported angular displacements correspond to average values obtained from these measurements.

The measured angular displacement exhibited an average value of approximately 0.3°, as determined from multiple experimental trials. Based on this measured angular increment, a net rotation of 1° requires approximately 4 actuation cycles.

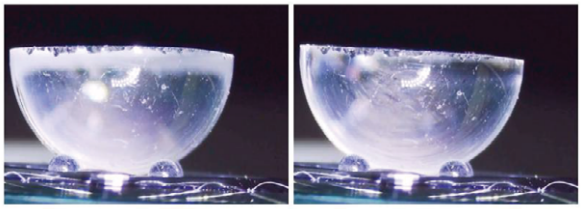


Figure 2 Microscopic image of the central hemisphere in initial position and in rotated position

5 Conclusion

An initial analytical estimation was performed to determine the rotation angle of the small hemisphere. Based on this calculation, the corresponding rotation of the central hemisphere was obtained and found to be approximately 0.093° per actuation cycle. Consequently, a full actuation cycle results in a central hemisphere rotation of ~0.093°, implying that approximately 11 complete actuation cycles are required to achieve a 1° rotation, as predicted theoretically.
Experimental characterization of multiple fabricated chips, however, showed a higher rotation per actuation cycle, with an average measured angle of approximately 0.3°. Accordingly, under experimental conditions, a full actuation cycle produces a significantly larger angular displacement, and a reduced number of cycles is required to reach 1° of rotation compared to the theoretical prediction.
These findings validate the second stage of the actuator's working principle and further experiments are being processed.

6 Acknowledgement

This research is funded by the German Research Foundation (DFG) within the priority program SPP2206 "KOMMMA", project "ADOPT – Adaptive optics for THz", grant number 424616052.

Special thanks to the technical staff for support in the cleanroom and H. Austenfeld for the stacked photographs.

Special thanks to the Center for Interface Dominated High Performance Materials (ZGH), Ruhr University Bochum, for the opportunity to use deep etching equipment.

7 Literature

[1] M. Yazdani and A. F. Payam, "A comparative study on material selection of microelectromechanical systems electrostatic actuators using Ashby, Vikor and topsis," *Materials & Design (1980-2015)*, vol. 65, pp. 328–334, Jan. 2015. doi:10.1016/j.matdes.2014.09.004

[2] I. Morkvenaite-Vilkonciene et al., "Development of electrostatic microactuators: 5-year progress in modeling, design, and applications," Micromachines, vol. 13, no. 8, p. 1256, Aug. 2022. doi:10.3390/mi13081256

[3] A. Veroli *et al.*, "An approach to the extreme miniaturization of rotary comb drives," *Actuators*, vol. 7, no. 4, p. 70, Oct. 2018. doi:10.3390/act7040070

[4] P. F. Van Kessel, L. J. Hornbeck, R. E. Meier, and M. R. Douglass, "A MEMS-based projection display," *Proceedings of the IEEE*, vol. 86, no. 8, pp. 1687–1704, 1998. doi:10.1109/5.704274

[5] J. E. Ford, V. A. Aksyuk, D. J. Bishop, and J. A. Walker, "Wavelength add-drop switching using tilting micromirrors," *Journal of Lightwave Technology*, vol. 17, no. 5, pp. 904–911, May 1999. doi:10.1109/50.762910

[6] D. Hah, H. Toshiyoshi, and M. C. Wu, "Design of electrostatic actuators for MOEMS applications," *SPIE Proceedings*, vol. 4755, pp. 200–207, Apr. 2002. doi:10.1117/12.462812

 DOI: 10.30420/456743010

Highly Conductive Metallic Thin Films on Flexible Substrates

Benjamin R. Zemlin[1,*], Jonas Hubertus[1], Dirk Göttel[1], Alberto Priuli[2], Saverio Addario[2], Gianluca Rizzelo[2], Stefan Seelecke[2], Günter Schultes[1], John Heppe[1]

[1]University of Applied Sciences of Saarland, Goebenstr. 40, 66117 Saarbruecken, Germany
*benjamin.zemlin@htwsaar.de
[2] Saarland University, Campus, 66123, Saarbruecken, Germany

Abstract

This paper investigates the electromechanical properties of RF-sputtered Au thin films on biaxially pre-stretched PDMS substrates for use as highly conductive, compliant electrodes in Dielectric Elastomer Transducers (DETs). While conventional compliant electrodes have high sheet resistance, pure metallic films offer superior conductivity but are typically brittle. By employing a pre-stretching strategy (37.5% and 57.5%), a wrinkled surface morphology is created that allows the metal to accommodate large deformations through out-of-plane buckling. The study demonstrates that 20 nm thin Au electrodes achieve an exceptionally low base resistance of approximately 4 Ω and maintain conductivity up to 300% uniaxial strain. Compared to similarly produced Ni films, Au exhibits higher stretchability due to its superior ductility and lower Young's modulus. These findings establish sputtered Au thin films as a high-performance solution for DETs and flexible electronics, combining unprecedented endurance with metallic-level conductivity.

1 Introduction

Flexible electronics are pivotal for emerging technologies such as wearables electronics, soft robotics, and biomedical devices, and demanding components capable of significant mechanical deformation while maintaining high conductivity [1, 2]. Dielectric Elastomer Transducers (DETs), often termed "artificial muscles," are key elements in this domain, offering large strains, high energy density, and rapid response [3]. The operational principle of DETs relies on an elastomeric dielectric layer sandwiched between two compliant electrodes; an applied electric field causes the elastomer to compress and expand. Crucially, the electrodes must maintain high electrical conductivity while accommodating these substantial strains to ensure efficient and reliable device performance [4].

Conventional compliant electrodes, typically made from conductive fillers like carbon black, graphene, or metallic nanoparticles embedded in elastomers, offer excellent stretchability but have high sheet resistance (tens of kΩ/□) [5]. This limits DET efficiency, actuation speed, and can lead to thermal management issues. In contrast, pure metallic thin films possess superior conductivity (resistivities orders of magnitude lower) but are inherently brittle, failing at only a few percent strain. This fundamental mismatch between the mechanical properties of highly stretchable elastomers and brittle metals presents a significant barrier to their direct integration. To overcome the limited stretchability of metallic thin films, various strategies have been developed. These include patterning the metal film (e.g., serpentine designs), moulding the substrate surface to create wavy topographies, or pre-stretching the elastomer before metal deposition [6]. The latter method, where a film is applied to a pre-stretched substrate and subsequently wrinkled upon relaxation (Figure 2), allows the out-of-plane buckling to accommodate large deformations by unfolding [7]. While effective, detailed studies focusing on the electromechanical behaviour of unstructured gold thin films on highly pre-stretched PDMS, particularly concerning their optimized performance and direct application in DETs, remain underexplored. Many approaches involve complex patterning or specific material choices, leaving room for a simpler, high-performance solution. This paper addresses the electromechanical properties of radiofrequency (RF) sputtered gold (Au) thin films deposited on biaxially pre-stretched PDMS membranes. Our primary objective is to evaluate their resistance under uniaxial stretch and their potential as highly compliant electrodes for DETs. We provide a direct comparison with similarly produced nickel (Ni) thin films, building on prior work by Hubertus et al. [7]. This study demonstrates an unprecedented combination of very low initial resistance and exceptionally high stretchability for unstructured metal films, offering a significant advancement for high-performance DETs.

The subsequent sections detail the experimental methodology (Section 2), present the electromechanical characterization results for Au electrodes compared to prior results with Ni electrodes (Section 3), discuss the findings and their implications for DETs (Section 4), and conclude with a summary and outlook (Section 5).

ISBN: 978-3-8007-6743-4 @ VDE VERLAG GMBH · Berlin · Offenbach

 DOI: 10.30420/456743010

2 Materials and Methods

This section outlines the fabrication of highly conductive metallic thin films on flexible PDMS substrates and their subsequent electromechanical characterization.

2.1 Substrate Preparation and Biaxial Pre-stretching

The PDMS used in this study is Elastosil 2030 (WACKER) with 50 µm thickness. To induce a wrinkled surface morphology, membranes are biaxially pre-stretched using a custom rig. First, the membranes are placed on silicone pins and subsequently stretched to uniform strain levels of 37.5% and 57.5% in both planar directions. While held in the stretched state, films are secured onto rigid metal frames equipped with magnetic tape (inner dimensions: 80 mm x 80 mm), as illustrated in Figure 2. A second metal frame is placed over the first, to shield the magnetic tape from the plasma during sputtering. This setup maintained the pre-stretch during subsequent metallization. Immediately before sputtering the membrane is cleaned using ultrapure water and a de-ionizing gun with nitrogen.

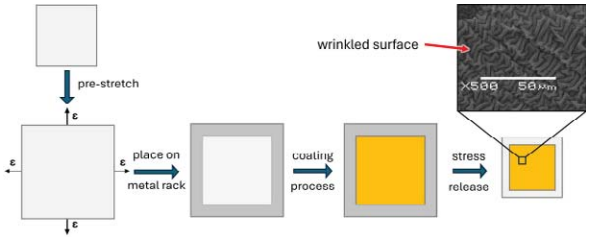


Figure 2 Process steps of manufacturing the electrode samples: a pre-stretched PDMS film is fixed on a metal frame and then coated. Afterwards, the membrane is allowed to relax, and a wrinkled surface is achieved.

2.2 Thin Film Deposition by RF Sputtering

Gold (Au) thin films are deposited onto the pre-stretched PDMS substrates using a multi-chamber sputtering system built by Aurion. A high purity (99.99%), 4" target is used. The chamber was evacuated to a base pressure below 5×10e−7 mbar, and Argon (99.99%) served as the process gas. The sputtering pressure is 20 µbar with an Ar flow rate of 40 sccm. RF power is 130 W, applied at room temperature for 300 s, yielding approximately 20 nm thick films. To verify the film thickness, glass plates are also placed in the process chamber. The thickness is measured using a surface profilometer (Dektak 150). After deposition, releasing the films from the frames allowed the pre-stretched substrate to relax, forming the characteristic wrinkled morphology.

2.3 Experimental Setup

The samples with the wrinkled surfaces are structured using a 355 nm ultra-short-pulse Laser. The structured electrode geometry is a 30 mm x 30 mm square. The membrane is fixed in 3D-printed clamps and contacted using copper tape. The test rig is equipped with a linear actuator and an LCR meter (Hemag HM 8118). The setup is controlled using a LabVIEW script running on a Windows PC. In Figure ***2*** each measurement point represents the average resistance over a 25 s period where the sample is held at the respective strain. After each step, the sample is completely relaxed before being stretched to the next strain level, to prevent the accumulation of creep due to the viscoelastic properties of PDMS.

3 Experimental Results

This section presents the experimental results of the strain-dependent electrical resistance behaviour of Au thin films compared to Ni thin films. Figure 2 shows the results of the strain-resistance measurements of Ni and Au thin films on PDMS membranes biaxially pre-stretched to 37.5% and 57.5%.

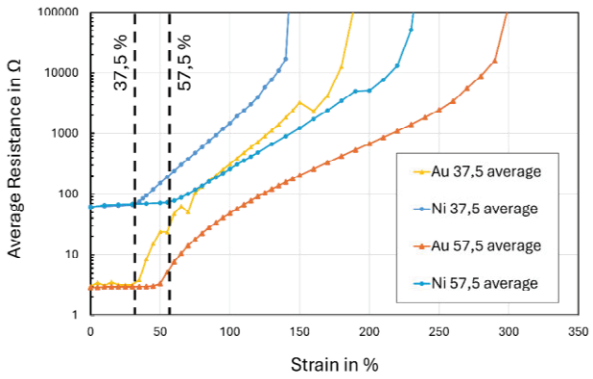


Figure 1 This figure shows the average resistance of Au and Ni electrodes versus uniaxial strain with pre-stretched substrates of 37.5% and 57.5% respectively. Each line represents the average of at least three individual measurements. The data for the Ni-samples is kindly provided by Hubertus et al [7].

For Ni electrodes the base resistance at zero percent strain is on average 60 Ω, compared to Au electrodes of 4 Ω. The difference in base resistance is explained by slight geometric differences and the lower resistivity of Au. Up to the level of pre-stretch (LOP) the resistance remains constant and increases when surpassing the LOP due to local microcracking of the thin film. The 20 nm, 57.5% pre-stretched, sputtered Au electrodes remain conductive (resistance < 100 kΩ) up to 300% of uniaxial strain. This is an unprecedented endurance for unstructured metal films. In comparison, similarly produced Ni thin films (10 nm, wrinkled from pre-stretch) showed initial average resistance of 60 Ω and samples with 57.5% pre-stretch, stayed conductive up to approximately 250% strain. These results demonstrate that sputtered metal films can combine very low resistance with large stretchability, potentially enabling improvement of DET performance.

4 Discussion

There are two important findings in the measurements regarding the use of gold thin films as electrodes for DETs. First, the very low base resistance of only around 4 Ω and second, the very high stretch of up to 300 %, which is for possible samples with LoP 57.5% while remaining conductive (resistance < 100 kΩ). This can be compared to Ni thin films, which reach 250% of stretch with a LoP of 57.5%. Additionally, the base resistance remains at this very low level up to reaching the level of pre-stretch. The sharp increase of resistance is attributed to cracks forming in thin films as was analysed in our previous work on Ni [7]. Up to the LoP, the wrinkles are being stretched out, leading to very little stress in the thin film itself. When the LoP is reached, stress accumulates in the thin film and cracks start forming. The higher maximum strain in the Au thin films is likely due to the higher ductility of gold. Au has a Young's modulus of approximately 79 GPa, whereas Ni exhibits a significantly higher modulus of about 200 GPa, therefore, cracks propagate more easily in the more brittle Ni films. In contrast, Au thin films can accommodate higher deformation before cracks form and propagate, which ensures more stable conductive pathways with lower electrical resistance. Since the electrodes´ ability to adapt to the deformation of the DET is critical, Au thin films can increase flexibility and maximum stroke. However, this is also dependent on several other parameters like adhesion, long term performance, electrical breakthrough strength and the achievable Maxwell force. These factors are part of ongoing research.

5 Conclusion and Outlook

In summary, our findings establish sputtered metallic thin films, particularly Au, on PDMS as a promising compliant electrode for DETs and suggest broader use in flexible electronics and soft sensors where both high conductivity and large deformability are required. In the context of the DECMAS project (part of KOMMMA), a miniaturized DEA array is currently being tested using sputtered metallic thin film electrodes that have been structured by means of ultra-short pulse laser ablation. Additionally, Au electrodes are under test regarding long-term stability and structurability, while DETs using Au thin films are being tested with high voltage.

Acknowledgements
We gratefully thank the DFG – German Research Foundation for funding the project DECMAS II (ID SCHU 1609/7-2). Furthermore, we thank the DFG for funding the SEM used in this work as part of the special Major Research Instrumentation program (INST 475/2-1).

6 Literature

[1] Y. Liu, L. Liu, Z. Zhang, und J. Leng, „Dielectric elastomer film actuators: characterization, experiment and analysis*“, Smart Mater. Struct., Bd. 18, Nr. 9, S. 095024, Juli 2009, doi: 10.1088/0964-1726/18/9/095024.

[2] R. Pelrine, R. Kornbluh, Q. Pei, und J. Joseph, „High-Speed Electrically Actuated Elastomers with Strain Greater Than 100%“, Science, Bd. 287, Nr. 5454, S. 836–839, Feb. 2000, doi: 10.1126/science.287.5454.836.

[3] I. A. Anderson, T. A. Gisby, T. G. McKay, B. M. O'Brien, und E. P. Calius, „Multi-functional dielectric elastomer artificial muscles for soft and smart machines“, Journal of Applied Physics, Bd. 112, Nr. 4, S. 041101, Aug. 2012, doi: 10.1063/1.4740023.

[4] M. Ghevondyan, M. Davtyan, und M. Aghayan, „Dielectric elastomer actuators: medical applications review“, Discov Mater, Bd. 5, Nr. 1, S. 43, Feb. 2025, doi: 10.1007/s43939-025-00225-7.

[5] B. Fasolt, M. Hodgins, G. Rizzello, und S. Seelecke, „Effect of screen printing parameters on sensor and actuator performance of dielectric elastomer (DE) membranes“, Sensors and Actuators, A: Physical, Bd. 265, Nr. October, S. 10–19, 2017, doi: 10.1016/j.sna.2017.08.028.

[6] S. Rosset und H. R. Shea, „Flexible and stretchable electrodes for dielectric elastomer actuators“, Appl. Phys. A, Bd. 110, Nr. 2, S. 281–307, Feb. 2013, doi: 10.1007/s00339-012-7402-8.

[7] J. Hubertus, J. Neu, S. Croce, G. Rizzello, S. Seelecke, und G. Schultes, „Nanoscale Nickel-Based Thin Films as Highly Conductive Electrodes for Dielectric Elastomer Applications with Extremely High Stretchability up to 200%“, ACS Appl. Mater. Interfaces, Bd. 13, Nr. 33, S. 39894–39904, Aug. 2021, doi: 10.1021/acsami.1c10686.

 DOI: 10.30420/456743011

Towards scaling Cooperative Dielectric Elastomer Actuator Systems

Saverio Addario*[1], Alberto Priuli[1], Andrej Schagaew[1], Benjamin Zemlin[3], J. Heppe[3], Stefan Seelecke [1,2], Gianluca Rizzello[1]
[1.] Saarland University, Department of Systems Engineering, Saarbrücken, Germany.
[2.] Smart Material Systems, Center for Mechatronics and Automation Technology - ZeMA gGmbH, Saarbrücken, Germany.
[3.] Department of Sensors and Thin Films, University of Applied Sciences of Saarland, Saarbrücken, Germany.

Abstract

Dielectric elastomers (DEs) are soft electroactive polymers that act as deformable capacitors, and can operate as actuators or sensors depending on the applied electrical configuration. In two-dimensional arrays, neighboring dielectric elastomer actuators (DEAs) interact mechanically and electrically, enabling cooperative behavior and distributed self-sensing. Large-stroke actuation requires a suitable mechanical biasing system, and negative-stiffness biasing is particularly attractive for stroke amplification. This work presents a force-displacement analysis of a downscaled two-dimensional cooperative DE array together with an evaluation of resized nonlinear polymeric biasing systems. The study investigates cooperative effects, identifies suitable materials for miniaturized biasing elements, and provides insight into the structural and fabrication constraints that govern the scalability of fully polymeric cooperative DEA architectures, including the potential of advanced 3D printing for compliant bias designs.

1 Introduction

Dielectric elastomers (DEs) are soft electroactive materials that convert electrical energy into controlled mechanical deformation through electrostatic forces [1]. They consist of a compliant dielectric membrane, typically made of silicone or acrylic elastomers, coated on both sides with compliant electrodes, thus forming a deformable capacitor. When a voltage difference is applied across the electrodes, the resulting electrostatic pressure compresses the membrane through its thickness and induces an in-plane expansion, which gives rise to actuation [2]. The achievable stroke can be further enhanced by coupling the DE membrane with a suitable external biasing or pre-loading mechanism, such as a mass, a linear spring, or a nonlinear buckling beam [3]. Characteristics of DEs include large actuation strain, fast response, high energy density, and low acoustic noise [4]. Owing to this distinctive combination of properties, dielectric elastomer actuator (DEA) technology has proven suitable for a wide range of engineering applications, including soft robotics [5], optical systems [6], medical devices [7], haptic interfaces [8], and acoustic systems [9]. These features make DEs an attractive actuation technology for compact, lightweight, and compliant mechatronic systems requiring efficient and adaptable mechanical performance. Although most current applications still rely on stand-alone DE devices, growing interest has recently shifted toward one- and two-dimensional arrays of independently addressable DEAs for multifunctional and distributed actuation [10].

Building on this trend, recent advances in DEA technology have increasingly moved toward cooperative architectures, in which multiple actuators are interconnected within a networked system. In such configurations, the mechanical biasing force required for DEA operation is commonly provided by pneumatic, fluidic, or rigid components [10]. Although these design strategies can support miniaturization [11], they generally lead to limited stroke, reduced efficiency, and comparatively stiff architectures, mainly because of the biasing elements.

In contrast to these rigid biasing strategies, the present work investigates the downscaling of a fully polymeric 3 × 3 cooperative dielectric elastomer actuator array, in which the biasing system is likewise polymeric to preserve the intrinsic compliance and flexibility of the architecture [12]. In this sense, the study represents a first step toward the miniaturization of cooperative DEA systems, with the actuator diameter reduced by approximately a factor of 3.8 compared with the corresponding macroscopic array [13], while the overall system dimensions are reduced by a factor of about 2.8.

The proposed prototype retains the same 3 × 3 layout as the larger-scale system, but adopts a multilayer DE architecture with sputtered metallic thin-film electrodes deposited on the PDMS membrane surface instead of screen-printed electrodes, thereby reducing the electrode thickness from micrometer-scale carbon-based films (≈ 5 μm) to nanometer-scale metallic layers (down to ≈ 10 nm), which are better suited for microscale applications. Since the system still relies on a shared membrane substrate, the mechanical coupling effects among adjacent elements are first characterized, with particular attention to the resulting nonlinear interactions and to their exploitation in the geometric design of the biasing system.

A further focus of this work concerns the negative-stiffness polymeric bias system to be coupled with the downscaled array. Although thermoplastic biasing elements proved effective at the macroscale, significant limitations emerge because fabrication inaccuracies on the order of a few millimeters become increasingly critical at smaller scale, ultimately compromising repeatability and performance. For this reason, alternative

 DOI: 10.30420/456743011

fabrication strategies capable of providing higher geometric precision and reproducibility, such as 3D printing techniques, are investigated, despite the higher hysteresis typically associated with printed polymeric materials. Four candidate materials are initially identified and subsequently analyzed through simulation, with the aim of designing downscaled biasing elements whose force-displacement characteristics can be matched to those of the individual DE units in the array. These results demonstrate a compact and scalable route toward dielectric elastomer actuator micro-arrays with cooperative actuation and sensing, while dispensing with pneumatic or fluid-based biasing elements. They also open promising perspectives for future developments in intelligent wearables, haptic interfaces, and autonomous micro-conveying systems, as well as enabling more advanced cooperative control strategies in fully soft microscale architectures.

2 DE matrix Design

DEs are soft electroactive transducers that can be described as deformable capacitors, typically consisting of an acrylic or silicone dielectric membrane placed between two compliant electrodes. Their operating principle relies on Maxwell stress: when a voltage difference is applied across the electrodes, the resulting electrostatic attraction generates a pressure through the thickness of the elastomer. This electromechanical loading compresses the dielectric layer and, owing to the nearly incompressible nature of the material, produces a corresponding expansion in the in-plane directions.

The downscaled design adopted in this work introduces several relevant modifications with respect to the original macroscale system from [13]. First, the screen-printed carbon-black electrodes used in the previous prototype are replaced by sputtered nickel thin films. Second, while the macroscale array consisted of eight stacked DE layers plus an additional protective layer for structural safety, the downscaled version achieves comparable force performance with a reduced stack composed of four DE layers, together with dedicated ground and protective layers, as shown in Figure 1a.

This work reports the design of a downscaled 3 × 3 DE array with overall dimensions of 55 × 55 mm², compared with the original macroscale platform, which had external dimensions of 150 × 150 mm², as shown in Figure 1b. The scaling process primarily concerns the geometry of the individual DE units, whose outer diameter is reduced from 39 mm to 11 mm and whose inner diameter is reduced from 12 mm to 3.5 mm, as illustrated in Figure 1c. In addition, the center-to-center pitch in both in-plane directions decreased from 47.5 mm to 17.7 mm. These reductions are implemented while preserving a minimum clearance of 3 mm between neighboring conductive regions, which is required for high-voltage operation and helps mitigate the risk of electrical arcing.

A further important difference concerns the electrical interconnection of the central element (2,2). In the 150 × 150 mm² array, electrical contacts were realized using silver conductive adhesive applied in the clamping regions, where the compliant electrodes were printed. In contrast, in the downscaled 55 × 55 mm² array, the electrical routing is achieved through conductive traces directly patterned onto the sputtered metallic thin film on the PDMS membrane surface. This approach provides a more uniform and monolithic contact scheme, which is better suited for miniaturized systems and compatible with microfabrication-oriented processes.

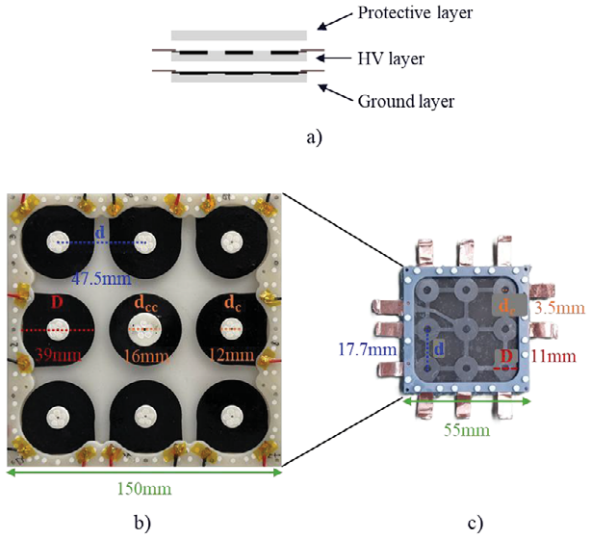


Figure 1 (a) DE Array multilayered structure. Comparison between the two array prototypes: (b) the macro-scale configuration and (c) the corresponding downscaled version developed in this work.

3 Cross-coupling mechanical characterization

The adopted manufacturing process provides highly repeatable device performance, both for single-membrane configurations and for systems based on stacked DE layers [13]. The experimental characterization was carried out by imposing a sinusoidal out-of-plane displacement from 0 to 4 mm at 1 Hz, under both low-voltage (LV, 0 V) and high-voltage (HV, 2.7 kV) conditions. As expected, the application of HV induced an electrostatic softening of the DE membrane, reducing the force required to achieve a given displacement.

This first characterization was performed in the flat configuration, i.e., with the neighboring DEs remaining undeformed out of plane. The resulting force-displacement curves exhibit moderate hysteresis under cyclic loading, which can be attributed to the viscoelastic behavior of the elastomer and compliant electrodes. Moreover, the results highlight three distinct mechanical responses within the matrix, corresponding to the different boundary conditions experienced by corner, side, and central DE units. Building on these results, the present work focuses on the integration of the downscaled DE array with the newly developed biasing element design. To assess the influence of the static out-of-plane deformation introduced by the biasing system,

 DOI: 10.30420/456743011

as well as the associated mechanical coupling between adjacent DE units, an additional characterization is performed.

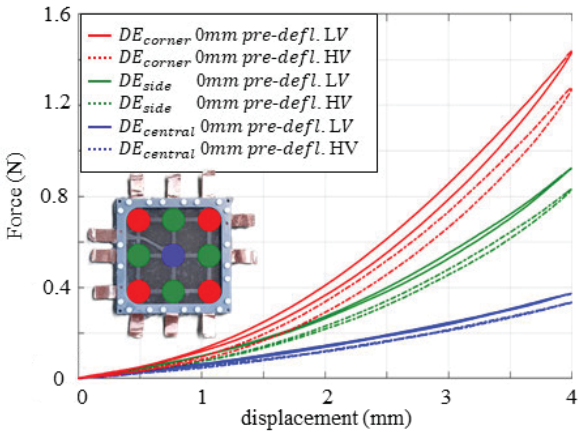


Figure 2 DE Array LV-HV force-displacement characteristic with neighboring flat configuration.

In this test, one DE element is tested as previously mentioned while the neighboring elements are pre-deformed out of plane by 3 mm, corresponding to the expected operating equilibrium defined by the intersection between the force-displacement response of a properly designed negative-stiffness biasing system and the 0 V curve of the DE element. This configuration allows each DE unit to be evaluated under conditions closer to the intended biased equilibrium state. The imposed pre-deflection of the neighboring elements leads to a general reduction in the absolute force levels measured during the second characterization. This effect is associated with the initial stress state induced in the reference membrane by the surrounding deformed DEs. In addition, the force-displacement curves exhibit an initial zero-force plateau, whose extent depends on the position of the measured element within the array. This plateau is most pronounced for the central DE and progressively decreases for side and corner elements. Although the measured DE starts from the same nominal reference position and undergoes the same imposed displacement as in the flat first configuration, the surrounding pre-deflected membranes modify its initial mechanical state. As a result, contact between the indenter and the reference membrane occurs at a larger imposed displacement, producing an initial region in which no contact force is measured.

The strongest coupling effect is observed for the central DE, as shown in Figure 3. In this case, the pre-deflection of the neighboring elements significantly reduces the available operating range, with positive force values appearing only for displacements above approximately 2 mm. This behavior introduces additional constraints for the design of the corresponding central negative-stiffness biasing element. The analysis also identifies the effective gap between the LV and HV force-displacement curves, which defines the actual actuation window available for the nonlinear biasing elements and provides the basis for the design choices discussed in the following section.

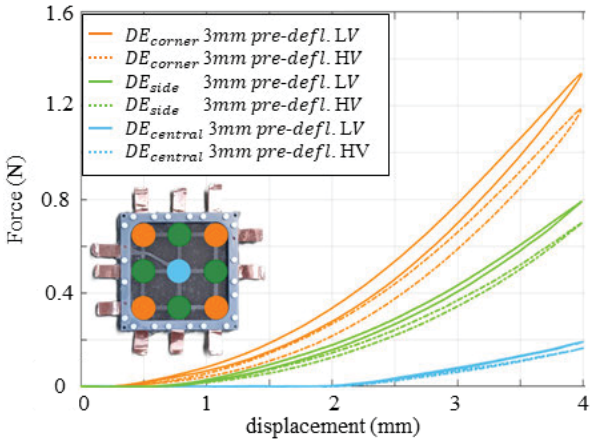


Figure 3 Mechanical coupling influence on the DE Array LV-HV force-displacement characteristic.

4 Negative-stiffness Biasing downscaling

Enhancing the actuation stroke of DE membranes requires an appropriately designed preloaded biasing system, since its mechanical response strongly affects the achievable displacement, stability, and repeatability of the actuator. In previous macroscale DE systems, such as the reference architecture shown in Figure 2, negative-stiffness biasing elements are implemented through thermoformed buckled-beam structures made of thermoplastic materials such as A-PET. These geometries introduce a negative-slope region in the force-displacement response, acting as a stiffness-compensation mechanism for the DE membrane and enabling millimeter-scale displacements with improved mechanical coupling and reduced long-term drift compared with softer silicone-based biasing elements. However, when the system is downscaled, this fabrication approach becomes increasingly critical.

At millimeter-scale dimensions, the tolerance to manual fabrication errors is significantly reduced, and even small deviations in the geometry of the thermoformed beams can strongly affect the mechanical response and, consequently, the overall actuator performance. For this reason, different materials and manufacturing strategies were investigated to assess 3D printing as a potential alternative to manual thermoforming for the realization of downscaled negative-stiffness biasing elements while maintaining large actuation stroke. Accordingly, four candidate materials were first evaluated, each associated with a different additive-manufacturing process: PEEK and PET-G for filament-based printing, BMF resin for stereolithography-based fabrication, and Nylon for selective laser sintering (SLS). Before fabricating complete NBS geometries, beam-like samples were tested in a cantilever configuration, as shown in Figure 4a, where one end is clamped and the free end is mechanically displaced by 3 mm. Based on

 DOI: 10.30420/456743011

Euler-Bernoulli beam theory, the measured force-displacement response was used to estimate the material stiffness through its flexural rigidity, allowing the Young's modulus of each printed material to be identified. The resulting values were E = 3.147 GPa for cured BMF resin, E = 2.498 GPa for PEEK, E = 1.887 GPa for PET-G, and E = 1.554 GPa for Nylon. These experimentally identified material properties will be then used as input parameters in COMSOL to design downscaled biasing geometries with force-displacement responses compatible with the requirements of the downscaled DE matrix. In particular, the design aims at identifying a local optimum in terms of overall DEA stroke, which depends on the intersections between the biasing force-displacement characteristic and the DE force-displacement curves under minimum and maximum voltage actuation.

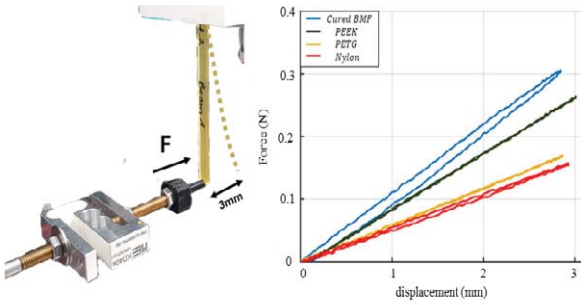


Figure 4 Experimental and simulated force-displacement response after the identification of the material parameters.

5 Conclusions

In this work, a downscaling strategy for a cooperative, fully polymeric, multidimensional DEA array is presented. The DE array is first characterized by measuring the force-displacement response of each membrane individually. The influence of the mechanical coupling between the membranes and the corresponding biasing elements in the actuated configuration on the measured force-displacement behavior is then analyzed. Based on this analysis, the material of the polymeric biasing element is investigated through cantilever tests to determine the elastic modulus of each candidate material. These properties provide the basis for the fabrication of the 3D-printed biasing elements that will be subsequently used to simulate and optimize the bias geometry, with the aim of matching it as closely as possible to the force-displacement behavior of the DE array presented in this work. Future work will focus on the characterization of polymeric biasing systems and on their subsequent integration with the downscaled DE array, with the aim of preserving the overall softness of the system while enabling millimeter-scale strokes. This will allow static and dynamic characterization of the actuation performance, paving the way for the investigation of sensing capabilities and, more broadly, for future soft smart applications.

6 Funding

Funded by the Deutsche Forschungsgemeinschaft (DFG, German Research Foundation) under grant no. 424608471.

7 Literature

[1] Kofod, G. "Dielectric elastomer actuators." Technical University of Denmark. (2001).

[2] Y. Zhao, L.-J. Yin, S.-L. Zhong, J.-W. Zha, Z.-M. Dang, "Review of dielectric elastomers for actuators, generators and sensors," IET Nanodielectrics (2020), 3, 4, 99–106.

[3] A. Marette, A. Poulin, N. Besse, S. Rosset, D. Briand, H. Shea. "Flexible zinc–tin oxide thin film transistors operating at 1 kV for integrated switching of dielectric elastomer actuators arrays", Advanced materials 29 (2017) 1700880.

[4] C. Lowe, X. Zhang, G. Kovacs, "Dielectric elastomers in actuator technology", Advanced Engineering Materials 2005, 7, 5 361.

[5] Koenigsdorff, M., Holzer, S., Konstantinidi, S., Civet, Y., & Perriard, Y. (2026). "A soft robotic fish with a dielectric elastomer actuator body and negative stiffness spine". *Advanced Robotics Research*.

[6] Lv, J., Hong, H., Zhang, M., Gan, et al. (2025). "Bio-inspired optofluidic focus-tunable imaging system with large two-dimensional field-of-view tuning capability". *Measurement, 253*, 117332.

[7] Benouhiba, A., Walter, A. M., Jahren, et al. (2025). "Soft Beats: A dielectric elastomer-based ventricular assist device for next-gen heart failure management". *Advanced Engineering Materials*, 27(20), 2501234.

[8] J.-H. Youn, S.-Y. Jang, I. Hwang, et al. "Skin-attached haptic patch for versatile and augmented tactile interaction", Science Advances 11 (2025)

[9] Shrestha, M., Lau, G.K., Chin, Y.W. *et al.* "A tunable acoustic absorber using reconfigurable dielectric elastomer actuated petals". *Commun Eng* **3**, 11 (2024).

[10] X. Qu, X. Ma, B. Shi, et al., "Refreshable braille display system based on triboelectric nanogenerator and dielectric elastomer", Advanced Functional Materials (2021).

[11] Shen, H., Dong, X., Li, X et al. "A dynamic modeling framework of a DE actuators miniature pump for enhanced power density". Extreme Mechanics Letters, 79, 102396. (2025).

[12] Addario, S., Priuli, A., Gratz-Kelly, S et al. "Multi-dimensional negative-stiffness thermoplastic bias mechanisms for high-stroke dielectric elastomer actuator arrays," in [Electroactive Polymer Actuators and Devices (EAPAD) XXVII], 1–10 (2025).

[13] Addario, S., Priuli, A., Schagaew, et al. "Downscaling of multidimensional cooperative arrays of dielectric elastomer actuators". *Proc. SPIE* 13945 (2026).

 DOI: 10.30420/456743012

Response Surface Modeling and Multi-Response Optimization of PVDF/$BaTiO_3$/CNT Films for Flexible Actuator Applications

Ahmed Attaoui[1,2,*], Ayda Bouhamed[3,4], Chokri Bouraoui[2] and Olfa Kanoun[1,*]

[1] Professorship of Measurement and Sensor Technology (MST), Chemnitz University of Technology, Reichenhainer Straße 70, 09126 Chemnitz, Germany; olfa.kanoun@etit.tu-chemnitz.de
[2] Laboratory of Mechanics of Sousse (LMS), National Engineering School of Sousse (ENISo), University of Sousse, Technopole de Sousse, Route de Ceinture Sahloul, 4054 Sousse, Tunisia; chokri.bouraoui@eniso.u-sousse.tn
[3] Faculty of Sciences of Gafsa (FSGF), University of Gafsa, 2112 Gafsa, Tunisia; aydabouhamed@gmail.com
[4] Laboratory of Electromechanical Systems (LASEM), National Engineering School of Sfax, University of Sfax, Soukra km 4, 3038 Sfax, Tunisia
* Correspondence: ahmed.attaoui@etit.tu-chemnitz.de; olfa.kanoun@etit.tu-chemnitz.de

Abstract

High-performance flexible piezoelectric actuators require precise tuning of electroactive, dielectric, and mechanical properties. However, optimizing multicomponent polymer nanocomposites through trial-and-error approaches remains inefficient and often fails to capture interactions between fillers. This work presents a systematic methodology for developing predictive analytical models to optimize PVDF/$BaTiO_3$/CNT nanocomposite films for flexible piezoelectric actuator applications. Response surface methodology (RSM) was employed based on a two-factor design of experiments (DOE), with $BaTiO_3$ and CNT contents selected as the main formulation variables. Following fabrication by solution casting, the films were characterized using Fourier-transform infrared spectroscopy, tensile testing, and impedance spectroscopy. Second-order polynomial models described the individual, quadratic, and interaction effects of the fillers, showing strong predictive capability with R^2 values of 0.934, 0.971, and 0.990 for β-phase content, Young's modulus, and dielectric constant, respectively. ANOVA and independent validation experiments confirmed the reliability of the models. Sensitivity analysis revealed that CNT loading strongly governs the mechanical and dielectric responses, while the $BaTiO_3$ × CNT interaction plays a critical role in electroactive β-phase formation. Multi-response desirability optimization identified an optimum composition window of 11.10-13.95 wt% $BaTiO_3$ and 0.46-0.64 wt% CNT, with the highest desirability, D_{max} = 0.849, predicted at 12.45 wt% $BaTiO_3$ and 0.55 wt% CNT. This approach reduces trial-and-error experimentation while clarifying filler interactions, providing an experimentally efficient framework for tailoring PVDF-based materials for next-generation flexible piezoelectric actuators.

1 Introduction

Actuators play a central role in modern technologies by converting external stimuli, such as electrical, thermal, magnetic, or pneumatic energy, into controlled mechanical motion [1]. They are widely used in robotics, biomedical devices, wearable systems, haptic interfaces, micro-electromechanical systems, prosthetics, adaptive structures, and human-machine interaction platforms [2-4]. As these technologies move toward miniaturized, lightweight, and body-conformable systems, the demand for compact actuators capable of producing precise, repeatable, and efficient motion has increased significantly. Conventional actuators, including electromagnetic motors, pneumatic actuators, hydraulic systems, and rigid piezoceramic actuators, have enabled major advances in automation and precision control. However, their use in emerging wearable and soft-interface applications remains limited by several drawbacks. Electromagnetic actuators often rely on bulky coils and magnets, whereas pneumatic and hydraulic systems require external pumps or fluidic components. Rigid piezoceramic actuators offer fast response and high force density, but their brittleness and mechanical mismatch with soft biological surfaces restrict their use in deformable systems. These limitations have motivated the development of lightweight and flexible actuator materials with direct electromechanical response. Soft actuator materials have therefore attracted increasing attention as promising candidates for next-generation actuation systems. Unlike rigid actuator architectures, flexible materials can conform to complex surfaces, withstand bending and deformation, and be integrated into thin films, textiles, wearable patches [5,6], and soft robotic structures [7]. Their intrinsic compliance allows better mechanical compatibility with the human body and enables distributed actuation over large or curved areas. This makes them particularly attractive for applications such as vibrotactile feedback, wearable interfaces, artificial muscles, soft grippers, adaptive sensors, and compact haptic devices.

Among the different classes of flexible actuator materials, electroactive polymers are especially appealing because they can generate mechanical deformation in response to an electrical stimulus while maintaining low density, processability, and mechanical flexibility [8]. These materials can be fabricated in thin-film form using scalable processing techniques, making them suitable for miniaturized and lightweight actuator platforms. Electroactive polymers can offer fast response, silent operation, design flexibility,

and the possibility of integration into multifunctional systems where sensing and actuation are combined within the same material structure [9,10]. In this context, poly(vinylidene fluoride) (PVDF) and its copolymers are among the most widely studied piezoelectric polymers for flexible energy harvesting, sensing, and actuator applications because of their electromechanical coupling, chemical stability, and mechanical flexibility [11]. The piezoelectric response of PVDF is primarily governed by the fraction of its electroactive β-phase, which exhibits the all-trans (TTTT) chain conformation responsible for spontaneous polarization [12]. However, pristine PVDF often requires material modification or processing optimization to enhance its electroactive phase content, dielectric properties, and mechanical performance for practical devices. To address these limitations, the incorporation of functional fillers into PVDF has become an effective strategy for developing high-performance flexible actuator materials [13]. Ceramic fillers such as $BaTiO_3$ act as nucleating agents that promote β-phase crystallization and simultaneously enhance the dielectric constant [14-16]. Conductive nanofillers such as carbon nanotubes (CNTs) contribute to mechanical reinforcement and provide percolation pathways that can amplify the local electric field and facilitate dipole alignment [14,17].

Design of experiments (DOE) coupled with response surface methodology (RSM) provides an efficient route to reduce experimental trial-and-error while quantifying the individual, quadratic, and interaction effects of formulation variables [18]. Although DOE-RSM is well established in broader composite processing and optimization, its application to multifunctional PVDF-based piezoelectric nanocomposites remains limited. Existing studies have mainly focused on specific systems such as electrospun PVDF fibers [19] and PVDF/SiC nanoenergy harvesters [20]. The objective of the present work is to develop analytical models that correlate the individual, quadratic, and interaction effects of $BaTiO_3$ and CNT loadings with the β-phase content, Young's modulus, and dielectric constant of PVDF-based nanocomposite films. By coupling DOE with experimental characterization and RSM, the resulting predictive models are intended to reveal the structure-property relationships of the nanocomposites and to identify an actuator-oriented composition window that balances electroactive phase formation, dielectric enhancement, and mechanical compliance for flexible piezoelectric actuator applications.

2 Materials and Methods

2.1 Materials

Poly(vinylidene fluoride) (PVDF) was purchased from Sigma-Aldrich and used as received without further purification. PVDF was selected as the polymer matrix because of its ferroelectric nature, density of 1.78 g/cm³, melting temperature of approximately 160-170 °C, and ability to form the electroactive β-phase. Barium titanate ($BaTiO_3$) powder, obtained from Sigma-Aldrich, was used as the ceramic filler owing to its high dielectric permittivity, particle size below 2 μm, purity of 99.5% trace metals basis, and density of 6.08 g/cm³. Multi-walled carbon nanotubes (CNTs), supplied by Nanocyl, were incorporated as conductive nanofillers because of their high electrical conductivity, purity above 95%, average diameter of 9.5 nm, average length of 1.5 μm, and Young's modulus exceeding 1 TPa. N,N-Dimethylformamide (DMF), supplied by Fisher Scientific, was used as the solvent due to its high polarity, ability to dissolve PVDF, and suitability for promoting effective filler dispersion. All materials were used without further treatment unless otherwise stated.

2.2 Elaboration Process

PVDF-based nanocomposites containing barium titanate ($BaTiO_3$) and multi-walled carbon nanotubes (CNTs) were fabricated using a solution casting process. The procedure was designed to ensure homogeneous filler dispersion within the polymer matrix and reproducible film quality. The elaboration process used to prepare the PVDF/$BaTiO_3$/CNT nanocomposite films is schematically presented in **Figure 1**.

Initially, $BaTiO_3$ powder was dispersed in *N*,*N*-dimethylformamide (DMF) and magnetically stirred at 55 °C and 800 rpm for 10 min, followed by ultrasonication at 30% amplitude for 5 min to reduce particle agglomeration. In parallel, CNTs were dispersed in DMF and ultrasonicated for 5 min at 30% amplitude to promote uniform CNT dispersion. Separately, PVDF powder was dissolved in DMF under continuous magnetic stirring at 55 °C and 800 rpm for 5 h until a homogeneous polymer solution was obtained. Afterward, the $BaTiO_3$ and CNT dispersions were combined and mixed, followed by the gradual addition of the PVDF solution to form the final ternary suspension. The resulting mixture was further stirred and subsequently ultrasonicated for 10 min to enhance filler distribution and interfacial mixing. The prepared suspension was then degassed under vacuum to remove entrapped air bubbles before being cast onto a flat substrate. A controlled volume of solution was deposited to obtain films with uniform thickness. Finally, the cast films were dried in an oven at 60 °C for 3 h to remove residual solvent and promote crystallization, yielding flexible PVDF/ $BaTiO_3$/CNT composite films for subsequent characterization.

2.3 Characterizations and measurements

The characterization methods used for the PVDF/$BaTiO_3$/CNT nanocomposite films are schematically summarized in **Figure 2**.

Fourier-transform infrared spectroscopy (FTIR) was performed using an INVENIO spectrometer (Bruker, Germany) equipped with an attenuated total reflectance (ATR) accessory. The spectra were recorded in the range of 650-1800 cm^{-1} with a resolution of 4 cm^{-1}, and 32 scans were averaged for each sample to improve the signal-to-noise

 DOI: 10.30420/456743012

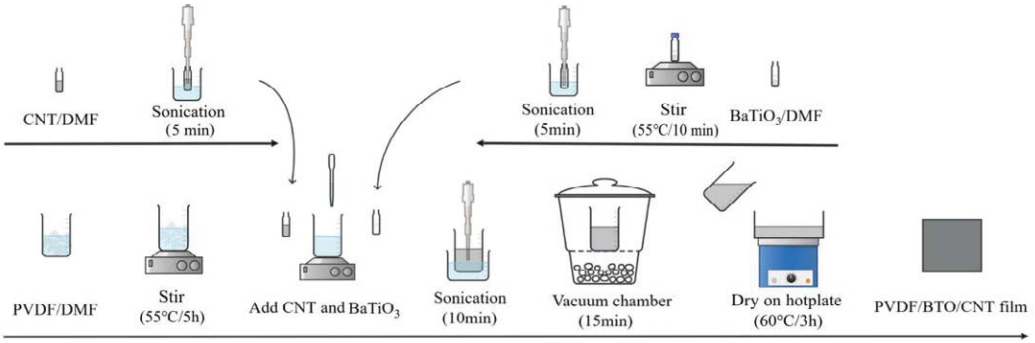


Figure 1. Schematic illustration of the elaboration process of PVDF/$BaTiO_3$/CNT nanocomposite films.

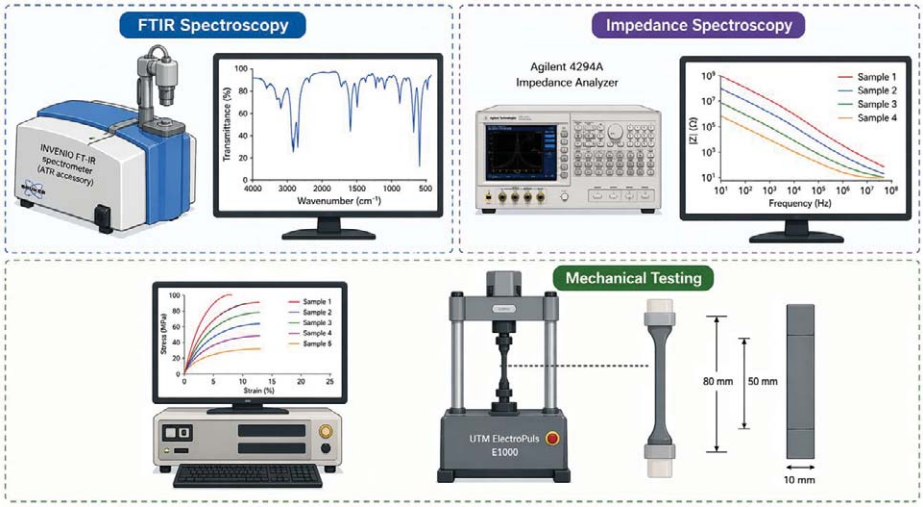


Figure 2. Schematic overview of the characterization methods used for the PVDF/$BaTiO_3$/CNT nanocomposite films.

ratio. The electroactive β-phase content was quantified from the FTIR spectra according to the method reported by Morali et al. [21], using Equation (1):

$$F_\beta = \frac{A_\beta}{(\frac{K_\beta}{K_\alpha}.A_\alpha + A_\beta)} = \frac{A_\beta}{(1.26.A_\alpha + A_\beta)} \quad (1)$$

where Aα and Aβ are the absorbance intensities corresponding to the characteristic α- and β-phase bands, respectively, and Kα and Kβ are the absorption coefficients of the respective crystalline phases.

For the mechanical characterization, Young's modulus was determined using a universal testing machine, ELECTROPULS® E10000. Rectangular specimens were prepared according to the ISO 527-3 Type 2 standard and tested at a crosshead speed of 10 mm/min. At least five specimens were tested for each composition to ensure statistical reliability.

Electrical and dielectric properties were evaluated by impedance spectroscopy using an Agilent 4294A impedance analyzer over a frequency range of 40 Hz to 110 MHz. The measurement system was interfaced with LabVIEW software for real-time acquisition of complex impedance data, allowing the dielectric response of the PVDF/$BaTiO_3$/CNT composite films to be analyzed. The real component of the complex permittivity ε′, was calculated from the measured complex impedance using Equation (2):

$$\varepsilon' = \frac{Z''}{\omega C_0 (Z'^2 + Z''^2)} \quad (2)$$

where Z′ and Z″ are the real and imaginary components of the complex impedance, respectively, ω = 2πf is the angular frequency, and C_0 is the vacuum capacitance of the electrode configuration.

2.4 Design of Experiments

In the present study, the experiments were designed using a full factorial design of experiments (DOE) approach to systematically evaluate the influence of filler composition on the multifunctional properties of PVDF-based nanocomposites. The main objective of the factorial design was to study the relationship between the input factors and the measured responses, namely β-phase content, Young's modulus, and dielectric constant. This approach enables the evaluation of both the individual effects of each factor and their interaction effects.

Barium titanate ($BaTiO_3$) content and CNT content were selected as the main input factors. Each factor was investigated at three levels, resulting in a 3^2 full factorial design with nine experimental runs. The design and statistical analysis were used to establish response surface models for predicting the material responses as a function of filler

 DOI: 10.30420/456743012

loading. Table 1 presents the selected factors and their coded and actual levels.

Table 1. Experimental factors.

Factors	Notation	Levels		
		-1	0	+1
$BaTiO_3$ (wt%)	A	10	15	20
CNT (wt%)	B	0.0	0.5	1.0

Table 2. Experimental results.

Exp. N°	A BT	B CNT	β-Phase (%)	E (MPa)	ε_r
1	-1	-1	86.20	2086.9	3.10
2	-1	0	91.30	2707.4	8.07
3	-1	+1	94.26	2890.4	7.60
4	0	-1	94.67	2454.1	3.65
5	0	0	94.33	2825.0	7.88
6	0	+1	95.45	2963.8	8.65
7	+1	-1	94.08	2779.6	3.70
8	+1	0	91.88	2804.1	8.21
9	+1	+1	89.43	2623.1	9.46

3 Results and discussion

In this section, the influence of $BaTiO_3$ and CNT contents on the β-phase content, Young's modulus, and dielectric constant of PVDF-based nanocomposites was investigated using response surface methodology (RSM). The experimental results obtained from the full factorial design were used to develop second-order polynomial regression models describing the relationship between filler contents and the selected responses. The adequacy and statistical reliability of the developed models were evaluated using the coefficient of determination, R^2, analysis of variance (ANOVA), and independent validation experiments. After validation, the models were used to generate response surface plots, Pareto charts, and desirability-based optimization maps to identify the PVDF/$BaTiO_3$/CNT nanocomposite composition most suitable for actuator applications. In this context, the desired material should provide a balanced combination of electroactive phase formation, enhanced dielectric performance, and controlled mechanical stiffness.

3.1 Development of mathematical models

Response surface methodology (RSM) was employed in this study to establish predictive relationships between the formulation parameters and the measured responses of the PVDF-based nanocomposites. RSM is a widely used statistical and mathematical technique for modeling, analyzing, and optimizing systems in which a response is influenced by several independent variables. In the present work, the experimental data generated from the full factorial design were used to construct regression models describing the combined influence of $BaTiO_3$ content and CNT loading on β-phase content, Young's modulus, and dielectric constant.

The general relationship between the response, Y, and the independent variables can be expressed as:

$$Y = f(X_1, X_2) + \varepsilon \qquad (3)$$

where X_1 and X_2 represent the coded values of $BaTiO_3$ and CNT contents, respectively, and ε is the experimental error associated with the measurements.

To accurately capture the linear, interaction, and curvature effects within the investigated design space, a second-order polynomial model was adopted. For two variables, the quadratic model is written as:

$$Y = \beta_0 + \beta_1 X_1 + \beta_2 X_2 + \beta_{12} X_1 X_2 + \beta_{11} x_1^2 + \beta_{22} X_2^2 \qquad (4)$$

where β_0 is the intercept term, β_1 and β_2 are the linear coefficients, β_{12} represents the interaction effect between the two factors, and β_{11} and β_{22} correspond to the quadratic terms.

The analytical expressions of the fitted quadratic models are given as follows:

$$\beta\text{-phase} = 96.268 - 0.615BT + 1.712CNT - 2.585BT \times CNT - 3.022BT^2 - 2.642CNT^2 \qquad (5)$$

$$E = 2844.88 + 87.02BT + 192.77CNT - 239.99BT \times CNT - 99.09BT^2 - 145.86CNT^2 \qquad (6)$$

$$\varepsilon' = 8.078 + 0.433BT + 2.543CNT + 0.315BT \times CNT - 0.037BT^2 - 2.027CNT^2 \qquad (7)$$

These analytical relationships represent the quadratic response surface models for β-phase content, Young's modulus, and dielectric constant.

Analysis of variance (ANOVA) was performed to evaluate the statistical significance of the developed models. The ANOVA results are summarized in Tables 3-5. The obtained R^2 values of 0.934, 0.971, and 0.990 for β-phase content, Young's modulus, and dielectric constant, respectively, indicate good agreement between the experimental and predicted responses, as presented in Figure 3a-c. The high R^2 values confirm that the second-order polynomial formulation is adequate to capture the nonlinear structure-property relationships within the studied composition space, validating the strong predictive capability of the models for optimizing PVDF/$BaTiO_3$/CNT compositions.

ISBN: 978-3-8007-6743-4 @ VDE VERLAG GMBH · Berlin · Offenbach

 DOI: 10.30420/456743012

Table 3. ANOVA results for the quadratic model of β-phase content.

Source	df	SS	MS	Contribution	F-value	p-value
Model	5	78.7948	15.7590	93.38%	8.4617	0.0544*
BT	1	2.2694	2.2694	2.69%	1.2185	0.3502
CNT	1	17.5788	17.5788	20.83%	9.4389	0.0545*
BT × CNT	1	26.7289	26.7289	31.68%	14.3520	0.0323**
BT^2	1	18.2609	18.2609	21.64%	9.8052	0.0520*
CNT^2	1	13.9568	13.9568	16.54%	7.4941	0.0715*
Residual	3	5.5871	1.8624	6.62%	--	--
Total	8	84.3820	--	100.00%	--	--

*p < 0.10, **p < 0.05, ***p < 0.01.

Table 4. ANOVA results for the quadratic model of Young's modulus.

Source	df	SS	MS	Contribution	F-value	p-value
Model	5	560975.1717	112195.0343	97.07%	19.8879	0.0166**
BT	1	45432.2718	45432.2718	7.86%	8.0534	0.0658*
CNT	1	222970.5049	222970.5049	38.58%	39.5242	0.0081***
BT×CNT	1	230386.5602	230386.5602	39.87%	40.8388	0.0078***
BT^2	1	19637.9865	19637.9865	3.40%	3.4811	0.1589
CNT^2	1	42547.8482	42547.8482	7.36%	7.5421	0.0710*
Residual	3	16924.0811	5641.3604	2.93%	--	--
Total	8	577899.2528	--	100.00%	--	--

*p < 0.10, **p < 0.05, ***p < 0.01.

Table 5. ANOVA results for the quadratic model of dielectric constant.

Source	df	SS	MS	Contribution	F-value	p-value
Model	5	48.5523	9.7105	99.00%	59.4909	0.0034***
BT	1	1.1267	1.1267	2.30%	6.9025	0.0785*
CNT	1	38.8113	38.8113	79.14%	237.7764	0.0006***
BT × CNT	1	0.3969	0.3969	0.81%	2.4316	0.2168
BT^2	1	0.0027	0.0027	0.01%	0.0165	0.9060
CNT^2	1	8.2148	8.2148	16.75%	50.3275	0.0058***
Residual	3	0.4897	0.1632	1.00%	--	--
Total	8	49.0420	--	100.00%	--	--

*p < 0.10, **p < 0.05, ***p < 0.01.

The ANOVA results demonstrate that the proposed quadratic response surface models are statistically suitable for describing the effects of $BaTiO_3$ and CNT contents on the selected responses. For all investigated responses, the model sum of squares was considerably higher than the residual contribution, indicating that the developed equations successfully captured the main experimental trends with limited unexplained error.

For the β-phase content, **Table 3** shows that the overall quadratic model exhibited marginal statistical significance, with p = 0.0544. This indicates that the second-order regression model can reasonably describe the evolution of the electroactive phase within the investigated composition range. Among the model terms, the BT × CNT interaction was statistically significant, with p = 0.0323, demonstrating that β-phase formation is strongly influenced by the combined effect of $BaTiO_3$ and CNTs rather than by their individual contributions alone.

The quadratic model developed for Young's modulus, presented in **Table 4**, was statistically significant, with p = 0.0166, confirming its suitability for predicting the stiffness behavior of the nanocomposites. The CNT linear term and the BT × CNT interaction term was highly significant, with p < 0.01, demonstrating that CNT incorporation and the synergistic reinforcement between $BaTiO_3$ and CNTs are the principal factors controlling the elastic response.

The dielectric constant model, reported in **Table 5**, exhibited the highest statistical significance, with p = 0.0034, indicating an excellent fit between the composition variables and the dielectric response. In this case, both the CNT linear and quadratic terms were highly significant, with p < 0.01, confirming that CNT concentration is the dominant parameter governing the relative permittivity.

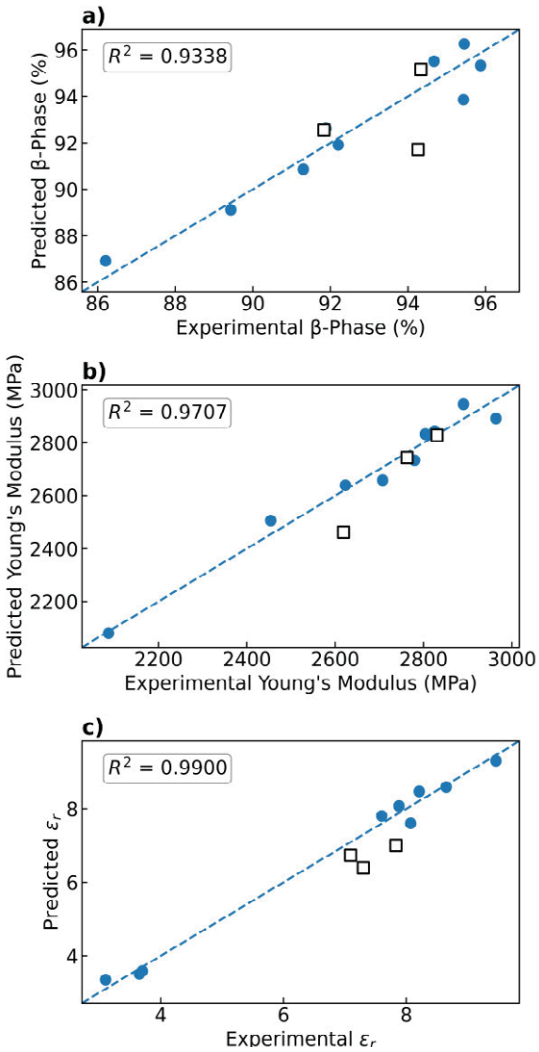


Figure 3. Goodness of fit of RS model (a) β-phase content, (b) Young's modulus, and (c) dielectric constant.

 DOI: 10.30420/456743012

The goodness-of-fit plots shown in **Figure 3** demonstrate strong agreement between the experimental and predicted values for all investigated responses. The data points are closely distributed around the parity line, confirming the adequacy of the developed quadratic models. High coefficients of determination were obtained for β-phase content, $R^2 = 0.9338$; Young's modulus, $R^2 = 0.9707$; and dielectric constant, $R^2 = 0.9900$, indicating excellent predictive accuracy.

To further evaluate the generalization capability of the models, additional validation experiments containing 0.3 wt% CNT were introduced as independent test points. These validation compositions were not included in the model fitting stage. In **Figure 3a-c**, the validation points are represented by open square symbols, while the direct comparison between experimental and predicted values is further summarized in **Figure 4a-c**.

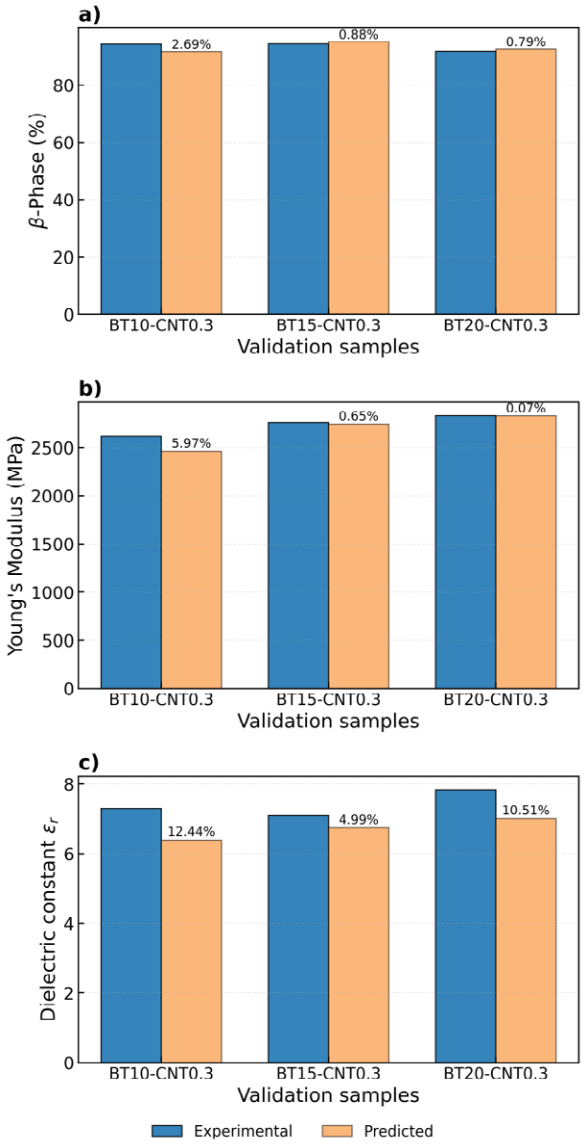


Figure 4. Experimental and predicted validation responses for PVDF/$BaTiO_3$/CNT nanocomposites (a) β-phase content, (b) Young's modulus, and (c) dielectric constant.

The validation results show good agreement between the measured and predicted values for the three studied responses. The average absolute prediction errors were 1.46% for β-phase content, 2.23% for Young's modulus, and 9.31% for the dielectric constant. The relatively low errors obtained for β-phase content and Young's modulus indicate that the developed quadratic models provide acceptable interpolation capability within the studied factor space. The larger deviation observed for the dielectric constant is expected because dielectric behavior is highly sensitive to nanoscale conductive network formation, filler dispersion, and interfacial polarization effects. Nevertheless, the overall validation confirms that the proposed quadratic models can be reliably used to predict and optimize the performance of PVDF/$BaTiO_3$/CNT nanocomposites.

3.2 Effect and sensitivity analysis of input factors

The influence of $BaTiO_3$ (BT) content and CNT loading on β-phase content, Young's modulus, and dielectric constant was further analyzed using main effects and interaction plots, as shown in **Figure 5**, together with Pareto charts of standardized effects, presented in **Figure 6**. The main effects plots illustrate the individual contribution of each filler to the selected responses, while the interaction plots reveal whether the response of the PVDF matrix is governed by independent or coupled filler effects. Complementarily, the Pareto charts provide a quantitative ranking of the linear, quadratic, and interaction terms, allowing the dominant factors controlling each material property to be identified.

This combined graphical and statistical analysis provides deeper insight into the composition–property relationships of the PVDF/ $BaTiO_3$/CNT nanocomposites. In particular, it enables direct evaluation of the sensitivity of the electroactive, mechanical, and dielectric responses to changes in filler loading, thereby clarifying the formulation parameters that most strongly govern the multifunctional performance of the films. Such understanding is essential for defining an optimized composition window suitable for flexible piezoelectric actuator applications.

The β-phase content response, shown in **Figure 5a-c**, exhibits a clear nonlinear dependence on both BT and CNT contents. Increasing CNT loading enhanced the β-phase fraction up to 0.5 wt%, followed by a slight decrease at higher concentration. This behavior can be attributed to the nucleating role of CNTs, which promotes electroactive phase crystallization at moderate loading, whereas excessive CNT content may favor agglomeration and restrict PVDF chain alignment [22]. A similar nonlinear trend was observed for BT, with the β-phase content reaching a maximum at approximately 15 wt% before decreasing at higher ceramic loading. The interaction plot further highlights a strong coupling between BT and CNT, indicating that the influence of CNTs on β-phase formation depends markedly

 DOI: 10.30420/456743012

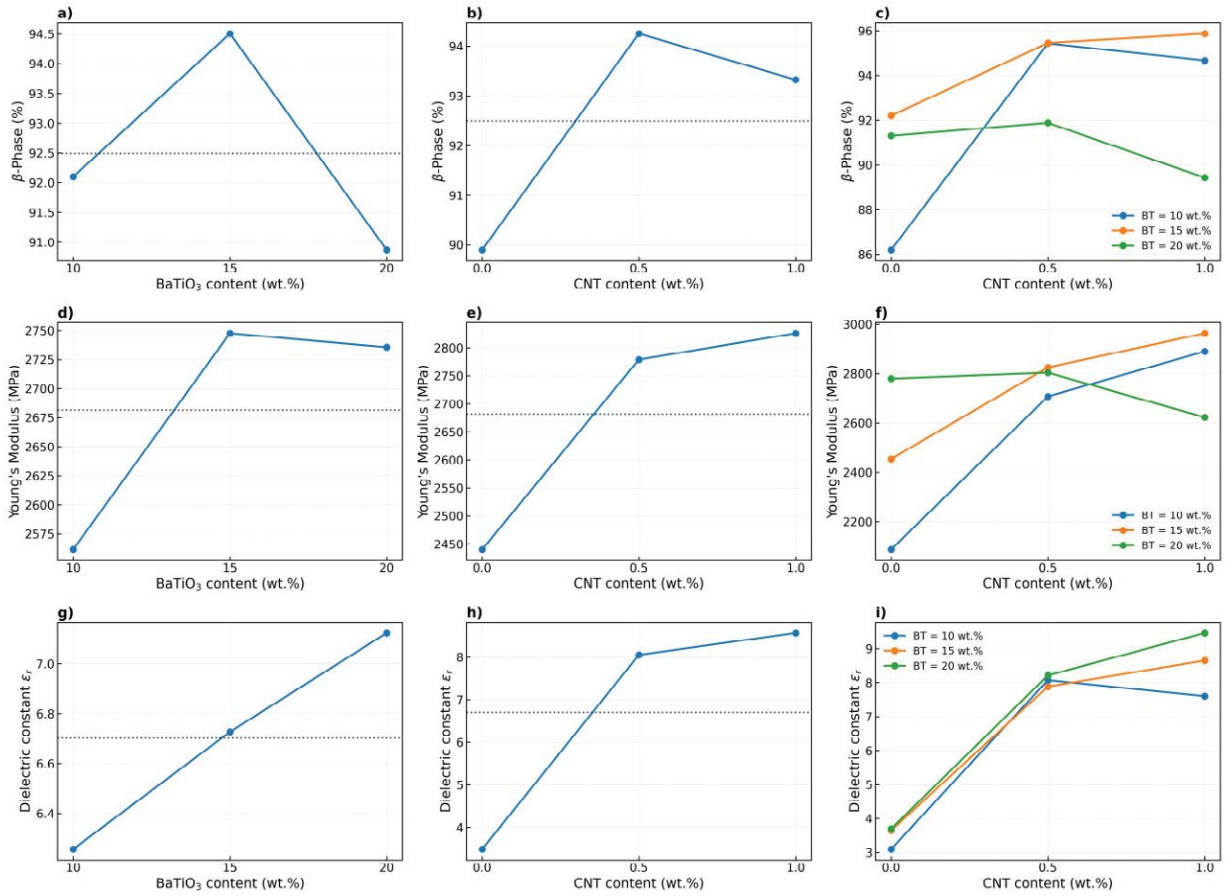


Figure 5. Main effects and interaction plots of $BaTiO_3$ (BT) and CNT contents on (a-c) β-phase content, (d-f) Young's modulus, and (g-i) dielectric constant.

on the BT concentration. This observation is consistent with the Pareto analysis in **Figure 6**, where the BT × CNT interaction showed the highest contribution, accounting for 27.4% of the total standardized effect. This was followed by BT², CNT, and CNT², with contributions of 22.6%, 22.2%, and 19.8%, respectively, while the individual BT effect was the least influential, contributing only 8.0%. These results indicate that β-phase formation is governed primarily by filler synergy and nonlinear compositional effects rather than by the isolated contribution of a single filler. Therefore, a moderate and balanced BT/CNT composition is more favorable for promoting electroactive phase formation than simply increasing the concentration of either filler.

The mechanical response, presented in **Figure 5d-f**, demonstrates that CNT loading is the dominant factor controlling Young's modulus. A pronounced increase in stiffness was observed with increasing CNT concentration, which is associated with the high intrinsic modulus of CNTs and their ability to improve load transfer within the PVDF matrix [23,24]. In contrast, BT exhibited a more moderate nonlinear effect, with Young's modulus reaching a maximum at 15 wt% before slightly decreasing at higher loading. This reduction at excessive ceramic content may be related to stress concentration, particle agglomeration, or reduced filler dispersion within the polymer matrix [25].

The interaction plot indicates that the reinforcing effect of CNTs is strongly dependent on BT content, becoming more effective at intermediate BT loading and less pronounced at higher ceramic concentration. This interpretation is supported by the Pareto analysis in **Figure 6**, where the BT × CNT interaction and CNT loading were the dominant terms, contributing 31.8% and 31.2%, respectively. Together, these two terms accounted for 63.0% of the total standardized effect, confirming that the mechanical stiffness is mainly governed by CNT reinforcement and its interaction with BT particles. The BT linear effect contributed 14.1%, while CNT² and BT² contributed 13.6% and 9.3%, respectively. These findings show that the elastic behavior of PVDF/BT/CNT nanocomposites is not controlled only by the intrinsic reinforcing effect of CNTs, but also by hybrid filler interactions that influence load transfer and local stress distribution within the polymer matrix.

The dielectric response, shown in **Figure 5g-i**, was mainly governed by CNT loading. The dielectric constant increased markedly with increasing CNT concentration, which can be attributed to enhanced interfacial polarization and the formation of micro-capacitive networks within the PVDF matrix, typically associated with the Maxwell-Wagner-Sillars polarization mechanism [26,27]. BT also contributed to dielectric enhancement owing to its high intrinsic permittivity and additional polarization contribution,

 DOI: 10.30420/456743012

but its effect was less pronounced than that of CNTs. The interaction plot suggests that the dielectric response can be further improved when BT and CNT are incorporated together, indicating a cooperative filler effect. Nevertheless, the overall behavior remains predominantly controlled by CNT concentration. This conclusion is strongly supported by the Pareto analysis in **Figure 6**, where CNT alone accounted for 57.5% of the total standardized effect, while the CNT² term contributed an additional 26.4%. Consequently, CNT terms collectively represented 83.9% of the overall influence on the dielectric constant. By comparison, the BT linear term contributed 9.8%, whereas the BT × CNT interaction and BT² terms contributed only 5.8% and 0.5%, respectively. These results confirm that the dielectric behavior of PVDF/BT/CNT nanocomposites is primarily controlled by CNT-induced interfacial polarization

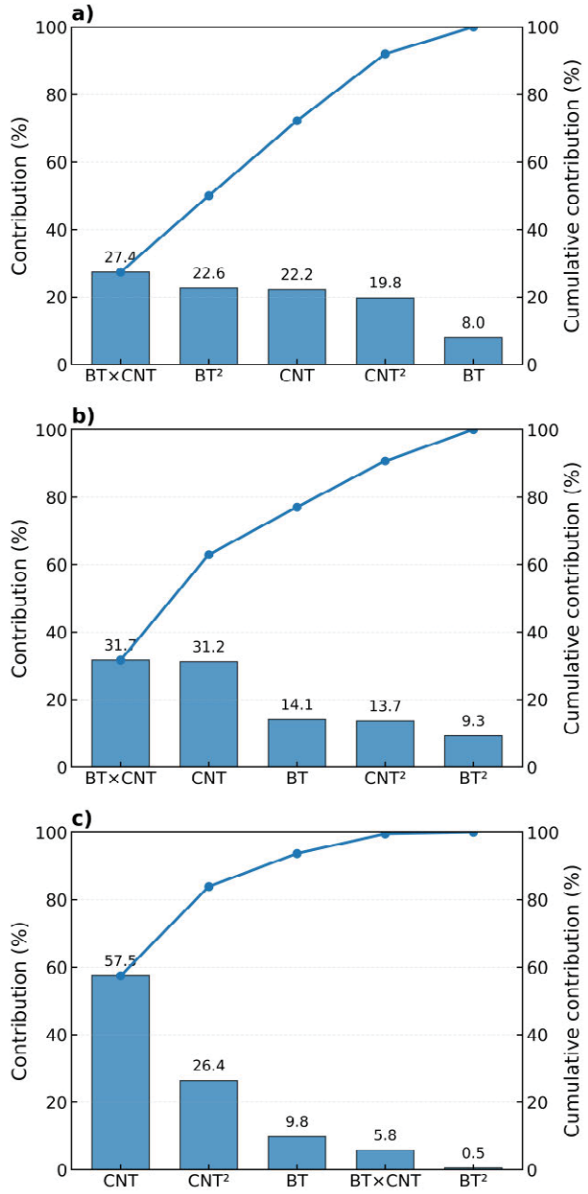


Figure 6. Pareto contribution plots of standardized effects for (a) β-phase content, (b) Young's modulus, and (c) dielectric constant.

and micro-capacitive network formation, with BT providing a secondary contribution through its intrinsic polarizability.

The combined interpretation of the main effects plots, interaction plots, and Pareto analyses confirms that CNT loading is the dominant compositional parameter governing the multifunctional response of the PVDF/BT/CNT nanocomposites, particularly with respect to dielectric constant and Young's modulus. $BaTiO_3$ exhibits a secondary but essential role by contributing to dielectric polarization and, more importantly, by modulating the formation of the electroactive β phase. The pronounced BT × CNT interaction observed for both β-phase content and Young's modulus indicates that the material response cannot be optimized by treating each filler independently. Instead, the overall functional performance results from a delicate balance between ceramic induced polarization, CNT driven interfacial polarization and micro-capacitive effects, and mechanical reinforcement produced by the combined filler system. These findings emphasize the importance of composition-based optimization for identifying formulations that simultaneously promote electroactive phase formation, enhance dielectric response, and maintain suitable mechanical stiffness for PVDF based nanocomposites designed for flexible actuator applications.

3.3 Response surface analysis

To further examine the coupled influence of $BaTiO_3$ and CNT contents on the investigated responses, three-dimensional response surface plots were generated from the developed quadratic models, as shown in **Figure 7**. These plots provide a continuous representation of the predicted response evolution across the investigated composition domain and allow the identification of formulation regions associated with favorable electroactive, mechanical, and dielectric performance.

Figure 7a presents the response surface of the β phase content. The surface exhibits a dome shaped profile, indicating a clear nonlinear dependence on both BT and CNT contents. The β phase fraction increases when moderate amounts of BT and CNT are incorporated, reaching a maximum region at intermediate filler loadings. However, a further increase in filler content leads to a reduction in the predicted β phase content. This behavior suggests that moderate filler addition promotes electroactive phase formation by enhancing dipole alignment and heterogeneous nucleation, whereas excessive filler loading may restrict PVDF chain mobility and promote filler agglomeration. Therefore, the β phase response is not governed by the isolated increase of a single filler, but rather by an optimized balance between BT and CNT contents.

The response surface for Young's modulus is shown in **Figure 7b**. The modulus increases markedly with increasing CNT loading, confirming the dominant reinforcing role of CNTs within the PVDF matrix. This behavior is attributed to the high aspect ratio and intrinsic stiffness of CNTs, which enable efficient load transfer through the polymer network. The surface also reveals a nonlinear effect of BT content. Stiffness improves with BT addition up to

 DOI: 10.30420/456743012

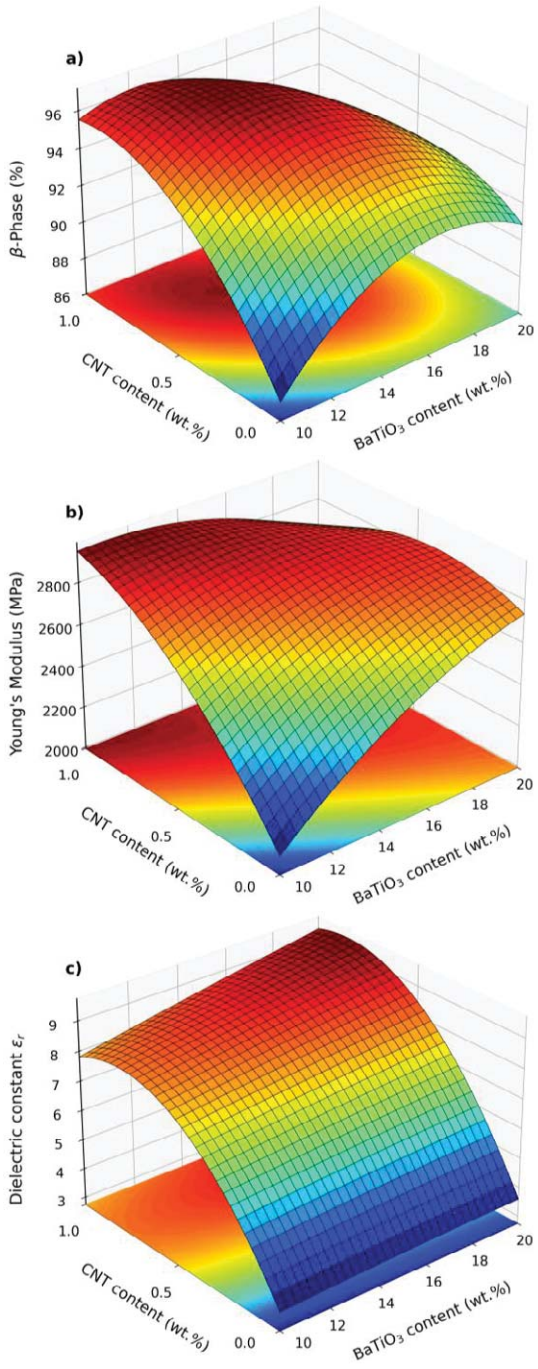


Figure 7. Response surface plots showing the combined effects of $BaTiO_3$ and CNT contents on: (a) β-phase content, (b) Young's modulus, and (c) dielectric constant.

an intermediate concentration, but excessive BT content does not lead to a continuous increase in modulus. The highest stiffness region is predicted at high CNT loading combined with low to intermediate BT content. This trend indicates that CNTs provide the main mechanical reinforcement, while excessive ceramic loading may introduce stress concentration, particle agglomeration, or reduced dispersion quality. The curvature of the surface further confirms the important coupled influence of BT and CNT in controlling the mechanical response of the nanocomposites.

Figure 7c shows the response surface for the dielectric constant. The dielectric constant increases strongly with CNT loading, demonstrating that CNT content is the dominant factor governing the dielectric response. This enhancement is associated with intensified interfacial polarization and the development of micro capacitive networks within the PVDF matrix. $BaTiO_3$ also contributes to the dielectric enhancement through its high intrinsic permittivity and additional polarization contribution; however, its influence remains secondary compared with the CNT driven dielectric response. The surface curvature indicates a nonlinear dielectric behavior, particularly at higher CNT contents, where the permittivity approaches a high response region.

3.4 Multi-response desirability optimization for actuator design

Following the development and validation of the quadratic response surface models, multiple response desirability optimization was performed to identify the most suitable PVDF/$BaTiO_3$/CNT composition for flexible actuator applications. In such piezoelectric nanocomposites, the selection of an optimal formulation cannot be based on a single response, since the overall functional performance results from a compromise between electroactive phase formation, dielectric polarization capability, and mechanical compliance.

Accordingly, β phase content and dielectric constant were selected as responses to be maximized, as both are directly associated with enhanced piezoelectric and electromechanical performance. In contrast, Young's modulus was defined as a target response rather than a maximization criterion, in order to avoid excessively stiff formulations while maintaining sufficient mechanical integrity. This optimization strategy therefore aims to identify a balanced composition that promotes electroactive phase formation, improves dielectric response, and preserves the flexibility required for actuator applications.

To incorporate the relative physical importance of the selected responses in actuator design, the overall desirability function was not calculated using equal weights. Instead, the response weights were assigned using the Analytic Hierarchy Process (AHP), based on a pairwise comparison of the selected material properties [28]. This approach allows the optimization process to reflect the functional relevance of each response rather than treating all responses as equally important.

In this weighting strategy, β phase content was considered more important than both dielectric constant and Young's modulus, because the electroactive β phase is the primary crystalline phase responsible for the piezoelectric activity of PVDF based materials [29–31]. The dielectric constant was assigned the second highest importance, since it is directly related to polarization capability and electric field response. Young's modulus was assigned a lower, but still

 DOI: 10.30420/456743012

relevant, importance because it mainly reflects the mechanical compliance and structural integrity of the film [30,32]. Therefore, the adopted weighting scheme prioritizes electroactive phase formation, followed by dielectric polarization capability and mechanical flexibility. The adopted AHP pairwise comparison matrix is expressed as:

$$A = \begin{array}{c|ccc} & \beta & \varepsilon_r & E \\ \hline \beta & 1 & 2 & 3 \\ \varepsilon_r & 1/2 & 1 & 2 \\ E & 1/3 & 1/2 & 1 \end{array} \quad (8)$$

Where β, ε_r, and E represent the β-phase content, dielectric constant, and Young's modulus, respectively. The response weights:

$$w_\beta = 0.540, \quad w_{\varepsilon_r} = 0.297, \quad w_E = 0.163. \quad (9)$$

The consistency of the pairwise comparison was evaluated using the consistency index (CI) and consistency ratio (CR). The obtained values of λ_{max} = 3.0092, CI = 0.0046, and CR = 0.0079, confirmed the high consistency of the adopted judgment matrix, since CR was far below the acceptable threshold (CR < 0.10). These results confirm that the assigned response weights are scientifically coherent and appropriate for the multi-response optimization strategy.

The individual desirability values of the three responses were then combined into a single overall desirability function using a weighted geometric mean, as expressed in Equation (10):

$$D = d_\beta^{0.540} . d_{\varepsilon_r}^{0.297} . d_E^{0.163} \quad (10)$$

where d_β, d_{ε_r}, and d_E represent the individual desirability values of β phase content, dielectric constant, and Young's modulus, respectively.

The resulting overall desirability map is shown in **Figure 8**. A well-defined high-desirability region was observed within the intermediate composition range, indicating that the optimal formulation for flexible actuator applications is achieved through a balanced combination of $BaTiO_3$ and CNT rather than by maximizing either filler content independently. The maximum desirability value, D_{max} = 0.849, was predicted at 12.45 wt% $BaTiO_3$ and 0.55 wt% CNT.

To assess the robustness of the predicted optimum, an optimal composition window was defined using the criterion $D \geq 0.99\ D_{max}$. Within this high-desirability region, the $BaTiO_3$ content ranged from 11.10 to 13.95 wt%, while the CNT content ranged from 0.46 to 0.64 wt%. The predicted responses remained consistently favorable across this region, with β-phase content ranging from 95.0 to 96.5%, Young's modulus from 2742 to 2856 MPa, and dielectric constant from 7.7 to 8.3. This result indicates that the optimized actuator-relevant performance is not confined to a single composition point, but is maintained across a stable formulation window.

The predicted optimum therefore represents an actuator-oriented material design point obtained from the simultaneous optimization of electroactive phase formation, dielectric polarization capability, and mechanical stiffness. However, since the desirability function was constructed from material-level responses, the predicted composition should be further validated under real actuation conditions. For this purpose, PVDF/$BaTiO_3$/CNT films will be evaluated through electromechanical actuator testing, including

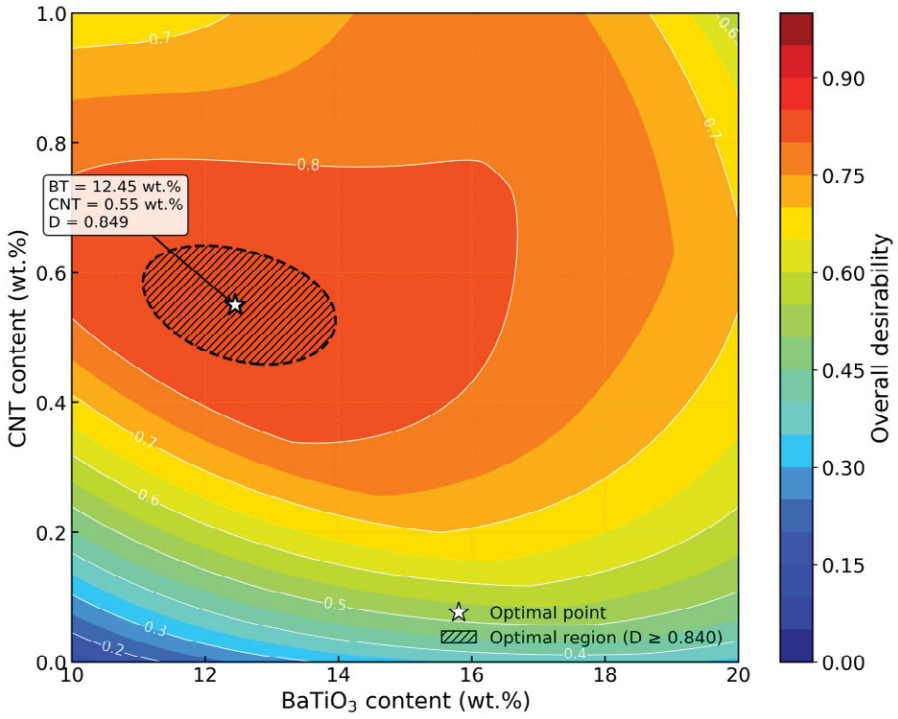


Figure 8. Overall desirability map for actuator-oriented optimization of PVDF/$BaTiO_3$/CNT nanocomposites.

displacement amplitude, dynamic vibration response, operating voltage requirement, and effective piezoelectric response. This validation step will determine whether the optimized material properties translate into improved device-level actuation performance and will provide the basis for selecting the final composition for flexible actuator implementation.

4 Conclusion

This work demonstrates a DOE-assisted strategy for the rational design and optimization of PVDF/$BaTiO_3$/CNT nanocomposites for flexible actuator applications. Second-order response surface models were successfully developed for β-phase content, Young's modulus, and dielectric constant. The models showed strong agreement with the experimental data, with R^2 values of 0.934, 0.971, and 0.990, respectively. Independent validation experiments further confirmed their predictive capability, demonstrating that the proposed models can reliably describe the composition-dependent behavior of the investigated nanocomposites.

Sensitivity analysis revealed that CNT loading is the dominant factor controlling the mechanical and dielectric responses, mainly through mechanical reinforcement, interfacial polarization, and micro-capacitive network formation. $BaTiO_3$ played a secondary but essential role by contributing to dielectric polarization and promoting the formation of the electroactive β-phase. The strong BT × CNT interaction observed for β-phase content and Young's modulus confirms that the functional properties are governed by hybrid filler synergy rather than by the isolated contribution of each filler.

The multi-response desirability optimization identified 12.45 wt% $BaTiO_3$ and 0.55 wt% CNT as the optimum actuator-oriented composition, corresponding to a maximum desirability of $D_{max} = 0.849$. At this composition, the predicted responses were approximately 96% β-phase content, 2800 MPa Young's modulus, and a dielectric constant of about 8. In addition, an optimal composition window was identified between 11.10 and 13.95 wt% $BaTiO_3$ and 0.46 and 0.64 wt% CNT, indicating that the optimized response is maintained within a stable intermediate filler range rather than at a single isolated composition.

These findings show that the optimal actuator formulation is not achieved by maximizing filler loading, but by balancing electroactive phase formation, dielectric enhancement, and controlled mechanical stiffness. The optimized composition provides a rational material design point for the development of flexible piezoelectric actuator films and will guide subsequent electromechanical validation under real actuation conditions.

5 Literature

[1] Miriyev, A.; Stack, K.; Lipson, H.: Soft material for soft actuators. *Nat. Commun.* 8 (2017), 596.

[2] Cianchetti, M.; Laschi, C.; Menciassi, A.; Dario, P.: Biomedical applications of soft robotics. *Nat. Rev. Mater.* 3 (2018), 143–153.

[3] Rus, D.; Tolley, M. T.: Design, fabrication and control of soft robots. *Nature* 521 (2015), 467–475.

[4] Kim, S.; Laschi, C.; Trimmer, B.: Soft robotics: A bioinspired evolution in robotics. *Trends Biotechnol.* 31 (2013), 287–294.

[5] Peng, C.; Chen, Y.; Yang, B.; Jiang, Z.; Liu, Y.; Liu, Z.; Zhou, L.; Tang, L.: Recent advances of soft actuators in smart wearable electronic-textile. *Adv. Mater. Technol.* 9 (2024), 2400079.

[6] Fang, C.; Xu, B.; Li, M.; Han, J.; Yang, Y.; Liu, X.: Advanced design of fibrous flexible actuators for smart wearable applications. *Adv. Fiber Mater.* 6 (2024), 622–657.

[7] Yang, Y.; Wu, Y.; Li, C.; Yang, X.; Chen, W.: Flexible actuators for soft robotics. *Adv. Intell. Syst.* 2 (2020), 1900077.

[8] Bar-Cohen, Y.: Electroactive polymer (EAP) actuators as artificial muscles: Reality, potential, and challenges. *Proc. SPIE* 4329 (2001), 1–10.

[9] Bar-Cohen, Y.; Sherrit, S.; Lih, S. S.: Electroactive polymer (EAP) actuators for planetary applications. *Proceedings of the 4th SPIE EAPAD Conference* 4695 (2002), 259–267.

[10] Poulin, A.; Rosset, S.; Shea, H. R.: Feedback controlled dielectric elastomer actuators with integrated stretchable strain sensors. *Appl. Phys. Lett.* 107 (2015), 244104.

[11] Ramadan, K. S.; Sameoto, D.; Evoy, S.: A review of piezoelectric polymers as functional materials for electromechanical transducers. *Smart Mater. Struct.* 23 (2014), 033001.

[12] Broadhurst, M. G.; Davis, G. T.; McKinney, J. E.; Collins, R. E.: Piezoelectricity and pyroelectricity in polyvinylidene fluoride—A model. *J. Appl. Phys.* 49 (1978), 4992–4997.

[13] Bouhamed, A.; Attaoui, A.; Mabrouki, F.; Tegenkamp, C.; Kanoun, O.: Enhanced flexibility and β-phase crystallization in PVDF/$BaTiO_3$ composites via ionic liquid integration for multifunctional applications. *J. Compos. Sci.* 9 (2025), 302.

[14] Attaoui, A.; Bouhamed, A.; Scholze, M.; Wagner, M. F.-X.; Tegenkamp, C.; Bouraoui, C.; Kanoun, O.: High-performance self-poled PVDF-$BaTiO_3$-CNT nanocomposites: A multifunctional material for flexible next-generation energy harvesting and sensing. *Nano Energy* 148 (2026), 111688.

[15] Ayadi, M. D.; Naifar, S.; Khlif, M.; Zouari, B.; Zschenderlein, U.; Wunderle, B.; Kanoun, O.: Natural fibers for performance boosting of $BaTiO_3$-PDMS flexible piezoelectric composite generators. *J. Alloys Compd.* 1008 (2024), 176485.

[16] Li, Y.; Su, X.; Liang, K.; Luo, C.; Li, P.; Hu, J.; Li, G.; Jiang, H.; Wang, K.: Multi-layered BTO/PVDF nanogenerator with highly enhanced performance induced by interlaminar electric field. *Microelectron. Eng.* 244 (2021), 111557.

[17] Huang, S.; Yee, W. A.; Tjiu, W. C.; Liu, Y.; Kotaki, M.; Boey, Y. C. F.; Ma, J.; Liu, T.; Lu, X.: Electrospinning of polyvinylidene difluoride with carbon nanotubes: Synergistic effects of extensional force and interfacial interaction on crystalline structures. *Langmuir* 24 (2008), 13621–13626.

[18] ManojKumar, N.; Muthukumaran, C.; Sharmila, G.: Optimization of process parameters using response surface methodology: A review. *Mater. Today: Proc.* 37 (2020), 1289–1294.

[19] Mittal, P.; Gupta, S.; Gupta, R. K.; Sharma, A.: Surface morphology and β-phase formation of single polyvinylidene fluoride (PVDF) composite nanofibers. *Nano-Micro Lett.* 9 (2017), 1–15.

[20] Khlif, M.; Naifar, S.; Ayadi, M. D.; Zschenderlein, U.; Wunderle, B.; Kanoun, O.: Structure dependent piezoelectricity in electrospun PVDF-SiC nanoenergy harvesters. *J. Alloys Compd.* 920 (2022), 165505.

[21] Morali, A.; Mandal, A.; Skorobogatiy, M. A.; Lopez, D.; Dufresne, A.; Michaud, V.: Unleashing the piezoelectric potential of PVDF: A study on phase transformation from gamma (γ) to beta (β) phase through thermal contact poling. *RSC Adv.* 13 (2023), 28843–28856.

[22] Cerrada, M. L.; Arranz-Andrés, J.; Caballero-González, A.; Blázquez-Blázquez, E.; Pérez, E.: The β form in PVDF nanocomposites with carbon nanotubes: Structural features and properties. *Polymers* 15 (2023), 1491.

[23] Manu, R.; Subba Rao, R.; Bhowmik, S.; Varshney, L.; Abraham, M.; Jayanarayanan, K.: Surface morphology and mechanical properties of poly(vinylidene fluoride) reinforced with carbon nanotubes. *AIP Conf. Proc.* 2630 (2022), 040002.

[24] Al-Munajjed, R.; Reyadh, M.; Al-Jumaili, A.; Yang, R.; Xiao, S.: Mechanical properties of carbon nanotube/polymer composites using different molecular dynamics methods. *Sci. Rep.* 4 (2014), 6479.

[25] Janićijević, A.; Filipović, S.; Sknepnek, A.; Salević-Jelić, A.; Jančić-Heinemann, R.; Petrović, M.; Petronijević, I.; Stamenović, M.; Živković, P.; Potkonjak, N.; Pavlović, V. B.: Structural, mechanical, and barrier properties of the polyvinylidene fluoride-bacterial nanocellulose-based hybrid composite. *Polymers* 16 (2024), 1033.

[26] Tsyganov, A.; Vikulova, M.; Artyukhov, D.; Bainyashev, A.; Goffman, V.; Gorokhovsky, A.; Boychenko, E.; Burmistrov, I.; Gorshkov, N.: Permittivity and dielectric loss balance of PVDF/$K_{1.6}Fe_{1.6}Ti_{6.4}O_{16}$/MWCNT three-phase composites. *Polymers* 14 (2022), 4609.

[27] Nath, N. K.; Parida, R.; Parida, B. N.; Nayak, N. C.: Synergistic effects of MWCNT–MXene nanohybrids on dielectric and ferroelectric properties of PVDF/PMMA blend composites. *ACS Appl. Electron. Mater.* 7 (2025), 1252–1266.

[28] Sukesh, S.; et al.: Analyzing the effectiveness of AHP methodology for material selection. *Int. J. Res. Publ. Rev.* 5 (2024), 1–10.

[29] Sencadas, V.; et al.: Smart and multifunctional materials based on electroactive poly(vinylidene fluoride): Recent advances and opportunities in sensors, actuators, energy, environmental, and biomedical applications. *Chem. Rev.* 123 (2023), 11393–11484.

[30] Martins, P.; Lopes, A. C.; Lanceros-Mendez, S.: Electroactive phases of poly(vinylidene fluoride): Determination, processing and applications. *Prog. Polym. Sci.* 39 (2014), 683–706.

[31] Baji, A.; et al.: Enhanced piezoelectricity of electrospun polyvinylidene fluoride fibers for energy harvesting. *ACS Appl. Mater. Interfaces* 12 (2020), 10763–10777.

[32] Kumar, B.; et al.: On the structural, dielectric, piezoelectric, and energy storage behavior of polyvinylidene fluoride (PVDF) thick film: Role of annealing temperature. *J. Appl. Phys.* 132 (2022), 224109.

 DOI: 10.30420/456743013

Energy efficient electro-mechanical wing ice protection system for future aircrafts

Denis Becker[1], Thorsten Koch[1], Christopher Davies[2], Valerian Palanque[3], Matthias Schmidt[1], Valentin Mees[1], Michael Matthias[1]

Organization(s): 1: Fraunhofer LBF, Darmstadt, Germany; 2: Parker Meggitt, Shepshed, Loughborough, United Kingdom; 3: Airbus, Toulouse, France

denis.becker@lbf.fraunhofer.de

Abstract

The accumulation of ice on aircraft surfaces is a critical issue that impacts both safety and efficiency. Traditional thermal bleed-air systems, which draw warm air from engines to combat ice, are energy-intensive and not viable for next-generation aircraft. This paper presents the development of an innovative electromechanical ice protection system utilizing piezo stack actuators to harness vibrational energy, achieving up to a 90% reduction in energy consumption compared to conventional methods.

1 Motivation:

Icing during flight significantly alters an aircraft's aerodynamic performance, leading to increased drag, reduced lift, and impaired controllability. The aviation industry's push towards sustainable practices necessitates the exploration of alternative ice protection systems that are more energy-efficient and compatible with emerging electric and hybrid propulsion technologies. Current systems are insufficient, as they rely heavily on thermal energy, which is incompatible with future aircraft designs that prioritize energy efficiency.



Figure 1 Iced aircraft wing

2 Approach:

This research focuses on a structural dynamic ice protection system that employs piezoelectric actuators to induce vibrations at the resonant frequency of the ice-covered leading edge. By using accelerometers embedded in the composite structure, the system actively monitors resonance frequencies, allowing for real-time adjustments to optimize ice shedding efficiency. The methodology includes extensive numerical simulations—modal, static deformation, and harmonic analyses—to assess the system's feasibility, followed by experimental validation in a controlled icing wind tunnel at Cranfield University.

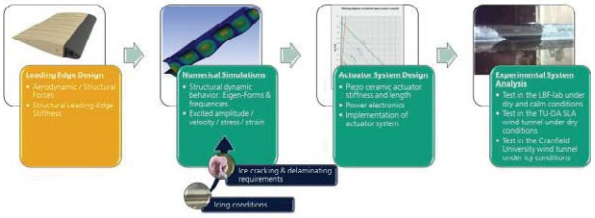


Figure 2 Approach for an electro-mechanical wing ice protection system

3 Results:



Figure 3 Iced CFRP leading edge at Cranfield University wind tunnel

The experimental setup demonstrated the efficacy of the developed system in shedding ice across various icing scenarios. The resonant excitation of the leading edge at optimal frequencies allowed for effective ice removal, with the maximum shear stress generated reaching approximately 1.6 MPa, sufficient to overcome the adhesion of ice to the

wing surface. The actuator system, powered by a piezoelectric amplifier, effectively operated at the desired frequencies of up to 4 kHz, indicating a successful integration of all components for real-time de-icing.



Figure 4 CFRP leading edge at Cranfield University wind tunnel after activation of the de-icing system

This electromechanical ice protection system shows promise as a sustainable and efficient alternative to traditional methods, aligning with the aviation industry's objectives for climate-neutral operations by 2050. By eliminating reliance on thermal energy, this innovative approach not only enhances flight safety but also contributes to the overall goal of reducing the environmental impact of aviation. Further developments and optimizations are anticipated to refine this technology for practical applications in future aircraft designs.

The project receives funding from the Clean Aviation Joint Undertaking under the European Union’s Horizon 2020 research and innovation program under Grant Agreement No 101101974.

4 Literature

[1] D. Olejniczak und M. Nowacki, "Evaluation of the Influ-ence of Icing on Wings on Aircraft Flight Parameters," Transportation Research Procedia, Jg. 35, S. 100–109, 2018, doi: 10.1016/J.TRPRO.2018.12.017.

[2] Z. Wang, "Recent progress on ultrasonic de-icing technique used for wind power generation, high-voltage transmission line and aircraft," Energy and Buildings, Jg. 140, S. 42–49, 2017, doi: 10.1016/j.enbuild.2017.01.072

[3] Y. Cao, W. Tan und Z. Wu, "Aircraft icing: An ongoing threat to aviation safety," Aerospace Science and Technology, Jg. 75, S. 353–385, 2018, doi: 10.1016/j.ast.2017.12.028.

[4] T. P. Ratvasky, B. P. Barnhart und S. Lee, "Current Methods Modeling and Simulating Icing Effects on Aircraft Performance, Stability, Control," Journal of Aircraft, Jg. 47, Nr. 1, S. 201–211, 2010, doi: 10.2514/1.44650.

[5] F. Jiang und T. Qiu, "Research on the effect of icing on aerodynamic performance of airfoil and power generation performance of wind turbine," J. Phys.: Conf. Ser., Jg. 1684, Nr. 1, S. 12141, 2020, doi: 10.1088/1742-6596/1684/1/012141.

[6] J. Wallisch und R. Hann, Hg., SAE Technical Paper Series. SAE International400 Commonwealth Drive, Warrendale, PA, United States, 2023.

[7] F. T. Lynch und A. Khodadoust, "Effects of ice accretions on aircraft aerodynamics," Progress in Aerospace Sciences, Jg. 37, Nr. 8, S. 669–767, 2001, doi: 10.1016/S0376-0421(01)00018-5.

[8] M. Santarelli, M. Cabrera und M. Calì, "Analysis of Solid Oxide Fuel Cell Systems for More-Electric Aircraft," Journal of Aircraft, Jg. 46, Nr. 1, S. 269–283, 2009, doi: 10.2514/1.38408.

[9] M. Henke et al., "Challenges and Opportunities of Very Light High-Performance Electric Drives for Aviation," Energies, Jg. 11, Nr. 2, S. 344, 2018, doi: 10.3390/EN11020344.

[10] V. PALANQUE, T. PLANÈS, P.-B. VALÉRIE, B. MARC und D. SCOTT, "Piezoelectric resonant ice protection systems - Part2/2 : benefits at aircraft level," Chinese Journal of Aeronautics, Jg. 37, Nr. 6, S. 50–63, 2024, doi: 10.1016/j.cja.2024.03.021.

[11] PI Ceramic, Piezoelektrische Aktoren - Bauelemente, Technologie, Ansteuerung.

 DOI: 10.30420/456743014

Giving Voice to Flat Plastic Panels with Piezoceramic Actuators: Vibrational Analyses with Feedback Interferometry

Elisabetta Bodo, Eindhoven University of Technology, Eindhoven 5600MB, The Netherlands, e.bodo@tue.nl
Carlo Anelli, University of Pavia, Pavia 27100, Italy, carlo.anelli01@universitadipavia.it
Valentina Bello, University of Pavia, Pavia 27100, Italy, valentina.bello@unipv.it
Sabina Merlo, University of Pavia, Pavia 27100, Italy, sabina.merlo@unipv.it

Abstract

Piezoelectrically actuated flat surfaces represent promising devices for next-generation loudspeakers, with performances strongly influenced by the choice of substrate material. We present the use of a compact, low-cost and self-aligned configuration based on laser diode feedback interferometry to provide an overview of the out-of-plane vibrations of two piezo-actuated panels made of Polypropylene and Plexiglas, with a perimeter frame. Spectral measurements performed by driving the actuator with electrical white noise in the frequency band up to 700 Hz reveal that the system resonances, corresponding to various vibration modes, appear at lower frequencies for Polypropylene compared to the Plexiglas panel, consistent with the lower Young's modulus of Polypropylene.

1 Introduction

Flat surfaces actuated by piezoelectric elements are emerging as promising candidates for next-generation loudspeakers, offering compactness, low power consumption, and efficient electro-acoustic conversion compared to traditional moving-coil systems. Their thin profiles make them simple to integrate and thus suitable for portable and wearable devices, as well as for the transformation of already existing display surfaces into sound-radiating elements [1- 2]. Their electromechanical performances strongly depend on the material properties of the vibrating structure: the stiffness, density, and internal damping determine the resonance frequencies, vibration amplitudes, and overall actuation efficiency. Therefore, understanding the influence of material parameters is essential for the optimization of piezoelectrically driven flat panels.

In this work, we experimentally compare the electromechanical spectral responses of two panels with identical geometry, made of Plexiglas and Polypropylene, provided with a piezoelectric ceramic actuator attached at the center and a perimeter frame, driven by electrical white noise. The optoelectronic configuration consists of a semiconductor feedback interferometer: we demonstrated that this very compact, low-cost and easy to handle setup allows vibration monitoring of diffusing targets, without the need of accurate alignment.

2 Materials and Methods

We tested two panels with identical dimensions (150 × 100 × 1 mm) with a piezo-electric actuator (Wisol4030, size 40 × 30 × 0.8 mm, nominal capacitance 6 µF ± 15%, by Wisol, Republic of Korea) attached with a double-sided adhesive tape at the center of the Polypropylene and Plexiglas panels. These materials exhibit different mechanical and optical properties. Plexiglas is stiffer and denser than Polypropylene. Plexiglas is optically transparent, whereas Polypropylene can be translucent or opaque. The mechanical properties of both tested materials are summarized in Table I. Both panels were supported at the edges by a 3D-printed carbon-fiber frame, raised approximately 1 cm above the optical bench. A layer of foam was placed underneath to minimize vibrations of the supporting structure, absorb acoustic waves and prevent unwanted reflections from the bench surface.

Table I: Mechanical properties of the tested devices

Mechanical property	Polypropylene	Plexiglas
Young's module (GPa)	1.3	2.5
Density (kg/m^3)	900	1180
Poisson ratio (kg/m^3)	0.42	0.35

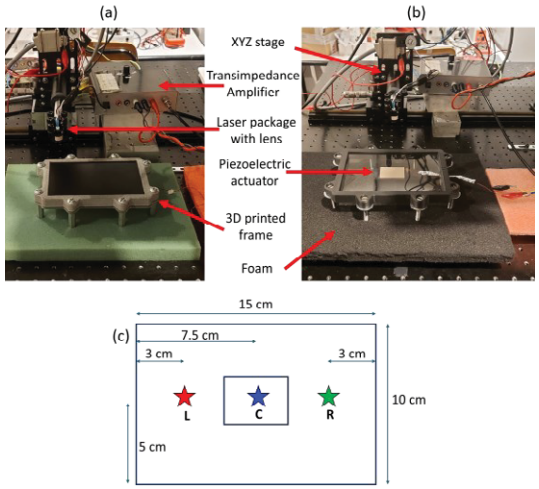


Figure 1 Photographs of the experimental setup showing the **(a)** Polypropylene and **(b)** Plexiglas panels. **(c)** Schematic of the panels with actuator (top view) and selected position for the interferometric measurements.

We drove the piezoactuators with a positive voltage between top and bottom electrodes by means of a signal generator (33500B Waveform Generator by KEYSIGHT, USA). Electrical driving causes in-plane stretching of the piezo-ceramic module which yields out-of-plane bending of the plate: the AC driving induces vibrations and excites structural modes. The air-pressure waves, generated by the

 DOI: 10.30420/456743014

oscillating motion of the panel, propagate as longitudinal sound waves through the surrounding medium and the frequency/amplitude of the air-pressure wave depend on the AC driving voltage and on the structural modes of the panel.

Figures 1(a) and **1(b)** show the photographs of the experimental setup with Polypropylene and Plexiglas panel provided with actuator, respectively. The semiconductor laser feedback interferometer [3-4] employs a near-infrared laser diode (HITACHI HL7851G, Japan) biased at 75 mA with peak emission wavelength of 780 nm and optical power output of approximately 5 mW. The radiation is focused perpendicularly on the surface of the device under test by means of a lens. The distance between the laser and the plate is about 5 cm so that the diffused light from the vibrating surface is coupled back into the laser cavity to induce frequency and amplitude modulation of the emitted field. The sensor head that incorporates laser package and lens is mounted on a XYZ-axis translation stage to locate the readout beam at different positions of the plates for vibration measurements.

Measurements were performed at three different positions of the plates to investigate the spectral response of the modes with out-of-plane displacements in the selected frequency range. **Figure 1(c)** shows a schematic of the panels with the measuring points indicated as L, R (left and right with respect to the actuator, red and green stars, respectively) and C (center of the device, blue star in the figure). We worked in conditions of small displacements ($\Delta z << \lambda/4$) so that the output signal is directly proportional to the displacement. By working in quadrature, the photodetected AC current I_z (provided by the monitor photodiode in the package) is given by: $I_z = I_o \cdot sen\left[\frac{4\pi}{\lambda} \cdot \Delta z\right]$, where I_o is the current amplitude that depends on the driving and feedback level, λ is the laser wavelength. The photogenerated current I_z was converted into a voltage signal by a custom-designed 100 kΩ transimpedance amplifier. We eventually acquired the signal with a dynamic signal analyzer (DSA 35670A by Agilent, USA).

3 Spectral Measurements

We investigated the influence of the material on the electro-mechanical response of the overall structure by performing spatially resolved interferometric measurements to identify the vibration modes in the range up to 700 Hz. By driving the actuator with electrical white noise and by analysing the output signal in frequency domain, we can directly extract the electromechanical spectral response that shows the resonances peaks of the devices under test.

We characterized the electro-mechanical response of both Polypropylene and Plexiglas panels: the results are shown in **Figure 2(a)** and **2(b)**, respectively. We can identify the peaks corresponding to the first and second vibration modes. They appear at around 150 Hz and 530 Hz for Plexiglas, and at 115 Hz and 460 Hz for Polypropylene, consistent with the lower Young's modulus of Polypropylene. Note that the absolute values of peak amplitudes can be compared only within a single acquisition: the interferometric signal amplitude is not only proportional to the displacement amplitude but is also affected by the feedback level and the slow phase changes that influence the quadrature condition.

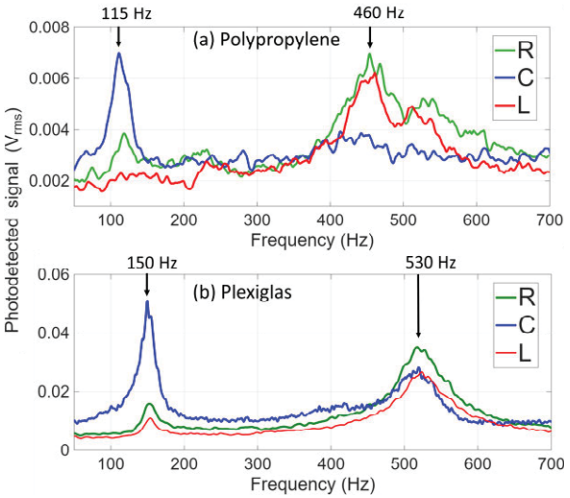


Figure 2 Experimentally measured spectral responses in the range 0 – 700 Hz at point L (red traces), C (blue traces) and R (green traces) for **(a)** Polypropylene and **(b)** Plexiglas panels.

4 Conclusions

Experimental results obtained with a very simple and low-cost setup highlight how the material stiffness and density affect the natural frequencies and vibration modes, providing useful insight for the design of efficient piezo-actuated acoustic surfaces. The photodetected signals in the frequency band 0 – 700 Hz allowed us to characterize plates in Plexiglas and Polypropylene: in particular, the first two vibrations modes are found at lower frequencies for Polypropylene with respect to Plexiglas, consistent with the lower Young's modulus of Polypropylene. The use of a laser-feedback interferometer allowed us to perform a fast and efficient characterization of vibrating transparent and opaque surfaces, without the need of a complex system and alignment. This kind of investigations provides significant feedback for the modelling and represents a powerful preliminary step to the more demanding phase of acoustic testing, requiring anechoic chamber and microphone arrays.

5 Literature

[1] Ganju, V.: Piezoelectrics enable displays to provide both high-quality audio and touch feedback. IEEE Spectrum. Vol. 61, No. 3, pp. 22–27, Mar. 2024

[2] Knight, P.: Smart speaker, tell me about your acoustic sensor. Phys World. Vol. 33, No. 12 pp. 25–29, Feb. 2021

[3] Bodo, E. et al: Assessment of vibration frequencies of piezo-actuated panel by model-assisted self-mixing interferometry. IEEE Open J. Instrum. Meas. Vol. 4, pp. 1-8, Art no. 9500408, June 2025

[4] Anelli, C. et al: Electro-mechanical frequency response of a piezo-MEMS speaker measured by laser diode feedback interferometry. J Microelectromech Systems. Vol. 34, No. 4, pp. 452-458, Aug. 2025

 DOI: 10.30420/456743015

High-resolution Rotating Piezo Motors for LISA Laser Interferometer Space Antenna

Jocelyn REBUFA, Jolan GAUTHIER, Nicolas BOURGEOT, Alexis GIERCZAK, Clement COTE, Olivia STADLER, François BARILLOT, Frank CLAEYSSEN
Cedrat Technologies, 38240 Meylan (France), frank.claeyssen@cedrat-tec.com

Abstract

The article presents the outcomes of Technology Development Activities (TDA) of several rotating piezo motors for the LISA mission. The Laser Interferometer Space Antenna (LISA) is the European Space Agency's (ESA) third large-class mission, aiming to become the first spaceborne gravitational wave observatory. It comprises three spacecrafts flying in a precise triangular formation, separated by 2.5 million kilometres. To ensure a stable environment for the scientific payload, motors must deliver ultra-low micro-vibration levels and exceptional magnetic cleanliness.
Cedrat Technologies (CTEC) worked within several consortiums on 3 different motors of various sizes in different parts of the satellites. These 3 motors have a large variety of specifications, but are all compact compared to the provided torque, low-speed, non-magnetic, and will answer the environmental constraints of the LISA missions (launch, radiation, cleanliness, low micro-vibration emissivity). In this article, the development processes are described, covering the conceptual, preliminary, and breadboard phases. Test results are presented and discussed, along with the lessons learned, demonstrating the potential of inchworm piezoelectric motors for space applications. From these results, CTEC has been selected for the development of the flight models FM (TRL 9) of 3 types of motors. These models should consider the space environment requirement constraints (resistance to launching shocks and vibration, etc) with margins, according to ECSS norms.

1 Context

1.1 LISA mission

ESA's Laser Interferometer Space Antenna (LISA) will be the first space-based observatory dedicated to studying gravitational waves: ripples in the fabric of space-time emitted during the most powerful events in the Universe, such as pairs of black holes coming together and merging.
LISA will consist of three spacecraft orbiting around the Sun in a triangular formation 2.5 million kilometres apart. It detects gravitational waves by laser interferometry, measuring tiny distance changes between test masses kept in free-fall condition inside each spacecraft. LISA is sensitive to low-frequency gravitational waves not accessible from Earth.
Cedrat Technologies (CTEC) worked within 2 consortiums to reach Technology Readiness Level 3 (TRL 3) for custom-made motors designed for specific satellite functions.

The first one (**fig.1**) is used in the Antenna Pointing Mechanism (APM) and was designed in collaboration with SENER Poland and SENER Spain [1]. There are two operational modes for the APM of the High Gain Antenna: continuous pointing and periodic repointing. In the continuous pointing, the APM continuously tracks the Earth performing a 1º rotation per day without stopping science observation. This mode required unprecedented low micro-vibration levels. In the periodic repointing mode, the antenna is only steered once every two weeks not breaking the link between spacecraft but pausing science interferometry. Key specifications included a full range of motion (0–360°) and high positioning accuracy (±0.05°).



Figure 1 APM breadboard for LISA HGA

The second motor (**fig.2**) is used in Optical Assembly Tracking Mechanisms (OATMs), also developed with SENER Poland and SENER Spain [2]. Each spacecraft uses two Optical Assembly Tracking Mechanisms (OATMs) to achieve and maintain optical links by adjusting telescope pointing with µrad accuracy. Once aligned, they work with spacecraft's Drag Free Attitude Control System (DFACS) to achieve nrad pointing stability in the interferometric link.

ISBN: 978-3-8007-6743-4 @ VDE VERLAG GMBH · Berlin · Offenbach

 DOI: 10.30420/456743015

Key specifications were to provide 5º angular stroke, 66 Nm torque and sub-nrad resolution.



Figure 2 OATM breadboard for LISA MOSA

The third piezoelectric motor (**fig.3**) is the Beam Alignment Mechanism (BAM), developed in collaboration with OHB System (Germany). On the satellite optical bench, the BAM rotary micromotors are used to compensate for parasitic variations in the optical path length by adjusting the transmitted beam position laterally.

These motors are compact, low-speed, hollow stepping motors that rotate a tilted glass plate to deviate the laser beam. They are equipped with new eddy current sensors (ECS) to monitor the angular position of the shafts. A pair of motors is needed to perform the alignment optical function.
The main specifications include continuous 360° rotation and an absolute positioning accuracy of ±0.15°.

The **table 1** gathers the main performances of each three motors. As a common point, all these motors exploit CTEC APA® and PPA piezo actuators. These actuators benefit from a rich space heritage, from space qualification to successful flights [3,4,5,6].

	APM	**OATM**	**BAM**
Motion range	0-360°	0-5°	0-360°
Torque	2 Nm	66 Nm	0.003 Nm
Resolution	~10 nrad	< 1 nrad	Not evaluated
Volume	Ø304x79 mm^3	128x61x162 mm^3.	42x42x55 mm^3
Mass (w\o harnesses)	2.1 kg	1.7 kg	< 20 g (actuators and sensors only)
Non-magnetic	yes		

Table 1 Performance of the 3 piezo motors for LISA

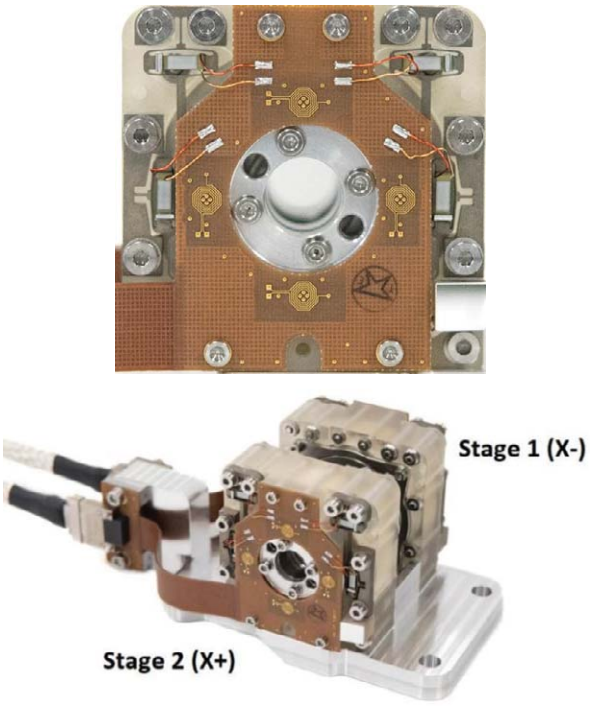


Figure 3 BAM breadboard for LISA optical bench

1.2 Inchworm motor principle

Piezoelectric inchworm motors have gained increasing prominence in various applications due to their unique capabilities and advantages ([7]). These motors are adapted for applications which require non-magnetic and radiation compatibility, high force/volume ratio, good unpowered stall force and low power consumption. There are operational applications of CTEC piezo motors for space, such as BSMA for IASI-NG and other harsh environment [8,9].

One possible architecture for inchworm motor is to use 2 pairs of actuators. For each pair, one actuator is the clamp, the other one is the extender (provides stroke to the payload). The operating principle is displayed in **fig.4**.

1. 1st actuator pair clamping phase
2. 1st actuator pair stroke phase
3. 2nd actuator pair clamping phase, followed by the 1st pair unclamping phase
4. 2nd actuator pair stroke phase, with 1st pair retraction

DOI: 10.30420/456743015

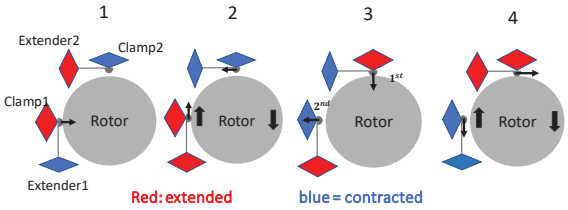


Figure 4 Inchworm motor operating principle

2 Antenna Pointing Mechanism (APM)

To support the space-to-ground communications and the orbit determination by tracking from the ground stations, each spacecraft will embark a Radio-Frequency Subsystem (RFS) and a High-Gain Antenna Subsystem (HGAS) operating in X-Band. The high gain antenna of each satellite is composed of two axes in series, azimuth and elevation. Each stage is equipped with an encoder.

The inchworm architecture is based on 6 modules. Each module is composed of two APA® amplified piezo actuators [10], one dedicated to clutching (clamp/unclamp actuator), the other one dedicated to drive the mobile part (sometimes called “expander” or “extender”).

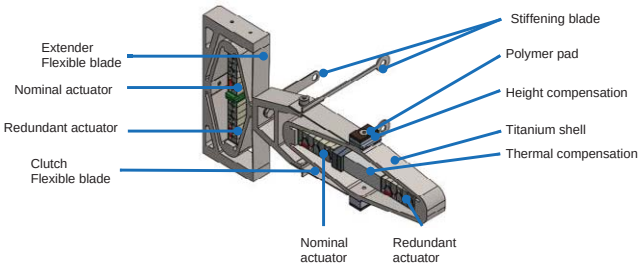


Figure 5 APM inchworm module assembly

The six modules are operated 3 by 3. The first important aspect is to drive the mobile part in constant velocity to avoid any export of accelerations due to driving.

To guarantee the correct motorization margin over the temperature range of the mission, a thermal compensation has also been realized inside the clamp actuator and before amplification as depicted in **fig.5**. It is accompanied by a precise adjustment of the clamp height, carefully dimensioned to have the proper interference with the mobile part and thus applying sufficient holding torque at rest, and proper clearance once actuated.

Another key aspect of the motor is to avoid any sudden release of motion when one triplet is opening. For this reason, the “backlash compensation method” introduced by Cedrat Technologies allowed to lighten the load of the releasing triplets, before the clamps open. A load cancellation parameter is varied until the best tuning is reached (**fig.6** and **fig.7**). Feedforward strategies are currently under investigation to track the optimal parameter over the full 360° stroke, thermal fluctuations and ageing.

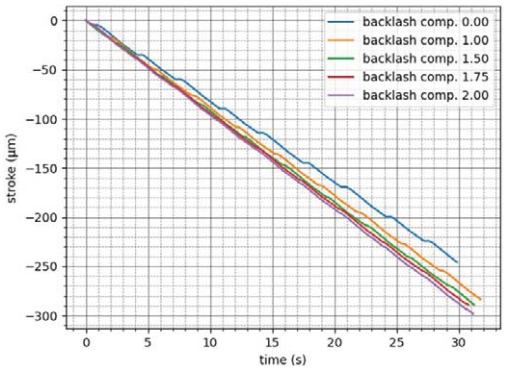


Figure 6 Typical motion results obtained after backlash compensation several steps to achieve constant velocity mode

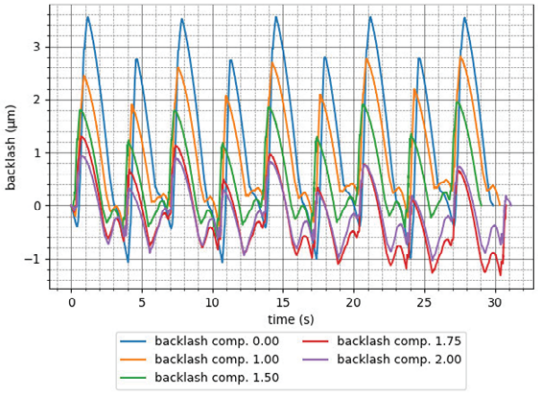


Figure 7 Typical motion results obtained after backlash compensation, removing the constant velocity slope

Eventually, the modules are designed to allow back driving during launch: the friction pad is expected to slip before the load damages the piezoelectric modules. Flexible blades are used to stiffen the other axis.

3 Optical Assembly Tracking Mechanism (OATM)

The central element of the LISA payload is the Mechanical-Optical Sub-Assembly (MOSA), that includes the test mass whose inertial trajectory is disturbed by the passage of a gravitational wave, laser interferometers for measuring the displacement of the test mass relative to the test mass located in a remote spacecraft and the Telescope for transmitting/receiving the interferometer laser beam between the spacecraft. The MOSAs will need to be actuated along one rotatory degree of freedom against the SC platform by means of the "Optical Assembly Tracking Mechanism" (OATM). Six OATM Flight models (FM) will be used, two per spacecraft. The OATM is the mechanism responsible for tracking the “breathing angle” of LISA constellation.

As per the Antenna Pointing Mechanism, a non-magnetic motor combining titanium and piezoelectric materials is designed. The main difference is that the required torque with safety margin is significantly higher, whether the required quality of motion is higher.

ISBN: 978-3-8007-6743-4

@ VDE VERLAG GMBH · Berlin · Offenbach

 DOI: 10.30420/456743015

For this purpose, a similar concept than depicted for APM in **fig.5** has been declined to larger and stiffer actuators in **fig.8.**



Figure 8: OATM inchworm module

The larger and direct actuation for the extenders using CTEC PPA [11] significantly reduces the sensitivity to external backlash. Also the full stroke of the extender is much smaller and thus allow finer resolution in motion.
The same backlash compensation as for the APM in open loop has been implemented (**fig.9**). Further developments are ongoing to dynamically control the residual backlash and the remaining motion error in close loop.

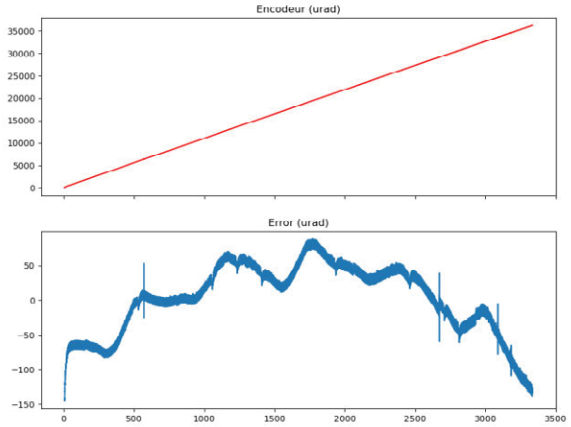


Figure 9: Position measurement (in µrad) vs time with encoder during acquisition mode and error, speed around 10 µrad/s

Additional testing successfully occurred at lower speeds, down to 4 nrad/s. With the TDA setting of the clamp actuators, up to 193N (66 N.m) has been measured as maximum force. Ongoing developments are implementing the same thermal compensation of the APM inside the OATM design.
The sub-nanorad resolution at low frequency has been measured at low bandwidth with capacitive sensor. Preliminary testing in air and with ambient thermo-elastic effects limited the resolution of the interferometric verification. Both methods are expected to reach their own noise floor compared to the motor resolution. Further testing in TVAC and interferometry are expected to refine the motor resolution.

4 Beam Alignment Mechanism (BAM)

The Beam Alignment Mechanism (BAM) aims to compensate for the tilt-to-length (TTL) effect induced by the long optical path between each satellite of the mission (2.5 million km). To achieve this function, two tilted optical plates are independently rotated by a piezoelectric motorisation located on the LISA Optical Benches (OB). The position of the optical plate is monitored by the mean of eddy current sensors (ECS), printed within a circuit board close to a tilted conductive target fastened on the rotating shaft.

The BAM breadboard (**fig.3,10**) have been developed in close collaboration with OHB System (Germany). OHB provided CTEC with a zerodur housing (CTE ~ 0 ppm/K at 20°C) including two sealed ball-bearings whose measured static friction torque was close to 3 mNm. The bearings were mounted with independent shafts integrating the optical plates and the conductive sensor targets.

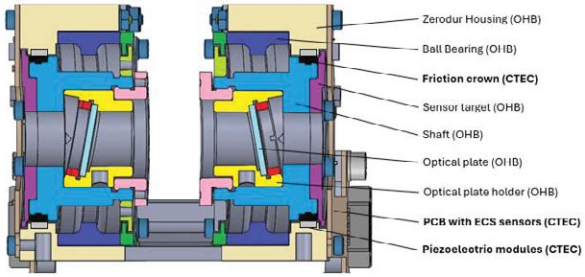


Figure 10 BAM breadboard internal structure

A tailored miniature piezoelectric motorization has been designed to comply with the stringent envelope, torque and speed requirements, featuring low voltage (75V) rectangular MLA piezoelectric ceramics (1.65x1.65x5 mm^3). Using the APA® concept from CTEC [10], these MLA were integrated in a titanium shell amplifying their 4 µm stroke to more than 20 µm. The shell also provides the ceramic with sufficient preload, preventing the piezoelectric ceramic to be submitted to tensile stresses during random vibrations and shock loads that occur during the in-orbit commissioning phase of the mission. With two piezoelectric ceramics per shell, the extender and clamp actuators are achieved in a single module (**fig.11**).

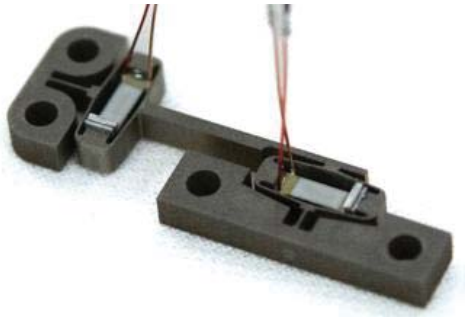


Figure 11: BAM breadboard piezoelectric actuators

 DOI: 10.30420/456743015

First evaluations of this miniature motorization have shown that achieving the inchworm drive requires a very accurate pre-tensioning of the piezoelectric modules containing the clamp actuators onto the driven shaft. A correct pre-tensioning of the clamps ensures the extenders are in contact with the shaft during the rotation phase (clamps closed), and that the extenders can properly be reset (clamps opens) to perform the next step (**fig. 4**). While it was not possible to achieve such settings on the breadboard, inertial drive principle derived from CTEC Stepping Piezo Actuators [7] was successfully used instead of the inchworm drive, without adding any additional element to the design. As inchworm mode would be preferred, future BAM versions will be optimised for this mode.

Inertial drive enabled the possibility to actuate the two independent shafts over 360° and achieve an angular speed between 4 and 6 rpm with a step size below 0.1° (**fig. 12**) when the extenders were actuated at full voltage and high frequencies (roughly 500 Hz). The resolution may be increased to some extent by lowering the extender maximum voltage.

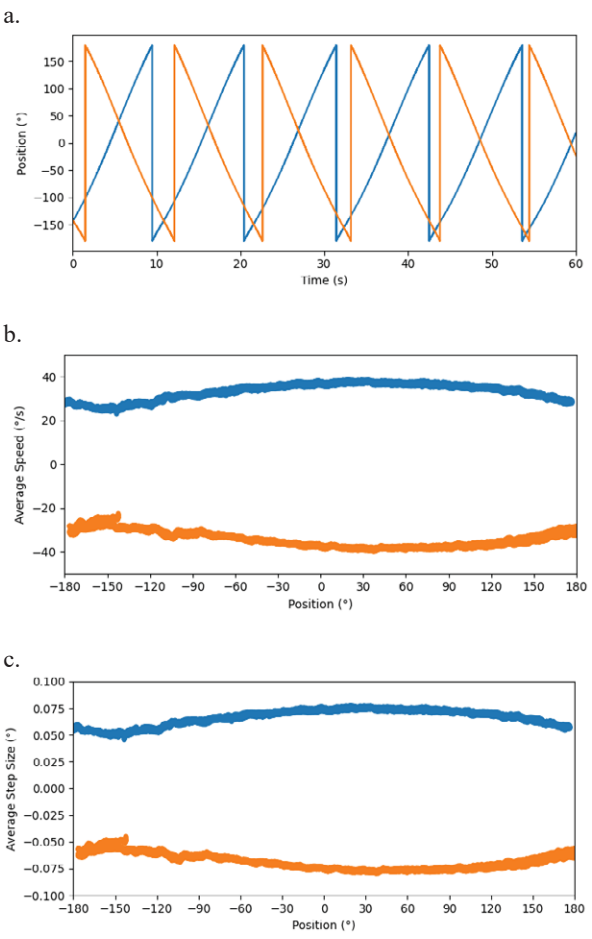


Figure 12 BAM motorization test
a. strokes b. steps c. speed

All the angular performances were measured using an embedded compact rotation encoder specifically developed for the project. It derives from CTEC PCB-based eddy current sensors (ECS) [12] and exploit the space heritage of ECS sensor developed for EUCLID [13]. These sensors were pre-calibrated using an external calibrated autocollimator.

These ECS coils and their target only require 3 to 4 mm height envelope to be implemented (excluding their potential conditioning electronics) making them very convenient for applications where available space is heavily constrained, such as miniature motors.

In the BAM breadboard sensors, an angular calibration residual error of less than ±0.15° (±0.05%) was demonstrated (**fig.13**) with an angular resolution close to 0.01° rms over a 10 kHz bandwidth for the overall measurement chain.

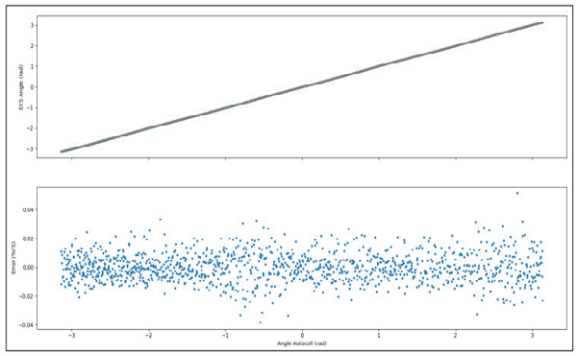


Figure 13 BAM ECS sensor calibration test – Stage 1

5 Conclusion

CTEC has developed successful 3 types of non-magnetic rotating piezo motors for LISA, with breadboards satisfying requirements of APM, OATM and BAM.
These motors are stepping motors offering very high resolution. All are based on APA and PPA piezo actuators.
BAM motor is equipped with a new compact rotation encoder based on Eddy Current Sensors ECS.
From these results, CTEC has been selected for the development of the flight models (FM) (TRL 9) of these 3 types of motors. These models should consider the space environment requirement constraints (resistance to launching shocks and vibration, etc) with margins, according to ECSS norms.

6 Acknowledgement

The authors acknowledge the financial and technical support provided for these activities from the European Space Agency (ESA). The authors are grateful to OHB for the collaboration in BAM and SENER for the collaboration in HGA and OATM.

 DOI: 10.30420/456743015

7 Literature

[1] M. Krakowczyk, J. Mugica, P. Campo, M. Stokowska, G. Aigouy, J. Rebufa, A. Gierczak, A. Tvaruzka, M. Sidz, A. Hoc, E. Dominguez, I. Gabiola, C. Cote, E. Mate, S. Wittig, V. Preda, Development of an ultra-low vibration actuator for LISA APM, ESMATS 2025

[2] J. Mugica, M. Stokowska, P. Campo, S. Frankowski, G. Aigouy, J. Rebufa, C. Cote, A. Gierczak, P. Zaltron, M. Sidz, M. Krakowczyk, O. Stadler, A. Hoc, E. Dominguez, I. Gabiola, J. Grzybo, Development of the LISA Optical Assembly Tracking Mechanism ESMATS 2025

[3] R. Leletty, A New Amplified Piezoelectric Actuator for Precise Positioning and Active Damping, Proc SPIE, Smart Systems and Mat., San Diego Ca, March 1996.

[4] P. Guay, Piezo Qualification for Space Applications, Proc Actuator 2002, Ed. Messe Bremen, B3.2, pp.284-287

[5] C. Allegranza, Actuators for Space Applications: State of the Art and New Technologies, ACTUATOR Conf, Review paper, Bremen (DE), 2014

[6] https://cedrat-technologies.com/wp-content/uploads/downloads/aerospace_heritage.pdf

[7] N. Bencheikh, N. Bourgeot, A. Pagès, G. Aigouy, J. Rebufa, E. Betsch, F. Claeyssen, Inertial and Inchworm piezoelectric motors: Design and Motorization selection key aspects. ACTUATOR 2024.

[8] F. Barillot CEDRAT TECHNOLOGIES - Nanometric positioning with IASI-NG ‘s Beam Splitter Mechanism Actuator, AMS 45th Aerospace Mechanisms Symposium, Houston Texas USA, 13-15 may 2020

[9] F. Barillot, J. Rebufa, E. Betsch, J. Gauthier, A. Pagès, N. Bencheikh, Tough precision piezoelectric motors for space applications, AMS, Virginia Beach, May 2024

[10] APA® Amplified piezo actuator, Registered trademark of Cedrat Technologies, https://cedrat-technologies.com/categorie-produit/amplified-piezo-actuator-piezo-actuators/

[11] PPA Parallel Prestress Actuator, Cedrat Technologies, https://cedrat-technologies.com/categorie-produit/piezo-actuators/amplified-piezo-and-parallel-pre-stressed/parallel-pre-stressed-actuator-piezo-actuators/

[12] O. Sosnicki, Eddy current sensors on Printed Circuit Board for compact mechatronic application, Proc SENSOR 2010, Ed ITG/GMA-Fachtagung Nürnberg, 18 May 2010

[13] J.C. Barriere, Qualification of euclid-near infrared spectro-photometer cryomechanism, Proc. ‘ESMATS 2017’, Univ. of Hertfordshire, Hatfield, U.K., 20–22 September 2017

 DOI: 10.30420/456743016

Improving the reliability of piezoelectric actuators and motors subjected to significant self-heating and several billion actuation cycles or severe environments

Nicolas Bourgeot[1], Frank Claeyssen[1], Guillaume Mansuy[1], Rasmus Lou-Møller[2], Iman Mehdipour[2], Yves Ruffieux[3], François Barrot[3]
(1) Cedrat Technologies, 38240 Meylan, France, guillaume.mansuy@cedrat-tec.com
(2) CTS Denmark A/S, 3490 Kvistgaard, Denmark, rasmus.moeller@ctscorp.com
(3) Centre Suisse d'Electronique et de Microtechnique, 2000 Neuchâtel, Switzerland francois.barrot@csem.ch

Abstract

Piezoelectric actuators provide high positioning accuracy and rapid dynamic response, making them well suited for applications requiring non-magnetic behaviour, radiation compatibility, high force-to-volume ratio, reliable unpowered holding force, and resistance to vibrational environments. However, during high-frequency or continuous operation, these actuators may experience significant self-heating, particularly when operated in vacuum or elevated-temperature environments. To address these challenges and enable reliable operation of piezo actuators in extreme conditions, the Eurostars-funded PROOFED project was launched. It brings together Cedrat Technologies (CTEC) as project Coordinator working on the piezo motor design, CSEM for thermal modelling and thermal drain development, and CTS for the development of high temperature piezo stacks. Results include experimental validation of 10 billion of actuations at temperature up to 200°C, thermal drain with 41% thermal resistance reduction and new definitions of RSPA Rotary Stepping Piezo Motors offering wide operational thermal range and resistance to magnetic fields as well as vibration and shocks.

1 Introduction

1.1 Inertial motors operating principle

Amplified Piezoelectric Actuators (APA®) [1-3] from CTEC are used in inertial motors use to move a payload through friction (Figure 1), in all CTEC Stepping Piezo Actuators (SPA) families [4-9]. They function via a stick–slip principle: a slow voltage ramp moves actuator and payload together (stick), whereas a rapid voltage drop causes the actuator to return quickly while the payload remains in place (slip). Reversing the voltage sequence reverses the motion.

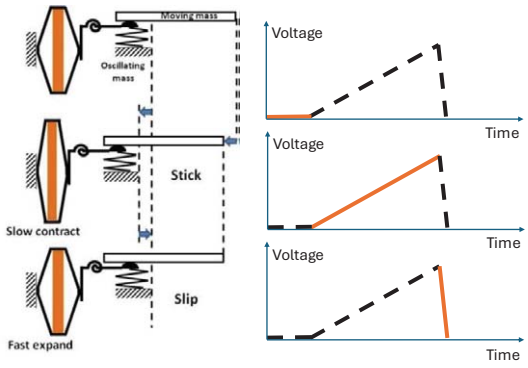


Figure *1*: Stick-slip actuation of inertial piezo motors [1] [2]

1.2 Target specifications and challenges

PROOFED project targets PiezoelectRic mOtOrs For Extreme conditions. When developing piezoelectric motor for extreme conditions (able to operate continuously under thermal, vacuum, radiation, vibrations, magnetic environment), ensuring the long-term durability of the piezoelectric stack is one of the main challenges. This is particularly critical at high temperatures or in the presence of significant self-heating effects.
Typical target specifications of PROOFED piezo motors are given in Table 1. The aim is to reach 300km of linear distance, corresponding to 10 billion actuations of the piezo actuator.

Specification	Value
Operating environment temperature	70°C
Non-operating environment temperature	[-40;250°C]
Magnetic field	3.5 T
Radiation	2.5 MGy
Cumulated equivalent linear distance	300 km
Equivalent number of piezo actuations	10^{10}

Table 1 Targeted specifications for PROOFED motors

2 Characterisation and modelling of self-heating

2.1 Self-heating modelling strategy

To assess the influence of actuator self-heating on its thermal behaviour under constrained environmental conditions, a three-dimensional finite element model of the actuator "APA40SM-SV" was developed using COMSOL Multiphysics (see Figure 2).

 DOI: 10.30420/456743016

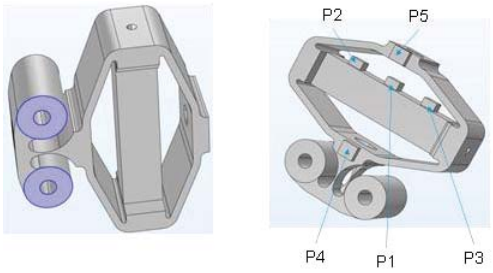


Figure 2 Piezoelectric actuator model implemented

In this model, the power dissipated within the piezoceramic is implemented as a volumetric heat source applied across the entire piezoceramic domain using the following general formulation:

$$P_{loss} = 2\pi \cdot f \cdot C_p \cdot \tan(\delta) \cdot U_{rms}^2$$

where

- P_{loss} is the heat power lost in the system,
- f is the operating frequency,
- C_p is the piezoelectric material capacitance,
- $\tan(\delta)$ is the dielectric dissipation factor, and
- U_{rms} is the rms value of the applied voltage.

To accurately reproduce the environmental conditions experienced by the actuator (70 °C and vacuum), the following boundary conditions are imposed:

- A fixed temperature of 70 °C is applied at the interface between the actuator and its mechanical support (highlighted in blue in Figure 2).
- Radiative heat exchange is applied to all external surfaces. The radiative heat flux is defined as:

$$\dot{Q_{rad}} = \varepsilon \cdot \sigma \cdot (T_{env}^4 - T_{sur}^4)$$

where

- $\dot{Q_{rad}}$ is the radiative heat flux,
- ε is the surface emissivity,
- σ is the Stefan–Boltzmann constant,
- T_{env} is the environmental temperature, and
- T_{sur} is the surface temperature.

Different emissivity values are assigned depending on the material and surface finish.

Finally, to enable direct comparison between simulated and experimental temperature measurements, five additional volumes representing the thermal sensor locations of the real actuator (see Figure 9) are included in the model. These are shown as volumes P1 to P5 in Figure 2.

2.2 Characterization of main piezoelectric parameters under relevant environmental conditions

Because the primary piezoelectric properties (namely the capacitance and dielectric loss factor) depend on both the applied electric field and the surrounding temperature, their characterization under representative environmental conditions is essential. To this end, two complementary measurement approaches are employed:

- **Sine wave characterization under operational temperature condition**: The actuators are placed inside a temperature-controlled oven to reproduce the thermal conditions encountered during vacuum operation. A sinusoidal voltage with amplitude and frequency equivalent to those of the sawtooth driving signal is applied. The piezoceramic parameters are extracted by fitting the measured voltage and current waveforms to a simplified equivalent circuit consisting of a parallel resistance and capacitance (illustrated in Figure 3).
- **Sawyer-Tower measurements**: To validate the values obtained from the sine-wave method, polarization curves are measured using a Sawyer–Tower configuration. As before, measurements are performed in an oven to replicate in-use conditions. A reference capacitor with a capacitance 100 times larger than that of the actuator is used to ensure accurate charge measurement. An example of a resulting polarization curve is shown in Figure 4.

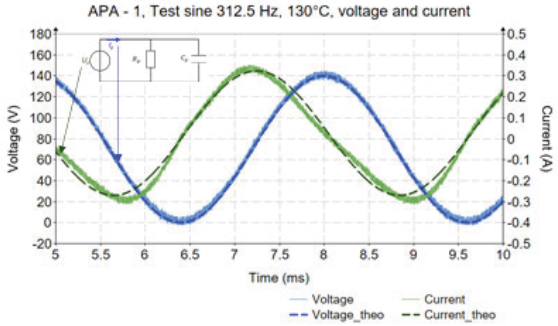


Figure 3 Outputs from the sine wave characterization

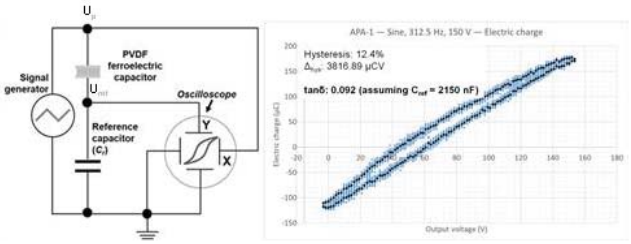


Figure 4 Outputs from the Sawyer-Tower measurements

From these two characterization methods, the piezoelectric properties reported in Table 2 are obtained for the two tested actuators.

Properties	APA-1	APA-2	Theory
Tan(δ) (-)	0.09	0.09	0.1
C_p (nF)	2150	2300	2844
P_{loss} (W)	0.71	0.76	1.05

Table 2 Measured piezoceramic properties at high-voltage and high-temperature

 DOI: 10.30420/456743016

3 Development of high temperature piezoelectric stacks

To ensure long-term reliability under high-temperature conditions, several joining methods between wire and the piezoelectric stacks were evaluated. Conductive epoxy demonstrated the highest durability during extensive lifetime testing and was therefore selected for stacks of varying sizes: 2x5x10mm^3 and 5x5x10mm^3 (Figure 5):
After assembly of the stacks, the electrode faces of each stack were bonded to a stranded, Kapton-insulated wire using the conductive silver epoxy.

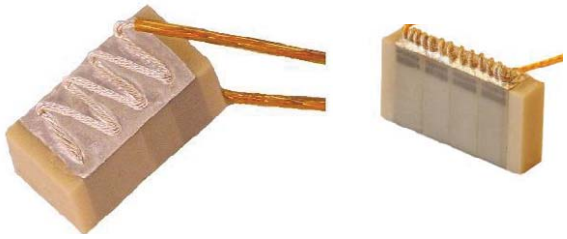


Figure 5 One piece coiled and external Kapton covered wire configurations for stacks of dimensions 2×5×10 mm³ and 5×5×10 mm³[10]

These stacks were subsequently integrated into actuator assemblies, which successfully completed endurance tests totalling 10 billion cycles [10]. During testing, the operating frequency was adjusted to maintain a self-heating temperature of approximately 200 °C. The actuators exhibited only minor and acceptable performance variations, confirming that both the enhanced stack design and the selected electrical connection method were robust under demanding thermal and mechanical conditions.

The corresponding specifications for the stacks, wiring configuration, and APA are summarized in Table 3.
Each APA40SM-SV incorporates two piezoelectric stacks of 5x5x10 mm, with each stack consisting of four piezo tiles compressed between two end plates (Figure 6).
The APA35XS-SV uses smaller 2x5x10mm stack.

Parameters	Values		Unit
Length (L)	5	2	mm
Width (W)	5	5	mm
Max width (WM)	8	6.8	mm
Height (H)	10	10	mm
Free capacitance @1 V_{RMS} 1kHz	640	250	nF
Operating voltage, Vmax	150		V
Free stroke 0V to Vmax	11	11	µm
Max. operating temp.	200		°C
PZT material	NCE51F		
External electrodes	Screen-printed Silvers		
Wire configuration			
Type	Kapton		
Wire attachment method	glued by conductive Silver epoxy		
Amplified Piezoelectric Actuator (APA®)			
APA40SM-SV		APA35XS-SV	
APA free stroke -20V to Vmax	54	54	µm

Table 3 Piezo stack with wire configuration and APA® specifications

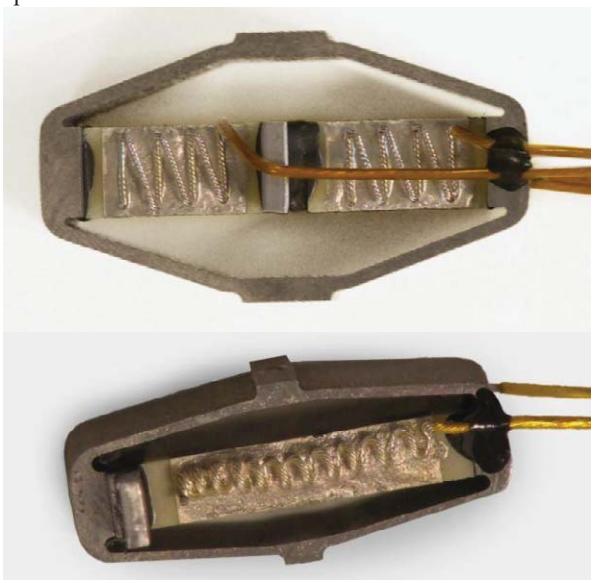


Figure 6 Top: APA40SM-SV with 5x5x10mm3 stacks ; Bottom: APA35XS-SV with 2x5x10mm3 stack

4 Design and integration of a dedicated thermal drain

4.1 Thermal drain design

Based on the 3D thermal model described above and the piezoelectric properties reported in Table 2, the piezoceramic is predicted to reach a temperature of approximately 170 °C during operation in 70°C vacuum environment. Self-heating would become even more problematic with higher-frequency signals or elevated operating temperatures. Therefore, the implementation of a thermal drain is being investigated to ensure the actuator's long-term reliability. Several design concepts were evaluated and compared in terms of performance and integration feasibility. Ultimately, the concept illustrated in Figure 7, consisting of a thermally conductive element inserted at the centre of the piezoceramic, was selected. This design was preferred for the following reasons:

- **Design simplicity:** The thermal drain consists of a metal sheet folded into the required geometry. Flexible features are incorporated into the design to minimize the impact of the drain on the actuator's global stiffness and to avoid significant degradation of its vibrational performance.

 DOI: 10.30420/456743016

- **Thermal performance:** Positioned at the centre of the piezoceramic, the thermal drain provides an efficient thermal path bypassing the inherently high thermal resistance of the piezoeletric. It channels heat away from the piezoelectric core toward the actuator fixation, effectively reducing the temperature of the piezoceramic element.
- **Compatibility with mechanical design constraints:** The chosen solution integrates seamlessly with the actuator architecture. It satisfies the thermal requirements while exerting only limited influence on the actuator's mechanical performance parameters such as stroke, speed, lifetime, and wear-compensation mechanisms. The inherent preload applied to the piezoceramic further ensures good thermal contact between the thermal drain and the ceramic element.

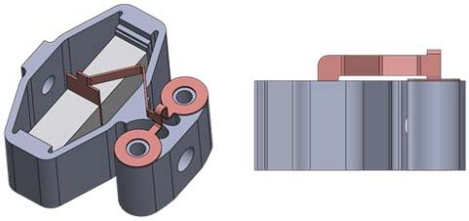
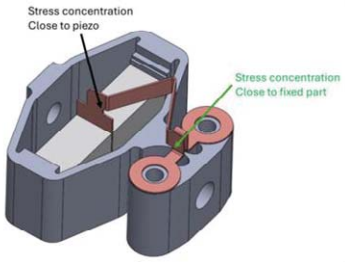


Figure 7 Actuator with thermal drain

A comprehensive set of analyses was conducted to verify compliance with the main design requirements. In particular, the following aspects were examined:

- **Impact on actuator temperature:** According to the thermal simulations, the implementation of the thermal drain yields an expected thermal resistance reduction of approximately 54%.
- **Impact on mechanical performance:** Because the thermal drain is designed to remain flexible in the direction of the actuator's operating vibration, the overall stiffness increase is limited to about 1% in the direction of actuation and 5% in tilting.
- **Stress behavior under multiple loading scenarios (thermal, actuation, and tilt loading):** Stress analyses were carried out in fatigue using Haigh's diagram. Two critical regions on the thermal drain were evaluated (see Figure 8): the stress concentration near the piezoceramic and the stress concentration near the fixed end. In both cases, the resulting stress levels lie well below the Goodman and VDI fatigue limits, confirming the suitability of the proposed design for long-term cycling operation.



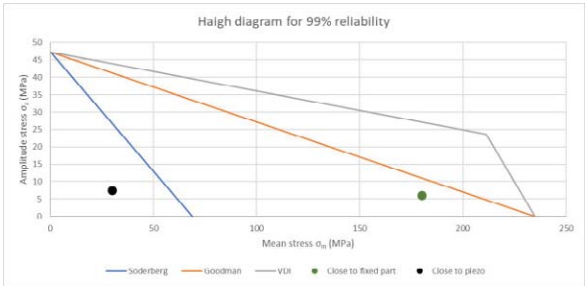


Figure 8 Static and alternating stresses at two critical thermal drain locations evaluated vs fatigue limits

4.2 Integration and testing

To validate the expected thermal performance, two actuators equipped with the thermal drain and five surface-mounted thermal probes were manufactured (Figure 9). These probes were bonded to the actuator surface to record the temperature distribution during operation. An additional reference probe was installed to measure the temperature of the fixation plate.

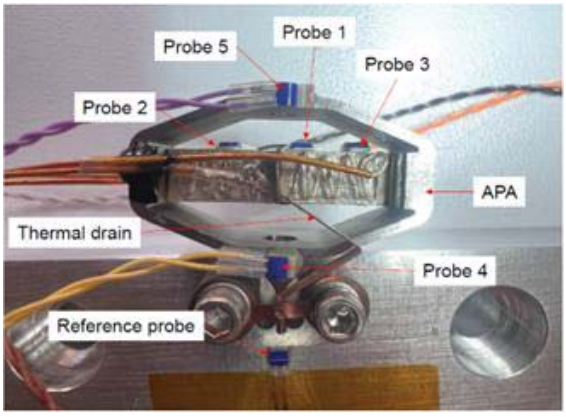


Figure 9 Instrumented actuator with thermal drain

Both actuators were placed in a thermal-vacuum chamber (Figure 10) featuring a temperature-controlled base plate and an actively thermalized cover. Prior to activation, the chamber environment was adjusted to ensure that all thermal probes stabilized at approximately 70 °C.

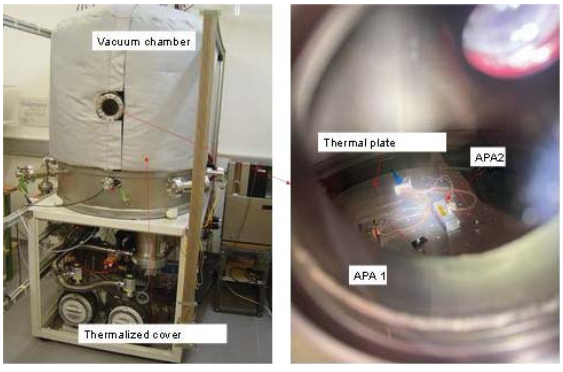


Figure 10: Environmental configuration during testing

DOI: 10.30420/456743016

Once thermal equilibrium was reached, the actuators were actuated and the resulting temperature rise was recorded.

A summary of the results for one of the tested units is presented in Figure 11 (the other being similar). These measurements confirm the effectiveness of the thermal drain: a reduction of the thermal resistance of ~41% is obtained.

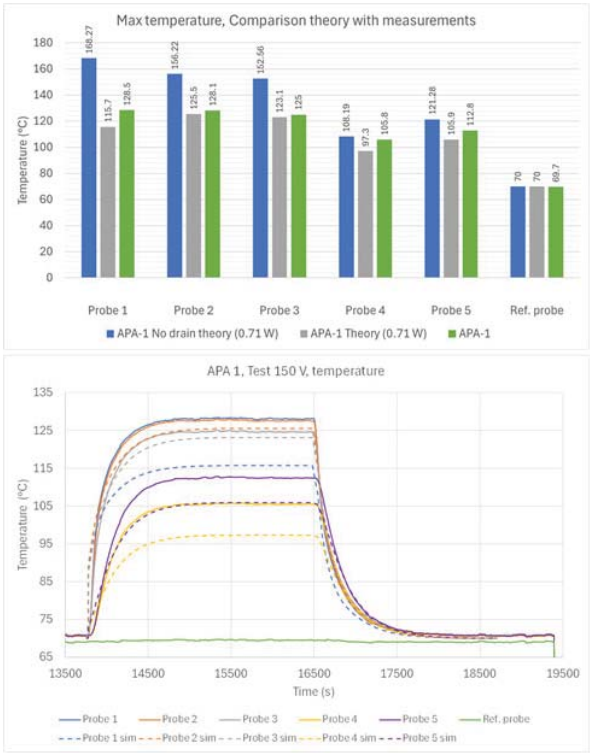


Figure 11 Test result of APA-1 in vacuum, at maximum applied voltage and environmental temperature of 70°C

Furthermore, comparison between the five measured probe temperatures and the model predictions shows excellent agreement (Table 3). The maximum deviation, observed near the primary heat source, was limited to 11%. This strong correlation validates the simulation approach and confirms its suitability as a predictive design tool for future actuator improvements.

	APA-1	APA-2
P1	+11%	+8%
P2	+2%	-
P3	+2%	-3%
P4	+9%	+2%
P5	+7%	+3%

Table 3 Obtained difference between simulated and measured temperatures

5 Inertial rotary piezo motors for severe environments.

The rugged APA40SM-SV with thermal drain was integrated by CTEC into RSPA inertial rotary piezo motors for continuous actuation under high temperature and vacuum.

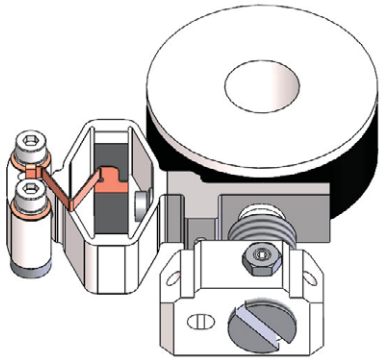


Figure 12 APA40SM-SV on a 34mm diameter payload

Using smaller piezo stacks and its expertise, CTEC miniaturized motors for harsh environment from "40SM" motors delivering 100N.mm torque with a 35mm friction radius to significantly more compact designs.

In these compact configurations, the piezo actuator and rotor are integrated within an envelope of Ø14 mm internal diameter and Ø27.5 mm external diameter to drive a payload (Figure 13 left). These RSPA motors have been tested successfully in vibration, shocks and thermal environment, following specifications of table 1.



Figure 13 Left: Cylindrical housing featuring an integrated RSPA uXS piezomotor and additional functions. Right: RSPA XS Compact rotary piezo motors for severe environments

Parameter	RSPA uXS	RSPA XS
Min. Holding torque	> 8N.mm	>13 N.mm
Min. driving torque	>2.6 N.mm	>4.5 N.mm
Volume of motor part	Ø14mm int. Ø27.5mm ext	Ø30*15mm Excluding output shaft
Mass of motor	<10g	<45g

Table 4 RSPA uXS & RSPA XS rotary piezo motors performances

ISBN: 978-3-8007-6743-4

@ VDE VERLAG GMBH · Berlin · Offenbach

6 Conclusion

Complementary measures implemented within the PROOFED project significantly enhanced the reliability and lifetime of piezoelectric actuators, even under prolonged high-cycle operation.

- Optimisation of the joining methods for piezoelectric stacks increased its lifetime for continuous actuation. 10 billion of actuations with 200°C surface temperature were demonstrated on several APA® actuators [10].
- A thermal drain was integrated into the APA® actuator. Experimental results closely matched simulations, confirming that the thermal drain effectively reduces operating temperature without degrading the actuator's dynamic performance.

Finally, the rugged actuators were integrated by CTEC to build RSPA inertial rotary piezo motors for severe environments. The range goes from "40SM" motors delivering 100N.mm torque with a 35mm friction radius to much more compact "uXS" motors.

Finally, some results are considered for use in the rotating piezo motors of LISA space project [9].

7 Acknowledgement

CTEC received funding from Eurostars under the PROOFED 2361 Consortium Agreement. The Eurostars Program is powered by EUREKA and the European Community. The Coordinator CTEC is supported by BPI FRANCE and the French state within the France 2030 program.

CTS gratefully acknowledge the support of Innovation Fund Denmark (E2361 - PROOFED - CTS Ceramics Denmark, Case no. 3109-00083B) whose project grant made this work possible.

CSEM has been co-funded by Innosuisse – Swiss Innovation Agency, in the framework of the Eurostars Programme (Project No. 2361 – PROOFED).

8 Literature

[1] R. Leletty, A New Amplified Piezoelectric Actuator for Precise Positioning and Active Damping, Proc SPIE, Smart Systems and Mat., San Diego Ca, March 1996.

[2] P. Guay, Piezo Qualification for Space Applications, Proc ACTUATOR 2002, Ed. Messe Bremen, B3.2, pp.284-287

[3] APA® Amplified piezo actuator, Registered trademark of Cedrat Technologies, https://cedrat-technologies.com/categorie-produit/amplified-piezo-actuator-piezo-actuators/

[4] F. Claeyssen, and al, Stepping Piezoelectric Actuators Based on APAs, Proc Actuator 2008

[5] C.Belly, F. Claeyssen, R. Le Letty, T. Porchez, Benefits from Amplification of Piezo Actuation in Inertial Stepping Motors and application for High Performance Linear Micro Motors, Proc Actuator 2010

[7] A. Guignabert, and al, Improvement of MSPA Module of Stepping Piezo Actuator, Proc Conference Actuator, A3.8 p121, 25-27 June 2018

[8] E. Betsch, J. Gauthier, N. Bencheikh, A Pagès, High power density Piezo motors for critical environments Proc. Actuator 2022.

[9] N. Bencheikh, N. Bourgeot, A. Pagès, G. Aigouy, J. Rebufa, E. Betsch, F. Claeyssen. Inertial & Inchworm piezoelectric motors: Design and Motorization selection key aspects, Proc. Actuator 2024

[10] R. Lou-Møller, I. Mehdipour, C. Mangeot, N. Bourgeot, F. Claeyssen, B. Laluc. Enhancing the Reliability of Piezoelectric Actuators and Motors Under Severe Self-Heating, High-Cycle Operation, and Harsh Environmental Conditions, Proc. Actuator 2026.

[11] J. Rebufa, J. Gauthier, and al, High-resolution Rotating Piezo Motors for LISA Laser Interferometer Space Antenna. Proc. Actuator 2026

 DOI: 10.30420/456743017

Adaptive Surface Actuation via Magnetoactive Elastomer Membranes

Ina Bregu[a], Abdelkarim Masoud[a], and Jürgen Maas[a]
[a]Technische Universität Berlin, Mechatronic Systems Laboratory, 10623 Berlin, Germany

Abstract

In this work, we present the modeling, simulation, and experimental characterization of a magnetoactive elastomer membrane (MAE membrane) whose surface topology can be actively controlled and reconfigured using electromagnetic coils. The actuation of the coils enables localized and programmable deformations, creating diverse application possibilities, including haptics, soft robotics, adjustable adhesion, and shape-changing interfaces. The proposed approach combines the Neo-Hookean hyperelastic material model with magnetic Kelvin force distributions to develop a predictive model for the reconfigurable surface structure. The derived analytical model is further evaluated experimentally. The final step is the implementation of an open-loop control strategy that maps desired MAE membrane deformations to the required coil current for targeted surface configurations without real-time feedback, thereby providing a foundation for fast and efficient control of reconfigurable surface topologies.

1 Introduction

Magnetoactive elastomers (MAEs) are a class of smart composites, consisting of magnetizable micro- or nanoparticles embedded within an elastomer matrix [1]. Unlike thermally or chemically responsive hydrogels that have a slow response time, MAEs can undergo very rapid and highly reversible mechanical deformations when exposed to external magnetic fields [2]. This combination of rapid response and reversibility makes them particularly suitable for applications in soft robotics, including biomedical and minimally invasive surgery, haptics, and human-machine interfaces. As these fields require increasingly complex and programmable interactions, the demand for precise design and actuation strategies for MAEs has increased significantly.

The macroscopic deformation of MAEs results from a complex magneto-mechanical coupling at the microscale. When subjected to a magnetic field, the embedded particles interact via dipole-dipole forces, while also experiencing Kelvin body forces in the presence of field gradients. These internal interactions are transferred to the hyperelastic elastomer matrix, resulting in global shape changes and modulus stiffening. [3]

The active control of the surface topography of MAE structures enables diverse application possibilities. In the field of haptics, multimodal MAEs have been used to achieve dynamic tactile interfaces and touch sensors capable of altering their surface roughness to provide information to the user [4]. In soft robotics, MAE materials serve as artificial muscles and soft grippers that can conform to delicate objects [5]. In the domain of adjustable adhesion, recent studies have shown that (bioinspired) MAE surfaces, can actively modulate capillary and pull-off forces by magnetically altering their apparent contact angle and surface roughness, enabling reversible attachment in both dry and wet environments [6]. Finally, the integration of MAEs into structural designs has led to the development of shape-changing interfaces and mechanical metamaterials, in which the local modulus and geometry can be tuned to control acoustic bandgaps or enable complex morphing structures [7].

Despite these advancements, achieving precise, localized, and dynamically programmable surface topologies remains a significant challenge, as most current proposed models rely on bulk magnetic fields that lack the resolution to isolate deformations. To address this, we propose a modeling framework that couples Neo-Hookean hyperelasticity with magnetic Kelvin volume force distributions to predict reconfigurable surface deformations. This model provides the foundation for an open-loop control scheme based on a displacement matrix that maps target membrane deformations to the coil current. By utilizing the resulting magnetic flux density field generated by the activated coil, the system can achieve a localized deformation across the membrane surface.

2 Theoretical Modeling

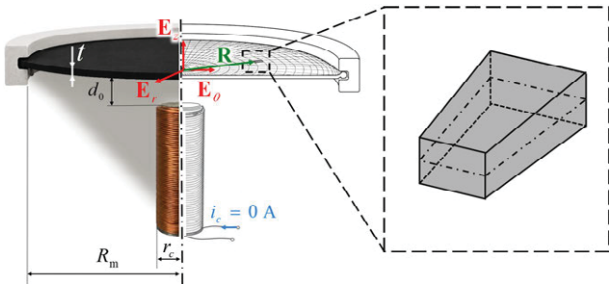
To derive an analytical model for the local deformation u of the MAE membrane, a continuum mechanics framework is formulated that couples hyperelasticity with magnetic body forces. The Neo-Hookean constitutive law describes the membrane's mechanical behavior when subjected to magnetic Kelvin forces generated by the electromagnetic coil current i_c.

2.1 Continuum Mechanics of the Membrane

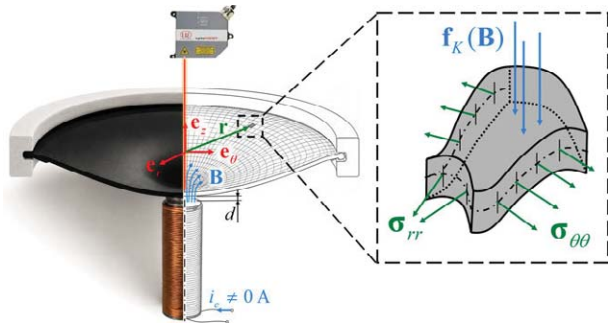
We consider an axisymmetric membrane in cylindrical coordinates and establish a mapping from the undeformed reference configuration, described by cylindrical coordinates (R, Θ, Z), to the deformed current configuration, de-

 DOI: 10.30420/456743017

noted by (r,θ,z). The geometric transition from the initial flat reference configuration to the deformed current configuration is illustrated in Figure 1.



(a) Undeformed configuration and geometric parameters.



(b) Deformed state under applied magnetic field.

Figure 1 Schematic representation of the MAE membrane actuator system with the electromagnetic coil, MAE membrane, laser triangulation sensor as well as a representative differential volume element illustrating the coupled magnetic-elastic response.

The positions of a material point in the undeformed reference configuration and the deformed current configuration are given by the vectors $\mathbf{R}$ and $\mathbf{r}$, respectively:

$$\begin{aligned}\mathbf{R} &= R\mathbf{e}_R + Z\mathbf{e}_Z,\\ \mathbf{r} &= r(R)\mathbf{e}_r + z(R,Z)\mathbf{e}_z.\end{aligned} \tag{1}$$

The displacement vector $\mathbf{u}$ is defined as:

$$\mathbf{u} = \mathbf{r} - \mathbf{R}. \tag{2}$$

To relate these geometric transitions to the mechanical deformation, we compute the deformation gradient tensor $\mathbf{F} = \nabla_0 \mathbf{r}$. In the local orthonormal basis, $\mathbf{F}$ is given by:

$$\mathbf{F} = \mathrm{diag}(\lambda_r,\lambda_\theta,\lambda_z) = \frac{\partial r}{\partial R}\mathbf{e}_r \otimes \mathbf{E}_R + \frac{r}{R}\mathbf{e}_\theta \otimes \mathbf{E}_\Theta + \frac{\partial z}{\partial Z}\mathbf{e}_z \otimes \mathbf{E}_Z. \tag{3}$$

Here $\mathbf{E}_R, \mathbf{E}_\Theta, \mathbf{E}_Z$ denote the material reference configuration basis vectors and $\mathbf{e}_r, \mathbf{e}_\theta$ and $\mathbf{e}_z$ the current configuration basis vectors. The principal stretches in the radial and hoop directions are defined respectively as:

$$\lambda_r = \frac{dr}{dR}, \quad \lambda_\theta = \frac{r}{R}. \tag{4}$$

Assuming the elastomer is perfectly incompressible, the volumetric deformation must be zero (the Jacobian of the deformation must satisfy $J = \det(\mathbf{F}) = \lambda_r\lambda_\theta\lambda_z \overset{!}{=} 1$), which is enforced by the constraint:

$$\lambda_r\lambda_\theta\lambda_z = 1 \iff \lambda_z = \frac{1}{\lambda_r\lambda_\theta}. \tag{5}$$

This condition reduces the degrees of freedom in the Neo-Hookean energy density function by allowing the transverse stretch λ_z to be expressed in terms of the in-plane stretches.

2.2 Constitutive Behavior

To characterize the mechanical behavior of the MAE composite, we adopt a Neo-Hookean hyperelastic material model. The strain energy density ψ is expressed in terms of Young's modulus Y and the first invariant of the right Cauchy–Green deformation tensor $\mathbf{C} = \mathbf{F}^T\mathbf{F}$:

$$\psi(I_1) = \frac{Y}{6}(I_1 - 3) = \frac{Y}{6}\left(\lambda_r^2 + \lambda_\theta^2 + (\lambda_r\lambda_\theta)^{-2} - 3\right), \tag{6}$$

where $I_1 = \mathrm{tr}(\mathbf{C})$ characterizes the deformation state. The incompressible Neo-Hookean model is appropriate for strain ranges $\lambda < 1.5$ typical in this work.

2.2.1 Derivation of Stress Components

The Cauchy stress components are derived by differentiating the strain energy. The second Piola–Kirchhoff stress tensor is:

$$\mathbf{S} = 2\frac{\partial\psi}{\partial\mathbf{C}} - p\mathbf{C}^{-1} = \frac{Y}{3}\mathbf{I} - p\mathbf{C}^{-1}, \tag{7}$$

where p is a Lagrange multiplier, physically interpreted as hydrostatic pressure for perfectly incompressible material and $\mathbf{I}$ referes to the identity matrix.
The Cauchy stress in the current configuration is obtained via the push-forward operation:

$$\sigma = \mathbf{F}\mathbf{S}\mathbf{F}^T = \frac{Y}{3}\mathbf{B} - p\mathbf{I}, \tag{8}$$

where $\mathbf{B} = \mathbf{F}\mathbf{F}^T$ is the left Cauchy-Green deformation tensor.
For the axisymmetric deformation with the diagonal deformation gradient $\mathbf{F} = \mathrm{diag}(\lambda_r,\lambda_\theta,\lambda_z)$, the principal stress components are:

$$\begin{aligned}\sigma_{rr} &= \frac{Y}{3}\lambda_r^2 - p,\\ \sigma_{\theta\theta} &= \frac{Y}{3}\lambda_\theta^2 - p,\\ \sigma_{zz} &= \frac{Y}{3}\lambda_z^2 - p.\end{aligned} \tag{9}$$

The radial stress σ_{rr} and hoop stress $\sigma_{\theta\theta}$ characterize in-plane deformation, while σ_{zz} represents the thickness-normal stress that drives the out-of-plane displacement u(r). The hydrostatic pressure p is determined during the numerical solution via the boundary conditions (zero displacement at the membrane edge).

 DOI: 10.30420/456743017

2.3 Magnetic Field Formulation

To describe the actuation behavior of the MAE membrane, a continuum mechanical modeling approach is adopted based on the Kelvin force density volume [9]. The magnetically induced force acting on the magnetizable particles within the elastomer matrix is expressed as a Kelvin volume force density $\mathbf{f}_K$:

$$\mathbf{f}_K = \mu_0(\mathbf{M}\cdot\nabla)\mathbf{H}, \tag{10}$$

where μ_0 is the permeability of free space, $\mathbf{M}$ is the magnetization, and $\mathbf{H}$ is the magnetic field strength. Using the constitutive relation

$$\mathbf{M} = \chi_{\text{eff}}\mathbf{H}, \tag{11}$$

with effective susceptibility (accounting for demagnetization) [9]:

$$\chi_{\text{eff}} = \frac{3\chi(\mathbf{H})}{3+\chi(\mathbf{H})}. \tag{12}$$

The susceptibility $\chi(\mathbf{H})$ accounts for demagnetization effects within the elastomer matrix, reducing the applied field experienced by the particles by a geometry-dependent factor [9]. The force density is reformulated as:

$$\mathbf{f}_K = \mu_0\chi_{\text{eff}}(\mathbf{H})(\mathbf{H}\cdot\nabla)\mathbf{H} \tag{13}$$

In cylindrical coordinates, the z-component of the force can be calculated as:

$$f_{k,z} = \mu_0\chi_{\text{eff}}(H)\left(H_r\frac{\partial H_z}{\partial r} + H_z\frac{\partial H_z}{.}\partial z\right) \tag{14}$$

For practical experimental applications, it is advantageous to express this force as a function of the magnetic flux density using $\mathbf{B}$, which can be measured directly using a teslameter with a Hall sensor for experimental validation. Therefore, substituting the relation

$$\mathbf{H} = \frac{\mathbf{B}}{\mu_0\mu_r} \tag{15}$$

into Equation (13) yields a force expression dependent solely on the magnetic flux density and the material's relative permeability. Therefore, the spatial distribution of the magnetic flux density $\mathbf{B}$ must be known. After substitution, the z-component of the force density becomes:

$$f_{k,z} = \mu_0\chi_{\text{eff}}\left(\frac{B}{\mu_0\mu_r}\right)\frac{1}{(\mu_0\mu_r)^2}\left(B_r\frac{\partial B_z}{\partial r} + B_z\frac{\partial B_z}{\partial z}\right), \tag{16}$$

which depends only on the measured magnetic flux density distribution $\mathbf{B}(r,z)$ obtained from COMSOL simulations and the material's relative permeability $\mu_r(B)$.

2.4 Derivation of the Governing ODE

For a thin membrane with axisymmetric transverse deflection $u(r)$, Equation (9) can be integrated through the thickness t, and the stress resultant or membrane tension can be defined as:

$$T_0 = \int_t \sigma_{zz}\,dz. \tag{17}$$

The equilibrium of the membrane surface in cylindrical coordinates yields:

$$\frac{1}{r}\frac{d}{dr}\left(rT_0\frac{du}{dr}\right) = f_{k,z}. \tag{18}$$

Expanding and assuming constant pre-tension T_0:

$$T_0\left(\frac{d^2u}{dr^2} + \frac{1}{r}\frac{du}{dr}\right) = f_{k,z}. \tag{19}$$

Dividing by T_0 and substituting the magnetic force from Equation (13):

$$\underbrace{\frac{d^2u}{dr^2} + \frac{1}{r}\frac{du}{dr}}_{\substack{\text{Membrane resistance}\\ \text{to bending (curvature)}}} = \underbrace{\frac{1}{T_0}\mu_0\chi_{\text{eff}}(B)\left(B_r\frac{\partial B_z}{\partial r} + B_z\frac{\partial B_z}{\partial z}\right)}_{\substack{\text{Applied magnetic force}\\ \text{driven by field gradients}}}, \tag{20}$$

where the membrane tension T_0 is a material property determined by the pre-stressed state from the Neo-Hookean constitutive model. For a membrane clamped at the edge, the following condition is defined:

$$u(r = R_{\text{m}}) = 0 \quad \text{(fixed edge)}, \tag{21}$$

where R_{m} denotes the radius of the MAE membrane.
The coupled magneto-mechanical equilibrium reduces to a single nonlinear ordinary differential equation (ODE) in one spatial dimension (radial coordinate r), which can be solved using standard numerical methods.

2.5 Magnetic Field Density Distribution and Numerical Fitting

Since magnetic scattering effects cannot be modeled using simplified equivalent magnetic circuits with lumped parameters, a numerical simulation in COMSOL Multiphysics is performed to obtain the magnetic field density distribution as a function of both the electromagnetic coil radius r_{c} and the coil-membrane distance d, see Figure 2.

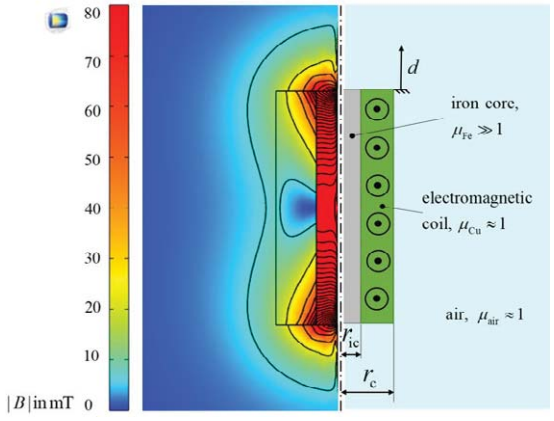


Figure 2 Cross-sectional schematic of the electromagnetic coil and COMSOL Multiphysics simulation results of the magnetic flux density distribution across the electromagnetic coil cross-section.

 DOI: 10.30420/456743017

The model consists of an iron core and a copper coil within an air domain, where infinite element layers are applied to the external boundaries to represent an infinite vacuum buffer.

The simulation also accounts for the non-linear magnetization characteristics $\mathbf{B} = f(\mathbf{H})$ of the iron core. Crucial to this model is the distance-dependent field distribution: as the membrane deforms under magnetic attraction, the distance d changes and consequently, the magnetic field $\mathbf{B}(r_c, d)$ must depend on both the radial coordinate and the instantaneous coil-membrane separation.

2.5.1 Radial Distribution of the Magnetic Field

From the simulation results, the radial distribution of magnetic flux density $\mathbf{B}(r)$ is extracted for multiple distances d from the coil surface.

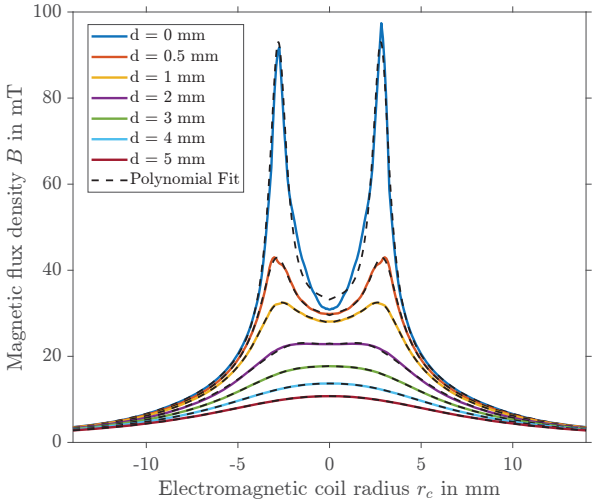


Figure 3 Numerical simulation results showing the radial distribution of the magnitude of magnetic flux density B at varying distances d from the coil surface.

The sharp peaks, visible in Figure 3, arise from material discontinuities at the iron-copper-air interfaces (at $r_{ic} = 3$ mm), where the permeability drops abruptly from $\mu_{iron} \propto 10^3 \mu_0$ to $\mu_{copper} \propto \mu_0$. This distance-dependent behavior is necessary for accurately modeling the membrane's attraction toward the coil. As the membrane deforms, the reduction in d leads to an increase in the local magnetic field density, which in turn amplifies the magnetic force.

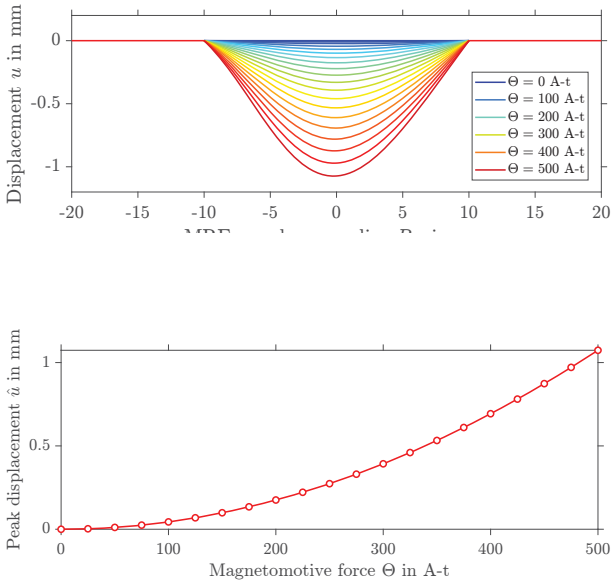
2.5.2 Polynomial Fitting for Numerical Integration

The simulation results are finally fitted to analytical functions for numerical efficiency during the numerical solution process. Polynomial fits $\mathbf{B}_{fit}(r, d)$ were generated using least-squares fitting for each distance d, with the polynomial order adaptively chosen to achieve a maximum relative error of <2% at material boundaries and <1% elsewhere. This fitted representation can be seen in Figure 3 and smooths minor numerical features at material boundaries while preserving the essential physics of the magnetic field concentration.

3 Numerical Simulation Method and Results

The transversal deformation of the MAE membrane is modeled as a boundary value problem (BVP) and solved using the `bvp4c` solver in MATLAB. This solver implements a collocation method based on the three-stage Lobatto IIIa formula, that approximates the displacement profile of the axisymmetric membrane by discretizing the radial domain into a set of grid points. From an initial guess by `bvpinit`, the solver iteratively adjusts the solution of the ODE until the boundary conditions are satisfied within the specified `RelTol` and `AbsTol` limits [10].

In this BVP, the magnetic volume force $f_{k,z}$ drives the membrane deformation $u(r)$, which alters the effective coil-membrane distance at each radial position. Since the displacement amplitude is comparable to the gap distance d, a fully coupled approach, re-solving the magnetic field



(b) Peak membrane displacement $\hat{u}$ as a function of magnetomotive force Θ.

Figure 4 Numerical results of the magnetically induced displacement of the MAE membrane.

The numerical results illustrating the membrane displacement and the relationship between the applied current and the membrane's peak displacement are presented in Figure 4 and show very good agreement with the expected physics and experimental results.

The MAE membrane shows a symmetric concave displacement profile with its peak displacement at the center and tapering to zero at the fixed edges. The peak displacement $\hat{u}$ demonstrates a nonlinear increase as the applied magnetomotive force Θ increases.

 DOI: 10.30420/456743017

4 Material Characterization and Experimental Validation

In this section, the theoretical predictions from the coupled magneto-mechanical BVP are compared with experimental measurements.

4.1 Magnetoactive Elastomer Composition

Two silicone elastomer matrices were investigated in this study: Silixson 10 and Silixson 25 (Wacker Silicones, nominal hardness ratings). Both matrices were reinforced with carbonyl iron particles (BASF, Ultrapure Carbonyl Iron, median particle radius $r_p = 3.125\,\mu$m) at a constant volume fraction of $c_v = 50\%$. The high particle concentration creates a mechanically reinforced composite material whose effective Young's modulus differs from that of the pure matrix. The elastomer matrix Young's moduli (Shore A hardness) were obtained from manufacturer datasheets [11], [12]:

- Silixson 10: $E_{\text{matrix}} \approx 0.5$ MPa
- Silixson 25: $E_{\text{matrix}} \approx 1.5$ MPa

For the particle-filled composite, the effective Young's modulus Y is enhanced by the presence of rigid iron particles.

Although simple composite mixing rules (e.g., rule of mixtures) would overpredict the stiffening for soft elastomers, the effective modulus for 50% volume-fraction iron-silicone composites typically ranges from $Y \approx 1$–5 MPa, depending on the matrix hardness and particle clustering effects. We adopt values within this range for the two materials:

- Silixson 10 + 50% CIPs: $Y \approx 1.2$ MPa
- Silixson 25 + 50% CIPs: $Y \approx 3.0$ MPa

These estimates are based on reported literature values for similar magnetoactive elastomer systems [13]. The chosen values (Y = 1.2, 3.0 MPa) represent mid-range estimates. A sensitivity analysis indicates that $\pm 20\%$ variation in Y produces $\pm 10\%$ variation in predicted u_p, which is within experimental noise for the displacement measurements.

4.2 Experimental Setup and Procedure

Four membrane samples were fabricated using a mold-casting process, producing circular clamped membranes with two thickness values: $t = 3$ mm and $t = 5$ mm, see Figure 1. Each membrane was mounted in a 3D-printed housing designed to maintain a constant clamped boundary condition directly above an electromagnetic coil. The coil-to-membrane distance was set to $d_0 = 5$ mm, ensuring strong magnetic coupling while maintaining a stable experimental configuration.

Transverse membrane displacement was measured using a high-precision laser triangulation sensor (optoNCDT, Micro-Epsilon, Germany) focused on the membrane peak displacement $\hat{u}$. The electromagnetic coil was driven by a controlled current source, varying the applied current from 0 to 2.0 A in increments of 0.1 A. All signals were recorded via a dSPACE MicroLabBox real-time control system, ensuring temporal recording between current commands and displacement measurements. The peak displacement was measured and recorded at each current step. The experimental setup can be seen in Figure 5.

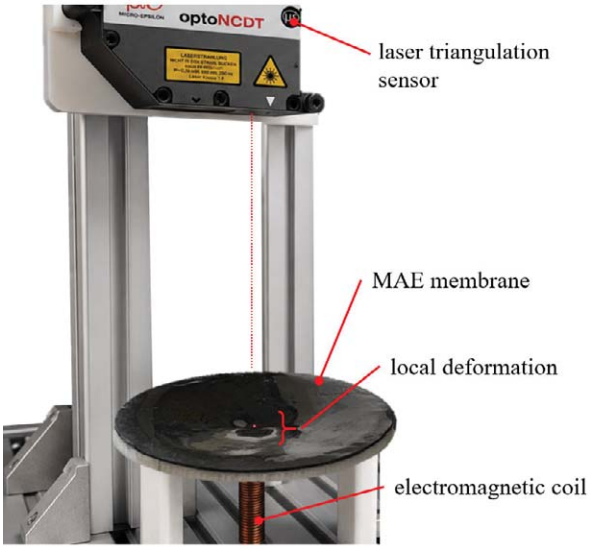


Figure 5 Experimental setup for measuring the peak displacement of a Magneto-Active Elastomer (MAE) membrane. The red laser spot indicates the measurement point at the center of the membrane for determining peak displacement $\hat{u}$.

4.3 Experimental Validation

As illustrated in Figure 6, utilizing the material moduli listed in Section 4.1 and the COMSOL-derived magnetic field distribution as input, the computed numerical results show very good agreement with experimental results for all four samples up to a critical electromagnetic current, i_{crit}. As expected, a softer silicon matrix (Silixson 10) shows significantly larger peak displacements compared to a stiffer matrix (Silixson 25). This effect is further amplified by the membrane thickness. Thinner samples achieve larger peak displacements for the same applied current. The nonlinear displacement-current relationship results from the coupled magnetoelastic interaction and geometric nonlinearities that vary with material stiffness.

Beyond a critical current value i_{crit}, the system undergoes a snap-through instability. This phenomenon occurs when the magnetic force, which scales as $\sim 1/d^2$ (from Kelvin force proportional to ∇B^2), as the gap distance d decreases and exceeds the elastic restoring force of the membrane. At this bifurcation point, a stable equilibrium configuration no longer exists, and the membrane is pulled rapidly toward the electromagnetic coil. This behavior is consistent with bifurcation theory; however, the currently formulated nonlinear BVP model does not capture the dynamics of this instability.

 DOI: 10.30420/456743017

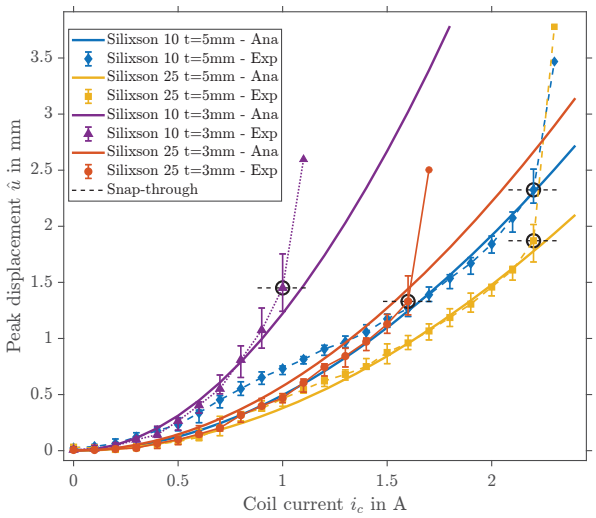


Figure 6 Comparison of numerical predictions (solid lines) and experimental measurements (symbols) for peak membrane displacement $\hat{u}$ as a function of coil current i_c.

Nevertheless, a safe operating window for controlled actuation, defined by $0 < i < i_{\text{crit}}$, can be estimated based on the limits of numerical convergence and experimental observation.

A comprehensive stability analysis, intended to further characterize the post-buckling regime and the complex bifurcation, is part of future work. Despite this limitations at the extremes, the model successfully predicts the qualitative behavior across the parameter range tested, confirming the validity of the proposed approach for design-relevant predictions of MAE membrane actuation.

5 Conclusion and Outlook

In this work, the analytical modeling and experimental evaluation of a magnetoactive elastomer (MAE) membrane actuated by electromagnetic coils has been presented. The results show good agreement between derived theoretical model and experimental observations across different material configurations. In particular, the Neo-Hookean constitutive model provides an adequate description of the membrane's hyperelastic response under magnetic loading. The presented control architecture establishes a systematic mapping from a desired surface deformation to the required actuation current.

Future work is dedicated to the extension of the presented framework to multi-coil array systems, enabling spatially resolved and programmable surface actuation. Such arrays can be used to achieve highly complex, localized deformation patterns by superimposing magnetic fields from multiple electromagentic actuators.

6 Literature

[1] G. Filipcsei, I. Csetneki, A. Szilágyi, M. Zrínyi: Magnetic Field-Responsive Smart Polymer Composites, Oligomers – Polymer Composites – Molecular Imprinting, Springer, Berlin, Heidelberg, 2007, pp. 137–189

[2] G. V. Stepanov, D. Yu. Borin, A. V. Bakhtiiarov, M. Storozhenko: Transient Response of Macroscopic Deformation of Magnetoactive Elastomeric Cylinders in Uniform Magnetic Fields, Polymers, 2024

[3] S. Chougale, D. Romeis, M. Saphiannikova: Field-Induced Transversely Isotropic Shear Response of Ellipsoidal Magnetoactive Elastomers, Polymers, 2023

[4] S. Costrell, M. Alam, R.L. Klatzky, M.E. McHenry, L.M. Walker, M.O. Martinez: A Magnetic Soft Device for Tactile Haptic Actuation of the Fingertip; Proceedings of the 2023 IEEE World Haptics Conference (WHC), Delft, The Netherlands, 10–13 July 2023, pp. 48–55

[5] X. Li, Z. Zhang, M. Sun, H. Wu, Y. Zhou, H. Wu, S. Jiang: A magneto-active soft gripper with adaptive and controllable motion; Smart Materials and Structures, Volume 30, Number 1, 2020

[6] S. Chen, Z. Qian, X. Fu, X. Wu: Magnetically Tunable Adhesion of Magnetoactive Elastomers' Surface Covered with Two-Level Newt-Inspired Microstructures

[7] C.D. Pierce, C.L. Willey, V.W. Chen, J.O. Hardin, J.D. Berrigan, A.T. Juhl, K.H. Matlack: Adaptive Elastic Metastructures From Magneto-Active Elastomers; Smart Materials and Structures, 29(6), 2020, p. 065004

[8] G. W. Holzapfel: Nonlinear Solid Mechanics; Wiley, New York, 2006

[9] J. Maas, D. Uhlenbusch: Smart Materials and Structures, 25(10), 2016, p. 104002.

[10] Shampine, L. F., & Kierzenka, J. (2001). *A Solver for Nondimensional Boundary Value Problems*. ACM Transactions on Mathematical Software, 27(3), 299-316.

[11] Silikonfabrik. (2026). *SILIXON 10 – 2K Silikonkautschuk (RTV2 Platin Gießsilikon)*. Technical Datasheet, Bad Bodenteich, Germany. (Accessed: 2026-05-04).

[12] Silikonfabrik. (2026). *SILIXON 25 – 2K Silikonkautschuk (RTV2 Platin Gießsilikon)*. Technical Datasheet, Bad Bodenteich, Germany.(Accessed: 2026-05-04).

[13] Johari, M. A. F., Mazlan, S. A., Nordin, N. A., Ubaidillah, U., Aziz, S. A. A., Nazmi, N., Johari, N., & Choi, S.-B. (2021). *The Effect of Microparticles on the Storage Modulus and Durability Behavior of Magnetorheological Elastomer*. Micromachines, 12(8), 948.

 DOI: 10.30420/456743018

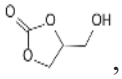
Electrostatically Actuated Liquid Lenses for an Anamorphotic Zoom

Debatri Das, Martin Hoffmann, Ruhr-Universität Bochum, 44801 Bochum, Germany
debatri.das@ruhr-uni-bochum.de

Abstract

The actuation of fluids is not restrained to mechanical pumps, rather electrostatic fields are able to actuate suitable liquids, especially highly polar fluids such as water or polyethylene carbonate. While unactuated small droplets tend to form spheres due to surface tension, actuated droplets can be adjusted in shape. The idea is to use stacked planar systems to enclose fluidic spheres and to actuate or elongate them by electrostatic forces. This effect is often called electrowetting on dielectrics as the liquid apparently wets the de-wetting surface, but in principle, it is the consequence of the electrostatic force on polar fluids (electrocapillarity).

1 Liquid Lens Formation

Fluids with high dielectric constant ($\varepsilon_{r,water}$ = 80; $\varepsilon_{r,glycerol\ carbonate}$ = 115) are preferred for examining electrowetting actuation (EWOD) effect, as dielectric properties [2] are responsible for electrowetting phenomenon by a polar droplet. In this research, 1 mm radius droplets of polar fluids such as water (H_2O) and glycerol carbonate,  , are studied. These droplets exhibit a Bond number of below 1 so that the surface tension is dominating against gravitational effects (Bo < 1) [3] is used for obtaining stretched out , deformed ellipsoid shape of the same under electrostatic force compared to the spherical shape under no influence of the electrostatic force. The reformation of a spheroid in a surface minimized structure is largely due to the influence of surface tension: water 72 mN/m, glycerol carbonate: 40 mN/m. Electric fields counteract surface tension and allow to reform the droplet shape.

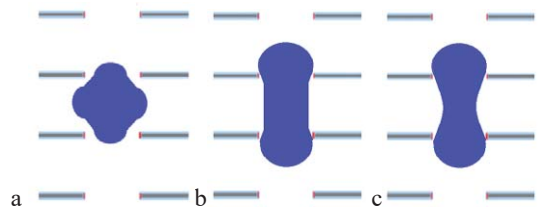


Fig 1. a: Droplet in an approximated spheroidal shape in a the high rack system and a convex shape; b: reformed droplet into a cylindrical shape and c: droplet transforming into a concave shape due to electrostatic actuation

By reshaping the sphere due to reduction of the volume while keeping its length, the sphere turns more and more into cylindrical lens. An optical zoom lens changes the magnification of an object from all direction arbitrarily. The formula of a deformed droplet turned into a liquid lens can be given by:

$$\frac{1}{FL} = (n_1 - n_2)\left(\frac{1}{r_1} - \frac{1}{r_2}\right)$$

FL: Optical focal distance
n_1: refractive index of water (1.33)
n_2: refractive index of air (1)
r_1: axisymmetric curvature radii on the vertical surface
r_2: axisymmetric curvature radii on the horizontal surface

Table 1: Variation of voltage and obtained optical focal length

Voltage (V)	Optical distance (mm)
0	0.3
100	1.06
150	1.51
200	3.03

ISBN: 978-3-8007-6743-4 @ VDE VERLAG GMBH · Berlin · Offenbach

 DOI: 10.30420/456743018

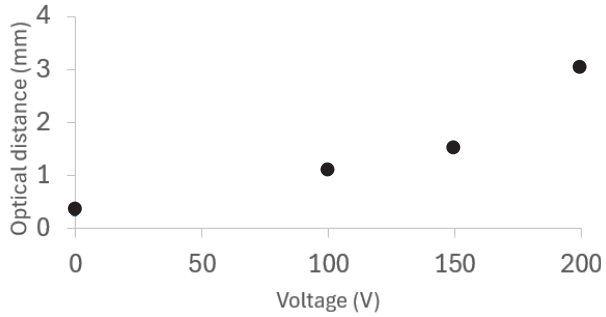
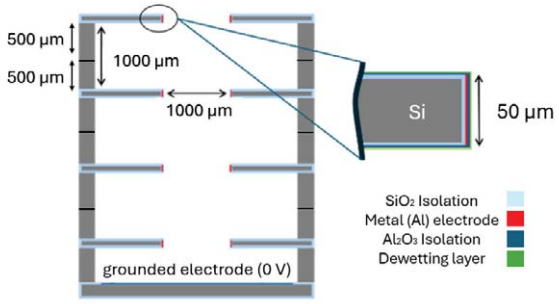


Fig 4. Linear graph with different voltage applied (X axis) and Optical distance of a spheroid (Y axis)

2 Realization of the Actuator

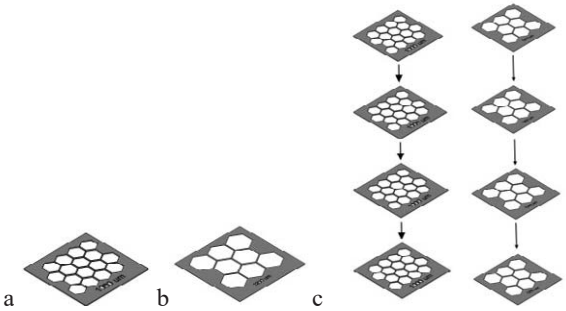
The actuator is realized by stacking aligned SOI wafers. The device layer forms the channels while the handle layer provides enough space for the droplet.

Two SOI substrates, (device layer of 50 µm Si, SiO_2 layer 2 µm, 500 µm Si handle layer) joined together is used to define channels within a stack of at least four wafers, a three dimensional sideview of a fabricated actuator is shown below.

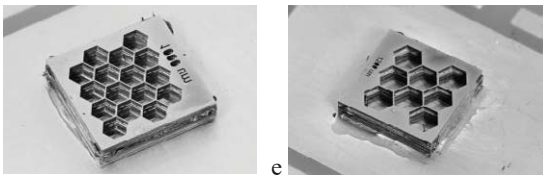


a b

Fig 2. a: wafer stacks designed as a high rack storage demonstrator, 2 SOI chips with 500 µm handle layer joined together creating a distance of 1000 µm between each stage, b: enlarged form of each layer with materials following different colour codes



a b c



d e

Fig 3.a:Schematic sideview of a microchip with 1000 µm diameter cavities, 2 SOI chips with 500 µm handle layers inversely joined together to create the distance of 1000 µm b: Schematic sideview of a microchip with 1200 µm diameter cavities c: High rack storage system consisting of 1000 µm (left) and 1200 µm (right) cavity design as all layers joined with conductive glue d: Top view of the actuator with stacked 1000 µm (4 stages) diameter chips, each such stage consists of two chips. e: Top view of the actuator with stacked 1200 µm (4 stages) diameter chips

The actuators are realized by stacking SOI chips, creating a high bay rack system. Each of the four modules consists of two SOI chips with 500 µm handle layer, joined inversely together to create an internal height of 1000 µm. The figures above show a schematic top view design with different material layer coated with 200 nm Silicon dioxide (SiO_2) as an isolation layer, 150 nm aluminum for a sidewall metallization for achieving conductivity, 150 nm pin hole free, conformal, dielectric layer with Al_2O_3 achieved by atomic layer deposition (ALD) and finally, a hydrophobic coating, here HMDS (hexamethyl-disilizane), for achieving the electrowetting on a dewetting surface.

Operating the system with AC potentials reduces the risk of surface charging within the isolation layers due to very high and constant field strengths.

3 Simulation

The simulations are performed using COMSOL Multiphysics® v.6.0 software.

Fig 6.a-c the simulations under applied electric potentials at 4 stacks labelled as P1 = 150 V, P2 = -150 V, P3 = -150 V and P4 = 150 V. Fig 6a indicates the starting position of a droplet on top of the storage and in a field-free regime holding a spherical shape (white coloured contour determining its surface cross section). As the voltage is applied (∓150 V in 6b), the droplet is pulled into the cavities, and it changes its shape due to the electrostatic field: While the field

 DOI: 10.30420/456743018

tends to pull the droplet apart, the surface tension tries to retract it into the central, field-free cavity. The field effects are shown as the black lines in the figure. Positive electric potentials are coded as red colour , and negative potentials are represented in blue colour respectively. Due to the asymmetry (closed electrode at the bottom, no electrode at the top, the shape of the droplet is not mirror-inverted in the vertical direction.

In fig 6c, the voltages are turned off again, and the droplet , under no electric field influences, the droplet turns into a surface minimized spheroid.

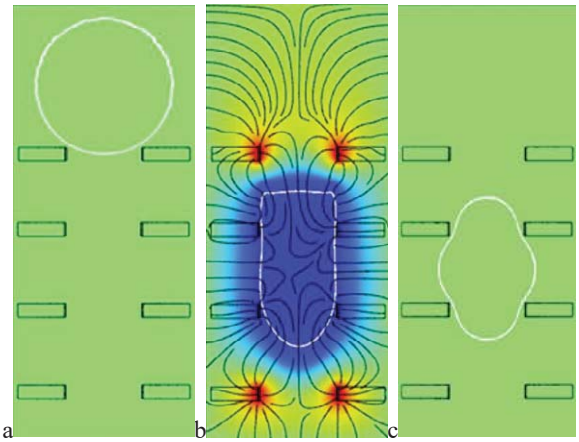


Fig 5. a: Droplet on top of the cavity, no potential applied. b: elongated shape of an actuated droplet inside of the 2nd and 3rd stacks, electric potential as ∓150 V applied sidewall electrodes (P1,P4 as 150 V, P2,P3 as -150 V).c: droplet reforms into a surface minimized ellipsoid shape after switching off the potentials

4 Experiments

For a first verification, water droplets are analyzed in a high rack storage microsystem. In the droplet shape analyzer, the electrowetting behavior of a water droplet is observed under the influence of electric potential.

Tests under electrostatic field show, that a conformal, pin hole free aluminum oxide dielectric layer has been achieved on the aluminum electrodes for an electric potential ranging up to ∓150 V; no water electrolysis due to a breakthrough of the isolation layer has been observed that would result in gas bubbles and increased current. Fig.5a shows the microsystem with four stacks of hexagonal structures, and a droplet on the top of the cavity before applying an electrical potential. The contact angle of the droplet in the beginning is approx.. 110°. Fig 5b and 5c show that eventually, when electric potential increases up to the range of ∓150 V, the actuation starts and droplet gradually moves in the cavities. The change in contact angle in between the surface and the droplet interface is also observed along with the electrostatic actuation. Once the droplet enters the cavity completely, the voltage is turned off. With no potential, the water droplet reshapes the structure and reforms into a surface minimized spheroidal structure due to the effect of surface tension.

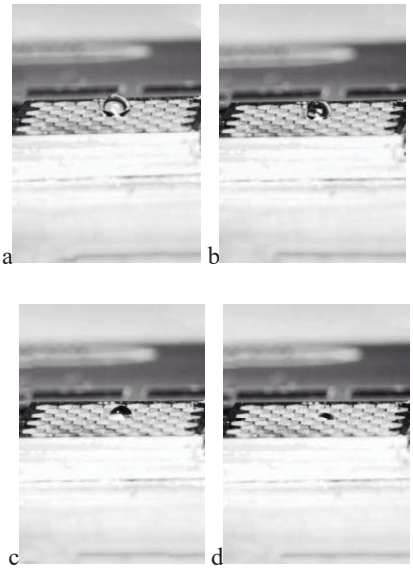


Fig 6. Schematic sideview of the gradually actuated droplet on 1000 µm cavities. a: the droplet on a hydrophobic surface at unactuated state. b-c: the droplet gradually actuated through 1000 µm radius cavities with electric potential applied at the sidewalls. d: the droplet goes into the cavity after actuation, and it holds the spheroidal shape.

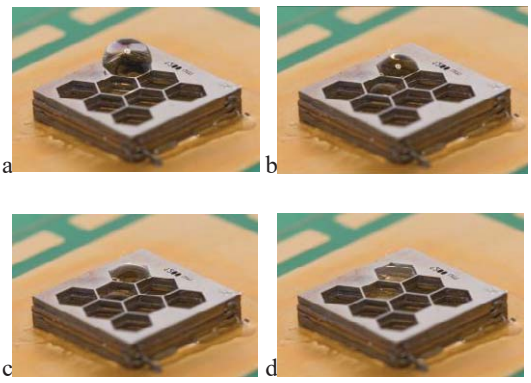


Fig 7. Schematic sideview of the gradually actuated droplet on 1200 µm cavities. a: the droplet on a hydrophobic surface at unactuated state. b-d: the droplet gradually actuated through 1200 µm radius cavities with electric potential applied at the sidewalls.

Areas with higher electric field leverage reshaping of the droplet into such a spheroid as shown in Fig 7 d, and the droplet stays stable at this position after switching the potential off. Another factor is the differences in focal length for each stage of the droplet, at potential, the droplet holds a concave bulge at the curvature radii, resulting in a smaller optical length. While gradually increasing electric potential on the electrodes, the droplet wets the surface. Reformation of the droplet, while transforming the curvature radii into longer shape as an elongated droplet, effectively makes the focal length longer. The difference in contact angles of the droplets is also seen in Fig 8 a(non actuated, hydrophobic) and b (actuated, hydrophilic).

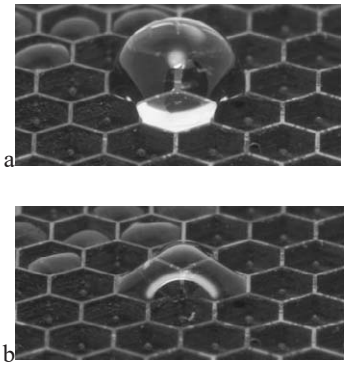


Fig 8. a: droplet with a shorter focal length at non actuated state. b: droplet with a longer focal length at actuated state, resulting contact angle change while wetting the surface.

Introducing AC voltages to switch different voltage at different stacks results in optimizing different shapes of a droplet. AC voltages can also sweep away intermittent surface charges between any two stacks.

5 Summary

By integrating microfluidic channels with electrostatic actuation, a novel concept is proposed for rapidly tunable liquid lenses. The underlying mechanism leads interfacial surface tension to act as a virtual membrane that dictates the geometric profile of the lens. At micro-scales, surface tension naturally minimizes interfacial energy, reshaping small fluid volumes into near-perfect spherical droplets. The application of an external electrostatic field modulates this profile, enabling dynamic tuning of the focal length while maintaining a continuously curved, aberration-free optical surface. This actuation framework operates on the principle of electrowetting on dielectrics (EWOD), such as the applied electric field reduces the effective contact angle, causing the conductive liquid to wet an otherwise hydrophobic substrate.

6 Acknowledgement

This is to acknowledge that the research is funded by DFG, German Research Foundation under the aspect of priority program SPP 2206 Project “KOMMMA-ELSA”. Center for Interface Dominated High Performance Materials (ZGH) is to be acknowledged for ASE process equipment. The chip photography credit goes to Mr. Harald Austenfeld, Ruhr University Bochum.

7 References

[1] S.Sinzinger, M.Hoffmann, D.Pätz, S.Leopold. Anamorphotisches System und seine Verwendung, German Patent DE102014005789B4; Aug. 3,2017. https://patents.google.com/patent/DE102014005789B4/de

[2] Schmitt, L.; Conrad, P.; Kopp, A.; Ament, C.; Hoffmann, M. Non-Inchworm Electrostatic Cooperative Micro-Stepper-Actuator Systems with Long Stroke. *Actuators* **2023**, *12*,150. https://doi.org/10.3390/act12040150

[3] Jean Berthier, Kenneth A. Brakke: Chapter 2 - Theory of Wetting, Micro-Drops and Digital Microfluidics (Second Edition), William Andrew Publishing,Pages 7-73,ISBN 9781455725502,2013.https://doi.org/10.1016/B978-1-4557-2550-2.00002-X.

[4] Jean Berthier, Kenneth A. Brakke: Chapter 3 - The Physics of Droplets, Micro-Drops and Digital Microfluidics (Second Edition), William Andrew Publishing, Pages 75-160,ISBN 9781455725502,2013. https://doi.org/10.1016/B978-1-4557-2550-2.00003-1.

[5] Manfred Kohl, Christoph Ament, Gowtham Arivanandhan, Tamara Bechtold, Peter Conrad, Sipontina Croce, Vincent Gottwald, Martin Hoffmann et al.: Active bi- and multistability in cooperative microactuator systems, In: Sensors and Actuators Reports 9 (2025) 100338, DOI: 10.1016/j.snr.2025.100338

 DOI: 10.30420/456743018

[6] P. Conrad, A. Berdnykov and M. Hoffmann, "Design of a Liquid Dielectrophoresis-driven Platform with Cooperative Actuation," ACTUATOR 2022; International Conference and Exhibition on New Actuator Systems and Applications, Mannheim, Germany, 2022, pp. 1-4.

[7] COMSOL Multiphysics® v. 6.0. www.comsol.com. COMSOL AB, Stockholm, Sweden

ISBN: 978-3-8007-6743-4 @ VDE VERLAG GMBH · Berlin · Offenbach

 DOI: 10.30420/456743019

Lead-free 4 layered piezoelectric motor

B. Delibas, B. Koc
Physik Instrumente (PI) SE & Co KG, Karlsruhe, Germany

Abstract

In this paper, we present a four-layer, lead-free piezoelectric ultrasonic actuator integrated into a precision test stage. The motivation for developing lead-free piezoelectric actuators stems from the toxicity of lead in conventional lead zirconate titanate (PZT) actuators and from European RoHS regulations, under which the current exemption for PZT may no longer be extended. However, the mechanical performance of lead-free bulk piezoelectric actuators remains challenging. The reduced efficiency of the actuator leads to excessive heat generation during operation, which limits performance reliability and motion stability under continuous drive at high duty cycles. To mitigate heat generation, we propose a novel actuator structure composed of four layers of lead-free piezoelectric plates bonded with elastic elements. These elements are designed not only to enhance thermal conductivity but also to incorporate a cavity structure that enables rapid heat dissipation for cooling. The cavity-embedded elastic elements are optimized to provide ideal clamping conditions for the actuators, minimizing oscillation amplitudes and thereby reducing mechanical losses.

Keywords: Lead-free, piezoelectric motor, layered structure, cavity elastic elements

1 Introduction

There are several reasons for developing lead-free ultrasonic motors. First, piezoelectric ultrasonic motors using lead-free ceramics may become mandatory in the near future due to the well-known toxicity of lead. The European RoHS exemption for PZT may not be extended. An environmentally friendly production process for lead-free materials that minimizes the volatilization of toxic substances during calcination and sintering would be desirable. Additionally, the disposal of lead-based piezoelectric materials is a major concern for PZT-based ceramics [1].

The performance of piezoelectric motors built with lead-free actuators is significantly lower than that of their PZT-based counterparts [2]. In addition to the lower d_{33} piezoelectric constants, heat generation in lead-free actuators poses a major challenge for achieving stable, reliable, and robust resonant drive in lead-free piezoelectric-motor stages [3-4]. The problem arises because the eigenfrequency of the motor shifts dramatically during operation.

This paper presents a lead-free piezoelectric motor constructed from four ceramic layers to reduce both the required voltage and the heat generation. Lead-free piezoelectric layers used in this actuator are based on copper-doped potassium sodium niobate (KNN) ceramics [5]. PIC GmbH (Lederhose, Germany) produced piezoelectric ceramics with dimensions of 25 mm × 11 mm × 1 mm that were used to fabricate composite-layered PILine® actuators by embedding elastic elements. The motion controller used for the performance test is the C-867.2U2, a piezoelectric motor controller for PILine® systems with PID (Proportional-Integral-Derivative) adaptive motion control. Various driving methods, such as single-source, dual-source, and dual-frequency excitation, which have been implemented for standard PILine® systems, can also be applied to this structure [6–7].

2 Design of piezoelectric motors

Four-layered lead-free ceramics are bonded to cavity-embedded elastic elements, made of copper and an alumina pusher, forming the contact element. This arrangement is illustrated in a CAD model and in a prototype showing the ideal clamping positions with minimized oscillation amplitudes (Figures 1 and 2).

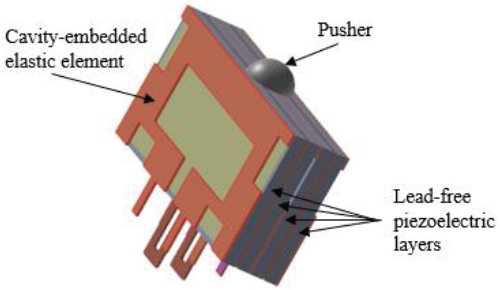


Figure 1 Four-layered lead-free actuator, CAD model

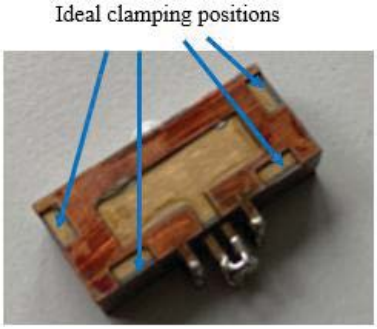


Figure 2 Four-layered lead-free actuator, prototype

 DOI: 10.30420/456743019

A four-layered lead-free actuator in metal housing is built and preloaded against friction bar of the stage (Figure 3).

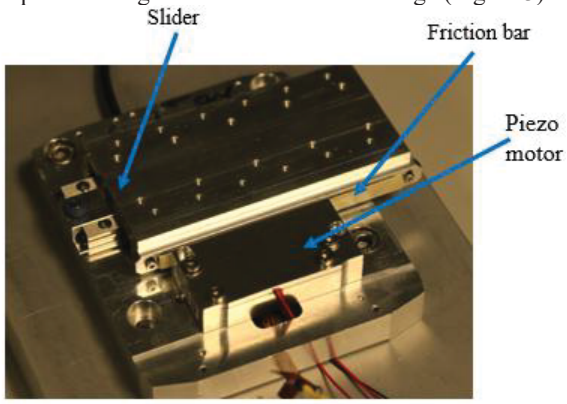


Figure 3 U-551K005 stage built with four layered lead-free piezoelectric motor.

The change in eigenfrequency during the burn-in test was measured. The required motor voltage at the start of operation did not increase significantly when the excitation frequency was between 194 and 196 kHz. After 10 minutes of operation, the motor output remained stable, which can be attributed to improved thermal conductivity from the composite design and the cavities between the layers. Burn-in measurements indicate that operation between 194 and 196 kHz is the optimal frequency range for continuous drive of the layered lead-free piezoelectric stage.

3 Experiments and results

The test stage with four-layered lead-free actuators was evaluated for impedance change, voltage requirement in auto-frequency mode, continuous drive in fixed-frequency mode, push/pull force, and current requirements.

3.1 Impedance measurements

The dynamic characteristics of the lead-free layered actuator were also examined with an impedance analyzer. The actuator was soldered to flexible cables and mounted in the stage with a 10 N preload. Using a small-signal impedance analyzer from Agilent, we measured the actuator's eigenfrequency to be 194.3 kHz (Figure 4).

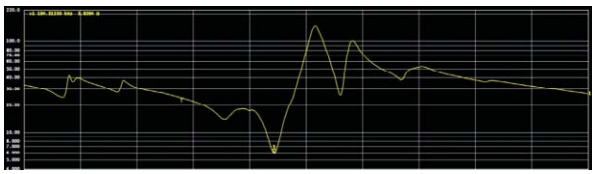


Figure 4 Impedance measurement

3.2 Voltage requirement at auto frequency mode

The test stage equipped with the lead-free actuator was driven continuously in auto-frequency mode, in which the controller's driver unit determined the optimum operating frequency for the piezoelectric ceramics. The auto-frequency search bandwidth was set from 192 kHz to 196 kHz. The required voltage (blue) and the optimum frequency (orange) as functions of operation time are plotted in Figures 5 and 6.

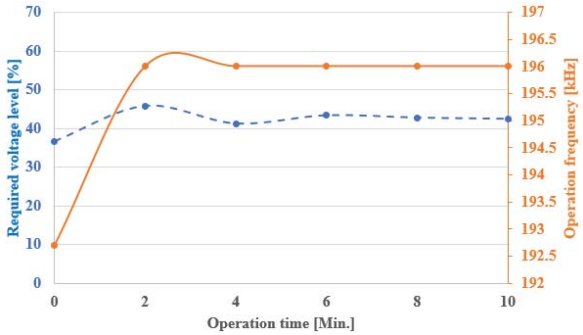


Figure 5 Voltage requirement and optimum operation frequency from controller over continuous drive during closed-loop velocity with 20 mm/s.

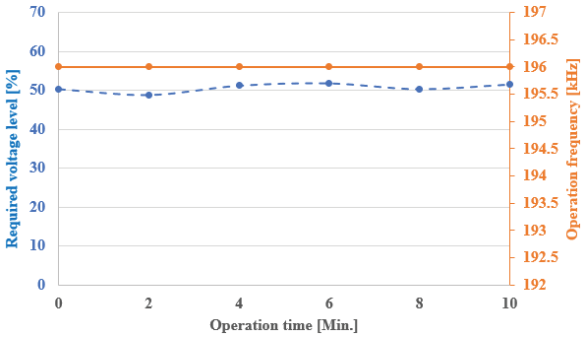


Figure 6 Voltage requirement and optimum operation frequency from controller over continuous drive during closed-loop velocity with 40 mm/s.

As shown in the figures, the motor output required for the velocity settings of 20 mm/s and 40 mm/s remained below 60% of the maximum allowable voltage supplied by the controller during 10 minutes of continuous operation. The optimum frequencies largely rose to the maximum value during operation; consequently, the optimum frequency was fixed at the maximum value, 196 kHz. This corresponds to fixed-frequency operation for continuous drive.

The continuous drive of the stages without the auto-frequency mode was tested with a closed-loop velocity of 20 mm/s. The frequencies chosen for this test ranged from 196 kHz to 198 kHz. The required voltage levels for various fixed-frequency settings over a 10-minute operation time are plotted in Figure 7.

ISBN: 978-3-8007-6743-4 @ VDE VERLAG GMBH · Berlin · Offenbach

DOI: 10.30420/456743019

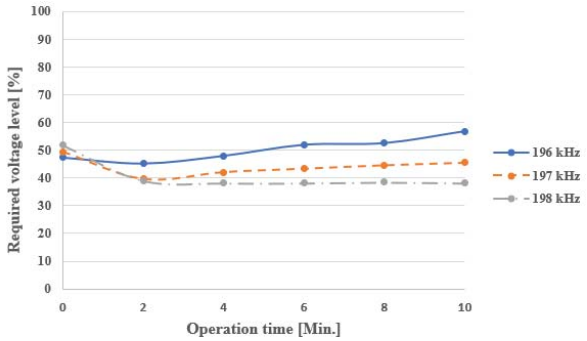


Figure 7 The required voltage level with various fixed frequency settings for a 10-minute operation time

The motor output at the start of operation did not increase significantly when the frequency was between 196 and 198 kHz. After 10 minutes of operation, the motor output remained constant, which could be attributed to improved thermal conductivity of the structure due to the composite design and the cavities between the layers. Measurements showed that operation frequencies in the 196–198 kHz range could be used as the optimum frequencies for the continuous drive of the lead-free layered piezoelectric stage.

3.3 Push/pull force with fixed frequency operation

As shown in Figure 8, the push-pull force capacity of the layered lead-free test stage against gravity was measured using a rope roller mechanism with dummy loads.

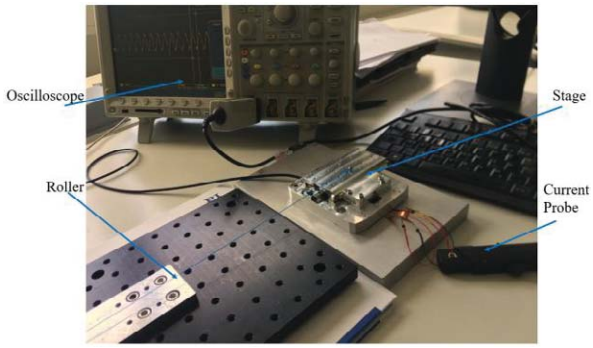


Figure 8 Test setup to measure push/pull force capacity and current requirements during closed-loop operation.

The U-551K005 stage with a four-layered lead-free actuator can handle push-pull forces of 3 N and 4 N at closed-loop speeds of 10 mm/s, 20 mm/s, 40 mm/s, and 60 mm/s, operating at frequencies of 192 and 194 kHz, as shown in Figures 9 and 10. For this stage, the required voltage remained below 70% of the maximum voltage supplied by the controller.

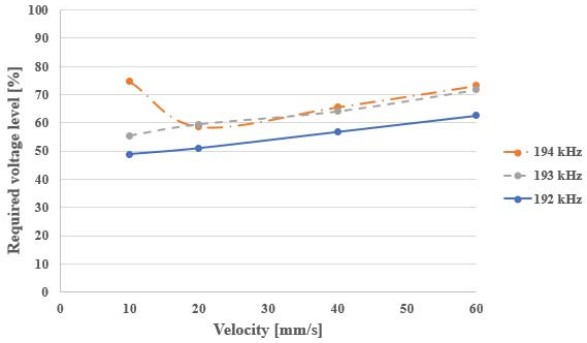


Figure 9 Required voltage at various closed-loop velocities and operation frequencies against 3 N push/pull force against gravity

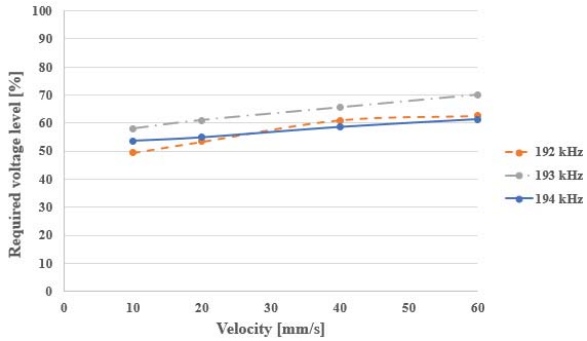


Figure 10 Required voltage at various closed-loop velocities and operation frequencies against 4 N push/pull force against gravity

Figure 8 shows that a TCP0030A (120 MHz) current probe was used for the measurements. Figures 11 and 12 present the current requirements at various velocities when the stage moved against 3 N and 4 N push/pull forces against gravity, respectively. The motor operated at 193 kHz.

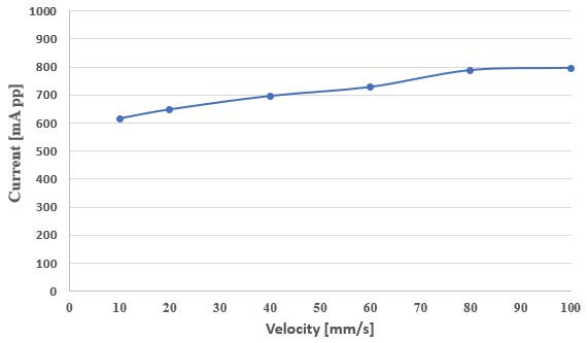


Figure 11 Motor current measurements at various velocities when it is 3 N loaded against gravity.

 DOI: 10.30420/456743019

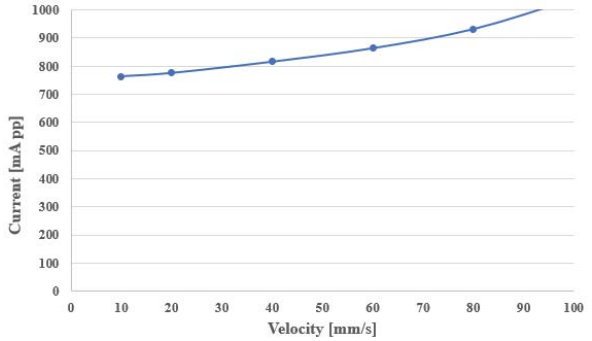


Figure 12 Motor current measurements at various velocities when it is 4 N loaded

Current measurements confirmed that the required current remained below 1000 mA (1 A), in line with the specifications of the C-867.2U2 controller. Although layered actuators demand higher current, the measured values are still compatible with standard controllers.

3.4 Life-Time Test

A layered lead-free actuator–based stage was tested at a velocity of 10 mm/s for more than 80 days as part of a compact life-time test. As shown in Figure 13, the stage remained stable over days of operation. There was no degradation in voltage levels over the lifetime. Additionally, there was no excessive heat generation during operation, since the stage operated at moderate voltage levels with fixed frequencies of 194 kHz and 195 kHz.

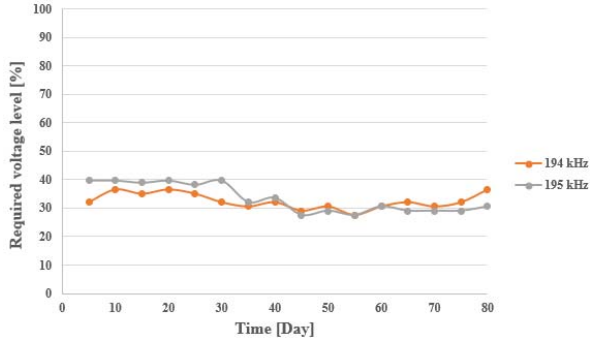


Figure 13 Life-time test for four-layered lead-free actuator at two operation frequencies

4 Conclusion

In this paper, we tested four-layer lead-free actuators in a composite structure. The actuator, composed of four lead-free ceramic plates bonded to cavity-embedded elastic elements, was housed in a metal casing and preloaded against a friction bar mounted on the stage. The eigenfrequency of the four-layer actuator inside the motor housing was measured as 194.3 kHz.

The eigenfrequency shift during operation was measured. Results show that the required motor voltage during the burn-in phase did not increase significantly when the excitation frequency was maintained between 194 and 196 kHz. After 10 minutes of operation, the motor output stabilized, which can be attributed to the improved thermal conductivity of the composite design and the cavities between the layers. These measurements confirm that this frequency range is the optimal window for continuous operation of the layered lead-free piezoelectric stage.

Push-pull force measurements showed that the test stage equipped with four-layer lead-free actuators could deliver a 4 N push/pull force against gravity at closed-loop velocities of 20, 40, and 60 mm/s, operating at driving frequencies of 192–194 kHz. During closed-loop operation, the required voltage remained below 70% of the controller's maximum supply voltage (71 V_{rms}).

As previously observed, self-heating in lead-free bulk piezoelectric ceramic actuators during continuous operation raises their eigenfrequency. Consequently, auto-frequency mode is unsuitable for stages based on lead-free bulk actuators, requiring a limit on the maximum operating frequency to maintain stability. In contrast, layered-structure piezoelectric motors can operate in auto-frequency mode because self-heating produces much smaller eigenfrequency shifts.

Additionally, lifetime testing of the layered actuator showed that the motor operated reliably without any degradation of performance, and the voltage requirement remained essentially constant.

5 Literature

[1] Ibn-Mohammed, T., et al. "Are lead-free piezoelectrics more environmentally friendly?." *Mrs Communications* 7.1 (2017): 1-7.

[2] Difeo, Mauro, et al. "Performance evaluation of lead-free potassium sodium niobate-based piezoceramics for ultrasonic motor design." *Ceramics International* 51.10 (2025): 13646-13653.

[3] Tsai, C.C.; Chu, S.Y.; Chao, W.H.; Hong, C.S. A Rotary-Linear Ultrasonic Motor Using MnO2-Doped (Ba0.97Ca0.03)(Ti0.96Sn0.005Hf0. 035)O3 Lead-Free Piezoelectric Ceramics with Improved Curie Temperature and Temperature Stability. Actuators 2022, 11, 248.

[4] Maeder, M. D., Damjanovic, D., & Setter, N., Lead free piezoelectric materials. *Journal of electroceramics*, *13*(1), 385-392, 2004.

[5] PI Ceramic GmbH [Online], https://www.piceramic.com/en/expertise/piezo-technology/piezoelectric-materials, Accessed on October 27, 2025.

[6] Makarem, Sarah, et al. "Data-driven tuning of PID controlled piezoelectric ultrasonic motor." *Actuators*. Vol. 10. No. 7. MDPI, 2021.

[7] Delibas, Bülent, et al. "A Method to Realize Low Velocity Movability and Eliminate Friction Induced Noise in Piezoelectric Ultrasonic Motors," in *IEEE/ASME Transactions on Mechatronics*, vol. 25, no. 6, pp. 2677-2687, Dec. 2020.

 DOI: 10.30420/456743020

Electromagnetic characterization of Magnetorheological Dampers

Gabriel Dias Mendes, M.Sc.[a]
[a]Cracow University of Technology, Warszawska 24, 31-155 Kraków, Poland

Abstract

Magnetorheological (MR) dampers are semi-active devices which take advantage of the field-controlled properties of MR fluids to provide a variable damping force. Next, MR fluids are representatives of magnetically activated smart materials. Naturally, in order to make use of the material's controllable characteristics a magnetic field of sufficient magnitude is needed. Therefore, it is fundamental to develop an electromagnetic model of a specific MR device. Thus, the work focuses on obtaining key electromagnetic characteristics of a commercial MR damper so that based on these characteristics relevant models and control strategies can be developed and implemented. Based on black laboratory measurements results, incl. voltage and current, the characteristics of the specific MR damper are obtained and the challenges in developing a damper controller identified. To summarize, the procedure can be easily reproduced and applied to other configurations of MR dampers or actuators.

1 Introduction

Magnetorheological (MR) fluids are well-known representatives of smart materials. When exposed to magnetic fields, they transition from a liquid state to a semi-solid state, and developing a yield stress in the material as a result of the magnetic stimuli application [1]. This change is fast and reversible, and directly related to the magnetic field flux density applied to the fluid [2], meaning that a higher flux density will result in a higher yield stress value, closer to a solid-like behavior, while a lower flux density provides a behavior closer to a fluid-like behavior.

Usually, automotive dampers are passive devices, meaning that the energy dissipation capability of the damper is defined once it is built and cannot be altered. For comparison, semi-active dampers are capable of regulating their damping characteristics, e.g. by means of controllable solenoid valves. MR dampers are unique semi-active devices in the sense that the variable characteristics are achieved solely by modifying the rheology of the MR material. With the MR dampers it is possible because the output force is related to the yield stress of the MR fluid, which is related to the magnetic flux density applied to it. Thus, when a higher damping force is required from the damper, the magnetic field applied to MR fluid is adjusted to meet the requirement. In a typical automotive MR damper the magnetic field is generated by a solenoid which is composed of a ferromagnetic core, a coil and an air gap (filled with MR fluid). A reliable model of the magnetic circuit thus allows the enhancement of already established control schemes of the damper and probing new strategies, aiming for a better and more robust dynamic behavior of the vehicle's suspension. With the context set, the focus of this work is to provide experimental means for characterizing flow-mode (vehicle suspension) MR dampers. Briefly, to accomplished the goals, in this study the damper is excited with input voltage signals across a range of frequencies and amplitudes, so the dynamic behavior of the damper can also be deduced and captured. The dynamic behavior of the damper is crucial since it is expected that the damper can handle a variety of road profiles and ride conditions. The authors is of the opinion that the result of this study shall improve the modeling of the nonlinearities intrinsic of such device in both transient and steady-state conditions, respectively.

This work is structured as follows: first, key aspects of the damper operation are defined; second, the experimental procedure is described. Finally, the results are presented and discussed, and conclusions drawn.

2 MR Damper Characterization

From the structural standpoint, MR dampers are simple devices, featuring a valve which is essentially a ferromagnetic core, an air gap gap, which is filled with MR fluid, a coil, or coils in a multi-coil damper configuration, which are wound around the ferromagnetic core, and the piston housing. In **Figure 1** the structure of a single coil MR damper is revealed. The coil is excited with an electrical current applied, inducing magnetic field. The field is confined to the solenoid's structure incl. the ferromagnetic core, MR fluid, and the housing. Therefore, a simple *RL* (resistor-inductor) model of the circuit can be proposed, L - coil inductance, R - coil resistance. It is assumed that the inductance depends on the current i is due to the inherent nonlinearities of the ferromagnetic materials. Figure 2 shows the proposed circuital model, where v_{coil} is the voltage at the coil's terminals, i_{coil} is the coil current, R_{coil} denotes the DC resistance of the coil, and L is the coil's inductance.

$$v_{coil}(t) = i_{coil}(t)R_{coil} + L(i_{coil})\frac{di_{coil}}{dt} \tag{1}$$

Since $\lambda = L(i_{coil})i_{coil}$, λ – flux linkage, the above model

 DOI: 10.30420/456743020

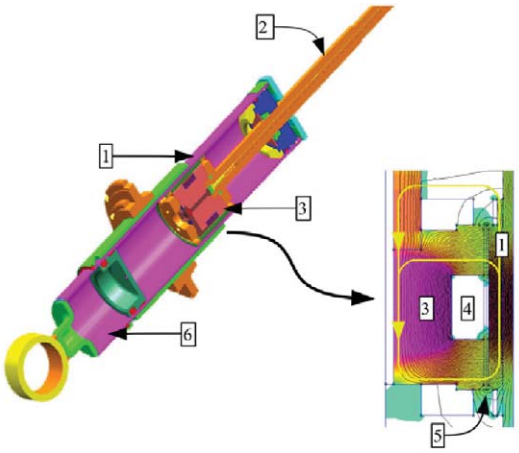


Figure 1 MR damper structure; 1-cylinder and ring, 2-rod, 3-core, 4-coil assembly, 5-annulus, and 6-gas chamber. Adapted from [3]

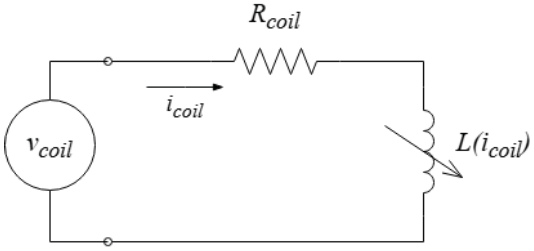


Figure 2 Electric circuit model of a MR damper.

can be rewritten as follows

$$\frac{d\lambda}{dt} = v_{coil}(t) - i_{coil}(t)R_{coil} \tag{2}$$

Considering sinusoidal scenarios, Ohm's law can be applied to estimate the impedance of the simple circuit

$$|Z_{damper}| = \sqrt{R^2 + (2\pi f L)^2} \tag{3}$$

Moreover, provided that the geometry of the solenoid and the number of wire turns of the coil are known, the actuator's magnetisation characteristics can be obtained

$$B = \frac{\lambda}{NA} \tag{4}$$

$$H = \frac{Ni_{coil}}{l} \tag{5}$$

where N – wire turns number, A – cross-section area of the surface that the magnetic flux passes through, l – magnetic path length. The obtained magnetization curve is an estimation – the approach assumes no magnetic flux leakage.

2.1 Experimental Setup

To accomplish the measurements, a data acquisition system was setup. The Speedgoat real-time target machine (Performance version) handles the measurements and commands outputs, the programmable power driver receives the commands from the Speedgoat machine and provides the MR damper with the required voltage, the current is sensed with a Fluke i30 current clamp, which is then measured by the Speedgoat machine. The object of interest was a commercial automotive MR damper with a dual coil valve. In the control valve the coils are wound in series, therefore, the equations (1)–(3) remain true for this damper. The damper was connected to the power supply, and was subjected to a sinusoidal voltage excitation input within the frequency range from 1–25 Hz in 1 Hz increments, and while in the frequency range from 25–50 Hz in 5 Hz steps, and from 50–100 Hz in 10 Hz. During the tests the amplitude varied 0.5 V to 4.5 V at 0.5 V increments. The measurements were sampled at 10 kHz, and filtering was applied offline to remove the measurement noise. The results are displayed in **Figures 3–6**.

3 Results

As already mentioned, the experiments were performed by exciting a stationary damper with known electrical inputs. The results are displayed in **Figures 3–6**. **Figure 3** shows that the damper's impedance increases inline with the increasing frequency. This brings a very practical issue causing i_{coil} to decrease as the frequency increases, for instance, for $v_{coil} = 4.5$ V i_{coil} at 5 Hz is more than 4 times higher than when excited at 100 Hz. The damping force provided by the damper is directly related to the magnetic field density, which is directly related to i_{coil}, therefore, if the damper is subjected to a road profile with a wide bandwidth input, it would have a significantly worse performance for higher frequencies if only the voltage applied to the coil was considered. Hence, various (flux or current) control strategies are usually employed in MR applications.

By decomposing the impedance into the resistance R and the inductance L, **Figure 4** is obtained. As expected, the resistance component increases while the inductance decreases at higher frequencies. This occurs because as the frequency increases the nonlinearities of the magnetic circuit become more apparent. It is known that the the eddy-current related losses tend to scale proportionally to $\sqrt{f}$ [4] which is especially problematic for MR dampers due to the fact that a non-laminated ferromagnetic core is usually used, making the management of eddy currents a major issue. The magnetic hysteresis is also affected by the rise in the frequency f since the magnetic domains have to change direction more frequently, even before reaching saturation; these micro effects cause losses that depending on the model are mapped to eddy-current losses, excessive losses, or anomalous losses [4]. Moreover, as a consequence of the direct relationship between inductance and the magnetic flux linkage, we also observe a reduction in the magnetic flux density in the damper, and as a result in the damping force as well.

Solving (2) for λ the impact of the frequency on the magnetic flux can be assessed. Based on the measurements of v_{coil}, R, and i_{coil}, λ can deduced in a straightforward manner. **Figure 5** displays the variation of λ for $v_{coil} = 4.5\sin(2\pi ft)$ V. The negative impact of the frequency on

 DOI: 10.30420/456743020

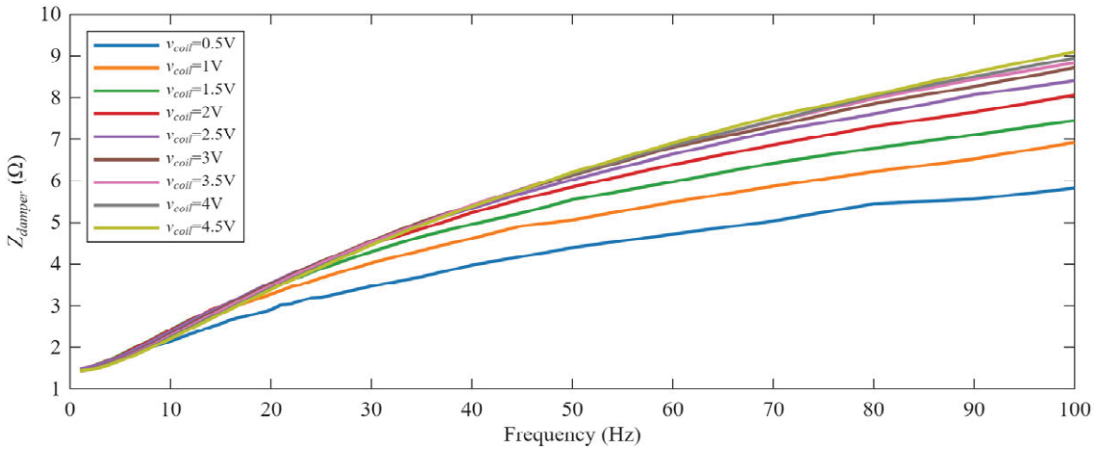


Figure 3 MR damper impedance variation with the voltage v_{coil} over the frequency range 1–100 Hz

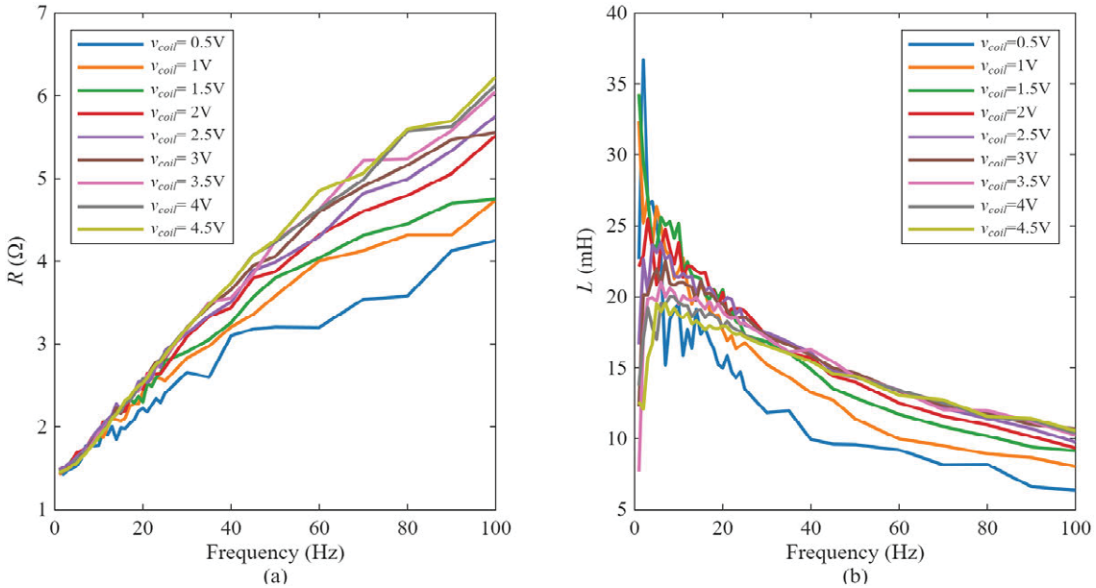


Figure 4 MR damper impedance breakdown over the frequency range 1–100 Hz: a) Resistance, b) Inductance

the damper's performance is even more evident in the illustration. The loop area decreases harshly as the frequency increases, showing how the magnetic flux drastically reduces as the frequency increases for the same voltage input, reinforcing how much performance is left at the table if an appropriate current control strategy is not used.

With λ available and with the knowledge of the damper's valve geometry and including the number of turns in the winding, the core's magnetization curve of can be deduced. The results are shown in **Figure 5**. The magnetization curve is a crucial characteristics that can be employed in the development of more effective controllers. First, due to the direct relationship between the flux density B and damping force. Second, it allows to model the nonlinearities of the magnetic circuit, e.g., hysteresis, which is needed both for design and control purposes. Although this curve is just an estimation, it provides satisfactory data for modeling the electromagnetic circuit, especially once we consider that it was obtained via simple black-box measurements. And it is known that manufacturing processes can cause significant variations in the magnetic properties of ferromagnetic materials, up to 30% in power loss [5]. Therefore, even the magnetization curve provided by the manufacturer cannot be completely trusted as they might have a significant error margin from batch to batch or even sample to sample.

4 Conclusion

In this work, the results of an electromagnetic characterization study of a commercial MR damper were presented. The procedure can be easily replicated with any other MR dampers. The results can be used, e.g. in the development of a math model of the damper's EM circuit as well as prototyping control schemes. It is also clear that any open loop strategy would be ineffective. Therefore, not surprisingly, at least a current control strategy should be employed in MR damper applications for handling different road sce-

 DOI: 10.30420/456743020

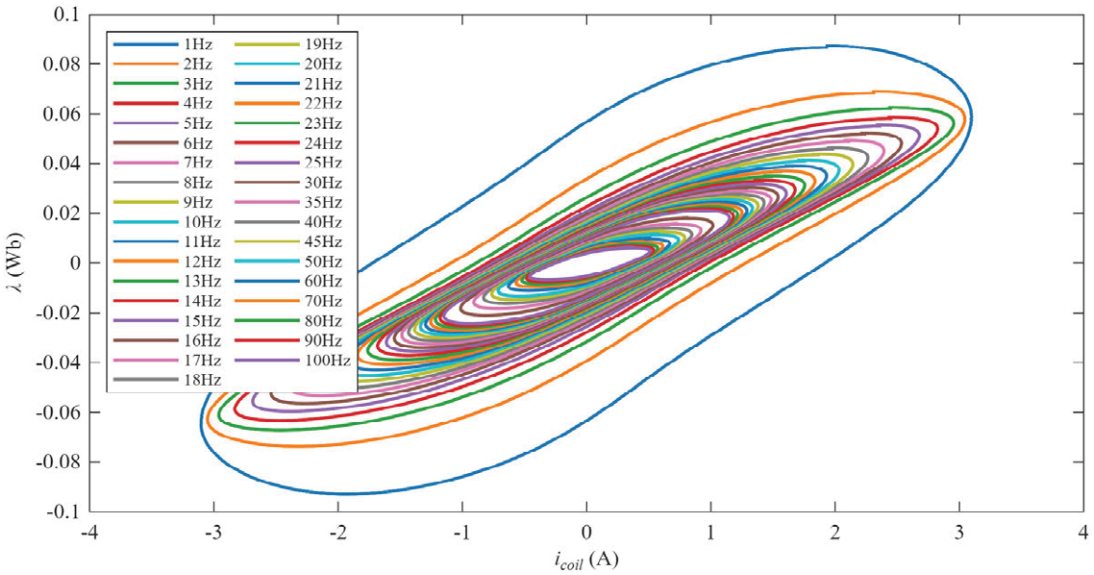


Figure 5 Magnetic flux linkage variation vs i_{coil}; $v_{coil} = 4.5$ V and $f = \{1 \ldots 100$ Hz.

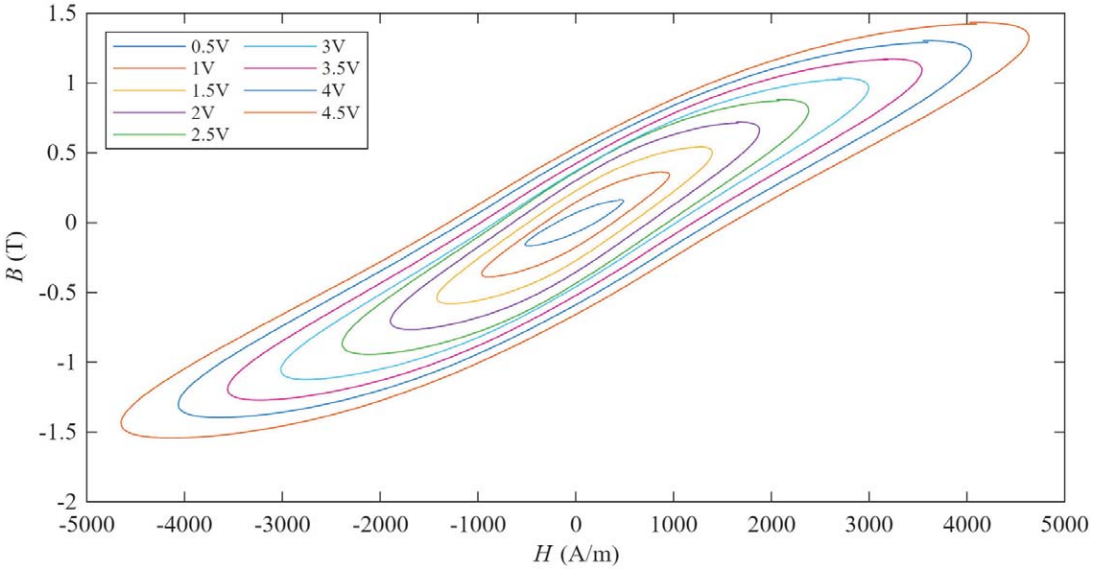


Figure 6 Magnetization curve of the magnetic core, $f = 5$ Hz.

narios and ride conditions. As continuation of this work, the author plans to develop an electromagnetic model of the damper (or control valve) to include both magnetic hysteresis and eddy currents effects used in the development of a model based control strategy, thus allowing for a robust controller driven by voltage and current measurements.

5 Literature

[1] J. Rabinov, “The magnetic field clutch,” AIEE Trans., vol. 67, pp. 1308– 1315, 1948.

[2] J. de Vicente, D. J. Klingenberg, and R. Hidalgo-Alvarez, “Magnetorheological fluids: a review,” Soft Matter, vol. 7, no. 8, p. 3701, 2011.

[3] Gołdasz J, Sapinski B, Jastrzębski Ł and Kubik M, “Dual Hysteresis Model of MR Dampers”, Front. Mater. vol 7, no. 236, 2020

[4] G. Bertotti, "General properties of power losses in soft ferromagnetic materials," IEEE Transactions on Magnetics, vol. 24, no. 1, pp. 621-630, Jan. 1988.

[5] K. Bourchas et al., "Quantifying Effects of Cutting and Welding on Magnetic Properties of Electrical Steels," in IEEE Transactions on Industry Applications, vol. 53, no. 5, pp. 4269-4278, Sept.-Oct. 2017.

 DOI: 10.30420/456743021

Piezo Actuated jet for stealth aircraft applications

D. Ferris (1), G. Mansuy (1), A. Barnique (1), G. Aigouy (1), E. Eglinger (2), J. Delva (2), F. Ternoy (2), J. Roháč (3)
(1) Cedrat Technologies SAS, Meylan, France,
(2) ONERA Lille, France
(3) ESC Defence, Čs. armády 14, 160 00 Prague, Czech Republic, jan.rohac@evolvsys.cz

Abstract

FACELIFT is a European Defense Funded project (101102557) to improve stealthiness and maneuverability compared to the current generation of military assets such as the European MALE-RPAS. This project proposes the use of fluidic actuators to reattach the flow with higher angle of aileron deflection. Sweeping jets and Synthetic jet actuators are assessed, first in wind tunnels, then on an aircraft. The piezoelectric Synthetic Jet Actuator (SJA) designed and chosen for this project reached a piston stroke of 2mm at 235Hz, creating a jet speed over 200m/s. Wind tunnel assessment showed that for a flow velocity of 30 m/s and aileron angle of 20°, the SJA can fully reattach the flow on the aileron. This SJA system will be tested in aircraft in flight conditions.
The FACELIFT consortium consists of 4 partners: Cedrat Technologies, Berliner Institut für Technologietransfer, ESC DEFENCE and ONERA. Moreover, Pipistrel Vertical Solutions has been chosen as aircraft manufacturer for this project.

1 Introduction & Design process

1.1 FACELIFT Challenge & state of the art

The FACELIFT (Fluidic Actuators for Control of stEaLth aIrcraFT) which is a European Defense Funded project (101102557) aims to improve strategic surveillance capability, survivability and operational resilience for future stealth aircraft, which will be more stealthy and more maneuverable than the current generation of military assets such as the European MALE-RPAS.
To overcome design conflicts between stealthiness and maneuverability of military aircraft, FACELIFT proposes the use of control flow actuators (CFA). Thereby, smaller stabilization and control surfaces can be used for an equal or better performance in terms of maneuverability. Two types of actuators are considered: Sweeping Jets and Synthetic Jets based on piezo actuators. It is expected that the implementation of closed loop-controlled CFA will deliver a 50% decrease of the Radar Cross Section (RCS) originating from a control surface for the same maneuverability by area reduction.
The FACELIFT consortium consists of 4 partners: Cedrat Technologies (CTEC), Berliner Institut für Technologietransfer (BIT), ESC DEFENCE (ESC) and ONERA. Moreover, Pipistrel Vertical Solutions (PVS) has been chosen as aircraft manufacturer for this project. The key technical challenge is to optimize aircraft aerodynamics, particularly by addressing boundary layer separation at the control surfaces.
This project is built on previous work conducted in the ASPIC and Synjet3C projects and a long collaboration between ONERA and CTEC [1-4]. It aims to demonstrate the effectiveness of an onboard Synthetic Jet Actuator (SJA) in aircraft under flight conditions. CTEC is adopting the approach developed in Synjet3C, prioritizing performance and compactness to meet the project's requirements.

1.2 Technical objectives of the SJA

The current state of the art highlights the promising performance of SJA, but also underscores their current limitations: thermal constraints, a wide range of resonance frequencies, challenges in miniaturization, and limited understanding of their dynamic behavior in embedded systems. These challenges apply to both the generation of high-speed jets and their mechanical and electronic integration into compact aerospace architecture.

The function of the SJA is to keep the airflow over the control surfaces attached up to high deflection angles of the control surface by blowing over them. To optimize the gain of this phenomenon, it is important to control the amount of airflow being provided by the fluidic actuator with a closed-loop system.
The expected aerodynamic performance (peak velocity, frequency) is defined by ONERA for both ground and flight assessments. The integration constraints for wind tunnel assessments as well as flight assessments are provided by PVS (available volume, shape constraints, maximum weight) and CTEC (characteristics of power supply, interfaces).

The main objective is to maximize the momentum coefficient defined below:

$$c_\mu \approx \frac{\rho_j S_j \langle U_j^2 \rangle}{(1/2)\rho_\infty U_\infty^2 S_{\text{ref}}}$$

where ρj is the jet density, Sj the orifice area, $\langle Uj^2 \rangle$ the quadratic mean of the jet velocity, ρ_∞ the ambient air density, U_∞ the incoming air speed and S_{ref} the projected wind area over the span of the aileron or rudder.
To maximize c_μ, we aim for a peak velocity (Uj)max as close as possible to the speed of sound. The peak velocity being fixed, the slot area is computed from the $c\mu$ and

 DOI: 10.30420/456743021

should be 77mm². SJA will blow on the suction side of one wing and on the pressure side of the other.
To avoid thermal degradation of piezo ceramics, the tests in laboratory should last no longer than ~1 min. However, there is no need in the scope of the project for a cooling system either in wind tunnel or in flight since the maneuvers are lasting less than 1 min.
The maximum available volume for equipment (batteries excluded) is 0.2m^3.

To perform the dynamic actuation, the concept of APA® Amplified Piezoelectric Actuators from CEDRAT TECHNOLOGIES [5,6] has been selected. This technology inherits space qualification and flights [7-9] and has been used for several control flow actuators, either flaps, pulse jet or synthetic jet actuators for aircraft [4,10-14].
A first draft of the APA® inside the SJA that could fit the expected performance is shown in Figure 1. According to preliminary computation, to reach those performances, two APA like this one per SJA should be used. The combined actuators generate more than 800µm of stroke with 6 ceramics (10x10x20mm) for a total capacitance of 26.5µF.

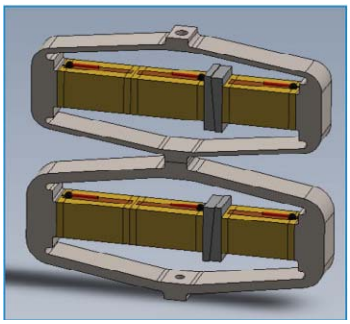


Figure 1 APA® design

For such an actuator, with about 150V pk-pk at a frequency of 300 Hz, a 6A 0-pk consumption is expected. As two aileron actuators are needed for one SJA, one SJA would need up to 12 A. Maximal driving Pk-Pk voltage may be a matter of further modification based on the conditions learnt in the wind tunnel experiments.

1.3 Design trade-off

CTEC and ONERA worked on the design of the SJA to be integrated into the airfoil structure based on the specifications defined. The SJA design shall be based on CTEC APA® amplified piezoelectric actuators and shall include position sensors, to be used for both characterization tests and health monitoring. In this design phase, two configurations were analyzed:

- Rotary RJA
- Linear SJA

The SJA has been designed so that the available force and displacement allow the compression of the air in the cavity with the piston up to sonic conditions. The amplification of displacement between the APA® and the piston is done by a pivot linkage.

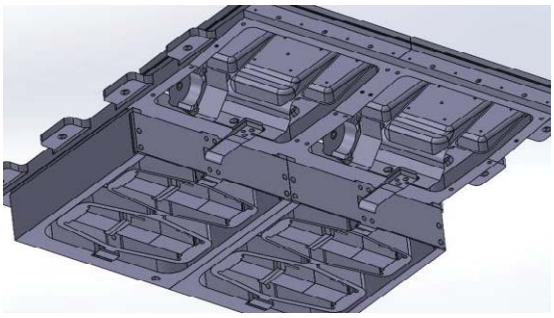


Figure 2 Rotary SJA design

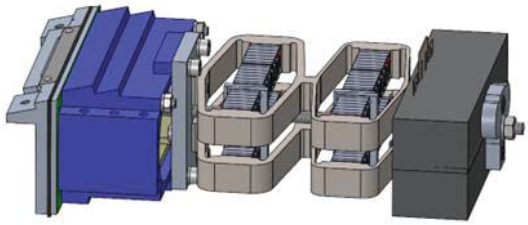


Figure 3 Linear SJA design

A piston is activated by 2 APA®. The displacement is amplified more than 2 times by another amplification mechanism. The air inside the chamber is expelled through a slot. A health monitoring sensor based on CTEC ECS measures the displacement of the piston to check that the rms stroke or peak-peak stroke stay at the desired level

The two configurations have been manufactured and tested in laboratory conditions. The performances are summarized in the table below.

Heading	Rotary SJA	Linear SJA
Pressure reached (bar)	1.4	1.55
Voltage (V pk-pk)	160	170
Frequency (Hz)	400	225

Table 1 Rotary vs linear SJA Perfo using same APAs

The linear SJA performs slightly better, is more reliable and has less power consumption, so this solution was chosen for the rest of the project.

2 Laboratory assessments

2.1 Prototypes tests

Several tests were performed on the linear SJA, to find the best operating point. The breadboard is tested at 170V and at the optimized 225Hz frequency.

 DOI: 10.30420/456743021

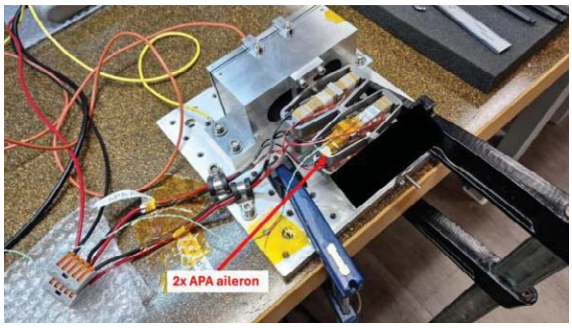


Figure 4 Laboratory test of SJA prototype

The maximum relative pressure amplitude is 0.86bar.

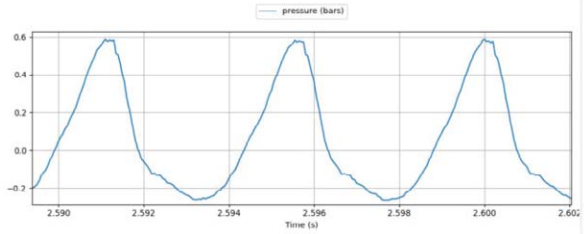


Figure 5 Overview of several pressure cycles

The table hereafter summarizes the performances of the linear SJA prototype:

	225 Hz; 170 Vpp ; 0.3x38 mm
APA Stroke pk-pk	890 µm
Piston Stroke pk-pk	1575 µm
Current 0-pk	12 A
Max absolute pressure	1.6 bar
Min absolute pressure	0.74 bar
Active power	136 W

Table 2 Linear SJA performance

ONERA performed a preliminary test to measure the air velocity at the slot exit. The SJA is mounted on an optical table, which serves to hold it in place and to mitigate vibrational phenomena. The air velocity is measured using a hot-wire anemometer.
This hot-wire is placed on a positioning system composed of a manual micrometer displacement table, topped with a camera for positioning the hot-wire relative to the slot.
The actuator is powered by the ESC driving unit, which is controlled by the SJA DRIVER GUI allowing for the management of frequency and voltage value (amplitude and offset).
The estimated peak velocity at 150V pk-pk reaches 195m/s for a maximum differential pressure (relative to ambient) evaluated at P = 0.48 bar. The visible suction phases are difficult to quantify because the hot-wire does not provide the direction of the flow.
This performance is achieved thanks to the second stage of mechanical amplification integrated into the SJA, which doubles the actuator stroke at resonance.

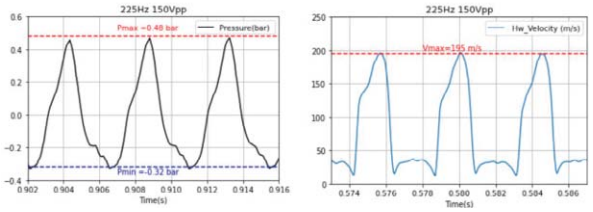


Figure 6 Generated pressure & air velocity @150V pk-pk

The second test at 170V pk-pk with greater oscillation amplitude reaches a maximum velocity of 211m/s for a maximal differential pressure of 0.58bar.

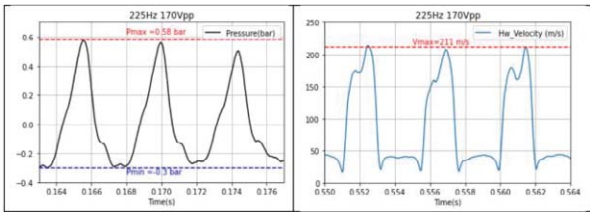


Figure 7 Generated pressure & air velocity @170Vpk-pk

2.2 Wingtip integration

A total of 7 SJA are installed in each wingtip. There is a strict mass constraint: the combined weight of all SJA within a single wingtip must not exceed 6.3 kg, which corresponds to a maximum of 900 g per unit.

There are 4 compartments in the wingtip: 3 slots for 2 SJA and 1 slot for 1 SJA. The wingtip will have a big opening to install the SJA. It will be closed partially by the SJA itself and partially with a lid.

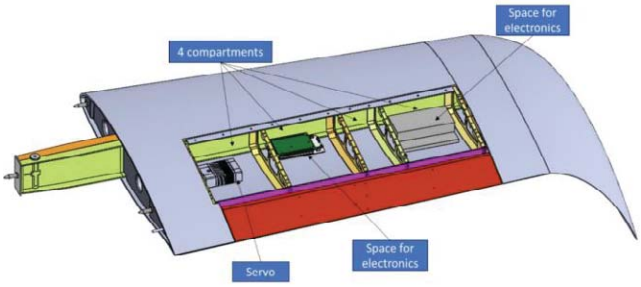


Figure 8 RHS Wingtip view

The 7 position sensors (health monitoring sensors) are routed through the openings in the ribs and connected to the 2 conditioners. These are Eddy Current sensors (ECS) developed and integrated by Cedrat Technologies into the SJA systems (see Figure 9)

 DOI: 10.30420/456743021

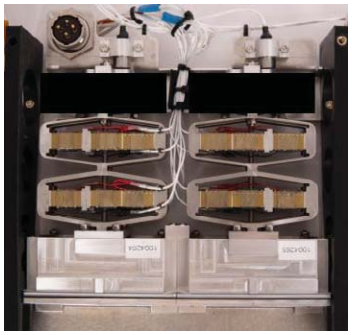


Figure 9 RHS Wingtip view

The SJA power, temperature sensors and pressure sensors are connected to the harness in the wingtip.

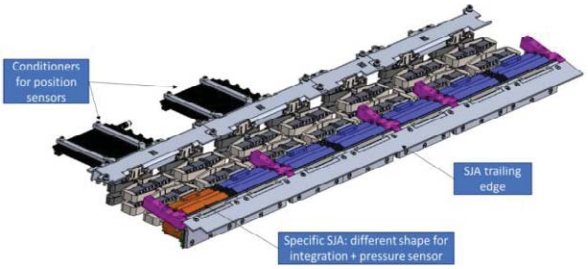


Figure 10 Full pre-assembly of 7 SJA

2.3 Functional test

The SJA for wind tunnels have been manufactured and all included sensors have been assembled.
Different tests have been performed at Cedrat Technologies to validate the SJA for the FACELIFT project:

- Quasistatic test: to verify that nothing reduces the piston stroke beyond normal.
- Operating frequency search: frequency sweeps to find the range with the maximum pressure where the stroke is not beyond the APA limit.
- Performance assessment at optimal frequency: to measure the main performances at full voltage (stroke, pressure, current, active power).



Figure 11 All SJA assembled

As shown in figure 6, the best operating frequency is 235Hz. It is not advised to actuate at 170Vpp below 235Hz because it could damage the SJAs. Actuate above 235Hz is possible but the pressure will be reduced, and the current will increase.

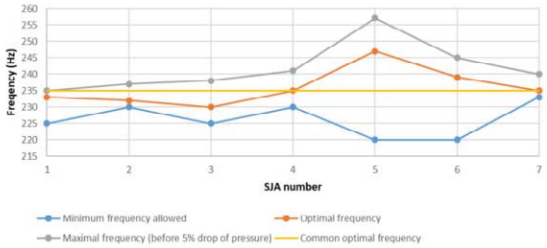


Figure 12 Optimal frequency search for each SJA

2.4 Wind tunnel tests

The objectives of the wind tunnel campaign were:

- To measure the performance of synthetic jets to control the flow separation in an open and closed-loop manner on the upper side of the aileron.
- To gather aerodynamic data to identify an aerodynamic reduced-order model of a wing equipped with active flow where this reduced-order model will be used in the design loop of an aircraft equipped with flow control actuators.
- To test the electronics and actuators before going to flight tests.

The following figure shows a picture of the model mounted vertically in the L1 test section. The closed-loop wind tunnel test section has a diameter of 2.4 m and is operated at speeds ranging between 15 and 68 m/s (Mach number from 0.04 to 0.2) for this experiment.



Figure 13 Model view in ONERA L1 wind tunnel

The results of the wind tunnel tests demonstrated that SJA actuation increased the lift even with high aileron angle. Figure 15 shows the lift increase versus aileron angle for several scenarios of angles of attack and flow velocities.

 DOI: 10.30420/456743021

$$\Delta CL = \frac{CL_{with\ control\ (\delta)} - CL_{without\ control\ (\delta)}}{CL_{with\ control\ (\delta)}}$$

where δ is the deflection angle.

This improvement is very good up to an angle of 20°, then the SJA reattach less the air flow on the aileron.

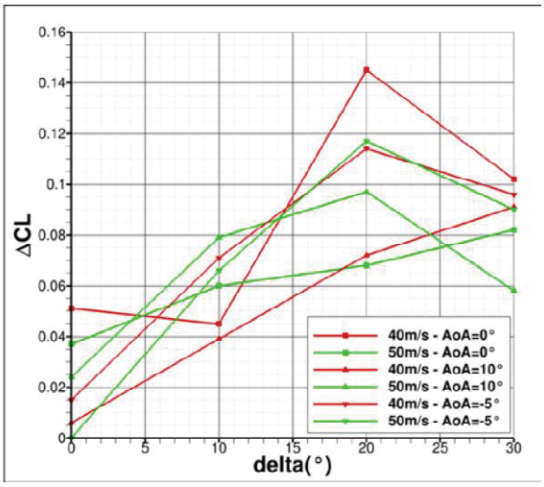


Figure 14 Lift coefficient versus aileron angle

The closed loop control was able to reduce the actuation voltage to the minimum necessary to reattach the airflow on the aileron.

3 Flight tests

The SJA has been designed to be integrated into a Pipistrel aircraft retrofitted to accommodate the project specifics needs. The flight tests planned at the end of the project (July 2026) will demonstrate performance in a real environment.
The figure 15 shows the aircraft retrofitted for this project.



Figure 15 Aircraft used for SJA flight tests

4 Acknowledgment

The project FACELIFT is funded by the EU under the Grant Agreement number: 101102557 – FACELIFT

5 Conclusion

In the framework of UE FACELIFT project, a new piezoelectric Synthetic Jet Actuator (SJA) has been designed and tested. It reaches a piston stroke of 2mm at 235Hz, creating a jet speed over 200m/s. Wind tunnel assessment showed that for a flow velocity of 30 m/s and aileron angle of 20°, the SJA can fully reattach the flow on the aileron. This SJA system will be tested in summer 2026 in a Pipistrel aircraft in flight conditions.

6 Literature

[1] F. Ternoy, Improvement of Synthetic Jet Actuator Technology for High Efficiency, Proc. Actuator 2022, Ed Messe Bremen, June 2022.
[2] F. Ternoy, Overview of ONERA Fluidic Actuators in Aerodynamics, Journal Aerospace Lab, Issue 6 - June 2013
[3] E. Eglinger, High performance Synthetic Jet Actuator for Aerodynamic Flow Improvement Over Airplane Wings, Proc. Actuator 2018, Ed Messe Bremen, June 2018
[4] G. Jaussaud, Ongoing progress in flow control actuators and required drive electronics, Proc. AEC Bordeaux 25-28 February 2020
[5] R. Leletty, A New Amplified Piezoelectric Actuator for Precise Positioning and Active Damping, Proc SPIE, Smart Systems and Mat., San Diego Ca, March 1996.
[6] APA® Amplified piezo actuator, Registered trademark of Cedrat Technologies, https://cedrat-technologies.com/categorie-produit/amplified-piezo-actuator-piezo-actuators/
[7] P. Guay, Piezo Qualification for Space Applications, Proc Actuator 2002, Ed. Messe Bremen, B3.2, pp.284-287
[8] C. Allegranza, Actuators for Space Applications: State of the Art and New Technologies, ACTUATOR Conf, Review paper, Bremen (DE), 2014
[9] https://cedrat-technologies.com/wp-content/uploads/downloads/aerospace_heritage.pdf
[10] P. Leconte, Experimental assessment and further development of amplified piezo actuators for active flap device, Proc. Conf Actuator 2002
[11] C. Bouchet, Pulsed air high performances valves improve aerodynamic flow over airplane wings, N°B6.2 p259, Proc. Conf Actuator 2016
[12] G.Aigouy, ASPIC High Power Synthetic Jet Actuator, Proc Conf ACTUATOR 2020, 16-18 june 2020
[13] G.Aigouy, SYNJET3C Improvement of Synthetic Jet Actuator Technology for High Efficiency, Proc ACTUATOR 2022
[14] Y. Schäfer 1, Effects of Tip Injection on a Turbofan Engine with Non-Invasive High-Speed Actuators, Int. J. Turbomach. Propuls. Power 2025, 10, 9

 DOI: 10.30420/456743022

Soft Robotic Artificial Muscles for End-Stage Heart Failure Management

Javad Foroughi[1,2], Arjang Ruhparwar[2]
[1]School of Mechanical and Manufacturing Engineering, University of New South Wales, Sydney, NSW, 2052, Australia
[2]Department of Cardiothoracic Transplantation and Vascular Surgery Hannover Medical School
Carl-Neuberg-Str., 130625 Hannover, Germany
J.foroughi@unsw.edu.au, Ruhparwar.Arjang@mh-hannover.de

Abstract: The development of artificial muscles using carbon nanotubes and polymer fibers has enabled new opportunities for next-generation ventricular assist devices (VADs). In this study, we present a novel soft robotic heart sleeve composed of electrothermally driven, polymer-based artificial muscles designed to augment cardiac function externally without direct blood contact. This implantable device addresses major limitations of conventional VADs including thrombogenicity, lack of pulsatility, and bulkiness while eliminating the need for long-term anticoagulation therapy. The silicone-coated artificial muscles can generate pressures up to 120 mm Hg and operate at 1.4 Hz (84 bpm), with adjustable frequency to meet physiological demands. Powered by a low-voltage system compatible with portable batteries, the device significantly reduces the size and weight of the power system. This work represents the first demonstration of a soft robotic heart sleeve delivering synchronized, biomimetic contractile forces to support both left and right ventricular functions, offering a safer, compact, and pulsatile alternative for end-stage heart failure treatment.

Introduction:
Heart failure (HF) is a major global health burden, affecting over 41 million people worldwide.[1–4] VADs offer a promising solution for patients with end-stage HF. However, existing VAD systems often lead to serious complications, including aortic valve regurgitation and bleeding (Fig. 1a), primarily due to their direct contact with blood and the need for lifelong anticoagulation therapy. To overcome these challenges, non-blood-contact VADs have emerged as a transformative approach, reducing anticoagulation dependency and associated risks.[1]
The ideal VAD should preserve physiological pulsatile flow, avoid blood contact, and eliminate anticoagulant use goals that require breakthroughs in miniaturization, complete implantation, and pulsation modulation. Soft robotics offers a promising platform to meet these requirements, with the ability to interface delicately with biological systems. This project aims to develop and validate artificial muscle-based soft robotic VADs, leveraging advanced materials and engineering to redefine treatment strategies for heart failure.[1] Recent progress in artificial muscle technology [5–8] particularly carbon nanotube and polymer fiber-based actuators has opened new directions in medical device development, especially in cardiomyoplasty and VADs. Despite promising results, significant hurdles remain, including actuator miniaturization, long-term biocompatibility, mechanical durability, and power efficiency. This study directly addresses these challenges by designing a novel soft robotic VAD: an implantable sleeve driven by electrically actuated polymer muscles.

Results and Discussion:
We successfully developed and demonstrated a prototype soft robotic VAD powered by electrothermally driven twisted and coiled polymer fiber artificial muscles (Fig. 1b-c). The device is designed to assist cardiac contraction externally, without blood contact, thereby mitigating the risks associated with thrombosis and anticoagulation.
The silicone-coated artificial muscles generated peak pressures of up to 120 mm Hg, sufficient to support left ventricular function. The system operates at 1.4 Hz (84 bpm) closely mimicking the physiological heart rate with the ability to modulate frequency in response to changing circulatory demands. The device is powered by a clean, low-voltage electrical system (32.5 V), which is compatible with compact batteries and control units, significantly reducing the overall system footprint compared to conventional VADs.
This work marks the first successful demonstration of a soft robotic heart sleeve capable of delivering synchronized, biomimetic contractile forces to support both left and right ventricular functions. The innovation presents a promising alternative to mechanical circulatory support systems by offering enhanced safety, reduced size, physiologic pulsatility, and long-term durability. Ultimately, this technology holds significant potential to transform the treatment landscape for end-stage heart failure, improving both clinical outcomes and patient quality of life.

Acknowledgements:
The authors acknowledge financial support from the NSW Cardiovascular Early–Mid Career and Senior Researcher Grants, as well as the Department of Cardiothoracic, Transplantation, and Vascular Surgery at Hannover Medical School.

 DOI: 10.30420/456743022

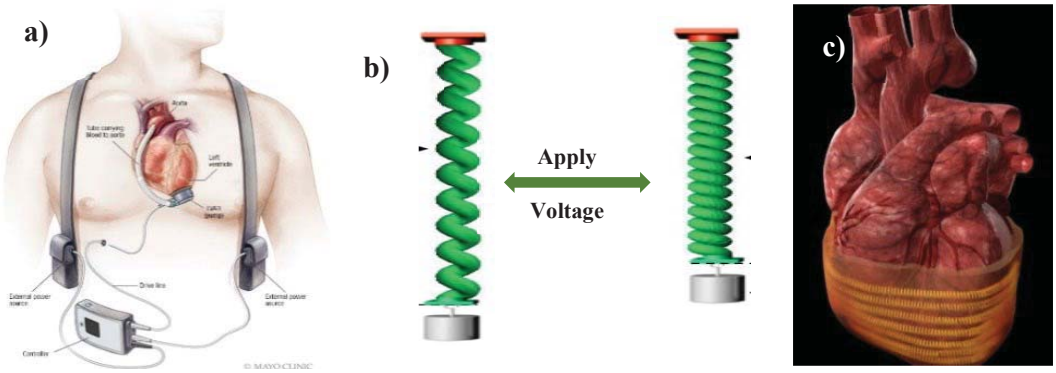


Figure 1: a) Illustration of a traditional left ventricular assist device (LVAD), b) Artificial muscles shown before and after actuation, and c) Proposed schematic of the heart sleeve concept, wrapped around the heart to avoid direct blood contact.

References:

1. Weymann, A., Foroughi, J., Spinks G., Aloko, S., Wang C. H., Ruhparwar, A., *et al., "Artificial Muscles and Soft Robotic Devices for Treatment of End-Stage Heart Failure"*. Adv. Mater. (2023).
2. Kongahage, D., Ruhparwar, A., Foroughi, J., *"High Performance Artificial Muscles to Engineer a Ventricular Cardiac Assist Device and Future Perspectives of a Cardiac Sleeve"*, Adv. Mater. Technol. 2021.
3. Ruhparwar, A., Foroughi J., Karck, M., Spinks, M.G., Kim S.J., *"Electrically contractile polymers augment right-ventricular function in the heart"*, Artificial Organs, 2014 ,38 (12).
4. Ruhparwar, A., Foroughi, J.; *et al., "Soft Robotic Dynamic Cardiomyoplasty with Electrically Contractile Artificial Muscle (AHM)"*, The Journal of Heart and Lung Transplantation, 2022. 4: p. S103.
5. Foroughi, J., et al., *"Torsional Carbon Nanotube Artificial Muscles"*, Science 334,494-497(2011)
6. Haines, C., Foroughi, J., *et al., "Artificial Muscles from Fishing Line and Sewing Thread"*, Science, 343, 868–872 (2014).
7. Mu J., Foroughi, J., *et al., "Sheath-run artificial muscles"*, Science 365,150-155(2019)
8. Chun, H., Foroughi, J., *et al., "Unipolar stroke, electroosmotic pump carbon nanotube yarn muscles"*, Science 371,494-498(2021)

ISBN: 978-3-8007-6743-4 @ VDE VERLAG GMBH · Berlin · Offenbach

 DOI: 10.30420/456743023

Antagonistic Bistable Actuator Based on Shape Memory Alloy Beams

Yasmina Frey, Zeliha Arabul, Ulrike Wallrabe, Albert-Ludwigs-Universität Freiburg, Freiburg, Germany
yasmina.frey@imtek.uni-freiburg.de, z.s.arabul@outlook.de, wallrabe@imtek.uni-freiburg.de

Abstract

This work presents the development of a compact bistable actuator based on two antagonistically arranged Nitinol shape memory alloy beams. The actuator is designed for reversible out-of-plane displacement with low energy consumption, requiring electrical power only during switching. The operating principle is based on thermally induced shape recovery of one beam, which forces the opposing beam into elastic deformation and triggers snap-through between two stable states.

Finite-element simulations were used to analyse the mechanical behaviour and to optimise the stiffness distribution of the coupled beam system. A symmetric beam configuration showed excessive structural stiffness and did not exhibit bistable switching. The geometry was therefore modified by introducing variable-width beam geometry and adapted curvature radii to homogenise the stress distribution and enable snap-through behaviour.

The optimised actuator demonstrates reproducible bistable operation with measured displacements of +3.2 mm and −3.1 mm and weighs 150 mg. Under external loading, the displacement decreases to approximately 2 mm for a mass of 1 g. The consumed energy per switching cycle is 8.4 J.

1 State of the Art

Shape memory alloy (SMA) actuators are widely used in microactuation due to their high energy density and scalability [1]. Recent developments focus on bistable concepts that maintain two stable equilibrium states without a continuous power supply [2]. In such systems, electrical energy is required only during switching, enabling energy-efficient operation [3].

Bistability in SMA actuators is commonly achieved by antagonistic coupling of two active elements [4]. When one element is activated and recovers its programmed austenitic shape, it forces the opposing element into elastic deformation. If the stored elastic energy exceeds a critical threshold, a snap-through transition between two stable equilibrium states occurs [5]. Recent work increasingly employs finite-element analysis to design such coupled beam structures and to identify reliable bistable switching [6].

2 Operating Principle

The actuator is based on two oppositely curved shape memory alloy beams arranged in an antagonistic configuration. Both beams are coupled at their apex and clamped at their outer ends. When one beam is heated above its transformation temperature, it recovers its programmed austenitic shape due to the shape memory effect [7]. This recovery motion forces the opposing beam into elastic deformation. If the stored elastic energy exceeds a critical threshold, the coupled system undergoes a snap-through transition into a second stable equilibrium.

This bistable behaviour allows switching between two positions without a continuous power supply, i.e. energy is required only during transitions between stable states. The thermal activation is achieved via Joule heating. Copper rivets provide both electrical contact and mechanical fixation.

3 Actuator design and fabrication

The actuator consists of two laser-cut Nitinol beams (provided by memetic GmbH, Karlsruhe, Germany), each 0.1 mm thick. A central hole at the apex of each curved section enables mechanical coupling of both beams with a copper rivet (**Figure 1A**). The outer beam ends are riveted to a ring-shaped printed circuit board (PCB), providing defined clamping conditions. The copper rivets serve both as mechanical fixation and as electrical contacts.

For shape setting, the beams are fixed in a brass mould defining the austenitic geometry (**Figure 1B**). The moulded beams are heat-treated at 500 °C for 5 min and subsequently quenched.

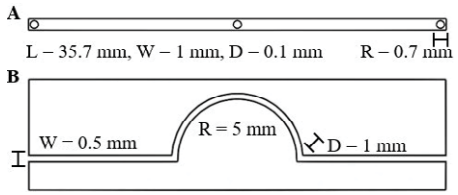


Figure 1 (**A**) Laser-cut SMA beam with contact and coupling openings for rivets. (**B**) Top view of the brass mould used for shape setting.

4 Symmetrical beam configuration

The base configuration consisted of two geometrically identical beams connected and fixed as explained before, with a central curved actuation zone and straight lateral segments (**Figure 2**).

To analyse the switching behaviour of this symmetric configuration, finite-element simulations were performed considering thermo-mechanical coupling, including Joule heating.

ISBN: 978-3-8007-6743-4 @ VDE VERLAG GMBH · Berlin · Offenbach

 DOI: 10.30420/456743023

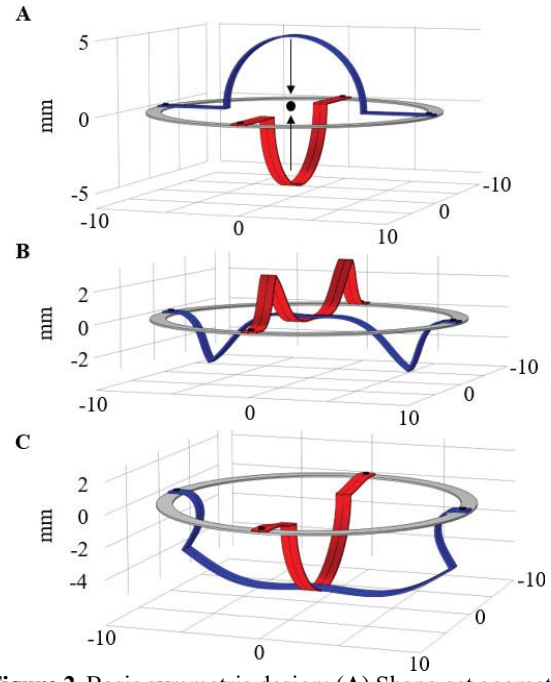


Figure 2 Basic symmetric design: (**A**) Shape-set geometry of the downward actuator (red) and the upward actuator (blue) before the mechanical connection at their apex points. Base segments are riveted to a PCB ring (grey). (**B**) Both actuators are connected at the apex, defining the neutral point. (**C**) Expected deformation when the downward actuator (red) is activated, inducing passive bending of the opposing beam (blue).

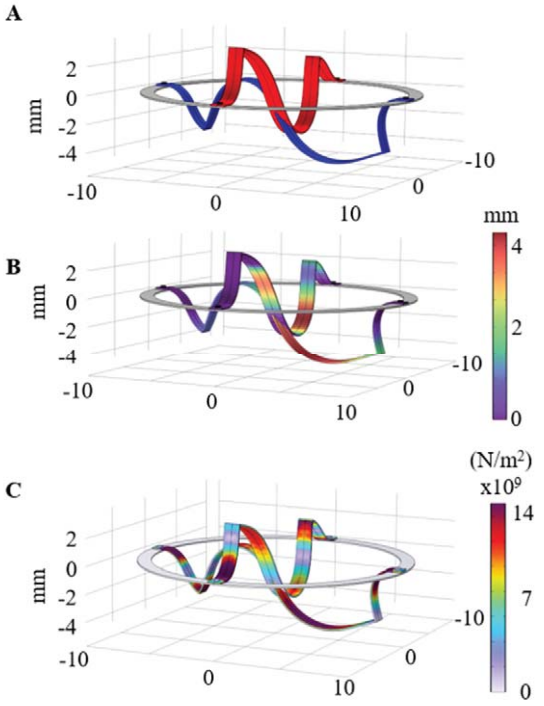


Figure 3 FEM simulation of actuation: (**A**) Colour code for comparison, (**B**) Simulated deflection of downward-actuated beam (red) at A_f = 85 °C. (**C**) Van Mises stress during actuation.

The simulation (**Figure 3**) showed that activation of one beam induced elastic bending of the opposing beam. However, the deformation of the curved actuator zone was limited, and the system remained monostable.
The von Mises stress distribution revealed pronounced stress concentrations at the transitions between curved and straight segments. The resulting inhomogeneous stress distribution thus limited the global out-of-plane motion and prevented the formation of a second stable equilibrium, i.e., no snap-through transition occurred.

5 Variable-width beam geometry

To enable bistable switching, the beam geometry was optimised to homogenise the stiffness within the coupled system. The curvature radius of the central actuator zone was increased from 5 mm to 6 mm. In addition, the beam width was varied along the beam length to balance flexibility and force transmission (**Figure 4**).

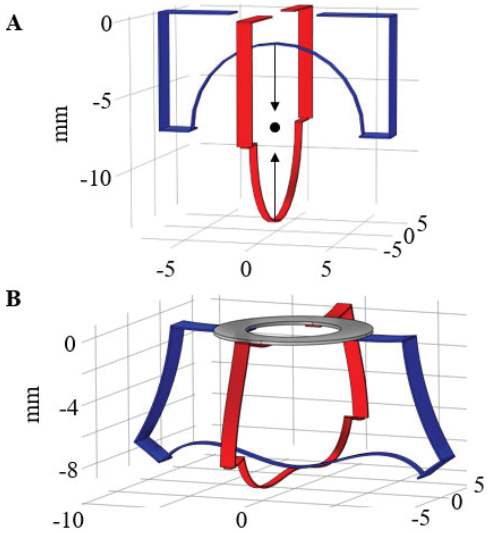


Figure 4 Optimised design incorporating hinges: (**A**) Shape-set geometry of the downward actuator (red) and the upward actuator (blue) before mechanical fixation at their apex. (**B**) Both actuators are connected at the centre of their curvatures (neutral point). Base segments are riveted to a PCB ring (grey).

Furthermore, defined vertical transition segments serving as hinges were introduced between the clamped horizontal part of the beams (Neumann boundary condition) and the curved actuation zone. These hinge segments reduce the stress concentrations and allow for lateral deflection during snap-through.
For this design, Finite Element simulations predicted the desired bistable behaviour with two stable equilibrium states (**Figure 5**).
The von Mises stress distribution appeared significantly more homogeneous compared to the symmetric configuration. Stress concentrations at the transition regions were reduced, as larger beam areas contributed to elastic energy storage (**Figure 6**). This homogenised stress distribution enabled the snap-through transition and sufficiently stabilised both equilibrium states.

ISBN: 978-3-8007-6743-4 @ VDE VERLAG GMBH · Berlin · Offenbach

DOI: 10.30420/456743023

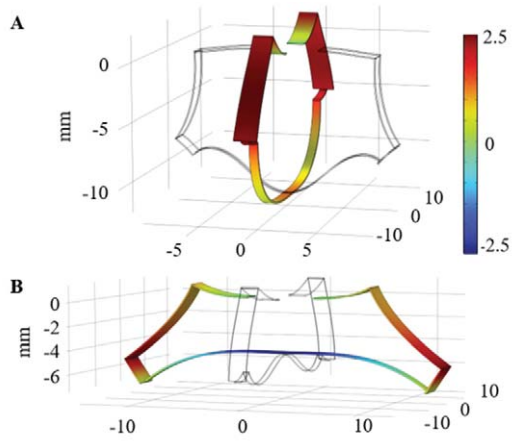


Figure 5 Simulated deflection at A_f = 85 °C. (**A**) downward-actuated beam, (**B**) upward-actuated beam.

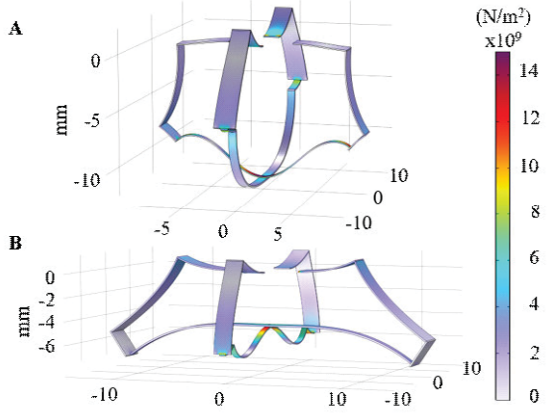


Figure 6 Van Mises stress of optimised design.

6 Experimental results

The fabricated actuator, with a total mass of approximately 150 mg, exhibited reproducible bistable switching via Joule heating at 1.2 A and 7 V, with displacements of +3.2 mm and −3.1 mm relative to the neutral position (**Figure 7**). Switching occurred within less than 1 s, corresponding to an energy consumption of 8.4 J. No continuous power was required to maintain the actuator position.
The unloaded actuator achieved a deflection of more than 6 mm, whereas under external loading up to a mass of 6 g, it decreased monotonically (**Figure 8**). At a load of 1 g, the deflection was already reduced to 1.8 mm. Higher loads suppress the displacement as the external force counteracts the SMA recovery force.

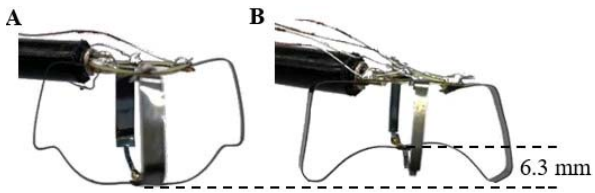


Figure 7 Experimental deflection of (**A**) downward-actuated beam, (**B**) upward-actuated beam.

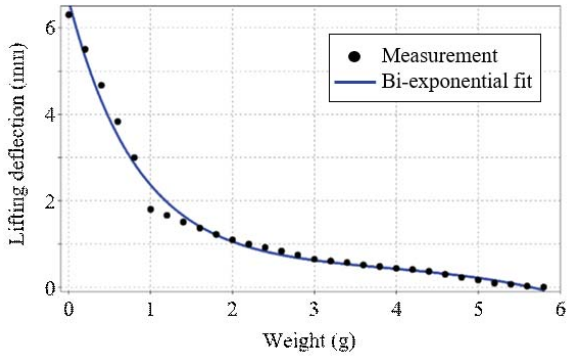


Figure 8 Experimentally determined maximum lifting deflection of the actuator dependent on an external load.

7 Conclusion

A compact bistable actuator based on antagonistic Nitinol beams was developed. An initial symmetric beam configuration exhibited excessive stiffness and remained monostable. By introducing variable-width beam geometries and adapted curvature radii, the stiffness distribution was homogenised, and snap-through behaviour was enabled.
The optimised actuator, having a mass of 150 mg, demonstrated reproducible bistable switching with a total displacement of 6 mm and an energy consumption of 8.4 J per switching event. It is therefore suitable for energy-efficient miniaturised systems. Under a load of 1 g, a displacement of 1.8 mm was maintained.

8 Literature

[1] Wilson, S. A., et al., New materials for micro-scale sensors and actuators: An engineering review, Materials Science and Engineering: R: Reports, 2007, vol. 56, no. 1-6, pp. 1-129.

[2] Shahsavari, Hamid, et al., Finite-Element Analysis of an Antagonistic Bistable Shape Memory Alloy Beam Actuator, Advanced Engineering Materials, 2024, vol. 26, no. 22, 2400969, pp. 1-16.

[3] LI, Haohang, et al., Bistable-shape memory synergy enables self-triggered snap-through with ultrahigh energy density, Advanced Functional Materials, 2026, vol. 36, no. 8, e14272, pp. 1-11.

[4] Arivanandhan, G., et al., Bistable In-Plane Switching by a Ni-Ti-Cu/Si Microactuator. IEEE 23rd International Conference on Solid-State Sensors, Actuators and Microsystems (Transducers), 2025, pp. 829-832.

[5] Chen, Xi, et al. Bistable actuation based on antagonistic buckling SMA beams. Actuators, MDPI, 2023, vol.12, no. 11, 422, pp. 1-18.

[6] Thomas, Sean, et al. Actuation displacement analysis of a self-switching shape memory alloy buckled beam. IEEE 21st International Conference on Electrical Machines and Systems (ICEMS), 2018, pp. 1771-1776.

[7] Lagoudas, D. C., Shape Memory Alloys – Modelling and Engineering Applications., TX, USA: Springer, 2008.

 DOI: 10.30420/456743024

Soft and Monolithic Variable Stiffness Clutches for Serial Elastic Actuators

Johannes Frey[a,b], Mohsen Jafarpour[a], Hugo de Souza Oliveira[b], and Edoardo Milana[a,b]
[a]Department of Microsystems Engineering - IMTEK, University of Freiburg, Germany
[b]Cluster of Excellence livMatS, University of Freiburg, Germany

Abstract

Series Elastic Actuators (SEAs) and Variable Stiffness Actuators (VSAs) are pivotal for safe human-robot interaction and energy efficiency. However, traditional designs often suffer from high mechanical complexity and a large number of components. This work introduces a monolithic variable stiffness clutch to address this limitation. The bistable, metamaterial-based clutch utilizes a circular arrangement of double-clamped curved beams that allow the clutch to be manually reconfigured between two stable states via elastic snapping. Experimental validation using 3D-printed TPU samples demonstrates that the clutch successfully toggles between distinct torsional stiffness regimes. Results show that "normally-open" fabricated clutches achieve higher stiffness changes of 8.4 Nmm/° (0.48 Nm/rad) compared to a "normally-closed" version. This shows that the fabrication state significantly influences the performance of the metamaterial. The demonstrated variable stiffness property of the clutch offers a customizable, low-part-count solution for retrofitting or integrating tunable compliance into robotic actuators.

1 Introduction

Robots interacting with humans or their environment require safe and efficient actuation. A key property in interaction is the compliance of a body and its actuators. While higher stiffness in actuators allows for very controlled and precise movements, introducing compliance can reduce vibrations and increase the safety of interaction as well as the energy efficiency of the system. Series elastic actuators (SEAs) utilise springs and other elastic components to address these challenges physically. Changing conditions, tasks, and environments further motivated the development of methods for stiffness modulation in system [1, 2]. Variable stiffness actuators (VSAs) allow tuning the actuator's properties during use, thus leveraging the advantages of SEAs [3]. SEAs and VSAs both feature an elastic element connecting the motor to its load. This enables energy to be stored and released as required, allowing the system to react to disturbances and limit the actuator's power for inherent safety. State-of-the-art VSAs, however, are complex devices composed of a large number of components [4, 5, 6]. This work introduces an alternative approach to VSAs, leveraging the stiffness change of a monolithic, bistable metamaterial that acts as a clutch between the motor and output shaft. This clutch can be manually reconfigured by opening and closing the element. Depending on the state, the clutch shows different torsional stiffness, making it ideal as a coupling element between actuator and load. The clutch is designed to be bistable, meaning it can hold two distinct states, which are switched through elastic deformation. By design, the load axis is decoupled from the reconfiguration mechanism. Therefore, the clutch can either be added to an actuator to retrofit it or it can be directly integrated into the actuator. The series configuration of the motor and the variable stiffness clutch thus depicts a variable stiffness series elastic actuator. Different robotic applications require variable-stiffness actuators with different specifications. The monolithic design enables the clutch to be customised and fabricated quickly, making it easy to be replaced and exchanged in case of wear or changing applications.

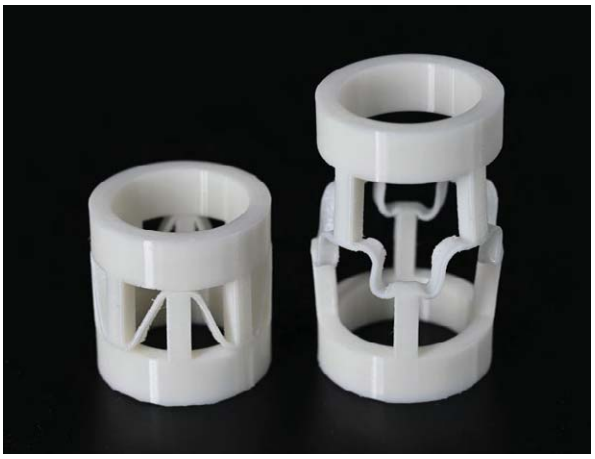


Figure 1 3D printed sample of the NC-clutch in closed (left) and open (right) state

 DOI: 10.30420/456743024

2 Methods

2.1 Design and Fabrication

The design of the variable stiffness clutch is based on the concept of non-linear metamaterials [7]. In particular, we base our design on a unit cell with characteristic double-clamped, curved beams [8]. These sine-shaped beams in each unit cell lead to a non-linear response of the metamaterial under tensile load, causing the unit cell to snap into a second, metastable state. This state is maintained until a critical opposing force is applied, causing the unit cell to snap back, which again changes the state of the clutch. Recent work showed that the state change of a planar metamaterial composed of such unit cells exhibits different shear stiffness in different states [9]. We follow an approach from literature by arranging four unit cells on a circular pattern to form a cylindrical topology that suits the application of a clutch [10, 11]. We chose the following dimensions of the unit cell:

Parameter	Dimensions
Outer diameter	33 mm
Inner diameter	25 mm
Thickness of the sine-shaped beams	1 mm
Height of the vertical beams	14 mm
Width of the vertical beams	4 mm
Gap height	0.5 mm

Table 1 Dimensions of the variable stiffness clutch

The bistable clutch can be fabricated in both open and closed states, which corresponds to two different application use cases: For the first option, the clutch will primarily operate in a soft configuration and is intended to be reconfigured during use to achieve greater stiffness in the VSA. The second option requires a clutch with an initially higher stiffness that can then be reconfigured to a more compliant state. In either case, the stable state should be used for the one that is likely to be used more frequently during the application. This is recommended since the clutch will undergo significant deformation in the metastable state, which will put additional strain on the structure over time. We further refer to the fabricated and stable states as "normally-open" and "normally-closed".
The clutches are FDM-3D-printed on a Prusa XL using TPU (Ninjatech Cheetah) with a Shore hardness of 95A. We use Verbatim BVOH as a soluble support material. The samples are printed with an infill of 50%, 0.2 mm layer height, a speed of 80 mm/s, a nozzle temperature of 240°C (for TPU), and a bed temperature of 50°C. Note that the infill setting only applies to the thicker vertical beams and the support rings of the clutch. The functional sine-shaped beams are unaffected by the setting due to their small thickness. All clutches are printed with their central axis perpendicular to the print bed. **Figure 2** shows the fabricated normally closed (left) and normally open (right) samples on the print bed. **Figure 1** shows the normally closed clutch in closed and open states.



Figure 2 3D printed samples fabricated from TPU with support material (soluble BVOH) on the Prusa XL. NO-configuration (right) and NC-configuration (left).

2.2 Experimental Setup

We study the response of the clutch under load in two separate series of experiments to explore its bistability, the variable stiffness property, and the influence of the state in which it was fabricated. All experiments are carried out on a ZwickRoell zwickiLine testing machine. A first tensile test examines the bistability, and thus the state change functionality of the design. For both the NC- and NO-fabricated samples, we start the deformation of the structure from the closed state and run 10 cycles with a maximum displacement of 25 mm at a rate of 500 mm/min. Note that this means that the NO-sample is already in its metastable state at the start of the experiment.
The variable stiffness of the samples is measured with a torsional test on the same machine. **Figure 3** shows how the NO-sample is mounted in the machine: We clamp the bottom and top rings of the clutch using a rigid support part and twist the top ring by a maximum angular deflection of 5° at a rate of $\pi/40$ rad/s. Again, we run 10 cycles to prove the consistency of the structural behaviour. Both configurations of the clutch are tested in open and closed states to compare their torsional stiffness. The difference between the stiffness in the open and closed states yields the stiffness change that the clutch can achieve.

3 Results and Discussion

The results of the tensile tests are depicted in **Figure 4** and show consistency over the individual load cycles of both samples. The force-displacement curve shows that with the initial displacement, the force increases rapidly, which shows high initial resistance of the structure against load. At a displacement of $\sim$3.5 mm, a maximum point is reached. Here, the maximum force of the NC sample is higher than for the NO sample, which shows the difference between a stable state (NC) and a meta-stable state

DOI: 10.30420/456743024



Figure 3 Testing sample (NO configuration) mounted in the ZwickRoell zwickiLine testing machine. The blue components are rigid and designed to support the clutch and allow for reliable mounting.

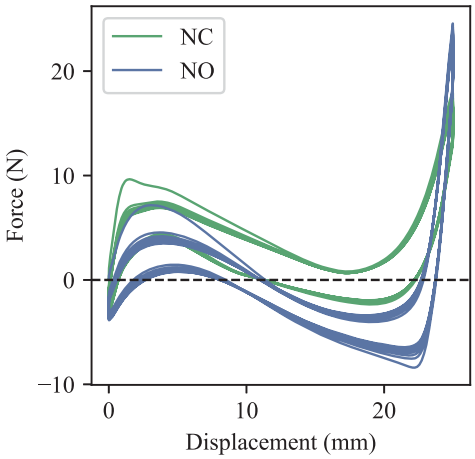


Figure 4 Results of the tensile test on the bistability of the variable stiffness clutch with 10 cycles. The Figure shows the force-displacement curves of the NC-printed sample (green) and the NO-printed sample (blue).

(NO). With further displacement, the force decreases to a point where it becomes a local minimum. Note that for the NO-sample, this minimum is at ∼-3.5 N, while the force of the NC-sample remains positive. This shows that only the NO-printed sample actively opens itself once a certain displacement is reached. From this minimum, the force continues to increase again until the maximum axial displacement of the clutch is reached at 25 mm. With unloading the clutch, the force-displacement curves of both samples cross the 0 N-level due to the hysteresis that arises from the viscoelasticity of the material. This global minimum marks the meta-stable state of the NC sample and the stable state of the NO sample. Further backward displacement deforms the clutch back into its initial, closed shape. Here, it can be observed how the force-displacement curve crossed 0 N again, implying that the structure actively pulls itself back into its initial shape. For the first stroke of each cycle, the force-displacement curves reach a higher maximum force than for all following cycles of the experiment. This is due to the viscoelasticity of the TPU material, which is also indicated by the backward motion finishing at a negative force for all testing cycles. The large hysteresis of the force-displacement curve shows the material-caused damping of the structure, with the enclosed area representing the energy dissipated. Comparing the curves of NO- and NC-configuration shows bistability for both samples (zero-crossing of the force-displacement curve). However, the results also show that the bistability is more pronounced for the NO sample.

Figure 5 and **Figure 6** show the results of the NC- and NO-configurations in the torsional test. In both cases, the slopes of the ten cycles indicate higher stiffness for the open state compared to the closed state. This matches the results for planar metamaterials with the same unit cell geometry [9]. The hysteresis of the samples again results from the damping of the TPU. However, the experiment shows a significantly more pronounced change in stiffness for the NO-printed sample, where a maximum torque of 60 Nmm is reached at the angular displacement of 5° in the open state (23 Nmm for the NC-configuration). This leads to a stiffness 12 Nmm/° for the open state of the NO-, and 4.6 Nmm/° of the NC-configuration. The closed state shows very similar results for both cases, with a maximum torque of 18 Nmm in the NO-configuration and 19 Nmm in the NC-configurations, leading to a torsional stiffness of 3.6 Nmm/° and 3.8 Nmm/°, respectively. Therefore, the achievable stiffness change with the variable stiffness clutch is 8.4 Nmm/° (0.48 Nm/rad) when printed in NO-configuration and 0.8 Nmm/° (0.05 Nm/rad) when printed in NC-configuration. This clearly indicates that the structure should be fabricated in the open state to generate a usable stiffness change between the two states.

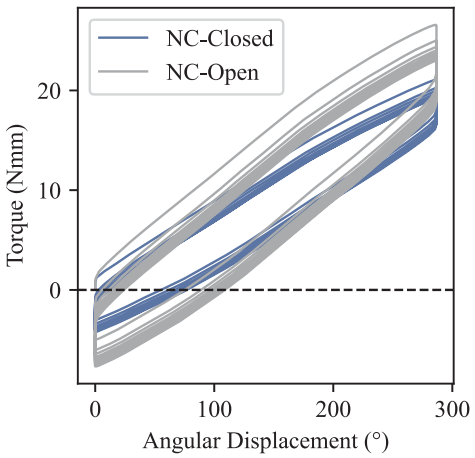


Figure 5 Results from the torsional test of the NC-printed, variable stiffness clutch in open (grey) and closed (blue) state.

ISBN: 978-3-8007-6743-4

@ VDE VERLAG GMBH · Berlin · Offenbach

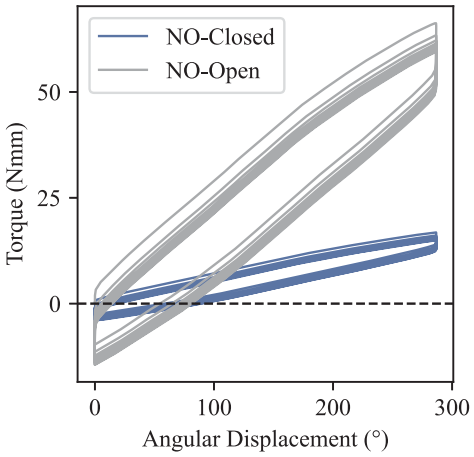


Figure 6 Results from the torsional test of the NO-printed, variable stiffness clutch in open (grey) and closed (blue) state.

4 Conclusion

The experimental results show that the design of the monolithic clutch enables switching between two characteristic torsional stiffness values by snapping it from a stable to a metastable state. The multimaterial 3D-printing allows for automated fabrication and customizability of the clutch. Regarding the stiffness of the two clutch states, it can be concluded that, regardless of the fabrication state, the open state exhibits higher stiffness than the closed state. However, the normally-open configuration leads to a substantially larger change of torsional stiffness between the open and closed state (0.48 Nm/rad). We therefore conclude that in order to obtain maximum stiffness change in the VSA, the clutch should be printed in the normally-open configuration. Bistability is given for both configurations, but is more pronounced for the NO sample. Based on this, we will aim to maximize the achievable stiffness change with the variable stiffness clutch. For this, we will systematically study the parametric geometry of the design and optimize it for both bistability and stiffness change. We will then also study different ways to trigger the state change of the clutch, following both an actuated and a passive strategy. This way, we will explore applications for the variable stiffness clutch and leverage the advantages it promises.

References

[1] Izabela K. Kuder et al. “Variable stiffness material and structural concepts for morphing applications”. In: *Progress in Aerospace Sciences* 63 (2013), pp. 33–55. ISSN: 0376-0421. DOI: https://doi.org/10.1016/j.paerosci.2013.07.001. URL: https://www.sciencedirect.com/science/article/pii/S037604211300064X.

[2] Zhang Li et al. “Variable stiffness methods for robots: a review”. In: *Smart Materials and Structures* 33.6 (May 2024), p. 063002. DOI: 10.1088/1361-665X/ad0753. URL: https://doi.org/10.1088/1361-665X/ad0753.

[3] Sebastian Wolf et al. “Variable Stiffness Actuators: Review on Design and Components”. In: *IEEE/ASME Transactions on Mechatronics* 21.5 (2016), pp. 2418–2430. DOI: 10.1109/TMECH.2015.2501019.

[4] Murat Reis and Kenan Tüfekci. “A Variable Clutch Mechanism for Adjustable Stiffness Actuators Based on Bending and Torsion of Prismatic Beams”. In: *Actuators* 12.1 (2023). ISSN: 2076-0825. DOI: 10.3390/act12010008. URL: https://www.mdpi.com/2076-0825/12/1/8.

[5] Irfan Hussain et al. “Design and Control of a Discrete Variable Stiffness Actuator With Instant Stiffness Switch for Safe Human-Robot Interaction”. In: *IEEE Access* 9 (2021), pp. 118215–118231. DOI: 10.1109/ACCESS.2021.3105587.

[6] G. Tonietti, R. Schiavi, and A. Bicchi. “Design and Control of a Variable Stiffness Actuator for Safe and Fast Physical Human/Robot Interaction”. In: *Proceedings of the 2005 IEEE International Conference on Robotics and Automation*. 2005, pp. 526–531. DOI: 10.1109/ROBOT.2005.1570172.

[7] Sicong Shan et al. “Multistable Architected Materials for Trapping Elastic Strain Energy”. In: *Advanced Materials* 27.29 (2015), pp. 4296–4301. DOI: https://doi.org/10.1002/adma.201501708. eprint: https://advanced.onlinelibrary.wiley.com/doi/pdf/10.1002/adma.201501708. URL: https://advanced.onlinelibrary.wiley.com/doi/abs/10.1002/adma.201501708.

[8] Hang Yang and Li Ma. “Multi-stable mechanical metamaterials by elastic buckling instability”. In: *Journal of Materials Science* 54 (Feb. 2019). DOI: 10.1007/s10853-018-3065-y.

[9] Hugo de Souza Oliveira et al. *Toggling stiffness via multistability*. 2026. arXiv: 2510.09511 [cond-mat.soft]. URL: https://arxiv.org/abs/2510.09511.

[10] Hang Yang and Li Ma. “1D and 2D snapping mechanical metamaterials with cylindrical topology”. In: *International Journal of Solids and Structures* 204-205 (2020), pp. 220–232. ISSN: 0020-7683. DOI: https://doi.org/10.1016/j.ijsolstr.2020.08.023. URL: https://www.sciencedirect.com/science/article/pii/S0020768320303280.

[11] Hugo de Souza Oliveira et al. “Meta-Ori: monolithic meta-origami for nonlinear inflatable soft actuators”. In: *2025 IEEE 8th International Conference on Soft Robotics (RoboSoft)*. 2025, pp. 1–6. DOI: 10.1109/RoboSoft63089.2025.11020947.

 DOI: 10.30420/456743025

Metamaterial for a localized simulated button-click

Mondher Ouari[1], Frédéric Giraud[2], Charles Croënne[3], Jean-Luc Bruyelle[2] and Christophe.giraud-Audine[2],
1 UMR 8520 - IEMN, Univ. Polytechnique Hauts-de-France, CNRS, Univ. Lille, Valenciennes, F-59313, France
2 Univ. Lille, Arts et Metiers Institute of Technology, Centrale Lille, Junia, ULR 2697 - L2EP, F-59000 Lille, France
3 UMR 8520 - IEMN F-59000 Lille, France
frederic.giraud@univ-lille.fr

Abstract

To realize a localized button click on a glass plate, a confinement system is designed which exploits the local resonance of a pillar array to create a resonating cavity. Two vibration modes are exploited and combined to generate a travelling wave.

1 Introduction

The tactile illusion of a button click can be generated using the elliptical particle motion at the substrate surface. For a flexural mode, the tangential component of the elliptical velocity drags the user's finger via friction [1]. To be efficient, the ratio between the normal displacement and the tangential one should be approximately equal to λ=1.

It has been demonstrated that 3D-printed pillars can create a band gap that confines the ultrasonic vibration inside a working area [2]. In this paper, we use this principle to create a disk shape haptic area on a large plate of glass. Compared with the aforementioned literature examples, our design is fitted to an already existing plate, showing a localized and confined vibration. Moreover, it exploits two vibration modes, making possible elliptic motion of the particles, which enables the simulation of a button click.

2 Design of the localized haptic actuator

2.1 Selected vibration pattern and frequency

The design proposed in this paper derives from the device presented in [3]; the elliptical motion is obtained on a disc from two standing waves, shifted in time by 90°, and which nodal lines are rotated in space by 45°. However, in this work, the disc is fixed at its external boundary, as presented fig. 1 a) and b), which differs from the aforementioned work which was in free condition. The value of Λ with this design can be estimated from the simulated results to $\Lambda = 0.28$.

2.2 Design of the confined vibration system

Three circular arrays of thirty six 5.05 × 2 × 2mm aluminum pillars are built on top of a 1.5mm-thick hollow aluminum disk, which is then placed on a 2mm-thick and 120mm-wide square glass plate, as shown on fig. 2 a). Their capability to confine the vibration inside the cavity is verified for the two modes.

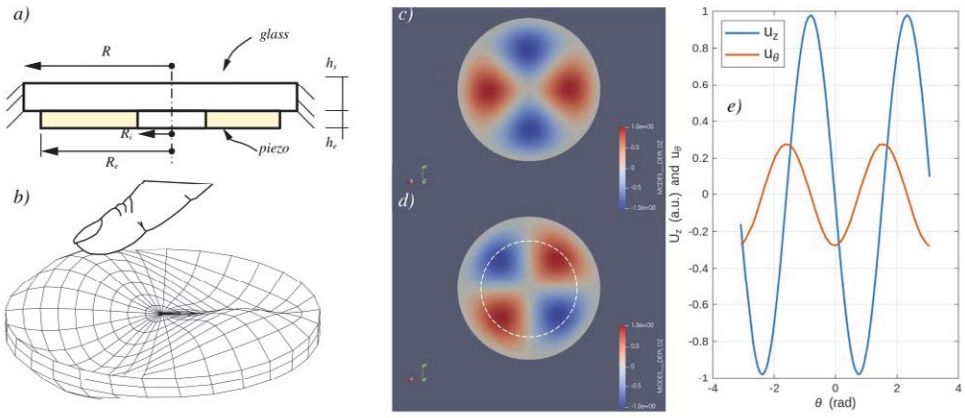


Fig. 1. Principle of the confined button click a) geometry b) Traveling wave used in this work c) and d) the simulation results for the two selected modes shifted in space by 90° at $47088Hz$ (top mode A , bottom mode B) and e) the displacement on u_z and u_θ along the dashed white circle.

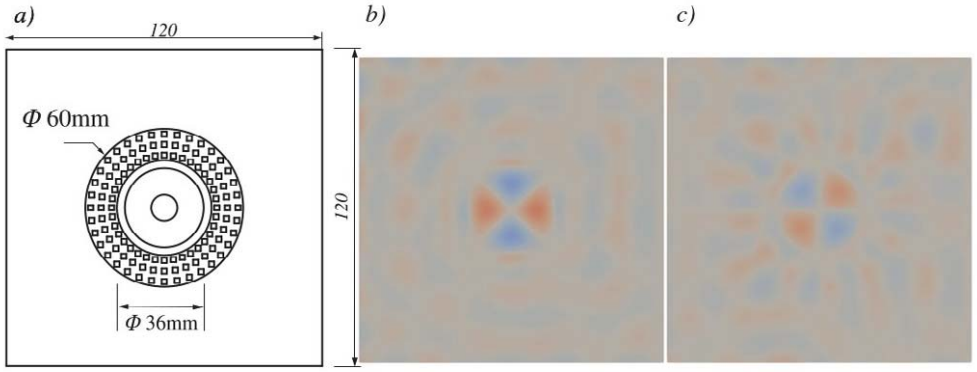


Fig. 2. Simulation of the confined vibration system a) schematic of the 3D simulated model b) the mode A at $46182Hz$ c) the mode B at $46247Hz$.

3 Experimental evaluation

The prototype is presented figure 3. The frequency response of the device, excited by one electrode shows a maximum vibration amplitude at f0 = 45909Hz, and the bandwidth is estimated to be 182Hz, leading to a quality factor of 252. The methodology is verified by the experimental measurements. Psychophysical tests will be shown to assess the capability of the interface to create localized stimuli on a large plate.

4 Acknowledgement

This research was funded by the Agence Nationale de la Recherche (ANR), grant ANR-21-CE33-0020 HASAME.

5 Literature

[1] Daunizeau, T., Gueorguiev, D., Haliyo, S., Hayward, V.: Phononic crystals applied to localised surface haptics. IEEE Transactions on Haptics 14(3), 668–674 (2021)

[2] Garcia, P., Giraud, F., Lemaire-Semail, B., Rupin, M., Kaci, A.: Control of an ultrasonic haptic interface for button simulation. Sensors and Actuators A: Physical 342, 113624 (2022).

[3] Gueorguiev, D., Kaci, A., Amberg, M., Giraud, F., Lemaire-Semail, B.: Travelling ultrasonic wave enhances keyclick sensation. In: Prattichizzo, D., Shinoda, H., Tan, H.Z., Ruffaldi, E., Frisoli, A. (eds.) Haptics: Science, Technology, and Applications. pp. 302–312. Springer International Publishing, Cham (2018)

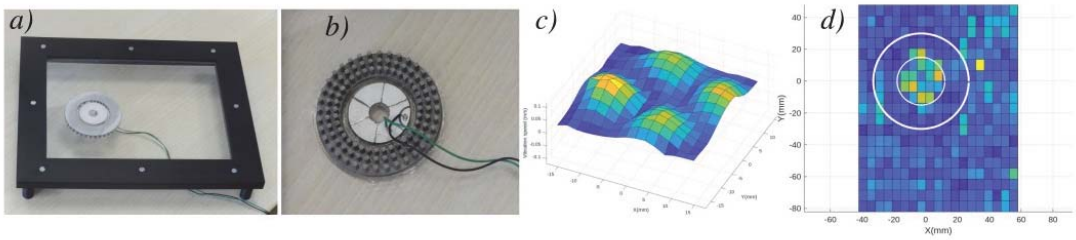


Fig. 3. Prototype of the confined button click device a) system on the glass plate b) view of the top electrode of the piezoelectric plate; the black wire is connected to the wrapped around electrode and is grounded c) Measurement of U_z in the cavity d) measurement of U_z on the plate.

 DOI: 10.30420/456743026

Assembly-oriented redesign of a shape memory alloy driven bistable gripper

Tom Gorges[1], Fabian Adler[3], Sarah Zimmer[3], Sophie Nalbach[1], Paul Motzki[1,2]

1 Depart. Smart Material Systems, ZeMA – Center for Mechatronics and Automation Technology, Saarbruecken, Germany
2 Saarland University, Depart. Systems Engineering, Saarbruecken, Germany
3 Depart. Assembly Systems, ZeMA – Center for Mechatronics and Automation Technology, Saarbruecken, Germany

Abstract

This paper presents the redesign of a shape memory alloy (SMA) driven gripper for industrial handling applications with a focus on assembly-oriented product development. Conventional pneumatic grippers are robust but energy-inefficient, while SMA actuators offer high energy density and compact integration potential. The developed gripper combines welded SMA wire bundles with a bistable mechanism for energy-free holding in both end positions and a compliant mechanism for motion transfer. Previous prototypes demonstrated the feasibility of the concept but were not suitable for industrial series production due to high assembly complexity, tolerance sensitivity, and unsuitable joining processes. Therefore, a systematic Design for Assembly (DFA) approach was applied to reduce part count, simplify assembly operations, and improve robustness. The redesign replaces conventional screw joints with snap-fit connections and hot-staked plastic pins, significantly reducing assembly effort and tooling requirements. The bistable mechanism was optimized to decrease tolerance sensitivity while maintaining functional performance. In addition, manually soldered SMA contacts were replaced by a PCB-based spring contact system enabling modular and reliable electrical integration. Functional integration within selective-laser-sintered components further reduced the number of parts and joining operations. Overall, the redesign reduced the part count from 76 to 14 and simplified manufacturing and assembly processes considerably. The presented gripper demonstrates how SMA-based actuation combined with DFA principles enables the transition from a laboratory prototype toward an industrially viable lightweight and energy-efficient handling system.

1 Introduction

In industrial production systems, grippers are essential components for automated handling processes and their importance continues to increase with the growing degree of automation [1], [2]. Pneumatically actuated grippers are widely used due to their robustness, dynamic performance, and compatibility with existing compressed-air infrastructures [3], [4]. However, pneumatic systems are associated with considerable energy losses and low overall efficiency [5]. As energy efficiency becomes increasingly important in industrial manufacturing, alternative actuation technologies are gaining relevance [6].

Electromagnetic actuators such as solenoids and electric motors are commonly used in automation systems, but their comparatively high mass and installation space requirements limit their suitability for compact and lightweight applications [7]. Shape memory alloys (SMAs) offer an alternative approach due to their high energy density, compact integration capability, and simplified actuator design [8], [9]. Consequently, SMA-based actuation systems have attracted increasing attention in robotics and lightweight automation applications [10]. Nevertheless, the industrial application of SMA technology remains challenging due to limitations regarding robustness, manufacturability, fatigue behavior, and system integration [11], [12].

To address these challenges, a novel SMA-driven gripper concept based on welded SMA wire bundles and a bistable mechanism was previously developed [13], [14], [15]. The bistable mechanism enables energy-free holding in both end positions, while a compliant mechanism transfers the actuator motion to the gripping jaws. Although earlier prototypes demonstrated the functional feasibility of the concept, they were not suitable for industrial series production due to high assembly complexity, tolerance sensitivity, and manufacturing-related limitations.

This paper presents the redesign of the SMA-driven gripper with a focus on assembly-oriented product development and industrial manufacturability. A systematic Design for Assembly (DFA) methodology is applied to simplify assembly processes, reduce complexity, and improve design robustness [16]. The objective is to transfer the existing laboratory prototype into a manufacturable and industrially viable handling system while maintaining the functional advantages of SMA-based actuation.

2 SMA Gripper Concept

The SMA gripper is based on a patented actuator concept (see Figure 1) that incorporates a bistable spring actuated by SMA wires. The spring, made of conventional steel, is preloaded and can assume two stable end positions. The transition between these positions is initiated by activating an SMA element on the tensioned side. Due to the resulting contraction of the SMA wires, the spring snaps into the opposite stable position and remains there without requiring additional energy input. The activation of the SMA wires is achieved by a short electrical pulse. Since SMA wires are attached to both sides, the second preloaded bundle can

 DOI: 10.30420/456743026

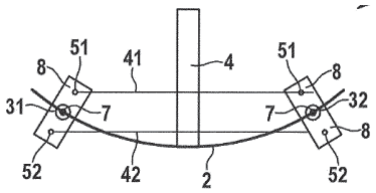


Figure 1: Sketch of an SMA actuator with a bistable pivot mounted leaf-spring and in-plane arrangement of the SMA wires *[15]*

subsequently be activated by another short current pulse. A CAD representation of the actuator concept integrated into a frame is shown in Figure 2.

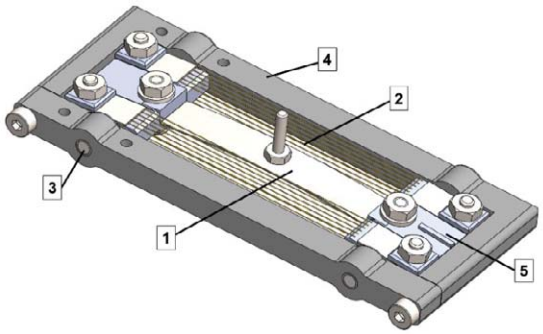


Figure 2: CAD model of the bistable SMA actuator with 1) leaf spring with shaft as stroke output, 2) SMA wire bundles, 3) Precisions pins as pivot bearings, 4) Frame with bushings and 5) spring clamp with wire bundle attachment points [14].

By extending this actuator with an output shaft located at the center of the spring, the displacement and force generated by the spring can be transferred to an external output. In the gripper developed in this work, the shaft is coupled to a compliant mechanism to which two gripper jaws are attached. Combined with a housing, this results in the gripper shown in Figure 3. Overall, the actuator design requires a coordinated dimensioning of displacement and force throughout the entire transmission chain, ranging from the SMA wire and leaf spring to the compliant mechanism. The force required to switch the spring between its two stable states is provided by two bundles, each consisting of six 100 µm SMA wires. Bundling the wires increases the achievable force while maintaining a high dynamic response due to the more favorable surface-to-volume ratio compared to a single thicker wire. The wires are attached to a contact plate using resistance welding.

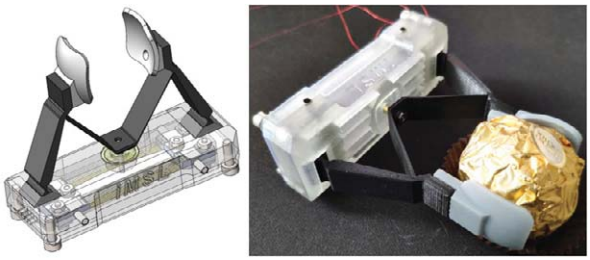


Figure 3: Left: CAD model of the gripper assembly with compliant kinematics, gripper jaws, transparent housing, and bistable SMA actuator unit. Right: Photograph of the final gripper setup holding a chocolate candy as a demonstrator [14].

At this stage of development, the gripper primarily serves as a proof of concept. As is typical for research prototypes, the focus is not yet on manufacturability, scalability, or design-for-assembly (DFA) principles. As a result, the gripper consists of 76 individual parts and requires several complex assembly steps, such as soldering electrical wires to the SMA contact plates, which increases the risk of assembly errors.

3 DFA-Based Redesign

To improve industrial manufacturability and enable potential series production, the SMA gripper was redesigned according to Design for Assembly (DFA) principles (see Figure 4). DFA aims to consider assembly-related aspects already during the design phase to reduce assembly effort, process complexity, and manufacturing costs. Key principles include reducing the number of parts, simplifying joining processes, and minimizing handling and assembly operations. Furthermore, functional integration enables multiple functions to be combined within individual components, reducing the number of additional fastening elements and assembly steps. Based on these principles, the mechanical and electrical subsystems of the existing gripper concept were systematically revised and optimized regarding assembly effort, robustness, and industrial applicability.

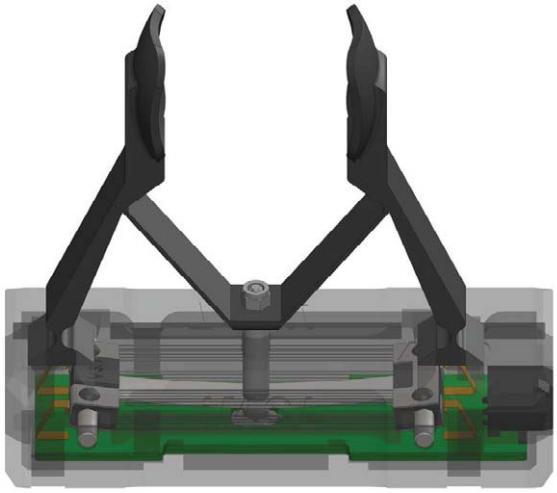


Figure 4: CAD model of the redesigned SMA-driven bistable gripper, showing the overall assembly with transparent housing

3.1 Electrical Connection

In the prototype version, electrical wires are soldered to the contact plates for electrical contacting. This is a complex manual process that needs to be replaced. As an alternative, spring contacts are used, which are mounted on a PCB with a connector socket. The contact plates of the SMA bundles

 DOI: 10.30420/456743026

are designed with a bent section at one end, allowing the spring contacts to make contact. In addition, the previously soldered bridge on the right side of the bundle (see Figure 5, top) is replaced by a modified bundle design. The new contacting concept, which mainly stands out due to the simplified assembly process, is shown in Figure 5 (bottom).

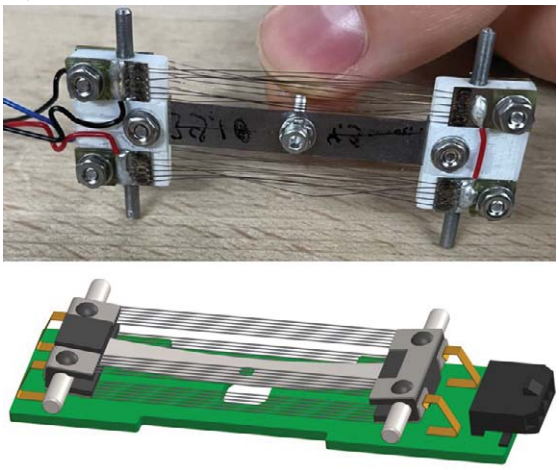


Figure 5: Electrical connection of the SMA bundles using soldered wires (top) and the redesigned spring-contact interface with PCB (bottom).

3.2 Housing

In the new design, the housing is manufactured using Selective Laser Sintering (SLS). Compared to the previously used Stereolithography (SLA) process, this provides greater design freedom, improved functional integration, and fewer post-processing steps. In addition, the selection of PA12 as the housing material eliminates the need for a bearing sleeve, since the material pairing with the stainless-steel shaft provides sufficiently low friction for the application.

In the initial design, the two housing parts are connected using four screws (see Figure 6, left). As part of the DFA redesign, these screws are replaced by four snap-fit connectors designed using Finite Element Analysis (see Figure 6, right). This functional integration simplifies the assembly process and reduces the number of components by four. Furthermore, the new design includes an integrated mounting feature for the PCB within the housing parts, eliminating the need for additional components.

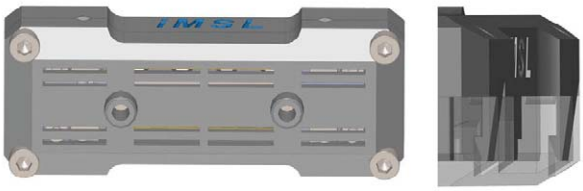


Figure 6: CAD model of the housing fastening design of the prototype version using screws (left) and integrated snap-fit features in the upper housing part of the redesigned version (right).

3.3 Leaf Spring and SMA Mounting

In the prototype design, the leaf spring is clamped between two plastic components using a bolted joint (see Figure 7, left). This assembly process is time-consuming and requires handling several small parts. In the redesigned version, a slot is integrated into the bearing shaft, allowing the leaf spring to be inserted directly into the shaft (see Figure 7, right). This simplifies the assembly process and reduces the number of components. In addition, the reduced number of interacting parts decreases the tolerance chain affecting the bistable leaf spring. Since the displacement of the leaf spring is sensitive to geometric tolerances, this aspect was also considered during the redesign of the housing, particularly at the bearing interface.

Furthermore, the SMA holder in the new design is manufactured from PA12 using the SLS process. As PA12 is a thermoplastic material, it enables the use of heat staking. In the previous design, the top and bottom contact plates are fastened using an M2 bolted joint. However, since the two contact plates must be electrically insulated from each other, an additional insulating plate is required between the connection and the SMA contact plate. This complex joining process requires many small parts that must be assembled in the correct order, resulting in a high risk of assembly errors (see Figure 7, left).

In the new SMA holder design, 2 mm pins are directly integrated into the component. These pins are initially used to position the SMA contact plates. After the plates are placed onto the pins, the pins are plastically deformed by heat staking, permanently securing the SMA bundles (see Figure 7, right). This results in a significant reduction in the number of components and a simplified joining process with high potential for automation.

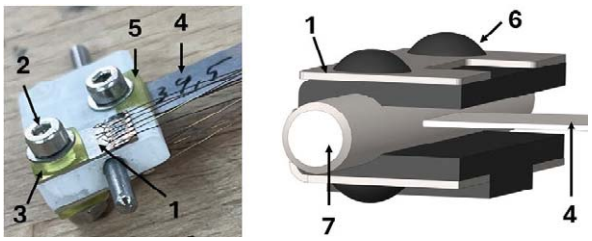


Figure 7: Left: Prototype SMA holder assembly with 1) SMA contact plate, 2) bolted joint with washer, 3) insulation plate, 4) bistable leaf spring, and 5) clamping block. Right: Redesigned SMA holder with 1) SMA contact plate, 6) heat-staked pins, 7) shaft with integrated slot for leaf spring and 4) bistable leaf spring.

3.4 Kinematic

The change in the manufacturing process also enables a reduction in the number of components within the kinematic structure. While the previous design used two different materials, the SLS process allows these parts to be manufactured as a single component. Complex structures such as the gripper jaws, previously manufactured using SLA, as well as compliant joints, previously produced using Fused Deposition Modeling (FDM), can now both be realized in PA12 using the same manufacturing process (see Figure 8).

ISBN: 978-3-8007-6743-4 @ VDE VERLAG GMBH · Berlin · Offenbach

As a result, one assembly step and two components are eliminated. However, due to the modified material properties, the compliant mechanism had to be redesigned accordingly.

In addition, the connection between the kinematic structure and the leaf spring is revised. Instead of using a screw connection with spacer sleeves and washers, a shaft with threaded ends and two self-locking nuts is used (see Figure 8, right). This reduces the number of components, although the comparatively complex tightening process remains necessary. No alternative solution could be identified without affecting the functionality of the system, which is also an important consideration in DFA-oriented design.



Figure 8: Left: Compliant mechanism with separate gripper jaws requiring assembly, Center: Compliant mechanism with integrated gripper jaws designed for SLS manufacturing, Right: Connection between the compliant mechanism and the leaf spring in the redesigned version.

4 Conclusion and Outlook

This work presents a redesign of an SMA-based gripper under consideration of design-for-assembly (DFA) principles. The applied design changes lead to a significant reduction in the number of components and a simplification of the overall assembly. In particular, several joining and assembly processes are simplified or eliminated through increased functional integration as well as modified manufacturing and material approaches.

The redesigned system improves assembly friendliness, reduces the risk of assembly errors, and increases the potential for automated assembly and future series-oriented manufacturing while maintaining the original functionality of the gripper.

Using this example, it is demonstrated how DFA methods can be applied to scientific prototypes, particularly in the field of SMA actuator systems. Future work will focus on investigating the long-term behavior of the redesigned gripper and identifying potential quantitative improvements where necessary.

5 Literature

[1] G. Fantoni *et al.*, “Grasping devices and methods in automated production processes,” *CIRP Annals*, vol. 63, no. 2, pp. 679–701, Jan. 2014, doi: 10.1016/J.CIRP.2014.05.006.

[2] V. Ivanov, V. Andrusyshyn, I. Pavlenko, J. Pitel’, and V. Bulej, “New classification of industrial robotic gripping systems for sustainable production,” *Sci. Rep.*, vol. 14, no. 1, p. 295, Dec. 2024, doi: 10.1038/S41598-023-50673-5.

[3] R. Abela, P. Refalo, M. Borg, and E. Francalanza, “Pneumatic Control for Sustainable Compressed Air Systems: Multi-criteria Optimisation for Energy Efficient Production,” *Procedia CIRP*, vol. 122, pp. 247–252, Jan. 2024, doi: 10.1016/J.PROCIR.2024.01.035.

[4] S. R. . Majumdar, *Pneumatic systems : principles and maintenance*. McGraw-Hill, 1996.

[5] R. Abela, P. Refalo, M. Borg, and E. Francalanza, “Pneumatic Control for Sustainable Compressed Air Systems: Multi-criteria Optimisation for Energy Efficient Production,” *Procedia CIRP*, vol. 122, pp. 247–252, Jan. 2024, doi: 10.1016/J.PROCIR.2024.01.035.

[6] V. Ivanov, V. Andrusyshyn, I. Pavlenko, J. Pitel’, and V. Bulej, “New classification of industrial robotic gripping systems for sustainable production,” *Sci. Rep.*, vol. 14, no. 1, p. 295, Dec. 2024, doi: 10.1038/S41598-023-50673-5.

[7] J. Mohd Jani, M. Leary, A. Subic, and M. A. Gibson, “A review of shape memory alloy research, applications and opportunities,” *Materials & Design (1980-2015)*, vol. 56, pp. 1078–1113, Apr. 2014, doi: 10.1016/J.MATDES.2013.11.084.

[8] P. Motzki and S. Seelecke, “Industrial Applications for Shape Memory Alloys,” in *Encyclopedia of Smart Materials*, Elsevier, 2021, pp. 254–266. doi: 10.1016/B978-0-12-803581-8.11723-0.

[9] P. Molitor, R. Britz, and P. Motzki, “High-Power Shape Memory Alloy Catapult Actuator for High-Speed and High-Force Applications,” *IEEE Access*, vol. 10, pp. 92373–92380, 2022, doi: 10.1109/ACCESS.2022.3202210.

[10] M. M. Kheirikhah, S. Rabiee, and M. E. Edalat, “A review of shape memory alloy actuators in robotics,” *Lecture Notes in Computer Science (including subseries Lecture Notes in Artificial Intelligence and Lecture Notes in Bioinformatics)*, vol. 6556 LNAI, pp. 206–217, 2011, doi: 10.1007/978-3-642-20217-9_18/SAVE-RESEARCH.

[11] D. Scholtes, S. Seelecke, and P. Motzki, “Electro-thermo-mechanical characterization of shape memory alloy wires for actuator and sensor applications—Part 1: The effects of training,” *Engineering Reports*, vol. 6, no. 10, p. e12867, Oct. 2024, doi: 10.1002/ENG2.12867;WGROUP:STRING:PUBLICATION.

[12] D. Scholtes, S. Seelecke, and P. Motzki, “Electro–Thermo–Mechanical Characterization of Shape Memory Alloy Wires for Actuator and Sensor Applications, Part 2: High-Ambient-Temperature Behavior,” *Adv. Eng. Mater.*, vol. 26, no. 10, p. 2400432, May 2024, doi: 10.1002/ADEM.202400432;REQUESTEDJOURNAL:JOURNAL:15272648;PAGE:STRING:ARTICLE/CHAPTER.

[13] D. Scholtes, S. Seelecke, G. Rizzello, and P. Motzki, “Design of a Compliant Industrial Gripper Driven by a Bistable Shape Memory Alloy Actuator,” *ASME 2020 Conference on Smart Materials, Adaptive Structures and Intelligent Systems, SMASIS 2020*, Nov. 2020, doi: 10.1115/SMASIS2020-2204.

[14] “CASMART 4th Design Challenge.,” https://www.casmart.org/home/student-design-challenges/casmart-4th-design-challenge.

[15] P. Motzki and S. Seelecke, “BISTABLE ACTUATOR DEVICE HAVING A SHAPE MEMORY ELEMENT,” WO2017194591A1, 2017

[16] G. Boothroyd, P. Dewhurst, and W. A. Knight, “Product Design for Manufacture and Assembly: Third Edition,” *Product Design for Manufacture and Assembly, Third Edition*, pp. 1–671, Jan. 2010, doi: 10.1201/9781420089288/PRODUCT-DESIGN-MANUFACTURE-ASSEMBLY-PETER-DEWHURST-WINSTON-KNIGHT-GEOFFREY-BOOTHROYD/RIGHTS-AND-PERMISSIONS.

 DOI: 10.30420/456743027

Multilayered electrohydraulic soft actuators for safe-to-touch wearables and underwater systems

Chinmay Gupta[a] , Krishnaprasad Rajagopalan[a] , Gaurav Khandelwal[ab], and Ajay Giri Prakash Kottapalli[a]

[a]Department of Bioinspired MEMS and Biomedical Devices (BMBD), Engineering and Technology Institute (ENTEG), University of Groningen, Groningen, Netherlands
[b]Department of Engineering Science, University of Oxford, Oxford, United Kingdom

Abstract

The versatility of soft actuators enables their deployment across diverse domains, including medical applications (e.g. precision surgery, prosthetics), assistive devices (e.g. haptics), environment exploration (e.g. underwater) and many more. The growing demand in various sectors necessitates the development of soft actuator systems that ensure human and environmental safety while maintaining reliability without compromising the performance. In this work, we have demonstrated a novel multilayered electrohydraulic actuator configuration that safely conceals the electrodes, enabling touch-safe operation for human-centric wearables, human-machine interaction and underwater applications, while maintaining comparable actuation performance. The actuator was successfully integrated with fish-tail model to replicate bio-inspired underwater tail motion, thereby confirming its suitability for aquatic applications.

1 Introduction

Soft actuators are an emerging class of systems designed to be flexible and conformable, enabling safe interaction with complex and unstructured environments. Unlike traditional robots, which are made up of rigid components and offer high accuracy and precision, soft actuators provide adaptability, compliance and safe interaction, making them suitable for applications such as healthcare, wearables and human-machine interactions[1], [2].

Soft actuators are broadly categorised based on type of stimulus used for actuation including, pneumatic[3], fluidic[4], electroactive[5], [6], magnetic[7], thermal[8] and chemical[9] mechanisms. Among these, electrostatic actuators driven by high electric fields offers advantages such as fast response, precise controllability, portability and ease of integration with electronic systems[10], [11]. Dielectric elastomer actuators (DEAs) are type of electrostatic actuators that utilize solid dielectric materials and consist of soft, stretchable rubber like material sandwiched between two flexible electrodes. Despite their fast response and large deformation, the essential requirement of rigid frames to provide pre-stretch needed for actuation, limits their use[12], [13]. To overcome these limitations, electrohydraulic actuators, a newer class of soft electrostatic actuators, have been introduced[2], [14]. Unlike DEAs, electrohydraulic actuators do not require any rigid and bulky frame for pre-stretch, enabling more compact and compliant design. They combine solid and liquid dielectrics and offer fast response, large deformation, high precision and design freedom with a flexible structure[15], [16].

Electrohydraulic actuators work through the coupling of electrostatic and hydraulic forces, enabling versatile modes of actuation depending on the shape, size, geometry and placement of the electrodes[6]. A typical structural design of these actuators consists of a thin, flexible, inextensible dielectric film, compliant electrodes and a dielectric fluid[2]. In conventional electrohydraulic actuators, electrodes are positioned on the outer surface of the actuator, which poses a potential hazard due to exposure to high voltage, especially in applications involving human interaction or underwater usage. To mitigate this, an insulating layer placement on top of the electrode has been introduced, enabling safe operation in both wearable and underwater environments. Wang et. al. utilized double sided adhesive tapes as an insulating layer on high voltage electrodes to enable the jellyfish operation in underwater environments[17]. In a similar approach, Tamayo et. al. insulated the high voltage electrodes of a haptic wristwatch by applying 60 um PET adhesive films[18]. Although insulating layer enhances safety and electrical protection, they reduce the actuator mechanical performance by increasing the stiffness of the actuator. Moreover, such layers are susceptible to wear, tear and delamination, potentially compromising reliability and introducing safety risks over time.

In this article, we propose a multilayered design approach that fully embeds the electrodes inside the actuator, ensuing waterproofing, safety and suitability for wearables applications[19]. Unlike

DOI: 10.30420/456743027

conventional design, where the dielectric shell serves as both structural and functional pouch with electrodes positioned on the outer surface, our design separates these functions. The dielectric shell act as a structural layer and houses the electrodes on the inner surface, while a functional layer is bonded on top of the electrode to complete the actuator (**Figure 1a, b**). Upon application of voltage across the compliant electrodes, an electric filed is established. The functional dielectric film prevents shorting between the electrodes and enables the electric field to induce opposite charges, thereby converting electrostatic force into mechanical motion. This results in zipping force that compress the actuator and displaces the dielectric liquid, leading to a reduction in actuator length, typically expressed as strain (**Figure 1c**).

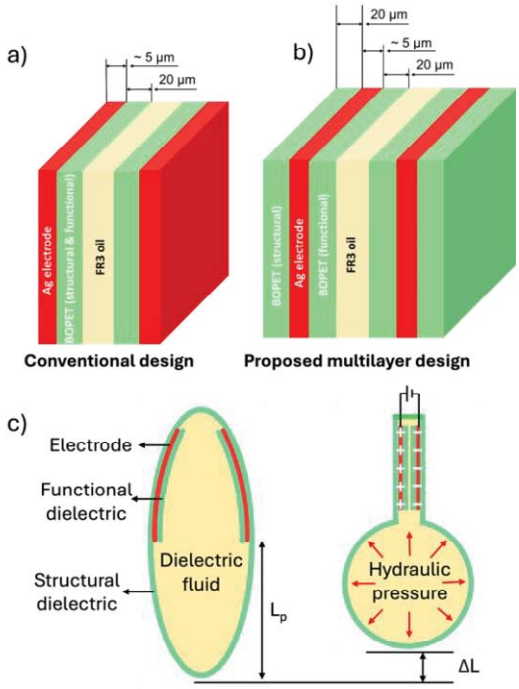


Figure 1: Design and working priciple of electrohydraulic actuators. a) and b) Structural components of conventional and proposed multilayer actuators, respectively, c) Schematic of actuator working prnciple: applied voltage causes electrode zipping, leading to linear contraction.

2 Fabrication of multilayered actuator

The fabrication of multilayered actuator involves several sequential steps and enables the use of various material combinations for structural and dielectric layers. The dielectric layer serves as the core functional layer that enables electrostatic actuation, while the structural layer encapsulates and stabilizes the actuator. In this work, we used biaxially oriented polyethylene terephthalate (BOPET) for both roles, owing to its high dielectric properties, mechanical strength and flexibility.

The fabrication begins with the deposition of electrode onto the structural layer (Mylar, 20 µm) (**Figure 2a**). Silver electrodes were patterned using an inkjet printer (Botfactory SV2). Following printing, the electrodes were cured at 75°C on hotplate for 25 minutes. After curing, a functional layer was laminated over the electrode using soldering rod, with a 2mm margin in all directions to ensure complete coverage and proper insulation (**Figure 2b**). Thereafter, the two films with deposited electrode and laminated functional layer were aligned and heat sealed, leaving a small vent for dielectric fluid filling (**Figure 2c**). Heat sealing was performed using a Fused Deposition Modelling (FDM) printer, which extruded a hot filament at 220°C, resulting into the heat sealing of the pouch in a specific pattern (**Figure 2d**). After heat sealing, the FR3 transformer dielectric liquid was injected through the vent, which was then sealed using a soldering iron (**Figure 2e, f**).

The final dimensions of the linear actuator were 2.3 cm in length and 5.5 cm in width, with electrode dimensions of 5.2 x 0.8 cm. The pouch was subsequently filled by 1.4 ml FR3 transformer oil.

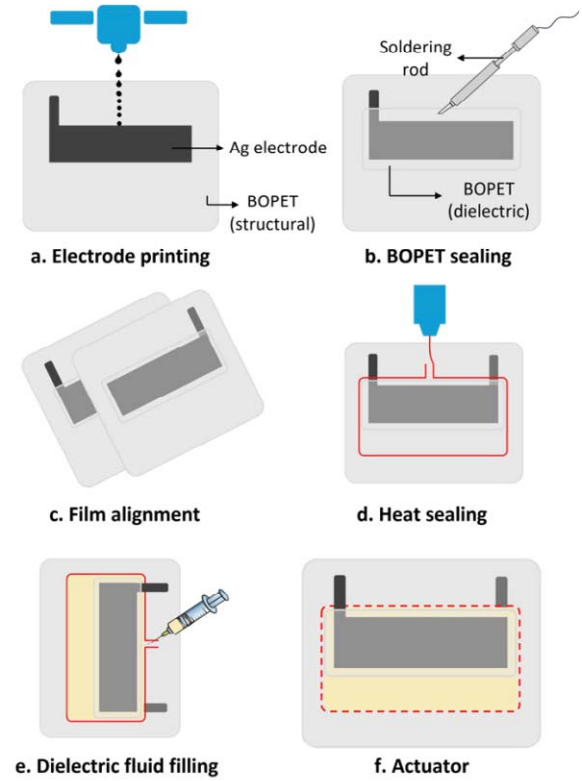


Figure 2: Schematic depiction of the fabrication process of the multilayered electrohydraulic actuator.

 DOI: 10.30420/456743027

3 Results

We used the conventional electrohydraulic actuator as a model system to explore the concept of multilayered structure. The conventional actuator consists of thin dielectric film that serves as both structural and functional structure, forming a pouch filled with dielectric liquid. The actuator shell is partially covered by compliable electrodes that are exposed to the external environment. Here, in this work we proposed a multilayered actuator design comprising separate structural and functional layer with embedded electrodes, thereby mitigating the risk associated with exposed electrodes.

The performance of the multilayered design was compared against the conventional actuator by fabricating actuators of identical size. As shown in **figure 3a**, the multilayered actuator achieved a maximum strain of 8.45 % at 7 kV. The strain-voltage curve across the applied range was comparable to that of the conventional actuator, indicating that embedding the electrode does not compromise actuation (**Figure 3b**). The load-strain characterization demonstrated that the actuator could lift weight over 100 g, approx. 40 times of its own weight (**Figure 3c**). Additionally, the actuator exhibited reliable and safe operation, maintaining safe-to-touch performance while actuation (**Figure 3d**). These results confirm that the multilayered design provided robust mechanical performance while ensuring safety and suitability.

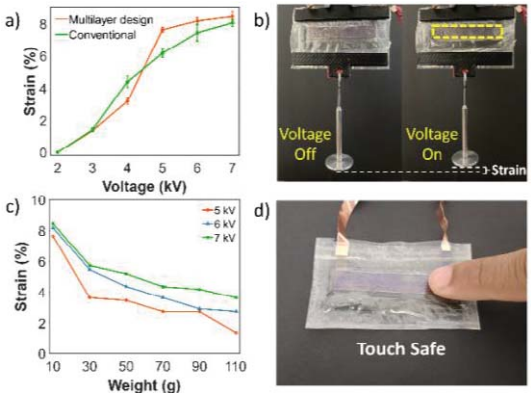


Figure 3: Strain performance characterization and demonstration of human-safe operation of the proposed multilayer actuator. a) Comparison of conventional and the proposed multilayer actuators, b) Image showing the strain under applied voltage, c) Strain-weight curve at different voltage, d) Demonstration of safe human contact on the zipped electrode region while the actuator is powered.

Along with mechanical robustness and safety, another important characteristic of soft actuator is the ability to respond quickly along a broad frequency range without compromising the actuation amplitude. The multilayered actuator exhibited a normalized strain over 75 % up to 7 Hz, demonstrating its capability for high-frequency operation (**Figure 4a**). The device exhibited a fast response time (60 ms) and quick recovery time (120 ms), highlighting its suitability for dynamic actuation in wearable devices and robotics (**Figure 4b**). To evaluate the operational stability, cyclic loading test was performed for 5000 cycles, with the actuator retaining over 85 % of its performance, indicating high reliability for long term operations (**Figure 4c**).

Overall, these results demonstrate that the multilayered actuator design achieves comparable mechanical performance while offering fast, repeatable actuation and enhanced safety, making it suitable for dynamic, wearable applications and underwater applications.

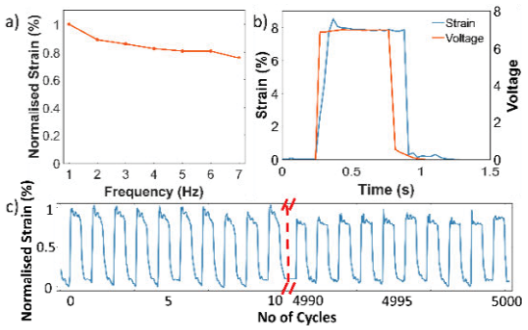


Figure 4: Repeatability and time response of the actuator. a) Actuator response across various frequencies, b) Response time of the actuator, highlighting actuation and recovery time, c) Cyclic actuation up to 5000 cycles, demonstrating long term stability.

To further highlights the underwater applicability of the multilayered actuator, a bio-inspired fish-tail actuator was fabricated. The fish tail was designed based on lunar tail concept and fabricated using a TPU (1 mm thickness) via an FDM 3D printer (Ultimaker S5). A multilayered electrohydraulic actuator of 13 in length and 9.5 cm in width, featuring a quarter circle electrode with an 8 cm diameter, was subsequently integrated with the fish tail. The actuator was filled by 7 ml of FR 3 oil, which was displaced toward the non-electrode region upon application of voltage, resulting into the bending of the tail (**Figure 5a**). This configuration enabled unidirectional motion of the fish tail in water and exhibited controllable bending angles at various corresponding voltages. The fish tail achieved a maximum of 17-degree angle at 7 kV, demonstrates its effectives for underwater applications (**Figure 5b**).

 DOI: 10.30420/456743027

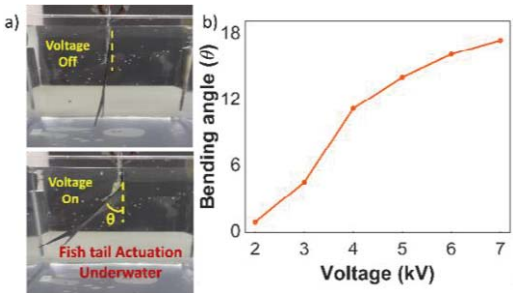


Figure 5: Demonstration of underwater fish tail actuation. a) Illustration of fish tail bending underwater under different actuation states (Off and on), b) Bending angle of the fish as a function of applied voltage.

4 Conclusion

The multilayered actuator design presented in this work effectively embeds without compromising actuation performance. The actuator demonstrated the ability to lift loads upto 40 times of its own weight while maintaining a safe-to-touch operation. Furthermore, its quick response, wide frequency range and stable long-term operation highlights its suitability for dynamic applications in wearables systems and robots. The successful demonstration of bio-inspired fish tail actuator further emphasizes its applicability in underwater environments. Overall, the proposed multilayered design significantly improves both the safety and functional versatility of electrohydraulic actuators, offering a promising approach for next generation soft robots. However, there remains room for improvement in operating voltage of these actuators. Through the careful selection of high-permittivity (high k) functional dielectric material, the required actuation voltage can be lowered. Additionally, employing structural material with higher dielectric strength material can enhance high-voltage performance by minimizing the risk for electrical breakdown.

5 References

[1] Y. Jung, K. Kwon, J. Lee, and S. H. Ko, "Untethered soft actuators for soft standalone robotics," *Nature Communications 2024 15:1*, vol. 15, no. 1, pp. 3510-, Apr. 2024, doi: 10.1038/s41467-024-47639-0.

[2] N. Kellaris, V. G. Venkata, G. M. Smith, S. K. Mitchell, and C. Keplinger, "Peano-HASEL actuators: Muscle-mimetic, electrohydraulic transducers that linearly contract on activation," *Sci. Robot.*, vol. 3, no. 14, p. 3276, Jan. 2018, doi: 10.1126/SCIROBOTICS.AAR3276.

[3] S. Conrad *et al.*, "3D-printed digital pneumatic logic for the control of soft robotic actuators," *Sci. Robot.*, vol. 9, no. 86, Jan. 2024, doi: 10.1126/SCIROBOTICS.ADH4060.

[4] S. Sridar *et al.*, "Hydro Muscle -a novel soft fluidic actuator," *Proc. IEEE Int. Conf. Robot. Autom.*, vol. 2016-June, pp. 4014–4021, Jun. 2016, doi: 10.1109/ICRA.2016.7487591.

[5] C. Gupta, A. O. Krushynska, B. Jayawardhana, L. Cheng, and A. G. P. Kottapalli, "Soft bionic actuation explains the functional role of whisking in seal whisker sensing," *npj Flexible Electronics 2026*, Mar. 2026, doi: 10.1038/s41528-026-00565-1.

[6] X. Wang *et al.*, "High-Strain Peano-HASEL Actuators," *Adv. Funct. Mater.*, vol. 30, no. 7, p. 1908821, Feb. 2020, doi: 10.1002/ADFM.201908821.

[7] D. Tang *et al.*, "Origami-inspired magnetic-driven soft actuators with programmable designs and multiple applications," *Nano Energy*, vol. 89, p. 106424, Nov. 2021, doi: 10.1016/J.NANOEN.2021.106424.

[8] X. Tian, Y. Guo, J. Zhang, O. M. Ivasishin, J. Jia, and J. Yan, "Fiber Actuators Based on Reversible Thermal Responsive Liquid Crystal Elastomer," *Small*, vol. 20, no. 24, Jun. 2024, doi: 10.1002/SMLL.202306952.

[9] Z. Han *et al.*, "Dual pH-Responsive Hydrogel Actuator for Lipophilic Drug Delivery," *ACS Appl. Mater. Interfaces*, vol. 12, no. 10, pp. 12010–12017, Mar. 2020, doi: 10.1021/ACSAMI.9B21713.

[10] M. Duduta, E. Hajiesmaili, H. Zhao, R. J. Wood, and D. R. Clarke, "Realizing the potential of dielectric elastomer artificial muscles," *Proc. Natl. Acad. Sci. U. S. A.*, vol. 116, no. 7, pp. 2476–2481, Feb. 2019, doi: 10.1073/PNAS.1815053116.

[11] S. K. Mitchell, T. Martin, and C. Keplinger, "A Pocket-Sized Ten-Channel High Voltage Power Supply for Soft Electrostatic Actuators," *Adv. Mater. Technol.*, vol. 7, no. 8, Aug. 2022, doi: 10.1002/ADMT.202101469.

[12] F. Zhou *et al.*, "Fabrication and modeling of dielectric elastomer soft actuator with 3D printed thermoplastic frame," *Sens. Actuators A Phys.*, vol. 292, pp. 112–120, Jun. 2019, doi: 10.1016/J.SNA.2019.02.017.

[13] R. Pelrine, R. Kornbluh, Q. Pei, and J. Joseph, "High-speed electrically actuated elastomers with strain greater than 100%," *Science*, vol. 287, no. 5454, pp. 836–839, Feb. 2000, doi: 10.1126/SCIENCE.287.5454.836.

[14] S. K. Mitchell *et al.*, "An Easy-to-Implement Toolkit to Create Versatile and High-Performance HASEL Actuators for Untethered Soft Robots," *Advanced Science*, vol. 6, no. 14, Jul. 2019, doi: 10.1002/ADVS.201900178.

[15] H. J. Joo *et al.*, "Ultralight soft electrostatic actuators based on solid-liquid-gas architectures," *Nature Communications 2026 17:1*, vol. 17, no. 1, pp. 1929-, Feb. 2026, doi: 10.1038/s41467-026-69463-4.

[16] C. Gupta, W. Hogenboom, B. Jayawardhana, and A. G. P. Kottapalli, "Inkjet-printed Electrohydraulic Actuator," *Proceedings of IEEE Sensors*, 2024, doi: 10.1109/SENSORS60989.2024.10784630.

[17] T. Wang, H. J. Joo, S. Song, W. Hu, C. Keplinger, and M. Sitti, "A versatile jellyfish-like robotic platform for effective underwater propulsion and manipulation," *Sci. Adv.*, vol. 9, no. 15, Apr. 2023, doi: 10.1126/SCIADV.ADG0292.

[18] N. Sanchez-Tamayo, Z. Yoder, P. Rothemund, G. Ballardini, C. Keplinger, and K. J. Kuchenbecker, “Cutaneous Electrohydraulic (CUTE) Wearable Devices for Pleasant Broad-Bandwidth Haptic Cues,” *Advanced Science*, vol. 11, no. 48, p. 2402461, Dec. 2024, doi: 10.1002/ADVS.202402461.

[19] S. D. Gravert *et al.*, “Low-voltage electrohydraulic actuators for untethered robotics,” *Sci. Adv.*, vol. 10, no. 1, p. 9319, Jan. 2024, doi: 10.1126/SCIADV.ADI9319.

 DOI: 10.30420/456743028

Three-phase SMA model with optimized fit for both strain and resistance

M.Sc. Max Hauber, Aalen University of Applied Sciences, Aalen, Germany
Dipl.-Ing. Markus Köpfer, Actuator Solutions GmbH, Gunzenhausen, Germany
Dipl.-Ing. Tobias Schumm, Actuator Solutions GmbH, Gunzenhausen, Germany
Prof. Dr.-Ing. Arif Kazi, Aalen University of Applied Sciences, Aalen, Germany

Abstract

In recent years, actuators based on Shape Memory Alloys (SMA) have become increasingly popular in various application fields. Both the design and the control of advanced actuators require SMA models that predict both mechanical strain and electrical resistance in response to changes in temperature and stress. Current SMA models typically focus on the phase transformations between the low-temperature martensite and high-temperature austenite phase. However, the formation of a third intermediate R-phase during cooling also has a significant impact on electrical resistance.
[1] presented an SMA model based on transformation surfaces that includes the relevant phase transformations between martensite, austenite, and the R-phase. Although the model achieved a good fit with experimental data for strain and resistance during cooling, discrepancies emerged during heating. This paper analyzes how an improved parameterization procedure can optimize the fit of the model during heating. The simulation results are compared with the experimental data.

1 Introduction

Innovative actuators driven by thin SMA wires provide benefits such as light weight, ease of miniaturization, high energy density, and noiseless actuation. SMA wires also change their electrical resistance with phase transformation, paving the way towards self-sensing actuator concepts. Nevertheless, the highly non-linear and hysteretic behavior of the SMA material poses significant challenges. SMA models to be used in advanced control schemes should reflect the complex behavior of SMA wires accurately, while being able to run on standard microcontrollers in real-time.
Macroscopic phenomenological SMA models that incorporate the phase transformation between martensite, austenite and also the R-phase have been proposed, but typically do not reflect the electrical resistance [2–6]. The phase-diagram-based model introduced in [7] accounts for electrical resistance, but is based on predefined decision paths to determine whether the R-phase will form. This approach does not represent the general case with variable degrees of R-phase formation. In [1], a three-phase SMA model based on transformation surfaces was presented that is capable of predicting both SMA wire strain and electrical resistance simultaneously. For the sake of simplicity, the phase transformations from martensite to austenite and from the R-phase to austenite used the same parameters. Although the resulting model accurately reproduced the experimental data during cooling, a noticeable discrepancy between the simulated and measured responses persisted during heating. The discrepancy is assumed to be caused by the pronounced influence of the R-phase on the specific electrical resistance at high temperatures. The present work builds upon this model and analyzes whether the independent parameterization of the martensite to austenite and the R-phase to austenite phase transformations can improve model accuracy.

2 Three-phase SMA model

Free energy-based SMA models typically involve time consuming iterative calculations, which make them appear less attractive for control purposes. Phase diagram-based models are usually computationally less demanding. However, conventional phase diagram-based SMA models may not be able to represent the contraction and electrical resistance behavior of the SMA wires with a sufficient degree of accuracy. [1] extends the concept of phase diagrams to transformation surfaces, which also reflect the variation of the shape of the phase transformation with the stress level. The novel ‘ihyp’ transformation function [8] was used to accurately model the measured transformation surfaces. The presented three-phase model covers both the formulation of the transformation processes between the individual phase fractions and the interactions between these processes. Figure 1 provides a schematic overview of the phase fractions with the phase transformations assigned.

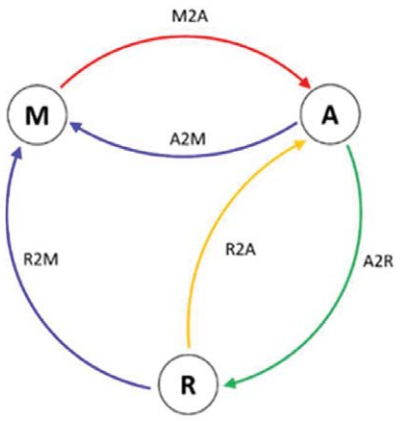


Figure 1 The three phase fractions martensite, austenite and R-phase with associated phase transformations processes.

 DOI: 10.30420/456743028

In Figure 1, ‘M’ stands for martensite, ‘A’ for austenite, and ‘R’ for the R-phase. Conventional two-phase models account for the transformation from martensite to austenite (‘M2A’) and vice versa (‘A2M’). When the R-phase is considered, austenite to R-phase (‘A2R’), R-phase to austenite (‘R2A’) and R-phase to martensite (‘R2M’) phase transformations need to be added. In [1], no indications were found for a sixth phase transformation from martensite to R-phase. Several of these phase transformation processes may occur simultaneously. Simultaneous phase transformation processes either act independently when sharing the same target phase fraction (e.g., A2M and R2M), or compete for the available initial phase fraction (A2M and A2R).

3 Improved Model Parameterization

The three-phase model introduced in [1] includes all five phase-transformation processes described in the previous section. For the sake of simplicity, the same parameters were used for the M2A and R2A phase transformations. The model achieved a good fit with experimental data for strain and resistance during cooling. However, discrepancies emerged during heating. This section examines how the parameterization process can be refined in order to improve model accuracy during heating.

The existing model is calibrated to experimental data recorded between a ‘practically fully austenitic’ state (defined at 150 °C) and a ‘practically fully martensitic’ state (defined at 20 °C), which will however still contain a small amount of R-phase. The experimental data were obtained from a highly precise test setup comprising a temperature-controlled silicone oil bath [9]. The parameter identification procedure begins by fitting the mechanical and electrical parameters associated with each phase fraction. Subsequently, the transformation temperatures are adjusted to the temperature regions where the rates of change in strain and specific resistance are at their maximum. In the final step, the curvature and asymmetry parameters of the transformation function [8] are adjusted.

Once a satisfactory parameter set has been obtained, these values are used as the starting point for the parameterization at the next higher stress level. The outcome of this procedure is a set of support points that are used to fit the functional relationships between each model parameter and the applied stress.

The objective of this study is to parameterize the R2A transformation individually. For this purpose, an experimental condition with a maximum content of R-phase is required. This condition was identified as the point on the cooling trajectory at the minimum stress level when the specific resistance is at its maximum. From this point on, phase transformation towards austenite is initiated by heating the wire at constant stress. Figure 2 presents the trajectories with the measured strain (left) and the measured specific resistance (right) at a stress level of 10 MPa, using the color scheme of Figure 1.

During the initial heating process (‘M2A’), the changes in strain and specific electrical resistance both occur at a temperature of around 77 °C. During cooling, the A2R transformation first induces an increase in specific resistance starting at 80 °C, followed by the R2M transformation, which leads to the elongation of the SMA wire around 45 °C. At 45 °C, the specific resistance is also at its maximum. The heating trajectory of the R2A transformation will need to start from this point.

In the first step of the parameterization process, the M2A, A2M, A2R, and R2M transformations are fitted using the iterative procedure described above. Then the R2A parameters are adapted to the inner hysteresis loop shown in Figure 2. The R2A transformation temperatures obtained from this step are close to the A2R transformation temperatures, but increased by around 4 °K. This observation is consistent with the findings reported in [2, 3, 7]. Compared to the original model, the R2A transformation temperatures in the optimized model are substantially decreased. Consequently, the influence of the residual R-phase during heating on the electrical resistance at temperatures above 80 °C is significantly reduced.

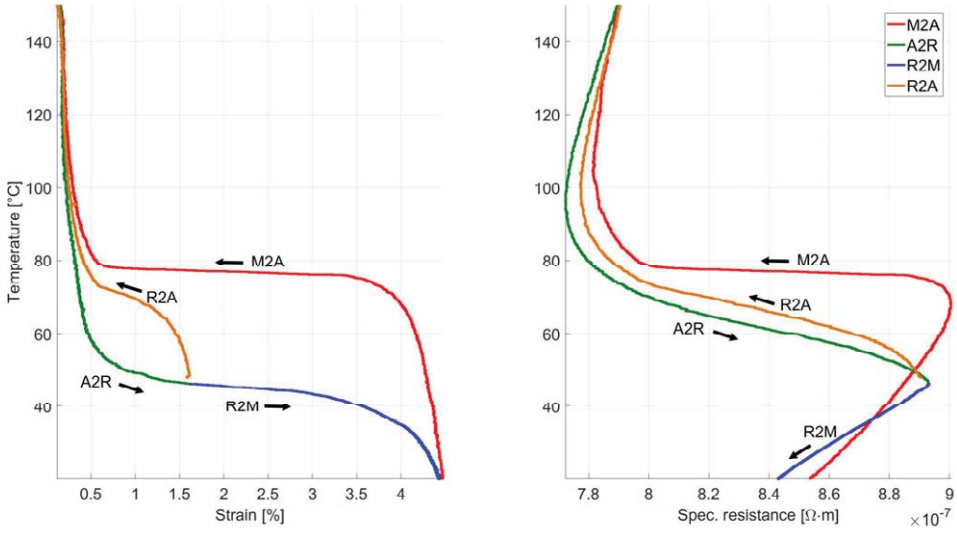


Figure 2 Recorded strain and specific resistance data sorted by phase transformation processes

 DOI: 10.30420/456743028

4 Simulation results

This section assesses the model's ability to accurately predict the experimentally measured strain and specific resistance. To investigate whether the fit during heating is improved, we first compare the optimized model with the original model and the experimentally measured data at a low stress level where the R-phase formation will be most pronounced. Second, the simulation results are compared with experimentally measured data at various stress levels to assess the overall accuracy.

Figure 3 shows the simulation results of both the original and optimized model along with the measured strain (left) and specific resistance (right) at a stress level of 10 MPa. Both models reproduce the steep transitions associated with the changes in strain and specific electrical resistance, as well as the smoother, rounded curvature towards high and low temperatures. In addition, both models accurately capture the changes in specific resistance that occur prior to the elongation of the SMA wire during cooling. When comparing the simulation results of the original and optimized model, the strain data show a high degree of consistency. In contrast, the simulated specific resistance exhibits a pronounced discrepancy. The heating trajectory of the original model underestimates the experimentally measured specific resistance and almost intersects the cooling trajectory at approximately 90 °C (**A**). The optimized model substantially improves the agreement with the experimental data, as the predicted trajectory remains at a higher specific resistance (**B**).

In a second analysis, the agreement between the simulated results and the experimentally measured data is examined at higher stress levels. Figure 4 shows the simulation results of the optimized model and the experimentally measured strain (left) and specific resistance (right) in a three-dimensional representation. For better clarity, only the trajectories spaced in 50 MPa intervals are displayed.

Overall, the simulation results and the experimental data are in good agreement.

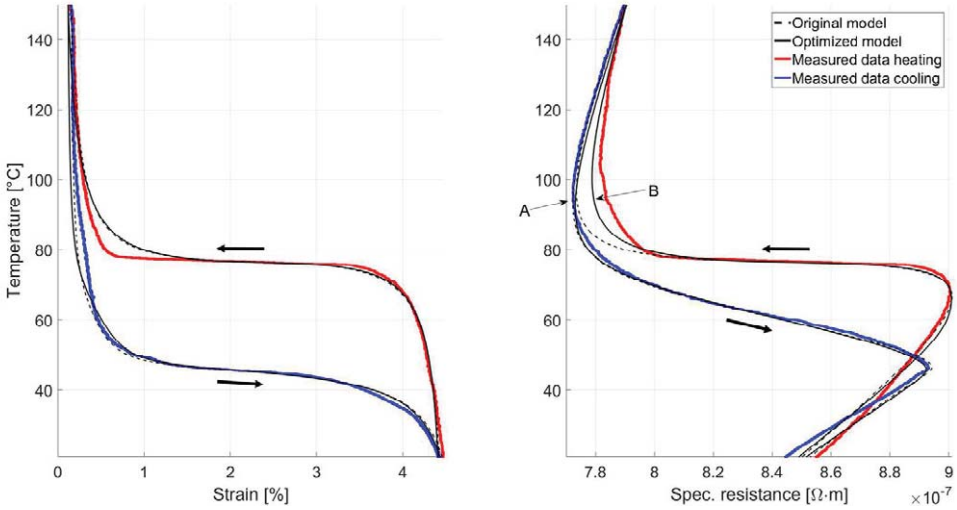


Figure 3 Simulation results of original model (black dotted) and optimized model (black solid) compared to measured data of heating (red) and cooling (blue) at 10 MPa stress level.

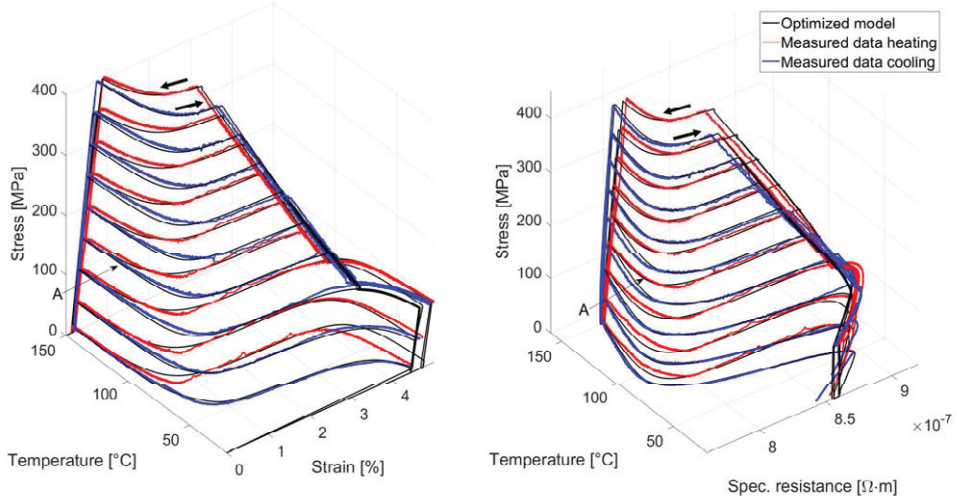


Figure 4 Simulation results of optimized model (black solid) compared to measured data of heating (red) and cooling (blue) in a three-dimensional representation

The transformation characteristics of the measured data, such as the steepness of phase transformation or the curvature at both ends of the steep transition, vary with the applied stress.
This stress-dependent behavior is accurately reproduced by the model through an appropriate adjustment of the steepness and curvature of the underlying transformation surface. With increasing stress level, the deviation between the optimized model and the experimental data is reduced. At stress levels above 150 MPa, the initial discrepancy between the simulated and measured responses - originally motivating this study - is hardly observable (**A**). Compared to the original model proposed in [1], the individual parameterization of the M2A and R2A phase transformations significantly improves the agreement with the experimental data up to stress levels of 250 MPa.

5 Summary and outlook

This paper proposes an improved parameterization procedure to optimize the accuracy of a three-phase SMA model during heating. The underlying SMA model presented in [1] includes the three phase fractions of martensite, austenite and the R-phase with five different phase transformation processes in between. While the model achieved a good fit with the experimental data during cooling, discrepancies emerged during heating. In this paper, this problem is addressed by an independent parameterization of the phase transformation processes during heating.
The refined procedure builds on measured data of an inner hysteresis loop starting from a wire condition with maximum R-phase content, identified as the point during cooling at a minimum stress level where the specific resistance is at its maximum. This approach yields significantly lower transition temperatures for the phase transformation from R-phase to austenite than that assumed in [1]. The reduced transition temperatures lead to an increased electrical resistance above 80 °C, reducing the observed discrepancies between the simulated and measured electrical resistance. This is true for low stress levels, where the formation of the R-phase is most pronounced, but also for higher stress levels up to 250 MPa. In conclusion, this study shows that in a three phase SMA model, an independent parameterization of the M2A and R2A phase transformations is necessary to accurately model the behavior of the electrical resistance.
While the optimized model predicts outer hysteresis loops with sufficient degree of accuracy, measurements still show discrepancies for inner hysteresis loops. Current research seeks to adapt the model such that inner hysteresis loops are also captured accurately.

Acknowledgements

The authors wish to thank the German Ministry of Education and Research (BMBF) for funding this work within the context of the project SMArtMed (grant no. 13FH080KX1)

Declaration of conflicting interests

The authors declared no potential conflicts of interest with respect to the research, authorship, and/or publication of this article.

6 Literature

[1] M. Hauber and A. Kazi, "A three-phase SMA model based on transformation surfaces", *Journal of Intelligent Material Systems and Structures*, 2026, doi: 10.1177/1045389X261417975.

[2] A. Sengupta and P. Papadopoulos, "Constitutive modeling and finite element approximation of B2-R-B19′ phase transformations in Nitinol polycrystals", *Computer Methods in Applied Mechanics and Engineering*, Jg. 198, 41-44, S. 3214–3227, 2009, doi: 10.1016/j.cma.2009.06.004.

[3] P. Sedlák, M. Frost, B. Benešová, T. Ben Zineb and P. Šittner, "Thermomechanical model for NiTi-based shape memory alloys including R-phase and material anisotropy under multi-axial loadings", *International Journal of Plasticity*, Jg. 39, S. 132–151, 2012, doi: 10.1016/j.ijplas.2012.06.008.

[4] D. Rigamonti, A. Nespoli, E. Villa and F. Passaretti, "Implementation of a constitutive model for different annealed superelastic SMA wires with rhombohedral phase", *Mechanics of Materials*, Jg. 112, S. 88–100, 2017, doi: 10.1016/j.mechmat.2017.06.001.

[5] G. Helbert *et al.,* "A uniaxial constitutive model for superelastic NiTi SMA including R-phase and martensite transformations and thermal effects", *Smart Mater. Struct.*, Jg. 26, Nr. 2, S. 25007, 2017, doi: 10.1088/1361-665X/aa5141.

[6] L. Wang, P. Feng, X. Xing, Y. Wu and Z. Liu, "A one-dimensional constitutive model for NiTi shape memory alloys considering inelastic strains caused by the R-phase transformation", *Journal of Alloys and Compounds*, Jg. 868, S. 159192, 2021, doi: 10.1016/j.jallcom.2021.159192.

[7] R. Brammajyosula, V. Buravalla and A. Khandelwal, "Model for resistance evolution in shape memory alloys including R-phase", *Smart Mater. Struct.*, Jg. 20, Nr. 3, S. 35015, 2011, doi: 10.1088/0964-1726/20/3/035015.

[8] A. Kazi, P. Frenzel and N. Bobic, *"Modelling the Stress-dependent Hysteresis of Shape Memory Alloys", ACTUATOR; International Conference and Exhibition on New Actuator Systems and Applications 2021, ISBN: 978-3-8007-5456-4*.

[9] A. Kazi, M. Hauber and M. Honold, "Thermomechanical characterization of phase transformation surfaces for thin SMA wires", *Journal of Intelligent Material Systems and Structures*, Jg. 34, Nr. 19, S. 2293–2306, 2023, doi: 10.1177/1045389X231174677.

 DOI: 10.30420/456743029

Pneumatic Cylinder Speed Control System using Particle-Excitation Flow Control Valve

Daisuke HIROOKA, Naomichi FURUSHIRO Tomomi YAMAGUCHI, Kansai University, Osaka, Japan
E-mail address : hirooka@kansai-u.ac.jp

Abstract

The authors have been developing a particle-excitation flow control valve using PZT element with the aim of application to small servo valves. The valve has the following advantages: small size, low weight, high responsiveness and continuous airflow control. In addition, we have developed this control valve, achieving proportional control. On the other hand, the characteristics of this control valve are affected by the pressure inside the valve, which makes it difficult to control the actuator stably. To address this issue, we propose using a feedback system for this control valve. In this report, we present a pneumatic cylinder speed control system that uses this valve to demonstrate a stable actuator control method.

1 Introduction

Pneumatic actuators have light weight and a high power/weight ratio compared to electromagnetic actuators and hydraulic actuators. Additionally, pneumatic actuators are characterised by their high compliance. In general, highly controllable devices like proportional flow control valves have large volume, heavy weight and low response. We have been developing a control valve using particle excitation by piezoelectric (PZT) elements, and this device can control air flow smoothly with small weight [1-3]. The authors succeeded in creating a proportional control valve by modifying these control valves [4]. This control valve uses a PZT element to vibrate the orifice plate, thereby moving the particles that function as the valve plug away from the orifice and controlling the valve opening area. This operating principle eliminates the need for a mechanism to hold the valve plug, making it easy to reduce the size and weight of the valve. Conversely, the holding force of the valve plug in this control valve is dependent on air pressure. Changes in internal pressure cause the orifice area of the valve to change. Consequently, the valve behavior becomes unstable while the actuator is operating. In this report, we present a stable actuator control method using this control valve and introduce a velocity control system for a pneumatic cylinder as an example.

2 Control system

2.1 Particle-excitation flow control valve

First, we explain the working principle of the particle-excitation flow control valve we have been researching [1-3]. The particle excitation valve consists of an orifice plate, a PZT elements, and particles. This valve controls the opening area to change the orifice plate vibration amplitude. Figure 1 shows a cross-sectional image of the flow control valve. In crossing stage, the particles seal the air flow by supplying air pressure (Fig. 1(a)). In the initial stage, the PZT element causes the orifice plate to vibrate, pulling the particles away from the orifices and opening them. The holding force of the valve plug are determined by the equation [1]. With m being the particle mass, r being the orifice radius, g being the acceleration due to gravity, and P being the applied air pressure, the holding force F on the orifice is as follows.

$$F = \pi r^2 P \pm mg \quad (1)$$

From equation (1), it can be seen that the holding force of the valve plugs depends on the air pressure. As a result, the opening area of the control valve is affected by air pressure change. Therefore, a dedicated control system is required to ensure stable operation of this control valve.

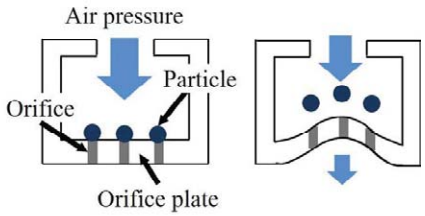


Figure 1 Basic working principle of particle excitation flow control valves

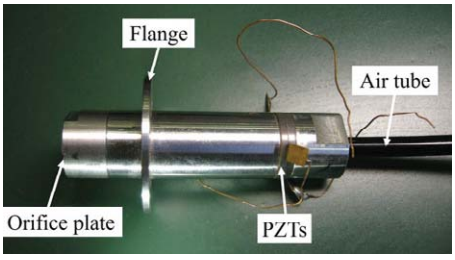


Figure 2 Prototype of the control valve

Figure 2 shows the prototype of the control valve. The main part of the prototype is the BLT, which is hollow and has an air chamber in contact with the orifice plate. The BLT has two ring-type PZTs for directional polarization of thickness, and this transducer generates longitudinal vibration. In this transducer, the tip acts as the antinode and the flange as the node of the wave. The orifice plate sits on top of the transducer and generates significant deformation. The prototype is 20 mm in diameter, 80 mm in length, and 150 g in weight. The prototype main body and orifice plate are made of stainless steel. The orifice plate has a diameter of 12 mm and a thickness of 1.2 mm. It has 12 orifices,

 DOI: 10.30420/456743029

each with a diameter of 0.4 mm. The orifices are positioned in such a way as to account for deformation of the orifice plate, thereby enabling proportional flow control [3]. The PZTs' outer diameters are 20 mm, inner diameters are 13 mm, and thicknesses are 2 mm. The prototype contains steel balls with a diameter of 0.8 mm. This prototype is capable of proportionally controlling flow rate under a constant air pressure.

2.2 Cylinder speed control system

Figure 3 shows the cylinder speed control system using this report. This system employs a meter-out method to regulate the exhaust air flow rate. In general, in the meter-out method, the cylinder velocity is proportional to the opening area on the exhaust side [4]. In this system, we think that implementing feedback control to maintain a constant cylinder speed would enable stable operation of the control valve. This system uses an encoder mounted on the cylinder to measure its speed. A microcomputer performs the speed calculation and feedback control. A function generator and a high-speed amplifier are used to generate the voltage applied to the control valve. Table 1 shows the details of the cylinders used in the experiment.

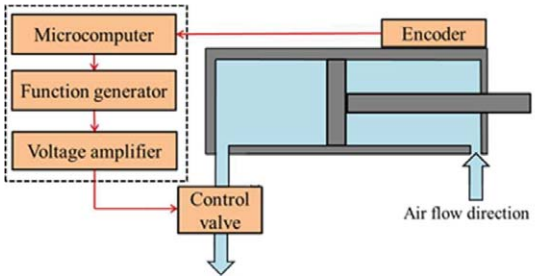


Figure 3 Cylinder speed control system

Table 1 Characteristics of the cylinder

Stroke	200 mm
Diameter	40 mm
Mass	1.64 kg

3 Experiment

Figure 4 shows the relationship between the voltage applied to the control valve and the cylinder speed, as measured in the experiment. The voltage applied to the control valve shall be 53.8 kHz, which is the resonant frequency of the transducer. As shown in Fig. 4, proportional control of the cylinder speed is possible within the range of 70 $V_{p\text{-}p}$ to 150 $V_{p\text{-}p}$. However, there is some variation in speed at 100 $V_{p\text{-}p}$, 120 $V_{p\text{-}p}$, and 140 $V_{p\text{-}p}$.We believe that this is caused by fluctuations in the pressure within the control valve. Figure 5 shows Cylinder speed with and without feedback control. We compare the case with constant voltage and the case with speed feedback at a target speed of 50 mm/s. When feedback is applied, the amplitude of the applied voltage is controlled within the range of 40 $V_{p\text{-}p}$ to 150 $V_{p\text{-}p}$ according to the cylinder's speed. In the absence of feedback, the voltage is kept constant at 100 $V_{p\text{-}p}$. From Fig. 5, the cylinder speed is stabilised by feedback control. We demonstrated that this control valve can respond to pressure fluctuations by using a control system.

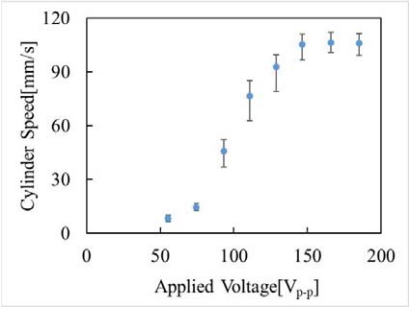


Figure 4 Relationship Between Cylinder Speed and Applied Voltage

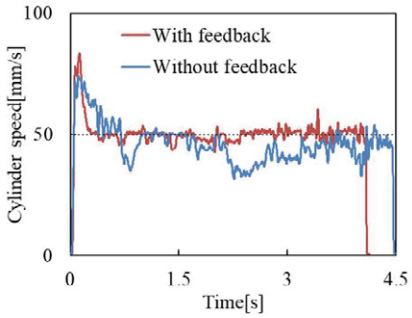


Figure 5 Results of the Cylinder Speed Feedback Control Experiment

4 Conclusion

In this report, we propose a method for the stable operation of the particle-excitation flow control valve. The method employed is a feedback control system for cylinder speed that generates an output proportional to the opening area. The results of the experiment demonstrated the potential for stable operation of the particle-excitation flow control valve through the use of feedback control.

5 References

[1] Daisuke. H. et al. : Flow control valve for pneumatic actuators using particle excitation by PZT vibrator, Sensors and Actuators A155, 2009, pp. 285-289

[2] Daisuke. H. et al. : Design and Evaluation of Orifice Arrangement for Particle-Excitaion Flow Control Valve, Sensors and Actuators A171, 2011 pp. 283-291

[3] Daisuke. H., et al. : Optimization of orifice position in particle-excitation valve for proportional flow control, Robomech Jounal Vol.4, 25, 2017, pp. 1-11,

[4] Toshinori, F., et al.: nalysis of Pneumatic Cylinder Responses Driven by Meter-out Circuit, Transactions of The Japan Hydraulics & Pneumatics Society Vol. 29, 4, 1998, pp.87-94 (in Japanese)

A steerable concentric push–pull suction device for single-port surgery

Finn Hoffmann[b], Robert Lathrop[a], Mouloud Ourak[a], Wouter Everaerts[c], Emmanuel Vander Poorten[a], and Paul Breedveld[b]
[a]Department of Mechanical Engineering, KU Leuven, Celestijnenlaan 300B, 3001 Leuven, Belgium
[b]Department of Mechanical Engineering, TU Delft, Mekelweg 2 2628 CD Delft, Netherlands
[c] Department of Urology, University Hospitals Gasthuisberg, Katholieke Universiteit Leuven, Herestraat 49 bus 802, B-3000 Leuven, Belgium

Abstract

This paper presents the design and evaluation of a lightweight steerable suction-irrigation system for single-port robotic surgery based on a concentric push-pull rod mechanism. The device was developed in two stages, progressing from a passive prototype to an actively actuated system using a pneumatically driven artificial muscle integrated with a notched flexible shaft. The final Steerable Suction Tube (SST) has a mass of 114 g and maintains a continuous suction lumen while enabling controlled tip bending. A benchtop surgical setup was used to evaluate actuation performance, fluid removal, and user workload. The system achieved distal tip deflections exceeding 90° with repeatable behaviour over a 0–6 bar pressure range. Comparative testing against a conventional ELEFANT suction device showed slightly improved fluid removal consistency and reduced variability. User evaluation using the Raw NASA-TLX ($n = 5$) indicated a tendency toward lower perceived workload for the SST, particularly in physical demand and effort, although results remain preliminary due to limited sample size and non-clinical conditions. Overall, the results demonstrate the feasibility of lightweight push-pull-based steering for suction tools in constrained surgical environments, while highlighting remaining challenges in control precision and ergonomics.

1 Introduction

Robotic surgery has become increasingly popular for various surgeries [1]. Intuitive's Da Vinci Xi is a common surgical robot, allowing 4 instruments through 4 ports. The Da Vinci Single-Port Access (SPA) system has recently entered the market and represents a major advancement in minimally invasive surgery, most commonly used for prostatectomy [2]. It allows three instruments plus a camera through a single port. Single Port (SP) surgery offers reduced invasiveness and shorter hospital stays [3]. However, since one arm is lost compared to the Xi, a suction arm or tube has to be maneuvered manually by an assistant standing next to the SPA system in the same port (see **Figure 1**) to remove excess blood or debris.

State-of-the-art suction devices, such as the ELEFANT by Coloplast, struggle to maneuver this new, more confined surgical workspace. In close collaboration with an academic surgeon, this paper explores a new type of steerable suction-irrigation device. The key requirements for the new instrument include: the ability to *(i)* operate as an add-on to make existing suction-irrigation devices steerable without impeding their normal function, *(ii)* maneuver around the other surgical instruments inside the body (see Figure 1) and *(iii)* offer a bending segment in 1 Degree of Freedom over at least 90 degrees of curvature.

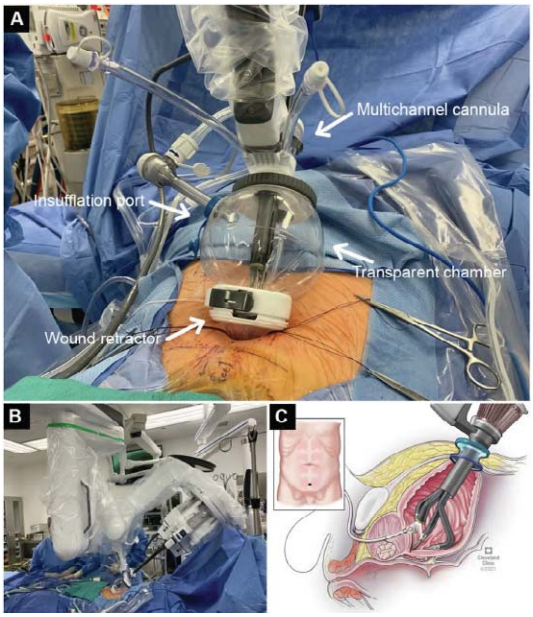


Figure 1 Example of surgery setup. A: setup of the entry port. B: Single Port overview. C: Illustration of robot inside bladder. Reproduced from Ramos-Carpinteyro et al. [4], licensed under CC BY-NC-ND 4.0.

2 Methodology

2.1 Prototype design

Cables in multilumen tubes can lead to large friction and actuation forces in bends [5], and notched nitinol tubes combined with cables can be complex, so a continuous push-pull segment was chosen [6]. A first prototype was 3D-printed in PLA on a Bambulab A1 (0.4 / 0.2 mm nozzle). (see **Figure 3**). The prototype features an ergonomic

 DOI: 10.30420/456743030

grip and a finger-operated trigger that adjusts the curvature of the distal segment. The hollow system accommodates a suction tube. Tube dimensions are stated in **Table 1**. The basics of a CPP segment are illustrated in **Figure 2**. The length of the overall shaft is 213 mm, and the flexible end is 78 mm in length with 20 notches. Representative bending angles are illustrated in **Figure 8**.

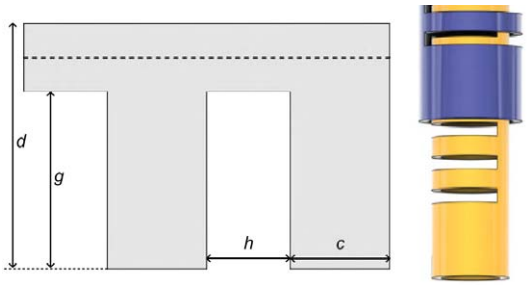


Figure 2 Left: notched tube. d=outer diameter, g=notch height, h=gap width, c=notch width. Dashed line illustrates the neutral axis. Right: two tubes assembled.

Table 1 Specification for tubes.

Specification	Outer tube [mm]	Inner tube [mm]
d	11.3	8.5
g	10.3	7.5
h	1.5	1.5
c	2.1	2.1

2.2 Activation and verification

To avoid fatigue by the operator, the addition of a Pneumatic Artificial Muscle (PAM) was explored. A test setup incorporating a Festo DMSP-5-100N-AM-CF actuator was developed. The PAM controls the curvature of the distal segment, while the setup is used to assess its actuation range. The artificial muscle connects to the inner tube of the continuous push-pull (CPP) segment and directly controls its translation.

2.3 Steerable suction tube (SST)

After successful testing, a pneumatically actuated suction device was developed, named the Steerable Suction Tube (SST). The device can be seen in **Figure 4**. This new device features a longer tube of 318 mm and a Pneumatic Artificial Muscle embedded inline with the inner tube. An adjustable potentiometer is used to control the deflection angle of the tip. It allows for constant repositioning of the distal tip from 0°to over 90°, similar to the prototype. The system is connected to an auxiliary Arduino R4, with a pressure regulator to handle the variable pressure of the PAM. The rest of this device is similar to the prototype of section 2.1, with a continuous suction tube running through the handle and a straight segment.

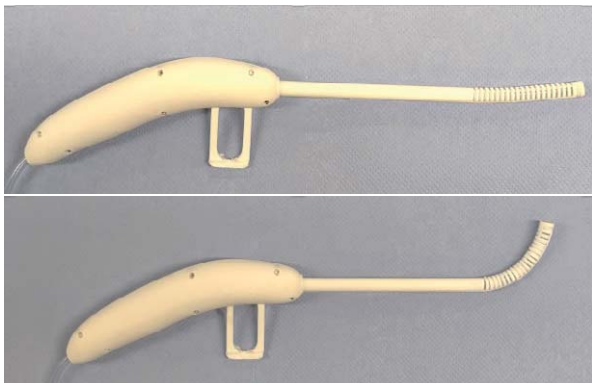


Figure 3 Photos of prototype showing the curved and straight segment.

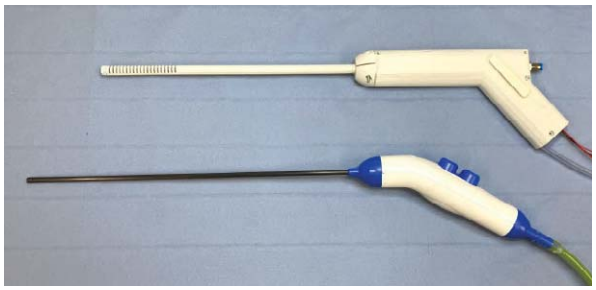


Figure 4 Above: improved Steerable Suction Tube. Below: ELEFANT by Coloplast, with an attached suction tube.

2.4 Surgery setup

To evaluate the performance of the SST relative to that of the ELEFANT, a dedicated experimental setup was constructed. The objective of the test was to assess both devices in terms of maneuverability as well as the associated cognitive and physical workload for the user.

A setup was designed consisting of a two-port access (d = 12.3 mm) into a simulated surgical environment. Within this workspace, 3D-printed structures are positioned to emulate arbitrary configurations of robotic surgical arms. A camera is mounted above the entry point, aligned centrally between the artificial arms, providing a top-down surgical view similar to an endoscopic perspective.

A custom-designed tray is placed beneath the simulated robotic arms (see Figure 6). The tray contains a water-based solution colored with food dye to enhance visual contrast. It is subdivided into multiple compartments representing different levels of accessibility and task difficulty. The central region and the outer annular segments each contain 2 ml of liquid, while the larger intermediate segments contain 8 ml. This spatial distribution is intended to replicate varying degrees of accessibility within a confined surgical field. Larger compartments are designed to be easily reachable, whereas smaller and more constrained regions introduce increased handling difficulty, where the potential advantage of an actuated suction device is expected to become more apparent.

To build a challenging test environment, three bigger op-

 DOI: 10.30420/456743030

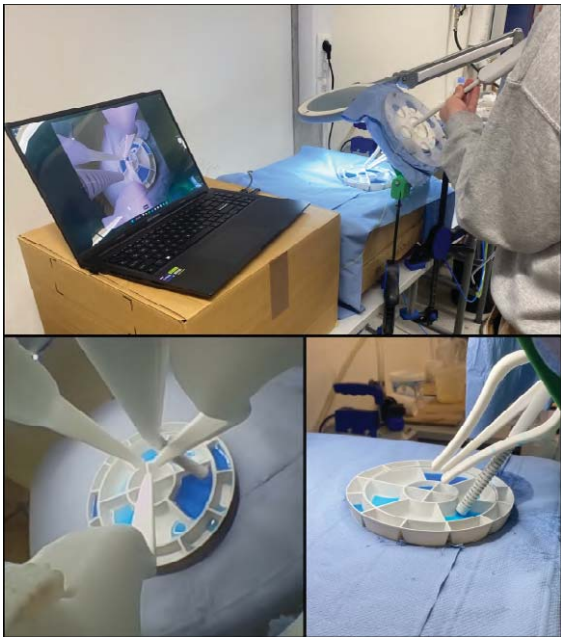


Figure 5 Full test setup. Top: test setup. Bottom left: camera view during test. Bottom right: side view of test setup.

posing segments, as well as one of the smaller inner segments of the tray, are filled with the liquid. Two segments of the far outer ring are also filled to challenge participants fully; see **Figure 6**. This way, the participants were forced to maneuver around the robotic arms. The order of device usage was randomized between participants to reduce learning-order effects. Five participants with no prior robotic surgery experience were recruited for the study. The goal of the test is to suck off all fluid present in the segments of the tray. Following a four-minute practice session, participants were given two minutes to clear the surgery area of all liquid, and the weight of the filled tray was measured before and after the test was completed. After each respective test, participants were asked to fill in a NASA-TLX questionnaire to assess mental and physical loads [7]. The final two-minute test was performed once per participant for each device.

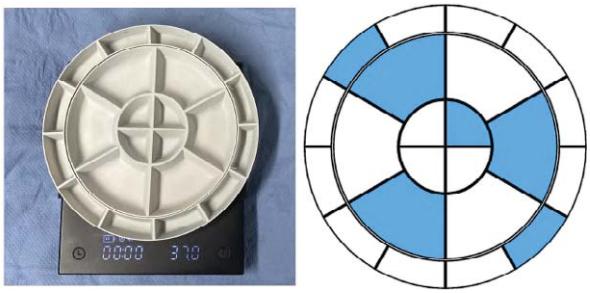


Figure 6 Left: custom tray. Right: illustration of the filled segments. The outer ring is made up of twelve bigger segments, the middle one is made up of six segments, and the smallest one is made up of four segments.

3 Experimental Results

3.1 Deflection test

To characterize the actuation behavior of the pneumatic artificial muscle (PAM), experiments were performed over a pressure range of 0 to 6 bar. This range corresponds to the operational limits of the system under manual actuation. The primary output metric is the distal tip angle, defined as the angular deflection of the end-effector relative to its neutral configuration. **Figure 7** shows the measured relationship between applied pressure and distal tip angle for three repeated trials.

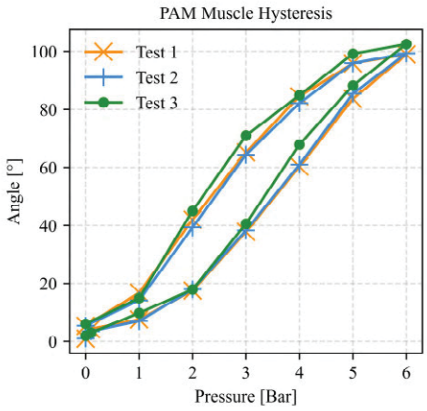


Figure 7 Plot showing the distal tip angle against pressure.

Across all trials, the distal tip angle increases with increasing pressure. The response is nonlinear, with smaller increments in angle at low pressures (0–2 Bar), larger incremental changes in the mid-range (approximately 2–5 Bar), and a reduced rate of change approaching the upper pressure limit. Variability between the three trials is observed at intermediate pressure levels, where the measured angles for identical pressure values are not identical across repetitions. However, at low (0–1 Bar) and high (5–6 Bar) pressure levels, the measurements are very repeatable between trials. **Figure 8** shows representative configurations of the distal segment at increasing pressure levels, illustrating the corresponding change in shape with actuation.

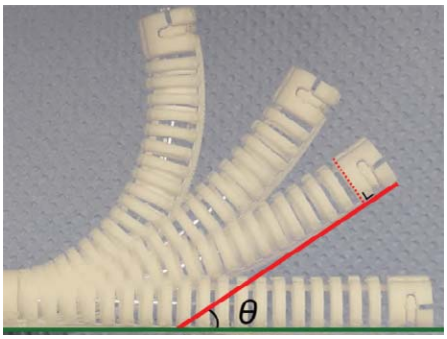


Figure 8 Selected images of the test visualizing a few different measured angles [°].

 DOI: 10.30420/456743030

3.2 Weight-Based Fluid Uptake Evaluation

To quantify the fluid removal performance of the custom tray, a pre- and post-test mass measurement was performed. The difference in mass was used to estimate the amount of liquid absorbed during the procedure. The mean fluid uptake can be seen in **Figure 9**. The absorbed fluid volume Δm was computed as:

$$\Delta m = m_{\text{initial}} - m_{\text{final}} \tag{1}$$

The Steerable Suction Tube demonstrated higher and more consistent fluid removal performance compared to the ELEFANT configuration. The reduced variance may indicate improved controllability of the distal suction orientation. However, the experimental setup does not fully replicate accurate fluid dynamics or tissue interaction encountered during surgery.

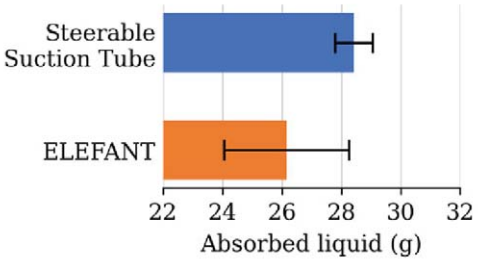


Figure 9 Mean and standard deviation of fluid uptake of each device [g].

3.3 Subjective Workload Assessment

Subjective workload was evaluated using the Raw NASA-TLX across six dimensions: mental demand, physical demand, temporal demand, performance, effort, and frustration. Each participant evaluated both devices after completing the task. Tests were performed with five participants over a period of two days. Averaged scores for both respective devices can be seen in **Figure 10**. Overall averaged scores were also determined and can be seen in **Figure 11**.

The SST resulted in lower workload scores across most NASA-TLX dimensions compared to the ELEFANT. The largest reductions were observed in physical demand and effort, whereas temporal demand showed smaller differences between devices. Inter-participant variability remained moderate, as indicated by the standard deviations in **Figure 10**.

Averaged Raw TLX scores are shown in **Figure 11**. The SST achieved a lower overall workload score compared to the ELEFANT device for four out of five participants. Individual participant scores are represented by white markers to illustrate the distribution of responses. The distribution of the scores differs slightly. The SST exhibits a wider spread of scores, whereas the ELEFANT shows a more compact distribution.

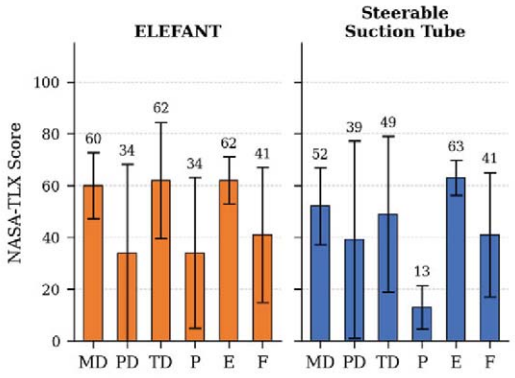


Figure 10 Mean Raw NASA-TLX subscale scores for both devices ($n = 5$). Error bars indicate one standard deviation. Lower scores correspond to lower perceived workload [7]. For the NASA-TLX performance metric, lower scores suggest improved perceived task performance. MD: Mental Demand, PD: Physical Demand, TD: Temporal Demand, P: Performance, E: Effort, F: Frustration.

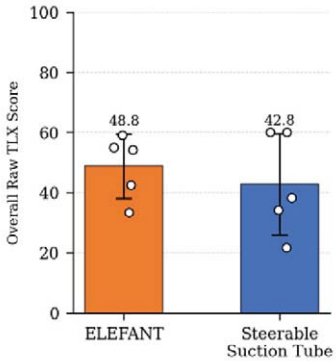


Figure 11 Mean overall Raw TLX scores for both devices. White markers indicate individual participant scores.

4 Discussion

4.1 Actuation Performance

The non-linear pressure-angle relationship observed in Figure 7 is consistent with the characteristic contraction behaviour of PAM-driven continuum structures. At low pressures, limited angular displacement may result from initial stiffness in the system. The slope in the mid-pressure range suggests more efficient force transmission once the actuator is fully engaged. The trials demonstrate comparable pressure-angle trajectories, indicating acceptable repeatability under quasi-static loading conditions.

Large distal articulation is particularly relevant for single-port procedures, where rigid instruments suffer from a restricted range. The demonstrated bending range may improve access behind structures, like the robotic arms of the Da Vinci SP.

4.2 Evaluation of ergonomics

Although the SST consistently produced lower raw TLX scores for most participants, the study population was limited ($n = 5$). Consequently, the workload findings should be interpreted as preliminary indications of improved ergonomics, rather than evidence of improvement. During testing, certain observations may also have impacted performance. The thicker shaft of the SST (d = 10.4 mm) struggled to enter and maneuver the two ports of the surgery setup, whereas the ELEFANT (d = 5.3 mm) allowed greater freedom of movement. Furthermore, control of the PAM proved challenging, since the distal tip did not articulate gradually but instead transitioned more abruptly from 0° to 90°. This limited fine positional control during manipulation.

4.3 Limitations

Several limitations should be considered when interpreting the presented results. First, the study population was limited to five participants. This hinders robust statistical analysis of performance assessment and of the NASA-TLX results. Furthermore, experiments were conducted in a benchtop environment that only approximates the spatial constraints of single-port surgery. The fluid tests were performed using simplified fluid surrogates and therefore do not fully replicate physiological conditions encountered during surgery. The study also did not evaluate distal tip force, long-term durability, sterilization compatibility, or fatigue behaviour of the actuator system.

4.4 Future Work

Future work will focus on reducing the shaft diameter to improve maneuverability within the port and potentially higher maneuverability in the surgery space. With the use of nitinol notched tubes, significant reduction of the diameter would be possible. An additional degree of Freedom, in the form of a rotation of the shaft, may further improve ergonomics. If implemented at the top of the grip and positioned within easy reach of the index or middle finger, such a mechanism could reduce wrist strain associated with awkward hand and wrist postures during manipulation.

5 Conclusion

This paper presented a steerable suction-irrigation device for single-port robotic surgery, based on a concentric push-pull mechanism actuated by a pneumatic artificial muscle. The prototype achieved distal tip deflections exceeding 90° and demonstrated repeatable actuation behaviour under quasi-static loading conditions. Preliminary user testing with the Steerable Suction Tube suggested reduced perceived workload and improved fluid removal performance compared to the ELEFANT device. Future work will focus on shaft miniaturization and further validation in more clinically representative environments.

Acknowledgements

The authors would like to acknowledge the contributions of Edwin Arnalsteen and Louis Pante, whose continued development of the project after the initial prototype phase supported the ongoing refinement of the system.

6 Literature

[1] Yeisson Rivero-Moreno, Sophia Echevarria, Carlos Vidal-Valderrama, Luigi Pianetti, Jesus Cordova-Guilarte, Jhon Navarro-Gonzalez, Jessica Acevedo-Rodríguez, Gabriela Dorado-Avila, Luisa Osorio-Romero, Carmen Chavez-Campos, and Katheryn Acero-Alvarracín. Robotic surgery: A comprehensive review of the literature and current trends. *Cureus*, 15(7), 2023.

[2] Richard J. Fantus, Andrew Cohen, Christopher B. Riedinger, Kristine Kuchta, Chi H. Wang, Katharine Yao, and Sangtae Park. Facility-level analysis of robot utilization across disciplines in the national cancer database. *Journal of Robotic Surgery*, 13(2):293–299, 2019.

[3] Antonio Franco, Antony A. Pellegrino, Cosimo De Nunzio, Morgan Salkowski, Jamal C. Jackson, Lucas B. Zukowski, Enrico Checcucci, Srinivas Vourganti, Alexander K. Chow, Francesco Porpiglia, Jihad Kaouk, Simone Crivellaro, and Riccardo Autorino. Single-port robot-assisted radical prostatectomy: Where do we stand? *Current Oncology*, 30(4):4301–4310, 2023.

[4] Roxana Ramos-Carpinteyro, Ethan L. Ferguson, Jaya S. Chavali, Albert Geskin, and Jihad Kaouk. First 100 cases of transvesical single-port robotic radical prostatectomy. *Asian Journal of Urology*, 10(4):416–422, 2023.

[5] Xiaohua Hu, Ang Chen, Yigang Luo, Chris Zhang, and Edwin Zhang. Steerable catheters for minimally invasive surgery: A review and future directions. *Computer Assisted Surgery*, 23(1):21–41, 2018.

[6] Kaitlin Oliver-Butler, Jake A. Childs, Adam Daniel, and D. Caleb Rucker. Concentric push–pull robots: Planar modeling and design. *IEEE Transactions on Robotics*, 38(2):1186–1200, 2022.

[7] Sandra G. Hart and Lowell E. Staveland. Development of NASA-TLX (task load index): Results of empirical and theoretical research. In Peter A. Hancock and Najmedin Meshkati, editors, *Human Mental Workload*, volume 52 of *Advances in Psychology*, pages 139–183. North-Holland, 1988.

 DOI: 10.30420/456743031

Lumped modelling of loss mechanisms in piezoelectric transducers

Jan Holterman, VIRO, Hengelo, The Netherlands
Bas Jansen and Henry Schmidt, ASML, Veldhoven, The Netherlands
j.holterman@viro-group.com

Abstract

A lumped-parameter model is introduced to describe a piezoelectric transducer, so as to explicitly visualize energy storage in both the mechanical and the electric domain, as well as two-way energy conversion between these domains. As this 'symmetric' model can easily be extended with energy dissipation elements, it allows for an intuitive interpretation of both dielectric and elastic loss (both extensive and intensive) and their impact on the dynamic behaviour of a piezoelectric transducer in terms of its electric impedance. The model is validated for a piezoelectric circular disc in radial vibration.

1 Introduction

1.1 Piezoelectric energy efficiency analysis

In many applications of piezoelectric transducers energy efficiency is a key design parameter, especially in high-frequency and high-power applications. For efficient energy conversion through a piezoelectric transducer, three conversion steps should be optimized:

1) energy transfer from the power source to the transducer, by appropriate impedance matching;
2) energy conversion within the transducer from the mechanical to the electric domain or vice versa;
3) energy transfer from the transducer to the load, again by appropriate impedance matching.

In this paper we focus on energy conversion within the piezoelectric transducer (2), whereas impedance matching (1 and 3) will only be mentioned briefly in section 3.4.

As in any transducer operating between two physical domains, energy transfer in a piezoelectric transducer takes place via consecutive energy conversion cycles; see e.g. [1]. For analyzing the efficiency of such energy conversion cycles two aspects should be distinguished:

2a) conversion ratio: upon each cycle, how much of the input energy is transferred from the electric domain to the mechanical domain or vice versa?
2b) dissipation: upon each cycle, how much energy is lost as heat, i.e., converted to the thermal domain?

The key parameter for the energy conversion ratio (2a) is the effective *coupling factor* of the piezoelectric transducer, which is in turn determined by the coupling factor of the piezoelectric material for the specific operating mode (e.g. k_{33}, k_{31}, k_t) and the geometry of the transducer (e.g. a multilayer stack or a disc). The key parameters for dissipation (2b) are the *loss tangents* of the piezoelectric material. Piezoelectric matrix equations and material parameters are revisited in section 2.

1.2 Lumped-parameter models: symmetric versus asymmetric model structure

For a practical piezoelectric transducer, the coupling factor and the loss tangents are typically determined from dynamic electric impedance measurements, in terms of its capacitance and its resonance and anti-resonance frequencies and associated quality factors. Moreover, for interpretation of the measured impedance, typically an equivalent electric circuit model is used, often with lumped elements with parameter values to match the observed resonant behaviour of one or more vibration modes of interest; see e.g. [2-5].

The equivalent electric circuit in its simplest form is known as the Butterworth-Van Dyke (BVD) model [4]. In section 3 we will argue that the structure of this model is 'asymmetric' and that, as a consequence, BVD-like models do not allow for an intuitive interpretation of storage, conversion, and dissipation of energy in a piezoelectric transducer. For energy efficiency analysis we therefore advocate the use of a 'symmetric' lumped-parameter model. In section 4 this model is experimentally validated for a piezoelectric circular disc in radial vibration.

2 Piezoelectric material parameters

2.1 Intensive and extensive parameters

Depending on the choice of independent variables, the linear constitutive equations for piezoelectric materials (relating stress *T* and strain *S* to electric field *E* and electric displacement *D*) come in four different sets (so-called *d*/*e*/*g*/*h*-notation; see Table 1).

T and *E* are referred to as 'intensive' variables. Here we also refer to the material parameters in *d*-notation (s^E, ε^T, d), defined for constant *T* or *E*, as intensive parameters.

S and *D* are referred to as 'extensive' variables. Here we also refer to the material parameters in *h*-notation (c^D, β^S, h), defined for constant *S* or *D*, as extensive parameters.

In the scalar case, as implicitly assumed in Table 1, the constitutive equations describe the behaviour of a two-port storage element, i.e., an element that is able to:

- exchange power with its environment through both a mechanical port and an electric port;
- store energy from both the mechanical domain and the electric domain;
- convert part of the energy from the mechanical to the electric domain (direct piezoelectric effect) and vice versa (inverse piezoelectric effect).

For a lossless piezoelectric material, i.e., without energy dissipation, all parameters in Table 1 are real-valued.

ISBN: 978-3-8007-6743-4 @ VDE VERLAG GMBH · Berlin · Offenbach

 DOI: 10.30420/456743031

d-notation (intensive):

$$\begin{pmatrix} S \\ D \end{pmatrix} = \begin{bmatrix} s^E & d \\ d & \varepsilon^T \end{bmatrix} \begin{pmatrix} T \\ E \end{pmatrix} \quad (1)$$

$$k^2 = \frac{d^2}{s^E \varepsilon^T} \quad (2)$$

$$d = k\sqrt{s^E \varepsilon^T} \quad (3)$$

e-notation (mixed):

$$\begin{pmatrix} T \\ D \end{pmatrix} = \begin{bmatrix} c^E & -e \\ e & \varepsilon^S \end{bmatrix} \begin{pmatrix} S \\ E \end{pmatrix} \quad (4)$$

$$c^E = 1/s^E \quad (5)$$

$$e = d/s^E \quad (6)$$

$$\varepsilon^S = (1-k^2)\varepsilon^T \quad (7)$$

g-notation (mixed):

$$\begin{pmatrix} S \\ E \end{pmatrix} = \begin{bmatrix} s^D & g \\ -g & \beta^T \end{bmatrix} \begin{pmatrix} T \\ D \end{pmatrix} \quad (8)$$

$$\beta^T = 1/\varepsilon^T \quad (9)$$

$$g = d/\varepsilon^T \quad (10)$$

$$s^D = (1-k^2)s^E \quad (11)$$

h-notation (extensive):

$$\begin{pmatrix} T \\ E \end{pmatrix} = \begin{bmatrix} c^D & -h \\ -h & \beta^S \end{bmatrix} \begin{pmatrix} S \\ D \end{pmatrix} \quad (12)$$

$$c^D = 1/s^D \quad (13)$$

$$\beta^S = 1/\varepsilon^S \quad (14)$$

$$k^2 = \frac{h^2}{c^D \beta^S} \quad (15)$$

$$h = k\sqrt{c^D \beta^S} \quad (16)$$

$$h = \frac{1}{d}\frac{k^2}{1-k^2} \quad (17)$$

Table 1 Constitutive equations for piezoelectric materials

extensive parameters	intensive parameters	
$\beta^{S*} = \beta^S(1 + j\tan\delta)$	$\varepsilon^{T*} = \varepsilon^T(1 - j\tan\delta')$	(18a,b)
$c^{D*} = c^D(1 + j\tan\phi)$	$s^{E*} = s^E(1 - j\tan\phi')$	(19a,b)
$h^* = h(1 + j\tan\theta)$	$d^* = d(1 - j\tan\theta')$	(20a,b)

Table 2 Material parameters including loss tangents

2.2 Conversion ratio: coupling factor

For a transducer described as a two-port storage element the key parameter for the energy conversion ratio is the coupling factor k. For piezoelectric materials the coupling factor is given by eq. (2) and (15). The extensive and the intensive material parameters are related through the coupling factor as illustrated by eq. (7), (11), and (17).

2.3 Dissipation parameters: loss tangents

Dissipation in piezoelectric materials is typically due to hysteretic behaviour, which can be described mathematically by means of complex-valued material parameters (marked with *; see Table 2). To this end the dielectric, elastic, and piezoelectric parameters can be extended with respective loss tangents (or loss factors), representing the imaginary part of the material parameters.

Here we follow the naming and notation of Uchino [5-7] in order to distinguish between:

- extensive loss tangents: without prime;
- intensive loss tangents: with prime.

Note: Ikeda [2] refers to extensive loss as 'intrinsic' loss.

In the scalar case as above, the relation between the intensive and the extensive loss tangents is given by [5-7]:

$$\begin{pmatrix} \tan\delta' \\ \tan\phi' \\ \tan\theta' \end{pmatrix} = \boldsymbol{K} \begin{pmatrix} \tan\delta \\ \tan\phi \\ \tan\theta \end{pmatrix} \quad (21)$$

$$\boldsymbol{K} = \boldsymbol{K}^{-1} = \frac{1}{1-k^2} \begin{bmatrix} 1 & k^2 & -2k^2 \\ k^2 & 1 & -2k^2 \\ 1 & 1 & -1-k^2 \end{bmatrix} \quad (22)$$

3 Piezoelectric transducer models

3.1 Equivalent electric circuit models

Both the conversion ratio and the dissipation parameters for a piezoelectric transducer can appropriately be determined from dynamic electric impedance measurements, in terms of the capacitance and the resonance and anti-resonance frequencies and associated quality factors (see e.g. Fig. 6). For interpretation of the measured impedance typically an equivalent electric circuit is used, often with lumped parameter values to match the observed resonant behaviour of one or more vibration modes of interest.

The equivalent electric circuit in its simplest form is known as the Butterworth-Van Dyke (BVD) model [4]. In Fig. 1 it is illustrated that the BVD-model directly relates to the piezoelectric equations in *e*-notation (eq. (4)), with (assumed real-valued) parameters as in eq. (23) as well as a coil L_1 and a resistor R_1 representing inertia m and dissipation d_m^U (often viscous damping) in the mechanical domain.

$$\begin{pmatrix} F \\ q \end{pmatrix} = \begin{bmatrix} k_\mathrm{m}^U & -e_\mathrm{comp} \\ e_\mathrm{comp} & C_\mathrm{el}^x \end{bmatrix} \begin{pmatrix} x \\ U \end{pmatrix} \quad (23)$$

In literature several extensions to the BVD-model can be found, not only to account for multiple vibration modes, but also to include complex-valued parameters to account for hysteretic losses. Ikeda [2] for example introduces a complex-valued transformer ratio, corresponding to adding a loss tangent to e_comp in eq. (23) and Fig. 1b. An example of an equivalent circuit accounting for dielectric, elastic, and piezoelectric loss is provided by Uchino (Fig. 2).

3.2 Drawbacks of asymmetric model

As the matrix equation in *e*-notation (eq. (4) and (23)) is of the mixed type, the resulting model structure in the BVD-model may be considered 'asymmetric' in the sense that energy storage in both domains is modelled in different ways: the mechanical parameter for energy storage is intensive ($k_\mathrm{m}^U \sim c^E$), whereas the electric parameter for energy storage is extensive ($C_\mathrm{el}^x \sim \varepsilon^S$).

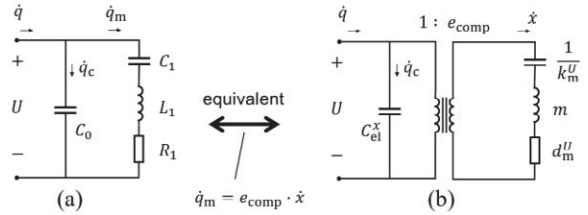


Figure 1 a) BVD-model and b) equivalent circuit based on piezoelectric transducer parameters in *e*-notation [8]

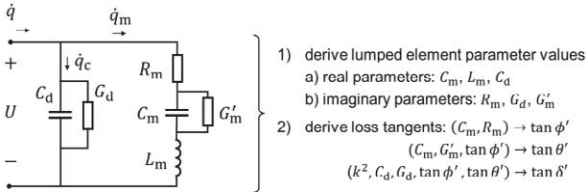


Figure 2 BVD-like model with extra lumped elements for derivation of (intensive) loss tangent values [5]

 DOI: 10.30420/456743031

A drawback of this asymmetry is that two-way energy conversion, i.e., the 'symmetry' of the direct and the inverse piezoelectric effect, is not intuitively clear. For that reason, in a previous publication [8] we advocated a 'symmetric' model, based on the piezoelectric equations in *h*-notation, i.e., on extensive material parameters. In the present paper, in addition, we argue that energy dissipation mechanisms are not intuitively clear from the asymmetric (*e*-notation-based) structure of BVD-like models.

In BVD-like models energy dissipation mechanisms are typically attributed, in a mathematical way, to the two (or three) elements in the electric circuit of Fig. 1a (or 1b):

- C_0 (equal to C_{el}^{x}) as a storage element then seems to relate to $\varepsilon^{S*} = 1/\beta^{S*}$, i.e., not only the real part but also the imaginary part, and thus to the *extensive* dielectric loss tangent $\tan\delta$; refer eq. (18a);
- C_1 comprises both e_{comp} and k_{m}^{U} and thus seems to relate to d^*/s^{E*} respectively $1/s^{E*}$, i.e., to the *intensive* elastic and piezoelectric loss tangents $\tan\varphi'$ and $\tan\theta'$; refer eq. (19b) and (20b).

From a physical or energy-based point of view however (see e.g. [1,2]), it is more convenient to attribute losses to the extensive variables x and q (and possibly to a combination of these), i.e., to the two (or three) branches for the current ($\dot{q}$, $\dot{q}_{\mathrm{m}}$, $\dot{q}_{\mathrm{c}}$) in the electric circuits in Fig. 1 and 2. For that reason in section 3.4 we will extend the symmetric model of [8] with only extensive loss elements. Based on this model we will give an intuitive interpretation of the extensive and intensive loss tangents and their relations.

3.3 Example transducer in *h*-notation

As an example transducer to be modelled we consider a multilayer actuator stack, characterized by geometry and material parameters as shown in Fig. 3. This transducer can be described as follows, with a diagonal transformation matrix $\boldsymbol{T}$ accounting for the geometry and (lossless) material parameters, and a dimensionless matrix $\boldsymbol{B}$ accounting for energy storage, conversion, and dissipation.

$$\begin{pmatrix} F \\ U \end{pmatrix} = \begin{bmatrix} k_{\mathrm{m}}^{q*} & -h_{\mathrm{comp}}^{*} \\ -h_{\mathrm{comp}}^{*} & (1/C_{\mathrm{el}}^{x})^{*} \end{bmatrix} \begin{pmatrix} x \\ q \end{pmatrix} = \boldsymbol{T}\cdot\boldsymbol{B}\cdot\boldsymbol{T}^{\mathrm{T}} \begin{pmatrix} x \\ q \end{pmatrix} \quad (24)$$

$$\boldsymbol{T} = \begin{bmatrix} \sqrt{k_{\mathrm{m}}^{q}} & 0 \\ 0 & \sqrt{\dfrac{1}{C_{\mathrm{el}}^{x}}} \end{bmatrix} = \begin{bmatrix} \sqrt{A/l}\,\sqrt{c^{D}} & 0 \\ 0 & \dfrac{1}{n}\sqrt{l/A}\,\sqrt{\beta^{S}} \end{bmatrix} \quad (25)$$

$$\boldsymbol{B} = \begin{bmatrix} 1 + j\tan\phi & -k(1+j\tan\theta) \\ -k(1+j\tan\theta) & 1 + j\tan\delta \end{bmatrix} \quad (26)$$

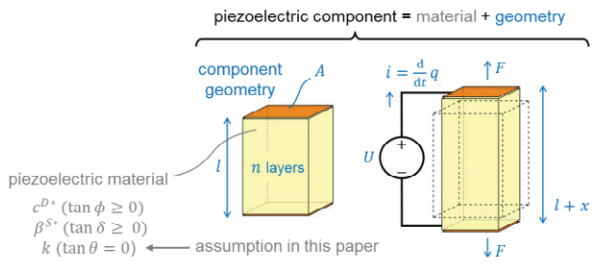


Figure 3 Example piezoelectric transducer

3.4 Symmetric lumped-parameter model

The choice for the *h*-notation (with positive '+' imaginary values) is crucial, as this means that lumped dissipation elements can simply be 'added' to a model structure with lumped storage elements. The choice for $\boldsymbol{T}$ is also crucial, as this results in a 'normalized' matrix $\boldsymbol{B}$, i.e., with the real part of both diagonal elements equal to 1, such that:

- the (absolute) real part of the (cross-domain) off-diagonal elements is equal to the coupling factor k;
- the (absolute) imaginary part of the diagonal elements equals a (single-domain) loss tangent.

As a consequence, both energy conversion (k) and domain-related energy dissipation ($\tan\phi$ and $\tan\delta$) can easily be visualized, e.g. in the lumped mechanical model in Fig. 4.

The lossless version of this model (introduced in [8], along with an even more intuitive orthogonal structure as well as a similar equivalent electric circuit) is fully symmetric. The model is extended here with hysteresis elements (shown as mechanical friction), related to the loss tangents as follows:

$$\tan\phi = h_{\mathrm{m}} + k h_{\mathrm{c}} \quad (27)$$

$$\tan\delta = h_{\mathrm{el}} + k h_{\mathrm{c}} \quad (28)$$

$$\tan\theta = k h_{\mathrm{c}} \quad (29)$$

In this paper, in line with Ikeda [2], but in contrast to Uchino [5-7], we assume no hysteresis in the coupled domain, i.e., zero extensive piezoelectric loss:

$$h_{\mathrm{c}} = 0 \;\Rightarrow\; \tan\theta = 0 \quad (30)$$

Note: hysteresis on the *d*-parameter (non-zero intensive piezoelectric loss: $\tan\theta' \geq 0$) is then only due to extensive dielectric and elastic loss; refer eq. (21) and (22).

The advantages of the overall resulting model are:

1) symmetric energy storage structure, showing two-way piezoelectric energy conversion, characterized by normalized values $(1-k)$ and k;
2) loss mechanisms only in hysteresis elements, i.e., no dissipation in storage and transformer elements;
3) hysteresis elements directly relate to extensive loss: h_{m} represents $\tan\phi$; h_{el} represents $\tan\delta$;
4) intuitive interpretation of intensive loss (see Fig. 5);
5) transformer elements accounting for geometry and material parameters, allowing for intuitive analysis of mechanical and electric impedance matching.

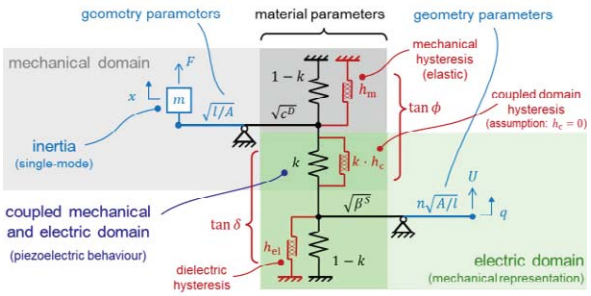


Figure 4 Symmetric lumped-parameter model of a piezoelectric transducer including friction elements to account for hysteresis losses (and a mass m to represent resonant behaviour at a single vibration mode; see Fig. 5)

 DOI: 10.30420/456743031

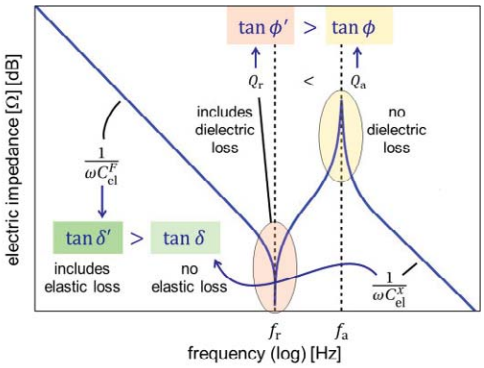


Figure 5 Interpretation of extensive and intensive loss tangents for a (single-mode) lumped-parameter model:
- high-frequency range: extensive dielectric loss ($\tan\delta$)
- low-freq. range: intensive dielectric loss ($\tan\delta' > \tan\delta$)
- at anti-resonance f_a: extensive elastic loss ($\tan\phi$)
- at resonance f_r: intensive elastic loss ($\tan\phi' > \tan\phi$)

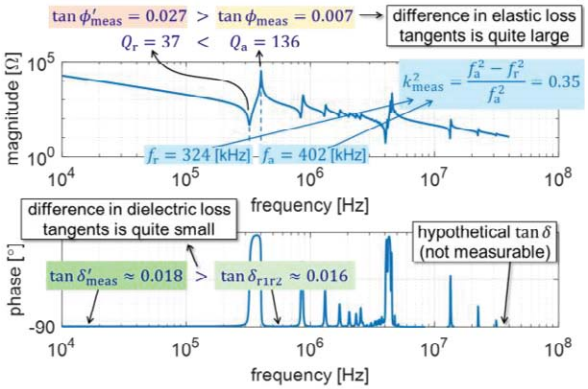


Figure 6 Impedance measurement for a piezoelectric disc

4 Validation of symmetric model

4.1 Qualitative and quantitative evaluation

The single-mode model interpretation of the loss tangents as shown above is experimentally validated for a piezoelectric circular disc (material: PIC255; diameter: 6 mm; thickness: 0.5 mm). Fig. 6 shows a measurement of the electric impedance, showing the first radial vibration mode at 320 kHz and the first thickness mode at 4 MHz. Here we focus on characteristic parameters derived from the frequency range including only the first radial vibration mode, thus ignoring the effect of higher-order modes.

Qualitative evaluation of the estimated loss tangents can be seen to be in accordance with the simplified single-mode interpretation of Fig. 5: for both the dielectric and elastic loss the intensive value is larger than the extensive value.

For *quantitative* evaluation we use eq. (21) and (22). With these we may e.g. estimate the dielectric loss tangent in the frequency range beyond the first radial (anti)resonance:

$$\begin{aligned}\tan\hat{\delta}_{\mathrm{r1r2}} &= (1-k^2_{\mathrm{meas}})\tan\delta'_{\mathrm{meas}} \\ &\quad -k^2_{\mathrm{meas}}\tan\phi_{\mathrm{meas}} \\ &= 0.65\cdot 0.018 - 0.35\cdot 0.007 \approx 0.009\end{aligned} \tag{31}$$

This value is significantly smaller (0.009/0.016 ≈ 58%) than the dielectric loss tangent derived directly (but due to the dynamics a bit uncertain) from the phase of the measured impedance in this frequency range.

In addition, we may estimate the intensive elastic loss tangent from the measured extensive loss tangent (at anti-resonance) and the measured dielectric loss tangent in the frequency range beyond the first radial (anti)resonance:

$$\begin{aligned}\tan\hat{\phi}' &= \frac{\tan\phi_{\mathrm{meas}} + k^2_{\mathrm{meas}}\tan\delta_{\mathrm{r1r2}}}{1-k^2_{\mathrm{meas}}} \\ &= \frac{0.007 + 0.35\cdot 0.016}{0.65} \approx 0.020\end{aligned} \tag{32}$$

This value equals only 0.020/0.027 ≈ 75% of the elastic loss tangent based on the quality factor at resonance. The observed quantitative discrepancies are discussed hereafter.

4.2 Discussion

A symmetric lumped-parameter model, extended with dissipation elements, has been advocated for intuitive interpretation of energy efficiency aspects in piezoelectric transducers. Experimental validation has shown how this model helps e.g. in understanding the qualitative relation between intensive and extensive loss tangents.

If extended to only a single-mode model, the underlying loss tangent equations show a quantitative mismatch with the piezoelectric disc in radial vibration. This mismatch is likely due to the higher-order modes (or non-linear effects) neglected in the model, and thus a direct result of its simplicity. The model can be extended to account for these effects, though at the cost of reduced clarity and simplicity. Further validation is therefore left for future research.

Literature

[1] Breedveld, P.C.: Integrated Modeling of Physical Systems, Lecture notes, University of Twente, Enschede, The Netherlands, 2013

[2] Ikeda, T.: Fundamentals of Piezoelectricity, Oxford University Press, Oxford, USA, 1990

[3] Kim, J.: Grisso, B.L.: Kim, J.K.: Ha, D.S.: Inman, D.J.: Electrical Modelling of Piezoelectric Ceramics for Analysis and Evaluation of Sensory Systems, Proc. IEEE SAS 2008, 122-127, Atlanta, USA

[4] Van Dyke, K.S.: The Piezo-Electric Resonator and its Equivalent Network, Proc.IRE, Vol. 16, 742-764, 1928

[5] Uchino, K.: Ferroelectric Devices & Piezoelectric Actuators: Research Misconceptions and Rectifications, DEStech Publ., Pennsylvania, USA, 2017

[6] Uchino, K.: Hirose, S.: Loss Mechanisms in Piezoelectric: How to Measure Different Losses Separately, IEEE Transactions on Ultrasonics, Ferroelectrics, and Frequency Control, Vol. 48, No. 1, Jan. 2001

[7] Uchino, K.: Zhuang, Y.: Ural, S.O.: Loss Determination Methodology for a Piezoelectric Ceramic: New Phenomenological Theory and Experimental Proposals, Journal of Advanced Dielectrics, Vol.1, No.1, 17–31, 2011

[8] Holterman, J.: Jansen, B.: Schmidt, H: Piezoelectric Transducer Modelling: A Comprehensive Overview, DSPE conf. 2025, St Michielsgestel, The Netherlands

 DOI: 10.30420/456743032

Piezoelectric Ultrasonic Mirror Tip/Tilt Stage

Jan Homberg[1] (j.homberg@pi.de), Alexej Wischnewski[1] (a.wischnewski@pi.de), Bülent Delibas[1] (b.delibas@pi.de),
[1] Physik Instrumente (PI) SE & Co. KG, Auf der Römerstraße 1, 76228 Karlsruhe, Germany

Abstract

This paper proposes a 2-degrees-of-freedom (2-DoF) miniature beam steering stage (16 × 16 × 16 mm³) driven by a single piezoelectric ceramic excited at resonant ultrasonic frequency. First, the module's components and structure are described. Second, finite element method (FEM) simulations, including modal analysis of the piezoelectric ultrasonic motor and direction-changing driving methods are presented. Finally, experimental results of a functional prototype under open-loop motion control are shown. Its angular motion range was measured using an autocollimator, demonstrating range limitations with a maximal angular motion of about ±10 mrad. Additionally, a laser vibrometer was used to measure oscillation amplitudes of the piezoelectric stator tips under resonant excitation, validating the simulation results.

1 Motivation

Lasers are used in many areas of technology, including metrology, medical technology, military, metal working, communications, and many more. The laser beams in such industries are usually precisely directed, or guided, via tip/tilt mirrors. The necessary precision in the guidance of the laser beam may be manually achieved via micrometer screws, e.g. in experimental setups on optical tables. However, industrial applications depend on automated solutions, with a growing demand for miniaturization. Piezoelectric drives are commonly used, e.g. for positioning tip/tilt mirrors.

Physik Instrumente (PI) offers a wide range of stages and positioners, including tip/tilt mirrors based on piezoelectric actuators with a parallel kinematic design, which exhibit high stiffness, high control bandwidth, position stability, and resolution [1]. Due to fundamental principles, further miniaturization of such devices comes with a significant loss in motion range and/or stiffness.

Complementary to such directly driven actuator stages, positioning stages based on piezoelectric motors are provided. In these systems, the motion of the rotor or runner element is generated by the piezoelectric ceramic via a frictional tip. The deformation or oscillation of the actuator, excited by an electrical signal, is transmitted to the driven element through this friction interface. In this way, a wide range of motion is achievable while maintaining a compact design and high stiffness.

A well-established approach involves screw designs driven by piezoelectric inertia motors for the movement of mirrors [2-5]. Here, the stator is threaded into a nut and maintains frictional contact with it. This nut is directly or indirectly connected to a piezoelectric actuator, which drives the screw via stick-slip motion based on the inertia principle.

The primary limitation of inertia-driven systems is the restricted speed of the moving or rotating components. This arises from the motor's inertia-based operating principle: the piezoelectric actuator cannot drive the screw at frequencies exceeding 10 kHz, as the static friction between the actuator and screw cannot transition to sliding friction beyond this threshold.
Additionally, inertia-driven systems with two piezoelectric actuators for 2-DoF movements and parts like screws or spindles require relatively large installation space.
Furthermore, the excitation frequency range of piezoelectric inertia drives is within the audible spectrum, which can be noisome during operation. In most closed-loop motion control systems, the impact forces of piezoelectric actuators occur within a frequency bandwidth in the order of 1 to 10 kHz [6].

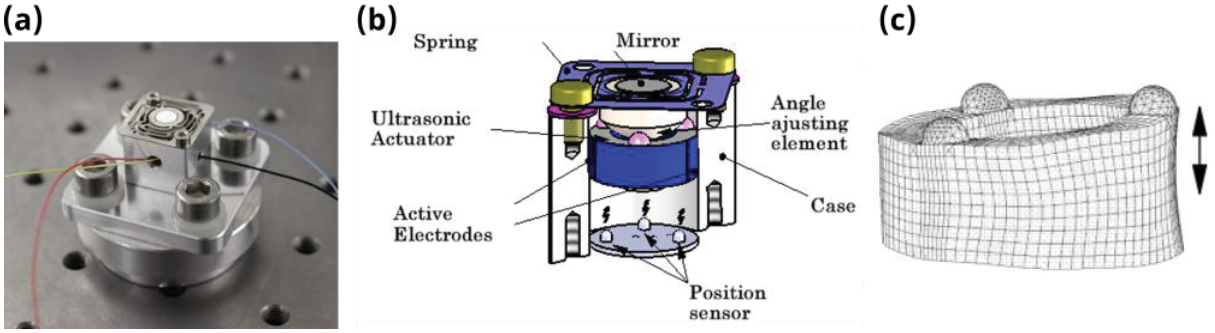


Figure 1. Proposed tip/tilt mirror drive a) functional sample b) CAD model of its interior c) FEM modal analysis when only one electrode is excited.

 DOI: 10.30420/456743032

These drawbacks of low traversing velocity, noisy actuation, and bulky spindle drive dimensions inherent to inertia-based systems can be mitigated by replacing the inertia drive with a piezoelectric ultrasonic motor for mirror adjustment. At the same time, general advantages of piezo motors are maintained, like e.g., wide range of motion and self-locking property, meaning the position is retained when electrical voltage is removed.

2 Approach

For the reasons mentioned above, we propose a tip/tilt mirror stage driven by an ultrasonic piezoelectric motor.
Figure 1 illustrates a functional sample (a) and a CAD model of its interior structure (b). The entire assembly has compact dimensions of about 16 × 16 × 16 mm³. The motor features an ultrasonic actuation element, i.e. a hollow cylindrical resonator fabricated from PIC 181 hard piezoelectric ceramic (PI Ceramic GmbH, Germany) [7]. The mirror is mounted inside a hemispherical ceramic element (rotor), which is driven via three 120°-spaced tip elements bonded onto the piezoelectric resonator. The rotor is spring-loaded to ensure sufficient friction force at the tip contacts.
The resonator features one common inner electrode and three outer electrodes, which divide it into three 120° segments. It exhibits certain vibrational modes, which can be excited by application of a sinusoidal voltage signal at one of the segments. Figure 1 (c) shows the FEM modal analysis of such a vibrational mode, with a resonance frequency of 406 kHz. Due to the high oscillation amplitude of the active segment, the rotor rotates out of plane. By driving the three electrodes sequentially, the mirror can be adjusted to any tip/tilt angle.
A key advantage of this design is its ability to achieve two-degree-of freedom (2-DoF) angular motion using only a single piezoelectric stator, enabling a very compact size. Additionally, the operation is silent due to the high operating frequency, which lies in the non-audible range.

A functional sample of this tip/tilt mirror stage was prepared for further testing. The piezoelectric tip/tilt actuator is designed to exert an actuation force on the order of 1 N at the contact surface between the spherical tips and the rotor. During operation, the flat spring applies a restoring force to the rotor that depends its angular position, thereby altering the effective actuation force. As the restoring force increases with the angular displacement, the achievable range of motion is limited. At the maximal tilting angle, the restoring force equalizes the driving force.

3 Results

The resonance frequency and oscillation amplitude of the functional sample were measured using a laser vibrometer (Polytec, Germany). The measurement setup is shown in Figure 2. An open-loop sinusoidal frequency sweep signal was applied, with a bandwidth of 380 to 430 kHz and a mean operating voltage of 15 Vrms. Figure 3 illustrates

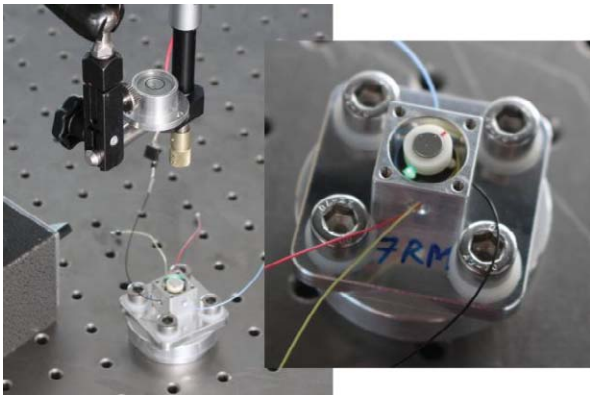


Figure 2. Test setup for the Vibrometer measurement of resonance frequency and oscillation amplitude of the functional sample.

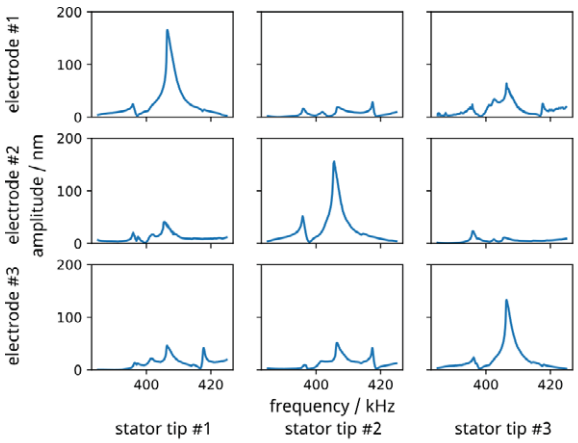


Figure 3. Actuation amplitudes of the stator tips upon single electrode driving at *Vrms* = 15 V, measured at various frequencies with a Vibrometer.

the oscillation amplitudes of all three stator tips upon activation of each individual electrode. All three diagonal measurements, where the measured stator tip corresponds to the active electrode, show oscillation amplitudes of about 150 nm at the resonance. These diagonal measurements confirm a consistent resonance frequency of approximately 406 kHz, aligning with the FEM simulation results. Measurements outside the diagonal cases (i.e., when non-corresponding electrodes are excited) reveal that tip movements are negligible compared to those observed during direct electrode excitation.
The 2-D tip/tilt angular movements of the functional sample were measured using an autocollimator, as shown in Figure 4. A set of 55 individual steps in alternating directions is presented in Figure 5. Due to the motor design constraints and the restoring force of the flat spring in particular, the attainable angle of rotation is restricted to a triangular area (yellow area in Fig. 5). To quantify the controllable angular range, we defined a circle enclosing the largest possible area within this triangular boundary (red area in Fig. 5). Within this definition, the functional sample achieved an angular motion range of ±10 mrad.

DOI: 10.30420/456743032

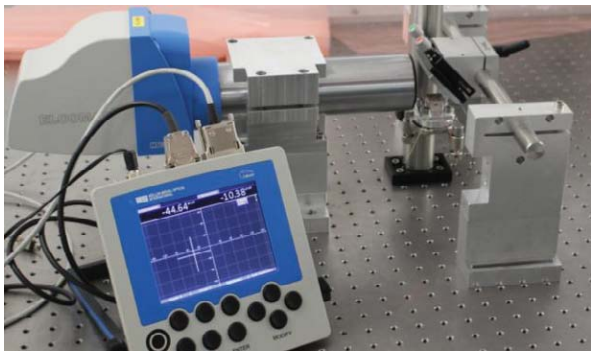


Figure 4. Test setup with autocollimator for the measurement of the angular movement range of the functional sample.

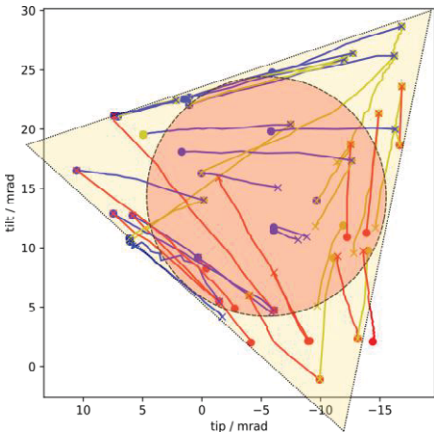


Figure 5. 2-DoF autocollimator measurement of the range of motion. The trajectories of 55 individual steps are shown. Each start (end) position is marked with an ‘x’ (full circle). Steps of axis 1, 2, 3 are depicted in blue, red, yellow, respectively. The circular motion range of ±10 mrad is marked in red.

4 Conclusion

A 2-DoF miniature tip/tilt mirror, driven by an ultrasonic piezoelectric motor using only a single piezoelectric ceramic, is presented. Experimental measurements from a laser vibrometer show close agreement with FEM modal analysis results. The functional sample demonstrates rotational motion of up to ±10 mrad in all directions. Future work will focus on integrated sensor development and closed-loop motion control strategies to enhance the performance of this compact tip/tilt mirror.

5 Literature

[1] Physik Instrumente (PI) SE & Co.KG, Germany, Piezo Flexure Tilting Mirrors, https://www.physikinstrumente.com/en/products/nanopositioning-piezo-flexure-stages/piezo-flexure-tilting-mirrors, Accessed on May 4, 2026

[2] Newport Corporation, USA, https://www.newport.com/p/8885, Accessed on Oktober 22, 2025

[3] Luecke, F.S.: Tuganov, A.: Piezoelectric actuator for optical alignment screws, US Patent, US5410206A, 1995

[4] Hübner, R.: Marth, H.: Piezoelectric rotary drive for a shaft, US Patent, US 9106158B2, 2015

[5] Physik Instrumente (PI) SE & Co.KG, Germany, N-480 High-precision Kinematic Mirror Mount, https://www.physikinstrumente.com/en/products/linear-actuators/piezomike-for-long-term-stability/n-480-high-precision-kinematic-mirror-mount-1000171, Accessed on Oktober 22, 2025

[6] Koc, B.; Delibas, B. Impact Force Analysis in Inertia-Type Piezoelectric Motors. Actuators 2023, 12, 52. https://doi.org/10.3390/act12020052

[7] Physik Instrumente (PI) SE & Co.KG: Piezoelectric Ceramic Products - Fundamentals, Characteristics and Applications, White paper (2016), pp. 18-19

 DOI: 10.30420/456743033

Change in stress-strain-characteristics of MSM-alloys in weak magnetic fields for adaptive interfaces

Marco Hutter, Institute of Design and Production in Precision Engineering (IKFF), University of Stuttgart, Stuttgart, Germany, marco.hutter@ikff.uni-stuttgart.de
Lukas Fuchs M. Sc., Institute for Engineering Design and Industrial Design (IKTD), University of Stuttgart, Stuttgart, Germany
Dr.-Ing. Peter Schmid, Institute for Engineering Design and Industrial Design (IKTD), University of Stuttgart, Stuttgart, Germany
Prof. Dr.-Ing. Thomas Maier, Institute for Engineering Design and Industrial Design (IKTD), University of Stuttgart, Stuttgart, Germany
Prof. Dr.-Ing. Bernd Gundelsweiler, Institute of Design and Production in Precision Engineering (IKFF), University of Stuttgart, Stuttgart, Germany

Abstract

Adaptive human machine interfaces offer promising capabilities to improve precision of operation, shorten learning times and to reduce user error. One way of adaptivity can be to create visual and tactile feedback matching with user tasks. In this work, possibilities to use multistability and magnetostress of magnetic shape memory alloys to create these types of adaptive feedback are discussed and experimental investigations into magnetostress are presented. To maintain the use of multistability, only weak fields below magnetically induced deformation are considered. The magnetostress range for 10M-NiMnGa-crystals is determined experimentally for compressive and tensile loading. Implications for the use of this principle are discussed and a viable magnetic configuration using moving permanent magnets is presented.

1 Introduction

Research into application of magnetic shape memory alloys (MSM) has mostly focused on actuators in fields such as fluid technology. We propose human machine interfaces (HMI) as a little explored field of application, utilizing the comparatively large strains of MSM and their energy product, which matches well with fine motor skill use cases, if suitable transmission is provided. In the field of HMI research, adaptivity is of great interest to improve metrics such as precision of operation and reduce time to learn and user error. In EN 894-3 [1], the standard about ergonomic requirements of control elements, visual and tactile checks of controls states are two of six more specific requirements for control elements. They are crucial in many applications where the user is not in constant contact with the control elements while using the machine. Users can therefore set the control elements and forget about it until they visually or tactilely check the status of the control element again [2]. Furthermore, the ability to change the stress-strain-characteristic enables adaptive feedback with regard to the force required to bring the control element into a desired state depending on the user's preferences or the context [3]. This is relevant for most of today´s HMIs, as they are just indirectly connected to the controlled function by wire. The feedback from controlling a function is therefore no longer directly perceptible [2]. Additionally, tactile feedback can also avoid eyes-off time from the main task, which is especially relevant for applications where distraction can lead to serious failures.
This can be combined with other types of feedback during a change in position such as vibrotactile feedback or a change in the force-distance-characterstic of the interface. This combination can be achieved by using multistability and magnetostress in MSM-alloys.

1.1 Multistability

Magnetic shape memory alloys exhibit a pseudoplastic shape change by a reorientation of their martensitic lattice structure. During reorientation the martensitic crystal structure changes from one martensite variant, also called twin, into another [4]. This is opposed by an internal resistance and is typically expressed by the twinning stress, i.e. the mechanical stress necessary to facilitate pseudoplastic deformation. As part of the deformation areas within the alloy change their orientation sequentially, creating volumes of exclusively one twin variant. Borders between these volumes are called twin boundaries and can be observed moving in the crystal during deformation. Twinning stress can be affected by internal parameters, such as defects of the crystal structure, its specific modulation and the number and type of twin boundaries, or by external parameters like loads and restrictions caused by clamping. [5] While twinning stress causes losses in the material during actuation cycles, and is thus usually desired to be as low as possible, it also enables MSM-alloys to retain their shape under limited external load without any power consumption, which is called multistability [6].

1.2 Magnetostress

The crystal structure of MSM-alloys shows magnetic anisotropy, which causes one of the crystals axes and thus the corresponding twin variant to be favored in parallel with an external magnetic field. Therefore, on a macroscopic level a magnetically induced stress, called magnetostress, can be

 DOI: 10.30420/456743033

perceived. If this magnetostress is higher than the twinning stress (and any mechanical load), reorientation of the crystal structure and thus strain of the macroscopic sample occurs [7]. This is not feasible for all types and modulations of MSM-alloys. In the case of the most commonly employed NiMnGa-alloys, magnetic field induced strain is generally possible for 10M-configuration, but not in NM-crystals [8]. However, magnetostress is still expected to occur in these crystals as well, even though it is not sufficient to create reorientation.

2 Magnetostress and multistability in adaptive HMI

A suitable connection between a control element and an MSM-sample will link the operation motion to a deformation of the crystal. Twinning stress will, as discussed above introduce multistability into this system and will need to be overcome during operation. Magnetostress, caused by an external magnetic field, can change the required operation force. As this does not require MFIS of the MSM-stick, magnetic fields can be relatively weak and magnetic systems therefore have the potential to be small. Following, investigations into magnetostress at sub-MFIS fields are shown and discussed in terms of their range and implications for use in HMI.

2.1 Experimental setup

The setup consists of an electromagnetic circuit, the MSM-sample and a test machine. The magnetic circuit contains a hand wound coil (n = 1000, 0.5 mm wire diameter) and flux guide of 1.0715 steel. It is intentionally oversized to minimize influence of saturation and heating on the measurements. The air gap for the MSM-stick is 2.2 mm long in parallel with the magnetic field for samples with a nominal length in this direction of 2 mm, leaving an air gap suitable for avoiding jamming of the stick during operation. Figure 1 depicts the setup including the clamps for tensile tests (see below), with part of the flux guide pulled back to reveal the MSM-stick and the lower clamp.

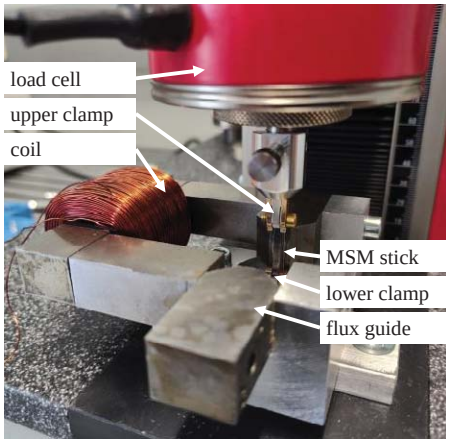


Figure 1 Experimental setup for measuring sub-MFIS magnetostress (tensile setup depicted).

Results in this work are given relative to the magnetic flux density in the MSM-stick. This is derived from the current in the coil by reference measurements and FEA simulations. The simulation model is created in Ansys Electronic Desktop containing the coil, the circuit and the MSM-stick. For the circuit steel and the MSM-alloy nonlinear magnetization curves are used. The MSM-material is modelled for its fully compressed and fully elongated states. In both cases, modelling includes the magnetic anisotropy of the MSM-alloys.

To achieve a good representation of the physical setup, the simulation is tuned to measurements taken in the air gap of the circuit with a hall probe (Magnet Physik FH55 Teslameter) by adjusting the coil parameters. For this tuning the MSM-material in the simulation is replaced with air to represent the empty air gap. The experimental data shows a magnetic field at zero current in the coil, which is caused be remanence in the steel core. As this will occur during subsequent testing, the remanence is also approximated in the simulation. This is done by introducing an additional constant current, which shows best agreement with the experimental data at 90 mA. Figure 2 shows simulation results for the empty air gap, the compressed as well as the elongated MSM-stick. The average magnetic flux density in the MSM-volume is displayed over the coil current (without the current representing remanence). The experimental data is included as well.

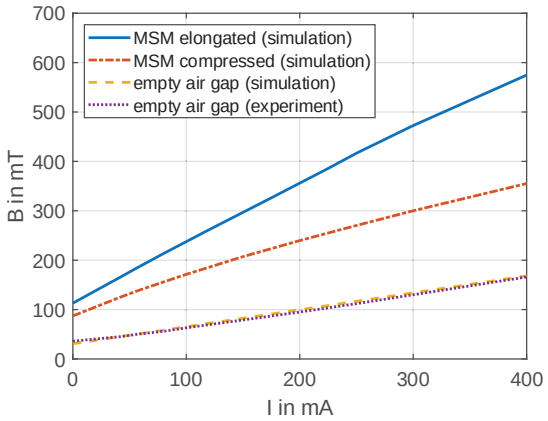


Figure 2 Correlation between coil current and magnetic flux density for the experimental reference and the tuned simulation model for the empty air gap, compressed and elongated MSM-stick.

The figure shows good agreement between the reference data and the simulation with empty air gap. From these results and tests with the MSM-samples the sub-MFIS range of the coil current is determined to be 0…300 mA. Any following flux density values in the MSM-stick are derived from the coil current using the above results for the compressed MSM-stick.

Nominal dimensions of the MSM-sample in the compressed state are 2 x 3 x 15 mm³. The MSM-material used here is a 10M-NiMnGa-alloy with MFIS of up to 6 %. Two types of measurement will be conducted. For compressive

 DOI: 10.30420/456743033

tests, the MSM-sticks will be held in in the air gap by a mounting of the type described in [9]. It is fully elongated with a strong magnetic field of over 800 mT and subsequently compressed under a varying weak magnetic field during the testing procedure.
For tensile tests, loads will be transferred via clamping at either end of the MSM-stick. Clamps and bolts are made of aluminum and brass to avoid interference with the magnetic field. The clamping length is 1.5 mm reducing the active length of the MSM-stick to 12 mm for these tests. Here, the weak field is applied during elongation. At the end of every test, the sample is compressed by the machine returning to its starting position.
The testing machine is a zwickiLine Z0.5 with an Xforce HP load cell capable of compressive and tensile tests of up to 100 N. The internal position sensor of the machine is used to derive sample strain.

2.2 Compressive tests

The compression of the MSM-stick is repeated three times for each current step and therefore magnetic field. The results in Figure 3 represent average curves for stress over strain calculated from the three tests.

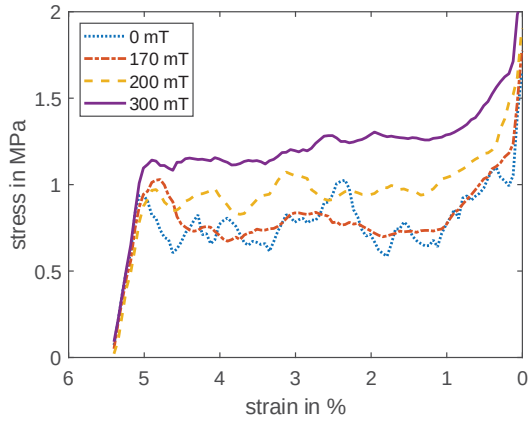


Figure 3 Stress-strain-characteristic for MSM-stick compression in weak magnetic fields.

There is a clear correlation between the magnetic field and the level of the martensitic plateau, which itself is clearly visible. The results are more irregular for weaker magnetic fields. The curves at magnetic fields of 0 and 170 mT also show a clear peak at the beginning of the martensitic plateau compared to the rest of the reorientation. This is associated with nucleation of twin boundaries, for which necessary stresses can be higher than for twin boundary movement [10]. At stronger fields this is likely to still happen, but not be visible, as it is similar to the level of stress necessary for twin boundary movement. For the MSM-sample magnetically achievable elongation has reliable been at 5.4 %. The average stress of the martensite plateau ranges from 0.75 MPa at no magnetic field to 1.22 MPa at 300 mT.

2.3 Tensile tests

In preliminary tests conducted for the tensile setup, high force peaks at the beginning of the elongation have been recorded. This is again attributed to twin boundary nucleation. As force peaks here have been even higher, than for compressive tests, the test procedure is modified to start at around 1.5 % of strain instead of a fully compressed stick. The bigger influence here is likely connected to the clamping of the MSM-stick, which hinders bending during formation of twin boundaries. Results of the modified test procedure are displayed in Figure 4. Here as well, averages from three cycles of strain testing are shown.

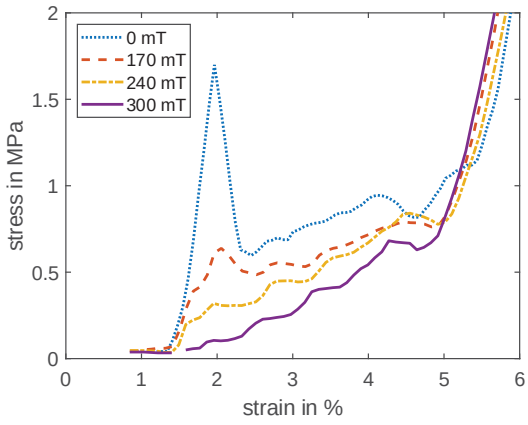


Figure 4 Stress-strain-characteristic for MSM-stick elongation in weak magnetic fields.

Once again, the correlation between magnetic field and deformation stress is visible. Despite the modified test procedure, for the test at 0 mT a high stress peak is still apparent, as well as a small one for 170 mT. This needs to be addressed for any application of this mechanism. The overall shape of the curves has a less pronounced martensitic plateau than for compressive tests. Results instead show a rising characteristic during elongation. To some extent, this might be linked to slipping in the clamping of the MSM-stick, which is as well suspected to be the reason for deviations in the maximum strain seen between curves. Here, slipping is a plausible explanation, as deviations are higher for higher forces. The range of average stress during deformation is 0.32…0.84 MPa. The value at no magnetic field for these tensile tests is in part higher than during compressive tests due to the spike at the beginning of the deformation. Omitting the spike yields an average stress of 0.80 MPa, which is closer to the result of the compressive test. The remaining difference can again be attributed to the clamping.

ISBN: 978-3-8007-6743-4 @ VDE VERLAG GMBH · Berlin · Offenbach

 DOI: 10.30420/456743033

2.4 Discussion

For both compressive and tensile tests, the influence and range of sub-MFIS magnetostress has been demonstrated. In both cases high force peaks at the beginning of the martensitic transformation have been observed, which are likely linked to twin boundary nucleation. For application of the presented mechanism samples with a stabilised twin structure are expected to produce smoother stress-strain-characteristics at the expense of limiting the maximum strain. Additionally, the clamping during tensile tests has been found to have significant impact on the results. Clamping was chosen here to enable changing and reusing of MSM-samples. For application it is however disadvantageous, as in addition to the influence on stress-strain-characteristics it limits the length of the MSM-stick exhibiting martensitic transformation. Other methods for transferring tensile loads include gluing and welding, which have both been demonstrated in literature [11, 12]. Independent of the chosen method, results here and in other research [13] indicate that smoothness of the MSM-stick deformation can be improved by limiting constraints in the fixation of the MSM-stick.

Overall findings here still show a change in average stress of about 0.5 MPa at a flux density of 300 mT, corresponding to a 63 % increase for compression and a 60 % reduction for elongation. For the intended use in an interface, this is promising, as it is expected to be clearly detectable for users. Haptic tests are however not part of this work, but will be conducted in the future. Design of an exemplary magnet configuration is given by simulation in the next section. The aim is to achieve a relatively compact and light magnetic circuit, as the necessary magnetic fields are relatively weak.

3 Design of a demonstrator circuit

For the design of a demonstrator magnetic circuit utilizing sub-MFIS magnetostress, the use of permanent magnets is advantageous, as it avoids Ohmic losses. Varying the magnetic field can then be achieved by changing the position of the magnets or by changing the magnetization of semi-hard magnetic material such as AlNiCo-alloys. The second option still requires coils for magnetization, which increase overall volume and is therefore not considered for now. Instead, a simulation using Ansys Electronic Desktop is employed to find a permanent magnet configuration suitable for achieving the range found in the experiments above.

For the simulation the MSM-stick is again modelled in the same way as before, representing the compressed stick. Two types of magnets are chosen for simulation and in each configuration two identical copies are positioned in line with the short axis of the MSM-sample (see **Figure 6**). The two types of magnets have dimension of 18 x 8 x 4 mm³ with an N48 magnetization and 20 x 4 x 2 mm³ at N45, respectively.

For the simulation the distance between the MSM-stick and the magnet on either side is varied. The resulting average flux density in the MSM-volume is given in Figure 5 with respect to the distance for both types of magnets.

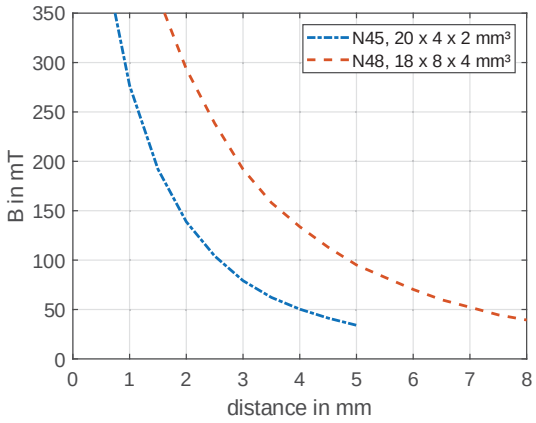


Figure 5 Magnetic flux density in the MSM-stick relative to the distance to the magnets for both types of magnets.

As can be seen, the necessary range of flux density can be achieved by both magnets. The higher end of the flux density range of 300 mT is achieved for distances of 1 mm and 2 mm. For distances over 4 mm and 7 mm respectively the flux density in the MSM-sticks drops below 50 mT, which is close to the remanence found in the electromagnetic circuit above and can be regarded as equivalent to no magnetic field. Subsequently, a demonstrator needs to provide 3 mm of movement for each of the permanent magnets to represent the desired range.

Apart from the average flux density in the MSM-stick, uniformity of the field is to be considered. It is evaluated here by calculating the standard deviation of the flux density in the MSM-volume relative to the average. This is below 10 mT for both magnet configurations. For visualization purposes, Figure 6 depicts the two magnets (red) at an intermediate distance of 2 mm each from the MSM-stick (yellow). The field is given by flux lines in one plane at halt the MSM-sticks height.

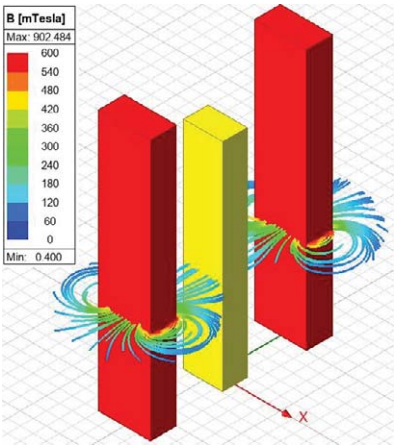


Figure 6 Field distribution at a distance of 2 mm between magnets (red) and MSM-stick (yellow).

These results are achieved without the use of flux guide. For the given magnets this is not necessary and would increase weight and volume of the setup. For different magnets, it might be advantageous. Mechanical design for positioning the magnets has a number of options, such as ratcheting, threading and flexure-based mechanisms. The chosen option should be self-locking to efficiently maintain magnet position during operation. A thread-based demonstrator is planned as a next step, to facilitate a possibility for haptic evaluation of the adjustable stress.
In an application with a dynamically (self-)adjusting interface, use of variably magnetized AlNiCo-magnets is expected to be more efficient than moving permanent magnets.

4 Conclusion

In this work, the influence of magnetostress at sub-MFIS fields on stress-strain-characteristics of a 10M-NiMnGa-alloys has been investigated. It was found that the stress necessary for compression and elongation can be altered by around 60 % at these weak magnetic fields. This is promising for use in adaptive human machine interfaces, offering variable operating forces while retaining the multistable potential of MSM. Implementation of this principle in a demonstrator based on permanent magnets has been shown by simulation of two suitable magnet configurations. Adjustment of the magnetic field is intended by moving the magnets in a range of 3 mm. As there is no steel necessary to achieve the desired magnetic fields, the configuration has the potential to be both light and compact.
Further work will include mechanical design of the demonstrator and its realization for testing haptic properties of the variable stress-strain-characteristic. Additionally, future tests are planned to incorporate stabilized twin structures to achieve smoother results and will include characterization of NM-alloys. These show higher twinning stress and maximum strain, thus having potential for more compact design. For characterization of these crystals, the clamping needs to be redesigned to avoid slipping.

5 Acknowledgement

Funded by the Deutsche Forschungsgemeinschaft (DFG, German Research Foundation) – project nr. 564608338.

6 References

[1] *DIN EN 894-3:2010-01, Sicherheit von Maschinen_- Ergonomische Anforderungen an die Gestaltung von Anzeigen und Stellteilen_- Teil_3: Stellteile; Deutsche Fassung EN_894-3:2000+A1:2008*, Berlin.

[2] M. Schmid and T. Maier, *Technisches Interface Design: Anforderungen, Bewertung und Gestaltung*. Berlin, Heidelberg: Springer Vieweg, 2017.

[3] F. Reichelt, D. Holder, A. Kaufmann, and T. Maier, “Strategies for User-Centered Adaptation of Future Vehicles,” in *Lecture Notes in Networks and Systems, Proceedings of the 21st Congress of the International Ergonomics Association (IEA 2021)*, N. L. Black, W. P. Neumann, and I. Noy, Eds., Cham: Springer International Publishing, 2021, pp. 798–805.

[4] M. Arndt, M. Griebel, V. Novak, T. Toubicek, and P. Sittner, “Martensitic Transformation in NiMnGa Single Crystals Numerical Simulation and Experiments,”

[5] I. Kulagin, M. Li, V. Laitinen, and H. Handroos, “Review of MSM Actuators: Applications, Challenges, and Potential,” *IEEE Access*, vol. 10, pp. 83841–83850, 2022, doi: 10.1109/ACCESS.2022.3197278.

[6] M. Raab and W. Schinköthe, Eds., *Active Gravity Compensation Actuator using the Multistability of Magnetic Shape Memory*, 2018.

[7] L. Riccardi, “Position Control with Magnetic Shape Memory Actuators,” Dissertation, 2014.

[8] A. Pérez-Checa *et al.*, “Study of the critical parameters for magnetic field-induced strain in high temperature Ni-Mn-Ga-Co-Cu-Fe single crystals,” *Scripta Materialia*, vol. 158, pp. 16–19, 2019, doi: 10.1016/j.scriptamat.2018.08.018.

[9] M. Hutter and B. Gundelsweiler, “Analysis of the impact of mechanical guidance on active MSM-stick elongation behavior,” in *ACTUATOR 2022; International Conference and Exhibition on New Actuator Systems and Applications*, 2022, pp. 1–4.

[10] R. W. Cahn, “Twinned crystals,” *Advances in Physics*, vol. 3, no. 12, pp. 363–445, 1954, doi: 10.1080/00018735400101223.

[11] R. Courant and J. Maas, “Design and characterization of an efficient multistable push-pull linear actuator using magnetic shape memory alloys,” *IEEE Access*, p. 1, 2024, doi: 10.1109/ACCESS.2024.3436809.

[12] P. Fleischmann, J. Happel, and B. Gundelsweiler, “Analysis and development of a sensor concept for multistable actuators with passive magnetic shape memory alloy,” *tm - Technisches Messen*, vol. 91, no. 5, pp. 255–267, 2024, doi: 10.1515/teme-2023-0158.

[13] M. Chmielus, I. Glavatskyy, J.-U. Hoffmann, V. A. Chernenko, R. Schneider, and P. Müllner, “Influence of constraints and twinning stress on magnetic field-induced strain of magnetic shape-memory alloys,” *Scripta Materialia*, vol. 64, no. 9, pp. 888–891, 2011, doi: 10.1016/j.scriptamat.2011.01.025.

 DOI: 10.30420/456743034

Experimental setup for piezoelectric relations identification

Bas Jansen[a], Ivan Staykov[b], Paul Vrancken[b], Hans Butler[a,b], Siep Weiland[b]
[a]ASML, Veldhoven, The Netherlands, [b]Eindhoven University of Technology, Eindhoven, The Netherlands
bas.jansen@asml.com

Abstract

The relations of the controlled and dependent variables for piezoelectric elements change with the imposed boundary conditions. For self-sensing control applications a verified model structure capturing all these varying (non-) linear relations is needed. This work describes an experimental setup that is capable of identifying all these 16 measured input-output relations such that they can be compared to a piezoelectric lumped model.

1 Introduction

Piezoelectric materials couple the electric and mechanical domain together. It depends on the application what is defined as the input (independent variable) and what is the output (dependent variable), see Figure 1.



Figure 1 A piezo couples voltage, charge, force and displacement, without prescribing input or output

The relation of the controlled and dependent variables change with the imposed boundary conditions, i.e. an electric open piezo element has a higher mechanical stiffness compared to an electric shorted one [1] and a voltage driven piezo actuator exhibits hysteretic behaviour towards displacement, while with charge control this is linear [2]. The four variables lead to a total of 16 input-output relations, see Table 1.
In self-sensing applications, the actuation and sensing capabilities of piezoelectric elements are exploited simultaneously [3] and signals flow in multiple directions through the model. A model, used for simulation, design and analysis, should capture these bidirectional relations correctly, including dynamics and non-linear hysteresis. The lumped model based on [1], see elements in dashed box labelled “Piezo” of Figure 1, has the ability to do this. In [3] various model evaluations are listed indicating that the majority neglects hysteresis. In [4] this model is implemented in multiple ways to evaluate a limited set of different input-output relations, but not the complete set. In [5] a similar approach is evaluated but here the focus lies on the identification of the embedded hysteresis operator for actuation purposes and considers a parallel rather than a series resistance, and again solely for actuation purpose. The model is seldomly implemented with full dynamics, including hysteresis, electromechanical losses and then evaluated in this full bidirectional sense.
This leaves the question if all relations between the four relevant signals, listed in Table 1: voltage, charge, force and displacement, are described properly if the model remains fully intact. Especially, the question is if the single hysteresis operator in the model describes all input output relations correctly.

This paper describes the experimental setup that is used to validate the linear and non-linear relations between all input-output combinations in order to compare this to the piezo model presented in Figure 2.

2 Main system requirements

The system must be able impose all inputs and measure all outputs as defined by Table 1. Some of these relations are relatively easy to evaluate, like applying a voltage and measure displacement, while others are less trivial e.g. applying a charge, keep the position constant and measure force. In order to realize this, a secondary *counter actuator* needs to be placed in series with the piezo element. By setting this in closed loop position control a defined position can be realized.
The critical parameters of this setup are the small displacement and the large force density of piezoelectric actuators. The first puts constraints on the position measurement system. The latter defines the required dimensions of the counter actuator. This paper focuses on these few requirements, the full set of requirements can be found in [6].

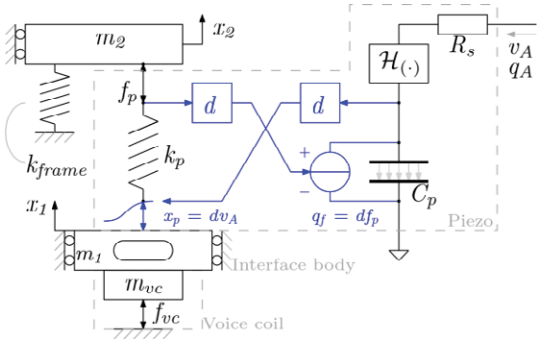


Figure 2 Schematic model representation of series coupled piezo [1] and a voice coil both mounted in frame.

Table 1 Set of 16 relations. For each input, two sets of outputs with their own relation can be identified

Input	Output set 1	Output set 2
Voltage	Charge & position	Charge & force
Charge	Voltage & position	Voltage & force
Force	Charge & position	Voltage & position
Position	Charge & force	Voltage & force

Public

 DOI: 10.30420/456743034

2.1.1 Position sensor accuracy vs piezo range

Piezo actuators have a limited range. A typical maximum actuation strain of $s_{\max} = 10^{-3}$ [−] leads to hysteresis under voltage steering of 10^{-4} [−] and under charge steering of 10^{-5} [−]. This means the actuator range should be $\times 1000$ compared to the sensor accuracy in order for the hysteresis to be detectable.

2.1.2 Piezo vs voice coil force

A piezo material stiffness of $c_{33}^{E} = 50$ GPa leads to a stress in the actuator of $T_{\max} = c_{33}^{E} s_{\max} = 50$ MPa which leads to an equivalent blocking force of $50 \frac{\mathrm{N}}{\mathrm{mm}^2}$. This number doubles to $100 \frac{\mathrm{N}}{\mathrm{mm}^2}$ in case of electric open conditions in which $c_{33}^{D} \approx 100$ GPa (with coupling factor of k = 0.7).

2.1.3 Frequency ranges

Charge amplifiers have a lower frequency bound below which they effectively behave as a voltage amplifier [2]. Typically this frequency is < 0.1 Hz.
The closed loop position control bandwidth limits the upper actuation frequency. This is set by the system dynamics, sampling delay and phase lag due to sensor filtering. Ideally this bandwidth needs to be $> 10 \cdot f_{\mathrm{setpoint}}$.

3 System design and realization

A subset of designs is selected for consideration based on the requirements, full design is available in [6].

3.1 Piezo and voice coil actuator

The selected piezo is the PC4WM; a long and thin monolithic multilayer stack. The selected counter actuator is the MMA9054 voice coil (vc) actuator that is capable of delivering the required force at a reasonable current and dimension. The key characteristics of both actuators can be compared in Table 2.

Table 2 Overview of piezo and voice coil properties

Actuator	Piezo	Voice coil	Unit
Type	PC4WM	MMA9054	n.a.
Blocking force	250	605	[N]
Free stroke	9.5×10^{-6}	$\pm 12 \times 10^{-3}$	[m]
Stiffness k_p	2.63×10^{7}	0	[N/m]
Capacitance C_p	180	–	[nF]
Current range	–	±24	[A]
Piezo constant d	63.3	–	[nC/N]
Force constant K_t	–	25.0	[N/A]
Dimensions	2 × 3 × 10	64 × ⌀90	[mm]
Mass	0.5×10^{-3}	0.7	[kg]

3.2 Mechanical realization

Figure 2 shows a schematic model of the series coupled actuators. The voice coil is modelled as an ideal force actuator that exerts force on its own mass and through a guided interface body to the piezo. The piezo is a lumped representation according [1]. The piezo element is mounted in between the interface body and the frame. The frame closes the force loop, with frame stiffness to the mechanical ground. To prevent off-axis and/or bending forces into the piezo, the mechanical interfaces are realized with half-spheres that sit in cup counterpart. A CAD drawing of the design is presented in Figure 6 and a photograph of the realized setup is shown in Figure 7.

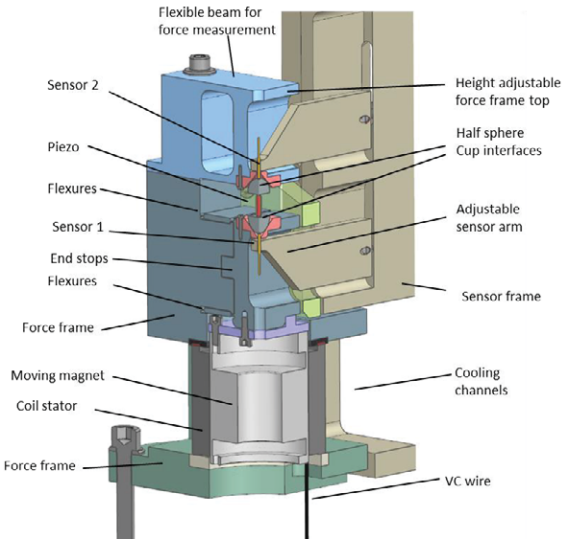


Figure 6 Cross section CAD view of the setup showing all mechanical system components [6]

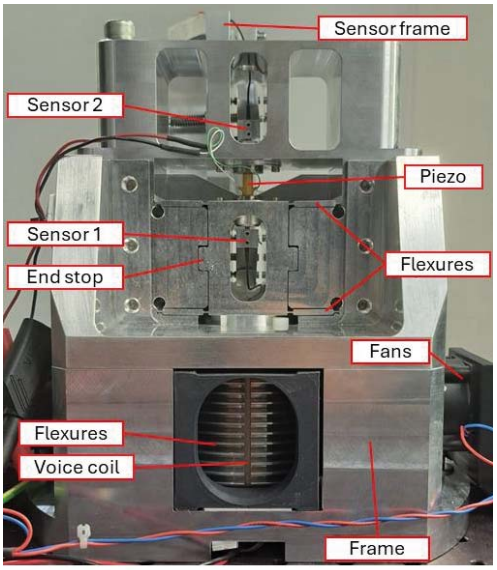


Figure 7 Photograph of the realized setup, identifying main system components

3.3 Position measurement

Two interferometers (Keyence SI-F01) measure the piezo length change, $\Delta L = x_2 - x_1$, at the half spheres at the top and bottom of the piezo. A small hole in the centre of the cups allow the measurement (almost) directly at the piezo. The sensor heads are supported with an external measurement frame outside the force paths of the actuators.

Public

 DOI: 10.30420/456743034

With filtering and averaging periodic signals, the accuracy is tens of nanometre which is sufficiently close to the required range-to-accuracy ratio of $\times\,1000$.

3.4 Mechanical dynamics

The relative heavy voice coil is placed at the bottom of the structure to limit the sway mode natural frequency. Cooling channels ensure that the dissipated vc-power is extracted from the system. The system dynamics in actuation direction is dominated by mass of the voice coil plus interface body on the series stiffness of the piezo and frame and is calculated (FEM) to be 700Hz which should allow for a position control bandwidth of tens of Hertz .

3.5 Driving amplifiers

On the electrical side the piezo is driven by custom voltage and analogue charge (±250V) amplifiers. The charge feedback is realized over a calibratedseries refrence capacitor $50 \cdot C_p = 9\mu F$. The voice coil is driven directly by a programable Delta SM7022 power supply unit (PSU).

3.6 Measurement electronics

Figure 8 contains the piezo voltage and charge measurement circuits. One of these circuits can be connected to the piezo depending on the measurement need. Figure 3 illustrates only the electrical force induced charge $q_f = d \cdot f_{vc}$ and the capacitance of the piezo element .

The voltage measurement circuit consists of a voltage follower with resistive 1:10 voltage divider with $R_1 = 11\text{M}\Omega$ and $R_2 = 99\,\text{M}\Omega$. At the actuation frequency of 1Hz, $Z_{Cp} = 884$ [kΩ], which is much smaller than the resistive path. With this configuration the open-circuit condition is realized while voltage measurements can be made.

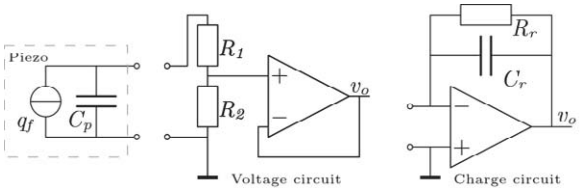


Figure 8 Voltage and charge analogue measurement circuits with TL062CP operational amplifier

The charge measurement circuit keeps both amplifier inputs at zero volt, mimicking an electric shorted piezo. The force induced charge is stored on C_r. Parallel resistor R_r prevents charge drift with corner frequency $f_q = \frac{1}{2\pi R_r C_r} =$ 10 mHz. With this circuit the short-circuit condition is realized while charge measurements can be made.

The force measurement is derived by multiplying the voice coil current, using the current monitor of the PSU, with the motor constant $f_{\text{vc}} = i_{\text{vc}} \cdot K_t$

3.7 Control topology

The control scheme of Figure 9 is capable of evaluating all cases from Table 1. The voltage and charge are provided, and measured by the respective amplifiers. The set force comes fromt the voice coil actuator. The position setpoint is created by closing the control loop over the measerd position.

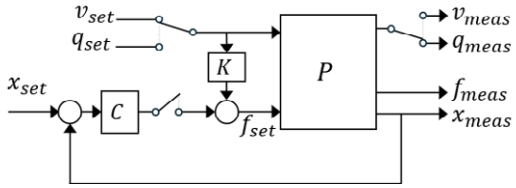


Figure 9 Control and configuration overview. The combinations of input and output signals can be configured

For the case where the charge is the input, the voltage is automatically the electrical free / measurement variable. When the position is measured, the force is controlled to a constant value. Vice versa, when the force is measured the position remains unchanged / controlled by the feedback loop. Feed-through filter K ensures the largerst portion of the force is created in advance such that the system does not have to rely solely on the feedback control.

The data acquisition and control is impemented in a Simulink Realtime real time PC with an IO104 I/O module.

4 Results

A few of the characteristic results of the setup are presented here. Figure 10 shows the displacement as function of both the voltage and the charge amplifier for a triangular 1 Hz input signal. The signals are low-passed at 50Hz and the average of a 100 periods is taken. The linear phase lag between the input and output is removed with a linear delay filter. The remaining eye opening can be fully assigned to hysteresis. The relative error, with respect to a linear fit, clearly show the presence of hysteresis in voltage control. Though not fully linear, the hysteretic part, or the eye opening, under charge control conditions <1%.

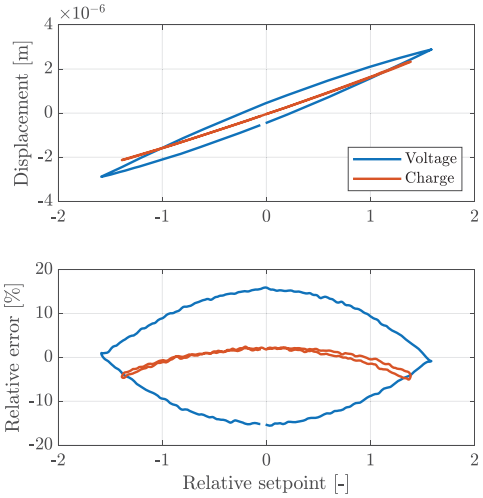


Figure 10 Hysteresis with voltage versus charge steering

Figure 11 shows the pure mechanical frequency response function (FRF) from actuation force to piezo length

Public

 DOI: 10.30420/456743034

change. It compares the results from FEM analysis [6] to the measured FRF. It shows a slightly lower main resonance around 650Hz and a smaller parasitic resonance just above 100Hz. Main difference is however a significant roll-off starting just above 20Hz. A second order transfer function fit is made that describes the roll-off shape. Part of this behaviour originates from the limited bandwidth of the power supply that drives the voice coil, yet the full explanation requires further investigation.
The open loop transfer will be dominated by this roll-off and not by the (initially assumed) first mechanical mode. The fitted transfer is used to tune a simple PI controller. With the given dynamics a bandwidth of 19Hz is realized, still sufficient to close the position loop.

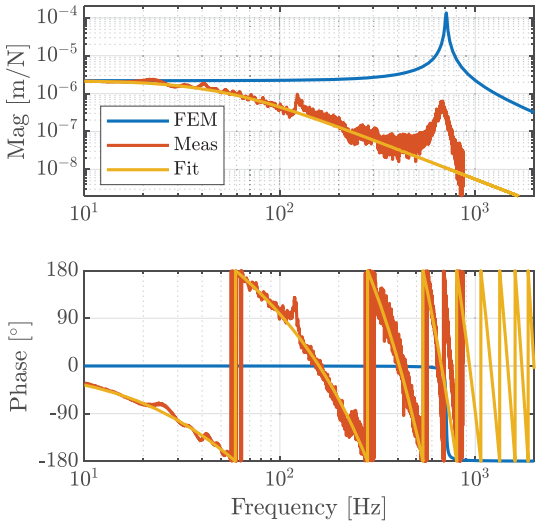


Figure 11 FRF comparison between FEM and measurement showing undesired roll-off in the measurement

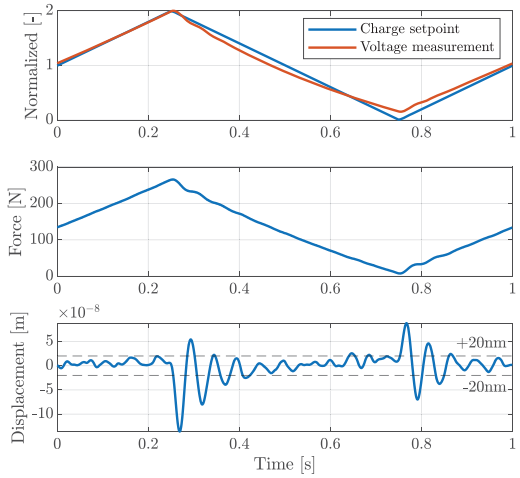


Figure 12 Measurement showing that while to the piezo is actuated by the charge amplifier, the voice coil exerts a counter force to keep the piezo elongation ‘zero’. The force and voltage are measurement variables that can be related to the charge input.

Figure 12 shows the case in which the piezo is driven by a charge and the force and voltage are the measured signals. The position remains constant ($x_{\text{set}} = 0$) by the closed loop position controller. The bottom subplot shows remaining small displacement error. After the settling, after the turnaround point of the triangular signal, it stays within a bound of $\pm 20\text{nm}$. The voice coil delivers a peak force of 250N on the tiny piezo stack to prevent it from elongating.

5 Conclusion

This paper presented the design and realization of an experimental setup in which all; input-output relations of a piezoelectric elements can be identified.
A large voice coil actuator is used to exert external force and to maintain the elongation of the piezo zero, while the piezo is driven by one of its own amplifiers, with a closed loop position control scheme.
Overall the system is capable of identifying the various input output relations with the configurable control schemes. With the selected PSU, the position loop has limited bandwidth. For future use cases a higher bandwidth amplifier can be added to increase the operating frequency.

Literature

[1] M. Goldfarb and N. Celanovic, “A lumped parameter electromechanical model for describing the nonlinear behavior of piezoelectric actuators,” Journal of dynamic systems, measurement, and control, 1997.

[2] C. Yang and K. Youcef-Toumi, “Principle, implementation, and applications of charge control for piezo-actuated nanopositioners: A comprehensive review,” *Mechanical Systems and Signal Processing*, vol. 171, p. 108885, May 2022.

[3] B. Jansen, H. Butler, S. Weiland and A. Ananthakrishnan, "Damping control using self-sensing signals for coupled piezo actuators," *ACTUATOR 2022; International Conference and Exhibition on New Actuator Systems and Applications*, Mannheim, Germany, 2022, pp. 1-4.

[4] J. B. Liseli, et al, “An Overview of Piezoelectric Self-Sensing Actuation for Nanopositioning Applications: Electrical Circuits, Displacement, and Force Estimation,” *IEEE Transactions on Instrumentation and Measurement*, Jan. 2020

[5] M. Al Janaideh, M. Al Saaideh, and M. Rakotondrabe, “On hysteresis modeling of a piezoelectric precise positioning system under variable temperature,” *Mechanical Systems and Signal Processing*, vol. 145, p. 106880, Nov. 2020

[6] Design of a Piezoelectric Stack Testing Setup, I.T. Staykov, BSc thesis, Eindhoven University of Technology, Aug. 2023.

Public

 DOI: 10.30420/456743035

Development of a highly dynamic and precise actuator with magnetic weight compensation for 3D-wafer scanning

Maik Kadias, ITK Precisioning GmbH, Lahnau, Germany, m.kadias@itknet.de
Matthias Böhle, ELSOMA GmbH, Schwerte, Germany, matthias.boehle@elsoma.de
Heiko Knoll, ITK Precisioning GmbH, Lahnau, Germany, h.knoll@itknet.de
Dr. Rolf Slatter, ITK Precisioning GmbH, Lahnau, Germany, r.slatter@itknet.de

Abstract

This paper presents the innovative concept of a highly dynamic linear actuator with adaptive magnetic weight compensation for 3D wafer scanning applications. The voice coil-based system combines millimeter-scale travel range with sub-micrometer repeatability, while the innovative magnetic compensation reduces required holding force by up to 90%, significantly minimizing power consumption and thermal effects. The actuator concept is designed to achieve millisecond response times and maintain constant sensor-to-sample distances of 10-100 µm at motion speeds exceeding 10 mm/s. This wear-free technology enables real-time adaptation to complex surface topographies e.g. for MEMS and microelectronics applications in dependence of the used sensor systems. Especially for the failure analysis and process control in microelectronics, for example, by means of Scanning Magnetic Field Microscopy (SMM), this actuator system offers improved performance and productivity.

1 Introduction

Quality requirements for electronic components in renewable energy, automotive (e-mobility), and medical technology are constantly increasing. So, there is a strong need for advanced inspection systems to supplement the established methods such as optical inspection or Scanning Acoustic Microscopy (SAM), to visualize structural defects.
However, these methods are not suited to detecting electrical faults like short circuits or interruptions. Such kind of defects only become apparent under current flow, causing characteristic discontinuities in electric and magnetic fields. For the analysis of such failures field extremely sensitive methods are used, e.g. Scanning Magnetic Field Microscopy (SMM) [1], for which a highly dynamic distance correction between the object surface and the sensor used for the field measurement is required.
Beyond failure analysis, several converging trends in semiconductor manufacturing are driving the demand for fast and accurate 3D wafer scanning. Heterogeneous integration and chiplet packaging introduce significant height variations from through-silicon vias, copper pillars, solder bumps and wafer-level mould caps. Microelectromechanical systems (MEMS) and microfluidic devices feature etched cavities, suspended membranes and channels with feature heights spanning tens to hundreds of micrometres, and in some cases millimetres. Wide-bandgap power electronics based on SiC and GaN, as well as wafer-level photonic integration, add further demanding topographies such as deep trenches, kerf profiles and microlens arrays. Across all these domains, classical inspection systems with fixed working distances reach their physical limits, since the sensor-to-sample distance must be actively controlled to maintain optimal signal quality.

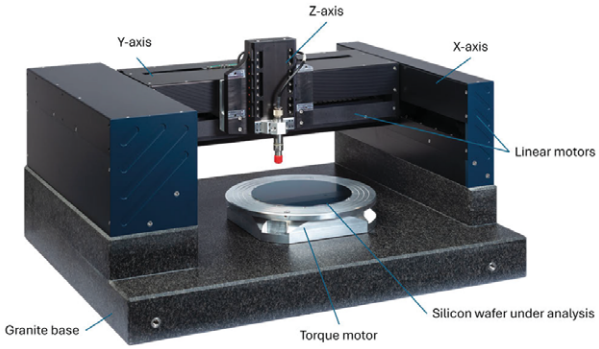


Figure 1 3D Wafer-scanner

2 Design requirements

The intended application as the vertical (Z-) axis of a 3D wafer-scanner (Figure 1), developed by ITK Precisioning, located in Lahnau near Wetzlar, imposes a demanding combination of performance and functional requirements. The system must carry a payload of up to 1.6 kg, provide a vertical travel of min. 12 mm and reach a maximum velocity of 200 mm/s and an acceleration of 5,000 mm/s² in order to enable on-the-fly topography following. The mean bidirectional repeatability shall be 100 nm, the maximum bidirectional repeatability 200 nm and the absolute positioning uncertainty less than 500 nm, measured according to ISO 230-2. On the functional side, the actuator must offer a variable weight compensation that can be tuned to different sensor masses, and the standstill power consumption shall be minimised in order to limit temperature rise and thereby reduce thermal drift of the scanner structure.

ISBN: 978-3-8007-6743-4 @ VDE VERLAG GMBH · Berlin · Offenbach

 DOI: 10.30420/456743035

3 Systematic design approach

The mechatronic development of the actuator concept was carried out following the V-model defined in VDI/VDE 2206, complemented by the systematic design methods of VDI 2221/2222. Once the requirements had been fixed, a functional analysis decomposed the Z-axis into four core functions: moving the payload, measuring the position, guiding the movement and compensating the payload weight. For each function, possible solution principles were compiled in morphological matrices, evaluated against the requirements, and combined into a coarse structural concept integrating all four sub-systems on a single moving slide. As a result, a voice coil motor was selected for the actuation (small moving mass, high dynamics, wear-free operation), a magnetoresistive (MR) linear encoder for the position measurement (high resolution and accuracy combined with high robustness and a competitive cost level), a linear ball bushing for the guidance, and a magnetic system for the weight compensation.

4 Actuator design

To achieve the highest spatial resolution and lowest noise levels, for some applications the distance between the sensor and sample must be continuously adjusted during scanning process. This can be achieved by combining, for example, an optical multi-camera system for 3D topography acquisition with fast and precise positioning mechanics. For high-precision vertical (Z-axis) positioning, two established solutions exist: spindle drives and piezo drives. Spindle drives enable large travel ranges but suffer from pitch errors and mechanical play. They also suffer from wear, particularly in short stroke applications with highly dynamic movements. Piezo drives offer high resolution but have extremely limited travel range. The idea described here employs an alternative approach: a linear direct drive based on a voice coil system. This drive type combines sufficient travel range with wear-free operation while enabling exceptionally high dynamics. Although lacking self-locking, this is compensated through a novel, adaptive magnetic weight compensation system (Figure 2).

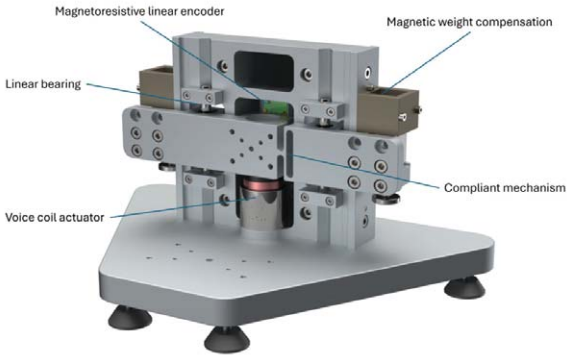


Figure 2 Prototype linear actuator

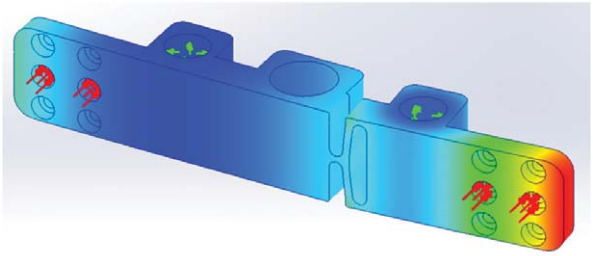


Figure 3 FEM analysis of compliant mechanism deflection

The actuator also features a compliant mechanism to ensure a consistent friction over the complete stroke (Figure 3) by avoiding “clamping” effects between the bearings due to parallelism errors or thermal expansion.

5 Development of a magnetic weight compensation system

The voice coil actuator lacks self-locking capability, requiring active control to prevent the moving mass from falling. An innovative magnetic weight compensation system is being developed by ELSOMA GmbH, located in Schwerte, near Dortmund, to address this challenge and minimize power consumption (Figure 4). The system utilizes permanent magnets, with a specially developed magnetization profile, arranged to generate a repulsive force counteracting the weight of the moving components. This passive compensation significantly reduces continuous power requirement, as the voice coil only needs to provide the difference between gravitational and acceleration forces and the magnetic compensation force. The system is adaptive, allowing fine-tuning to match different sensor masses and operating conditions. Key advantages include reduced power consumption and heat generation, improved positioning stability, enhanced dynamic response, and wear-free operation. This compares favourably to previous work to develop magnetic compensation systems [2-7].

The compensation unit must provide an adjustable axial force in the range of up to 20 N within a build envelope of 120 × 100 × 50 mm³, deliver a near-constant force over at least 10 mm of travel and exhibit only a limited stray field. The selected design comprises a soft magnetic outer ring made of annealed steel with high saturation flux density, a sintered anisotropic NdFeB ring magnet, and a coaxial sintered anisotropic NdFeB cylinder magnet. The axial force is varied continuously by rotating the inner cylinder magnet relative to the outer ring magnet, which changes the superposition of the two magnetic fields. An iterative simulation and experimental optimisation led to a “square” implementation that makes more efficient use of the available cross-section:

The magnetic design also had to limit the stray field outside the build envelope, since residual fields could perturb sensitive sensors mounted close to the moving slide. A 2D and 3D finite-element simulation environment was used to

ISBN: 978-3-8007-6743-4 @ VDE VERLAG GMBH · Berlin · Offenbach

 DOI: 10.30420/456743035

evaluate alternative magnet topologies, magnet grades and geometries, before the most promising candidates were verified on physical prototypes.

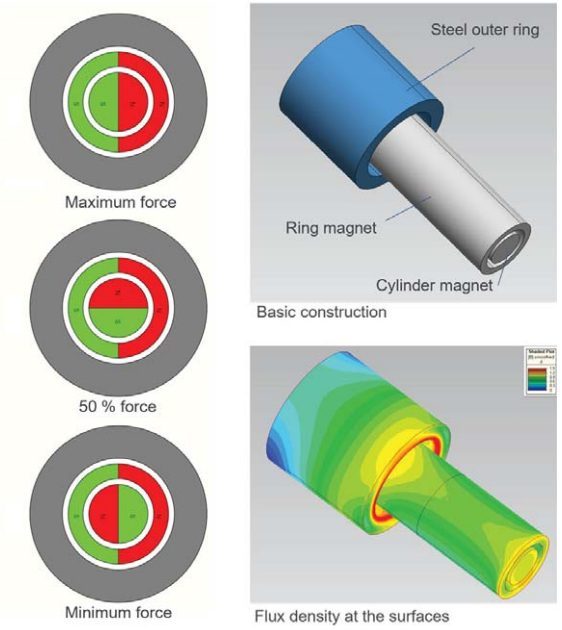


Figure 4 (a) Principle of operation of magnetic weight compensation (left) (b) Magnetic simulation of surface flux density (right)

6 Compliant joint

A pair of linear ball bushings is statically over-determined, so any parallelism error or thermal expansion of the slide induces additional stresses and a position-dependent friction. To avoid this effect, a compliant joint was introduced into the linear guidance system that allows torsion around the X-axis, bending around the Y-axis and a small expansion or compression along the X-direction, while remaining stiff in the actuation direction. The geometry was dimensioned by extensive FEM stress and deflection analyses to ensure fatigue resistance over the expected number of load cycles (Figure 3).

7 Prototype assembly and test setup

The complete prototype actuator integrates the voice coil motor, the MR linear encoder, the pair of linear ball bushings, the compliant joint and the magnetic weight compensation system on a single moving slide (Figure 2). The voice coil and the MR encoder are aligned along the actuation axis, while the compensation unit is arranged in parallel to balance the static load of the moving mass. The compliant joint is placed between the slide and the second linear bearing, where it absorbs residual misalignments without degrading the actuation stiffness. The resulting design is highly compact and offers a build height comparable to a conventional spindle drive, while delivering significantly higher dynamics and a fundamentally different power-consumption signature.

For verification, the prototype was instrumented in a dedicated test setup comprising the actuator, its dedicated controller and a measurement PC. Positional accuracy was characterised against an interferometer reference, while functional and thermal tests were performed in a climate-controlled chamber. The test programme compared variants of the actuator with and without the compliant joint, as well as the adjustable magnetic weight compensation against a “fixed” magnetic spring. A representative 1 kg payload was used to emulate a typical sensor head mass during the functional verification of the weight compensation system.

8 Results

The highly dynamic actuator with magnetic weight compensation has achieved significant milestones. The novel, highly integrated design enables a travel range of several millimeters while maintaining sub-micrometer repeatability. Initial simulations and prototypes demonstrate that magnetic weight compensation reduces required voice coil holding force by up to 90%, significantly decreasing power consumption and thermal effects. Dynamic performance tests show millisecond response times, enabling real-time adaptation to surface topography during on-the-fly scanning. The system has the perspective to achieve a positioning bandwidth suitable for maintaining constant sensor-to-sample distances of 10-100 µm even at motion speeds exceeding 10 mm/s in the vertical direction. The combination of optical topography pre-scanning and predictive control algorithms further enhances the system's ability to follow complex 3D surface profiles. The wear-free operation ensures long-term stability and reliability, critical for industrial deployment in quality control and failure analysis.

The prototype was tested extensively. Positional accuracy was determined according to ISO 230-2 with an interferometer as reference, performing 100 movements at 501 measurement positions in a Class 2 metrology room (VDI/VDE 2627) at 20 °C. The mean bidirectional repeatability error was 266 nm, the maximum bidirectional repeatability error 397 nm and the position uncertainty 1.74 µm. Although these values exceed the targets of 100 nm, 200 nm and 500 nm respectively, the analysis attributes the residual deviation largely to a sub-optimal control parameterisation, which contributes approximately 200 nm peak-to-peak position noise. Power consumption was measured in a thermal chamber between 0 and 40 °C and compared to a reference design with a “fixed” magnetic spring. With the adjustable magnetic weight compensation, the stand-still power consumption dropped to 4 mW at 20 °C, against 1.65 to 3.2 W for the design with a (not perfectly matched) fixed magnetic spring – a reduction of more than two orders of magnitude. The compliant joint additionally reduced the mean power consumption by 6.72 %. The proto-

 DOI: 10.30420/456743035

type weight compensation system achieves a maximum axial force of 22 N, an adjustable range of 2 to 22 N, and a force variation below 5 % over 16 mm of travel (Figure 5).

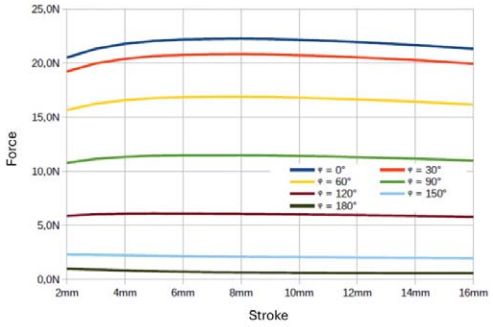


Figure 5 Force vs. stroke characteristic

9 Discussion

The chosen combination of voice coil motor and adjustable magnetic weight compensation offers several advantages over the established alternatives. Compared to a spindle-driven Z-axis, the moving mass is smaller and there is no backlash or stick-slip behaviour, both of which are frequent error sources in scanning applications. Compared to a piezo solution, the available travel range is at least one order of magnitude larger while still maintaining sub-micrometer repeatability. Compared to a counterweight-based gravity compensation, no doubling of the moving mass and no rope or guide system is required, while a pneumatic compensation would require a compressed air supply and offer only limited adjustability. The combination of the magnetic compensation with the compliant joint additionally relaxes the requirements on the linear bearing alignment, making the system more robust against assembly tolerances and thermal expansion and easier to qualify in series production.

10 Summary and Outlook

A highly integrated mechatronic system for the vertical axis of 3D wafer scanners has been designed and verified by combining a voice coil motor, a magnetoresistive linear encoder, a pair of linear ball bushings with a compliant joint, and a novel adjustable magnetic weight compensation system. The systematic V-model development approach according to VDI/VDE 2206 has been employed throughout, from the requirements specification via functional decomposition and morphological analysis to detailed design and experimental verification. The prototype meets the functional requirements and demonstrates the value of a fully passive weight compensation: the standstill power consumption was reduced from 1.65 to 3.2 W with a conventional fixed magnetic spring to only 4 mW with the adjustable compensation, while millisecond response times and sub-micrometer repeatability were retained.

The developed actuator technology opens new possibilities for high-precision scanning applications e.g. for the magnetic field microscopy. Future work will focus on further optimization of the magnetic compensation system to accommodate larger mass ranges and extending travel distance while maintaining accuracy. Integration with advanced control algorithms including machine learning-based predictive positioning is planned to improve dynamic performance. The modular design enables adaptation to other high-precision scanning applications, including confocal microscopy, and automated optical inspection systems. For ITK as an SME, this concept opens opportunities to develop innovative positioning systems more rapidly and establish them in various fields with similar requirements, strengthening the competitiveness of European microelectronics industry.

To close the remaining gap to the accuracy targets, the next development steps therefore focus on three areas: an improved parameterisation of the position controller, expected to remove most of the residual peak-to-peak noise; a refined magnetic design with a flatter force-versus-stroke characteristic of the weight compensation; and an error look-up table to compensate systematic geometric errors. The voice coil itself is also an excellent force sensor and thereby opens the possibility of a fully closed-loop adaptive weight compensation that automatically tracks changes in the payload mass. Combined with measurements of the angle-dependent axial force, this approach yields a calibration table linking the rotation angle of the inner cylinder magnet to the resulting compensation force, which the actuator firmware can use to drive a separate motor to set the appropriate angle for a given payload mass.

11 Literature

[1] M. Kögel, F. Altmann, S. Tismer, S. Brand: Magnetic field and current density imaging using off-line lock-in analysis, Microelectronics Reliability 64 (2016) 346–351

[2] D. Ausderau: Konstantkraftgeber, Europäische Patentanmeldung EP 1 378 986 A1, 30.01.2003

[3] J. Janssen, J. Paulides, E. Lomonova: Study of magnetic gravity compensator topologies using an abstraction in the analytical interaction equations, Progress in Electromagnetics Research, Vol. 128, 75-90, 2012

[4] B. Mrak, B. Lenaerts, W. Driesen, W. Desmet: Optimal Magnetic Spring for Compliant Actuation – Validated Torque Density Benchmark, Actuators 2019, 8, 18

[5] B. Schulte Westhoff, A. Elkarim Massound, J. Maas: Miniaturized electric linear drive with permanent magnetic weight compensation, Proc. of ACTUATOR 2021, GMM Fachbericht 98, 265 – 268

[6] M. Emrad Hossein, J.Z. Bird, V. Albarran, D. Che: Analysis and Experimental Testing of a New Type of Variable Stiffness Magnetic Spring with a Linear Stroke Length, Proc. of IEEE Energy Concerison Congress and Exposition (ECCE), 2021

[7] B. Mrak, J. Willems, J. Baake, C. Ganseman: Novel Adaptive Magnetic Springs for Reliable Industrial Variable Stiffness Actuation, Actuators 2023, 12, 191

 DOI: 10.30420/456743036

Experiencing Coupled Resonance Dynamics when Designing with Vibrotactile Actuators*

Prof. Dr. Thorsten A. Kern[a,b], Dr. Mohammad Sadeghi[a], Dr. Ornella Tortorici[a,b], Maximilian Becker[a], Juliana Lüer[a,b], and Ali Elnwegy[a,b]
[a]Institute for Mechatronics in Mechanics, Hamburg University of Technology, Hamburg, Germany
[b]*ligeti center*, Hamburg, Germany

Abstract

Vibrotactile actuators are used in touchscreens to create tactile feedback and defined crispy surface dynamics. Being mounted on such plastic structures the resulting surface dynamics can differ substantially from what idle actuator specifications predict. This paper identifies the root cause as a coupled resonance interaction between the actuator's internal spring-mass-damper-system and the structural modes of the systems, and demonstrates that this interaction is very predictable from two standard measurements performed on the actuator alone. As a representative setting five rectangular polycarbonate plates of varying thickness are studied under three conditions: bare plate, bare plate with mounted actuator as a bare mass, and actuator with free moving mass. Laser Doppler vibrometer measurements show that when the plate's natural frequency approaches the actuator's internal resonance, the free actuator acts as a dynamic vibration absorber (DVA), splitting the structural resonance and introducing a pronounced anti-resonance. A Rayleigh-Ritz plate model coupled to a lumped-parameter actuator model parameterised exclusively by idle and blocked test measurements predicts all three response conditions without any fitting to plate data. The results establish internal mechanical impedance as the missing design parameter in vibrotactile system integration, and motivate a standardised two-test characterisation methodology applicable across many actuator types.

Keywords: vibrotactile actuators, dynamic vibration absorber, coupled resonance, mechanical impedance, lumped-parameter model, structural dynamics, haptic system design

1 Introduction

Haptic user interfaces with functional surfaces are a well-established product category across consumer electronics, automotive controls, and medical devices. Their structural elements are predominantly made of engineering lightweight, formable, and acoustically suitable for transmitting surface vibrations [1]. To deliver tactile sensations on these surfaces, vibrotactile actuators are embedded in or mounted to the plastic structure, exciting it at frequencies within the range of human mechanoreceptor sensitivity [2, 3]. Among the actuator types employed for this purpose, modern designs increasingly rely on electrodynamic voice-coil principles, which offer wideband frequency response and independent control of force and displacement amplitude across the full tactile bandwidth [4, 5].

The integration of such actuators into lightweight structures, however, frequently reveals dynamic behaviour that deviates substantially from the predictions of simple design tools. Engineers observe that the same actuator, driven with the same signal, produces markedly different surface vibrations depending on the structural context into which it is mounted different plate thicknesses, boundary conditions, or attachment rigidity all alter the resulting haptic sensation in ways that are difficult to anticipate from actuator's specifications alone. The root cause is a mechanical coupling between the actuator's internal dynamics and the resonant structure it is attached to: the actuator is not an ideal force source but a dynamic system with an internal impedance that interacts with the load [6, 7, 8].

The characterization of vibrotactile actuators in the literature has predominantly focused on their frequency response most notably the unloaded acceleration amplitude or a loaded condition with an ideal mass, as established in the modeling work of *Yao et al.* [9] and the measurement methodology of *McMahan et al.* [5]. Together they constitute the prevailing best practice. Load-dependent effects have been documented qualitatively [6, 10], and systematic characterization has been applied to specific actuators such as the "Haptuator" series [11, 12, 13] and isolated wideband designs [4, 14].

A methodology that makes the coupled dynamic interaction between actuator and host structure quantitatively predictable and that is applicable across actuator types without destructive testing is, however, absent from the literature. Recent work has exploited impedance variation implicitly as a sensing signal [15], confirming that the load-dependent impedance shift is physically significant, yet its role as an explicit structural design parameter remains un-

*This research was funded under the Program "Innovative Hochschule" (Innovative University) by the Federal Ministry of Research, Technology and Space (BMFTR) of Germany (Grant No. 13IHS232C) and the City of Hamburg.

DOI: 10.30420/456743036

addressed.

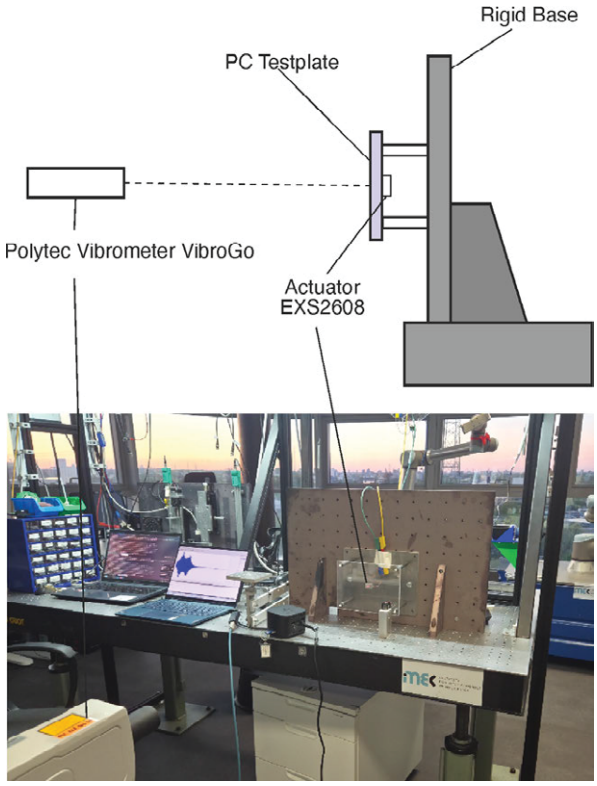


Figure 1 Experimental setup: PC plate of dimensions 200×150 mm^2 clamped at four corner points, EXS 2608L-03 A actuator attached at the plate centre, laser Doppler vibrometer aimed at the coupling point. Configuration A (blocked mass) and Configuration B (free oscillator) differ only in whether the actuator's internal mass is arrested or free.

2 Experiments

This paper addresses this gap through a systematic experimental and analytical investigation. A series of five rectangular polycarbonate plates of varying thickness, clamped at their four corners, serves as a representative model structure for a plastic haptic interface. A single electrodynamic actuator (Grewus, EXS 2608L-03 A) is coupled to each plate under three distinct conditions:

1. In the unloaded plate state, the plastic plate is clamped at its corners by four screws into a fixed position.
2. In the state with the blocked mass, the actuator is mounted centered on the plate, but the coil is short-circuited. This provides a high emf-based damping to the actuator, which results in it acting as an almost ideal mass without moving elements.
3. In the free-oscillating state the actuator is open-circuited allowing the mass to move freely in the internal dynamics of the system.

In all cases a reproducible impulse with a small electrodynamic hammer was used to excite the harmonics of the plates. unloaded plate. For analysis and model-verification the plate velocity is measured by a Polytec VibroGo scanning laser Doppler vibrometer across the relevant frequency. range (Fig. 1). The EXS 2608L-03 A has a mass of 5.5 gram of which 4.2 gram are moving.

As expected, the added total actuator mass shifted the resonance frequency of the unloaded oscillating plates to lower frequencies (Fig. 2, indicator 1 and 2). When the actuator is allowed to oscillate freely as a dynamic vibration absorber (DVA), the first eigenmode of the 2, mm plate is barely affected, while the eigenmode of the 6 mm plate significantly alters its frequency response (indicator 3).

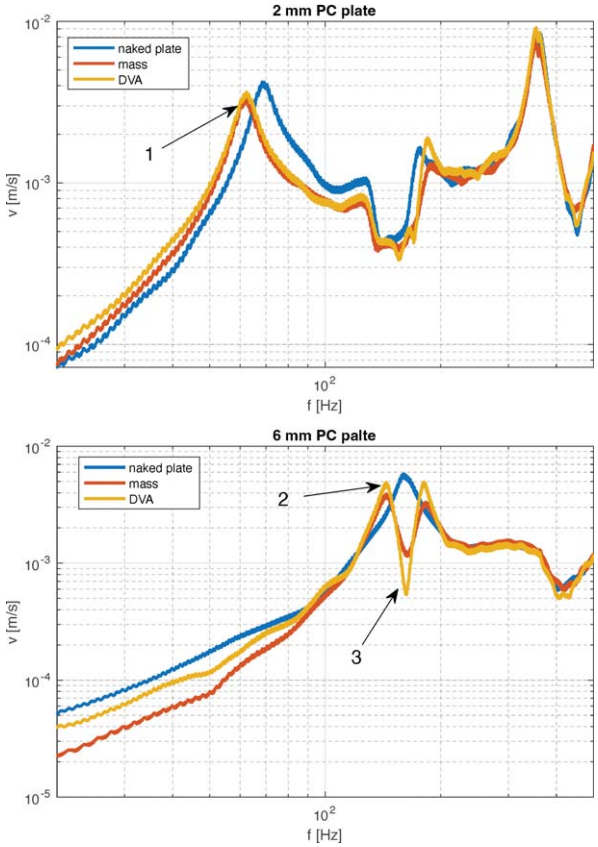


Figure 2 Measured frequency response examples of the 2mm and 6mm polycarbonate plate in the conditions of a bare-plate, with added mass and with DVA (dynamic vibration absorber)

3 Dynamic Modeling

The observations motivate a two-component analytical model with a model of the plate and the actuator coupled in joint analysis.

3.1 Plate-Model

The dynamic response of a rectangular plate with elastic point supports at its four corners is approximated via the

 DOI: 10.30420/456743036

Rayleigh–Ritz [16, 17] method using the basis functions

$$\varphi_{mn}(x,y) = \cos(m\pi x/l)\cos(n\pi y/b)\,|\,m,n = 0,\ldots,N \quad (1)$$

This, unlike a sine–sine basis, attains non-zero values at the corner coordinates and therefore allows the support stiffness k_{fix} to couple into all elastic modes, not merely the rigid-body bounce mode. The generalized stiffness matrix $\mathbf{K} = \mathbf{K}_{\text{plate}} + \mathbf{K}_{\text{corner}}$ and diagonal mass matrix $\mathbf{M}$ are assembled analytically, with

$$K_{\text{corner},ij} = k_{\text{fix}} \sum_{c=1}^{4} \varphi_i(\mathbf{x}_c)\varphi_j(\mathbf{x}_c) \quad (2)$$

summing over the four corners $\mathbf{x}_c$, and the natural frequencies ω_r together with mass-normalized mode shapes Ψ_r follow from the generalized eigenproblem $\mathbf{K}\mathbf{v} = \omega^2\mathbf{M}\mathbf{v}$. The point-force receptance at the plate center is then reconstructed by modal superposition,

$$H(\omega) = \sum_r \frac{\Psi_r^2(\mathbf{x}_0)}{\omega_r^2 - \omega^2 + \mathrm{i}\,\omega(2\zeta\omega_r + C_r)}, \quad (3)$$

where $\zeta = \eta/2$ is the material loss factor and $C_r = \mathbf{v}_r^\top \mathbf{C}_{\text{corner}}\mathbf{v}_r$ is the modally projected viscous damping contribution of the corner supports.

Based on measurements of the fundamental resonance frequency across five polycarbonate plates of thicknesses $h \in \{2,4,5,6,8\}$ mm, the corner support stiffness was identified by minimizing the sum of squared relative frequency errors, yielding $k_{\text{fix}} = 239$ kN/m with a root-mean-square deviation of 6 % across all specimens; the resulting model parametrization is summarized in Table 1.

Table 1 Rayleigh–Ritz plate model parameters.

Sym.	Description	Value
Geometry		
l	Plate length	200 mm
b	Plate width	150 mm
h	Plate thickness	2 mm to 8 mm
Material (polycarbonate)		
E	Young's modulus	2.40 GPa
ρ	Density	1240 kg m^{-3}
ν	Poisson's ratio	-
η	Loss factor	-
Corner support (identified)		
k_{fix}	Stiffness at corner	239 kN m^{-1}
d_{fix}	Damping at corner	2.0 N s m^{-1}
N	Ritz truncation order	10

3.2 Actuator Model

Following the best-practice methodology established by *McMahan et al.* [5], the vibrotactile actuator is represented as a lumped-parameter model comprising a 9-element spring-mass-damper network (Fig. 3). In the 2nd (mobility) analogy, this network captures the internal compliance k_M, internal damping d_M, and internal moving mass m_{int} as elements whose interaction with the external load impedance determines the actuator output.

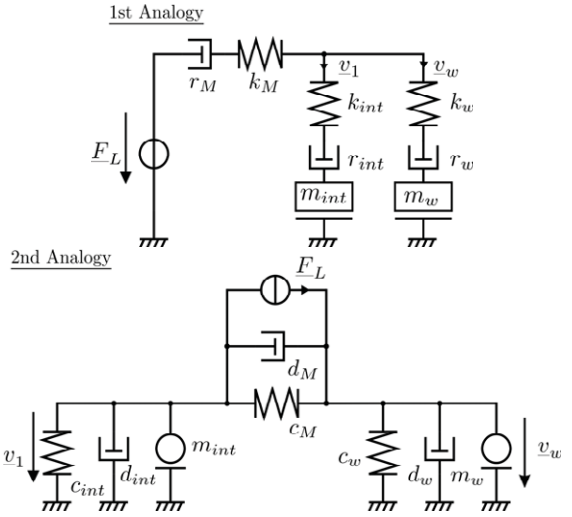


Figure 3 Lumped-parameter model of a linear resonant actuator in the 1st analogy (top) and 2nd analogy (bottom), adapted from [5]. The internal subsystem (m_{int}, k_M, d_M) couples to the external load (m_w, k_w, d_w) via the primary force source $\underline{F}_L$.

To identify the internal model parameters without disassembly, two complementary tests are applied. In the **idle (open-circuit) test**[1], the actuator is mounted on a membrane that is compliant in the actuation direction but stiff transversely, so the actuator moves freely; this yields the open-circuit velocity $\underline{v}_{\text{open}}(\omega)$. In the **blocked (short-circuit) test**[2], the actuator is rigidly coupled to a force sensor on a stiff base, suppressing all displacement; this yields the short-circuit force $\underline{F}_{\text{short}}(\omega)$. Together, these two measurands define the internal mechanical impedance

$$\underline{Z}_i = \frac{\underline{F}_{\text{short}}}{\underline{v}_{\text{open}}}, \quad (4)$$

which encapsulates all load-relevant dynamic properties of the actuator in a single complex-valued frequency function. Figure 4 shows this representative measurement for the *Grewus* EXS 2608L-03 A: The idle test delivers acceleration (and its velocity and displacement integrals) over the tactile frequency range, the blocked test delivers force, and the computed impedance clearly exhibits the resonance–anti-resonance transition at the actuator's internal resonance near 160 Hz.

A least-squares system identification constrained to physically admissible parameter ranges is applied to fit the model of Fig. 3 to the measured data (Fig. 5). The fit is accurate across the primary resonance region; deviations above 500 Hz reflect higher-order spring eigenmodes not captured by the 9-element model. Two parameter sets are retained: a *best-fit* set minimizing the residual norm, and a

[1] In analogy to an electrical source being tested without a load attached.

[2] In analogy to an electrical source being tested under short-circuit conditions.

 DOI: 10.30420/456743036

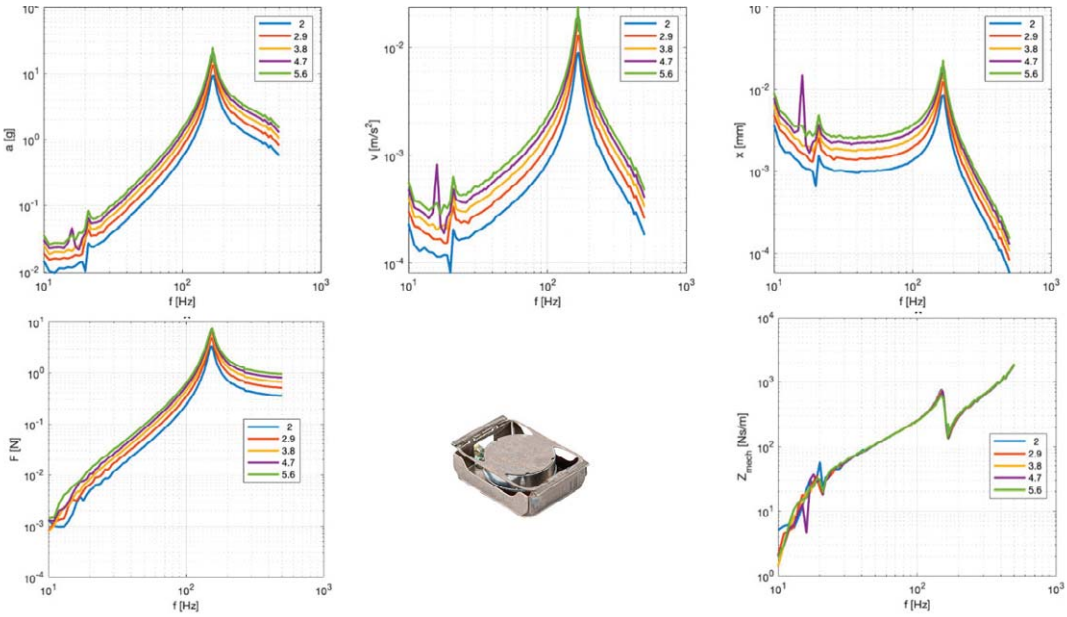


Figure 4 Complete characterization dataset for the *Grewus* EXS 2608L-03 A obtained by the two-test procedure: idle test (acceleration and integrated velocity and displacement; top row) and blocked test (short-circuit force at multiple drive voltages; bottom left), yielding the internal mechanical impedance $\underline{Z}_i$ (bottom right). Two frequency sweeps on a single test stand are sufficient to determine all parameters required for coupled system prediction. The resonance–anti-resonance transition near 160 Hz in the impedance curve is the spectral fingerprint that governs the dynamic vibration absorber effect observed in Fig. 2.

physics-informed set constrained to values consistent with the known actuator geometry and material.

Table 2 Identified lumped-parameter model of the *Grewus* EXS 2608L-03 A (internal subsystem only; world parameters not included).

Sym.	Description	Value
m_{int}	Moving mass	$4.3 \times 10^{-3}\,\text{kg}$
k_{int}	Sec. stiffness	$1.0 \times 10^{-5}\,\text{N m}^{-1}$
d_{int}	Sec. damping	$1.3 \times 10^{-2}\,\text{N s m}^{-1}$
k_M	Prim. stiffness	$4885\,\text{N m}^{-1}$
d_M	Prim. damping	$0.1\,\text{N s m}^{-1}$

4 Model vs. Measurement

The parameterized coupled model is then compared against the experimental measurements (Fig. 6). In the vicinity of the plate's first eigenmode the influence of the actuator on the structural frequency response is clearly evident (indicator 4). Even the secondary plate dynamics near 140, Hz (indicator 5) are reproduced by the model, albeit at a reduced amplitude. The contrast between the two extreme cases is particularly instructive: the 2, mm plate, whose first eigenmode lies near 70, Hz, is well below the actuator's internal resonance and is therefore largely unaffected by its dynamic vibration absorber effect. The 6,mm plate, by contrast, has a natural frequency of approximately 170, Hz close to the actuator resonance and consequently exhibits a pronounced anti-resonance and frequency splitting characteristic of a strongly coupled DVA. The theoretical model captures both limiting cases and the intermediate behaviour with good fidelity.

Future Use and Perspective

The data presented in this paper based on a a single actuator type, two plate configurations, five thickness values are deliberately minimal. Their purpose is not completeness but proof of principle: to demonstrate that a pair of standard measurements, idle and blocked, is sufficient to predict the full coupled dynamics of an actuator-structure system without any additional fitting inside the relevant frequency ranges for tactile systems.

The broader implication becomes visible when the methodology is applied across the actuator landscape which our team did and made accessible at *Coupled Resonance Dynamics*. This compression of apparent diversity into a common physical currency is only possible once internal actuator impedance is treated as a first-class design parameter.

Vibrotactile actuator engineering stands today at precisely the point that circuit design reached when Thévenin's theorem was formulated. Before that theorem, engineers designed around the open-circuit voltage of a source. Afterwards, they designed with source and load as an inseparable pair, and the full power of impedance matching became accessible. The plate experiment in this paper is the haptic analogy of that insight: the same actuator, the same signal, and yet qualitatively different structural dynamics depend-

DOI: 10.30420/456743036

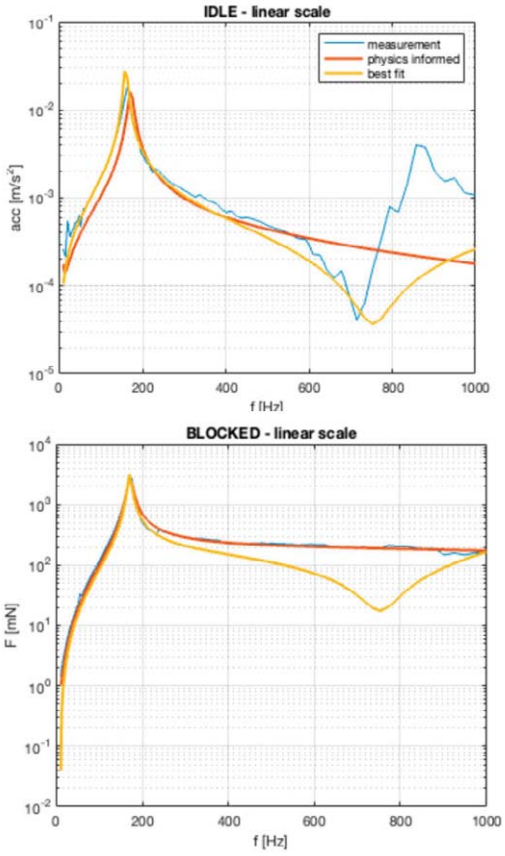


Figure 5 Least-squares model fit (Fig. 3) to the measured idle and blocked data of the *Grewus* EXS 2608L-03 A. Solid line: measurement; dashed line: model fit.

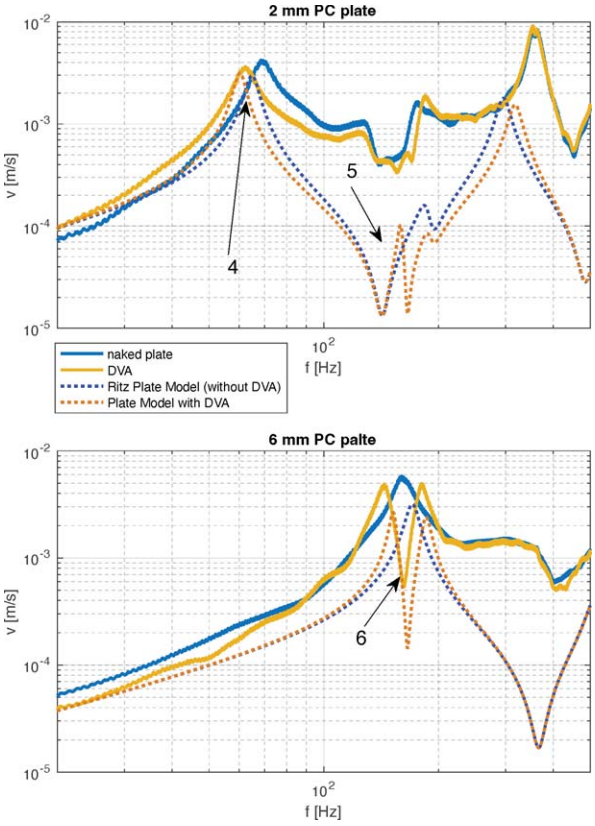


Figure 6 Comparision of Ritz-Model without and with DVA and vibrometer measurements. Whereas the frequency response beyond the first eigenmode is still challenging (indicator 6), the characteristics at the first resonance can clearly be proven with the model and its parameterization.

ISBN: 978-3-8007-6743-4

@ VDE VERLAG GMBH · Berlin · Offenbach

ing solely on whether the source impedance is engaged. Idle acceleration, the prevailing specification metric, cannot predict this. Internal impedance, measured once by the two-test procedure, can.

The practical consequence is direct. A manufacturer who characterizes an actuator according to this methodology delivers, in two frequency sweeps, all the information a system designer needs to predict resonance shifts, anti-resonance positions, and maximum power transfer for any mechanical load without access to the actuator's internals, without destructive testing, and without iteration on physical prototypes.

5 Literature

[1] Thorsten A. Kern, Christian Hatzfeld, and Alireza Abbasimoshaei, editors. *Engineering Haptic Devices*. Springer Series on Touch and Haptic Systems. Springer International Publishing, Cham, 2023. ISBN 978-3-031-04535-6 978-3-031-04536-3. doi: 10.1007/978-3-031-04536-3. URL .

[2] Seungmoon Choi and Katherine J. Kuchenbecker. Vibrotactile Display: Perception, Technology, and Applications. *Proceedings of the IEEE*, 101(9):2093–2104, September 2013. ISSN 1558-2256. doi: 10.1109/JPROC.2012.2221071. URL . Conference Name: Proceedings of the IEEE.

[3] Claudio Pacchierotti, Stephen Sinclair, Massimiliano Solazzi, Antonio Frisoli, Vincent Hayward, and Domenico Prattichizzo. Wearable haptic systems for the fingertip and the hand: Taxonomy, review, and perspectives. *IEEE Transactions on Haptics*, 10(4): 580–600, 2017. ISSN 23294051. doi: 10.1109/TOH.2017.2689006. Publisher: Institute of Electrical and Electronics Engineers.

[4] Zhixiong Jiang and Sangmoon Hwang. Design and Analysis of Wide-Bandwidth Actuator for Haptic Controller With Novel Magnetic Circuit. *IEEE Transactions on Magnetics*, 59(12):1–5, December 2023. ISSN 1941-0069. doi: 10.1109/TMAG.2023.3284814. URL . Conference Name: IEEE Transactions on Magnetics.

[5] William McMahan and Katherine J. Kuchenbecker. Dynamic modeling and control of voice-coil actuators for high-fidelity display of haptic vibrations. In *2014 IEEE Haptics Symposium (HAPTICS)*, pages 115–122, February 2014. doi: 10.1109/HAPTICS.2014.6775442. URL . ISSN: 2324-7355.

[6] Bruce Mortimer and Gary Zets. Vibrotactile transduction and transducers. *The Journal of the Acoustical Society of America*, 121:2970–7, June 2007. doi: 10.1121/1.2715669.

[7] Ayoub Ben Dhiab and Charles Hudin. Confinement of Vibrotactile Stimuli in Narrow Plates: Principle and Effect of Finger Loading. *IEEE Transactions on Haptics*, 13(3):471–482, July 2020. ISSN 2329-4051. doi: 10.1109/TOH.2020.2986727. URL . Conference Name: IEEE Transactions on Haptics.

[8] Thorsten A. Kern, Christian Hatzfeld, and Fady Youssef. The User's Role in Haptic System Design. In Thorsten A. Kern, Christian Hatzfeld, and Alireza Abbasimoshaei, editors, *Engineering Haptic Devices*, pages 109–131. Springer International Publishing, Cham, 2023. ISBN 978-3-031-04536-3. doi: 10.1007/978-3-031-04536-3. URL .

[9] Hsin-Yun Yao and Vincent Hayward. Design and analysis of a recoil-type vibrotactile transducer. *The Journal of the Acoustical Society of America*, 128 (2):619–627, August 2010. ISSN 0001-4966. doi: 10.1121/1.3458852. URL .

[10] Lynette A. Jones and Anshul Singhal. Perceptual dimensions of vibrotactile actuators. In *2018 IEEE Haptics Symposium (HAPTICS)*, pages 307–312, March 2018. doi: 10.1109/HAPTICS.2018.8357193. URL . ISSN: 2324-7355.

[11] Nils Landin, Joseph M. Romano, William McMahan, and Katherine J. Kuchenbecker. Dimensional Reduction of High-Frequency Accelerations for Haptic Rendering. In Astrid M. L. Kappers, Jan B. F. van Erp, Wouter M. Bergmann Tiest, and Frans C. T. van der Helm, editors, *Haptics: Generating and Perceiving Tangible Sensations*, pages 79–86, Berlin, Heidelberg, 2010. Springer. ISBN 978-3-642-14075-4. doi: 10.1007/978-3-642-14075-4-12.

[12] Heather Culbertson, Juan José López Delgado, and Katherine J. Kuchenbecker. One hundred data-driven haptic texture models and open-source methods for rendering on 3D objects. *IEEE Haptics Symposium, HAPTICS*, pages 319–325, 2014. ISSN 23247355. doi: 10.1109/HAPTICS.2014.6775475. Publisher: IEEE Computer Society ISBN: 9781479931316.

[13] Heather Culbertson and Katherine J. Kuchenbecker. Importance of matching physical friction, hardness, and texture in creating realistic haptic virtual surfaces. *IEEE Transactions on Haptics*, 10(1):63–74, January 2017. ISSN 19391412. doi: 10.1109/TOH.2016.2598751. Publisher: Institute of Electrical and Electronics Engineers.

[14] Radu Olaru, Alexandru Arcire, Camelia Petrescu, Marius Mugurel Mihai, and Bogdan Gîrtan. A novel vibration actuator based on active magnetic spring. *Sensors and Actuators A: Physical*, 264: 11–17, September 2017. ISSN 0924-4247. doi: 10.1016/j.sna.2017.07.041. URL .

[15] Matthew Davison and Andrew P. McPherson. A self-sensing vibrotactile transducer for bidirectional tactile interaction. In *Proceedings of EuroHaptics 2024*, Lille, France, July 2024.

[16] Arthur W. Leissa. *Vibration of Plates*. NASA SP-160. NASA Office of Technology Utilization, Washington, D.C., 1969.

[17] G. B. Warburton. The vibration of rectangular plates. *Proceedings of the Institution of Mechanical Engineers*, 168(1):371–384, 1954. doi: 10.1243/PIME_PROC_1954_168_040_02.

 DOI: 10.30420/456743037

Creep modeling and stability of PNZT shape memory piezoelectric actuators

Jurrien Keulen[a], Mireny Ugalde Reygadas[a], Monica Acuatla Meneses[a], and Bayu Jayawardhana[a]
[a]University of Groningen, Engineering and Technologoy Institute, Groningen, The Netherlands
j.r.keulen@rug.nl

Abstract

Niobium doped lead zirconate titanate (PNZT) piezoelectric shape memory actuators are well-suited for set-and-forget applications, where long-term positioning stability is critical. Compared to conventional piezoelectric actuators, PNZT actuators exhibit a strong hysteresis memory. This property is exploited to achieve stable remnant positioning without continuous power supply. However, creep causes slow displacement drift, limiting long-term accuracy. This paper presents a parallel model structure combining a Preisach hysteresis model with a Kelvin-Voigt (KV) creep model to characterize hysteresis and creep in the PNZT actuator. A feedforward compensation strategy is derived from the identified models and numerically validated. The results demonstrate the suitability of the proposed parallel Preisach-KV structure for open loop set-and-forget applications.

1 Introduction

Shape memory, or set-and-forget piezo actuators are a class of quasi-static piezoelectric actuators designed for long term positioning stability, without requiring continuous power or feedback control. The shape memory piezo actuator operates based on the hysteretic memory of the ferroelectric material, defined by the remnant polarization state after removal of the electric field. This type of actuator was first introduced in [1] as shape memory piezoelectric actuator. A commercially available implementation was later presented in [2], known as PIRest. While PIRest actuators use PZT (lead zirconate titanate) ceramics, our actuator employs a niobium-doped PZT ceramic, PNZT. The niobium dopant enhances the asymmetry of the strain–electric field loop, which is often depicted and known as the butterfly loop. This enables a wider range of remnant strain. Advantages of the shape memory actuators include lower power consumption, long term stability and a potential reduction in electrical shielding complexity. Iterative control strategies are proposed in [3] and experimentally validated in [4]. Despite these advantages, the creep behavior of shape memory piezo actuators has not been characterized or compensated for in the literature.

Creep is a time-dependent phenomenon in piezoelectric actuators in which the displacement continues to drift after the input voltage is applied or removed, affecting both short-term and long-term positioning accuracy. For set-and-forget actuators in particular, creep poses a direct challenge to positioning stability, as we do not want to correct continuously for this drift. While creep in standard PZT actuators has been studied in [5], its characterization and compensation in PNZT-based shape memory actuators remains unaddressed.

The creep in piezoelectric actuators is commonly described using logarithmic models [5]. While the logarithmic models offer a simple formulation, it comes with a fundamental limitation. The predicted displacement grows unbounded when $t \to \infty$, which is physically unrealistic of PNZT set-and-forget actuators. This motivates the use of Kelvin-Voigt (KV) elements, which capture the time-dependent behavior through a parallel combination of spring-damper elements [6]. While fractional-order models offer improved accuracy [7], the added identification complexity makes KV elements an attractive and physically interpretable alternative. As shown in Figure 1, K_0 is omitted from the KV model, as the instantaneous elastic response is already captured by the hysteresis model. In this paper, we propose a parallel interconnection of a Preisach hysteresis model and a KV creep model for PNZT shape memory actuators, based on [6]. We further present a feedforward compensation strategy that suppresses creep after a desired remanent position has been reached.

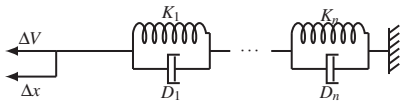


Figure 1 Kelvin Voigt model used to characterize piezoelectric creep. The model comprises n spring–damper pairs connected in parallel, relating input voltage ΔV to creep displacement Δx.

2 Model Identification.

The input-output behavior of the piezo actuator, from voltage to displacement, is described by an interconnection of a rate-independent hysteresis model and a time-dependent creep model whose outputs are summed, as shown in Fig-

DOI: 10.30420/456743037

ure 1. The hysteresis component is identified using a Preisach model and the creep component using a Kelvin Voigt model. Creep identification is restricted to short-term behavior (≤ 1 s) because of slow drift in the laser interferometer readout over longer windows.

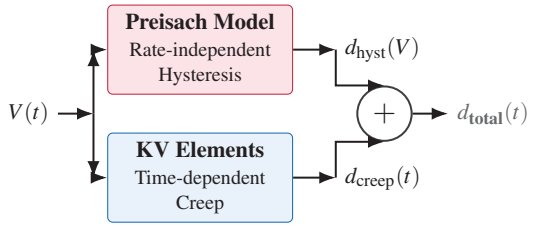


Figure 2 Parallel model structure for piezoelectric displacement, consisting of a Preisach hysteresis model and a Kelvin-Voigt creep model.

Experimental data for model identification is gathered using a single PNZT pellet with a thickness of 0.88 mm and diameter of 8 mm, placed in the piezo holder unit of an aixACCT TF2000. Displacement is measured using a SIOS laser interferometer at a sampling rate of 1000 samples/s. The input signals are designed using the waveform editor to capture a range of actuation amplitudes. Since the displacement is always centered at zero, a bipolar prepolarization pulse of $V_{\text{max}} = 2000$ V is applied to reset the polarization state of the piezo. The prepolarization is followed by a 0.9 s rest period, after which a record trigger initiates the measurement over the desired recording window. For creep identification, a trapezoidal voltage pulse is applied with rising and falling ramps at a slew rate of 1.6×10^5 V/s and a hold duration of 0.1 s at the target amplitude. The voltage is then returned to 0 V and the creep response is recorded for 1 s; longer windows are avoided due to drift in the interferometer readout. This procedure is repeated for amplitudes of 1600, 1700, 1800, and 1900 V, with five repetitions per amplitude to reduce measurement noise.

2.1 Hysteresis Identification

Piezo actuators exhibit hysteresis and creep simultaneously, making independent identification of the hysteresis non-trivial. Since we characterize the creep by using trapezoidal input signals, an excitation signal for hysteresis identification that does not match the slew rate of the trapezoidal signals, could potentially lead to inconsistent hysteresis estimates due to rate-dependent effects.

To account for this, triangular input signals are used whose slope matches exactly the rising and falling ramps of the trapezoidal creep measurements, at a slew rate of 160 000 V/s. At this rate, the transition time should be sufficiently fast such that creep is negligible, allowing the hysteresis to be isolated cleanly. The Preisach model is identified by by triangular signals from small to large amplitude, in steps of 100 V ranging from 1000 V to 2000 V, with five averages per amplitude. This exploits the wipe-out property of the Preisach model, ensuring consistent initialization of the ferroelectric domains state by erasing all previous extrema of the smaller magnitude. The Preisach

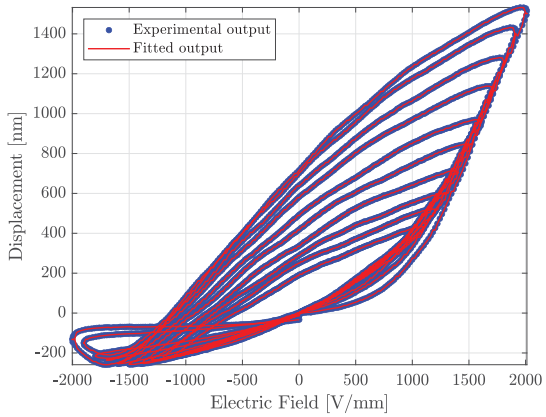


Figure 3 Measured and fitted butterfly loops using slope-matched triangular input signals 20-36Hz, discretization level M = 175, ≈ 1 % error.

weight plane is then identified using least squares and singular value decomposition [8], which is computationally expensive due to the large number of relay operators, but yields an accurate fit of the weighting plane. The resulting butterfly loops are shown in Figure 3.

2.2 KV Identification

With the hysteresis model identified, the creep component is isolated by subtracting d_{hyst} from the total measured displacement under trapezoidal excitation. As shown in Fig. 4, measurements are performed at input amplitudes of 1600, 1700, 1800, and 1900 V. Before each measurement, a bipolar sinusoidal prepolarization pulse of 2000 V amplitude is applied to bring the actuator to the same initial state. The residual displacement d_{creep} is plotted alongside the input signals, clearly exhibiting the characteristic vis-

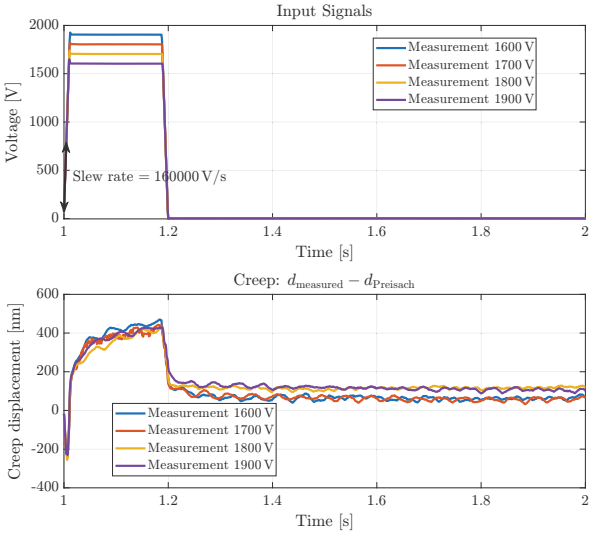


Figure 4 Trapezoidal input signals at 1600–1900 V and the resulting residual creep displacement d_{creep}, obtained by subtracting d_{hyst} from the total measured displacement.

ISBN: 978-3-8007-6743-4

@ VDE VERLAG GMBH · Berlin · Offenbach

DOI: 10.30420/456743037

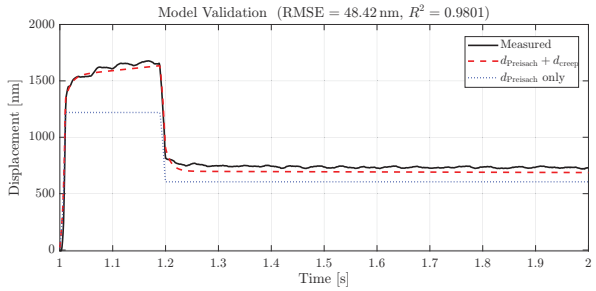


Figure 5 Measured and modeled displacement for a 1650 V trapezoidal input, comparing the Preisach-only and combined Preisach–Kelvin-Voigt models.

coelastic response during the step and the subsequent creep upon return to zero.

However, the KV model does not fully capture all observed dynamics. Negative residual values at the initial part of the d_{creep} suggest either a rate-dependent component in the Preisach model that is not fully accounted for, or insufficient prepolarization consistency between the measurements and Preisach model. A possible solution would be to adopt a Hammerstein structure for d_{hyst}, which could better capture the rate-dependent hysteresis contribution [9].

For identification, two KV elements are employed, yielding a creep transfer function

$$G_{\text{creep}}(s) = \frac{k_1}{\tau_1 s + 1} + \frac{k_2}{\tau_2 s + 1}, \tag{1}$$

where k_i is the steady-state gain and $\tau_i = D_i/K_i$ is the time constant of the i-th element. Two elements are sufficient to capture the dominant fast and slow creep modes observed within the 1 s identification window; adding further elements yielded marginal improvement in fit quality. Each term represents the creep contribution of a KV element, and the parallel combination with the hysteresis model enables the combined model to capture creep dynamics across multiple time scales. The parameters k_i and τ_i are identified by fitting $G_{\text{creep}}(s)$ to d_{creep} using least-squares optimization. The fitted transfer function, given by

$$G_{\text{creep}}(s) = \frac{0.185}{0.011\,s + 1} + \frac{1.685}{5.918\,s + 1},$$

is validated against a new measurement with a 1650 V trapezoidal input of similar shape as in Figure 5, where the combined Preisach-KV model is compared against the Preisach only prediction. The identified time constants confirm that the parallel structure captures both a fast and a slow creep mode, with the slow element dominating the long-term displacement drift. A significant amount of the differences between the measured and modeled displacement are caused by variability in the PNZT pellet response across repeated measurements [4].

3 Compensation Strategy

With the combined model identified, a feedforward compensation strategy can be developed to minimize long-term

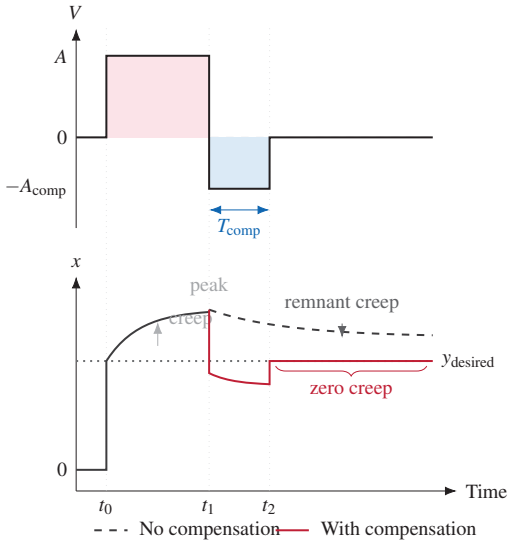


Figure 6 Feedforward compensation strategy. After the main excitation pulse of amplitude A, a negative pulse of amplitude A_{comp} and duration T_{comp} is applied to suppress remnant creep and hold the displacement at y_{desired}.

displacement drift for the PNZT set-and-forget actuator. The strategy consist of applying a negative voltage pulse of amplitude $-A_{\text{comp}}$ and duration T_{comp} immediately after the main excitation pulse. The duration T_{comp} is chosen beforehand and kept short to ensure a fast control strategy and not all remnant displacement is removed by depolarizing the piezo in the other direction. A schematic of the compensation strategy is shown in Figure 6. The amplitude of the driving signal A and the compensation pulse A_{comp} is determined by minimizing the weighted cost function

$$J = w_{\text{pos}} \left(\frac{e_{\text{pos}}}{y_{\text{desired}}} \right)^2 + w_{\text{drift}} \left(\frac{e_{\text{drift}}}{y_{\text{desired}}} \right)^2,$$

where $e_{\text{pos}} = \hat{y}(t_s) - y_{\text{desired}}$ is the predicted position error at steady state t_s, and e_{drift} is the state of the slow KV element at the end of the compensation pulse t_2, which governs the remaining long-term drift. Both terms are normalized by y_{desired} and weighted by w_{pos} and w_{drift} respectively, enabling a tunable trade-off between steady-state positioning accuracy and long-term drift suppression. The compensation strategy is simulated for a remnant position of $y_{\text{desired}} = 350$ nm. As shown in Figure 7 the optimizer yields a steady-state position of 343.8 nm, corresponding to a positioning error of 6.2 nm. The compensation pulse reduces the residual long-term drift to 26.67 nm. The residual drift stems from the slow Kelvin-Voigt element. Because $\tau_2 \gg T_{\text{comp}}$, the slow element is still evolving at t_2, leaving residual long-term drift. The compensation pulse can only act on the state that has already built up; it cannot preemptively cancel drift that has not yet occurred. As a result, a small but nonzero residual drift remains after compensation. A practical limitation of this approach is the loss of remnant position $\Delta = 248.8$ nm induced by the negative compensation pulse, which partially depolarizes the actuator. This must be accounted for when selecting the target

 DOI: 10.30420/456743037

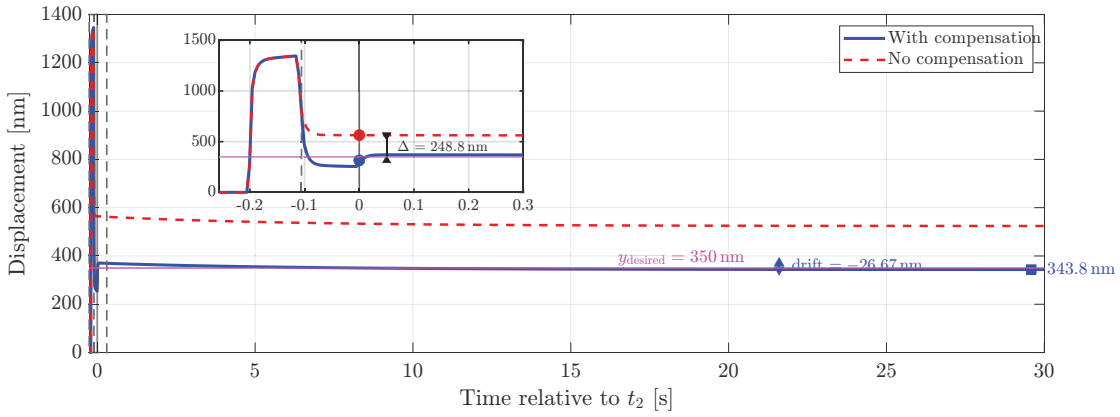


Figure 7 Simulated actuator displacement with and without creep compensation for a target remnant position of $y_{\text{desired}} = 350$ nm. Time is plotted relative to the end of the compensation pulse t_2.

position, as a higher initial remnant position is required to achieve the desired displacement after compensation.

4 Conclusion

In this paper, a Preisach hysteresis model and a Kelvin Voigt creep model were combined in a parallel interconnection to describe thequasi-static displacement of a PNZT shape memory actuator. The two components were identified independently using dedicated excitation signals, with the creep contribution isolated by subtracting the predicted hysteresis response from the measured displacement. A feedforward compensation strategy was then developed, applying a short negative voltage pulse after the main excitation to suppress long-term displacement drift. The pulse amplitude is determined offline by minimizing a weighted cost function that balances short-term positioning accuracy against residual drift, using the combined model as a surrogate.

Simulation results for a target remanent position of $y_{\text{desired}} = 350$ nm show that the strategy reduces residual long-term drift to 26.67 nm, at the cost of a depolarization loss of $\Delta = 248.8$ nm that must be accounted for when selecting the initial driving amplitude. These results indicate that the proposed parallel Preisach–KV structure is suitable for open-loop set-and-forget applications.

Future work will focus on experimental validation of the compensation strategy on the PNZT actuator. The rate-dependent residuals observed during creep identification also require more attention: it remains to be established whether they reflect a genuine rate-dependent hysteresis, which could for example be captured by a Hammerstein structure [9].

References

[1] T. Morita, Y. Kadota, and H. Hosaka, “Shape memory piezoelectric actuator”, *Applied Physics Letters*, vol. 90, no. 8, 2007, ISSN: 00036951. DOI: 10.1063/1.2709985.

[2] J. Reiser and H. Marth, “Pirest technology-how to keep the last position of pzt actuators without electrical power”, in *ACTUATOR 2018; 16th International Conference on New Actuators*, VDE, 2018, pp. 1–4.

[3] M. Vasquez-Beltran, B. Jayawardhana, and R. Peletier, “Recursive algorithm for the control of output remnant of preisach hysteresis operator”, *IEEE Control Systems Letters*, vol. 5, no. 3, pp. 1061–1066, 2020.

[4] J. Keulen, M. Ugalde-Reygadas, N. Hamelynck, J. Roorda, M. Acuautla, and B. Jayawardhana, “Development and validation of remnant control for PNZT hysteretic piezo actuators”, In preparation, 2026.

[5] H. Janocha and K. Kuhnen, “Real-time compensation of hysteresis and creep in piezoelectric actuators”, *Sensors and actuators A: Physical*, vol. 79, no. 2, pp. 83–89, 2000.

[6] K. Seki, J.-Y. Hirata, M. Ruderman, and M. Iwasaki, “Creep modeling with time-dependent damping parameters in piezoelectric actuators”, in *2019 IEEE International Conference on Mechatronics (ICM)*, IEEE, vol. 1, 2019, pp. 135–140.

[7] S. Tashakori, V. Vaziri, and S. S. Aphale, “A comparative quantification of existing creep models for piezoactuators”, in *International Conference on Wave Mechanics and Vibrations*, Springer, 2022, pp. 419–426.

[8] L. Liu, K. K. Tan, S.-L. Chen, S. Huang, and T. H. Lee, “Svd-based preisach hysteresis identification and composite control of piezo actuators”, *ISA transactions*, vol. 51, no. 3, pp. 430–438, 2012.

[9] Y. Guo, J. Mao, and K. Zhou, “Rate-dependent modeling and $\mathscr{H}_\infty$ robust control of gma based on hammerstein model with preisach operator”, *IEEE Transactions on Control Systems Technology*, vol. 23, no. 6, pp. 2432–2439, 2015.

 DOI: 10.30420/456743038

Reliability and drift behaviour of CNT-modified grippers for soft robotics applications

Ivica Kolaric[a], Rolf Nothhelfer-Richter[a], Jonas Heldt[a], Hirosato Monobe[b], and Takushi Sugino[b]
[a]Fraunhofer Institute for Manufacturing Engineering and Automation IPA
[b]Mechano-Activated Materials Research Group, Research Institute of Core Technology for Materials Innovation (CTMI), National Institute of Advanced Industrial Science and Technology (AIST)

Abstract

Since their discovery, CNT have fascinated numerous scientists worldwide due to their outstanding intrinsic properties. Their high electrical conductivity in particular opens up new possibilities for the development of electrode materials in electroactive polymers. Once the effectiveness of CNTs as actuators in aqueous environments had been proven [1], formulations were developed that enable the creation of "dry" actuators [2]. These actuators have been continuously improved and investigated for new applications.

1 Soft Robotic Grippers

The implementation of advanced gripping systems in soft robotics marks a fundamental paradigm shift in modern automation technology, positioning itself at the intersection of flexible logistics and delicate agricultural harvesting [13]. While conventional, rigid robotic end-effectors consistently fail when confronting highly unstructured geometries, irregular form factors, or mechanically fragile organic objects, soft robotic grippers leverage inherent material compliance to achieve biomimetic adaptability [12]. By distributing contact pressures evenly across the surface topology of the target object, these compliant manipulators drastically suppress local stress concentrations and eliminate the risk of structural bruising or micro-scale tearing [14]. Although widespread architectures still rely heavily on FEA or granular jamming configurations, these legacy methodologies increasingly encounter engineering bottlenecks due to their bulky external pneumatic supply lines, system-wide cycle-time latencies, and complex control infrastructures [12].

Among EAP alternatives, ionic CNT actuators have emerged as a particularly attractive compliant gripper element [1]. In these tri-layer systems, a thin ionically conductive membrane—such as Nafion or a PVDF-based ionomer—is sandwiched between two flexible carbon nanotube electrode layers. Voltage application at $\leq 2\,\mathrm{V}$ drives cation migration within the membrane, generating an asymmetric swelling stress that deflects the composite structure in a bending motion suited to delicate pick-and-place tasks[2]. Unlike FEAs, ionic CNT actuators require no external pneumatic infrastructure, enabling silent, lightweight, and electrically addressable gripper fingers compatible with miniaturised and MEMS-scale implementations. However, as multi-material composites subjected to repeated large-amplitude bending, they are susceptible to coupled degradation pathways—including electrode delamination, resistive network fatigue, membrane dehydration, and electrochemical side reactions—that limit operational lifetime [1] [2]. Characterising and mitigating these mechanisms is the primary objective of this work; the underlying failure modes are reviewed in Chapter 2 .

Picking operations—defined as the selective removal of items from storage media or natural growth environments to fulfil specific orders or processing streams—are foundational to modern supply chains. In warehouse logistics, order picking accounts for up to 55 % of total operating costs, making it a primary focal point for optimisation [13]. In agriculture, manual harvesting represents one of the highest variable costs and faces chronic seasonal labour shortages globally [15].

While rigid automation has successfully transformed structured environments (e.g., automotive assembly lines), it consistently struggles in unstructured, variable, and delicate contexts. Consequently, human labour remains the dominant force in both material handling and fruit harvesting. This reliance introduces systemic vulnerabilities—including musculoskeletal disorders, occupational injuries, and inconsistent throughput. To bridge this gap, soft robotics has emerged as a novel paradigm, utilising highly compliant materials to mimic the adaptability of the human grip while offering the tireless reliability of automated systems [12].

1.1 Manual Order Picking in Warehouse Logistics

1.1.1 Operational Requirements and Paradigm Shifts

In industrial distribution centres, order picking must satisfy strict KPIs centred around throughput, lead time, and picking accuracy. Operational paradigms are broadly categorised into two frameworks:

- **P2P:** The picker travels through aisles to retrieve items from static racks. Travel time often constitutes

 DOI: 10.30420/456743038

over 50 % of the entire picking shift, leading to significant physical fatigue [16].

- **PtP:** AS, RS or AMRs deliver bins directly to a stationary picker at a workstation. While this eliminates travel time, it increases picking frequency, escalating repetitive strain on the upper extremities [13].

Regardless of the paradigm, pickers must continuously execute cognitive tasks, including visual verification, counting, sorting, and scanning via RF terminals or Pick-by-Voice systems.

1.1.2 Throughput Performance Metrics

Human picking rates vary significantly depending on layout, technology, and item characteristics [13]: Paper-based Picker-to-Part: 50–80 picks/h, RF-Scanner / Pick-by-Voice: 100–150 picks/h, Pick-by-Light / Part-to-Picker workstations: 250–450 picks/h.
Error rates in manual picking typically range from 0.1 % to 1 %, requiring secondary quality assurance processes that add to overall operational overhead.

1.2 Human Picking and Harvesting in Agriculture

Unlike the controlled, climate-regulated environments of industrial warehouses, agricultural harvesting occurs in highly unpredictable outdoor conditions. The objects to be picked are not standardised boxes or bottles, but living organisms characterised by biological variability, varying maturity stages, and high mechanical fragility [12].

1.3 The Integration of Soft Robotics in Picking Operations

To combat labour scarcity and mitigate physical strain, the robotics industry is transitioning toward soft robotics [12]. Rigid robotic grippers apply concentrated point forces that crush fragile fruits and fail to conform to the irregular geometries found in logistics and agriculture.

1.3.1 Materials and Principles of Soft Actuation

Soft robotics utilises highly compliant materials—such as silicone elastomers (e.g., EcoFlex, DragonSkin), polyurethane, and woven textiles—to achieve structural deformation without mechanical joints [12]. The primary actuation methods include:

- **FEAs:** Pneumatic networks (PneuNets) embed internal chambers within an asymmetric elastomer structure. When pressurised, the chambers expand, causing the finger to curl gently around an object.
- **Granular Jamming Grippers:** A flexible membrane filled with granular media (e.g., coffee grounds) flows around an unknown shape, then jams rigid under vacuum to grip it conformally.

1.3.2 Application in Warehouse Logistics

In e-commerce fulfilment centres, robots must pick thousands of distinct items (e.g., cosmetics, packaged food, electronics) with unknown form factors. Soft grippers provide inherent physical adaptability, allowing a single end-effector to grip a soft t-shirt, a rigid phone case, or a flexible pouch without reprogramming. Coupled with machine vision systems, soft robotic workstations can achieve pick rates of 300–400 items/h, approaching human performance while operating continuously without fatigue [13].

2 Degradation Mechanisms in Ionic CNT Actuators

Ionic CNT actuators are tri-layer composites: a thin ionically conductive polymer membrane (e.g., Nafion or sulfonated PVDF) sandwiched between two compliant CNT electrode layers. Applied voltages $\leq 2\,\mathrm{V}$ drive cation migration, generating asymmetric swelling stress and controlled bending [1, 2]. The fundamental incompatibility of the stiff CNT network, viscoelastic membrane, and their interface gives rise to coupled degradation pathways, classified as *physical* and *electrochemical*.

2.1 Physical Degradation

Electrode–membrane delamination is the most critical structural failure mode. The large elastic modulus mismatch ($E_{\mathrm{CNT}} \approx 1\,\mathrm{TPa}$ vs. $E_{\mathrm{mem}} \approx 100$–$300\,\mathrm{MPa}$) generates cyclic interfacial shear stress, nucleating microscale voids that propagate into macroscopic delamination, reducing active electrode area and causing stress concentrations [2].
CNT network fatigue (R-fatigue): Conductivity depends on quantum-tunnelling across inter-tube junctions. Cyclic bending widens these gaps through progressive plastic deformation, causing a monotonic sheet resistance increase that reduces drive current, actuation force, and tip displacement [9].
Back-relaxation and viscoelastic creep: Under DC voltage, slow counter-ion redistribution partially reverses the initial bending (back-relaxation). Over many cycles, viscoelastic creep accumulates irreversible strain, manifesting as neutral-position drift and asymmetric stroke amplitudes [10].

2.2 Electrochemical Degradation

Membrane dehydration: Ionic conductivity is strongly coupled to membrane solvent content. In open-atmosphere operation, solvent evaporation increases bulk ionic resistance, directly measurable as a rising low-frequency impedance in EIS [11].
Faradaic side reactions: At the recommended 2 V drive voltage, the 1.23 V electrolysis threshold is exceeded, enabling water oxidation ($2\,\mathrm{H_2O} \rightarrow \mathrm{O_2} + 4\,\mathrm{H^+} + 4\,\mathrm{e^-}$) and proton reduction ($2\,\mathrm{H^+} + 2\,\mathrm{e^-} \rightarrow \mathrm{H_2}$). Resulting microbubbles disrupt interfacial adhesion and accelerate delamination [2].
Ion concentration polarisation: Continuous asymmetric excitation creates persistent cation concentration gradients, causing a non-zero neutral position, asymmetric strokes, and progressive amplitude decay [10].

 DOI: 10.30420/456743038

2.3 Summary

These mechanisms are coupled: Faradaic gas evolution accelerates delamination; dehydration amplifies junction fatigue; and ion polarisation compounds back-relaxation drift. Two complementary methods address these pathways: **EIS** provides a non-destructive, frequency-resolved fingerprint of membrane resistance, charge-transfer resistance, and diffusive transport over cycle count; **endurance testing** tracks macroscopic performance (tip displacement, blocking force, temperature) over continuous bipolar cycling.

3 Experimental

3.1 Impedance spectroscopy

Impedance was measured using a potentiostat *Interface 1010* from *Gamry Instruments, Warminster* capable of performing all techniques, including electrochemical impedance spectroscopy. Frequency sweeps were done covering a frequency range from 1.1 MHz downto 0.01 Hz. The Voltage was varied between 10 mV and 1000 mV.
All experiments were carried out in a climate chamber at 23 °C and 50 % relative humidity

3.2 Actuator test bench

To assess the long-term durability of the EAP actuators, a dedicated test bench for cyclic endurance testing was set up. Throughout the tests, displacement (or blocking force), electrical response, and actuator temperature were continuously monitored. The temporal evolution of these quantities was used to evaluate performance degradation and to characterize the long-term operational stability of the actuators.
The electroactive polymer (EAP) actuator was mounted in a vertical, suspended configuration using a mechanical clamping fixture that also provided the electrical contacts for voltage application. The test bench allows the actuator to freely bend in both directions. The tip displacement is measured using an *OptoNCDT* laser displacement sensor from *Micro-Epsilon*. In both configurations, the actuator surface temperature was monitored contactlessly using an *Infratherm IN 5 plus* infrared thermometer *IMPAC electronic GmbH*. All measurements were performed inside a climate chamber maintained at 23 °C and 50 % relative humidity to ensure stable boundary conditions.
Excitation voltages and frequencies for the actuator were generated and controlled through a LabVIEW-based program and applied by a Potentistat/Galvanostat *1030 PC.T.* from *Jaissle Elektronik GmbH*, which simultaneously acquired the resulting voltage and current signals. An overview of the experimental setup is provided in Figure 1.

3.3 Fabrication of three-layered actuator element

A three-layered actuator element was fabricated by heat-pressing the electrode films and the electrolyte film. Preparation and materials used are described in detail in [6] An

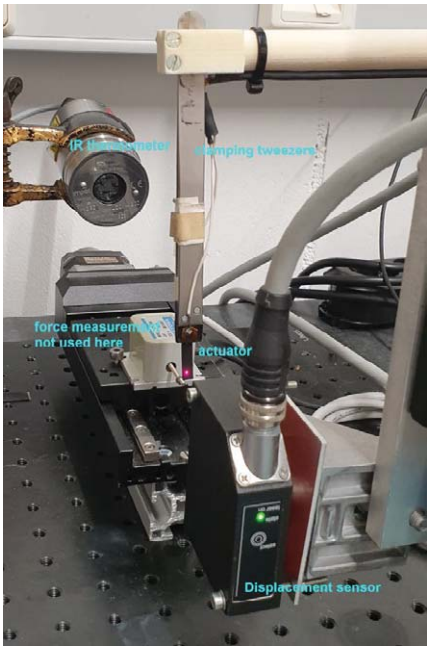


Figure 1 Experimental setup of the actuator test bench.

electrolyte film was laminated between two electrode films to make a symmetrical three-layered actuator element. The heat-pressing was performed at 70 °C with 10 N for 90 s in the first pressing process, then with 270 N for 90 s in the second pressing process. The electrode films adhered to the electrolyte film by this thermal treatment. The configuration of the three-layered actuator element is illustrated in Fig. 2. The total thickness of the actuator element was between 98 μm and 363 μm. The total thickness is mainly controllable by the thickness of the electrode film.

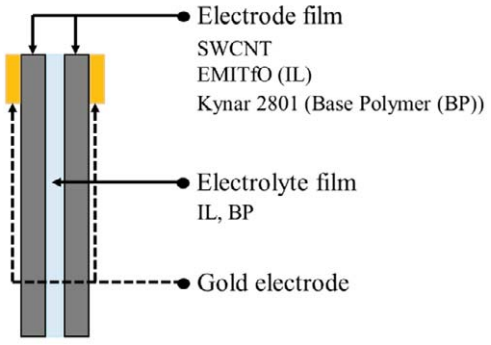


Figure 2 Schematic view of the three-layered actuator and chemical structures of EMITfO and PVDF-HFP

4 Results

4.1 Impedance spectroscopy

Ionic films without carbon nanotube electrodes were examined by Electrochemical Impedance Spectroscopy (EIS). The electrodes (16 mm diameter) were punched out

DOI: 10.30420/456743038

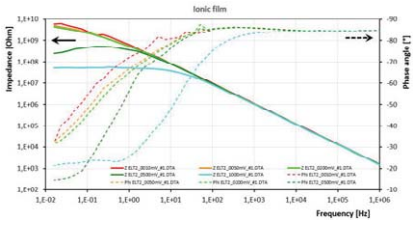


Figure 3 EIS of electrolyte film at excitation voltages of 10 mV, 50 mV, 200 mV, 500 mV and 1000 mV

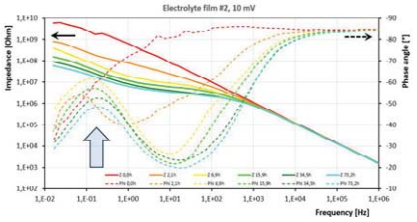


Figure 4 EIS spectra at 10 mV excitation over time

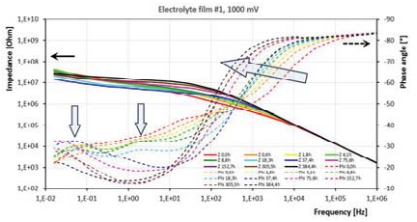


Figure 5 recording of EIS at 1000 mV excitation over time

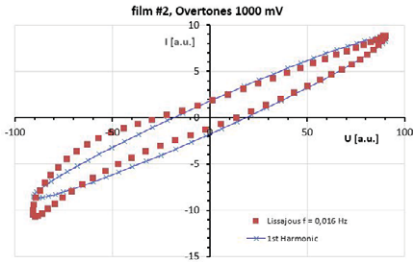


Figure 6 red curve: Lissajous figure at 0.016 Hz and 1000 mV excitation, blue curve: Lissajous figure of the fundamental frequency

of self adhesive copper strips.

The impedance spectroscopy shows a behavior of a coating soaked with electrolyte [4, 5]. At high frequencies the spectrum is dominated by capacitance indicated by a phase angle of -90° and gradient of the impedance of -1 in double logarithmic plot. From this part a capacitance of 120 pF was calculated, which is comparable with the capacitance of a 19 µm thick PET film (100 pF).

At low frequencies the impedance reaches a plateau and the phase angle is near 0° indicating ohmic behaviour. Fig. 3 shows that with increasing sinusoidal excitation voltage the ohmic impedance plateau at low frequencies is more pronounced. The higher voltage provokes a polarization of the film. A subsequent cycling of the excitation voltages (rms) of 10 mV, 50 mV, 200 mV, 500 mV and 1000 mV (Fig. 4) over a time of 73 hours showed that the polarization remains. At low frequencies a maximum in phase angle appears which can be assigned to the constraints in ion mobility. At the highest applied excitation voltage of 1000 mV - shown here at another film over a time of 384 hours - the impedance plateau is lower as at excitation with 10 mV. With time the transition from capacitive to resistive behaviour shifts to lower frequencies.

[3] showed that the the kinetics of a relaxation process in polymers is indicated by the frequency, whereas the number of contributing elements find its expression in the magnitude of the dielectric effekt. Based on this findings we conclude that the shift of a maximum in the phase spectrum to lower frequencies with duration of load indicates that a ionic charge transport mechanism slows down. The magnitude of the maximum ist nearly unchanged, so there is no consumption of ions. At short stress load times the maximum is partly hidden beneath the capacitive behaviour.

At high excitation voltages nonlinear behavior during the recording of impedance spectra especially at low frequencies was observed. The impedance recording software displays Lissajous figures during recording, where one can see a significant deviations from the elliptical shape. For later evaluation the software provides harmonics up to the tenth order, from which the Lissajous figures can be reproduced. Fig. 6 shows the Lissajous figure of the lowest frequency of 0.016 Hz and the corresponding Lissajous figure of the fundamental frequency. For the excitation voltage the amplitude of all harmonics are below 0.1 % of the amplitude of the fundamental frequencies. The harmonics of the current reach up to 10 % at frequencies below 1 Hz.

The authors attribute the occurrence of harmonics to a limited ion mobility and the resulting saturation of the polarisation of the dieletric film. The impedance spectra show only minor changes over the 384-hour observation period, indicating that the dielectric film is reasonably stable.

4.2 Endurance test

To test the durability of the actuators, they were subjected to a endurance test. Free movement was observed over a period of 15 days (or 380 hours). The actuator was driven by a 2-volt square-wave signal at 1 Hz. Fig 8 shows an overlay of the extreme positions of the movement at the beginning of the durability test and after 77, 191 and 380 hours. Initially the bending of the actuator corresponds to the bending of a beam. With increasing time under stress a discrete position of maximum curvature develops and the rest of the beam tends to stay straight.

Fig. 7 shows the displacement of the actuator and the electrical current. When the polarity of the voltage is reversed, the current shows a peak and then drops to a plateau. This corresponds to the charging and discharging of a capacitor. The corresponding displacement increases, but the frequency is too high to reach a plateau.

It took a few excitation cycles to reach a almost constant temperature of the actuator up to 45 to 50 °C. The frequency of 1 Hz is too high to see a temperature change

ISBN: 978-3-8007-6743-4

@ VDE VERLAG GMBH · Berlin · Offenbach

 DOI: 10.30420/456743038

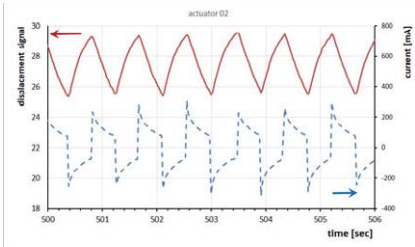


Figure 7 typical displacement (left axis) and current (right axis) of actuator 02

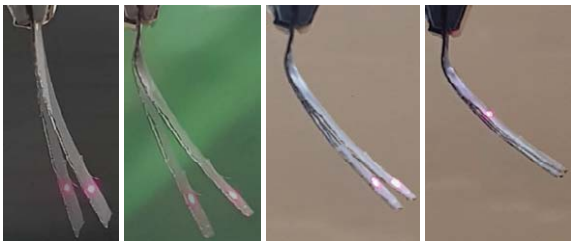


Figure 8 from left: overlay of the displacement after 0.13, 77, 191 and 380 hours

within one cycle, just as is the case at frequencies below 0.1 Hz. During the test the static bending of the actuator near the clamp increased. So the laser of the displacement sensor hits the actuator in an increasingly lower angle, which makes it difficult to measure the actuator's movement precisely.

Table 1 summarizes the changes in surface temperature and power consumption from the start of the experiment to the end of the endurance test.

Table 1 Overview of the changes in characteristic values over the endurance test

	Start	End
Time	500 s	380 h
Cycles	500	$\approx 1.2 \times 10^6$
Temperature [°C]	42.15	36.08
average Current [mA]	114.02	81.47
average Power [mW]	227.55	162.64

After the test the actuator was examinded visually and by microscope. A partial delamination of the conducting layers was observed on the convex side of the actuator . Fig. 9 shows a 3d image (Laser scanning microscope, Keyence) of both sides of the actuator at the bending point.

5 Discussion

In summary, CNT EAP actuators demonstrate considerable potential as multifunctional components for next-generation soft robotic systems. Their combination of mechanical compliance, actuation capability, and intrinsic sensing functionality makes them particularly suitable for adaptive, safe human–environment interaction, as well as for agricultural harvesting technology, where soft and

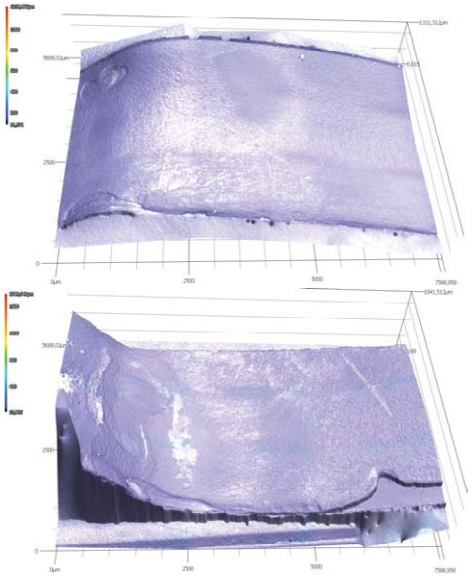


Figure 9 bending point of the actuator from the convex (left) and concave side (right) after test

functionally integrated actuator systems are of growing interest.

Nevertheless, endurance investigations clearly reveal that significant challenges remain. Improvements in energetic efficiency, operational reliability, and long-term durability are necessary for robust real-world deployment. A key aspect will be the development of dedicated packaging strategies that reconcile high flexibility with sufficient resistance to abrasion and mechanical wear. Further progress will additionally depend on advanced printing technologies capable of producing functional gradients and complex multilayer architectures with high precision, alongside improved process reproducibility to ensure consistent performance and scalable fabrication.

Future research should therefore address materials selection, structural design, packaging integration, and manufacturing control in parallel with actuator-level performance optimization. Deeper investigation of the individual actuator components will be equally important: the mechanical and viscoelastic properties of the membrane warrant characterisation via DMA and thermal expansion analysis, while EIS offers further insight into ion concentration and mobility. Of particular interest is the temporal variation of phase-spectrum maxima, from which molecular-level relaxation processes can be inferred.

6 Conclusion

CNT EAP actuators hold strong potential for soft robotics and medical applications, combining mechanical compliance, low weight, large deformation, and intrinsic sensing within a single material platform. This multifunctionality makes them particularly attractive for adaptive robotic systems and minimally invasive medical devices. Their applicability to gripping devices has been demonstrated, further underlining their practical relevance.

However, significant challenges remain before these actuators can be deployed in robust real-world applications. Long-term endurance tests reveal clear limitations in efficiency, reliability, and durability. A key weak point is the adhesion of the electrode material to the active membrane. Improved electrode materials, applied via a **drop-on-demand** technique [7, 8], offer a promising path forward: this approach enables precise, defined electrode structures, eliminates short-circuit risks associated with knife-cutting, and allows deposition of an additional isolating top layer.

More broadly, future progress requires advances in materials selection, actuator architecture, electrode stability, packaging, and manufacturing reproducibility. Dedicated packaging concepts must balance high flexibility with abrasion resistance, while advanced printing technologies will be essential for producing functional gradients and complex multilayer structures. Ultimately, realizing the full potential of CNT EAP actuators demands a concurrent focus on actuation performance, lifetime, operational stability, and scalable fabrication.

7 Acknowledgments

The author gratefully acknowledges Prof. Ray H. Baughman, Dr. Kinji Asaka, and Dr. Siegmar Roth for their inspiration and support over many years. Sincere thanks are also extended to the National Institute of Advanced Industrial Science and Technology (AIST), Japan, for its long-standing support in this important endeavor. The author further thanks Artur Potapenja for his valuable assistance in hardware construction.

8 Literature

[1] R. H. Baughman et al., “Carbon nanotube actuators,” Science, vol. 284, no. 5418, pp. 1340–1344, 1999. DOI: 10.1126/science.284.5418.1340

[2] K. Asaka, K. Mukai, T. Sugino, and K. Kiyohara, “Ionic electroactive polymer actuators based on nanocarbon electrodes,” Polymer international, vol. 62, no. 9, pp. 1263–1270, 2013.

[3] Mansour, A.A., Happ, E., Wolf, T. et al. Dielectric relaxation of polystyrene with side-chain- and chain-end-labels. Colloid Polym Sci 272, 894–902 (1994). https://doi.org/10.1007/BF00658887

[4] Gamry Instruments, EIS of organic coatings and paints, Application Note, https://www.gamry. com, 2023.

[5] M.Wanner, Elektrochemische Impedanzspektroskopie (EIS): Anwendung und Aussagen der Messtechnik, Webinar, Fraunhofer IPA, Stuttgart, 2022

[6] T. Sugino, Y. Shibata, K. Kiyohara, and K. Asaka, “Actuation mechanism of dry-type polymer actuators composed by carbon nanotubes and ionic liquids,” Sensors and Actuators B: Chemical, vol. 273, pp. 955–965, 2018, ISSN: 0925-4005. DOI: https : / / doi . org / 10 . 1016 / j . snb . 2018 . 05.006 [Online]. Available: https://www.sciencedirect.com/science/article/pii/S0925400518309006

[7] O. Tiedje, T. Hess, W. Niemeier, and Q. Ye, “Overspray-free painting: Requirements to equipment and material,” in Swedish Surface Treatment Cluster, Sweden, 2022.

[8] O. Tiedje, “Einführung selektiver beschichtung mittels digitaler methoden,” in PIAE by VDI – Internationaler Fachkongress f¨ur Kunststoffe im Automobilbau, Baden-Baden, Germany, 2026.

[9] S. Nemat-Nasser, “Micromechanics of actuation of ionic polymer–metal composites,” Journal of Applied Physics, vol. 92, no. 5, pp. 2899–2915, 2002. DOI: 10.1063/1.1495888

[10] S. Nemat-Nasser and J. Y. Li, “Electromechanical response of ionic polymer–metal composites,” Journal of Applied Physics, vol. 87, no. 7, pp. 3321–3331, 2000. DOI: 10.1063/1.372343

[11] M. Shahinpoor and K. J. Kim, “Ionic polymer–metal composites: I. Fundamentals,” Smart Materials and Structures, vol. 10, no. 4, pp. 819–833, 2001. DOI: 10.1088/0964-1726/10/4/327

[12] D. Rus and M. T. Tolley, “Design, fabrication and control of soft robots,” Nature, vol. 521, no. 7553, pp. 467–475, 2015. DOI: 10.1038/nature14543

[13] R. de Koster, T. Le-Duc, and K. J. Roodbergen, “Design and control of warehouse order picking: A literature review,” European Journal of Operational Research, vol. 182, no. 2, pp. 481–501, 2007. DOI: 10.1016/j.ejor.2006.07.009

[14] E. Ochoa and C. Mo, “Design and field evaluation of an end effector for robotic strawberry harvesting,” Actuators, vol. 14, no. 2, p. 42, 2025. DOI: 10.3390/act14020042

[15] T. Duckett, S. Pearson, S. Blackmore, and B. Grieve, “Agricultural robotics: The future of robotic agriculture,” UK-RAS Network, White Paper, 2018. DOI: 10.31256/WP2018.1

[16] T. Gudehus and H. Kotzab, Comprehensive Logistics. Springer Science Business Media, 2012

 DOI: 10.30420/456743039

Theoretical and experimental investigations regarding small electric drive systems overload potentials in short-term operation

Ulrike Kurz, M. Sc., ulrike.kurz@ikff.uni-stuttgart.de [1]
Dr.-Ing. Andreas Wagener, andreas.wagener@faulhaber.de [2]
Prof. Dr.-Ing. Bernd Gundelsweiler, bernd.gundelsweiler@ikff.uni-stuttgart.de [1]

[1] Institute of Design and Production in Precision Engineering, University of Stuttgart, Stuttgart, Germany
[2] Dr. Fritz Faulhaber GmbH & Co. KG, Schönaich, Germany

Abstract

Intermittent operation in general or even more short-term operation of electric drive systems provides the opportunity to take advantage of overload capacities. This means that motors can be smaller for a given application, which offers advantages in terms of installation space, materials and cost. To maximize the utilization of according potentials, this paper examines torque overload using two motor types: A coreless and a slotted motor. This involves experimental investigations, theoretical estimates and comparisons. The experimental investigations examine different methods for estimating winding temperature. The theoretical analysis considers both the single-body and two-body model approaches. The results show that significantly higher overload factors or longer switch-on times are thermally feasible than previously estimated theoretically. It is therefore concluded that specifying thermal parameters based on the operating mode could be a solution for more accurate estimates.

1 Introduction

1.1 Motivation

Applications using small electric drive systems often require an intermittent operation of the system. On the contrary, continuous operation is rarely required. Therefore, the overload capability of electric drive systems could be applied in many cases. This corresponds with reduced space requirements, use of material, weight and purchase costs. In order to exploit these potentials, a suitable theoretical estimate of the applicable overload is relevant. A corresponding estimate of the allowed power and torque overload can be retrieved from literature [1, 2]. A previous experimental study showed differences between theoretically and experimentally determined torque overload values, with the experimental results exceeding the calculations [3]. Therefore, this matter should be investigated further.

1.2 State of the art

A specification of a thermally allowed power overload regarding the excitation coil of a DC magnet was described by Kallenbach in [1]. This approach can be rediscovered in literature until now, when regarding intermittent operation of small electric drive systems [2]. The following equation is mentioned in this context for torque and short-term operation:

$$k_{\mathrm{S2,1-b}} = \frac{1}{\sqrt{1 - e^{-\frac{t_e}{\tau_e}}}}. \tag{1}$$

The torque overload factor (compared to continuous operation) equals $k_{\mathrm{S2,1-b}}$. This factor is influenced by the switch-on time t_e as well as a single thermal time constant of the drive system τ_e. The formula can be used to estimate the torque overload when considering single-body models. As described in [4] the use of a single-body model in comparison to a two-body model leads to relevant deviations regarding the resulting overtemperatures and thus overload factors. Thereby, lower overtemperatures respectively higher overload factors are obtained from the single-body model. This is because the winding heats up much faster than the housing of an electric drive system. The single-body model does not account for this behavior because it only considers one thermal time constant – the time constant of the housing. Instead using the related thermal time constant of the winding within the framework of the single-body model underestimates the overload capabilities due to its housing reference. This was evident in previous work [3]. An alternative approach is to calculate overload factors using the two-body model. Neglecting losses other than ohmic losses, the following formula results for torque overload calculation within the framework of the two-body model:

$$k_{\mathrm{S2,2-b}} = \sqrt{\frac{\theta}{\theta_1 \cdot \left(1 - e^{-\frac{t_e}{\tau_1}}\right) + \theta_2 \cdot \left(1 - e^{-\frac{t_e}{\tau_2}}\right)}}. \tag{2}$$

Thereby, the winding part is labelled with 1, the housing part with 2. The total of the winding overtemperature θ_1 and housing overtemperature θ_2 equals θ. [1, 2, 3, 4, 5]

1.3 Aim

This paper aims to theoretically and experimentally explore the overload potentials of brushless direct current motors (BLDC motors) in short-term operation: Duty type S2 according to the relevant standard [6]. Regarding experiments different approaches for identifying the winding temperature are compared. The latter limits the usable overload in first place and an accurate estimate is important to reach a high usage level. The experimental results are compared to theoretical approaches considering

 DOI: 10.30420/456743039

the single-body model as well as the two-body model and their applicability. The calculation of an adapted thermal time constant regarding the single-body model is proposed for easier overload calculation. The overall aim is therefore to identify the overload capabilities of the selected motors and verify them against the theoretical assumptions.

2 Approach

The overload potentials of small electric drive systems in short-term operation were tested with two BLDC motor types: A coreless motor (FAULHABER 3242G012BX4) and a slotted motor (FAULHABER 3216W012BXTH). Both motor types are comparable regarding diameter and power. The rated torque equals 39.2 mNm for the slotted motor and 50.3 mNm for the coreless motor, as described in the data sheets by rated current and motor constant (torque constant) [7, 8]. The following overload factors are referencing to those values.



Figure 1 Tested BLDC motor types; left: coreless motor, right: slotted motor

Concerning the theoretical assessment, the above-mentioned equation (2) for S2 operation and two-body models was used. Moreover, an approach using the overload calculation for single-body models (1) combined with an adapted thermal time constant found consideration. Using the two-body model requires knowledge about the temperature distribution between winding and housing. If the corresponding thermal parameters are not given by the manufacturers data sheet qualifying measurements are required. The single-body model on the other hand only requires one thermal time constant. As described above, using the housing or winding thermal time constant in this course is not expedient. Regarding the winding thermal time constant this is due to the fact, that the temporal behavior of the winding´s overtemperature with reference to the housing is described, not the ambient. Therefore, the following section proposes the calculation of an adapted thermal time constant that can be used for overload calculation with the single-body model and takes the discussed topic into account:

$$\tau_{\mathrm{adap}} = \frac{C_{th,W} \cdot \Delta T}{I_{DC}^2 \cdot R_{DC} \left(1 + \alpha_{co} \cdot \frac{T_{W,lim} - T_{amb}}{2}\right)} \cdot \qquad (3)$$

The adapted thermal time constant of the winding τ_{adap} is thereby retrieved from the product of the winding´s thermal capacity $C_{th,W}$ and the thermal resistance. The latter is calculated from the temperature difference ΔT divided by the ohmic power losses $I_{DC}^2 \cdot R_{DC}$. Thereby, the resistance increase due to the temperature difference between winding temperature limit $T_{W,lim}$ and the ambient temperature T_{amb} is considered using the temperature coefficient α_{co} of copper. To prevent an overly conservative view, this temperature difference is only considered as mean value (division by two). Otherwise the increased resistance at the final temperature would be taken into account. This procedure assumes a linear temperature curve. The general framework of the depicted formula is derived from the well-known thermal relationships [9]. The values required for the calculation can commonly be found in data sheets (I_{DC}, R_{DC}), are freely accessible (α_{co}) or depend on the specific operating conditions of the drive system ($\Delta T, T_{W,lim}, T_{amb}$). In case of missing data regarding the thermal capacity of the winding $C_{th,W}$ an estimate of the value based on motor size and corresponding copper mass could be used. Accordingly, it is possible to calculate overload factors for any desired winding temperature limit needing a limited number of (thermal) parameters.

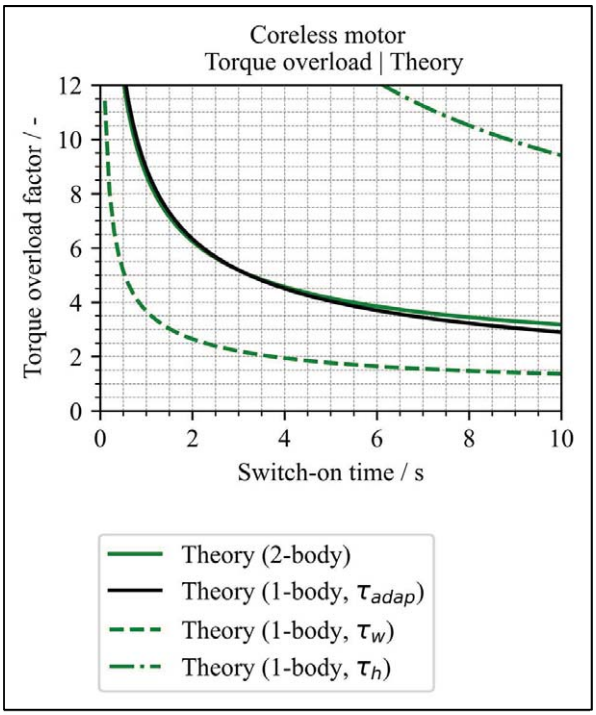


Figure 2 Coreless motor: Torque overload in theory

Figure 2 and **Figure 3** show theoretical overload curves (torque overload factor over switch-on time) using the different described calculation methods. Underestimation and overestimation caused by the single-body model combined with the winding thermal time constant or housing thermal time constant are depicted by the dashed or dashed/dotted curves. For the coreless motor the two-body model approach and the single-body model with adapted thermal time constant show a relatively comparable course regarding switch-on times less than 5 s. The following deviation can be led back to the fact, that no heat dissipation is considered regarding the single-body

 DOI: 10.30420/456743039

approach. Concerning the slotted motor, there is a greater discrepancy between the curve based on the two-body model and that based on the single-body model with adapted thermal time constant. This can be traced back to a different ratio of the winding and housing thermal parameters. Therefore, it is necessary to determine whether using a single-body model with an adapted thermal time constant leads to overestimation in certain cases. Furthermore, it should be noted here that the applicability of the standard two-body system and the according thermal parameters are currently under evaluation for the slotted motor. At this point, more complex approaches to temperature estimation have already been considered, but will not be included in this discussion [10]. For the coreless motor, however, the data from the data sheet was used [7]. In general, the coreless motor comes with higher thermal time constants, which is why higher torque overload factors result for this motor type.

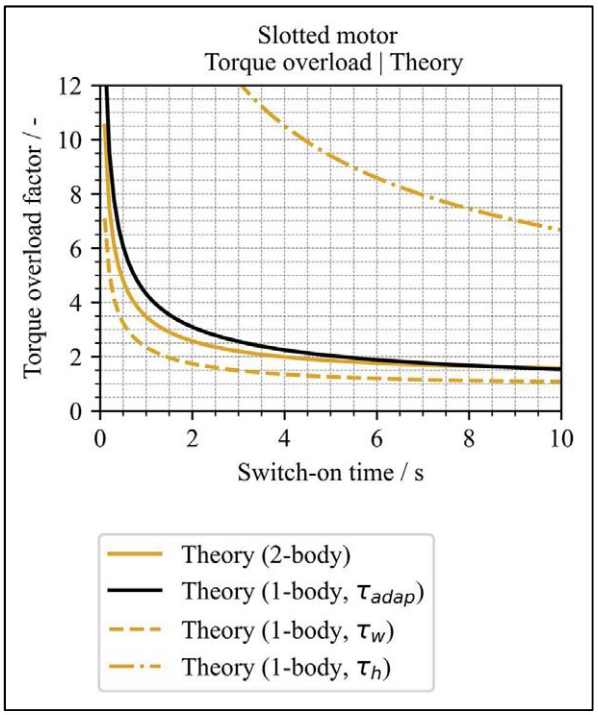


Figure 3 Slotted motor: Torque overload in theory

For the experimental considerations three motors of each architecture were operated sinusoidal commutated using digital hall sensors and a magnetic encoder (FAULHABER IE3-1024 L | IEF3-4096 L for BX4 | BXTH). The commutation and the speed-control were based on a field-oriented control (FOC) of the motors implemented in a MATLAB/Simulink R2022a environment using a dSPACE MicroLabBox combined with dSPACE ControlDesk 2022 B for Rapid Control Prototyping (RCP). A FAULHABER MC 5010 S power output stage was used in this setup as the prototyping amplifier, where the control signals were connected to the MicroLabBox which replaced the product logic. The power board is capable of delivering 50 V and 30 A (short-term). Starting with a torque value of 40 mNm and switch-on time of 10 s the torque level was increased in every test run. Each measurement started with an unloaded acceleration to 3000 rpm. The specified load was then applied without ramping and the measurements lasted for the defined switch-on time, or were previously terminated due to reaching the maximum winding temperature. The latter was defined 115 °C for the coreless motor and 125 °C for the slotted motor. The winding temperature for the brushless motor at rated current is also 125 °C; the choice of 115 °C is based on the available data regarding overtemperatures. The winding temperature was estimated using three approaches. First, a type K thermocouple located on/nearby the winding was used. Second, the ohmic losses and an adiabatic approach were used, as described in [3]. The latter means, that exclusively the heat capacity of the winding was considered. Third, the resulting difference in resistance retrieved from the measured current and voltage values was recalculated to the temperature:

$$R_S = \frac{U_q - U_{emf}}{I_q}. \tag{4}$$

In equation (4) the phase resistance is described by R_S and calculated using the q-values of voltage and current. The voltage component which is related to the electromotive force was subtracted, as the operation mode included considerable rotational speed. This method is only valid for short switch-on times as the magnets start to warm up at longer load phases which reduces the magnetic flux density and thus the back EMF (electromotive force). That means that the effect of increased winding resistance and accordingly increased voltage demand is affected in the opposite direction.

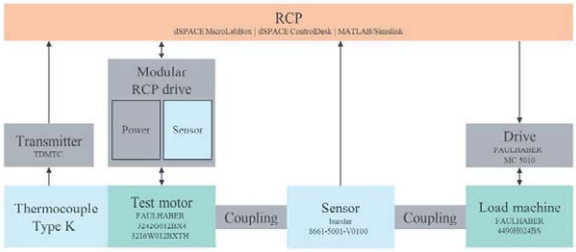


Figure 4 Measuring regime

The complete set-up of the experimental investigation is shown in **Figure 4**. A FAULHABER 4490H024BS BLDC was used as the load machine of the dynamometer. Thereby the torque was controlled by a standard FAULHABER MC 5010 S operated using the FAULHABER Motion Manager 7 software. Torque as well as speed were measured using a burster 8661-5001-V0100 torque sensor. The temperature of the winding was calculated as described above, the temperature of the motor housing as well as the ambient temperature were measured using thermocouples type K in combination with TDMTC transmitters. The phase currents were measured using the hall-based in-line current sensors of the power board extracted from a FAULHABER MC 5010 S Motion Controller. Information about the applied voltage was retrieved from the FOC. After finishing a

 DOI: 10.30420/456743039

measurement there was a cooling-off period. A new measurement was only realized when the housing temperature had less than or was equal to 27 °C.

3 Results and discussion

The results for the coreless and slotted motor are presented separately below. Each section is organized according to the method used to estimate winding temperature. The analysis considers the mean values and standard deviations from three motors each.

3.1 Coreless motor

3.1.1 Temperature monitoring via Type K

Regarding the coreless motor the results are presented in **Figure 5** and **Table 1**. During the maximum switch-on time of 10 s three overload operating points could be reached. Higher torque overload values than operating point no. 3 were not possible due the capabilities of the periphery (output stage).

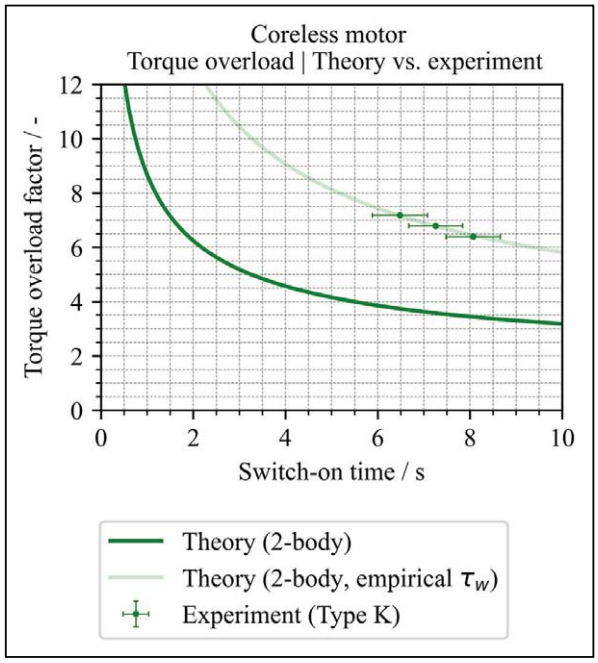


Figure 5 Coreless motor: Theory vs. experiment (Type K)

Table 1 Coreless motor: Torque overload factors and according switch-on times (mean values and standard deviations)

Point no.	1	2	3
$k_{S2,exp}$ / -	6.40 ± 0.01	6.79 ± 0.01	7.18 ± 0.01
t_e / s	8.07 ± 0.59	7.26 ± 0.58	6.48 ± 0.60

For the operating points no. 1 to 3 the winding temperature measured with a Type K thermocouple reached the defined limit of 115 °C. The resulting standard deviations are attributable more to the temperature measurement than to the test specimens themselves. With regard to the mean values, it appears that the measurement points follow the theoretical course as displayed by the light green curve calculated from the two-body model but using an empirical thermal time constant for the winding. Instead calculating with the data retrieved from the data sheet leads to the deep green curve. Accordingly, an underestimation is made by the theoretical calculation.

3.1.2 Temperature monitoring via power loss

Figure 6 and **Table 2** show the same measurement data as before but evaluated with a different winding temperature termination criterion. In this chapter the switch-on time resulting from the winding temperature retrieved by power loss, thermal heat capacity of the winding and an adiabatic assumption is discussed. In comparison to the previous **chapter 3.1.1** considerably smaller switch-on times are resulting. The reproducibility is very high in this case, since the only variable is the (controlled) current. The comparison with theoretical curves shows that the measurement points are close to both the two-body model as well as the single-body model with adapted thermal time constant (see **chapter 2**). It follows that the theoretical and practical approach generally coincide. However, the thermal parameters describe an adiabatic situation that does not actually exist - as shown in the previous chapter.

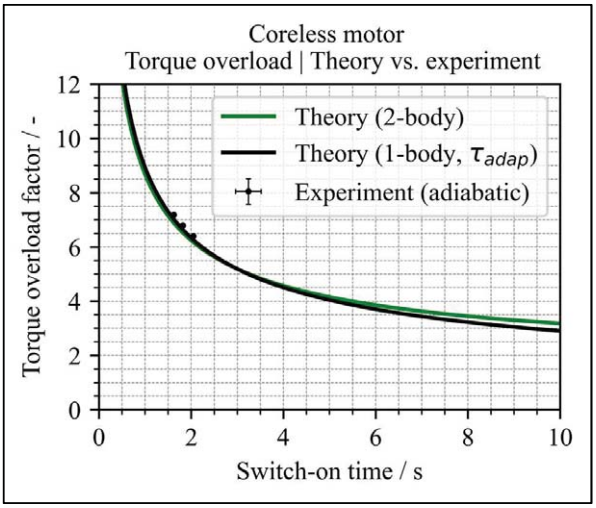


Figure 6 Coreless motor: Theory vs. experiment (adiabatic)

Table 2 Coreless motor: Switch-on time resulting from power loss calculation in context of overload measuring points (mean values and standard deviations)

Point no.	1	2	3
$k_{S2,exp}$ / -	6.40 ± 0.01	6.79 ± 0.01	7.18 ± 0.01
$t_{e,adiabatic}$ / s	2.05 ± 0.03	1.82 ± 0.03	1.62 ± 0.01

3.1.3 Temperature monitoring via resistance change

Beside from using Type K thermocouples and calculation via power losses the winding temperature was monitored via the resulting resistance delta. The according theory is described in **chapter 2**. The results are shown in **Figure 7** and **Table 3**. Larger standard deviations can be observed for the switch-on time, which are attributable to the noisy current and voltage signals. The input variables used in the calculation were averaged over a period of 10 ms.

 DOI: 10.30420/456743039

Fluctuations beyond this range are accordingly reflected in the temperature signal. Overall, switch-on times based on the Delta R criterion are slightly below the values presented in **chapter 3.1.1**. See also the comparison of the purple and green curves in **Figure 7**. The lower operating times observed may be due to the fact that the first valid value was used for the temperature limit. However, if the signal fluctuates, this has a corresponding effect rather than matching the average of the estimated temperatures. Refining the method would resolve this issue. Overall, it has been demonstrated that a temperature sensor is not necessarily required to achieve full utilization while ensuring thermal safety.

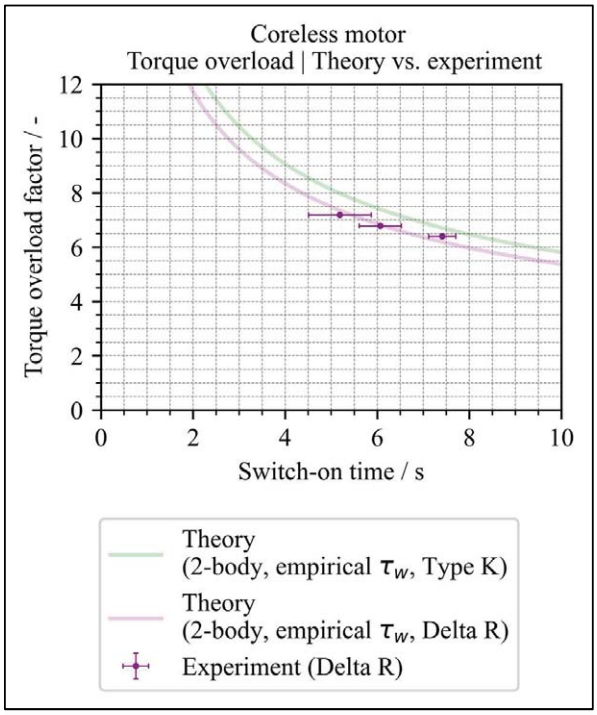


Figure 7 Coreless motor: Theory vs. experiment (Delta R)

Table 3 Coreless motor: Switch-on time resulting from Delta R calculation in context of overload measuring points (mean values and standard deviations)

Point no.	1	2	3
$k_{S2,\mathrm{exp}}$ / -	6.40 ± 0.01	6.79 ± 0.01	7.18 ± 0.01
$t_{e,Delta\ R}$ / s	7.41 ± 0.29	6.06 ± 0.46	5.19 ± 0.68

3.2 Slotted motor

3.2.1 Temperature monitoring via Type K

The results for the Type K termination criterion are presented in **Figure 8** and **Table 4**. Thereby operation points no. 2, 3 and 4 deviate from the theoretical course. This is due enlarging saturation effects where increased current no longer increases the torque one to one as already presented in previous work [3]. All measurement points exceeded the expected theoretical value in terms of current level - saturation occurred in all cases. Accordingly, overload factors $k_{S2} \geq 2.5$ are limited useful in terms of efficiency when considering the given slotted motor. Moreover, the theoretical estimate would need an according adaption. In general, the results also indicate that the overload potential is underestimated for the slotted motor when using the two-body model and currently available thermal parameters.

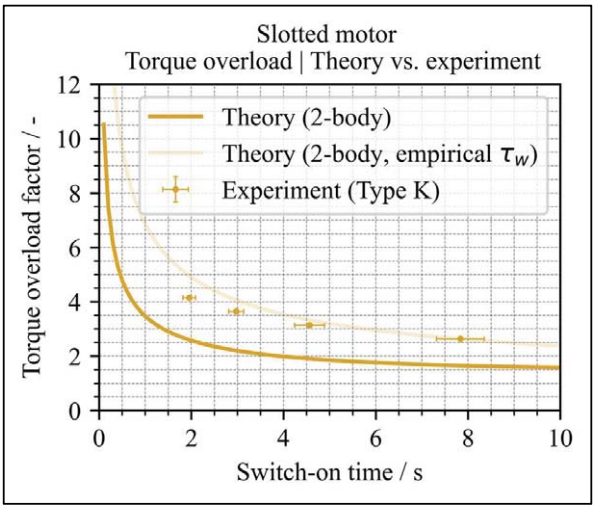


Figure 8 Slotted motor: Theory vs. experiment (Type K)

Table 4 Slotted motor: Torque overload factors and according switch-on times (mean values and standard deviations)

Point no.	1	2	3	4
$k_{S2,\mathrm{exp}}$ / -	2.64 ± 0.01	3.14 ± 0.00	3.65 ± 0.00	4.15 ± 0.00
t_e / s	7.83 ± 0.52	4.56 ± 0.32	2.97 ± 0.16	1.95 ± 0.14

3.2.2 Temperature monitoring via power loss

The switch-on times retrieved from power loss calculation are presented in **Figure 9** and **Table 5**. The experimentally determined values fall within the range of theoretical estimates based on the two-body model. The single-body model with an adapted time constant overestimates at this point. However, it is important to take the saturation effects into account as discussed before. The comparability

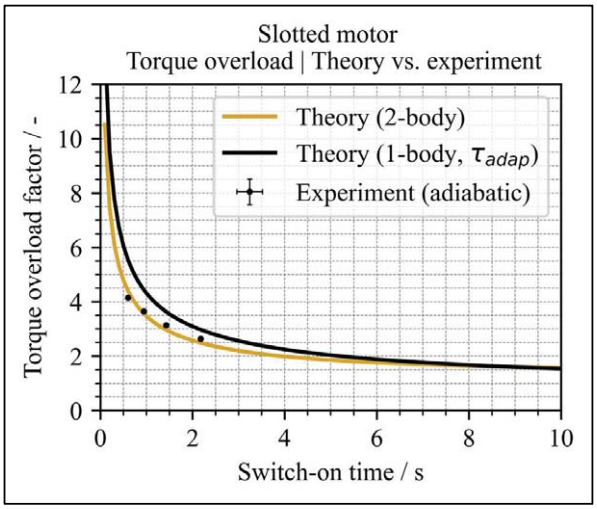


Figure 9 Slotted motor: Theory vs. experiment (adiabatic)

 DOI: 10.30420/456743039

with theory is therefore limited since the theoretical curves are based on rated currents. Consequently, it is not possible to determine whether the experimental data correspond more closely to the behavior of the two-body model or to that of the single-body model with an adapted time constant. However, higher current levels cause the measurement points to shift to the left.

Table 5 Slotted motor: Switch-on time resulting from power loss calculation in context of overload measuring points (mean values and standard deviations)

Point no.	**1**	**2**	**3**	**4**
$k_{S2,\mathrm{exp}}$ / -	2.64 ± 0.01	3.14 ± 0.00	3.65 ± 0.00	4.15 ± 0.00
$t_{e,adiabatic}$ / s	2.18 ± 0.04	1.43 ± 0.03	0.94 ± 0.03	0.60 ± 0.02

3.2.3 Temperature monitoring via resistance change

Regarding the winding temperature monitoring using resistance change no figure could be retrieved from the results as the according temperature always remained below the limit of 125 °C for the slotted motor. **Table 6** shows the final values for the Delta R temperatures. This behavior could be explained by the fact that the temperature sensor is located at a temperature hotspot on the winding, whereas the Delta R method calculates the average temperature rise. Furthermore, it was observed in some measurements that the initial temperature fell below the starting temperature of 25 °C. This can occur depending on the timing of the initial value calculation and the according overshoots in current and voltage.

Table 6 Slotted motor: Temperature values calculated by resistance change in context of overload measuring points (mean values and standard deviation)

Point no.	**1**	**2**	**3**	**4**
$k_{S2,\mathrm{exp}}$ / -	2.64 ± 0.01	3.14 ± 0.00	3.65 ± 0.00	4.15 ± 0.00
$T_{Delta\,R}$ / °C	84 ± 4	88 ± 10	95 ± 4	108 ± 3

4 Conclusion and outlook

Compared to previous work [3], this paper expands upon the method for determining overload potentials using thermocouples and resistance change for winding temperature estimation. It could be shown that considerably higher torque overload factors or greater switch-on times for a given overload factor are possible without damaging the motor in first place. In future, additional measurements should be conducted to expand the data set, considering longer switch-on times as well. Furthermore, higher overload factors could also be tested for the coreless motor by upgrading the peripheral equipment. For the slotted motor, this is not recommended due to saturation. With regard to the termination criteria, it has been shown that the Delta R method generally provides an appropriate estimate, if the switch-on time is short enough not to heat the magnet. Refining the method could eliminate the need for a temperature sensor. The theoretical calculations using the two-body model and the single-body model with an adapted thermal time constant were also verified in principle. At this stage, however, further work is needed to determine appropriate thermal parameters for both the coreless and slotted motor. This means that a thermal time constant for the winding based on the corresponding heat capacity is, in principle, correct as shown in **chapter 3.1.2**. However, during short-term overload operation, additional heat capacities of the motor come directly into play. This could be addressed by extending the two-body model to a three-body model, and so on. However, to minimize complexity, it would be conceivable to adjust the thermal parameters accordingly and explicitly focus on providing different specifications for overload operation and continuous operation. Furthermore, the analysis of the entire topic can be extended to include intermittent operation (e.g. duty type S3). Another topic that could be addressed in the future is the long-term damage caused to motors by overloading, for example, with regard to the lifetime of the insulation.

5 Literature

[1] E. Kallenbach, *Der Gleichstrommagnet*. Leipzig: Akademische Vertragsgesellschaft Geest & Portig K.-G., 1969.

[2] W. Amrhein and C. Fräger, Eds., *Handbuch Elektrische Kleinantriebe. Band 2: Kleinantriebe, Systemkomponenten, Auslegung*, 5., Stark überarbeitete, Erweiterte und aktualisierte Auflage. Berlin/Boston: De Gruyter Oldenbourg, 2022.

[3] U. Kurz, M. Olbrich, A. Wagener, and B. Gundelsweiler, "Experimental study on boosting small electric drive systems in short-term operation," in *Elektromechanische Antriebssysteme 2025, Tagungsband der 10. Fachtagung (VDE OVE)*, München, 2025, pp. 7–13.

[4] J. Vogel, Ed., *Grundlagen der elektrischen Antriebstechnik mit Berechnungsbeispielen*, 2., Durchges. Aufl. Heidelberg: Hüthig, 1980.

[5] J. Vogel, "Erwärmungsberechnung und Typenleistungsbestimmung elektrischer Maschinen nach dem Zweikomponentenmodell," Dissertation, 1982.

[6] *IEC 60034-1, DIN-EN 60034-1: Rotating electrical machines - Part 1: Rating and performance*. 2010.

[7] "FAULHABER Bürstenlose DC-Servomotoren Serie 3242 ... BX4." Accessed: Feb. 18, 2025. [Online]. Available: https://www.faulhaber.com/fileadmin/Import/Media/DE_3242_BX4_DFF.pdf

[8] "FAULHABER Bürstenlose DC-Flachmotoren Serie 3216 ... BXT H." Accessed: May 14, 2025. [Online]. Available: https://www.faulhaber.com/fileadmin/Import/Media/DE_3216_BXTH_DFF.pdf

[9] M. Németh-Csóka, *Thermisches Management elektrischer Maschinen: Messung, Modell und Energieoptimierung*. Wiesbaden: Springer Fachmedien Wiesbaden, 2018. doi: 10.1007/978-3-658-20133-3.

[10] D. Wöckinger, G. Bramerdorfer, T. Krainer, W. Amrhein, R. Keller, and B. Mund, "Advanced Data-based Temperature Modeling of an External Rotor PM Machine Considering an Optional Housing," presented at the IKMT 2022; 13. GMM/ETG-Symposium, Linz, Austria, 2022, pp. 161–167.

 DOI: 10.30420/456743040

Multi-DOF steerable endoscope for robot-surgeon collaborative control

Robert Lathrop[a], Mouloud Ourak[a], and Emmanuel Vander Poorten[a]
[a]Department of Mechanical Engineering, KU Leuven* , Celestijnenlaan 300B, 3001 Leuven Belgium

Abstract

Steerable devices for minimally invasive surgery enable surgeons to access remote anatomic locations and safely perform previously impossible procedures. Novel devices designed for surgeon-robot collaborative control are needed to expand the utility and adoption of these procedures, and enable further advances through the integration of robot-assisted surgical systems. This study details the design of a steerable endoscope with two controllable degrees of freedom: a bending tip driven by a group of pneumatic artificial muscles embedded in the device shaft, and a rotating shaft driven by a Dual-Chamber pneumatic artificial muscle. This flexible design uses multiple fluidic actuation strategies to produce a light-weight, compact instrument suitable for use as a handheld surgical instrument or for collaborative control with a robot-assisted surgery system. An initial prototype is built and its workspace is characterized, achieving bending of up to 71° and rotation of up to 133° with a weight of only 39 grams.

1 Introduction

Ongoing advances in the development of systems for Robot-Assisted Surgery (RAS) provide surgeons with new treatment options for a wide range of minimally invasive surgical (MIS) procedures. RAS procedures are performed across many specialties, enabling surgeons to access remote anatomy and perform procedures that would be inordinately risky or impossible via conventional methods [1, 2]. One key challenge limiting the adoption of RAS systems is the difficulty of designing instruments which provide new clinical capability without requiring surgeons to undergo significant retraining or alteration of existing techniques. Many steerable robotic surgical tools rely on bulky, heavy extrinsic drive systems to steer device motion from tele-operation systems which remove the surgeon from the patient's bedside. Recently developed intrinsically actuated MIS devices aim to address this challenge by producing lightweight, compact tools that are ergonomically similar to the clinical state-of-the-art, but with additional capability to navigate the surgical space [3, 4].

In particular, fetoscopic procedures such as Fetoscopic Laser Coagulation (FLC) are a compelling application for the development of new RAS systems due to their vital impact on patient's lives and the severely limited by the currently available instrumentation. FLC is a minimally invasive intervention used by surgeons to address Twin-Twin Transfusion Syndrome (TTTS), in which the blood supply between two fetuses sharing a placenta is imbalanced, resulting in malnourishment, developmental complications, and a mortality rate from $80-100\%$ if not treated [5].

In a FLC procedure, surgeons access the placenta by placing a fetoscope into the amniotic sac through a cannula in the mother's abdomen, and navigating the device tip to the placenta under sonographic and endoscopic video guidance as shown in Fig. 1. Vessels along the surface of the placenta are then selectively coagulated, balancing nutrient delivery between the fetuses and facilitating proper development. Current FLC procedures are performed with straight or curved rigid instruments which provide limited access to the placental surface, especially in cases where the placenta is located on the anterior wall of the uterus. The rigid fetoscope's inability to navigate the amniotic space also leads to a dangerous scenario in which a sur-

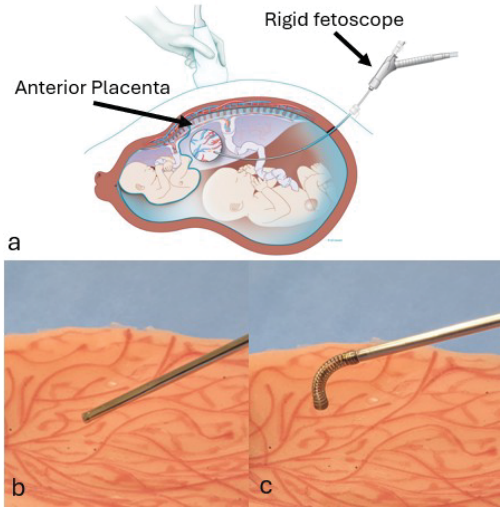


Figure 1 a) Illustration of a Fetoscopic Laser Coagulation procedure (courtesy of UZ Leuven), showing the challenge of anatomic access to the placental surface using rigid devices. b) Rigid fetoscope tip accessing the placenta at an angle dictated by the entry cannula position. c) Steerable fetoscope tip bending and rotating to align the laser fiber with the coagulation target.

DOI: 10.30420/456743040

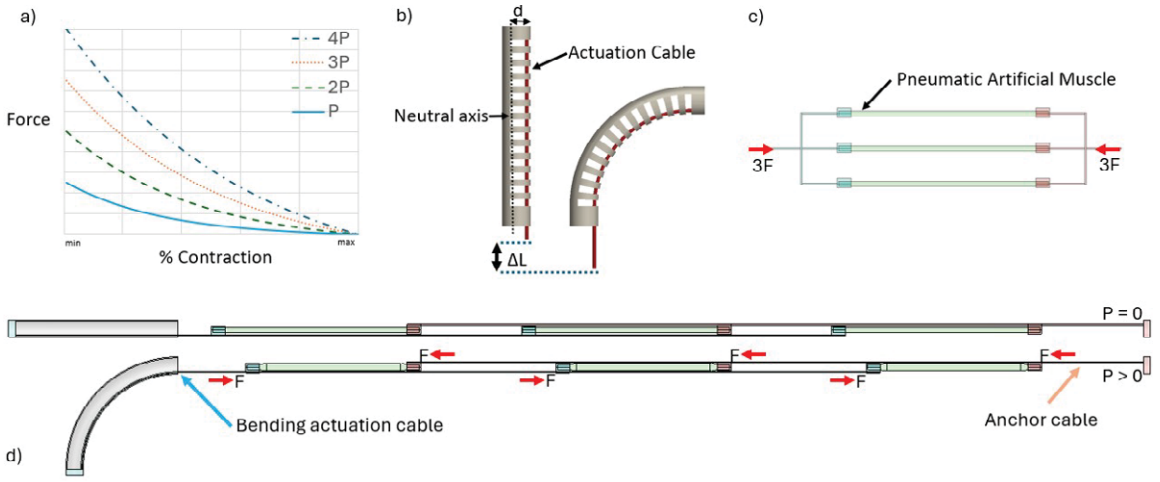


Figure 2 Bending Degree of Freedom actuation scheme and design. a) Isobaric workspace graph of a single pneumatic artificial muscle, showing the reduction in force output as the PAM contracts. b) Cable driven endoscope tip with stroke length required to achieve desired bending. c) Schematic of PAMs connected in parallel to increase force output in low-stroke-length applications. d) Interior view of the endoscope shaft showing the full bending actuation scheme. Three pneumatic artificial muscles are suspended in parallel between the device tip and the base of the device shaft. Each PAM acts as a tension source between tip and base, collectively bending the device when pressurizing the PAMs.

geon may (consciously or not) apply significant force to the entry cannula while trying to maneuver the fetoscope tip into position, potentially damaging the surrounding tissue and contributing to severe complications such as Preterm Premature Rupture of Membranes (PPRoM), endangering both fetus and parent [7].

Several devices and systems have recently been developed to address the challenges of FLC, including single degree-of-freedom (DOF) steerable handheld fetoscopes [4], an extrinsically actuated system to magnetically reposition a fetoscope in the womb [6], [8], [9] and a system for collaborative control of the tip position of a handheld steerable fetoscope. In the latter, Ahmad et. al. developed an actuated fetoscope driven by a system which used a convolutional neural network on images from the endoscopic video feed to make fine adjustments to the bend angle of the device [10]. This collaborative control approach gave the surgeon the freedom to maneuver the device as they would with traditional instruments while ensuring a consistent angle of attack for uniform laser coagulation on the placental surface, though the prototype device was somewhat larger than currently used rigid fetoscopes.

This work presents the design of a novel multi-degree of freedom (DOF) intrinsically actuated steerable endoscope for use in minimally invasive surgeries such as FLC. The design improves accessibility of the surgical space, without adding significant weight or bulk compared to state-of-the-art devices. It is intended to be suitable for use both as a standalone instrument or in collaborative control with a RAS system. The device leverages multiple miniature pneumatic artificial muscles that steer the device tip and rotate it along the axis of the endoscope shaft, enabling precise control of the device orientation relative to the surgical site. An initial prototype is constructed and evaluated for range of motion, weight, and accessibility.

2 Methods, Materials, and Design

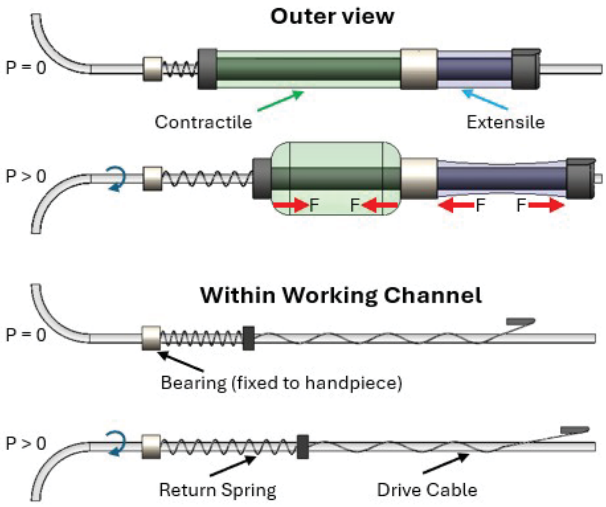


Figure 3 Actuation scheme of the rotational degree of freedom. A Dual-Chamber Pneumatic artificial muscle generates linear displacement. The middle connector of the DC-PAM is fixed to the endoscope's handpiece. When pressurized, the DC-PAM pulls on a drive cable attached to the extensile segment, rotating the endoscope shaft.

2.1 Multi-PAM Actuated Bending

The prototype endoscope uses two different compact pneumatic actuation schemes to actuate its two DOFs. The bending degree of freedom requires an actuator small enough to fit inside the footprint of the endoscope shaft while producing a high enough force to drive movement

ISBN: 978-3-8007-6743-4

@ VDE VERLAG GMBH · Berlin · Offenbach

 DOI: 10.30420/456743040

of the endoscope tip through its full range of motion. As shown in Fig. 2b, the force provided by a cable-driven bending actuator acts on the endoscope tip via an effective moment arm determined by the distance between the neutral axis of the bending segment and the attachment point of the actuation cable. This small moment arm necessitates the generation of a high actuation force, to produce a moment sufficient to bend the shaft and stiff elements such as the laser ablation fiber used in TTTS procedures.

The blocked force output of a PAM is commonly modeled using the principle of virtual work to calculate force as a function of the actuator's change in volume during pressurization [11]. This gives:

$$F = \frac{P\pi D_o^2}{4}(3\,cos^2(\theta) - 1) \tag{1}$$

where:

F = Force

P = Actuation pressure

D_o = Maximum diameter when $\theta = 90^o$

θ = Angle between braid strand and long axis of PAM

Notable in this relationship is that the maximum output force of a PAM is related to its initial diameter and braid geometry, but not to its initial length. A longer PAM will produce a higher effective actuation force than a short PAM of otherwise identical construction, because the force output of a PAM decreases as a function of its contraction percentage as shown in Fig. 2a. Cable-driven actuation of the endoscope bending tip requires a very short contraction length, which, assuming a constant curvature bending, can be calculated from the geometry of the bending segment as:

$$\Delta L = \theta_b r, \tag{2}$$

where:

ΔL = Stroke length for full actuation,

θ_b = Desired bend angle, and

d = Radial offset between neutral axis and drive cable.

The short contraction length required to bend the tip of the endoscope coupled with the device's long shaft length makes it possible to significantly increase the actuation force generated within the device shaft by coupling multiple short PAMs together in parallel, significantly expanding the device's actuatable design space [4]. To drive bending of the device's tip, a chain of 3 pneumatic artificial muscles with 1.9 mm diameter and 60 mm length are suspended inside the device shaft. The proximal end of each PAM is rigidly connected to the base of the endoscope's shaft, while each distal end is connected via cable to the bending segment at the device tip, as shown in Fig. 2. The PAMs are manufactured from silicone tubing wrapped in a polyimide braid and pneumatically sealed into stainless steel endpieces, as detailed in a previous study [4]. In this configuration, the PAMs are placed serially along the device shaft, but with their ends connected in parallel, causing them to act together to increase the maximum force that can be applied to the bending segment.

The chain of PAMs are pressurized via one pneumatic supply line passed from the distal end of each to the proximal end of the next, with sufficient slack left between actuators that the supply line is not tensioned during actuation. The small pressurized diameter of 1.9 mm PAMs leaves sufficient space inside the endoscope for the inclusion of important components such as a working channel for the introduction of surgical tools and wiring for an endoscopic digital camera and light source.

2.2 Dual-Chamber PAM Actuated Rotation

Rotation of the endoscope is driven by a dual-chamber PAM (DC-PAM) concentric to the endoscope, as shown in Fig. 3. This recently introduced actuator [3] consists of a 10 mm outer diameter, 9.4 mm inner diameter, 60 mm long contractile PAM pneumatically connected to a 10 mm outer diameter, 9 mm inner diameter, 40 mm long extensile PAM. A working channel runs through the actuator, rigidly connected to the outer ends of the contractile and extensile segments. When pressurized, the two pneumatic chambers act together to drive linear motion of the middle connector relative to the end connectors and shaft. The use of paired contractile and extensile chambers makes it possible for the hollow working channel running through the actuator to be pneumatically sealed at both ends without the need for an o-ring or similar element, which may introduce significant friction in miniaturized designs. This hollow actuator enables compact concentric designs with higher force output relative to traditional PAMs [3].

To convert the linear motion of the DCPAM to rotation of the endoscope, a capstan drive is formed by wrapping a 0.5 mm steel cable around the endoscope's shaft. The cable is fixed to the proximal end of the DCPAM shaft at one end and coupled to a return spring which is attached to a bearing at the distal end. The bearing and midpoint connector of the DCPAM are fixed to the endoscope handpiece.

When pressurized, the working channel and end connectors of the DCPAM are driven towards the proximal end of the endoscope. This pulls the drive cable, rotating the shaft, while the return spring ensures consistent reverse-rotation during depressurization. The bearing ensures concentricity of the shaft during rotation. Assuming there is no slippage between the drive cable and shaft, the maximum rotation produced by this mechanism can be modeled similarly to a Capstan drive, with the linear motion of the DC-PAM producing a corresponding unwinding of the drive cable:

$$\theta_r = \frac{\Delta L_{DC}}{r_{shaft}} \tag{3}$$

where:

θ_r = Angle of maximum rotation,

ΔL_{DC} = Stroke length of DC-PAM, and

r_{shaft} = Radius of endoscope shaft.

ISBN: 978-3-8007-6743-4 @ VDE VERLAG GMBH · Berlin · Offenbach

 DOI: 10.30420/456743040

3 Experiments and Discussion

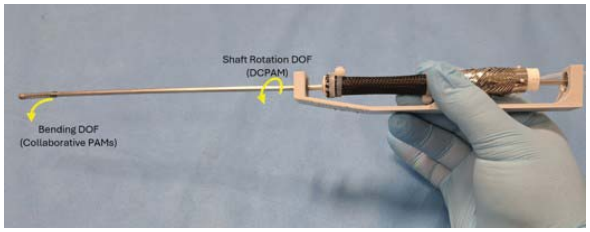


Figure 4 Prototype multi-DOF steerable endoscope

To assess functional performance of the prototype endoscope, a characterization of the range of motion for each degree of freedom was performed. The handpiece of the endoscope (shown in Fig. 4) was fixed in place in a vise and repeatedly actuated, with the achieved bending and rotation captured by a camera as shown in Fig. 5. Bend and rotation angle measurements were performed by comparing the baseline and fully actuated positions of the device using the image analysis software ImageJ (U. S. National Institutes of Health, Bethesda, MD, USA, version 1.54f). Results of this testing and measurements of the final prototype are summarized in Table 1. Measurements were repeated across 5 actuations cycling from 0 to 6 bar of pressure, producing an average maximum of $71.2 \pm 2.1^\circ$ of bending. The rotational ROM reached an average maximum of $133 \pm 4.4^\circ$. No significant axial displacement of the endoscope shaft was observed during actuation of the rotational DOF.

Rotation	Bending	Weight	Handpiece Volume
133°	71.2°	39 grams	130 x 20 x 25 mm

Table 1 Summary of prototype endoscope maximum range of motion for each DOF, weight, and size.

The achieved actuatable ranges of motion show significant promise for the utility of the multi-DOF endoscope for shared-control robot-assisted surgical applications. The ability to reorient the prototype endoscope tip over such a wide range of poses provides greater ability to reach surgical sites whose access would otherwise be obstructed, and to do so entirely within the surgical space, reducing the risk of unintentional pressure on the cannulae used for introduction of MIS devices.

In terms of weight and size, the prototype compares favorably to existing rigid endoscopes used in procedures such as FLC. One such device, the Karl Storz model 11506*AA* Miniature Straight Forward Telescope, was measured to weigh 109 grams, with a hub footprint of 84 x 36 x 20 mm. At only 39 grams and 130 x 25 x 20 mm, the prototype is significantly lighter, and comparable in volume. Future steerable endoscope design iterations have significant potential for further miniaturization and functional improvement. In particular the use of a smaller diameter endoscope shaft would enable both the use of a smaller DC-PAM actuator, and an increase in the rotational ROM produced by the DC-PAM's linear displacement, as shown in equation 3. The bending ROM could be improved by the use of a less rigid bending segment, by increasing the number of PAMs suspended in the device shaft (though a significant increase to shaft length to accommodate additional PAMs may become unwieldy for surgeons), or by the use of a bending segment design requiring a shorter stroke length, at which the PAMs are capable of producing higher forces.

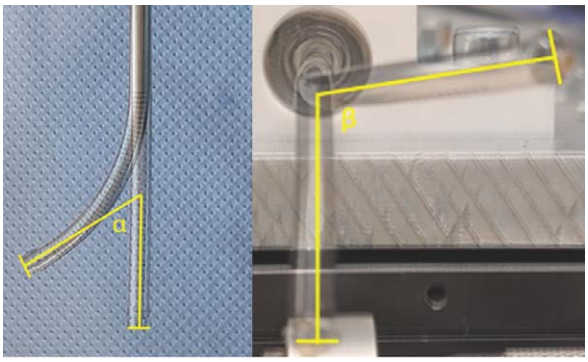


Figure 5 Tip of the endoscope bending during actuation of the shaft-embedded PAMs (α) and rotating during actuation of the dual-chamber PAM (β).

An important finding of the initial characterization testing was the capacity for independent actuation of the degrees of freedom. Further testing should be done to assess the dynamic performance of the mechanisms to confirm initial observations, but the ability to independently control both device bend and rotation simplifies the development of systems for robot-surgeon collaborative control.

Further optimization of the device dimensions, manufacturing method, and actuator dimensions should be undertaken to improve the steerable range of the device. Though this prototype is proposed for collaborative control applications not typically involving contact between the endoscope and objects in the surgical field, dynamic stability of the device tip in response to external forces should be studied. Future in-silico and pre-clinical evaluation will require the integration of elements such as an ergonomic handpiece, intuitive controls to enable surgeons to steer the device without adding cognitive burden, functional elements such as endoscopic visualization and illumination, and the addition of shape-sensing elements such as fiber-optic shape sensors or electromagnetic trackers to enable closed-loop control of the position of the device tip.

4 Conclusion

The prototype developed in this study demonstrated the capability of the selected actuation schemes to drive actuation of a steerable endoscope through clinically relevant ranges of motion. This lightweight and compact design provides a promising path towards the development of unobtrusive MIS devices that provide surgeons new capabilities while maintaining a similar form factor to the devices currently in clinical use. Future work should focus on the optimization of the device design to further increase steerable ranges, in-

tegration of shape sensing elements to enable closed-loop control, assessment of the dynamic performance and independent actuation of the actuation schemes, and integration of endoscopic imaging capabilities to enable more realistic in-silico evaluation of the endoscope's performance.

Acknowledgments

This project received funding from a KU Leuven internally funded project FLEXFET (3E200384).

5 Literature

[1] Rivero-Moreno, Y. et al.: Robotic Surgery A Comprehensive Review of the Literature and Current Trends,: Cureus, Vol. 24, 2023

[2] Burgner-Kahrs, J. et al.: Continuum Robots for Medical Applications, A Survey,: IEEE Transactions on Robotics, Vol. 31, 2015

[3] Lathrop, R. et al.: Concentric Dual-Chamber Pneumatic Artificial Muscles: Miniature Actuators Designed for Use in Minimally Invasive Surgical Instruments,: Journal of Medical Robotics Research, Vol. 07, 2022

[4] Lathrop, R. et al.: Tug-of-War-Style High-Force Fluidic Actuation for Small Diameter Steerable Instruments,:Actuators, Vol. 13, 2024

[5] Djaafri, F. et al.: Twin–twin transfusion syndrome – What we have learned from clinical trials,:Seminars in Fetal and Neonatal Medicine, Vol. 22, 2017

[6] Mesot, A. et al.: Teleoperated magnetic endoscopy: A case study and perspective,: Advanced Intelligent Systems, Vol. 7, No. 10, 2025

[7] Van der Schot, A. et al: Impact of cannula diameter on pregnancy outcomes after minimally invasive fetal laser surgery in the treatment of twin-to-twin transfusion syndrome: A systematic review and meta-analysis,:Acta Obstet Gynecol Scand., Vol. 103, 2024

[8] Gervasoni, L. et al: Magnetically Guided Laser Surgery for the Treatment of Twin-to-Twin Transfusion Syndrome,:Adv. Intell. Syst., Vol. 4, 2022

[9] Mattille, M. et al: Advancing Minimally Invasive Precision Surgery in Open Cavities with Robotic Flexible Endoscopy,; arXiv preprint arXiv:2511.14458, 2025

[10] Ahmad, MA. et al: Deep learning-basedmonocular placental pose estimation: towards collaborative robotics in fetoscopy,:Int J CARS, Vol. 15, 2020

[11] Chou, C. et al.: Static and dynamic characteristics of McKibben pneumatic artificial muscles,:Proceedings of the 1994 IEEE International Conference on Robotics and Automation, Vol. 1, 1994

 DOI: 10.30420/456743041

Finite Element Analysis of Asymmetric Inflatable Snapping Actuators

Xin Li, Ye Jin, and Edoardo Milana
Department of Microsystems Engineering - IMTEK, University of Freiburg, Freiburg, Germany
Cluster of Excellence livMatS @ FIT, University of Freiburg, Freiburg, Germany
E-mail address: edoardo.milana@imtek.uni-freiburg.de

Abstract

Snapping structures are widely used in soft robotics due to their ability to store and rapidly release elastic energy, enabling fast actuation and mechanically encoded behaviors. However, most existing snapping structures are designed symmetrically, while asymmetric snapping motion has received relatively limited attention. This work presents a finite element analysis of asymmetric inflatable snapping actuators (AISA) capable of generating controllable asymmetric snapping motion through an eccentric dome design. By introducing a geometric offset into a conventional snapping shell, the actuator exhibits directional snapping trajectories during inflation and deflation. Finite element simulations based on a fluid–structure interaction framework were conducted to investigate the influence of shell depth and eccentricity on the snapping behavior. The results show that appropriate combinations of geometric parameters enable stable asymmetric trajectories, while excessive or insufficient asymmetry leads to unstable deformation or numerical instability. The proposed actuator demonstrates a simple mechanical approach for achieving programmable asymmetric motion in soft pneumatic systems without additional electronic control.

1 Introduction

Soft robotics is advancing rapidly thanks to innovations in materials, design tools, and fabrication techniques. However, most existing systems still rely on bulky, tethered components such as valves and pumps, which limit their autonomy. In contrast, many biological organisms embed physical intelligence directly within their bodies, where geometry and material gradients naturally govern deformation and motion without centralized control [1]. Inspired by this concept, integrating physical control into soft robots offers a promising route toward compact, autonomous, and self-regulated systems.

One promising strategy for achieving physical control is the use of snapping structures [2]. Snapping structures can store elastic energy and release it rapidly once a critical threshold is exceeded. Common examples include curved beams and domes. Such mechanisms are particularly attractive for physical intelligence because they exhibit clear state transitions during actuation, analogous to binary states in computation, and can also introduce time delays that enable sequential behaviors. Through careful geometric design, snapping structures can therefore be programmed to achieve specific mechanical responses and functionalities.

Extensive research has explored this concept. For instance, Gorissen et al.[3] developed an inflatable jumping robot utilizing a simple snapping shell, achieving a jumping height of 42.9 mm independent of actuator size. Similarly, Comoretto et al.[4] integrated mechanofluidic memory into soft robots, using bistable snapping behavior to realize autonomous switching without electronic control. These studies demonstrate that snapping mechanisms can serve diverse functions in soft robotic systems, ranging from rapid actuation to embodied physical control.

Despite significant attention on energy storage and release in snapping structures, the asymmetric motion occurring during snapping transitions has been less explored. Most snapping structures are designed symmetrically, consisting of two identical sides. When an actuation force is applied, elastic energy is distributed and stored symmetrically within the structure. [5, 6]Once the applied force exceeds the snapping threshold, the structure loses stability and rapidly transitions to another state, releasing the stored energy. In practice, however, the two sides can never be perfectly identical, resulting in slight asymmetries during the snapping process. Consequently, one side often becomes mechanically weaker, leading to asymmetric snapping motion. To intentionally amplify this behavior, researchers have introduced geometric asymmetries such as localized cuts, thickness gradients, and offset curvatures, which help guide the snapping direction.

For example, Li et al.[7] demonstrated a semi-open elastomeric dome with a T-shaped cut that consistently snapped in a preferred direction under pneumatic pressure. Luo et al.[8] developed a multistable soft actuator in which internal asymmetries induced mixed-mode snapping between stable states. Bell et al.[9] introduced a thickness gradient into a bistable snapping shell to create an asymmetric snapping actuator, enabling mechanically programmed complex locomotion gaits under periodic fluidic actuation. These studies highlight the potential of geometric asymmetry in controlling snapping direction and motion.

In this work, we focus on the design of an actuator with a controllable asymmetric snapping direction. We first de-

 DOI: 10.30420/456743041

veloped an inflatable snapping actuator with asymmetric geometric features and systematically investigated the influence of different design parameters on the snapping trajectory. The fabrication process is presented, and numerical simulations are conducted to analyze how various parameters affect the snapping behavior. Finally, we discuss potential applications of the proposed actuator.

2 Design and Simulation

2.1 Design of AISA

Inspired by the work of Van Raemdonck et al.[10], who developed an inflatable snapping shell with tunable snapping behaviors through geometric modifications, we designed an asymmetric inflatable snapping actuator (AISA) consisting of a sealed chamber and a functional snapping shell made from Silicone(Smooth-Sil 950). During inflation, the snapping shell responds to the internal pressure variation within the chamber. Specifically, an eccentric dome design is adopted to achieve asymmetric snapping behavior. Specifically, asymmetry is introduced by shifting the center of the dome by a prescribed offset distance, thereby weakening one side of the shell geometry (**Figure 1**).

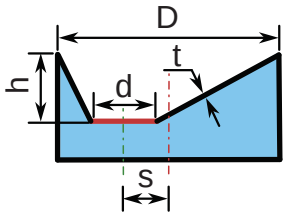


Figure 1 Structure design of AISA

Due to the eccentric design, one side of the shell possesses a larger effective contact area than the other. Consequently, the pressure-induced deformation on the larger side becomes more pronounced. During inflation, the larger side of the shell (the right side in this study) responds first and rises earlier, causing the center region of the shell to tilt toward the left. As the internal pressure further increases, the opposite side also deforms and rises, gradually restoring the center region to a horizontal configuration. During deflation, a similar but reversed process occurs. The right side collapses first, followed by the left side, resulting in the center region first tilting toward the right before returning to the horizontal state. Therefore, within a complete inflation–deflation cycle, the shell sequentially undergoes four distinct states: tilted left, horizontal, tilted right, and horizontal again. This shows the asymmetric nature of the snapping transition. More details on design, fabrication and integration of these actuators in a soft robotic walker can be found in [11].

The geometric parameters associated with the eccentric design strongly influence the asymmetric snapping trajectory. To investigate these effects, the dome depth and eccentric offset are tuned to generate different shell configurations. The detailed geometric parameters are summarized in (**Table 1**).

Table 1 Geometric parameters of AISA

Parameter	Symbol	Value(mm)
Shell height & Eccentric offset	h & s	1.6 & 2.2 3.0 & 2.0 3.4 & 1.0 4.0 & 3.0
Tip diameter	d	3.0
Shell diameter	D	10.0
Shell thickness	t	0.2

2.2 Finite element simulations

A numerical simulation of the inflation–deflation process was conducted in *Abaqus/CAE 2025* using a fluid–structure interaction (FSI) framework with a `*FLUID CAVITY` definition. A dynamic implicit analysis was performed to capture the deformation evolution under controlled volumetric loading and to evaluate the corresponding pressure–volume response.

The membrane was modeled as a Neo–Hookean hyperelastic material [12, 13] with shear constant $C_1 = 0.34$ MPa. Rayleigh damping was introduced with coefficients $\alpha = 0.0001$ and $\beta = 0.0001$ to suppress numerical oscillations. Both the inflation and deflation stages lasted 1 s, using a Dynamic, Implicit step with nonlinear geometric effects enabled. The time increment was limited between $\Delta t_{\min} = 1 \times 10^{-5}$ s and $\Delta t_{\max} = 1 \times 10^{-4}$ s.

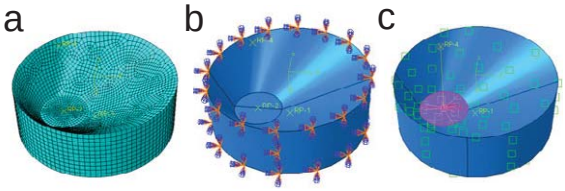


Figure 2 a) Mesh model of the AISA. b) Boundary conditions and constraints applied to the model. c) Bonding of the tracking point.

A prescribed fluid flux was implemented through the `*FLUID FLUX` function to apply a ramp volumetric flow rate with a peak value of 0.4 mL s^{-1}. **Figure 2**(a) shows the mesh configuration of the actuator model. The structure was discretized using S4R reduced-integration shell elements with a global mesh size of approximately 0.3 mm. To reproduce the experimental boundary conditions, the base plane was fully constrained as a fixed boundary condition, as illustrated in **Figure 2**(b). In addition, a 5 mm support bar was tied to the central plane of the actuator to amplify the snapping displacement during deformation, as shown in (**Figure 2**)(c).

3 Results

We conducted simulations on models with different parameter combinations under identical loading conditions. The results show that the snapping trajectories vary significantly with changes in shell geometry and eccentricity.

 DOI: 10.30420/456743041

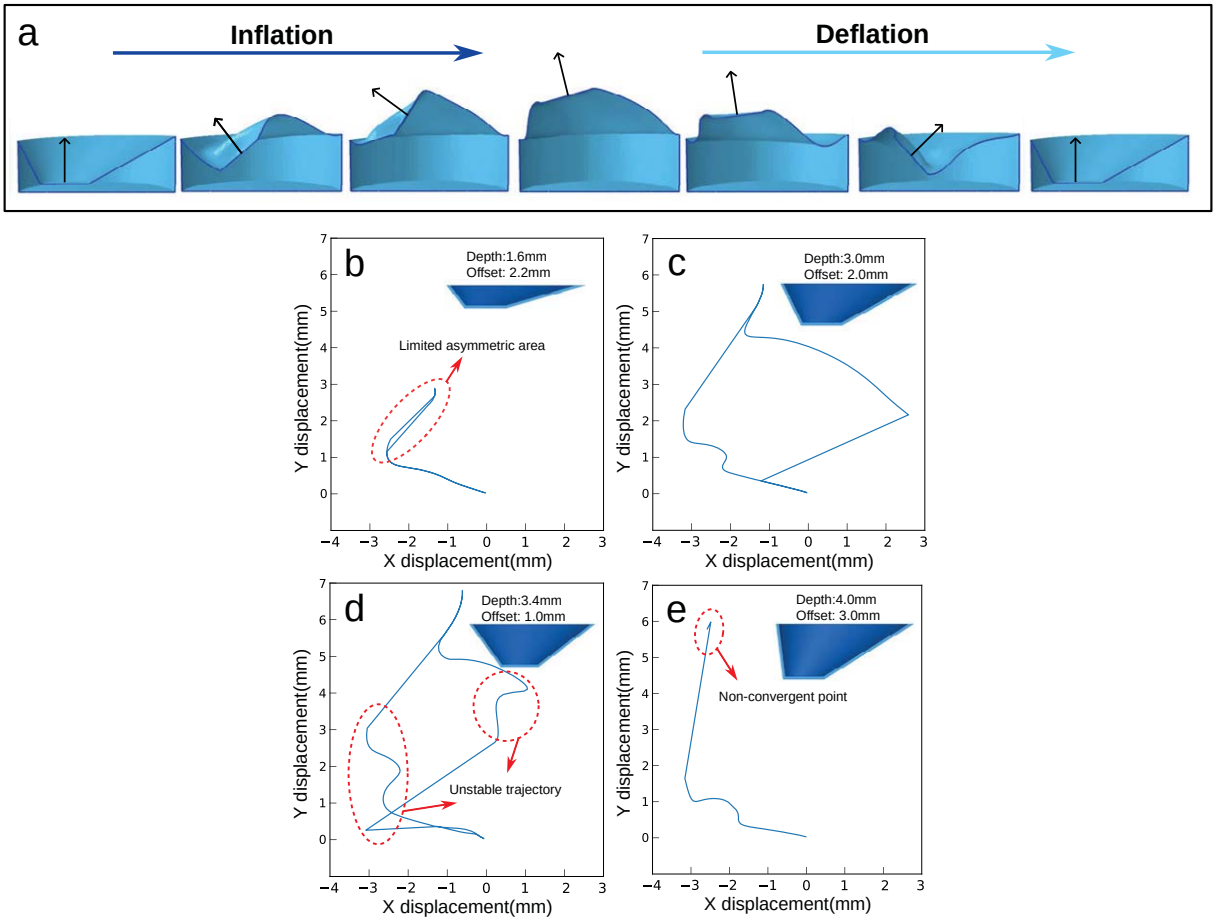


Figure 3 a) Illustration of asymmetric snapping during inflation–deflation cycle. b) Simulated trajectory for the parameter combination of 1.6 & 2.2. c) Simulated trajectory for the parameter combination of 3.0 & 2.0. d) Simulated trajectory for the parameter combination of 3.4 & 1.0. e) Simulated trajectory for the parameter combination of 4.0 & 3.0.

As shown in **Figure 3**(a), the complete inflation–deflation cycle of asymmetric snapping is illustrated. The black arrow represents the normal vector of the shell center, clearly demonstrating the asymmetric snapping behavior throughout the cycle. The figure also shows how the left and right sides of the shell experience different loading conditions during the cycle, ultimately resulting in asymmetric motion.

As shown in **Figure 3**(b), the parameter combination **1.6&2.2** corresponds to a shallow shell with a relatively large eccentricity. Under this condition, the overall trajectory appears nearly symmetric rather than asymmetric. Nevertheless, a small asymmetric region can still be observed during the snapping process. This indicates that the eccentric loading effect is still present. However, because the shell depth is too small, the available deformation space for asymmetric motion is limited, preventing the asymmetric behavior from fully developing.

In **Figure 3**(c), the parameter combination **3.0&2.0** produces a deeper shell while maintaining a large eccentricity. In this case, the actuator exhibits a stable and well-defined asymmetric trajectory. The increased shell depth provides sufficient deformation space during snapping, allowing the eccentric geometry to effectively guide the asymmetric motion throughout the inflation–deflation cycle.

As shown in **Figure 3**(d), the parameter combination **3.4&1.0** still generates an asymmetric trajectory, but the motion becomes noticeably unstable. Although the shell remains relatively deep, the eccentricity is much smaller and closer to a symmetric configuration. As a result, the geometric difference between the left and right sides is insufficient to fully dominate the snapping direction. During the snapping process, the elastic energy alternates between the two sides of the shell, leading to oscillatory left–right motion in the trajectory. Despite this instability, the remaining eccentricity still introduces an overall asymmetric tendency.

In **Figure 3**(e), the parameter combination **4.0&3.0** results in a non-converged simulation. Under this configuration, the shell is both very deep and highly eccentric. Although such geometry would theoretically enhance asymmetric snapping, severe local buckling occurs during deformation. Specifically, the left side of the shell becomes nearly perpendicular to the boundary. As the right side rises during inflation, the left side can no longer deform smoothly and instead undergoes local buckling until the snapping threshold is reached, after which it rapidly jumps upward. This behavior produces the sharp discontinuity observed in the

trajectory. During deflation, the right side collapses first, while the left side buckles again under compression. Because the right side simultaneously pushes the structure laterally, the buckled left side bends further toward the left, causing excessive deformation and ultimately leading to numerical instability in the simulation.

4 Conclusion

In this work, an asymmetric inflatable snapping actuator (AISA) was proposed to investigate asymmetric snapping behavior in soft pneumatic structures. By introducing an eccentric dome geometry into a conventional snapping shell, controllable asymmetric motion was successfully achieved during the inflation–deflation cycle. Unlike conventional symmetric snapping structures, the proposed design exhibited asymmetric snapping trajectory.

Finite element simulations based on a fluid–structure interaction framework were conducted to analyze the influence of geometric parameters on the snapping behavior. The results demonstrated that both shell depth and eccentricity play critical roles in determining the trajectory characteristics. Shallow shells limited the available deformation space and suppressed asymmetric motion, while insufficient eccentricity led to unstable oscillatory behavior. In contrast, an appropriate combination of shell depth and eccentric offset enabled stable and repeatable asymmetric snapping trajectories. Excessive depth and eccentricity, however, introduced severe local buckling and numerical instability during deformation.

The study shows that geometric asymmetry can effectively guide snapping direction and deformation evolution in inflatable soft actuators. The proposed actuator provides a simple and fully mechanical approach for generating directional motion without relying on additional control systems or electronics. These findings offer a potential strategy for developing physically intelligent soft robotic systems with programmable motion behaviors, and may inspire future applications in soft locomotion, adaptive structures, and mechanically encoded control systems.

5 Acknowledgment

This research was Funded by the Deutsche Forschungsgemeinschaft (DFG, German Research Foundation) under Germany's Excellence Strategy – EXC-2193/1 – 390951807.

6 Literature

[1] Edoardo Milana, Cosimo Della Santina, Benjamin Gorissen, and Philipp Rothemund: Physical control: A new avenue to achieve intelligence in soft robotics, Science Robotics, Vol. 10, No. 102, AAAS, 2025.

[2] Aniket Pal, Vanessa Restrepo, Debkalpa Goswami, and Ramses V. Martinez: Exploiting Mechanical Instabilities in Soft Robotics: Control, Sensing, and Actuation, Advanced Materials, Vol. 33, No. 19, Wiley, 2021.

[3] Benjamin Gorissen, David Melancon, Nikolaos Vasios, Mehdi Torbati, and Katia Bertoldi: Inflatable soft jumper inspired by shell snapping, Science Robotics, Vol. 5, No. 42, AAAS, 2020.

[4] Alberto Comoretto, Stijn Koppen, Tanaya Mandke, and Johannes T. B. Overvelde: Embodying Mechano-Fluidic Memory in Soft Machines to Program Behaviors upon Interactions, Device, 2025.

[5] J. T. B. Overvelde, T. A. de Jong, Y. Shevchenko, S. A. Becerra,G. M. Whitesides, J. C. Weaver, C. Hoberman, and K. Bertoldi,"Amplifying the response of soft actuators by harnessing snap-through instabilities,"*Proc. Natl. Acad. Sci. U.S.A.*, vol. 112, no. 35, pp. 10863–10868, 2015.

[6] P. Rothemund, Y. Ainla, L. Belding, M. D. Preston, S. Kurumaya, Z. Suo, G. M. Whitesides, and D. J. Preston, "A soft, bistable valve for autonomous control of soft actuators," *Sci. Robot.*, vol. 3, no. 16, eaar7986, 2018.

[7] Min Li, Huikai Zhang, Wei Fang, Jian Wu, and Xi-Qiao Feng: Directional Soft Jumper by Harnessing Asymmetric Snapping of a Semi-Open Shell, Extreme Mechanics Letters, Vol. 72, 2024.

[8] Yichi Luo, Dinesh K. Patel, Zefang Li, Yafeng Hu, Hao Luo, Lining Yao, and Carmel Majidi: Intrinsically Multistable Soft Actuator Driven by Mixed-Mode Snap-Through Instabilities, Advanced Science, Vol. 11, No. 18, 2024.

[9] M. A. Bell, L. Cattani, B. Gorissen, K. Bertoldi, J. C. Weaver, and R. J. Wood: A Soft, Modular, and Bi-Stable Dome Actuator for Programmable Multi-Modal Locomotion, 2020 IEEE/RSJ International Conference on Intelligent Robots and Systems (IROS), pp. 6529–6535, 2020.

[10] Bert Van Raemdonck, Edoardo Milana, Michael De Volder, Dominiek Reynaerts, and Benjamin Gorissen: Nonlinear Inflatable Actuators for Distributed Control in Soft Robots, Advanced Materials, Vol. 35, No. 35, Wiley, 2023.

[11] Xin Li, Ye Jin, Mohsen Jafarpour, Hugo de Souza Oliveira, Edoardo Milana: Snapping Actuators with Asymmetric and Sequenced Motion, 2026 IEEE 9th International Conference on Soft Robotics (RoboSoft), IEEE, 2026.

[12] Matheus S. Xavier, Andrew J. Fleming, and Yuen K. Yong: Finite Element Modeling of Soft Fluidic Actuators: Overview and Recent Developments, Advanced Intelligent Systems, Vol. 3, No. 2, Wiley, 2020.

[13] Narendra Gariya, Pushpendra Kumar, and Brijesh Prasad: Stress and Bending Analysis of a Soft Pneumatic Actuator Considering Different Hyperelastic Materials, Materials Today: Proceedings, 2022.

 DOI: 10.30420/456743042

Dual-Chevron Optothermal Rotary Microactuator for High Force and Large Displacement Actuation

Yanze Li[1], Alex J Thompson[1], Alfredo Fantetti[2], and Belal Ahmad[1]
[1]The Hamlyn Centre, Department of Surgery and Cancer, Imperial College London, London, UK
[2]Department of Mechanical Engineering, Imperial College London, London, UK
alex.thompson08@imperial.ac.uk, a.fantetti@imperial.ac.uk, b.ahmad@imperial.ac.uk

Abstract

This paper presents a optothermal rotational microactuator that converts translational motion into rotational displacement through a toothed torsional spring mechanism. The design employs two optothermal chevron actuators to sequentially engage the spring teeth and generate controlled cyclic rotation with high force potential and compact footprint. A detailed kinematic model of the actuation cycle is developed together with a tooth contact design incorporating frictional interaction and tolerance compensation for parasitic shifts. Finite element and multibody dynamic simulations are conducted to evaluate spring stiffness, contact dynamics, actuation force, and rotational behavior during a full actuation cycle. The device is fabricated using two photon polymerization and coated with aluminum to enhance optical absorption. Experimental results demonstrate repeatable optothermal rotational actuation with an average angular displacement of 0.6° per cycle, validating the proposed motion conversion principle. The proposed architecture provides a promising foundation for high force, large displacement optothermal microactuators for future multi degree of freedom microrobotic systems.

1 Introduction

Microactuators have emerged driven by the need for precise handling and manipulation at the micro scale, becoming increasingly utilized in microtechnology and biomedical applications. These actuators are integrated into devices such as microrobots and microgrippers, which facilitate their deployment in applications ranging from microassembly of minute components to manipulation of single cells [1]. They can be actuated using different techniques including magnetic, thermal, acoustic, optical, and optothermal, each providing advantages and disadvantages [2]. Among these actuation techniques, optothermal actuation, where focused laser beam is used to heat material and deflect it, is highly promising due to its remote nature and high selectivity, enabling the individual actuation of multiple actuators. This opens the way for microrobots and microgrippers with multiple degrees-of-freedom that can offer higher dexterity and functionality. However, most optothermal microactuators fail to provide ample force while achieving large deflection, especially for rotational movements, due to the trade-off between material stiffness and flexibility and their small footprints [3]. On this basis, this work aims to provide proof of concept of an optothermal rotational microactuator that provides high force outputs with large angular displacements.

2 Design and Fabrication

To achieve both large displacement and high force, this work employs the principle of accumulating translational motion and converting it into rotation. This requires: (1) a linear actuator with high force capacity and (2) an energy storage mechanism that converts kinetic energy into elastic potential, realized through a torsional spring. Among translational microactuators, the chevron actuator achieves ample translation displacements ranging from several microns to tens of microns and forces ranging from hundreds of micronewtons to millinewtons, making it suitable for the proposed device [4]. The chevron-shaped microactuator in its basic form consists of two symmetric beams connected to a base and a common node that translates when heated due to the thermal expansion along the beams. The torsional spring is used as a rotational joint to replace a traditional ball-bearing structure.

The design of the microactuator is shown in Fig. 1(a). It incorporates two chevron actuators to facilitate rotation and locking motions in clockwise and counterclockwise directions and a torsional spring with teeth on both sides that aligns with the chevron actuator tips. When a chevron actuator is actuated, its tip moves towards the spring and contact with the spring's teeth, offering a force on the tangential direction that makes the spring rotate. Rotation to the other direction is realized by the spring elasticity.

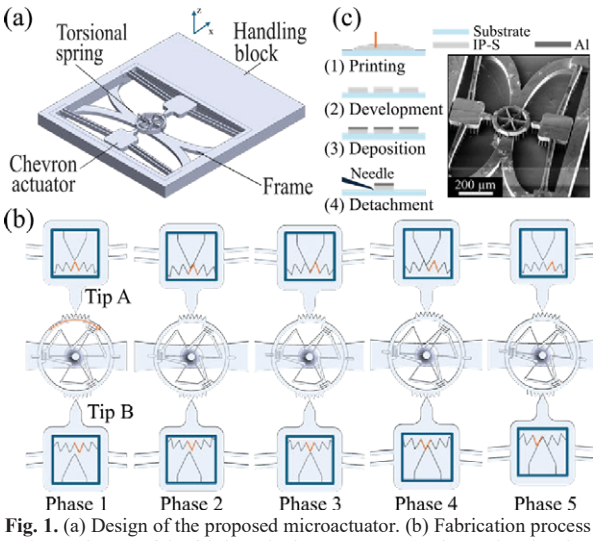


Fig. 1. (a) Design of the proposed microactuator. (b) Fabrication process and SEM image of the fabricated microactuator. (c) Kinematics showing the differnt actuation phases of the microactuator.

 DOI: 10.30420/456743042

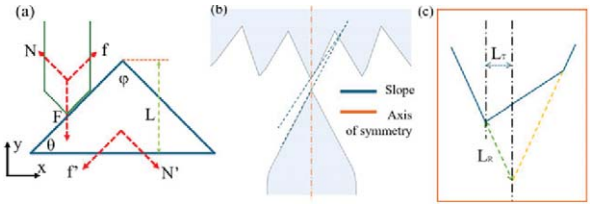


Fig. 2. (a) Teeth contact model, (b) Teeth slope, (c) Slope modelling.

When actuated, the spring rotates cyclically with each cycle divided into working phases (Fig. 1(b)). The top and bottom chevron tips are respectively denoted as A and B, with the teeth contacting tips highlighted to indicate rotation. Consecutive rotation requires the opposing teeth to be offset by half a tooth. In phase 1, tip A aligns with a tooth crest and tip B with a trough, marking the cycle's starting point. In phase 2, the top actuator is activated with tip A pushing the spring to rotate clockwise. In phase 3, tip A reaches a trough, while tip B aligns with a crest. In phase 4, the bottom actuator is activated with tip B pushing the spring to rotate clockwise. Meanwhile tip A gradually retrieves while holding the spring in place. In phase 5, tip B reaches a trough, while tip A realigns with a crest. The process then repeats, producing continuous clockwise rotation. Each step rotates the spring by half a tooth, while a complete actuation cycle of both actuators results in one full-tooth rotation. To maintain a desired angle, one actuator may remain activated to hold the spring in place. Reverse rotation can be achieved by deactivating both actuators, allowing backward motion, and then reactivating an actuator once the target angle is reached.

For better performance of the spring, the teeth contact is modeled. In Fig. 2(a), a Columb friction model is introduced considering a static coefficient of 0.5, a dynamic coefficient of 0.3, a stiction transition velocity of 2 µm/s and a friction transition velocity of 5 µm/s. These parameters were adopted from values for unlubricated polymers in [5]. The tangential and radial forces can be denoted as:

$$R_t = \frac{1}{2}Fsin\varphi - \frac{1}{2}\mu F(1-cos\varphi)$$
$$R_r = \frac{1}{2}F(1-cos\varphi) + \frac{1}{2}\mu Fsin\varphi \quad .$$

The teeth angle φ is selected at 63° to maximize R_t facilitating rotation while preserving moderate R_r causing parasitic shift. A special slope design (Fig. 2(b, c)) is introduced at the spring teeth to regulate the rotational direction and to add tolerance to the misalignment caused by parasitic shift, where maximum tolerance is determined by L_T and is also governed by fabrication resolution L_R, which is governed by the following geometry:

$$L_R = \frac{L_T}{\sin\left(\frac{\varphi}{2}\right)} \approx 2L_T.$$

These parameters are later validated in the simulation section.

For high force output, spring stiffness should be selected carefully. For an underdamped spring system released from maximum deflection, the velocity and kinetic energy increase as the system approaches the neutral position. To maximize dynamic performance, the spring mechanism should exhibit high stiffness, low rotational inertia, and minimal damping. Therefore, a spring inspired by a crossed flexure pivot spring [6] is adopted in order to minimize parasitic shifts of the rotational axis while retaining sufficient stiffness. It integrates three double-decker joints for cushioning, three straight beams for rotation, and flexure beams reinforcing the joints against translation.

The fabrication process follows a standard Nanoscribe two-photon polymerization printing procedure (Fig. 1(c)). A drop of IP-S resin is first placed on a glass substrate, and the structure is then printed within the resin. The structures are then developed using PGMEA for 20 minutes to remove unpolymerized resin. Finally, a 200 nm aluminum layer is sputtered onto the structure to enhance optical absorption. Cylindrical pillars are added beneath the structure to provide support for overhanging parts. Empirically, pillars with diameters as small as 2 µm can support the structure while allowing easy release. Fig. 1(b) also shows a scanning electron microscope (SEM) image of the fabricated actuator while visualizing the supporting pillars underneath the structure. Finally, the structure is released by attaching it to a double-sided tape on a coverslip, which breaks supporting pillars cleanly.

3 Simulation Results

The torsional spring is modelled in SolidWorks 2024 and finite element analysis (FEA) is conducted in COMSOL Multiphysics 6.0. Stiffness is defined as the rotational angle per unit torque, while resistance is defined as the parasitic shift per unit normal force.

Simulation of actuation is conducted in MSC Adams 2023 (Fig. 3(f)). The spring geometry is simplified as a cylinder with teeth connected to the ground by bushing, which offers stiffness for both rotation and translation. The chevron actuators are replaced with two pushes with prescribed translation. A nonlinear penalty contact model with damping is adopted for contact with Colomb friction. The contact normal force is:

$$F_n = K_c x^e + D_c \dot{x}^e.$$

The allowable penetration is set to 0.1% of contact part dimension while the stiffness is estimated by assuming the contact force to be on the order of five times the gravitational force. All damping is tuned into underdamping based on the stiffness and inertia properties, similar to macroscale springs. For all simulations, the GSTIFF integrator with IS2 formulation and HHT integrator both with an error tolerance of 10^{-5} are selected and cross-validated. Convergence study is carried out to ensure sufficient time steps and tolerance.

Table 1 Spring simulation parameters

Property	Value
Material Young's modulus	2.1 GPa
Material Poisson ratio	0.3
Mass	0.37 µg
Moment of inertia	2.56 mg·µm^2
Spring stiffness K_S	0.44 mN·µm/deg
Spring resistance K_c	0.07 mN/µm
Contact stiffness	397
Force exponent	2.2
Penetration depth	0.02 µm

 DOI: 10.30420/456743042

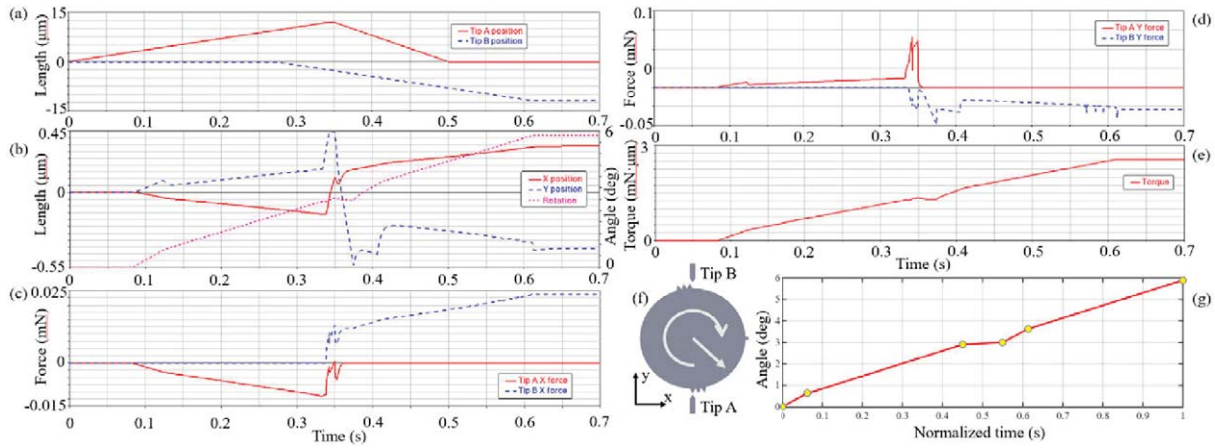


Fig. 3. Simulation of actuation (a) Chevron actuator position, (b) Spring pose, (c) Pusher force on X axis, (d) Pusher force on Y axis, (e) Spring torque, (f) Simulation setup, (g) Fitted actuation cycle.

Simulation of one full actuation cycle is carried out. Consecutive pushes are applied using two chevron actuators with prescribed 12 μm translation at constant speed (Figure 3.4). In Phase 1, both tips align with the spring teeth. Tip A advances (Phase 2), rotating the spring until reaching the tooth trough at 0.33s (Phase 3), then continues to 0.34s and holds until 0.35s. Tip B then engages and continues the rotation (Phase 4). An overlap period occurs when both tips contact the teeth, which is necessary for continuous actuation but should be minimized to reduce additional loads. The process is treated as quasistatic, where only tip positions but not the velocities govern the response.

Spring pose is recorded in Fig. 3(b). The rotation is approximately linear, indicating satisfactory controllability. At 0.125s, a change in rotational derivative and nonlinearity in Y displacement are observed, mainly due to the contact point shifting off the tooth slope, explaining the linear behavior before and after. A nonlinear region occurs from 0.33s to 0.42s, where the spring briefly stops and reverses by 0.29° before resuming rotation. This corresponds to abrupt variations in Y motion, where the spring shifts parasitically in +Y up to 0.33s, continues translating under direct pushing until 0.34s, and reaches a maximum at 0.35s. It then moves in −Y as Tip A retracts and Tip B advances, producing another extremum.

The forces on both tips are shown in Fig. 3(c). A change in force derivatives occur at 0.125s due to the tooth profile. Nonlinear behavior in X and Y forces follows the nonlinear Y position, while the spring torque remains consistent with rotational response, matching the ideal spring model. The peak actuation force is 0.06 mN, within the capability of chevron actuators.

It is observed that a full push can only achieve 2.9° (Phase 3) of rotation instead of 3°, the angle across half a tooth by design. This deficit is defined as θ_D. The deficit is doubled at phase 5, reaching 0.2°. It is assumed that this deficit remains this pattern for phase 3 and 5 in following actuation cycles, since the torque for rotation is scaled yet the force for parasitic shift remains unchanged because the shifts are unchanged. The slope size is mainly designed to tolerate this misalignment:

$$L_T = L_X + L_D, \tag{1}$$

where L_X is the shift of spring center on X and $L_D = 2\theta_D R$ is the shift caused by rotation deficit, in which $R = 110$ μm is the radius to teeth tip. Therefore L_T should be larger than 1.5μm. The deficit of rotation may be caused by the compliance of spring and the pushers introduced by the contact model, when the tips mesh with the teeth yet parasitic shift on X axis still exists.

The position within an actuation cycle can be fitted as a function of normalized time (Fig. 3(g)) and is linearly correlated with tip displacement. Each cycle comprises two identical periods driven by alternating chevron actuators, each exhibiting two linear regions. An intermediate region occurs when both actuator tips contact the spring, contributing only 0.1° of rotation. However, two actuators exhibit nonlinear coupling and are now only empirically controlled, which results in extra loads when two chevron actuators simultaneously contact the spring. Multi-cycle rotation could be handled by iterative application of the model.

4 Experimental Results

The experimental setup [7] is illustrated in Figure 4(a). A continuous-wave laser diode (532 nm, 2500 mW) serves as the laser source, with its beam directed to a digital mirror device (DMD). The reflected beam is coupled into a 19-core fiber bundle using a beam minimizer to match the fiber diameter, and the bundle projects the beam onto the microactuator mounted on an XYZ stage. A CMOS camera records the experiments through a microscope positioned above the structure. The DMD projects custom pattern, enabling selective illumination of individual fibers and on demand actuation of each chevron actuator.

Fig. 4(b, c) show the actuation results. In this experiment, only the left chevron actuator is activated repeatedly more than 50 times to validate the conversion of translation motion to rotational one. The chevron actuator translates upon optothermal heating, allowing its tip, aligned initially with the tooth crest, to reach the tooth trough and generate rotational motion of the torsional spring. Fig. 4(d) shows the measurement of the rotation displacement, with initial angles (minima), final angles (maxima), and the difference

DOI: 10.30420/456743042

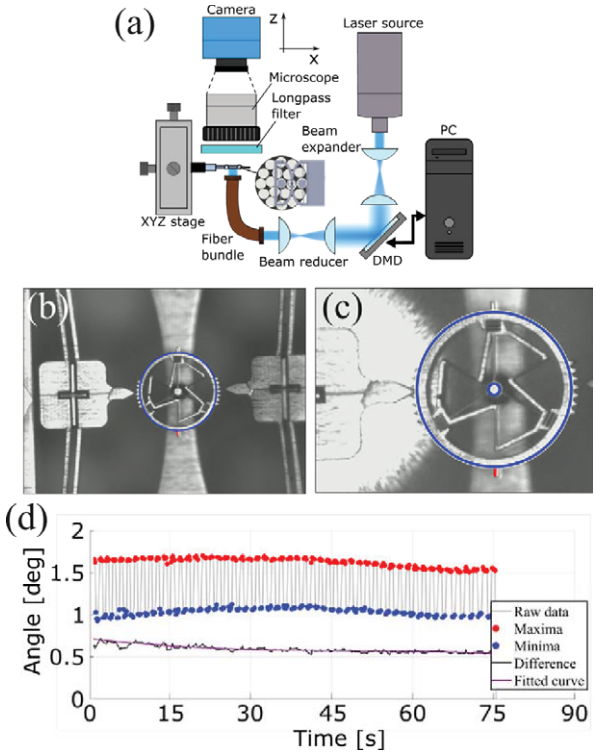


Fig. 4 (a) Experimental system. (b, c) Optothermal actuation and the resultalnt rotational displacement. (d) Repeatability test of the rotational displacement.

between them are shown in blue dots, red dots, and black line, respectively. The results show an average rotation of 0.6°.

The results prove the ability of the microactuator to generate repetitive rotational motion. The chevron actuators degrades with consecutive actuation while the spring deforms due to external load, which jointly causes minor shift in spring pose. However, accumulating these small rotations is challenging due to the difficulty in maintaining the original alignment between the chevron tips and the spring teeth after the release step in the fabrication process, even with the teeth slope accustomed to (1). In addition, the material degrades after laser illumination or mechanical pushes, resulting in shifts of deactivated pose. The spring outer ring deforms visually especially when pushed by both chevron actuators.

5 Conclusion

This work introduced a optothermal rotary microactuator capable of generating rotational motion through sequential tooth engagement and torsional deformation. The actuator combines two optothermal chevron actuators with a compliant toothed torsional spring to realize cyclic rotational actuation within a compact microscale structure. The rotational mechanism, tooth interaction, and contact behavior were analyzed through kinematic modelling and dynamic simulation, including the effects of friction, parasitic shift, and actuator coupling during one complete actuation cycle. The proposed device was fabricated using two photon polymerization with aluminum coating for enhanced optical absorption. Experimental studies demonstrated repeatable rotational actuation with successful tooth meshing and measurable angular displacement, validating the feasibility of the proposed rotational actuation strategy for future optothermal microrobotic applications.

Future work will investigate the relationship between spring stiffness, damping, and parasitic resistance to further improve rotational efficiency and force transmission. More accurate modelling of contact compliance and dynamic coupling between the two chevron actuators will be developed to reduce undesired loading during overlapping actuation phases. Additional studies on timing control, response bandwidth, and frequency characteristics will also be conducted to improve actuation stability and enable reliable continuous rotation. Further optimization of the spring geometry and fabrication robustness is expected to enhance rotational accumulation accuracy and support future multi degree of freedom microrobotic systems.

References

[1] L. V. Pasaguayo, Z. Al Masry, S. Lescano, and N. Zerhouni, “Surgical Microgrippers: A Survey and Analysis,” *Journal of Medical Devices*, vol. 17, no. 3, Jul. 2023.

[2] B. Ahmad, A. Barbot, G. Ulliac, and Aude Bolopion, “Hybrid Optothermal-Magnetic Mobile Microgripper for In-Liquid Micromanipulation,” *IEEE Robotics and Automation Letters*, vol. 8, no. 3, pp. 1675–1682, Feb. 2023.

[3] B. Ahmad, A. Barbot, G. Ulliac, and Aude Bolopion, “Remotely Actuated Optothermal Robotic Microjoints Based on Spiral Bimaterial Design,” *IEEE/ASME Transactions on Mechatronics*, vol. 27, no. 5, pp. 4090–4100, Feb. 2022.

[4] B. Ahmad, H. Chambon, P. Tissier, and A. Bolopion, “Laser Actuated Microgripper Using Optimized Chevron-Shaped Actuator,” *Micromachines*, vol. 12, no. 12, p. 1487, Nov. 2021.

[5] J. M. Fee and D. P. Solheid, “Coefficient of friction effects of polymers, silicone oil, and mini-rollers in cable pulling,” *Proceedings of IEEE/PES Transmission and Distribution Conference*, pp. 317–322, Apr. 1994.

[6] E. Thalmann and S. Henein, “Triple Crossed Flexure Pivot Based on a Zero Parasitic Center Shift Kinematic Design,” *Journal of Mechanisms and Robotics*, pp. 1–23, Jan. 2022.

[7] K. Chen, A. J. Thompson, and B. Ahmad, “Multi-DoF Optothermal Microgripper for Micromanipulation Applications,” *IEEE Robotics and Automation Letters*, pp. 1–8, Jan. 2025.

ISBN: 978-3-8007-6743-4

@ VDE VERLAG GMBH · Berlin · Offenbach

 DOI: 10.30420/456743043

Dual-Joint Cable-Driven Soft Actuator for Miniaturized Flexible Endoscopy

Zijian Liu, School of Medicine, University of Dundee, Dundee, UK, zzqliu@dundee.ac.uk;
Luigi Manfredi, School of Medicine, University of Dundee, Dundee, UK, l.manfredi@dundee.ac.uk

Abstract

Early colorectal cancer diagnosis and intervention require compact and compliant endoscopic steering in narrow, tortuous anatomy. This work presents a dual-joint cable-driven soft actuator with internally routed tendons, where distal tendons pass through proximal internal channels to improve compactness and enable compound postures such as S-shapes. An open-loop teleoperation baseline is implemented on Jetson + PCA9685 in C++, with independent joystick control of the proximal and distal joints. Magnetic sensing provides multi-point motion measurement, while the current simulation outputs the top-point workspace only. Experimental results are reported as partial-coverage validation and show trend-level consistency between model predictions and measured trajectories within explored sectors.
Key words : soft actuator, tendon-driven soft robot, flexible endoscopy, dual-joint steering, open-loop teleoperation.

1 Introduction

Early colorectal cancer diagnosis and intervention rely on effective endoscopic navigation through narrow, tortuous, and compliant anatomy. Conventional steering can still suffer from limited distal manoeuvrability and elevated friction/contact forces, motivating compact and compliant robotic steering mechanisms. Soft continuum actuation is attractive for this purpose, but many pneumatic/hydraulic solutions remain difficult to package and control at millimetre scale. Tendon-driven soft actuation remains appealing due to compact external actuation and fast response. Compared with single-section or single-segment tendon-driven soft/continuum designs [6,7], the present study investigates a dual-joint internally routed actuator that enables compound postures such as S-shapes. While tendon-driven continuum robots for minimally invasive and endoscopic applications have also been reported [1,2,8–10], the present work emphasizes a compact dual-joint soft structure, simplified length-based modelling, and sensing-enabled trend-level evaluation.

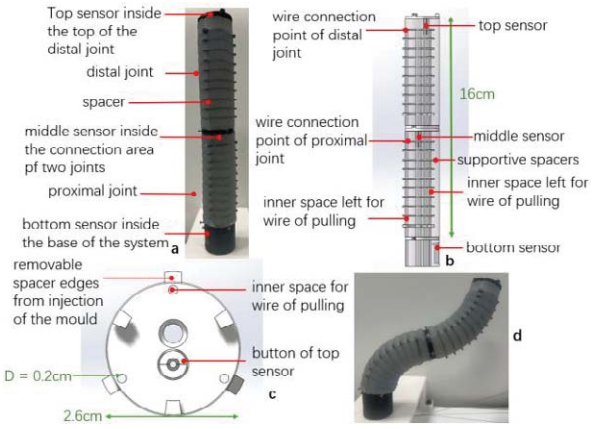


Figure 1 Mechanical design of the proposed dual-joint cable-driven soft actuator. (a) Photograph of the fabricated actuator. (b) CAD view of the overall dual-joint structure. (c) Cross-sectional CAD view showing the tendon-channel layout. (d) Complex ‘s’ shape displacement within the control of both joints.

2 Materials and Methods

2.1 Mechanical design and tendon routing

The actuator consists of two serial soft bending joints arranged along a common axis, referred to as the proximal and distal joints, as shown in Fig. 1(a,b). The distal tendons are routed through dedicated internal channels across the proximal segment before reaching the distal tendon connection region, while the proximal tendons terminate within the proximal joint. This dual-joint architecture preserves a compact cylindrical profile and enables compound bending configurations.

Each joint is driven by three tendons distributed evenly around the central axis, as shown in Fig. 1(c). Compared with externally routed layouts, the present internal routing improves compactness and reduces external interference during bending, but also introduces inter-joint coupling because proximal bending changes the distal tendon routing geometry and effective path length.

2.2 Tendon actuation principle and coordinated payout

For each joint, the joystick input $(x, y)$is represented in polar form as (θ, r), where θdenotes bending direction and $r$actuation intensity. The command is mapped to three tendons distributed approximately 120° apart around the actuator axis. Tendon actuation is determined by a projection-based rule:

$$u_i = k\, r\cos(\theta - \phi_i), i = 1,2,3$$

where $k$is a proportional gain and $\phi_i$denotes the angular location of tendon i. Positive $u_i$corresponds to reel-in, and negative $u_i$to controlled pay-out.

This coordinated reel-in/pay-out scheme keeps all tendons engaged during bending, reduces slack accumulation, and improves tension distribution. The same mapping is used

 DOI: 10.30420/456743043

for both joints in the present open-loop teleoperation baseline.

2.3 Modelling and coupling formulation

Rather than using curvature as a direct control input, the present study formulates segment actuation in terms of tendon length changes, which are more directly related to the servo–spool actuation chain used in the experimental platform. Similar tendon-driven continuum formulations have been used in segment-level robot modelling and in medical continuum robot studies, although the present work adopts a deliberately simplified, control-oriented baseline [7–9]. This choice provides a simple and interpretable baseline for open-loop control and experimental comparison, without claiming a high-fidelity description of the full distributed deformation of the soft body.

The actuator consists of two serial segments, indexed by $i \in \{1,2\}$, corresponding to the proximal and distal joints, respectively. Each segment is driven by three tendons indexed by $k \in \{1,2,3\}$, with angular locations $\alpha_{i,k}$ distributed approximately 120° apart in the cross-section. For segment i, the actuation command is described by a direction angle φ_i, a length-change amplitude q_i, and an optional common bias term b_i. The tendon length change of tendon kin segment iis written as

$$\Delta l_{i,k} = b_i - q_i \cos(\alpha_{i,k} - \varphi_i), \quad i \in \{1,2\}, k \in \{1,2,3\}$$

Here, tendons located near the commanded bending direction are shortened, whereas tendons on the opposite side are released proportionally. The common term b_i is used to represent shared pretension or slack adjustment applied to all three tendons of the same segment.

To extract the directional bending component independently of the common bias, the mean tendon-length change of segment i is first defined as

$$\overline{\Delta l_i} = \frac{1}{3}\sum_{k=1}^{3} \Delta l_{i,k},$$

and the corresponding zero-mean relative tendon-length changes are

$$\widetilde{\Delta l_{i,k}} = \Delta l_{i,k} - \overline{\Delta l_i}.$$

A planar actuation vector is then defined as

$$V_i = -\frac{2}{3}\sum_{k=1}^{3} \widetilde{\Delta l_{i,k}} \begin{bmatrix} cos\alpha_{i,k} \\ sin\alpha_{i,k} \end{bmatrix}$$

The negative sign ensures that the resulting vector points toward the actual bending direction, since tendon shortening corresponds to negative $\Delta\ell_{i,k}$. The normalization factor $\frac{2}{3}$ is chosen so that, for an ideal three-tendon symmetric layout, the vector magnitude is consistent with the input length amplitude q_i. The equivalent bending direction is therefore defined as

$$\phi_i = atan2(v_{i,y}, v_{i,x}),$$

and the corresponding actuation magnitude is

$$m_i = \|V_i\|$$

In the ideal symmetric case, m_i matches the commanded length amplitude q_i; in practice, it is interpreted as an equivalent actuation magnitude derived from the relative tendon-length changes.

To generate a simulated top-point motion, the actuation magnitude is mapped to an equivalent bending angle through an empirically calibrated proportional coefficient c_i,

$$\theta_i = c_i m_i$$

where the unit of c_i depends on the unit used for m_i (for example, rad/mm if m_i is expressed in mm). This mapping is not intended as a strict geometric derivation, but as a simple calibration-based approximation for the current actuator.

Each segment is then approximated using a constant-curvature-inspired geometric mapping. For a segment of active length H_i, the segment tip position expressed in its local base frame is written as

$$p_i = \frac{H_i}{\theta_i}\begin{bmatrix} cos\phi_i(1-cos\theta_i) \\ sin\phi_i(1-cos\theta_i) \\ sin\theta_i \end{bmatrix}, \quad \theta_i \neq 0.$$

with the limiting straight configuration

$$p_i = \begin{bmatrix} 0 \\ 0 \\ H_i \end{bmatrix} \quad as\ \theta_i \to 0.$$

The corresponding unit tangent direction at the segment tip is

$$u_i = \begin{bmatrix} cos\phi_i, sin\theta_i \\ sin\phi_i, sin\theta_i \\ cos\theta_i \end{bmatrix}.$$

For serial composition, the rotation matrix associated with segment iis defined explicitly as

$$R_i = R_z(\phi_i)R_y(\theta_i)R_z(-\phi_i),$$

so that the two-segment top-point output can be written unambiguously. Segment 1 produces (p_1, u_1), while Segment 2 produces local quantities (p_2, u_2) expressed in the frame attached to the tip of Segment 1. The final simulated top-point position is then

$$p_{top} = p_1 + R_1 p_2,$$

and the corresponding distal-end direction is

$$u_{top} = R_1 u_2.$$

Because the distal tendons are internally routed through the proximal segment, the real actuator exhibits routing-induced inter-segment coupling. In the present baseline model, this effect is not represented by a full nonlinear tendon-path correction; instead, the model treats each segment through its commanded tendon-length changes and uses the resulting deviations from measurement to interpret coupling-related behaviour in the experiments.

Accordingly, the present model should be understood as a simplified, control-oriented baseline for simulated top-

 DOI: 10.30420/456743043

point motion generation and trend-level comparison with experiments. It is not intended as a high-fidelity reconstruction of the full distributed deformation of the actuator. Effects such as friction, hysteresis, backlash, and routing-induced nonlinear coupling are not explicitly modelled here and are instead discussed as sources of deviation between simulation and measurement.

2.4 Electronics, open-loop teleoperation, and sensing

The actuation system was implemented on a Jetson Orin NX platform in C++, with PWM signals generated through an external PCA9685 driver board (Fig. 2). Joystick inputs were read through USB and interpreted as two independent 2D commands for the proximal and distal joints. For each joint, the input was converted into a directional command and actuation magnitude, then mapped to three tendon-driving servo outputs according to the coordinated reel-in/pay-out strategy described in Section 2.2. Identical safety constraints were applied to both joints before PWM output through the I2C-connected PCA9685 to six servo channels in total. The present implementation was intentionally kept as an open-loop teleoperation baseline without PID regulation or real-time sensor-based correction. For experimental characterization, a 3D Guidance trakSTAR magnetic tracking system was used as an external sensing device, with three sensor channels attached at the bottom, middle, and top of the actuator to monitor base, intermediate, and distal motion. The system outputs 6DoF data at $T_s = 0.01$ s(100 Hz), and all measurements were transformed into an actuator-centered object frame. Since the current kinematic simulation outputs only the top-point trajectory and workspace, quantitative comparison was performed mainly at the top point, while the middle and bottom measurements were retained for qualitative interpretation of inter-joint coupling.

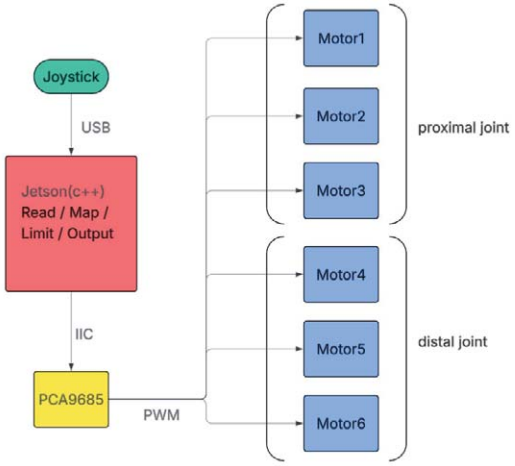


Figure 2 Open-loop teleoperation and actuation architecture of the dual-joint soft actuator.

3 Results

3.1 Repeatability and return-to-centre stability

To evaluate repeatability under fixed commanded postures, repeated trials were performed for both a target posture and a return-to-centre posture. For each condition, 29 repetitions were recorded using the magnetic sensing system at the top and middle sensing points. As shown in Figure 3, the repeated measurements formed compact point clusters for all four conditions (centre-top, centre-mid, target-top, and target-mid), indicating stable posture reproduction under repeated open-loop actuation. The centre and target clusters were clearly separated in the object-frame projection, which confirms that the actuator responded consistently to distinct commanded postures. Both joints were controlled by hardcode through Jetson to make the same and constant movement. (60° of bending on x axis for proximal joint and 60° bending on y axis for distal joint)

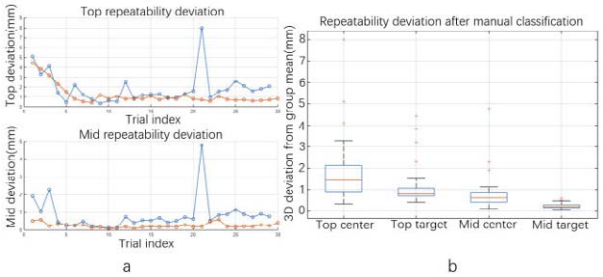


Figure 3 Repeatability deviation after manual classification of stable hold segments. (a) Trial-wise 3D deviation from the group mean for the top and middle sensing points under center and target postures. (b) Boxplot summary of the corresponding deviation distributions, with outliers indicating occasional larger return-to-center or target-reaching errors..

3.2 Workspace exploration and compound postures under random teleoperation

To characterize the motion capability of the actuator under open-loop operation, random joystick inputs were applied during teleoperation, and the resulting motion was recorded by the magnetic sensing system. The measured trajectories were reconstructed in the actuator-centred object frame to visualize the experimentally explored motion range. As shown in Figure 4, random teleoperation allowed the actuator to explore a continuous three-dimensional region of the workspace within the tested time window, indicating that the dual-joint structure can generate broad steering motion under open-loop actuation and support compound multi-segment bending. Because the input sequence was random and limited in duration, the measured trajectories represent an explored subset of the reachable workspace rather than an exhaustive workspace boundary.

ISBN: 978-3-8007-6743-4 @ VDE VERLAG GMBH · Berlin · Offenbach

 DOI: 10.30420/456743043

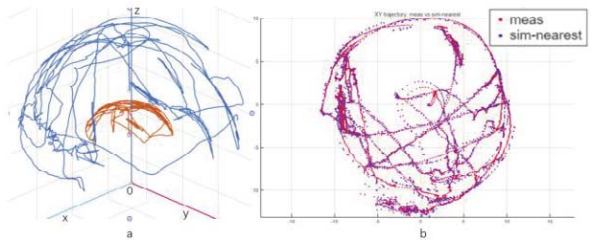


Figure 4 (a) Three-dimensional trajectories recorded during random teleoperation, illustrating the experimentally explored motion range of the actuator, which blue is representing the top sensor and orange represent the middle sensor. (b) XY-plane comparison between the measured joystick-driven trajectory (red) and its pointwise nearest-neighbour projection onto the simulated reachable set (blue, "sim-nearest"), with one-way meas→sim NN error summarized in the inset.

3.3 Model–measurement comparison under partial coverage

To compare the simplified model with the experimental data, the simulated top-point reachable set and the experimentally measured top-point trajectories were aligned in the common object frame and evaluated in the same projection. As shown in Figure 4b, the measured trajectories covered only a subset of the modelled reachable region, reflecting the limited exploration produced by the random teleoperation trial rather than an exhaustive scan of the full workspace.

Because the experimental data represent only the visited portion of the workspace, the comparison is interpreted as a partial-coverage evaluation rather than a full-boundary validation. The main objective is therefore to assess whether the measured top-point motion follows the local shape and scale of the modelled reachable set within the explored sectors.

The overlay shows visible trend-level correspondence between the measured trajectories and the model-predicted envelope in the visited regions. Quantitative evaluation was performed using nearest-neighbour error statistics. In the present dataset, the one-way measurement-to-simulation nearest-neighbour statistics mean = 0.404 cm, standard deviation = 0.278 cm, P50 = 0.322 cm, P95 = 0.926 cm, and maximum = 1.866 cm. These values indicate that the simplified model captures the main top-point motion trend within the explored sectors, while the remaining deviations are consistent with unmodeled effects such as friction, hysteresis, backlash, and routing-induced nonlinear coupling.

4 Discussion

The dual-joint internally routed design enables compact steering and richer postures, including S-shapes, relative to single-segment tendon-driven designs [6,7]. Internal routing improves compactness but introduces inter-joint coupling, which contributes to prediction error and repeatability limits. Given that experiments cover only a subset of the workspace, the present results should be interpreted as partial-coverage, trend-level validation rather than full-boundary agreement. The simplified kinematic model is therefore intended to capture the main top-point motion trend, while remaining deviations are consistent with friction, hysteresis, backlash, and routing-induced coupling.

5 References

[1] Shi, J., Shi, G., Wu, Y., & Wurdemann, H. A. (2023). A Multi-Cavity Touch Interface for a Flexible Soft Laparoscopy Device: Design and Evaluation.

[2] Chen, M., & Wang, D. (2019). A Multi-Module Soft Robotic Arm with Soft End Effector for Minimally Invasive Surgery. Proceedings of the 2nd World Conference on Mechanical Engineering and Intelligent Manufacturing (WCMEIM).

[3] Chen, A., Yin, R., Cao, L., Yuan, C., Ding, H., & Zhang, W. J. (2017). Soft Robotics: Definition and Research Issues. Mechatronics and Machine Vision in Practice.

[4] Aljaber, F., & Althoefer, K. (2018). Towards Creating a Flexible Shape Sensor for Soft Robots. IEEE International Conference on Soft Robotics (RoboSoft), Livorno, Italy.

[5] Xu, F., & Wang, H. (2021). Soft Robotics: Morphology and Morphology-Inspired Motion Strategy. IEEE/CAA Journal of Automatica Sinica, 8(9), 1500–1522.

[6] Seleem, I. A., Naeem, M. A., Takemura, H., & Ishii, H. (2025). Tendon-driven based extensible soft robot with variable stiffness. Robotics and Autonomous Systems, 190, 104988.

[7] Grassmann, R. M., Rao, P., Peyron, Q., & Burgner-Kahrs, J. (2022). FAS—A Fully Actuated Segment for Tendon-Driven Continuum Robots. Frontiers in Robotics and AI, 9, 873446.

[8] Kato, T., Okumura, I., Song, S.-E., Golby, A. J., & Hata, N. (2015). Tendon-Driven Continuum Robot for Endoscopic Surgery: Preclinical Development and Validation of a Tension Propagation Model. IEEE/ASME Transactions on Mechatronics, 20(5), 2252–2263.

[9] Kato, T., Okumura, I., Kose, H., Takagi, K., & Hata, N. (2016). Tendon-driven continuum robot for neuroendoscopy: validation of extended kinematic mapping for hysteresis operation. International Journal of Computer Assisted Radiology and Surgery, 11(4), 589–602.

[10] Gao, Y., Takagi, K., Kato, T., Shono, N., & Hata, N. (2020). Continuum Robot With Follow-the-Leader Motion for Endoscopic Third Ventriculostomy and Tumor Biopsy. IEEE Transactions on Biomedical Engineering, 67(2), 379–390.

 DOI: 10.30420/456743044

Enhancing the reliability of piezoelectric actuators and motors under severe self-heating, high-cycle operation, and harsh environmental conditions

Rasmus Lou-Møller[1], Iman Mehdipour[1], Charles Mangeot[1], Nicolas Bourgeot[2], Frank Claeyssen[2], Boris Laluc[2]
(1) CTS Denmark A/S, 3490 Kvistgaard, Denmark, rasmus.moeller@ctscorp.com
(2) Cedrat Technologies, 38240 Meylan, France, nicolas.bourgeot@cedrat-tec.com

Abstract

Piezoelectric actuators are increasingly used in aerospace, medical, and precision industrial systems where reliable operation under extreme conditions is required. However, long-term performance is limited by combined stressors such as self-heating, high-cycle loading, and elevated temperatures, which may cause depolarization, fatigue, and electrical interconnection failures. Within the Eurostars PROOFED project—a collaboration between Cedrat Technologies and CTS Denmark—this work examines the fabrication and reliability of soft-doped NCE51F multilayer piezoelectric stacks. These stacks are integrated into Amplified Piezoelectric Actuators (APAs) and tested under high-temperature, high-cycle operating conditions. Different electrical interconnection methods, including fired silver paste, high-melting-point solder, and high-temperature conductive epoxy, were evaluated using sine-wave excitation at 150 V peak-to-peak with self-heating temperatures up to 200 °C. Conductive epoxy provided the most reliable electrical connection, while silver paste and solder joints failed due to thermal stress and insufficient adhesion. The optimized epoxy-based interconnection and wire configuration were implemented in piezoelectric stacks and validated through lifetime testing up to 10 billion cycles at approximately 200 °C. Only minor performance variations were observed after testing, demonstrating stable electrical and mechanical behaviour. The proposed stack design and interconnection approach enable reliable operation of multilayer piezoelectric actuators in demanding long-term applications.

1 Introduction

Piezoelectric actuators are widely used in aerospace, medical, and precision industrial systems where compact size, high resolution, and fast response are required. In many of these applications, actuators must operate reliably under demanding conditions involving elevated temperatures, continuous operation, and high numbers of actuation cycles [1, 2]. Ensuring long-term stability under such conditions remains a major challenge for multilayer piezoelectric actuators [3, 4].

During operation, dielectric and mechanical losses generate heat inside the actuator, leading to self-heating. Elevated temperatures combined with cyclic loading may cause depolarization, microstructural degradation, and fatigue damage. In addition, electrical interconnections between the multilayer stack and external wiring represent a critical reliability factor, particularly under high-temperature conditions where thermal expansion mismatch and mechanical stress may lead to cracking or loss of adhesion.

This work was carried out within the Eurostars PROOFED project in collaboration between Cedrat Technologies and CTS Denmark. The objective of this study is to investigate the reliability of multilayer piezoelectric stacks and their electrical interconnections under extreme operating conditions [5]. The main contributions of this paper are:

- Evaluation of high-temperature electrical interconnection methods
- Optimization of wire configurations for multilayer stacks
- Integration into Amplified Piezoelectric Actuators (APAs)
- Lifetime validation up to 10 billion cycles at approximately 200 °C

2 Multilayer Actuator Design and Materials

2.1 Piezoelectric Material

The multilayer actuators investigated in this study were fabricated from soft-doped NCE51F piezoelectric ceramics supplied by CTS [6]. This material was selected due to its high piezoelectric coefficients and suitability for actuator applications requiring large displacement at moderate driving voltages.

Key material properties are summarized in Table 1.

Table 1 – NCE51F material properties [6].

Property	Value	Unit
d_{33}	443	pC/N
Relative Dielectric Constant	1900	-
Coupling Coefficient k_{33}	0.74	-
Curie temperature	360	°C
Maximum operating temperature	200	°C

Multilayer technology enables large electric fields to be applied at relatively low driving voltages, allowing compact actuator designs with high performance.

2.2 Multilayer Stack Design

Preliminary experiments were performed at tile level using multilayer samples with dimensions 2×5×2 mm³ and 5×5×2 mm³ and an operating voltage of 150 V. The tiles were equipped with silver termination electrodes suitable for external electrical connections.

These samples were used to evaluate the reliability of different electrical interconnection methods under high-temperature self-heating conditions.

 DOI: 10.30420/456743044

Based on the tile-level results, multilayer stacks with dimensions (Figure 1) were fabricated for further investigation.

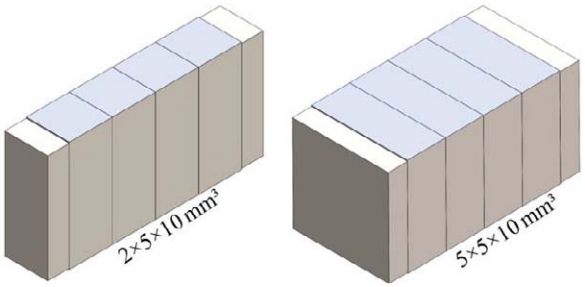
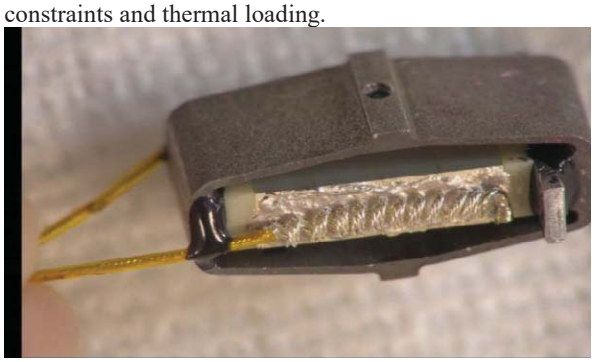


Figure 1. Two stacks in different sizes (2×5×10 mm³ and 5×5×10 mm³)

2.3 APA Integration

Selected multilayer stacks were integrated into Amplified Piezoelectric Actuators (APAs) to validate performance at system level.
The stacks were mounted inside APA mechanical frames providing displacement amplification (Figure 2).
The APAs provided a free displacement of approximately 54 µm at an excitation voltage of 150 V.
APA testing allows evaluation of actuator performance under realistic operating conditions including mechanical constraints and thermal loading.



APA35XS



APA40SM

Figure 2. APA35XS with mounted a stack 2×5×10 mm³ and APA40SM with mounted two stacks 5×5×10 mm³.

3 Electrical Interconnection Methods

3.1 Wire Materials and test setup

Electrical connections were made using single-strand nickel–chromium (NiCr) wires with a diameter of approximately 0.2 mm.
NiCr wire was selected due to its high temperature stability and mechanical robustness under cyclic loading conditions.
After establishing the electrical connections on the tiles using single-strand nickel–chromium (NiCr) wires (Ø ≈ 0.2 mm), as described in the following section, the tiles were assembled in parallel with their wire connections for the lifetime test setup shown in Figure 3.



Figure 3. test setup for wire connection techniques on the tile.

Then, the setup was driven continuously using sinusoidal excitation at:
Voltage:150 V peak-to-peak
Frequency: approximately 1.5-1.6 kHz for operating at temperatures close to 200 °C due to self-heating.

3.2 Connection Techniques

Three electrical connection methods were evaluated.

Fired thick-film Silver electrode

Electrical connections were first produced using fired silver paste applied between the termination electrode and the NiCr wire. Figure 4 shows the connection and the failures at different cycles.
The paste was fired at approximately 650 °C according to the manufacturer's recommendations.
This method is commonly used in multilayer ceramic devices and provides low electrical resistance connections.

 DOI: 10.30420/456743044

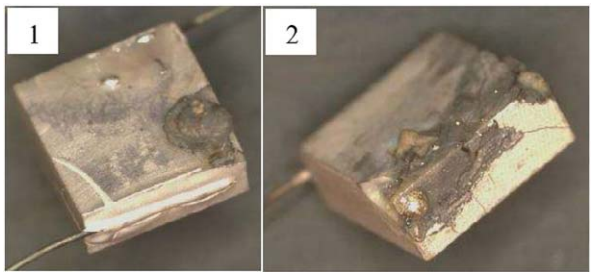


Figure 4. 1) failure at @ 920M and 2) failure at @ 3.7B May be related to internal stress

HMP Solder

Connections were also produced using lead-based high-melting-point solder with a melting temperature of approximately 300 °C (Figure 5).
This method is commonly used for electrical interconnections but may introduce thermal stresses during processing.

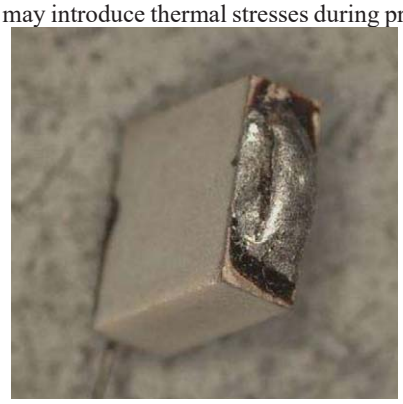


Figure 5. HMP @2.2B, Wire detached, Poor adhesion of NiCr to HMP

Conductive Epoxy

High-temperature conductive epoxy was used as an alternative connection method.
The epoxy was cured at approximately 100 °C for 1 hour.
This method provides mechanical compliance and is expected to reduce thermally induced stresses between the ceramic and the wire.

3.3 Wire Configurations

Two wire configurations were evaluated at stack level.

Bus Wire Configuration

The first configuration used a coiled bus wire connected to the stack electrodes. External connections were made using crimped connectors (Figure 6).
This configuration allows modular assembly but requires additional space inside the actuator.

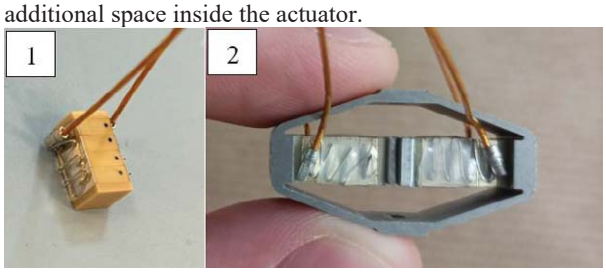


Figure 6. bus wire connection to Kapton wire by crimping

Kapton Wire Configuration

The second configuration used a one-piece coiled external wire with Kapton insulation (Figure 7).
This configuration provides improved flexibility and reduced assembly space requirements.
Based on preliminary testing, the Kapton wire configuration was selected for lifetime testing.

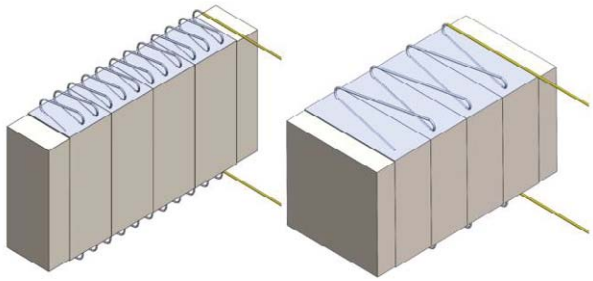


Figure 7. Stacks with wire configurations and their attachment

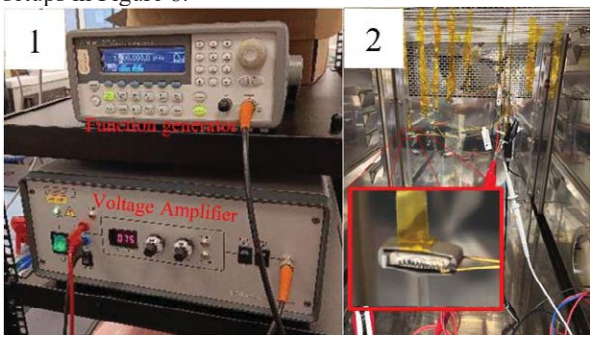
4 Experimental Procedures

4.1 Self-Heating Tests

Self-heating tests were performed using sinusoidal excitation at 150 V peak-to-peak.
The excitation frequency was varied in the range 1.1-1.4 kHz for *APA40SM* with stacks in size 5×5×10 mm^3 and 1.8-2.6 kHz for *APA35XS* with a stack in size 2×5×10 mm^3 to generate internal heating through dielectric and mechanical losses.
The temperature was measured using infrared camera to measure the surface temperature on the stacks.
Maximum temperatures up to approximately 200 °C were achieved.

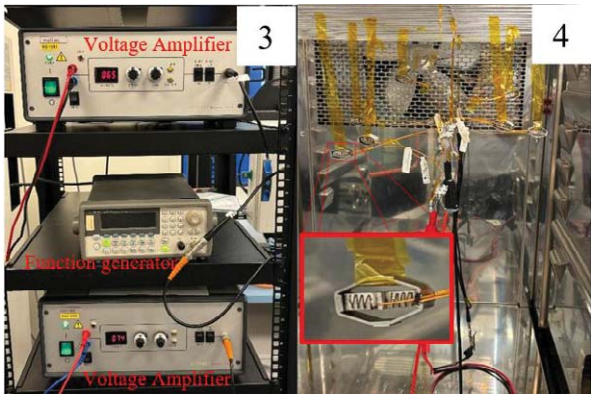
4.2 Lifetime Testing

Lifetime tests were performed on multilayer stacks integrated into *APA35XS* and *APA40SM* as in the following setups in Figure 8.



APA35XS

 DOI: 10.30420/456743044



APA40SM

Figure 8. Life-time setups for APA35XS and APA40SM.

The actuators were driven continuously using sinusoidal excitation at:
Voltage:150 V peak-to-peak
Frequency: approximately 2.3 kHz for *APA35XS* and 1.3 kHz for *APA40SM*.
The actuators operated at temperatures close to 200 °C due to self-heating.
The total number of cycles reached approximately 10 billion cycles corresponding to a test duration of approximately 50 days for *APA35XS* and 89 days for *APA40SM*.

5 Results and Discussion

5.1 Tile-Level Connection Reliability

The three electrical interconnection methods showed significantly different performance during self-heating tests.
Connections produced using fired silver paste failed after approximately 0.92 and 3.7 billion cycles due to cracking caused by thermal stresses (Figure 4).
High-melting-point (HMP) solder connections showed poor adhesion and resulted in wire detachment after approximately 2.2 billion cycles (Figure 5).
In contrast, conductive epoxy connections remained intact during testing with no failures observed.
These results indicate that conductive epoxy provides improved mechanical compliance and resistance to thermal stress.

5.2 Stack-Level Interconnection Performance

The conductive epoxy method was applied to multilayer stacks.
Both wire configurations were successfully implemented.
The bus wire configuration provided stable electrical connections but required additional assembly space.
The Kapton wire configuration provided improved flexibility and reduced mechanical stress on the electrodes.
No connection failures were observed during stack-level testing.

5.3 Lifetime Performance of APAs

Stacks assembled using conductive epoxy connections were integrated into APAs and subjected to lifetime testing.
After approximately 10 billion cycles at temperatures close to 200 °C, the actuators remained fully operational.
The free displacement showed (in Table 2) an increase of roughly 3%, while the resonance frequency measured under free-free boundary conditions decreased by about 4%.

Table 2. Comparison of the mean performance before and after the lifetime test

	APA35XS		*APA40SM*	
	Before life-time test	*After life-time test*	*Before life-time test*	*After life-time test*
free stroke -20V to Vmax (µm)	*54*	*56*	*54*	*56*

5.4 Discussion of Failure Mechanisms

The failures observed for silver paste and solder connections are attributed primarily to thermally induced stresses resulting from differences in thermal expansion between the ceramic, electrodes, and wires.
Conductive epoxy provides improved reliability due to its mechanical compliance, which allows partial relaxation of thermal stresses.
After the lifetime test, partial detachment of the wire from the silver epoxy was observed, indicating that further optimization of this interconnection method is still required.
The results demonstrate that electrical interconnections represent a critical reliability factor in high-temperature multilayer actuators.

6 Conclusion

This study investigated the reliability of multilayer piezoelectric actuators and their electrical interconnections under extreme operating conditions.
Among the evaluated methods, conductive epoxy provided the most reliable electrical connection and showed stable performance during self-heating tests up to approximately 200 °C.
Stacks assembled using conductive epoxy and optimized wire configurations demonstrated reliable operation during lifetime testing up to 10 billion cycles.
The results confirm that the proposed stack design and interconnection method are suitable for multilayer piezoelectric actuators operating under demanding conditions.

7 Acknowledgement

CTEC received funding from Eurostars under the PROOFED 2361 Consortium Agreement. The Eurostars Program is powered by EUREKA and the European Community. The Coordinator CTEC is supported by BPI FRANCE and the French state within the “France 2030” program.
CTS gratefully acknowledge the support of Innovation Fund Denmark (E2361 - PROOFED - CTS Ceramics Denmark, Case no. 3109-00083B) whose project grant made this work possible.

8 Literature

[1] E. Betsch, J. Gauthier, N. Bencheikh, A Pagès. High power density Piezo motors for critical environments ACTUATOR2022

[2] N. Bencheikh, N. Bourgeot, A. Pagès, G. Aigouy, J. Rebufa, E. Betsch, F. Claeyssen. Inertial & Inchworm piezoelectric motors: Design and Motorization selection key aspects ACTUATOR2024

[3] C. Mangeot. Temperature dependence of Soft/Hard PZT material properties and impact on the design choice, IWPMA 2015

[4] C. Mangeot, B. Andersen. Full characterisation of PZT actuators in quasistatic, large signal operation at elevated temperature, ACTUATOR 2016, MESSE BREMEN

[5] Nicolas Bourgeot, Frank Claeyssen, Boris Laluc, Rasmus Lou-Møller, Iman Mehdipour, Yves Ruffieux, François Barrot, Improving the reliability of piezoelectric actuators and motors subject-ed to significant self-heating and several billion actuation cycles or severe environments, ACTUATOR 2026, Wiesbaden Germany.

[6] https://www.ctscorp.com/Product-Series/NCE51.htm.

 DOI: 10.30420/456743045

3D nano-printed optical MEMS with closed-loop control

Florian Lux, Elijah Ditchendorf, Çağlar Ataman
Microsystems for Biomedical Imaging Group, Department of Microsystems Engineering (IMTEK), University of Freiburg, 79110 Freiburg, Germany
florian.lux@imtek.uni-freiburg.de

Abstract

3D nano-printing allows for the monolithic fabrication of Micro-Opto-Electro-Mechanical Systems (MOEMS). However, these polymer-based devices are subject to positioning errors caused by viscoelastic creep and temperature-dependent stiffness. We present a compact closed-loop control approach by incorporating a Hall sensor into a monolithically 3D nano-printed electromagnetic lens scanner. The magnetic field of the micro-magnet, already present for actuation, is used as a position-dependent signal. This approach enables a calibrated field-to-displacement mapping for a closed-loop control scheme that achieves a mean absolute accuracy of 0.86 µm and a precision of 0.49 µm across a displacement range of 150 µm, while eliminating creep-induced drift. Additionally, it reduces displacement drift caused by coil self-heating. This approach allows for precise positioning in monolithically 3D nano-printed optical microsystems for miniaturized imaging instruments that require reliable focus control.

1 Introduction

3D nano-printing enables the integration of micro-optics with complex actuators, without the need for optical assembly [1-3]. The monolithic fabrication solves the problem of alignment tolerances and allows for the fabrication of freeform optics and complex geometries, which cannot be realized with conventional MEMS fabrication processes [2, 3]. However, due to nonlinear material properties, the accuracy of open-loop operation cannot match that of silicon mechanics [1-3]. Therefore, integrated position sensors are essential to make these devices practically useful.
In this work, we integrate magnetic position sensing [4] into a large-aperture, 3D nano-printed lens scanner [1], and demonstrate that the detrimental effects of the nonlinear mechanical properties of photopolymers can mostly be eliminated through closed-loop control.

1.1 Concept and implementation

The actuator on which the proposed closed-loop control mechanism is demonstrated is based on a previously developed 3D-printed lens actuator designed for focus shifting [1]. In this actuator, a moving shuttle carries both a microlens and a micro-magnet. This shuttle is connected to a mechanical support structure by four ortho-planar linear motion springs, as shown in **Figure 1** (a). By placing this unit between two electromagnetic coils in an anti-Helmholtz-like configuration, a displacement of the shuttle is achieved by electromagnetic actuation. To sense the actual displacement of the shuttle, a Hall sensor is placed between the two electromagnetic coils, as close to the actuator as possible, as shown in **Figure 1** (b). The magnetic field measured by the Hall sensor comprises the electromagnetic field generated by the coil pair, which varies linearly with the applied current, and the magnetic field of the micro-magnet, which varies with shuttle position. Since the coil current is known, its magnetic field contribution can be subtracted using a calibration-based linear model. The displacement of the micro-magnet, and thus the shuttle carrying the microlens, can then be inferred from the remaining magnetic field using calibration data.

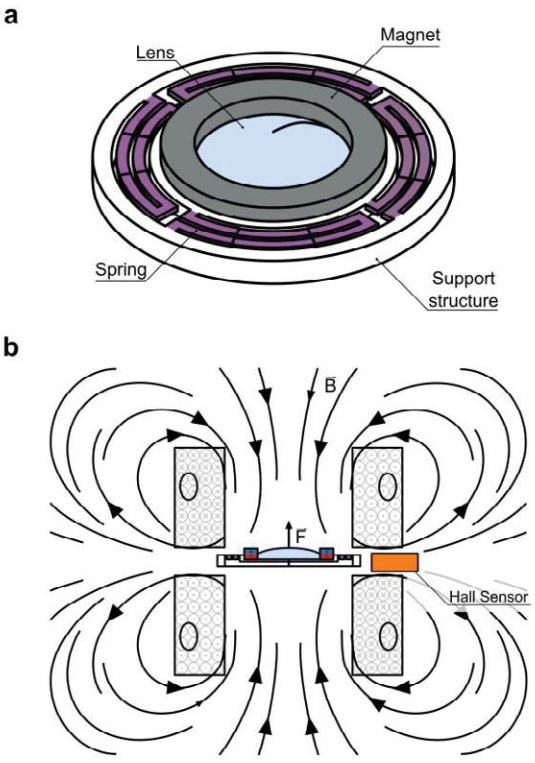


Figure 1 Working principle of the actuator. (a) A moving shuttle containing a microlens and a micro-magnet is connected to the outer support structure by four ortho-planar linear motion springs. (b) A coil pair in an anti-Helmholtz-like configuration generates the magnetic field gradient for displacement. A Hall sensor sandwiched between the coils measures the magnetic field originating from both the coil pair and from the moving magnet. Adapted from [1].

 DOI: 10.30420/456743045

2 Manufacturing

To enable lift-off, a 20 nm-thick polyvinyl alcohol layer was deposited on the silicon substrate prior to printing. (87–89 % hydrolyzed, Mw 13,000–23,000, Sigma-Aldrich 363081, 1 wt% aqueous solution, 1750 RPM, static dispense). The actuator was printed using a commercial two-photon polymerization-based printer (Photonic Professional GT+, Nanoscribe GmbH, Germany) using IP-S photoresin with a 10×/0.3 NA objective. **Figure 2** shows an SEM image of one spring with varying thickness.

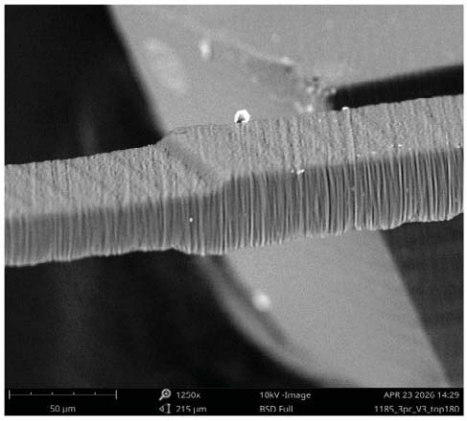


Figure 2 Representative image of a 3D nano-printed spring with varying thicknesses of 30 µm and 40 µm.

Following printing, the sample was developed in propylene glycol methyl ether acetate for 2 hours and rinsed in isopropyl alcohol for 30 minutes. During rinsing, flood illumination at 365 nm was applied to enhance the crosslinking of the polymer [5]. The substrate containing the printed actuator was then immersed in water to dissolve the sacrificial polyvinyl alcohol layer. The actuator, now detached from the substrate, was then transferred onto the lower coil. After fixing the actuator in place using UV-curable adhesive, the second coil was placed on top of the first coil, and the Hall sensor was inserted into a dedicated passive alignment groove. Both the second coil and the Hall sensor were fixed in place using UV-curable adhesive. The coil bodies were fabricated out of fused silica using selective laser-induced etching. Photographs of the fully assembled device are shown in **Figure 3**.

3 Results

The displacement was measured using a laser Doppler vibrometer (VGo-200, Polytec GmbH, Germany). The feedback loop was implemented on a microcontroller (Teensy 4.0 USB development board). The control signal calculated by the microcontroller was converted into a coil current by a custom-developed low-drift voltage-to-current converter.

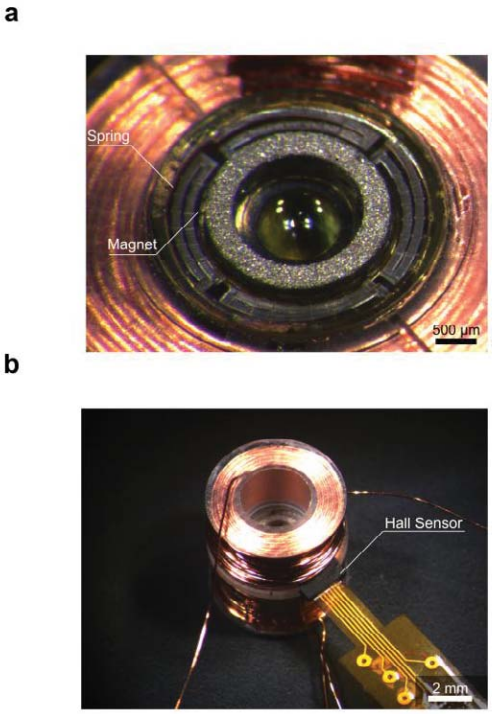


Figure 3 Photographs of the actuator. (a) Close-up of the springs, micro-magnet, and microlens. (b) Complete device with the Hall sensor on a flexible printed circuit board.

3.1 Accuracy and precision

To assess the precision and accuracy of the system, the setpoint for the position of the shuttle was increased and decreased in steps of 5 µm until a displacement of ± 75 µm was reached. The results shown in **Figure 4** indicate a displacement-independent mean precision of 0.49 µm.

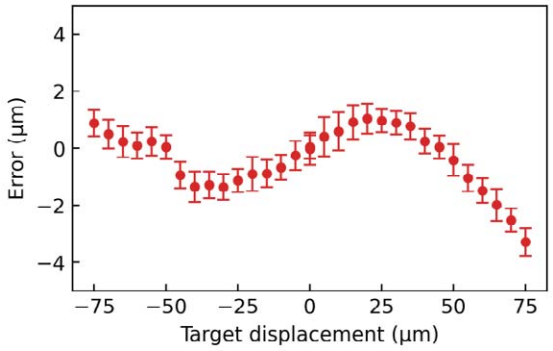


Figure 4 The proposed mechanism for closed-loop control achieves a mean precision of 0.49 µm, independent of displacement. The mean absolute accuracy is 0.86 µm, exhibiting a systematic trend.

The mean absolute accuracy is 0.86 µm, showing a systematic trend. This trend could arise from a mismatch of the

 DOI: 10.30420/456743045

assumed linear model to the actual position-dependent magnetic field, nonlinearities of the Hall sensor, or temperature effects, which may be influenced by the thermal history of previously set setpoints.

3.2 Step response

To evaluate the effectiveness of closed-loop control in compensating for creep caused by the viscoelastic properties of the polymer springs, a 75 µm step input was applied. The viscoelastic creep of more than 20 µm following the step response in open-loop operation further stresses the importance of closed-loop control for 3D nano-printed actuators. As can be seen in **Figure 5** (a), the drift following the step input is eliminated in closed-loop operation. The residual error during the closed-loop operation matches the systematic error observed in the accuracy characterization.

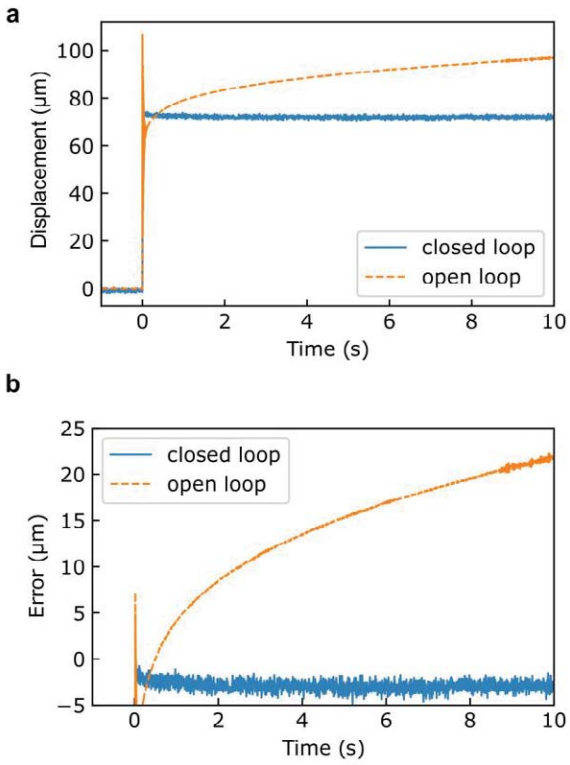


Figure 5 Step response in open-loop and closed-loop operation. (a) Following a step input, the actuator in open-loop operation shows a significant viscoelastic creep. In closed-loop operation, this creep is eliminated. (b) The relative error in open-loop operation is approximately 25 %. In closed-loop operation, a static error remains due to systematic calibration or model errors.

3.3 Long-term stability

During continuous actuation, the current in the electromagnetic coils leads to an increase in the actuator temperature, including the springs. This temperature increase causes a reduction of the Young's modulus of the springs [6]. As a result, the spring constant is reduced, leading to an increased displacement at a given current. To characterize

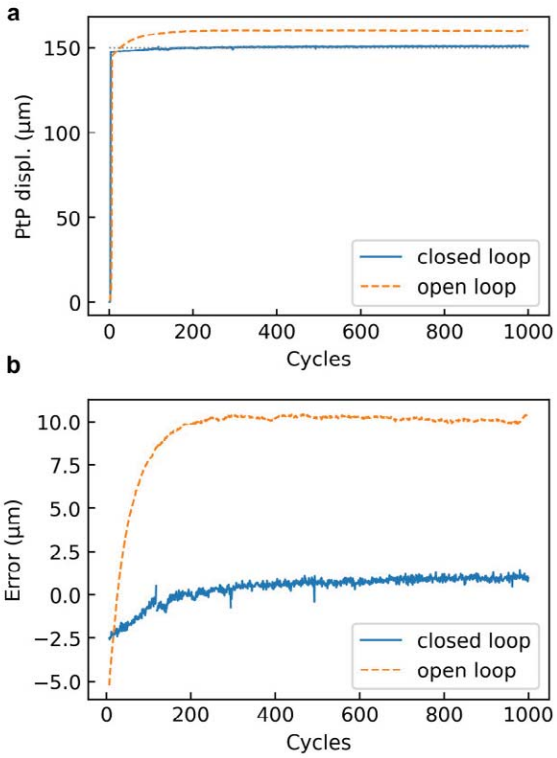


Figure 6 Long-term actuation over 1000 cycles at 1 Hz with a peak-to-peak amplitude of 150 µm. (a) Measured peak-to-peak displacement. (b) There is an error of up to 10 µm in open-loop operation. This error is reduced in closed-loop operation.

the ability of the closed-loop control to compensate for this temperature-induced drift, a long-term test was carried out. A sinusoidal signal with a peak-to-peak displacement of 150 µm and a frequency of 1 Hz was applied for 1000 cycles. In **Figure 6** (a), the peak-to-peak displacement is shown, while **Figure 6** (b) shows the deviation from the setpoint. In open-loop operation, this deviation reaches up to 10 µm, corresponding to a relative error of 6.7 %. The time constant of this drift is similar to the time constant of the temperature increase of the coil pair [1]. In closed-loop operation, the relative error was reduced to 1.6 %. The residual drift that can be observed in closed-loop operation is associated with thermal effects beyond the temperature dependence of the Young's modulus. For example, the remanence of the micro-magnet changes with −0.115 % $°C^{-1}$.

4 Discussion

The proposed closed-loop control mechanism compensates for two key intrinsic limitations of 3D nano-printed polymer actuators, namely viscoelastic effects and the pronounced temperature dependence of the Young's modulus. While the precision is limited by the noise of the utilized Hall sensor, the systematic error in the accuracy can arise from multiple origins. For example, a temperature depend-

 DOI: 10.30420/456743045

ence of the magnetic field-to-position mapping, nonlinearities of the Hall sensor, a model mismatch, or the temperature dependence of the remanence of the micro-magnet.

5 Conclusion

We demonstrated a closed-loop control mechanism for 3D nano-printed electromagnetic actuators that achieves a precision of 0.49 µm and a mean absolute accuracy of 0.86 µm. This control loop enables 3D nano-printedactuators to take the next step from proof-of-concept demonstrations to real-world applications.

6 Literature

[1] F. Lux, A. Calikoglu, and Ç. Ataman, “Monolithically 3D-nanoprinted millimeter-scale lens actuator for dynamic focus control in optical systems,”Advanced Photonics Nexus, vol. 4, no. 4, p. 046015,2025.

[2] F. Rothermel, S. Thiele, C. Jung, A. Krapf, S. E. Ilse, B. Merle, H. Giessen, and A. M. Herkommer, “Fabrication and characterization of a magnetic 3d-printed microactuator,” Advanced Materials Technologies, vol. 9, no. 12, p. 2302196, 2024.

[3] A. Calikoglu, F. Lux, H. Zappe, and Ç. Ataman, “3d nano-printed bistable microlens actuator for reconfigurable micro-optical systems,” Advanced Functional Materials, vol. 34, no. 48, p. 2408867, 2024.

[4] A. Calikoglu, G. González-Cerdas, D. Ilioae, M. Kienzler, F. Lux, Y. Taege, and Ç. Ataman, “Magnetic position sensing for self-calibration and image registration of scanning fiber endoscopes,” Journal of Optical Microsystems, vol. 4, no. 1, p. 014003, 2024.

[5] J. Purtov, A. Verch, P. Rogin, and R. Hensel, “Improved development procedure to enhance the stability of microstructures created by two-photon polymerization,” Microelectronic Engineering, vol. 194, pp. 45–50, 2018.

[6] N. Rohbeck, R. Ramachandramoorthy, D. Casari, P. Schürch, T. E. Edwards, L. Schilinsky, L. Philippe, J. Schwiedrzik, and J. Michler, “Effect of high strain rates and temperature on the micromechanical properties of 3d-printed polymer structures made by two-photon lithography,” Materials & Design, vol. 195, p. 108977, 2020.

ISBN: 978-3-8007-6743-4 @ VDE VERLAG GMBH · Berlin · Offenbach

 DOI: 10.30420/456743046

Magnetoelectric cantilever beam with reduced bending mitigates power nulls in Wireless Power Transfer systems.

Hidelberto Macedo Zamudio, Pascal M. Weber, Tobias Gräf and Ulrike Wallrabe, University of Freiburg, IMTEK – Department of Microsystems Engineering, Laboratory for Microactuators, Georges-Koehler-Allee 102, 79110 Freiburg, Germany.
E-mail address: hidelberto.macedo-zamudio@imtek.uni-freiburg.de, pascal.weber@imtek.uni-freiburg.de, tobias.graef@imtek.uni-freiburg.de and wallrabe@imtek.uni-freiburg.de

Abstract

Poor alignment weakens coupling in inductive wireless power transfer (WPT) systems and may even lead to power nulls within the charging area, reducing positioning freedom and affecting charging. This research presents a novel approach using a smart magnetoelectric fluxguide to actively distribute the magnetic field based on the receiver's position. The fluxguide consists of a 3-layered magnetostrictive/piezoeletric cantilever beam. We optimised its suspension to minimise bending during actuation by choosing a holder material that allows a free-free boundary condition, aiming for a uniform and controllable magnetic field. Experimental results show that our fluxguide is suitable for WPT systems within the Qi standard, operating from 87 kHz to 205 kHz.

1 Introduction

The growing demand for portable electronic devices has intensified the need for highly efficient and reliable energy transmission systems. To address this need, different Wireless Power Transmission (WPT) technologies have been developed [1]. Among them, inductive WPT systems are particularly suitable for short-distance applications, where compact and efficient designs are important. Such WPT systems generally consist of two well-aligned inductive devices: an emitter and a receiver.
However, maintaining a high level of alignment between these two elements is essential for proper operation. For instance, lateral offsets can significantly affect their efficiency and reduce the output voltage, resulting in poor misalignment tolerance and limited position freedom [2].
These issues become more pronounced with a larger transmission area, especially when a row of coils operates as the emitter, leading to spots of null energy (power null) within the charging area [3].
Current methods to improve tolerance to misalignment and reduce the impact of power nulls add complexity to the WPT system, increasing power consumption and costs, ranging from incorporating various supporting components [4] and position-dependent coils [5] to complex control mechanisms [6], and complex coil topologies [7,8].
This research presents a new approach by incorporating a smart magnetoelectric (ME) fluxguide into the WPT system to improve misalignment tolerance and cancel power nulls without modifying the system. By adjusting the magnetic permeability of our fluxguide through applied strain, we can effectively guide and distribute the magnetic field.

2 Power nulls phenomena

To illustrate the impact of misalignment in WPT systems, we simulated the system seen in **Figure 1**, consisting of two emitting coils (L_1 & L_2) and one receiving coil (L_3), each made of 18 windings, a height h_c of 4 mm, and an inner radius R_{in} of 5 mm. L_1 and L_2 are connected in series, with 1 V applied at an operating frequency of 200 kHz, thus keeping the same current $I_{1,2}$ through both coils. L_3 is at a distance $D_{receiver}$ from L_1 and L_2, a gap $D_{emitters}$ of 30 mm separates the center of L_1 and L_2. No parasitic resistance or capacitance was considered for the coils.

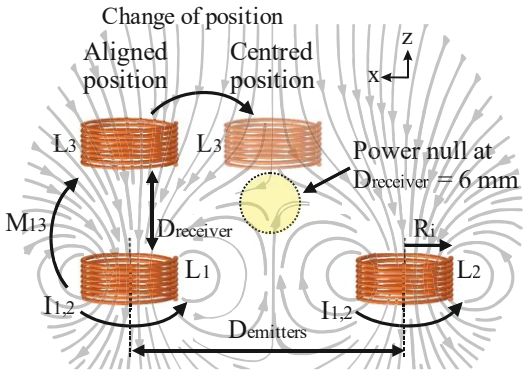


Figure 1 WPT system showing a power null at $D_{receiver}$ = 6 mm when centred.

The resulting magnetic flux is shown by gray arrows. The coupling factor k and the mutual inductance M_{31}, taking into account the self-inductances L_{11} and L_{33} from L_1 and L_3, are described as follows:

$$M_{31} = \frac{N\Phi_{31}}{I_{in}} \quad (1)$$

$$k = \frac{M_{31}}{\sqrt{L_{11}L_{33}}} \quad (2)$$

where Φ_{31} is the change in magnetic flux captured by L_3 coming from L_1 or L_2 due to $I_{1,2}$, according to Ampere's law. k is affected by L_3's position relative to the emitters. Φ_{31} and M_{31} change as L_3 shifts horizontally and vertically above L_1 and L_2. When L_3 aligns co-axially with L_1 or L_2, many magnetic flux lines pass through L_3, resulting in a strong k and high M_{31} as per **Equations (1)**, and **(2)**. At this point, misalignment is 0%, referred to as the “aligned position," as shown in **Figure 1**. When L_3 is horizontally centred between L_1 and L_2 and vertically at $D_{receiver}$ = 6 mm, i.e.in the yellow spot of **Figure 1,** most magnetic field lines

ISBN: 978-3-8007-6743-4 @ VDE VERLAG GMBH · Berlin · Offenbach

 DOI: 10.30420/456743046

bypass the coil, as they align parallel to the receiver. This leads to a very low M_{31} and weak k, in fact representing a pronounced power null, referred as "centred position". The misalignment is calculated as follows:

$$\text{Misaligment}(\%) = \frac{d}{R_i \cdot 2} \times 100 \quad (3)$$

where d is the horizontal displacement of L_3, which equals $D_{emitters}/2$ at the centered position. With a $D_{emitters}$ of 30 mm, the centered position reaches a 150% of lateral misalignment. Next, we simulated the horizontal misalignment in the WPT system by shifting L_3 by 110% left and right from the center while keeping $D_{receiver}$ at 6 mm. **Equations (1)** and **(2)** were used to calculate k, which was then normalized, as shown in **Figure 2**.

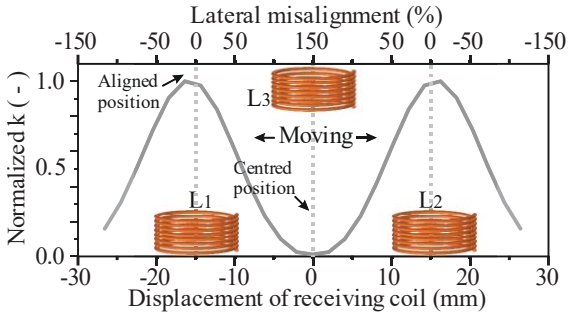


Figure 2 Simulated k while shifting L_3 26 mm to the left and right from the centered position at $D_{receiver}$ = 6 mm.

The maxima in the aligned positions and the power null in the centre are clearly visible. The shown situation is the worst-case scenario for wireless charging. At other vertical positions of L_3, some magnetic flux lines pass through the coil, enabling at least low coupling and resulting in non-zero mutual inductance. Thus, to demonstrate the effectiveness of our approach, we conducted our analysis on purpose at the power null location.

3 Active cantilever beam with reduced bending.

An active guiding and distribution of a magnetic field can enhance misalignment tolerance and avoid power nulls [9]. Our smart magnetoelectric fluxguide follows a strain-controlled approach, also known as magnetoelectric coupling [10], in which the permeability of our fluxguide can be tuned according to the receiver location. Thus, we selected the amorphous Fe-Si-B Metglas alloy due to its magnetostrictive properties (λ = 27 ppm [11]) and high permeability (μ_r = 2500 [12]) to guide the magnetic field. To control and apply the desired strain, we selected PZT M1100 from Johnson Matthey™ due to its high piezoelectric coefficient (d_{31} = -3.15 × 10^{-10} m V^{-1} [13]).

Our fluxguide was designed as a strain-mediated, layered composite, with a unimorph cantilever configuration to hold the Metglas™ layers above the coils while allowing free deformation, as seen in **Figure 3**. It consists of a piezoelectric layer (46 mm × 12 mm × 100 µm) sandwiched between two magnetostrictive layers (40 mm × 10 mm × 30 µm each). The magnetoelectric composite is suspended to two holders of which one is clamped (glued) to the beam, and the other remains loose and just allows for sliding, helping to avoid accidental mechanical contact or shocks during handling or operation. The whole assembly is mounted on a polylactide (PLA) frame.

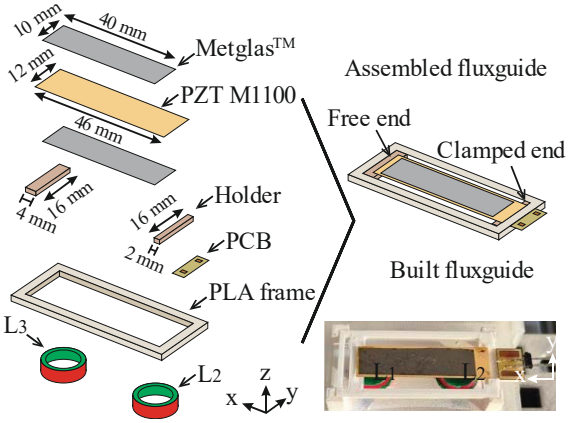


Figure 3 Schematic and picture of the fluxguide, disassembled on the left and assembled on the right, also showing L_1 and L_2.

Despite the symmetric Metglas/PZT/Metglas stack, we observed severe bending during actuation. In unimorph piezoelectric cantilevers with a single passive layer, bending is expected due to the length change of the piezo material during actuation. In contrast, cantilevers with two passive layers only bend if there is asymmetry in their stiffness or geometry [14] which, in practice, is introduced by the clamped suspension affecting the system behaviour. Thus, we optimized our fluxguide design, resp. its suspension, to reduce bending and prevent non-uniformity caused by unwanted shape changes.

According to Euler-Bernoulli theory, the boundary conditions for an ideal cantilever with length L along the x-axis and fixed at one end consist of a fully clamped end (4) and a free end (5), as described below:

$$w|_{x=0} = 0 \quad \& \quad \frac{dw}{dx}|_{x=0} = 0 \quad (4)$$

$$\frac{d^2w}{dx^2}|_{x=L} = 0 \quad \& \quad \frac{d^3w}{dx^3}|_{x=L} = 0 \quad (5)$$

where w is the deflection of the tip. To model this, our holder is represented as an elastic block with height h_e, width w_e, and length j_e as shown in **Figure 4(a)**. The clamped end boundary conditions are described using a lumped spring model with translational K_T and rotational K_R spring constants as shown **Figure 4(b)**. The translational spring resists vertical displacement, while the rotational spring opposes cantilever slope (rotation), as [15]:

$$K_T w(0) = EI\frac{d^3w}{dx^3}|_{x=0} \;\&\; K_R\frac{dw}{dx}|_{x=0} = EI\frac{d^2w}{dx^2}|_{x=0} \quad (6)$$

K_T can be calculated from Hook's law, considering the holder as a uniform elastic rod with a force F applied to its top, keeping it flat and horizontal after deformation. When F is applied in the Z direction, the displacement is expressed as follows:

$$\Delta h_e = \frac{F h_e}{Y_e w_e j_e} \quad (7)$$

ISBN: 978-3-8007-6743-4 @ VDE VERLAG GMBH · Berlin · Offenbach

 DOI: 10.30420/456743046

where Y_e is the Young's modulus of the holder. Then K_T is defined as:

$$K_T = \frac{Y_e w_e j_e}{h_e} \quad (8)$$

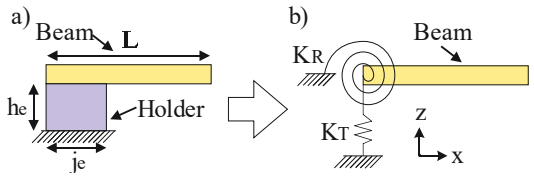


Figure 4 a) schematic of the piezoelectric beam attached to an elastic holder and b) its boundary conditions

K_R can be approximated when it is considered as a torsional spring. According to Hooke's theory, the spring constant can be calculated upon a uniform applied moment M as follows:

$$K_R = \frac{M}{\theta} \quad (9)$$

where θ is the rotational angle. To determine θ, we assumed the holder to behave as a flexible beam attached by the face parallel to the Z axis at the clamped end, with a moment M applied at its free end causing an angular displacement.

$$\theta = \frac{M j_e}{Y_e I_e} \quad (10)$$

being I_e the inertia of the holder. As bending occurs in the Z direction, the rotation is around the Y-axis, then I_e can be defined as follows:

$$I_e = \frac{w_e h_e^3}{12} \quad (11)$$

Finally, K_R can be estimated as:

$$K_R = \frac{Y_e w_e h_e^3}{12 j_e} \quad (12)$$

The boundary conditions change with K_R and K_T. As $K_R \to \infty$ and $K_T \to \infty$, the holder behaves as a perfectly rigid clamped end, and the conditions in (4) apply. As for, $K_R \to 0$ and $K_T \to 0$, the free end boundary conditions (5) apply. For small K_R and K_T (soft materials), the tip displacement increases with load or moment [16]. The piezoelectric layer is attached to the holder with length j_e along a beam section parallel to the X-axis, behaving like an actuator against a spring load, as shown in **Figures 3** and **4(a)**. When coupled to an elastic layer, the effective displacement of the piezoelectric beam Δj_{eff} on the holder is reduced by the joint constraints, as follows [17]:

$$\Delta j_{eff} = \Delta j_e \left(\frac{K_{pzt}}{K_{pzt} + K_e} \right) \quad (13)$$

being Δj_e the nominal displacement of the piezoelectric beam without constraints and K_{pzt} its stiffness. K_e describes the holder's stiffness, representing the combined effect of K_R and K_T in the cantilever system. The upper face of the piezo remains free, i.e., $K_e = 0$, so Δj_{eff} equals Δj_e, which causes shear deformation of the piezoelectric beam and results in an upward bending of the free end.

To show the influence of the holder stiffness, we simulated the cantilever's response during actuation with varying holder Young's modulus Y_e from 1 MPa to 100 GPa. Piezoelectric poling and DC electric field E_{piezo} were along the positive Z-axis. **Figure 5(a)** shows the free-end bending. Holders with low stiffness (Y_e<1GPa) exhibit limited bending, whereas hard holders (Y_e~40GPa) approach the maximum tip deflection.

Therefore, we chose polyurethane (PUR) with an Y_e = 2 MPa [18] for the holder to minimize bending and achieve a uniform magnetic field distribution. Our device is supported by a PLA frame, which may impose additional constraints. To study the mechanical performance of the complete structure, we simulated our cantilever supported by a PUR holder during actuation, as seen in **Figure 5(b)**.

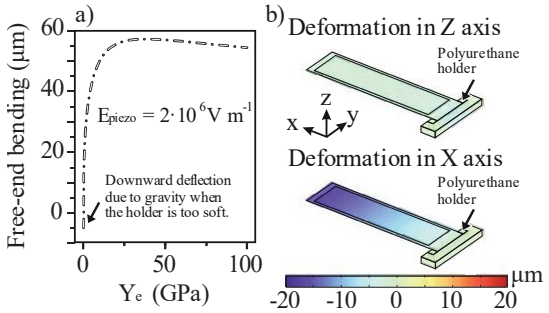


Figure 5 a) Simulation of the beam tip bending sweeping the holder's Y_e. b) Bending simulation with a PUR holder.

The low stiffness of PUR allows near-free deformation of the piezoelectric layer over the holder, reducing Z-axis bending while maintaining large X-axis strain.

4 Experimental verification.

To validate our approach, our fluxguide and an inductive-coupling WPT system were built according to the dimensions and materials specified in the preceding section. The picture in **Figure 3** presents the assembled device, mounted on a polylactide frame over L_1 and L_2. The bending of the fluxguide was measured with an optic profilometer Polytec CL4 under an AC signal E_{piezo} at 2 Hz, as seen in **Figure 6**.

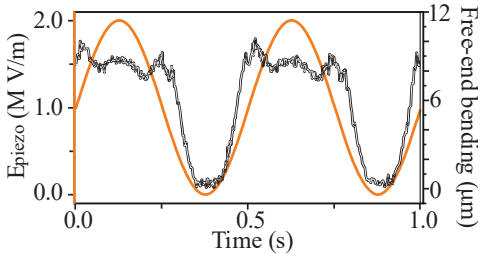


Figure 6 Measurement of beam tip bending.

At maximum polarization, the free end of our cantilever bends up by about 8 µm. To evaluate the effect on the magnetic field distribution, k was measured in the WPT system using a DG8SAQ Vector Network Analyzer from SDR-Kits, both with and without the fluxguide, which was placed 1 mm below L_3, as seen in **Figure 7(a)**. A voltage of 10 V was applied to L_1 and L_2 using a HAMERTM HMF2550 function generator at 200 kHz. L_3 was shifted to the left and right, like in **Figure 2**, with $D_{receiver}$ = 6 mm, to address the power null. The grey line in **Figure 7(b)** shows

ISBN: 978-3-8007-6743-4 @ VDE VERLAG GMBH · Berlin · Offenbach

 DOI: 10.30420/456743046

the normalised k without fluxguide, representing the case of **Figure 2**. The green line shows the obtained k with the passive fluxguide in the WPT system, which smoothens the magnetic field distribution, thus, k increases by about 40% in the centre, but also drops nearly 40% at the aligned position. E_{piezo} was then applied to the fluxguide to switch it to an active state and compensate for k losses at the aligned position, shown by the red line. The strain-induced permeability reduction decreases losses to 20% at alignment, preserving 80% of the coupling without fluxguide. The intersections of red and green lines indicate the switching positions between active and passive states of the fluxguide.

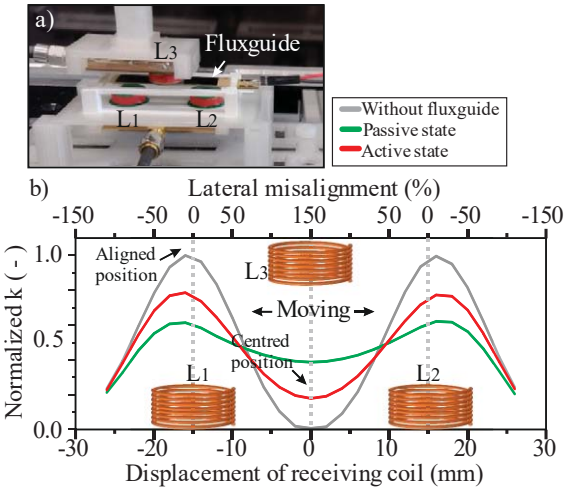


Figure 7 a) picture of the setup with L_3 centred and b) normalized k of the WPT system moving L_3 along the X-axis.

5 Conclusions.

Our fluxguide enhances positioning freedom and ensures coupling in WPT systems facing nulls or misalignment, using Metglas™'s high permeability and magnetoelectric coupling with a piezo-actuator. It is optimised to reduce bending during actuation and suits Qi-standard (f_0 = 87kHz - 205 kHz [19]).

6 Acknowledgements

This research was supported by the European Union's Horizon 2020 research and innovation program under the Marie Skłodowska-Curie grant agreement No 861145.

7 Literature

[1] K. Detka and K. Górecki, "Wireless Power Transfer— A Review", Energies, 15, 2022.

[2] J. Wang , J. Li , S. L. Ho , W. N. Fu , Y. Li , H. Yu , M. Sun., "Lateral and angular misalignments analysis of a new PCB circular spiral resonant wireless charger", IEEE Transactions on Magnetics, 48, 2012.

[3] F. S. Sandoval, S. M. T. Delgado, A. Moazenzadeh, U. Wallrabe, "A 2-D Magnetoinductive wave device for freer wireless power transfer", IEEE Trans. Power Electron., 34, 2019.

[4] J. C. Quirós, E. V. Guerrero, J. K. Sangeno, A. Triviño, "Magnetic Integration of Circular Pads and LCC-LCC for EV wireless charging tolerant to misalignment", IEEE Access, 11, 2023.

[6] T. Lim, Y. Lee, "Stacked-coil technology for compensation of lateral misalignment in nonradiative wireless power transfer systems", IEEE Transactions on Industrial Electronics, 68, 2021.

[5] S. Zhou, C. Chris Mi, "Multi-Paralleled LCC reactive power compensation networks and their tuning method for electric vehicle dynamic wireless charging", IEEE Trans. Ind. Electron., 63, 2016.

[7] C. Rakluea, A. Worapishet, S. Chaimool, Y. Zhao, P. Akkaraekthalin, "True nulls-free magnetoinductive waveguides using alternate coupling polarities for batteryless dynamic wireless power transfer applications", IEEE Trans. Power Electron., 37, 2022.

[8] Y. Li, Y. Feng, Y. Guo, "Triangulated transmitter coils with high design freedom for free-positioning and omnidirectional wireless power transfer system", IEEE Trans. Power Electron., 40, 2025.

[9] H. Macedo-Zamudio, U. Wallrabe, "Tunable Magnetoelectric Fluxguide Cancels Power Nulls in WPT Systems With Highly Misaligned Coils", Energy Technol., 14, 2026.

[10] D. K. Pradhan, S. Kumari, and P. D. Rack, "Magnetoelectric composites: applications, coupling mechanisms, and future directions," Nanomat., 10, 2020.

[11] M. Ali, and R. Watts, "Measurement of saturation magnetostriction using novel strained substrate techniques and the control of the magnetic anisotropy", J. Magn. Magn. Mater., 202, 1999.

[12] M. Price and K. Overshott, "The variation of initial permeability of amorphous ribbons with frequency and annealing conditions," IEEE Transactions on Magnetics, 19, 1983.

[13] HOERBIGER Motion Control GmbH, Data-Sheet-Piezoceramic-Masses-v2000004, https://www.piezoproducts.com, accessed: January 2025.

[14] M. R. A. Nabawy and W. J. Crowther, "Dynamic electromechanical coupling of piezoelectric bending actuators," Micromachines, 7, 2016.

[15] S. Bashmal, W. A. Oke, and Y. Khulief, "Vibration analysis of an elastically restrained microcantilever beam under electrostatic loading using wavelet-based finite element method," Nano-Micro Lett., 10, 2015.

[16] D. V. Bambill, G. I. Guerrero, and D. H. Felix, "Natural vibrations of micro beams with nonrigid supports", Journal of Vibration and Control, 23, 2017.

[17] V. L. Dsouza and M. Rao, "Development of an integrated flexure based inchworm drive for high precision linear positioning", Eng. Res. Express, 7, 2025.

[18] Y. Yanagihara, N. Osaka, S. Iimori, S. Murayama, and H. Saito, "Relationship between modulus and structure of annealed thermoplastic polyurethane," Materials Today Communications, 2, 2015.

[19] Wireless Power Consortium, "Qi Specification", https://www.wirelesspowerconsortium.com, Accessed: April 2023

ISBN: 978-3-8007-6743-4 @ VDE VERLAG GMBH · Berlin · Offenbach

 DOI: 10.30420/456743048

Compact piezo-driven inchworm rotary mechanism with high rotational accuracy for LISA Space mission

Narendra Mahavar[1, 2], Shashwat Kushwaha[1, 2], Dominiek Reynaerts[1, 2]
[1]Department of Mechanical Engineering, KU Leuven, Belgium
[2]Member Flanders Make, Belgium
dominiek.reynaerts@kuleuven.be

Abstract

A precision rotary mechanism is being developed as a part of a beam alignment mechanism for the LISA space mission. It will be integrated with the optical bench of the measurement system. This paper talks about the design and development of a space-qualified compact piezo-driven inchworm rotary mechanism adhering to LISA requirements. The mechanism allows bi-directional full rotation of the shaft with high rotational accuracy. The design makes use of V-grooves along with flexures for deterministic positioning and ensures pure incremental rotation about the axis of the shaft. Piezoelectric actuators integrated with displacement amplification mechanisms are used to actuate the rotary mechanism. Based on the simulation results, the device can rotate a shaft by 22.4 mDeg in a single actuation cycle while maintaining the parasitic translational displacements within ± 0.1 µm.

1 Introduction

LISA (Laser Interferometer Space Antenna) is an ongoing joint-European effort to develop a system capable of detecting low-frequency gravitational waves in space with high precision [1]. The system consists of three spacecrafts arranged in an equilateral triangle form where each arm length is about 2.5 million kilometers. Each spacecraft carries two optical benches housing optical components to detect and measure interference between different pairwise combinations of laser beams, both incoming beams (from the other two spacecraft) and local beams (from the spacecraft itself). This interferometry-based measurement system suffers from tilt-to-length coupling noise (TTL noise) leading to misalignment of laser beam with the telescopic interface. To address this, an optical beam alignment mechanism (BAM) is required to displace the incoming beam (Fig. 1) in any direction orthogonal to its axis within a circle of radius ≤ 225 µm and with a positional accuracy of 0.2 µm [2]. To achieve this functionality, it is proposed [3] to use two tilted optical flats (Fig. 1) which can be independently rotated about the beam axis. This paper focuses on a rotary mechanism to rotate the optical flats and to be integrated with the optical bench of the LISA measurement system. Some of the important functional requirements [2] for LISA-BAM are shown in Table-1.

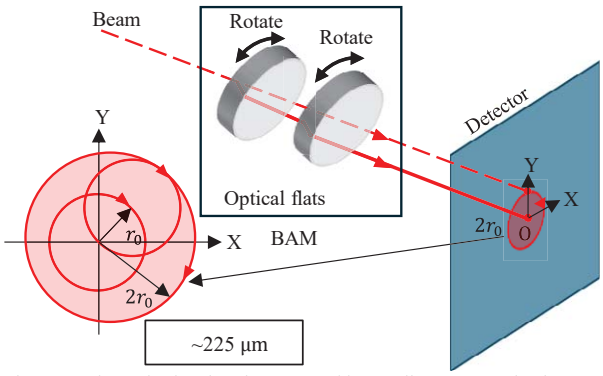


Figure 1 Schematic showing the proposed beam alignment mechanism using optical flats for LISA-BAM.

Materials	Avoid ferromagnetic material and optical sources
Cleanliness	Avoid particle generation
Speed	≥ 0.1 °/s
Parasitic transl. disp.	< ±1 µm
Parasitic angular disp.	< 10 mDeg

Table 1 LISA-BAM functional and material requirements for pre-development [2]

Restrictions on ferromagnetic materials make electrodynamic motors unsuitable for this mechanism. Electrostatic motors, as often employed for micro-electro-mechanical systems (MEMS) where the required forces are in micro- or milli-newtons [4], cannot provide the required force (and torque) at the length scale of LISA-BAM. So they were also opted out for this rotary mechanism. Finally, non-magnetic piezo-driven precision motors can be divided into three categories based on their working principle namely ultrasonic or resonance motors, inertia driven (stick-slip) motors, and inchworm motors. Ultrasonic and stick-slip principle-based motors beat inchworm motors in terms of speed but they generate particles [5]. On the other hand, inchworm principle-based motors produce minimal particles but are relatively slow. Since the desired speed for LISA-BAM mechanism is quite low (rotation speed of 0.1 °/s.), the proposed design is based on inchworm motors.

Maximal parasitic displacements present another challenging design requirement. Generally speaking, there are solutions with and without bearings. Unfortunately, most published bearings-less inchworm rotary mechanism [6,7,8,9] provide little detail about the parasitic radial translations and angular tilts. In the previous work, a prototype of design [6] has been developed and characterized [10]. It was observed that the design does not satisfy the LISA-BAM functional requirements. In most designs [6,7,8,9], the rotor has unknown and multi-point contacts (e.g. due to undefined contacts using a C-clamp concept)

 DOI: 10.30420/456743048

with the stator, which results in poor positioning accuracy of these designs.

For best possible positioning accuracy of the mechanism, the rotor should have three symmetric lines of contact. Therefore, all these designs have identical top and bottom modules separated by a small gap. They are cut out of 1 piece using the wire EDM process. At rest, the shaft is in contact with both modules, resulting into minimum six lines of contact.

Nevertheless, a prototype was developed where each section had three line contacts at 120° apart [10]. This design improved the repeatability of the mechanism but also failed due to two major drawbacks. Firstly, at rest, the rotor has six lines of contacts, leading to non-unique position after each rotation cycle. Secondly, the centre of the rotation did not coincide with the axis of the shaft, leading to parasitic tilts during the handover of the rotor between two modules of the inchworm mechanism.

At this point, there were two ways to proceed: the first is to improve the bearing-less design by ensuring symmetric three lines of contacts with the rotor at rest along with its pure rotation. The second way is to employ bearings in the inchworm rotary mechanism. Unfortunately, most published bearing-based inchworm rotary mechanisms [11,12,13,14] also provide little detail about the parasitic radial translations and angular tilts. Their main motivation for using bearings is to provide radial and axial support to the rotor in their mechanisms rather than leveraging the high precision positioning and rotation capabilities of bearings. Some advantages of the bearing-based design are as follows

- In [13] it is shown that it is possible to employ just two piezo electric actuators for the inchworm rotary mechanism. The fact of using only two piezo actuators is a major advantage as it requires less power electronics on the LISA satellite.
- Furthermore, compared to bearing-less designs, a single plate/module is enough for clamping and rotation, which simplify the design process and manufacturing.
- In addition, the bearings ensure rotation of the shaft about their axis, hence avoiding any parasitic tilts during rotor handover to the walking drive.

On the other hand, one major disadvantage of the bearings is their internal radial and axial clearances, which allows shaft's radial translations and wobble. In general, a pair of preloaded bearings are used to reduce the clearances as per the application.

It was decided to first work on the second solution. A prototype was developed where the rotor was supported by preloaded pair of angular contact ball bearings (7200 BECBP, SKF). Without preload, these bearings have a radial internal clearance in the range 12.6 - 19.3 µm. After characterization of the developed prototype, it was found that due to internal clearances of the bearings, the performance of the mechanism did not fully conform to the requirements for LISA-BAM [15]. The results show the parasitic translation displacement up to ±11.3 µm, and parasitic tilt of the shaft about the Z-axis up to ± 40 mDeg during three full cycles of rotations. The lightly preloaded bearings allow too large shaft displacements and tilts due to remaining internal clearances. On the other hand, higher preload lead to higher friction in the bearing, hence no rotation was observed due to low torque of the developed piezo-driven mechanism.

The measurement results conform to the specifications of the selected low precision bearings. With more expensive, high precision class bearings, it may be improved further, but, to achieve a run-out of less than 1 µm, the bearings need to be highly preloaded. Furthermore, to rotate the assembled shaft with these bearings, the rotary mechanism needs to have sufficiently high torque, which can be achieved with bigger, higher blocking-force piezos. This would eventually lead to a bigger footprint of the BAM mechanism exceeding the volume requirements. Apart from bearings, all other components (e.g., shaft, housing, etc.) need very tight tolerances around ~ 0.5 µm. Overall, it becomes extremely difficult to design the BAM with bearings. To satisfy the smaller footprint requirement for LISA-BAM, we turn to the first solution without bearings. This paper proposes a novel piezo-driven bearing-less inchworm rotary mechanism focusing on high precision rotation requirements for LISA-BAM. The design makes use V-grooves along with flexures for deterministic positioning and ensures pure incremental rotation about the axis of the shaft.

The rest of the paper is divided as follows: Section-2 talks about the design and working operation of the proposed mechanism. Section-3 discusses the simulation results, while section-4 discusses the overall actuation and measurement system including results. The conclusion and future work are discussed in section-5.

2 Design and Method

2.1 Design of the proposed mechanism

Fig. 2(a) shows the schematic of the assembled mechanism which consist of two square modules on top of each other and a rotor in the middle. Three locating holes (S1, S2, S3) are used in both plates for their in-plane alignment. There is a small gap between both modules at the middle, while they contact each other at the shown island faces. These contact faces are polished to ensure parallelism between the two modules.

The schematic of the lock/unlock module is shown in Fig. 2 (b). The stationary V-groove is shown with line contacts at 'C', and 'B', while the third line contact is shown with 'A' on a flexure mechanism, which can be translated horizontally by actuating the gripper piezo. This allows clamping and unclamping of the shaft within the top V-groove. The gripper piezo is integrated within a bridge-type displacement amplification mechanism to amplify the piezo stroke. The displacement amplification allows movement of contact line at 'A' by a sufficiently large amount to account for the tolerances of the shaft and manufacturing process. On the left side of this module, there is a push mechanism to push the shaft horizontally out of the top V-groove during single cycle of actuation (Fig. 3). The pushing head also has a V-groove shown with line contacts at 'D', and 'E'. The mechanism is actuated by the push piezo actuator, which is integrated within a reverse bridge displacement

DOI: 10.30420/456743048

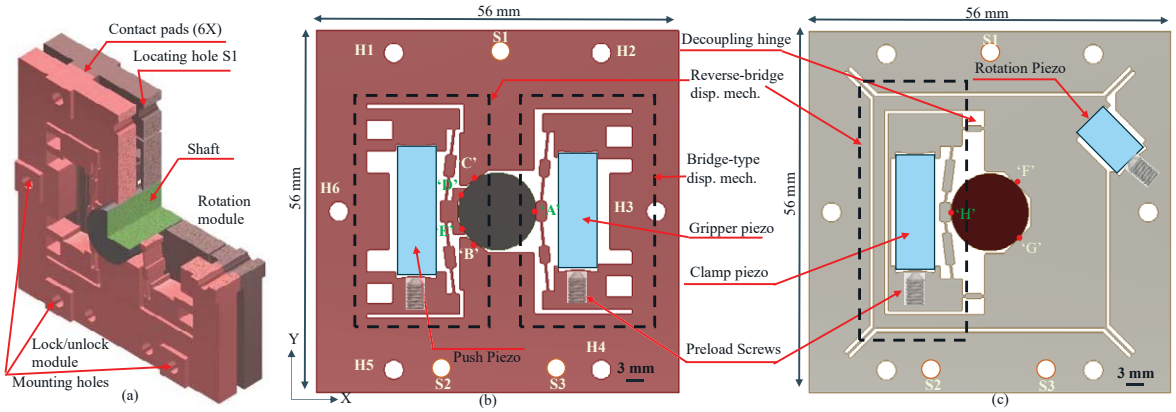


Figure 2 Schematic of (a) assembled mechanism, (b) lock/unlock module, and (c) rotation module.

amplification mechanism. The push head moves horizontally along the positive X-axis when push piezo is actuated. To push the shaft out of the top V- groove, both piezos should be actuated together.

Where the piezos make contact with the mechanism, both faces have a small circular curvature to ensure line contacts with the piezo faces. This reduces the effect of bending moments on the piezo and protects them under heavy compressive loads. For each piezo, the top and bottom sections of the mechanism are symmetric and uses parallelogram flexures to ensure that they displace by same amount when piezo is actuated. This eventually ensures that the push head and gripper head at 'A' moves horizontally and does not apply any tangential load on the shaft. Both the piezos are preloaded with screws at the bottom.

The schematic of the rotation module is shown in Fig. 2 (c). It consist of a clamp and a rotation mechanism. The V-groove is shown with line contacts at 'F', and 'G', while the third line contact is shown with 'H' on a flexure mechanism, which can be translated horizontally by actuating the clamp piezo. This allows clamping and unclamping of the shaft within the rotation module V-groove. The clamp piezo is integrated within a reverse-bridge-type displacement amplification mechanism to amplify the piezo stroke for the same reason as explained above for the lock/unlock module. In addition, the clamped shaft can be rotated by actuating the rotation piezo. The middle square section of the mechanism, which holds the shaft, is connected to the outer section through four symmetric leaf springs, whose neutral lines intersect through the center of the shaft. Furthermore, rotation piezo is oriented such that it applies tangential load on the springs to ensure pure incremental rotation about the axis of the shaft. Both the piezos are preloaded with screws as shown in the Fig. 2(c).

It can be seen that the design of the reverse-bridge displacement amplification mechanism in the rotation module is quite different from the one in the lock/unlock module. The former has no parallelogram flexure due to space constraints on the left hand side. To close the force loop around the piezo, the top and bottom section are directly connected with a slender beam at the left hand side. Furthermore, decoupling hinges are added to the right side of the top and bottom sections, which serves two purposes. Firstly, they ensure that the top and bottom section moves equally with the help of slender beam without over constraining them.

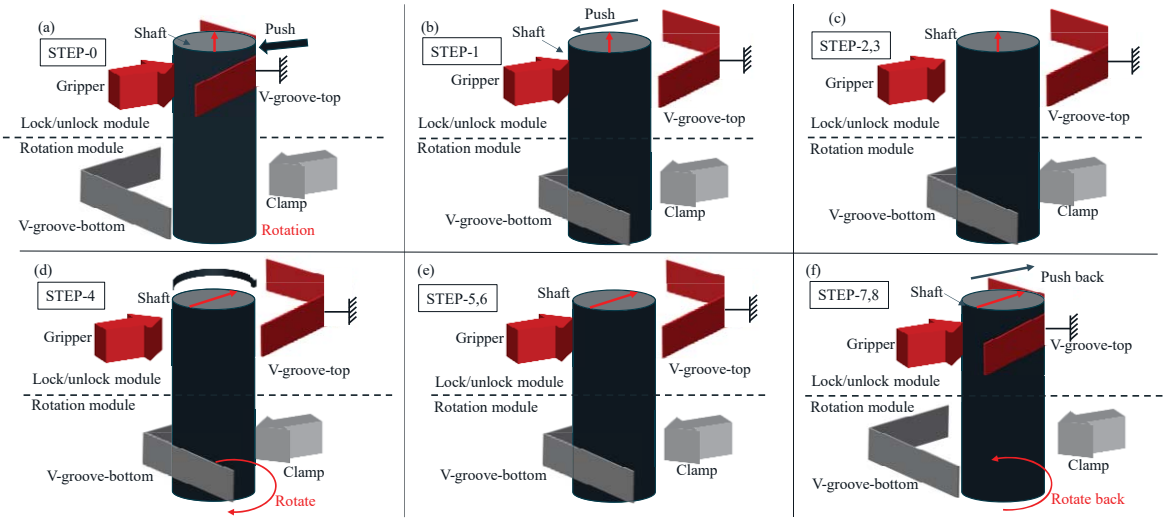


Figure 3 Schematic showing the single cycle of rotation (a) The shaft is locked in lock/unlock module at rest, (b) Shaft is pushed out of top V-groove to bottom V-groove, (c) Shaft is released from the lock/unlock module and clamped by the rotation module, (d) Shaft is rotated, (e) The rotated shaft is clamped by the lock/unlock module and released from the rotation module, (f) The rotated shaft is pushed back inside the top V-groove and locked, rotation module returns to original orientation.

ISBN: 978-3-8007-6743-4

@ VDE VERLAG GMBH · Berlin · Offenbach

DOI: 10.30420/456743048

	Lock/Unlock	Push	Clamp/unclamp	Rotation
Piezo	AE0505D18H18	AE0505D16DF	AE0505D18H18	AE0505D18H18
Piezo size (mm^3)	5x5x18	5x5x20	5x5x18	5x5x9
Piezo stiffness (N/µm)	47.2	48.9	47.2	106.3
Mechanism stiffness (N/µm)	18.2	16.9	10.06	0.41
Displacement gain (G)	6.3	5.7	6.2	NA
Max. developed stress (MPa)	82.5	82.7	138	26.3

Table 2 Showing the simulation results and properties of each mechanism module.

Secondly, they fully decouple the clamp and rotation mechanisms.

2.2 Working operation of the proposed rotary inchworm mechanism

Fig-3 (a) shows the schematic of proposed inchworm rotary mechanism at rest, where the shaft is held inside the top V-groove with three line contacts. The push mechanism and the rotation module are not in contact with the shaft at rest. This is to ensure that the shaft has unique orientation with only three lines of contacts after each cycle of rotation.

The inchworm mechanism rotates the shaft by a small incremental angle in a single cycle of rotation. A single cycle of rotation (Fig-3) consists of nine steps, which are described as follows.

- Step-0: At the start, all piezo are off and the shaft is at rest with a mechanical lock (Fig. 3(a): clamped by the three contact lines at 120° apart).
- Step-1: Push piezo is turned on to push the shaft out of the top V-groove to the bottom V-groove (Fig. 3(b)).
- Step-2: Clamp piezo is turned on to clamp the shaft in the bottom V-groove.
- Step-3: Push-piezo is turned off and gripper piezo is turned on to completely release the shaft from lock/unlock module (Fig. 3(c)).
- Step-4: Rotation piezo is turned on to rotate the shaft by a small incremental angle (Fig. 3(d)).
- Step-5: Push piezo is turned on and gripper piezo is turned off to clamp the rotated shaft.
- Step-6: Clamp piezo is turned off to release the shaft from the rotation module (Fig. 3(e)).
- Step-7: Push piezo is turned off to push the shaft back in the top V-groove (Fig. 3(f)).
- Step-8: Rotation piezo is turned off to get back to the original orientation.

For the next cycle, this becomes the initial state and the cycle repeats to achieve large angle of rotation. It can also be noted that these steps can be reversed to rotate the shaft in the other direction, which allows this mechanism to be used for clockwise and anticlockwise rotations of the shaft.

3 Simulation results

Finite element static structural simulations were performed in Ansys Mechanical, 2023. Tetrahedral meshing was used with an element size of 0.1 mm for critical components such as the hinges, leaf springs, and faces with the contact lines. The six holes at the corners were defined as fixed constraints. A frictional contact ($\mu = 0.1$) was defined between the shaft and the contact faces of the mechanism. Tokin multi-stack piezo actuators with a blocking force of 850 N are used in this prototype whose properties are mentioned in Table-2. To actuate each mechanism in simulation, equal and opposite forces are applied at the faces where piezo makes contacts. These forces are applied along the normal vector to these faces, while their magnitude is decided by the required piezo stroke for each mechanism. The stiffness of the mechanism reflected along the piezo length, the developed maximum von Mises stress, and displacement amplification gains are shown in the Table-2. The developed stresses are well below the yield strength of Titanium (900 MPa). All displacement gains are sufficiently high to account for tolerances of components and manufacturing process. The displacement gain for each mechanism and the results are discussed below.

Gripper mechanism (lock/unlock module)

Fig. 4(a) shows the deformation profile of the gripper mechanism when gripper piezo is actuated. This results into movement of contact line 'A' away from the shaft. The displacement gain (G) of this mechanism is defined as the ratio of 'displacement of point 'A' along the X-axis and the piezo stroke'.

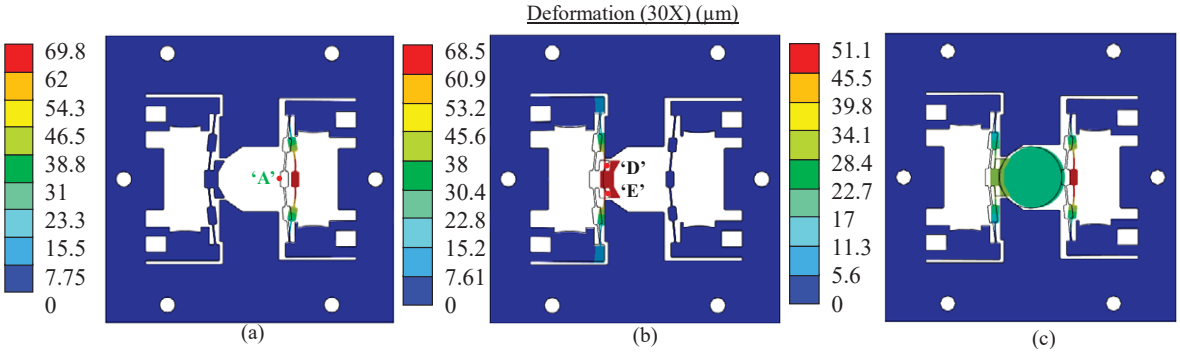


Figure 4 Plot showing deformations after (a) gripper-piezo actuation, (b) push piezo actuation, and (c) shaft coming out of top V-groove after push and gripper piezo actuation.

 DOI: 10.30420/456743048

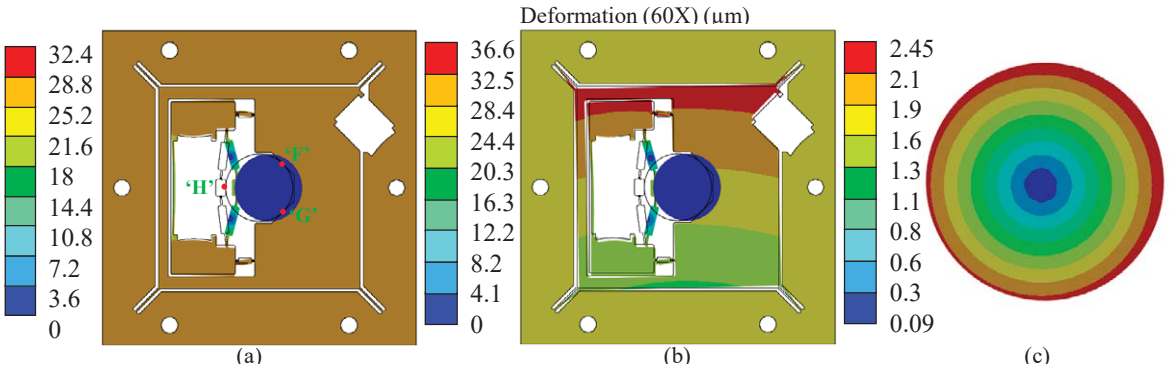


Figure 5 Plot showing deformations after (a) the shaft is moved inside the bottom V-groove and clamped, (b) rotation piezo is actuated to rotate the clamped shaft, (c) deformation of the shaft after the rotation.

Push mechanism (lock/unlock module)

Fig. 4(b) shows the deformation profile of the push mechanism when push piezo is actuated. This results into movement of contact lines 'D' and 'E' towards the shaft. The displacement gain (G) of this mechanism is defined as the ratio of 'displacement of point 'D' or 'E' along the positive X-axis and the piezo stroke'. Fig. 5 (c) shows the displacement of the shaft out of the top V-groove when both gripper and push piezos are actuated.

Clamp mechanism (rotation module)

Fig. 5(a) shows the deformation profile of the clamp mechanism when clamp piezo is actuated. This results into movement of contact line 'H' towards the shaft to clamp it inside the bottom V-groove. The displacement gain (G) of this mechanism is defined as the ratio of 'displacement of point 'H' along the X-axis and the piezo stroke'.

Rotation mechanism (rotation module)

Fig. 5(b) shows the deformation profile of the rotation module when the rotation piezo is actuated, while Fig. 5(c) shows the deformation profile of the shaft after the rotation. The rotation piezo was actuated by 8.5 µm, which results in an average rotation of 22.4 mdeg/cycle. During rotation, the simulated parasitic center displacement of shaft was found to be less than 0.1 µm. To satisfy the minimum rotation speed requirement for LISA-BAM, the mechanism should do at least 5 rotation cycles in a second which should not be a problem.

Contact force simulations

The developed prototype uses stainless-steel shaft of 12 mm diameter and 20 mm length as the rotor of the mechanism. The aim of this prototype development is to verify the functional requirements for the mechanism, rather than satisfying all space environment related constraints. The prototype will be assembled and characterized under gravity. Hence, it is necessary to hold the shaft in place under gravitational force.

The weight (F_g) of the shaft is 0.18 N. At each step, the shaft is clamped by at least three radial line contacts. To hold the shaft in place without slipping, the total frictional force must be more than the gravitational force.

$$F_f = \mu F_N \geq F_g$$

Taking $\mu = 0.1$, $F_N \geq 1.8$ N. Furthermore, considering a safety factor of 2, the sum of all the radial normal forces passing through the center of the shaft (F_T) should be ≥ 3.6 N.

A multi-step simulation was performed in Ansys to calculate the contact forces on the shaft while clamped in each step.

- Step-0: At rest, the 12 holes of the BAM are fixed. The shaft is outside of mechanism.
- Step-0.1: Gripper piezo was actuated to move contact line 'A' to the right side. This creates space for shaft insertion.
- Step-0.2: The shaft is moved inside the mechanism along the Z-axis.
- Step-0.3: Gripper piezo is turned off to clamp the shaft.

The rest of the steps (1-8) are exactly the same as described in single cycle of rotation.

At the end of step-0.3, the radial normal reaction forces at 'A', 'B', and 'C' were found to be 3.35 N, 2.9 N and 2.9 N respectively.

At the end of step-1, the radial normal reaction forces at 'A', 'D', and 'E' were found to be 1.9 N, 1 N and 1 N respectively.

At the end of step-3, the radial normal reaction forces at 'H', 'F', and 'G' were found to be 1.7 N, 1.4 N and 1.4 N respectively. These results shows that the mechanism generates enough frictional forces to hold the shaft in place without slipping.

4 Measurement system and results

4.1 Experimental setup and manufacturing

Power amplifiers (PDu150, Piezodrive and 790A01, AVL) were used to actuate the piezos while actuation waveforms were generated using NI data acquisition system (PXI 7851R, National Instruments). A coordinate measurement machine (Werth Video Check HA CMM) with SP25 touch probe (MPE = 1.57 µm) was used to measure the position of the shaft and calculate its incremental angle of rotation. Titanium was chosen for the prototype due to its excellent strength to weight ratio. The prototype was manufactured by wire-EDM of the two modules (rotation module and locking/unlocking module). The contacts between both

 DOI: 10.30420/456743048

modules were lapped to obtain parallelism, while the planar alignment is assured by 3 locating pins.

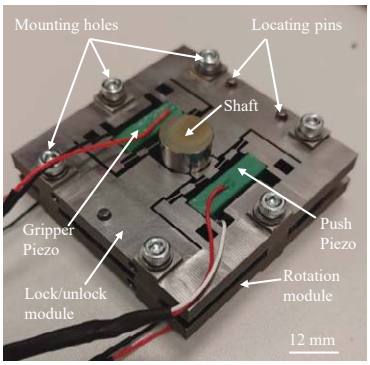


Figure 6 Image of the assembled prototype of the developed inchworm rotary mechanism.

4.2 Results

Fig. 6 shows the image of the assembled prototype with the piezo actuators and two modules of the mechanism mounted on top of each other. The characterization results will be published upon completion of the test program.

5 Conclusion and future work

This paper presents the design and development of a compact piezo-driven inchworm rotary mechanism for LISA table-top beam alignment module. The design uses two parallel square modules separated by a small gap in the middle. Each module has V-grooves with symmetric three line contacts with the shaft in each step of the single cycle of rotation. This improves the repeatability and positioning accuracy of the mechanism which is the main requirement for LISA-BAM. Based on the simulation results, the device can rotate a shaft by 22.4 mDeg in a single actuation cycle while maintaining the parasitic translational displacements of the driven shaft within ± 0.1 µm. To allow testing the device in terrestrial conditions the sum of all the radial normal forces passing through the center of the shaft allow to carry the weight of the shaft.

Future work include characterizing the performance of the developed prototype. Upon successfully achieving the functional requirements for LISA-BAM, the future tasks involves improving the current design in terms of space qualification. Some of those tasks are as follows: Coating the contact faces of the module and/or shaft with ceramic or any other materials to reduce the wear during its operation. Furthermore, large number of rotation cycles to be performed to assess the fatigue or life cycle of the developed mechanism. Finally, integrating the optical flats and characterizing the beam alignment performance in near vacuum environment to assess suitability for the LISA space mission is the end goal.

6 References

[1] K. Danzmann, *"LISA Mission Overview"*, Advances in Space Research Vol. 25, Issue 6, 2000, 1129 – 1136.

[2] LISA-BAM EBB Specifications Requirements (ref. doc. LISA-BAM-TN-00025-RDW, 2023).

[3] LISA OB Mechanism Architecture Trade (ref. doc. LISA-UKOB-INST-TN-009)

[4] I. Morkvenaite-Vilkonciene, V. Bucinskas V, et. al, *Development of Electrostatic Microactuators: 5-Year Progress in Modeling, Design, and Applications.* Micromachines. 2022; 13(8):1256.

[5] K. Spanner, and B. Koc, (2016, February). *Piezoelectric motors, an overview.* In Actuators (Vol. 5, No. 1, p. 6). MDPI.

[6] S. Shao, S. Song, K. Liu, and M. Xu, (2019). A piezo-driven rotary inchworm actuator featured with simple structure and high output torque. *International Journal of Applied Electromagnetics and Mechanics*, 59(1), 317-325.

[7] Li, Jianping, et al. "A piezoelectric-driven rotary actuator by means of inchworm motion." Sensors and Actuators A: Physical 194 (2013): 269-276.

[8] S. Song, S. Shao, M. Xu, Y. Shao, Z. Tian, & B. Feng, (2018). Piezoelectric inchworm rotary actuator with high driving torque and self-locking ability. Sensors and Actuators A: Physical, 282, 174-182.

[9] J. Li, H. Zhao, M. Shao, X. Zhou, H. Huang, & Z. Fan, (2014). *Design and experiment performances of an inchworm type rotary actuator.* Review of Scientific Instruments, *85*(8).

[10] N. Mahavar, S. Kushwaha, J. Menu, M. Houben, and D. Reynaerts, 2024. *Exploring a compact piezo-driven inchworm motor for LISA space mission.* In: European Societies, (Paper No. O6.01), (441-444). Presented at the euspen's 24th International Conference & Exhibition, Dublin, Ireland. Northampton, NN4 8JD, UK. ISBN: 978-1-9989991-5-6.

[11] Jia, Y., Wei, Y., Tang, H., Chen, X., Yang, Z. X., & Tian, Y. (2025). A new inchworm piezoelectric rotary motor with optimized vibration and frictional slipping effects. *Precision Engineering*, *96*, 123-133.

[12] Zhao, H., Fu, L., Ren, L., Huang, H., Fan, Z., Li, J., & Qu, H. (2013). Design and experimental research of a novel inchworm type piezo-driven rotary actuator with the changeable clamping radius. *Review of Scientific Instruments*, *84*(1).

[13] Ma, X., Liu, J., Deng, J., Chang, Q., & Liu, Y. (2023). A simplified inchworm rotary piezoelectric actuator inspired by finger twist: design, modeling, and experimental evaluation. *IEEE Transactions on Industrial Electronics*, *70*(12), 12660-12669.

[14] An, Y., Zhao, J., & Ji, S. (2024). A multipoint regulated inchworm rotary piezoelectric actuator inspired by hula hoop motion. *IEEE Transactions on Industrial Electronics*, *72*(3), 2852-2862.

[15] N. Mahavar, S. Kushwaha, and D. Reynaerts, 2025. *A Compact Piezo-driven Inchworm Rotary Mechanism for LISA Space Mission.* Presented at the Special Interest Conference: Micro/Nano Manufacturing & 6th AET Symposium on ACSM and Digital Manufacturing, Paris-Saclay University, France.

 DOI: 10.30420/456743049

Piezoelectric Transducer for High Intensity Reversible Acoustic Rotational Field Generation

Dalius Mažeika[1], Piotr Vasiljev[2], Andrius Čeponis[1], Regimantas Bareikis[2], Sergejus Borodinas[2]
[1] Vilnius Gediminas Technical University, Saulėtekio al. 11, Vilnius, Lithuania
[2] Vytautas Magnus University, K. Donelaičio str. 58, Kaunas, Lithuania
Dalius.Mazeika@vilniustech.lt

Abstract

Ultrasonic agglomeration uses high-intensity acoustic radiation forces to induce particle collision, providing a non-contact and energy efficient method for particle control in gas and fluid media. Its effectiveness depends on generating stable acoustic fields with strong rotational components to enhance mixing and collision rates. Conventional methods rely on multi-transducer arrays, which introduce challenges such as frequency and phase synchronization as well as field non-uniformity. This work presents a novel single-unit piezoelectric transducer designed to generate a reversible rotational acoustic field for enhanced particle agglomeration. The device combines a conical waveguide with a Langevin-type piezoelectric transducer and utilizes four-phase harmonic excitation with $\pi/2$ phase shift to produce a controllable acoustic vortex, eliminating the need for transducer arrays. Modal and harmonic response analyses were conducted to optimize the design, while acoustic simulations evaluated pressure distribution and vortex formation. The sound pressure level was quantified over a range of voltages and frequencies. A prototype was fabricated and experimentally validated, showing good agreement with simulations and demonstrating effective rotational field generation, particle levitation. The proposed design provides a compact and robust platform for high-efficiency acoustic manipulation and particle-processing applications.

1 Introduction

Ultrasonic agglomeration has gained significant attention as an effective method for controlling fine particles in gaseous and liquid media. By using high-intensity acoustic fields, this technique enhances particle interactions via acoustic radiation forces, orthokinetic effects, and induced fluid motion, thereby increasing collision frequency and particle coalescence. Acoustic radiation forces remain fundamental in describing particle behaviour in sound fields, and ultrasonic excitation can significantly improve agglomeration efficiency, particularly for submicron particles that are otherwise difficult to capture using conventional methods [1–3].

The structure and stability of the acoustic field strongly influence the performance of ultrasonic agglomeration systems. Traditional standing or traveling wave configurations often result in non-uniform particle distributions and limited mixing. To address these limitations, recent research has focused on acoustic vortices and rotational fields, which introduce angular momentum and enhance particle transport and collision probability. Such fields have been shown to improve particle trapping, clustering, and agglomeration efficiency [3-5].

However, generating stable rotational acoustic fields typically requires multi-element phased transducer arrays. While effective, these systems present several challenges, including phase synchronization complexity, sensitivity to fabrication tolerances, and non-uniform acoustic field formation [4]. These drawbacks limit their practical implementation, particularly in compact or industrial systems where robustness and simplicity are critical.

Langevin-type piezoelectric transducers are widely used for high-power ultrasonic applications due to their high efficiency and mechanical reliability. Different type shaped waveguides, such as disc or conical, are used to amplify displacement and improve acoustic energy concentration [4, 6]. Nevertheless, achieving controllable rotational acoustic fields using a single transducer unit remains challenging. Recent advances in excitation strategies suggest that phase-controlled harmonic excitation may enable the generation of asymmetric vibration modes capable of producing rotational acoustic components [4].

In this study, a novel design and excitation principle of a single-unit piezoelectric transducer are proposed to generate reversible rotational acoustic fields for enhanced ultrasonic agglomeration. Numerical and experimental studies were performed to validate the transducer's operating principle and measure dynamic and acoustic characteristics.

2 Design and operating principle

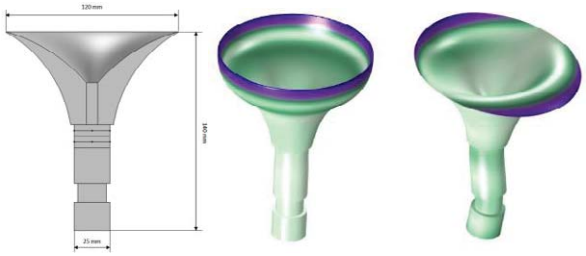
Design of the piezoelectric transducer includes a Langevin-type transducer and a conical-type waveguide (**Figure 1a**). Four thickness-polarized PZT-5H piezoceramic rings are employed to generate the mechanical vibrations of the transducer. The piezoelectric rings are divided into two groups. The first two rings constitute the first group and are used to excite the transducer's first longitudinal vibration mode. The remaining two rings form the second group. The electrodes of the first group are continuous, whereas the electrodes of the second-group rings are divided into four equal segments. The transducer body is manufactured from

 DOI: 10.30420/456743049

structural steel, whereas the conical waveguide is fabricated from Beta 21S titanium alloy. The transducer dimensions are optimized to ensure that the resonant frequency of the 1st longitudinal vibration mode coincides with that of the 2nd bending mode. The transducer is excited using four electrical signals. The electrodes of the piezoelectric rings in the primary group are driven by a single harmonic signal at the resonant frequency, whereas the second group is excited by four harmonic signals with phase shifts of $\pi/2$.

3 Numerical modelling

A numerical investigation of the proposed transducer was conducted to validate its operating principle and evaluate its mechanical, electrical, and acoustic characteristics. A finite element model was built using COMSOL Multiphysics 6.2. Firstly, the modal-frequency analysis was performed to analyze vibration modes and natural frequencies. A closed-circuit electrical boundary condition was applied, while no mechanical clamping constraints were used. The optimization process was carried out iteratively through a parametric sweep of the transducer geometry, including variations in length, diameter, cut-out dimensions, and cut-out position. The objective was to achieve coupling between the longitudinal and bending vibration modes required for rotational acoustic field generation. Following optimization, the natural frequency of the first longitudinal mode was obtained at 18.743 kHz (**Figure 1b**), whereas the second bending mode occurred at 18.694 kHz (**Figure 1c**). The frequency separation between these modes was only 49 Hz, indicating favourable conditions for modal coupling and efficient excitation of the rotational acoustic field.



a) b) c)

Figure 1 Design of the actuator (a); modal shapes of 1st longitudinal mode at frequency of 18.743 kHz (b) and 2nd bending mode at frequency of 18.694 kHz (c)

The admittance and phase–frequency characteristics of the transducer were investigated within the frequency range from 16 kHz to 21 kHz (**Figure 2**). Numerical simulations were performed by exciting the primary group of piezoelectric ring electrodes with a harmonic voltage of 50 $V_{p\text{-}p}$, while the remaining segments of the piezo ceramic ring were assigned open circuit boundary condition. The obtained results indicate that the resonance frequency associated with the bending vibration mode occurred at 18.75 kHz, whereas the longitudinal vibration mode resonance was identified at 18.99 kHz. A slight discrepancy between the natural frequencies obtained from modal analysis and the resonance frequencies observed in the harmonic response analysis was identified. This difference is attributed to the variation in electrical boundary conditions applied in the respective simulations, since modal analysis was conducted under closed-circuit conditions, while the harmonic response analysis employed mixed excitation and open-circuit electrode configurations.

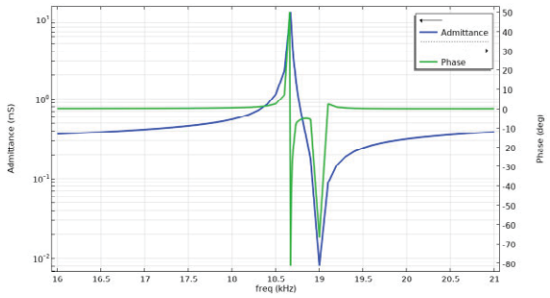
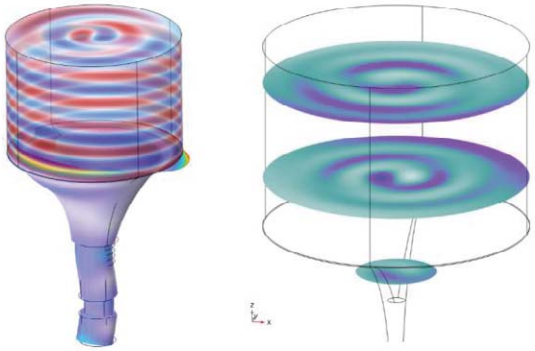


Figure 2 Admittance and phase-frequency characteristics in the frequency domain

Figure 3a illustrates the spatial distribution of the acoustic pressure generated by the proposed transducer. The results demonstrate the formation of a rotational acoustic field characterized by a spiral pressure-wave structure along the axial direction of propagation. Alternating high and low pressure regions can be observed as concentric helical layers, indicating the presence of a stable acoustic vortex generated by the phase-shifted excitation of the piezoelectric elements. Figure 3b presents the simulated acoustic pressure distribution in a transverse cross-sectional plane. The results reveal the formation of a distinct spiral pressure pattern, confirming the generation of a rotational acoustic field with vortex characteristics.



a) b)

Figure 3 Spatial distribution of the rotational acoustic pressure field (a) and cross-sectional distribution of the rotational acoustic pressure field (b)

The acoustic pressure is distributed in the form of concentric rotating wavefronts with a clear azimuthal phase variation around the central axis. Two dominant pressure regions are observed above the radiating surface, indicating the propagation of a stable multi-layer acoustic vortex structure. The pressure maxima and minima form spiral-

DOI: 10.30420/456743049

shaped contours, which are characteristic of acoustic fields carrying angular momentum. The central low-pressure region corresponds to the vortex core, where acoustic radiation forces promote particle confinement and rotational motion.

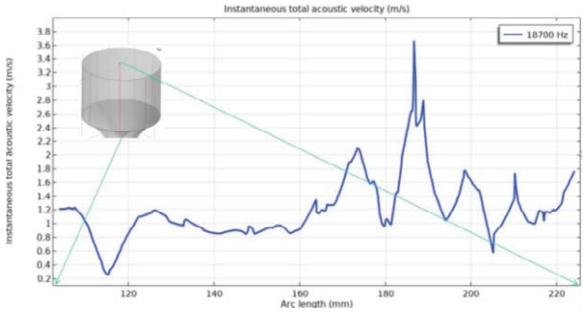
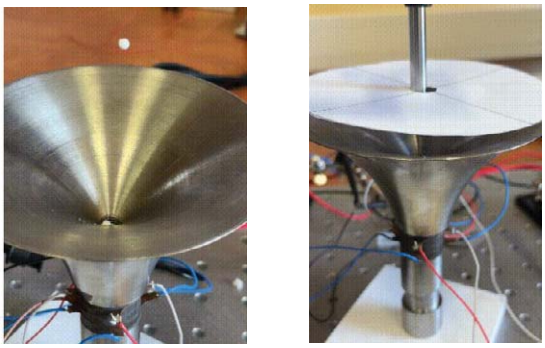


Figure 4 Distribution of the instantaneous total acoustic velocity along the investigated axial path

Distribution of the instantaneous total acoustic velocity along the investigated axial path within the generated acoustic field at an excitation frequency of 18.7 kHz is shown in Figure 4. The evaluated region extends through the central zone of the acoustic vortex above the radiating surface of the transducer. The results indicate a non-uniform velocity distribution characterized by alternating regions of relatively low and high acoustic particle velocity. As the distance from the transducer increases, several localized velocity peaks are observed, indicating the formation of intensified acoustic flow regions associated with constructive interference and vortex-induced energy concentration.

4 Experiments

A prototype of a piezoelectric transducer was made for the experimental study (**Figure 5**). Measurements of electrical, mechanical and acoustic characteristics were performed to validate the operating principle of the actuator and the results of numerical simulation.



a) b)

Figure 5 Prototype transducer: and levitation particle (a), levitating disc (b)

Firstly impedance–frequency characteristics of the transducer were measured to determine the resonant frequencies (**Figure 6**). The measurement results indicate that the resonant frequency corresponding to the 2nd bending mode and the 1st longitudinal mode were obtained at 20.11 kHz and 21.49 kHz, respectively. The discrepancy between the measured and calculated resonant frequency does not exceed 13.5%.

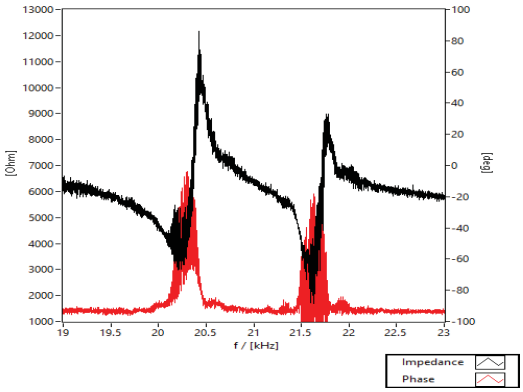


Figure 6 Measured impedance-frequency characteristics

Dependance of open air sound pressure level on excitation voltage was measured at two different excitation frequencies (**Figure 7**). The results demonstrate a monotonic near linear increase in sound pressure level with increasing excitation voltage, varying from 65.1 dB to 131.2 dB at the frequency of 20.1 kHz. An increase up to 25% in sound pressure level can be observed when transducer operated at the 1st longitudinal vibration mode. The sound pressure level rises monotonically with excitation voltage but saturates above 160 $V_{p\text{-}p}$.

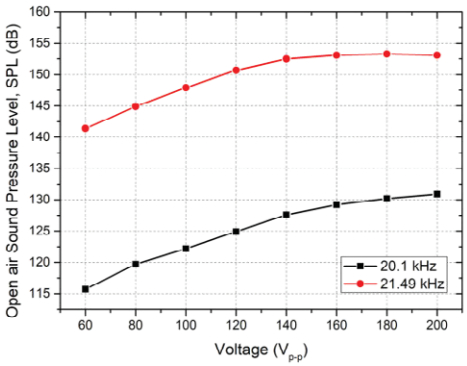


Figure 7 Dependance of open-air sound pressure level on applied voltage

The dependence of the sound pressure level inside the acoustic chamber on the excitation voltage was experimentally investigated at two excitation frequencies (**Figure 8**). The obtained results demonstrate an approximately linear increase in SPL with increasing excitation voltage for both operating frequencies. At an excitation frequency of 20.1 kHz, the SPL increased from 123 dB to 130 dB as the excitation voltage was raised from 100 $V_{p\text{-}p}$ to 200 $V_{p\text{-}p}$. However, a saturation tendency was observed at voltages exceed ing approximately 160 $V_{p\text{-}p}$, indicating a reduction in

 DOI: 10.30420/456743049

the rate of acoustic pressure increase at higher voltage levels. A similar trend was obtained at the excitation frequency of 21.49 kHz. In this case, the measured SPL varied from 140 dB to 149 dB within the same excitation voltage range. The higher SPL values observed at 21.49 kHz indicate more efficient acoustic energy conversion near the longitudinal resonance mode of the transducer. Overall, the results confirm that the generated acoustic pressure increases monotonically with excitation voltage, while nonlinear saturation effects become evident at elevated driving amplitudes.

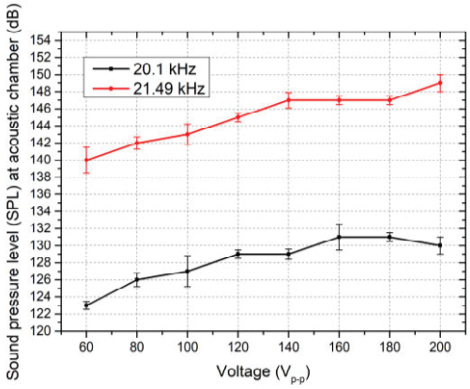


Figure 8 Dependance of sound pressure level at acoustic chamber on applied voltage

The angular motion velocity of the special light weight paper disc as a function of applied load (g) for both clockwise (CW) and counter-clockwise (CCW) rotational directions was measured and is presented in Figure 9. The experiments were conducted at two frequencies of 21.48 kHz and 20.2 kHz when the voltage of 100 V_{p-p} and 200 V_{p-p} was applied, respectively. As the load increases from 0.95 g to 2.41 g, a decreasing trend in angular velocity is observed for both rotational directions. The CW rotation consistently exhibits higher angular motion compared to the CCW rotation across all tested loads. Specifically, the CW motion decreases from approximately 24 RPM at 0.95 g to 15 RPM at 2.41 g, while the CCW motion decreases from 22 RPM to 13 RPM over the same load range. This behavior indicates that the actuator's rotational performance is load-dependent, with a more pronounced reduction observed in the CCW direction. The observed asymmetry between CW and CCW motions suggests potential anisotropy in the actuator structure.

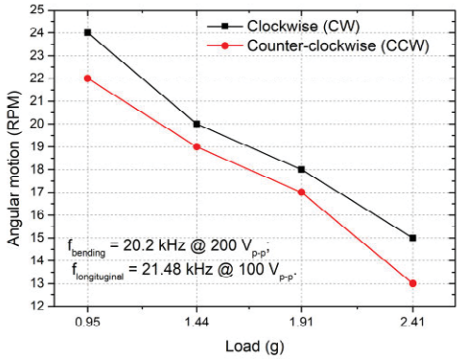


Figure 9 Angular motion characteristics of the transducer under varying load conditions

5 Conclusions

A novel piezoelectric transducer for the generation of reversible rotational acoustic fields was proposed and investigated. Numerical simulations and experimental studies successfully validated the operating principle of the developed actuator. The numerical results confirmed that the superposition and coupling of the longitudinal and bending vibration modes enable the formation of a stable rotational acoustic field characterized by a spiral pressure-wave structure propagating along the axial direction. Experiments showed that the maximum open-air sound pressure level achieved by the transducer reached 153.5 dB at an excitation voltage of 180 V_{p-p}, while the highest sound pressure level measured inside the acoustic chamber was 149 dB at 200 V_{p-p}. In addition, the transducer generated a maximum angular velocity of 24 RPM under a load of 0.95 g, confirming the formation of a controllable rotational acoustic flow. The experimental results showed that both the generated sound pressure level and angular velocity increase approximately linearly with excitation voltage and applied load within the investigated operating range. The obtained results demonstrate that the proposed single-unit transducer provides a compact, efficient, and robust solution for the generation of rotational acoustic fields and has strong potential for ultrasonic agglomeration, acoustic levitation, and particle manipulation applications.

Acknowledgment

This research has received funding from the Research Council of Lithuania (LMTLT) under grant agreement No. S-MIP-25-43.

6 References

[1] Gorkov, L. P. On the forces acting on a small particle in an acoustic field in an ideal fluid. Sov. Phys. Dokl., vol. 6, 1962., pp. 773–775.

[2] Hoffmann T. L., Koopmann G. H. Visualization of acoustic particle agglomeration: theory and experiments. Journal of the Acoustic Society of America, vol. 99, no. 4, 1996, pp. 2130–2141.

[3] Baresch D., Thomas J.-L., Marchiano R. Orbital angular momentum transfer to stably trapped elastic particles in acoustic vortex beams. Physical Review Letters, vol. 116, no. 2, 2016, pp. 2130- 2141.

[4] Wang S, Wang X, You F, Xiao H. Review of Ultrasonic Particle Manipulation Techniques: Applications and Research Advances. Micromachines. 2023; 14(8):1487.

[5] Cosgrove J.A., *et al*. Numerical simulation of particle motion in an ultrasound field using the lattice Boltzmann model. Ultrasonics, vol. 43, iss. 1, 2004, pp. 21-25.

[6] Jung, H.; Shung, K.K.; Lim, H.G. Ultrasonic High-Resolution Imaging and Acoustic Tweezers Using Ultrahigh Frequency Transducer: Integrative Single-Cell Analysis. Sensors, 2023, 23, 1916.

DOI: 10.30420/456743050

Compact piezoelectrically driven inchworm motor with large forces and strokes using advanced control

Ulrich Mescheder[1,4], Sonja Müller[1,3], Jahangir Khosravi[2], Bahman Azarhoushang[2,4],
[1] Institute for Microsystems Technology (iMST), [2]Institute for advanced manufacturing (KSF)
Furtwangen University, 78120 Furtwangen, Robert-Gerwig-Platz 1, Germany
[3] Department of Microsystems Engineering – IMTEK, University of Freiburg, Georges-Köhler-Allee 106,
[4]Associated to the Faculty of Engineering, University of Freiburg, 79110 Freiburg im Breisgau, Germany
Ulrich.mescheder@hs-furtwangen.de

Abstract

A compact and flat piezoelectric inchworm linear motor designed for forces up to 30 N was developed. By monolithic design of the inchworm walker (36 x 18 x 3 mm³) and the matching guide rail the motor consists of only eight parts simplifying assembly and reducing costs. Inchworm walker's clamping on the high-precision guide rail and normally latched operation are achieved by two oval clamps and by alignment of all piezoactuators in direction of movement. The holding forces are defined by the stiffness of the clamps and the allowance between inchworm walker and guide rail. Holding forces of 15-20 N were obtained. Using an advanced control strategy, straightness errors, influences of surface roughness of the contact areas of inchworm and guide rail and differences in the clamping performance of the two clamps can be reduced or even compensated. The control parameters can be derived from measurements of force differences occurring during operation (closed loop capability). The presented performance in respect to compactness, large forces (tens of N), stroke (> 30 mm) and speed (some mm/min) has not yet been demonstrated in the state of the art.

1 Introduction

Piezoelectrically actuated inchworm motors (IWM) provide several mm displacement with nanometer resolution and have large force capability. However, miniaturized, compact and structural simple (no complex assembly) IWM achieving large forces are rare. In a standard IWM two clamping actuators engage the clamps to a guideway and a feed actuator moves the clamp which is in the fee state forward. In a recent review of piezoelectric actuators (PA) including IWM Zhou et al. concluded that a structural simplification comes along with the backlash phenomena [1]. The load capacity was reviewed also showing typical loads of less than 10 N, only one listed was reaching up to 100 N. However, this motor was rather large, particularly 15 mm thick structural elements were utilized [2].
High forces were achieved by Park et al [8] with MEMS ridges to realize a clamping system without backlash problem. Displacement of that motor was small and step resolution was depending on the ridge's pitch (11 µm).
In ridgeless and latch free IWMs, the force which the motor can provide in forward direction is related to friction forces in the engaged state of one clamp. Clamping is provided by flexure guides through specific flexure hinges as lever system which amplifies the small movement of the clamping PA to a mechanically manageable movement of the clamps [3, 4, 5]. The major design challenge is to achieve a proper figure of merit between clamp force and clamp stroke. Li Ma et al. obtained with a flexure hinge design 21 N. The footprint of the motor was some tens of cm² [6].
The stiffness interaction between the frame and the PA is a key parameter for the possible clamping forces and how this interaction affects the positioning accuracy especially when working against an external in-axis load. Galante et al. showed a loading capability of 200 N and a stall force of 40 N, however with a large, particularly thick device (60 x 40 x 20 mm³). They observed backwards slipping which was more pronounced for larger loading forces. They concluded that the maximum load force for the motor is limited by the clamping force, not by the force capability of the pushing stack [7].
A new type of flexure hinges was introduced by Kim and Lee [9]. By using a ring-shaped shell structure with flexure oval structures for clamping and feed and orienting the two clamp PAs and the feed PA all in movement direction, they achieved self-blocking. Due to limitations of machining the flexure oval structures, large PAs were required with a stroke of 38 µm to ensure large friction forces by a large interference of the oval clamps and the guideway, and a complete disengagement of the oval clamps from the guideway when activated. The load was limited to some few N and size was in the order of some tens of cm² with a thickness or around 6 mm.
Oval shaped structures were also used in the IWM presented in [10]. The concept of the according motor was published in [11]. The conceptually proposed motor is rather small (6.6 × 2.6 × 3 mm³), however can provide holding forces of some N only according to the shown low clamp stiffness and the low clamping stroke of the very small PAs used (2 µm free stroke). Additionally, the reported maximal internal stress of around 4 GPa occurring under large load is much higher than the yield strength of the used Ti (880 MPa). No experimental data were shown.

In this paper we will present an IWM using also oval clamps for engagement. However, different to [11] a monolithic and high precision guideway without any adjustment screws was used and the clamp stiffness was scaled for large holding forces of 30 N.

ISBN: 978-3-8007-6743-4

@ VDE VERLAG GMBH · Berlin · Offenbach

DOI: 10.30420/456743050

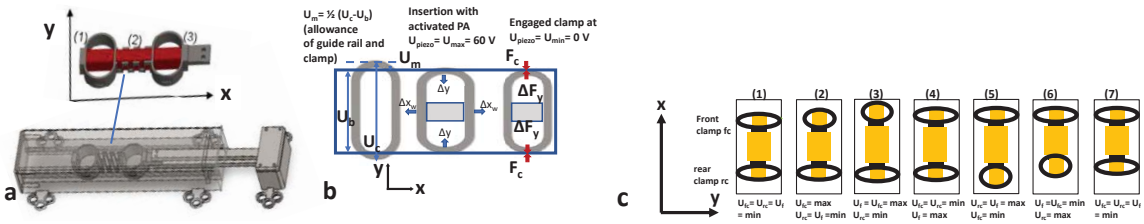


Figure 1: a) IWM with IWW within guideway (PAs not shown). The insert shows the IWW with three PAs (red). b) schematic assembly of IWW into GR with allowance U_m c) schematic driving cycle with engagement and disengagement actions (2), (4), (5) and (7)) of the oval clamps to GR and with push/pull actions (3) and (6).

2 Methods

The design of the inchworm walker (IWW), especially that of the most critical clamps, was derived from simulation using COMSOL Multiphysics. The mechanical stress in the clamps under typical loads and modal frequencies were also investigated with COMSOL. The system behaviour was derived from the obtained properties of the inchworm and the characteristics of the PAs from analytical models for PAs under load and working against a spring-like system [12].

The actuator system was manufactured out of titanium using a water-based wire electrical discharge machining (WEDM) machine (Mitsubishi Electric MP2400 precision series), equipped with an additional rotary spindle (ITS Technologies RSI-55). A 0.2 mm diameter brass wire was used to erode the actuator system. Two sets of WEDM parameters were applied for manufacturing the parts. The general surfaces were eroded using a four-pass WEDM sequence (one main cut and three trim cuts). To ensure high dimensional accuracy and superior surface roughness (expected R_a value of 0.32 µm), a second parameter set was employed, consisting of eight passes (one main cut and seven trim cuts). Multilayer piezostacks (NAC2002-H8 and -H6, cts) were used as PAs.

The actuator system was analysed using FIB-SEM (Carl Zeiss, Crossbeam 550) and 3D laser scanning microscopy (Keyence VK-X3100). Whenever defined constraints (i.e., fixation of a reference point) were in place, the unidirectional deformations and movements of the system were measured contactless with an interferometer (SIOS SP500, resolution of 0.1 nm). However, in some cases the system behaviour had to be derived from measurements of the two ends of IWW. In that case, additionally a triangulation sensor (Keyence LC-2430, resolution of 20 nm) was used. The holding forces of the IWW clamped in the guide rail were measured with spring scales. To investigate the load on the feed unit during operation, a 2 mm PA (stack NAC2001 from cts) was placed in series with the feed PA. Using the direct piezoelectric effect, the charging current due to a load on the feed unit was measured with the femto/picometer B2981A from Keysight.

3 Concept and modelling

The IWW is built up by two oval clamps (1, 3) for clamping and a central feed unit (2) (Fig. 1a). By choice of semi-major and semi-minor axes of the ellipse forming the oval clamps the force amplification and the stroke attenuation factor can be adjusted. A typical design is characterized by a force amplification of around 1.5 and stroke attenuation of 0.6667 (x related to y direction). Due to uniaxial alignment of all three PAs the forces on the PAs are acting in axial direction of movement, reducing shear and pull loads on the PAs.

Shims with precisely defined thicknesses (feeler gauge tapes) are inserted and preload the clamping PAs in the oval shaped clamps. The shims compensate for the length tolerances of the used PAs (typically some 10 µm) and provide a preload of the clamp in x-direction for a fine adjustment of the resulting allowance (Δy).

The IWW fits into a stiff guideway with precise T-shaped profiles at the sidewalls forming a stiff guide rail (GR) for according four recesses in the clamps. An important feature of this layout is self-blocking capability as the two clamping PAs (1) and (3) are orientated perpendicular to the clamping and parallel to the movement direction. The IWW is inserted into the guideway under power due to defined little allowance U_m of the GR compared to the walker's width (Fig. 1b). Maximal U_m is therefore defined by the maximal obtainable clamp stroke in clamping direction (Δy_{max}). For large holding forces both, large stiffness and stroke is needed. As a result, for stiff clamps the stiffness of the PA stacks is typically only 3x larger than the clamp stiffness. Therefore, stroke of the PAs will decrease with clamp stiffness as the clamps introduce a load on the PAs which will change the working points F_w, x_w of the PA (eq. (1a, b)). The resulting contact force F_c is calculated from eq. (2a, b). Here, a maximal allowance U_m equal to the achievable stroke under load is considered and R is the friction coefficient.

$$F_w = \frac{piezo\ \ stroke}{\left(\frac{1}{S_x} + \frac{piezo\ \ stroke}{blocking\ \ force}\right)} \quad (1a), \qquad x_w = \frac{piezo\ \ stroke}{\left(1 + S_x \frac{piezo\ \ stroke}{blocking\ \ force}\right)} \quad (1b)$$

$$F_c = -\Delta F_y = S_y \cdot U_m \quad (2a) \qquad F_h = 2 \cdot F_c \cdot R \quad (2b)$$

The dynamic behavior of an inchworm is described by differential eqn. for a second order spring mass damper system. We propose the model shown in Fig. 2 which is based on [14], but expanded by several elements: The stiffnesses of the PAs are represented by the spring constants k_{rp}, k_{fp} and k_{fup} for the rear and front clamp PAs and the feed PA, respectively. In the two clamping units the clamps are considered as springs parallel to the according clamping PAs with the spring constants k_{fc} and k_{rc}. The same holds for the

ISBN: 978-3-8007-6743-4

@ VDE VERLAG GMBH · Berlin · Offenbach

DOI: 10.30420/456743050

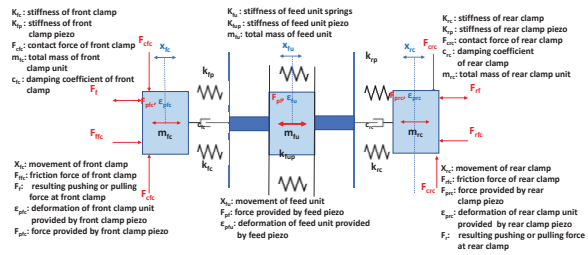


Figure 2: Lump model of the proposed IWM. Input properties are provided in the top row, outputs at the bottom.

feed unit where the feed PA (k_{fup}) is parallel to the feed unit spring (k_{fu}). This spring ensures pull back of the feed unit once the feed actuator power is turned off. Additionally, spring elements within the clamp units might be considered mimicking shim elements which are used to define proper comprehensive force conditions of the PAs within the clamps. Even though modelling is not the scope of this paper, it should be mentioned that the shown model is needed to analyze the system behavior and the results shown in chapt. 4. This model holds only under compression like conditions where the different structural elements are pressed together. Under pull conditions on the clamps, their stiffness is smaller and defined by k_{rc} and k_{fc} only. It is also worth mentioning that the clamping forces slightly differ between pulling and pushing loads: When pushed from both sides, the clamping force will increase as the clamps are loaded similar to "engagement" conditions, whereas under pulling load on both clamp sides, engaged clamps are partially released from the GR, thus reducing the effective clamping force. However, under force by the feed actuator the clamping quality is almost constant as the forces acting on one side of the oval clamp are transferred via the stiff clamping PAs to the other side, thus increasing and decreasing contributions to clamping force by opposite convex/concave deformation of the two sides of an oval clamp are compensating each other.

Two different designs with soft and stiff clamps were simulated, realized and characterized (Table 1). The stiffness depends on several material and geometrical properties such as Youngs Modulus of the used titanium, thickness and height of the walls and lengths in semi-major and semi-minor axes of the ellipse forming the oval clamp. Among the geometrical properties the wall thickness is the most important one. In Fig. 3, the stiffness of the clamps in clamping (y) and movement direction (x) is plotted together with the maximal contact force F_c and the maximal effective clamp stroke (y) derived using equation (1a, b). Due to the opposite dependence of stiffness and stroke, the gain of resulting force by increasing clamp wall thickness is slightly less than the gain of stiffness S_y. The different slope of S_y and S_x shows another interesting feature of the oval clamp design: the stroke attenuation and force amplification are depending on wall thickness: The stroke attenuation factor AF increases with increasing clamp wall thickness (AF→1) which supports the resulting effective clamp stroke and the achieved contact force F_c.

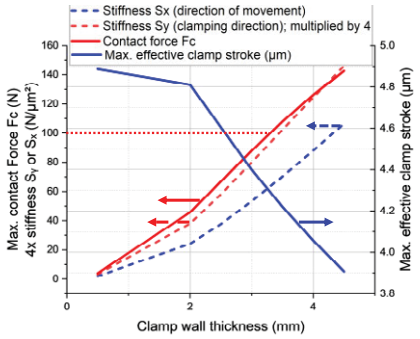


Figure 3: Thickness dependence of clamp stiffness S_y and S_x, of clamp stroke in clamping direction and resulting contact force F_c between clamp and guideway for engaged clamps (eq. (2)). The clamp stiffness values are multiplied by a factor 4 to plot those on the left axis scale. The dashed line marks the needed contact force for a holding force of 30 N (friction coefficient 0.3 for Ti on Ti)

As most IWMs our concept provides a coarse step mode with step size typically ranging from 1-5 µm and a fine motion mode with a resolution limited by the feed PA, thus mainly by the stability of the driving electronic supply, i.e., some ten nanometers.

property / clamp design	Wall thickness (mm)	S_y (N/µm)	S_x (N/µm)	Maximal contact force F_c (N)	Inchworm walker size (mm³)
Soft	0.5	0.814	0.467	4	21.94x11.08x3
stiff	3.0	19.99	13.33	107	36.38x18.3x3

***Table 1** Basic properties of the investigated inchworms with two different clamp types (soft and stiff). Stiffness of clamp piezos is 44 N/µm.*

4 Results and discussion

The characterization is divided into two parts: first the main two components of the IWM are characterized separately, i.e., the inchworm walker (IWW: two clamps and feed unit) and the guide rail (GR). Finally, the motor function is analyzed, especially the complex movement of the interconnected clamps during a stepping cycle.

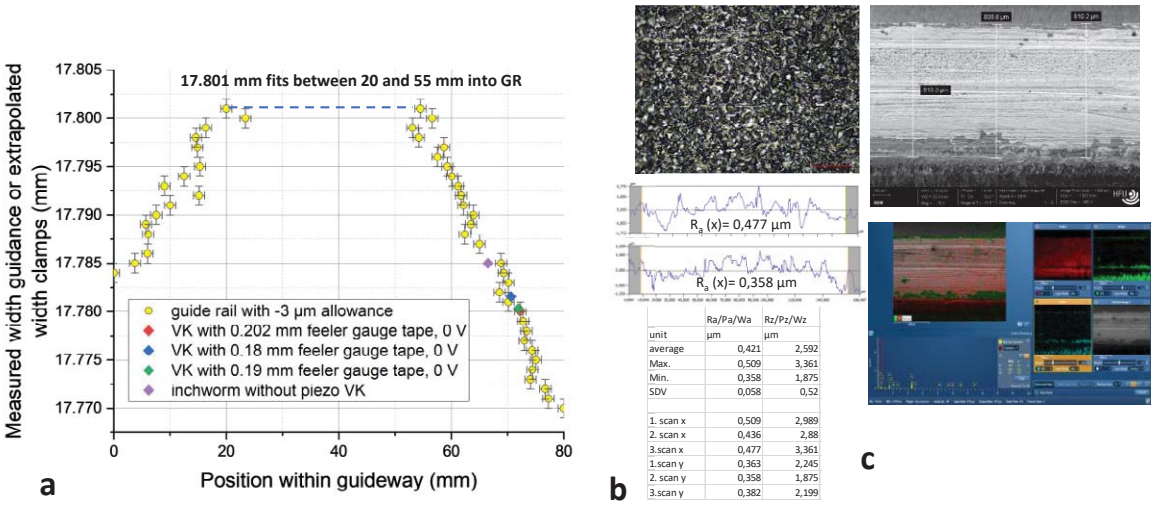
4.1 Characterization of IWW and GR

Due to the little available stroke of small PAs (some µm), the motor function relies critically on the achieved precision of the GR width in relation to clamp width, i.e., on an exact control of allowance over the complete length of the guideway. The GR width was measured with high-precision end gauges (resolution 1 µm). A typical result is shown in Figure 4a. Whereas the straightness in the central part between 20 mm and 60 mm is within the specification of the used WEDM machine (± 1.0 µm), the width decreases towards both ends. This behaviour may result from a combination of residual stresses released when the guideway is separated from the material block, as well as non-optimally chosen parameters of machining strategies used during the manufacturing process. Considering the length

ISBN: 978-3-8007-6743-4

@ VDE VERLAG GMBH · Berlin · Offenbach

DOI: 10.30420/456743050



	Ra/Pa/Wa	Rz/Pz/Wz
unit	µm	µm
average	0,421	2,592
Max.	0,509	3,361
Min.	0,358	1,875
SDV	0,058	0,52
1. scan x	0,509	2,989
2. scan x	0,436	2,88
3.scan x	0,477	3,361
1.scan y	0,363	2,245
2. scan y	0,358	1,875
3.scan y	0,382	2,199

Figure 4: Characterization of straightness of GR and surface roughness. a) Straightness of GR measured with end-gauges (resolution 1 µm), the triangles on the right slope mark stop positions for the characterization of a specific IWW at different applied voltages (compare Fig. 5, insert). b) surface roughness (x and y direction) of clamp contact area: R_a *(av.) = 0.421µm; c) for fine definition of GR width, the GR was coated by ALD with 1 µm thick* Al_2O_3*. FIB-SEM of the GR surface after use and cleaning, EDX provides information about the elements on the GR surface.*

of the guideway (80 mm), an additional finish grinding process may be required to ensure the dimensional accuracy and parallelism of the part.

The surface roughness R_a of the contact area (Fig. 4b) is 0.3-0.5 µm (y and x-direction). The eroded surface shows a clearly discernible grain structure with a lateral surface grain size of 5-10 µm. For test purposes the guideway was coated by atomic layer deposition (ALD) with 1.001 µm Al_2O_3 to check if a fine tuning of the GR width is possible by thin film technology. Fig. 4c shows that the coating's adhesion was poor and did not withstand some movement cycle tests and cleaning procedures. The FIB-SEM and EDX measurement clearly show that the coating was almost completely removed from the contact site and remained only at the guide walls. We also observed a material transfer to the counter surface on the clamps: Al_2O_3 was found preferably in the valleys of the rough surface. We conclude that for standard ALD deposition on titanium the adhesion is too low for used contact force and friction.

The clamp width is determined by two factors: a) CAD and manufacturing precision; b) preload defined by the effective gap within the clamp for the PA stacks and the used shims. High precision shims (feeler gauge tape) are used for slip free and effective stroke transfer from the PAs (length tolerance specified as 200 µm, typically in the range of 10 µm) to the oval clamps, which can be also coated by ALD for exact definition of the proper plate thickness. The preload by the inserted shim will change the stroke of the PA and thus of the according clamp (eq. (1b) and allows additionally a fine alignment of the allowance for a given GR width. The influence of the shim thickness on the clamp stroke in direction of movement provided by the PAs, i.e., Δx_w (eq. 1b), is plotted in Figure 5. The according clamp stroke in y-direction towards the GR and thus the possible clamping force is directly related to the shown stroke Δx_w. The linear slope represents the simulated decrease of clamp stroke due to stiffness relation of clamp (13.33 N/µm) and PA (43.95 N/µm). The measured clamp stroke is first increasing and saturates close to the expected maximum stroke of 6.5 µm for the used PA working against a spring load of 13.33 N/µm, however does not show the expected decrease even for shim thicknesses much larger than the gap. This missing decrease is associated with material creeping and a small plastic deformation of the clamps when inserting shims with increasing thicknesses. This hypothesis was evaluated by determining the absolute clamp width with the so-called stop method with a suitable guideway: the stop position at $U_{f,r} = 0$ V applied to the clamp PA can be used to determine the fabricated clamp width by using the pre-measured GR width and the

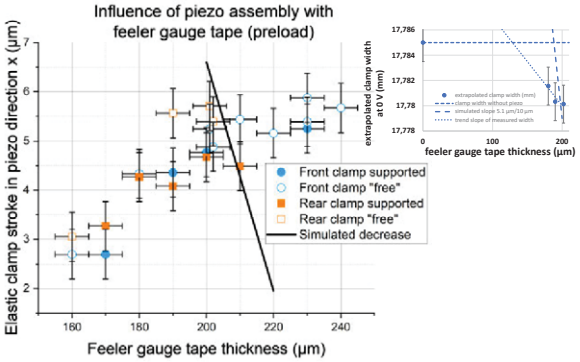


Figure 5: Elastic clamp stroke in direction of movement (x) as function of feeler gauge tape thickness. Due to slightly different length of the used PAs in the clamps, different feeler gauge thicknesses were used for the two clamps. The filled symbols represent measurement with higher reliability (free inch worm needs support when fixed at one clamp). The grey line shows the expected stroke decrease of a preloaded PA. Insert: influence of feeler gauge tape thickness on absolute clamp width derived with the stop method using the guideway shown in Fig. 4 (triangles on the right slope). The data at 0 µm corresponds to a clamp without PA.

ISBN: 978-3-8007-6743-4

@ VDE VERLAG GMBH · Berlin · Offenbach

DOI: 10.30420/456743050

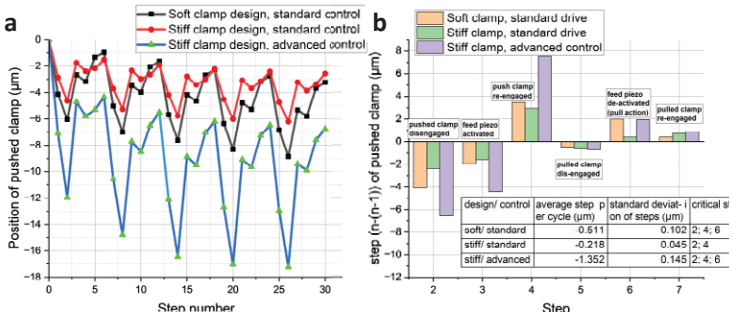


Figure 6: Motor function of two different designs and with two different control schemes. a) Measured position of the pushed clamp over 5 cycles, b) average step (position change) within IWM-cycle for given actions. The table summarizes most important findings.

measured clamp stroke as function of voltage applied to the PA (insert). From the data we can conclude that even at a feeler gauge tape thickness of 180 µm (so well below the expected gap of 200 µm), a preload is introduced in the clamps resulting in a reduction of clamp width in y-direction of around 3 µm. When increasing the feeler gauge tape thickness further, the stroke increases up to a saturation value of about 5.5 µm, whereas the clamp width decreases with a slope of around 0.7 µm/10 µm which is much less than 5.1 µm/10 µm which we calculated for an assumed elastic deformation of clamp and PA when inserting the PA with feeler gauge tape that is thicker than the gap. We assume that a plastic deformation had occurred during insertion of PA and shim as this was done by pressing the clamps together in y-direction to widen them in x-direction. From FEM simulation we expect to reach the Rp_{02} yield strength of Ti at a deformation of 16 µm. We conclude that the insertion has to be done under well controlled pressing to avoid plastic deformation. We developed an according protocol by using end-gauges as stops during assembly and increasing the shim thicknesses for optimization starting with a shim thickness well below the expected gap. However, under PA stroke < 6 µm and external load < 200 N the stress in the clamps will keep below Rp_{02}.

By optimization of the shims' thicknesses in the two clamps a clamp width difference of 1 µm was measured which is within the measurement accuracy.

4.2 Characterization of functional IWM

Figure 6a shows the movement patterns of two different designs (compare Table 1) and two control schemes. In all cases the position was measured at the so-called push clamp which defines the direction of movement (here front clamp). Even though clamp stiffness and size are very different, the movement patterns are very similar and show especially large position changes on the dis- and re-engagement actions (2 and 4) of the pushed clamp. This becomes even clearer when analyzing the average position change (step) within the IWM cycle (Fig. 6b). Obviously, largest position changes are found during these actions. This reciprocating movement during engagement and disengagement of the clamps has considerable influence on the performance of the motor and might be critical in some application, however favorable in others (e.g., callus massage function in distraction osteogenesis). Important features characterizing the movement quality are summarized in the inserted table. Besides actions (2) and (4), also the pull-action (6) has critical influence on the performance, as this corresponds to a backlash movement of the engaged push clamp. The measured data include clamp deformation, slipping and real translation movements as we measure the position at the outer clamp side. Additionally, it is obvious from the model (Fig. 2) that the actions of pushed and pulled clamp are interfering. That is why we also measured the movements of both clamps using sensors positioned on opposite sides. These movements were analyzed and shown in detail in a previous paper [13] where we identified elastic strokes (same amplitude for increasing and decreasing applied voltage) up to 6 µm, slipping movements ranging from 0.18 µm to 0.94 µm (largest value for the so-called passive = engaged clamp by feed action) and very little drift/creeping values between 16 and 36 nm. Most important, the clamping performance of the two clamps can be different and depend on position of the clamps' contact sites which are 22 mm apart in case of stiff design. The difference of clamping performance is mainly caused by slightly different widths of preloaded clamps (Fig. 5 insert) and additionally by limited straightness of the GR (around 1 µm, Fig 4a). In case that the engaged (passive) clamp does not provide large enough contact force (eq. (2)) it responds to the actions of the active ("free") clamp and feed actuations. Therefore, any asymmetry of clamping performance and local variation of guide rail width (including roughness) has influence on the ÍWM performance.

To address this problem, we have developed an advanced control concept. By optimizing the voltage applied to each PA individually (advanced control), it is possible to improve the performance of the motor considerably as shown in Fig. 6. Based on an analysis of the clamping performance of the two clamps separately as function of applied voltage we adjusted the voltage settings (both, min. and max. voltages). With advanced control the step size per cycle increased considerably to 1.352 µm which is however still less than the stroke of the feed PA in free condition as there is some loss during pull action (6). In the opposite direction (rear clamp as pushed clamp) 1.4592 µm step/cycle was obtained showing that the movement of the IWM is much better balanced using advanced control.

Further improvement of IWM's reliability can be achieved by an active control where the control settings are derived from the actual clamping situation of the IWW. For such a control loop an according input is required. For this purpose, we integrated a very small (2 mm long) PA into the feed unit and used that PA to measure the forces acting on the feed unit through the charging current on load change

ISBN: 978-3-8007-6743-4

@ VDE VERLAG GMBH · Berlin · Offenbach

DOI: 10.30420/456743050

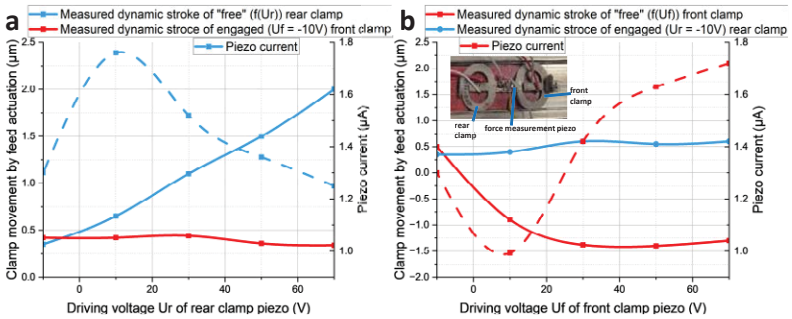


Figure 7: Correlation of clamp movement by feed actuation at different clamping properties and measured charging current peak from sensor PA. Feed potential: 1 Hz, triangular ramping U_{pp}=60 V. a) front clamp engaged, changing lamping condition of rear clamp. b) rear clamp engaged, changing clamping condition of front clamp. The insert shows the measurement set-up.

(direct piezoelectrical effect). We measured these forces as function of clamping performance, which was changed by according clamp voltages applied to the specific clamp and measured by the movement and/or deformation of that clamp. The according correlation is shown in Figure 7. The clamping conditions in Fig. 7a are regular: the engaged front clamp side moves only slightly (most probably a pure clamp deformation) whereas the stroke of rear clamp increases proportional to the voltage at the rear clamp, i.e., this clamp is getting more dis-engaged with increasing U_r. As the force sensing PA measures the net counter force of forces acting on both clamp sides, a maximum current (force) occurs at around U_r = 10 V. In Fig. 7b, an irregular clamping behavior is shown and characterized: For $U_f \geq$ 10 V the "free" (in fact with U_f changing clamping conditions) front clamp moves opposite to the feed actuation ("pulled", indicated by a negative sign) instead of being pushed away whereas the engaged rear clamp is moving slightly in phase with the feed actuator (again most probably this movement is a pure clamp deformation). Here a different current, i.e., force, profile is measured with a minimum at around U_f = 10 V. With increasing U_f, the behavior of the front clamp is getting more regular, however, without reaching a complete in-phase situation. This behavior can be understood by the according characteristics of clamp stroke f(U_f) and the model shown in Fig.2; which is not scope of this paper. We conclude that it is possible to derive the clamping performance from the force depending charging current of the sensing PA and thus to build up a closed control loop with adjusted voltages applied to the clamps. Additionally, the results in Fig. 7 show that an active control on clamping conditions can be achieved by according adjustment of the specific voltages applied to the clamping piezos for disengagement of the clamps.

The obtained clamping forces range for the stiff design typically between 15-20 N and reflect the different clamping performance due to GR's straightness. Wear was investigated on clamps' contact surface by high resolution SEM and confocal microscopy after use. Stripe-like 2 µm deep scratches were found. These scratches are allocated to the contact zone between GR and the according recess in the clamps. Different to the design, the flat part of the recess was around 100 µm smaller than the corresponding GR. We assume that this was caused by the radius of the wire used in WEDM. Therefore, we expect that these scratches occurred due to a contact stripe and can be avoided by a proper areal contact of an adjusted design of the recess.

The total range of travel is limited only by the straightness of the GR, in the fabricated demonstrator to around 40 mm. So far, we worked close to static conditions. However, working at 100 Hz which is well below resonance of all spring elements in the system, a speed of around 1.5 mm/min is expected.

Acknowledgement:

This work was founded by the BMBF project PersonaMedB within the CoHMed project, grant number 13FH5I06IA. FIBSEM device is funded by the DFG within the program Major Research Instrumentation (Project number: 505067193) under GG91b and by the state Baden-Wuerttemberg as well as by Furtwangen University.

5 References

[1] Zhou, X., Front. Mech. Eng. 2024, 19(1): 6, https://doi.org/10.1007/s11465-023-0772-0].
[2] Tahmasebipour M, Sangchap M, Smart Materials and Structures, 2020, 29(1): 015034
[3] U. Mescheder et al., Proceedings Actuators 98, Intern. Conf., Bremen, Juni 1998, p. 327-331
[4] Hassanpour PA, et al., Proc SPIE Int Soc Optic Eng 6463, (2007). doi:10.1117/12.701202
[5] Ye G, et al., Robot 33(2):251–256, (2011). doi:10.3724/SP.J.1218.2011.
[6] Li Ma et al, J Micro-Bio Robot (2014) 9:11–21, DOI 10.1007/s12213-014-0075-y
[7] T. Galante et al., Journal of intelligent Material systems and structures, Volume 10 iss.12, (1999), https://doi.org/10.1106/21LN-RUYY-35CH-C1FD
[8] J. Park et al., Sensors and Actuators A: Physical, Volume 90, Issue 3, 2001, Pages 191-202, ISSN 0924-4247, doi.org/10.1016/S0924-4247(01)00521-0
[9] J. Kim and J.-Ho Lee, Smart Mater. Struct. 14, 934, 2005, DOI 10.1088/0964-1726/14/5/030
[10] H. Kloub, Piezoelektrischer Inchworm Linearmotor, DE Patent DE102020002199A1, 2020
[11] H. Kloub, ACTUATOR; International Conference and Exhibition on New Actuator Systems and Applications 2021, *Online, 2021, pp. 1-4*
[12] https://usermanual.wiki/Physik-Instrumente/PI-CAT128ER3PiezoelectricActuatorspdf.1667988643, accessed 6.4.2026
[13] S. Müller et al., Proceedings Mikrosystemtechnik-Kongress 2025, 27.-29.10.2025, Duisburg https://doi.org/10.5162/SMSI2023/P48
[14] Sandip, J. et al, Precision Engineering 93 (2025) 481–496]

 DOI: 10.30420/456743051

Design Methodology for Electromechanical Functional Interfaces

Mr, Tom MIGLIACCIO[a], Dr, Thomas HUGUET[a], and Pr, François PIGACHE[a]
[a]Université de Toulouse, Toulouse INP, CNRS, LAPLACE, Toulouse, France

Abstract

This paper presents an algorithmic methodology for the optimal design of multi-actuated and highly coupled systems in the context of electromechanical functional interfaces. The development of the method is based on a 2D articulated and deformable truss. The objective is to redefine the initial truss according to the principle of least action so that it can adopt a set of predefined topologies.

1 Introduction

In materials science or chemistry, a "functional interface" describes the interaction region between two entities where specific properties are exploited to achieve a particular functionality. This generic term "functional interfaces" can easily be extended to electromechanical systems when adopting one or more particular surface topologies, either static or dynamic. These deformations are usually induced to transmit information, to apply or withstand forces, or to adapt the structure of a device to its various uses. Electromechanical functional interfaces thus find applications in various domains, such as haptic interfaces [1], [2] reconfigurable robotic devices [3], automotive and aeronautical sectors [4], biomedical applications [5] and more. The design process of such system is usually requirement-driven, yielding solutions that are either singular (minimally adaptable) or over-actuated, the latter increasing cost and potentially reducing reliability. The introduction of an articulated structures that create mechanical couplings between actuators might reduce the number of actuator needed. To design multi-actuated systems and reach optimal architectures efficiently, a systematic methodology is required. The aim is to develop a rational design approach that minimizes actuator count and energy consumption. This involves solving an inverse problem: determining the electromechanical system from the desired surface deformations. The approach draws inspiration from auxetic structures [6] to exploit multiple mechanical couplings. To the authors' knowledge, mechatronics and electrodynamics literature does not address methods for optimizing multi-actuated system kinematics. Civil engineering, however, has developed articulated and motorized truss structures to reduce weight or increase modularity (e.g., retractable roofs) of buildings, while resisting external forces [7], [8]. The kinematics and actuator minimization of such structures have been studied by [9]. This paper builds on these studies using similar truss-based structures. This paper first introduces the design methodology. It then demonstrates its application through several example surface topologies. Finally, the results are discussed and future research directions are outlined.

2 Mechanical Modelling

The structure under study is 2D truss structures composed of nodes connected by ideal passive pivot joints and two types of segments: deformable segments, whose length varies as L(t)=f(t) and rigid segments, whose length remains constant at L(t)=L_{ref}. The deformable segments can be of two types active or passive the latest following then the Hooke's law. Bending and torsion of segments are neglected; only longitudinal deformation is considered. The upper part of the truss — the upper chord — constitutes the interaction surface: it must conform to the target topologies. It is composed of upper chord nodes (whose positions are imposed to meet surface requirements) and anchored nodes (fixed boundary points). Nodes and segments below the upper chord are therefore referred as auxiliary; they introduce mechanical coupling and must remain below the upper chord at all times without intersecting it. An example of such structure is shown below (**Figure 1**), the example shows a cross-braced truss also called X-truss.

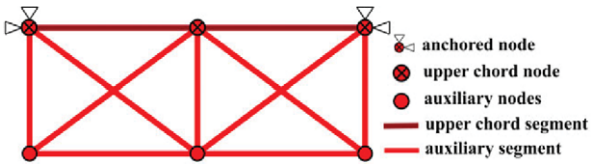


Figure 1 Illustration of a 2D X-shaped truss structures

In order to compute the kinematics of such structures a mechanical model is required. Here he mechanical model is based on Lagrange's equations in generalized coordinates. Masses are lumped at nodes; segments are massless and gravity is neglected. The system is integrated numerically using an implicit Euler scheme, which ensures convergence in the vicinity of the target configurations. The equation of motion in matrix form reads $A(q)\ddot{q} = b(q)$, where A is the generalized mass matrix and b collects generalized forces and potential energy gradients.

 DOI: 10.30420/456743051

3 Methodology

The objective is to find a system able to reach all prescribed target topologies. A brut-force solution to such a problem would assign two actuators per upper chord node, anchored to the ground, each node could therefore reach any position independently from the other nodes. The goal of the methodology is to create mechanical coupling between the upper chord nodes induce by the introduction of a truss architecture. This truss structure will required the fewest possible deformable segments (and hence actuators) while being able to reach all prescribed target topologies. For n_u upper chord nodes the goal is a solution using fewer than $2n_u$ actuators. The methodology proceeds in five stages, summarized in (**Figure 2**).

3.1 Stage 1 - Interaction surface definition

Target topologies are provided as continuous curves. The first stage is to determine the minimal numbers of nodes composing the functional interfaces allowing it to correctly represent the target topologies, according to a given precision criterion. Once the continuous curves have been discretized numerically with high precision. A curve reduction algorithm (adapted from [10]) is used to iteratively removes the least significant point — defined as the apex of the triangle with smallest height among three successive points — until the prescribed precision criterion is violated. The number of upper chord nodes is set by the most demanding topology. A reference configuration is then defined as the unique state in which all upper chord segments are at their reference lengths, i.e. the potential energy of the upper chord is zero. The span condition $\sum_j L_{ref_j} = D$ ensures this uniqueness, with L_{ref_i} being the reference length of the segment i and D being the total span of the system.

3.2 Stage 2 - Configurations definitions

As with the previous stage each required topologies might not required the same number of points to ensure their associated precision criterion Some upper chord nodes are undetermined for some of the required topologies - their positions are only defined for the most demanding topology. A hybrid optimization algorithm have been made in order to places them for all other topologies: First a combinatorial search selects on which upper chord segment each undetermined node is placed; Then a constrained continuous optimization (using fmincon with interior-point algorithm in MATLAB) minimizes the standard deviation of segment lengths across all configurations, so as to reduce energy variation: $min \sum_j \sqrt{\frac{1}{N_c} \sum_i (L_{ij} - L_{mean_j})^2}$ s.t. $L_{min_j} < L_j < L_{max_j}$

3.3 Stage 3 - Initial truss definition

Once all the configurations of the upper chords have been defined, auxiliary nodes and segments are added to ensure mechanical coupling. In this study, a single-layer cross-braced truss was chosen, as shown in (**Figure 1**). Any truss topology (Pratt, Warren, multilayer) could have been selected here. At this stage, all auxiliary segments

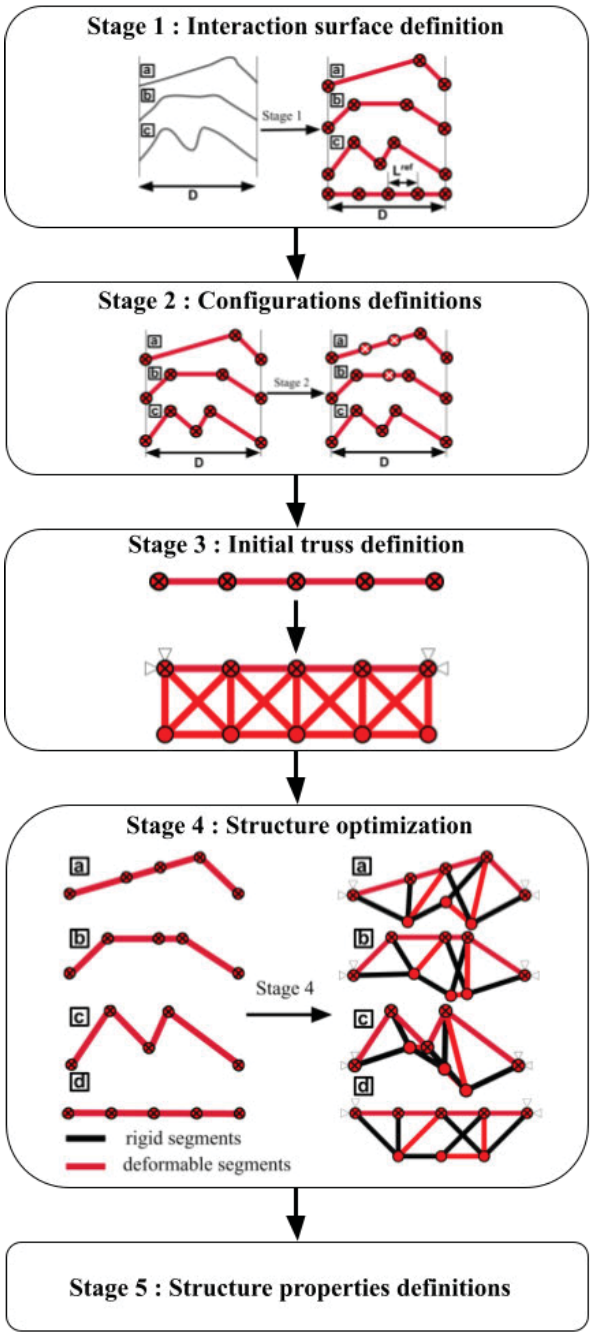


Figure 2 Flowchart of the five-stage design methodology

are deformable and considered passive, in accordance with Hooke's law. The initial truss is defined in its reference configuration, that is, with zero potential energy.

3.4 Stage 4 - Structure optimization

This is the core stage of the methodology. The auxiliary segments are, in an iterative and discrete manner, either stiffened or removed—one segment per iteration—until at least one target topology becomes unreachable. Indeed, stiffening a segment increase the mechanical coupling between the two nodes connected by that segment, while

 DOI: 10.30420/456743051

removing it lightens the structure. These two operations reduce the number of deformable segments and, consequently, the number of active segments. Each iteration can be broken down into four steps:

3.4.1 Step 1 - Auxiliary node placement

For each target topology, the position of all the upper chord is already set by stage 1 and 2 but the positions of auxiliary nodes are still to be defined. Their positions are determined by a continuous optimization procedure using fmincon function on MATLAB with the sequential quadratic programming (SQP) algorithm. The objective function of the problem is to minimize the total elastic energy of the deformable auxiliary segments. This problem is solved by satisfying certain geometric constraints: the auxiliary nodes must be located below the upper chord, and there must be no intersection between the auxiliary segments and the upper chord, as both of these phenomena would alter the shape of the functional interface as perceived by its environment.

3.4.2 Step 2 - Natural trajectory computation

Once all system configurations have been defined—that is, once the position of each node is known for all required topologies—it is necessary to determine a path that allows moving from any configuration to the target configurations. Here, we have chosen to always use the reference configuration as the starting point for reaching any required topology. Using a mechanical model in generalized coordinates, based on Lagrange's equations, it is possible to calculate the position of each node in the system under the influence of various forces. The methodology used here exploits the system's natural path as a trajectory, allowing the system to transition from the reference configuration to the required ones. Indeed, the reference configuration has been defined as the unique configuration for which the system has zero potential energy. If the system is placed in a different configuration, it will find a "natural path" allowing it to reach its reference configuration according to the principle of least action.

By recording the length of all segments at each time step, and assuming that all deformable segments are perfectly controlled active segments, it is possible to reach the target topologies by stepwise imposing the length of all segments in the reverse order of that in which they were recorded. This approach makes it possible to determine a path between the target topology and the reference topology, and vice versa. These paths must be calculated and validated for each of the required topologies. Along these paths, certain node displacements are not permitted, such as those of auxiliary nodes passing through the upper chord and/or auxiliary segments intersecting nodes of the upper chord, due to the mechanical constraints incorporated into the models.

3.4.3 Step 3 - Discrete stiffening/removal decision

In the previous step, the history of the lengths of all segments during each trajectory was recorded. Based on this deformation history, the standard deviation of each segment is calculated; the median value of this criterion is also calculated; the segment with the greatest deviation from the median is selected. If it lies below the median—meaning that, across all trajectories, it has been less deformed than the other segment—it is then stiffened; if it lies above the median—meaning that, across all trajectories, it has been more deformed than the other—it is then removed.

3.4.4 Step 4 - Validation

After every structural change to the system, a check is performed to ensure that all target topologies remain accessible from the reference configuration. Two independent safety lists are maintained: a list of elements that cannot be stiffened and a list of elements that cannot be removed. If a modification renders a topology inaccessible, the last valid structure is restored and the responsible segment is added to the corresponding list—a segment belonging to the list of elements that cannot be stiffened may later be removed, and vice versa. The procedure stops when no further modifications are possible.

3.5 Stage 5 - Structure properties definitions

The final stage distinguishes, among the remaining deformable segments, which are active (linear actuators) and which remains passive. Optimal mechanical properties might then determined by minimizing energy consumption under robustness and stability constraints. This stage has not yet been implemented and constitutes a direct continuation of this work.

4 Results

The methodology is applied to a case study involving three target topologies provided as continuous curves (**Figure 3**, a–c). The most demanding topology (c) requires five constrained nodes, yielding the initial single-layer cross-braced truss shown in Figure 3d.

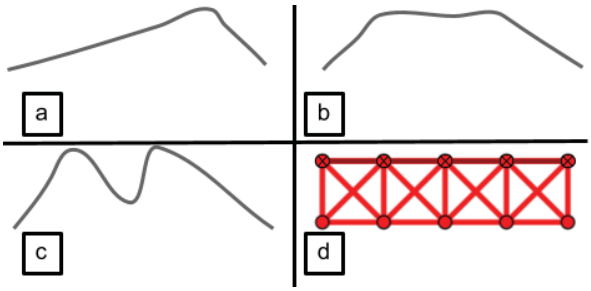


Figure 3 Initial requested topologies (a,b and c) and the initial truss structure (d)

After applying Stages 1 through 4, the final structure is obtained (**Figure 4**). Since Stage 5 has not yet been implemented, all remaining deformable segments act as actuators. The resulting architecture requires 5 actuators to position the three constrained nodes in the 2D plane. For comparison, a brute-force approach would need only 6 ac-

tuators, but such a configuration is not self-supporting — in contrast to the solution obtained here. The solution is a fully actuated upper chord with one auxiliary actuator to allow the structure to move away from its reference configuration. The resulting structure may seem vulnerable to external forces, particularly its own weight when gravity is taken into account. Applying external forces during the generation of trajectories could result in a more robust structure, that is, one with more segments and likely stiffer segments. The non-uniqueness of the solution should be noted: different final architectures can be obtained depending on the objective function, the optimization algorithm, the stiffening/removal criterion, and numerical parameters (time step, stiffnesses, nodal masses). The kinematics of the final structure are accessible via the following URL: https://hal.science/view/index/docid/5616845

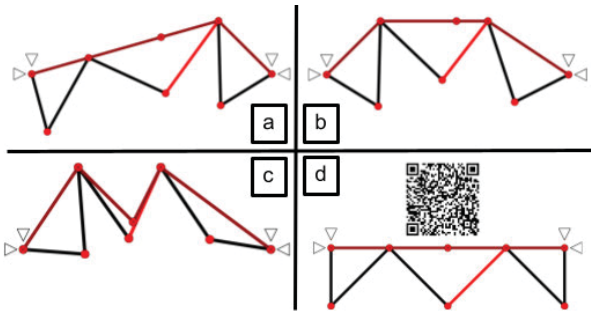


Figure 4 Final truss structure in the different requested configurations (a,b and c) and in the reference configuration (d)

5 Conclusion

A rational design methodology and its associated algorithms have been developed for the optimal design of electromechanical functional interfaces based on articulated 2D trusses. The methodology solves an inverse problem in five stages, guided throughout by energy minimization principles. Stage 4, the core of the approach, relies on discrete, iterative stiffening or removal decisions informed by natural trajectory analysis under the principle of least action. When applied to a case study involving three target topologies, this methodology results in a structure that uses one less actuator than with a “brute-force” approach, but is self-supporting. Key directions for future work include: add external forces that the structure must withstand both during final configurations and trajectories, exploring more complex initial truss topologies (multi-layer, long-range connections, additional auxiliary nodes), enabling pivot joint locking to extend mechanical coupling, defining alternative trajectories via a variational approach, and implementing Stage 5 to fully distinguish actuators from passive springs among the deformable segments.

6 Literature

[1] A. Mazzone, C. Spagno, et A. Kunz, "A haptic feedback device based on an active mesh", Proceedings of the ACM symposium on Virtual reality software and technology, 2003, p. 188 195.

[2] I. Qama, R.Groh, D. Holman, et A.Roudaut. "A Literature Review of Morphing Materials for the Design of Shape-Changing Interfaces", Conference on Human Factors in Computing Systems (CHI 2018). Association for Computing Machinery, New York, NY, USA, Paper 374, p.1–23.

[3] G. J. Hamlin, A. C. Sanderson, "Tetrobot : A Modular Approach to Reconfigurable Parallel Robotics", 1998, isbn 9781461554714.

[4] M. Braza, J.F. Rouchon, G. Tzabiras, F. Auteri, et P. Flaszynski, "Smart Morphing and Sensing for Aeronautical Configurations",Springer International Publishing, vol 153, 2023.,

[5] Z. Qaiser, et al., "Case study of a novel multi-actuated optimized reconfigurable freeform surface (MORFS) mold for custom foot orthoses", International journal of advanced manufacturing technology, 120.5-6, 2022, p. 3831-3842.

[6] J. Ou, Z. Ma, J. Peters, S. Dai, et al., "KinetiX - designing auxetic-inspired deformable material structures", Computers & Graphics, vol 75, pp. 72-81, 2018.

[7] P. Marker, A. Bleicher, "A Hierarchical Optimization Method for the Design of Active Hybrid Structures", Frontiers in Built Environment, 2022.

[8] G. Senatore, P. Duffour, et P. Winslow, "Synthesis of minimum energy adaptive structures", Structural and multidisciplinary optimization, 60.3, 2019, p. 849-877.

[9] R. Sachse. "Variational motion design for adaptive structures", Stuttgart: Institut für Baustatik und Baudynamik, Universität Stuttgart, 2020.

[10] M. Visvalingam et JD. Whyatt, "Line Generalization by Repeated Elimination of the Smallest Area", The Cartographic Journal, vol 30, number 1, 1993

 DOI: 10.30420/456743052

Dual-Mode Electrosurgical Device for Selective Tissue Perforation via Electrically-Induced Bubbles and Discharge

Shigeaki Miura, Yuudai Aokusa, Mayu Nakahigashi, Nobutoshi Ota, Yoko Yamanishi
Dept of Mechanical engineering, Kyushu University, Japan

Abstract

We have developed a method that allows for easy switching between isotropic perforation, which utilizes microjets and shock waves generated by the collapse of electrically-induced bubbles, and anisotropic perforation, which utilizes electrical discharges, all within a single device. By controlling the distance from the target, this device functions as an actuator capable of delivering either mechanical or electrical stimulation. We conducted perforation experiments using pig skin and demonstrated that by controlling the energy applied to the device, we can precisely control bubble size and discharge energy, thereby varying the perforation depth of the target tissue. Furthermore, we have newly demonstrated that switching between the anode and cathode connected to the device allows for switching between incision mode and coagulation mode.

1 Introduction

Electrosurgical devices are indispensable instruments in surgical procedures and have been used in a wide range of surgical techniques. However, since their invention several decades ago, challenges such as the difficulty in controlling the size, depth, and shape of incisions has persisted [1], and no significant progress has been made. On the other hand, laser devices have undergone remarkable development and are currently used in procedures such as cataract surgery [2]. However, the use of lasers still requires considerable caution due to issues such as reflection [3]. Therefore, in this study, we propose a novel method for perforating targets by selectively utilizing two types of phenomena: electrically-induced bubbles and electrical discharge. By controlling the distance between the target and the device, this method enables either (i) isotropic perforation using electrically-induced bubbles, or (ii) anisotropic perforation using localized heating generated by electrical discharge at the device tip.

2 Concept

The new knife we propose, called the “electrically-induced bubble knife,” performs two distinct operations within a single device. The concept is illustrated in Figure 1. The formation of electrically-induced bubbles, triggered by the voltage applied to the bubble knife, causes a rapid increase in local temperature at the device tip due to current flow [4]. The growth and collapse of these bubbles generate microjets and shockwaves, which result in the perforation of the target. Alternatively, grounding the bubble knife to the target prevents bubble formation, enabling direct target perforation via the thermal energy at the tip.

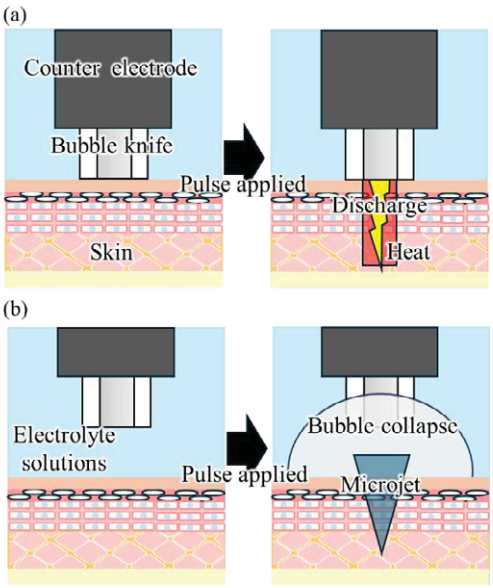


Figure 1 Concept of bubble knife. (a) Perforation using shockwaves and microjets that are generated by the collapse of a bubble. (b) Perforation using electrical discharge.

3 Experimental

The experimental setup is shown in Figure 2. The core-shell bubble knife was fabricated by inserting a tungsten wire into a glass capillary and trimming the tip to ensure a flat end face. A pulsed power supply was connected to the bubble knife. A 0.9% NaCl solution (saline) was used as the aqueous solution.

3.1 Evaluation of Voltage, Current, and Bubbles

A high-speed camera was used to record the behavior of the bubbles from their formation to their collapse, and

ISBN: 978-3-8007-6743-4 @ VDE VERLAG GMBH · Berlin · Offenbach

 DOI: 10.30420/456743052

changes resulting from the applied voltage were investigated. To evaluate bubble behavior, we binarized the differences between the first frame of the video and each subsequent frame. We calculated the volume based on the diameter obtained by treating the projected area as a circle, and used the resulting time-series data. The velocity of the microjet generated after bubble collapse was calculated by averaging the microjet's displacement per frame over 25 frames (1 frame = 1 µs), starting from the point where the bubble volume was minimal. An oscilloscope was used to measure the applied voltage and current when the bubble knife was connected to the anode and when it was connected to the cathode.

3.2 Evaluation of perforation

The distance between the pig skin and the bubble knife was adjusted, and skin perforation experiments were conducted. The depth of perforation was measured using a white-light interferometer, and the size of the holes was measured using a microscope. CT scan images were used to measure the maximum width and depth of the holes. The shape of the holes was evaluated by calculating the aspect ratio.

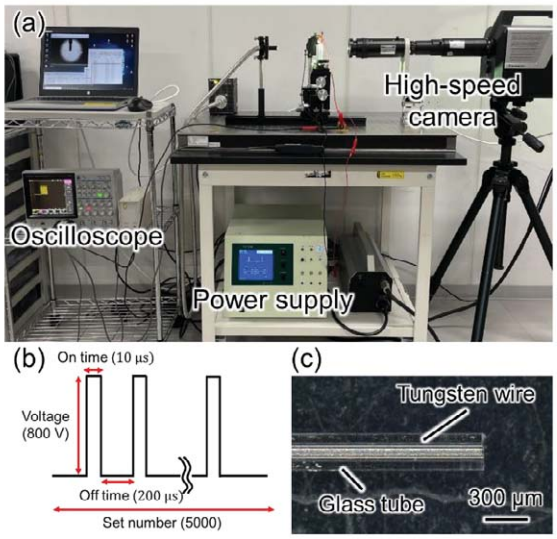


Figure 2 Perforation System. (a)Experimental setup. (b) Power conditions. (c) Image of bubble knife, fabricated by threading tungsten wire (diameter is 100 µm) through glass tube (outer diameter is 300 µm).

4 Results

4.1 Evaluation of Voltage, Current, and Bubbles

Figures 3 and 4 present the experimental results. Figure 3 demonstrates that connecting the bubble knife as the anode suppresses current flow, enabling minimally invasive perforation of the target. Conversely, connecting it as the cathode facilitates current flow, resulting in the coagulation of the target. Figure 4 illustrates the temporal evolution of bubble volume. It was observed that the cathode connection yields a smaller bubble volume and a shorter bubble growth period compared to the anode connection. Furthermore, the data show that increasing the applied energy enlarges the bubble, which correspondingly increases the microjet velocity. The increase in perforation depth with higher applied voltage can potentially be explained by Equation [6]:

$$\Delta P = \rho a \Delta V$$

where a is the speed of sound, ρ is the fluid density, and V is the mean velocity. Since larger bubbles generate faster microjets, the pressure surge upon collapse is amplified. This localized pressure elevation is believed to enable deeper perforation of the target. On the other hand, when electrical discharge is employed, a higher applied voltage enhances current flow, which subsequently amplifies Joule heating and allows for deeper target perforation.

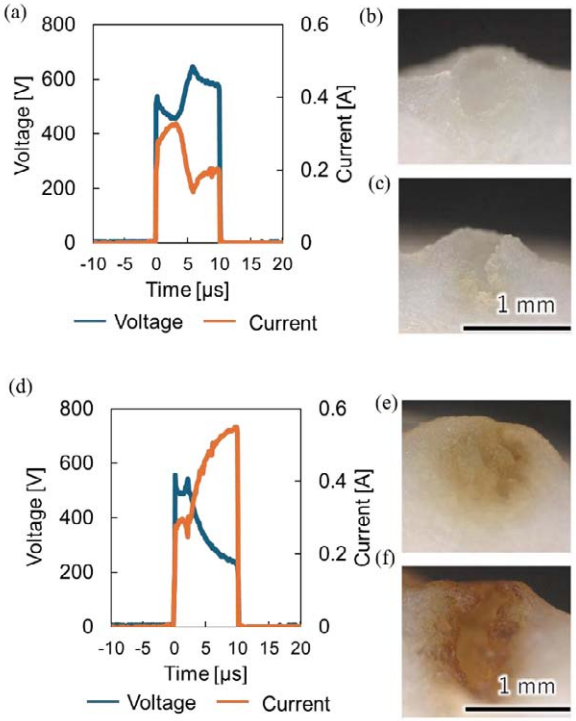


Figure 3 Evaluation of voltage and current characteristics and their effects on perforation, comparing anode and cathode connections of the bubble knife. (a), (d) Voltage and current waveforms for (a) anode and (d) cathode connections. (b), (e) Perforation via bubble collapse (shockwaves and microjets). (c), (f) Perforation via electrical discharge. (n = 3 for each data point.)

4.2 Evaluation of perforation

Figures 5 and 6 present the results of perforation experiments conducted using porcine skin. Figure 5 demonstrates that the use of electrical discharge enables anisotropic perforation of the target, whereas the use of bubbles results in isotropic perforation. Figure 6 shows that when employing electrical discharge, the pore diameter can be kept small even as the perforation depth is varied within the range of approximately 600 µm to 1200 µm. In contrast, when bubbles are used, the pore diameter remains

DOI: 10.30420/456743052

approximately twice as large as that observed with electrical discharge across the same depth range (600–1200 µm). In conclusion, this dual-mode electrosurgical device, the electrically-induced bubble knife, has the potential to contribute to precision surgery in the biomedical field.

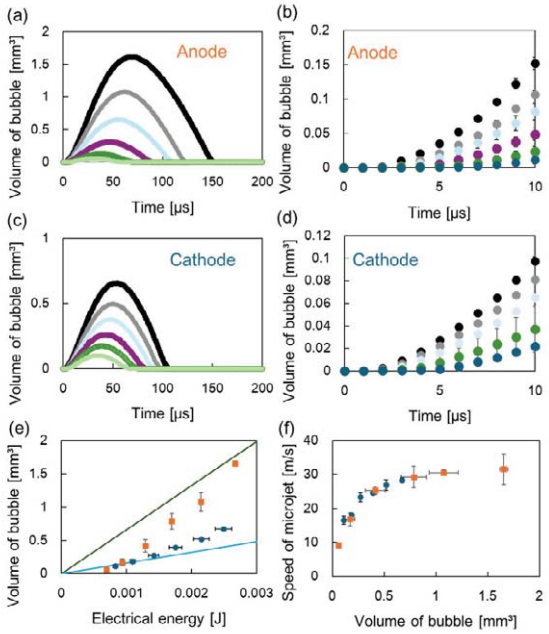


Figure 4 Variation of bubble growth with time and relationship between bubbles and microjets. (a), (c) Variation in the volume of the bubbles generated in the anode and cathode, respectively. (b), (d) Corresponding variation in bubble volume up to 10 µs. (e) Relationship between electrical energy and bubble volume. (f) Relationship between bubble volume and microjet speed. In the above graphs, the orange and blue marks correspond to the contact of the bubble knife to the anode and cathode, respectively; the black, gray, cyan, purple, green, and light-green curves and marks correspond to applied voltages of 1100 V, 1000 V, 900 V, 800 V, 700 V, and 600 V, respectively; the green and cyan curves represent the volume of bubbles generated by water vaporization and decomposition, respectively. (n = 3 for each data point) [5]

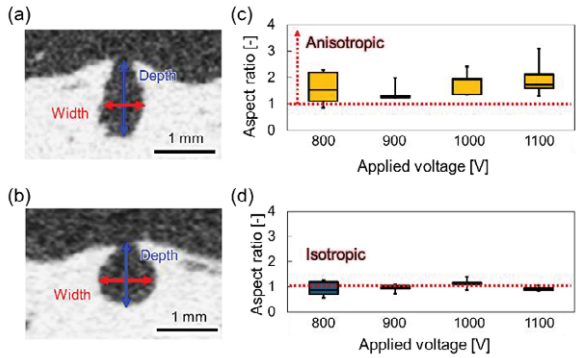


Figure 5 Results of perforation experiments using pig skin. (a, b) Cross-sectional views of the perforated holes captured by CT scan. (c, d) Changes in the aspect ratio as a function of the applied voltage. (n = 10 for each data point.)

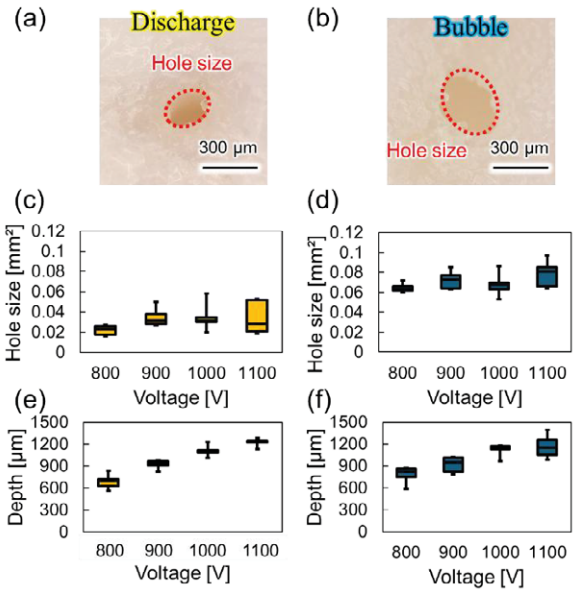


Figure 6 Perforation of pig skin (Bubble knife is connected to anode). (a), (c), (e) The depth and size of holes perforated via electrical discharge. (b), (d), (f) The depth and size of holes perforated via bubble collapse. (n = 10 for each data point.)

5 Literature

[1] Shiver, Austin L., et al. "Bigger Is Not Always Better: Effects of Electrocautery Setting on Tissue Injury in a Porcine Model." *Cureus* 14.7 (2022).

[2] Nagy, Zoltan, et al. "Initial clinical evaluation of an intraocular femtosecond laser in cataract surgery." *Journal of refractive surgery* 25.12 (2009): 1053-1060.

[3] Chandna, Shalu, and Suresh Dyamappa Kedige. "Evaluation of pain on use of electrosurgery and diode lasers in the management of gingival hyperpigmentation: A comparative study." *Journal of Indian Society of Periodontology* 19.1 (2015): 49-55.

[4] Ichikawa K, et al, "Plasma-induced bubble microjet metallization of elastomer." *Micromachines* 10.6. (2019) doi: 10.3390/mi10060389

[5] Aokusa. Y, et al. "A Needle-Free Bubble Injector Enabling Depth-Controlled Isotropic and Anisotropic Perforation Using Electrically Induced Bubbles and Heat Generated by Electric Discharge." *Biomedical Microdevices*, (2026) in press.

[6] Pal S, Hanmaiahgari PR Karney BW "An overview of the numerical approaches to water hammer modelling: The ongoing quest for practical and accurate numerical approaches." *Water* 13.11: 1597 (2011)

 DOI: 10.30420/456743053

Optimizing laser-induced graphene microstructure to enhance ion diffusion and actuation performance in PI-LIG-Ppy ionic actuators

David Morales Morales, Alejando Vega Rios, Sergio Flores Gallardo.

Centro de Investigación en Materiales Avanzados (CIMAV), Chihuahua, México.
david.morales@cimav.edu.mx

Abstract

Laser-induced graphene (LIG) has emerged as a promising conductive platform for electrochemical devices; however, its role in ionic actuators remains underexplored. In this work, LIG electrodes fabricated under different laser parameters were systematically studied to establish structure–electrochemical performance relationships. Raman spectroscopy, scanning electron microscopy, and electrochemical impedance spectroscopy revealed that laser conditions strongly affect defect density, porosity, and charge transport. The optimized LIG exhibited lower impedance and improved ionic accessibility, enabling uniform electropolymerization of polypyrrole (PPy). The resulting LIG–PPy system demonstrated a reversible actuation response with angular deflections up to 30° under ±1 V. These results highlight the importance of substrate engineering for improving ion transport and actuation performance in conductive polymer-based ionic actuators.

1 Introduction

Ionic actuators based on conductive polymers have attracted significant attention due to their ability to generate large deformations at low voltages [1] . However, their performance is strongly limited by ion transport and electrochemical resistance. While most studies focus on optimizing the active polymer layer, the role of the conductive substrate remains underexplored.

Laser-induced graphene (LIG) has emerged as a promising material due to its tuneable structure, high conductivity, and porous morphology [2] . In this work, LIG electrodes fabricated under different laser conditions are systematically analysed to establish structure–electrochemical performance relationships for ionic actuator applications.

2 Experimental

LIG was fabricated on 25 µm polyimide using a CO_2 laser under varying power (11–13%) and scan speeds (100–125 mm/s). Structural characterization was performed by Raman spectroscopy and SEM. Electrochemical behavior was evaluated using EIS in 0.5 M $LiClO_4$. Selected samples were used for PPy electropolymerization via cyclic voltammetry (0.2–0.8 V, 50 mV/s, 100 cycles). Actuation was evaluated under ±1 V in 0.5M using $LiClO_4$ electrolyte.

3 Results

3.1 LIG structure

Raman spectra of the LIG samples fabricated under different laser conditions are shown in **Figure 1**.
All samples exhibit the characteristic D (~1330 cm^{-1}), G (~1580 cm^{-1}), and 2D (~2650 cm^{-1}) bands, confirming the formation of graphitic carbon structures [3]. Clear differences are observed in the relative intensity of the D band, indicating variations in defect density induced by the laser parameters [4]. The LIG-12-125 sample shows a lower D-band intensity, suggesting a higher structural order, whereas LIG-12-100 exhibits a more pronounced D band, indicating increased disorder. Meanwhile, LIG-12.5-125 presents an intermediate behavior, combining a moderate D-band intensity with a more defined 2D band, which may indicate a better development of graphitic domains [5].

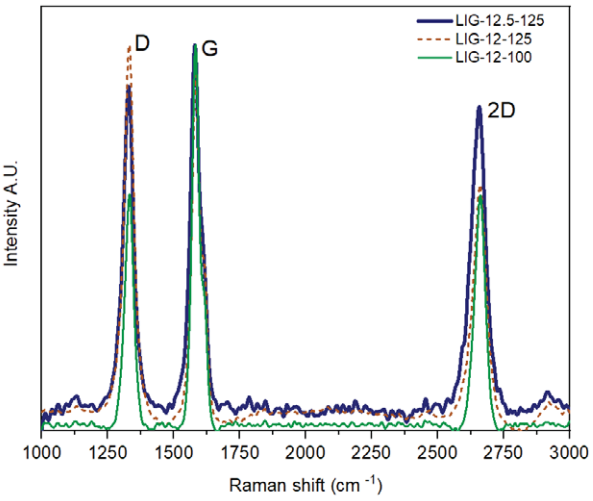


Figure 1 Raman spectra of LIG samples: LIG-12.5-125, LIG-12-125 and LIG 12-100.

 DOI: 10.30420/456743053

3.2 Electrochemical performance LIG

Electrochemical impedance spectroscopy (EIS) was used to evaluate the charge transport properties of the LIG samples. **Figure 2** shows the Bode plots of the impedance magnitude (|Z|) as a function of frequency.

All samples exhibit the typical decrease in |Z| with increasing frequency, indicating a transition from resistive behavior at high frequencies to capacitive behavior at low frequencies. However, significant differences are observed at low frequencies, where LIG-12-125 presents the highest impedance values, suggesting a higher resistance to charge transport. In contrast, LIG-12-100 exhibits the lowest impedance across the entire frequency range, indicating improved electrochemical performance [6].

These results suggest that increased structural disorder and porosity enhance ionic transport and reduce the overall impedance.

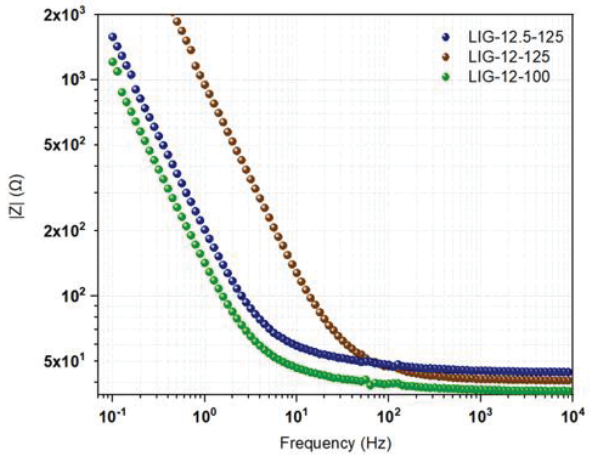


Figure 2. Bode plots of the impedance magnitude (|Z|) for LIG samples fabricated under different laser conditions. Differences at low frequencies indicate variations in charge transport resistance associated with structural changes.

The Nyquist plot of LIG-12-100 in the **Figure 3** shows a nearly vertical trend, indicating a predominantly capacitive response associated with efficient charge storage at the electrode/electrolyte interface. The absence of a well-defined semicircle suggests low charge-transfer resistance, while the limited 45° Warburg-type region indicates that ion diffusion is not the dominant process in the bare LIG electrode [7].

This behaviour is consistent with porous carbon structures and highlights the suitability of the optimized LIG as a conductive platform for ionic actuators [8].

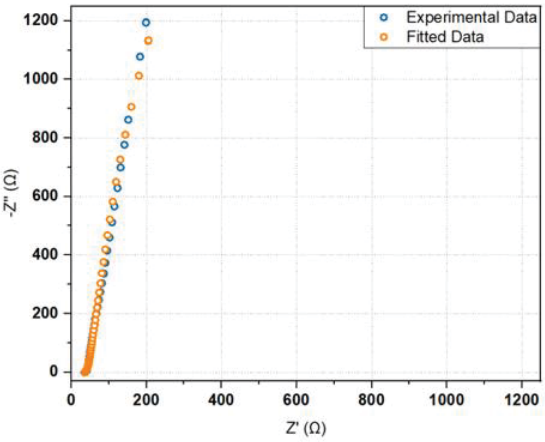


Figure 3. Nyquist plot of the optimized LIG sample with experimental and fitted data.

3.3 Morphological growth of PPy on LIG

The morphology of the LIG–PPy system was analysed by SEM after electropolymerization. As shown in Figure 4a, the characteristic parallel grooves induced by the laser scanning process are preserved after polymer deposition, indicating that the electropolymerization does not alter the macroscopic structure of the LIG. At higher magnification (Figure 4b), a porous and interconnected network is observed, where the PPy coating conforms to the underlying LIG structure. The polymer grows along the carbon framework, increasing the thickness of the walls while maintaining open porosity. This is further evidenced in the inset (Figure 4c), where a nodular morphology characteristic of electropolymerized Polypyrrole is observed. Electropolymerization of PPy on LIG-12-100 resulted in a uniform coating that preserved the porous structure [9]. The preserved porosity ensures efficient ion accessibility within the composite structure.

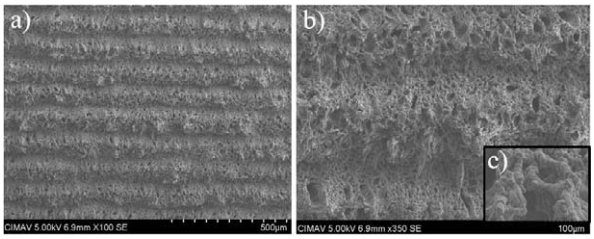


Figure 4. SEM images of the LIG–PPy system after electropolymerization. (a) Low magnification image x100. (b) x350 magnification and (c) x5000 magnification.

3.4 Electrochemical performance LIG-Ppy.

After PPy electropolymerization, the electrochemical response changes significantly, as shown in the Figure 5, the LIG–PPy system exhibits a more inclined profile, approaching a Warburg-type behavior, which indicates the

 DOI: 10.30420/456743053

introduction of diffusion-controlled processes associated with ion insertion and extraction within the electroactive polymer matrix [10].

This transition confirms that PPy incorporation modifies the charge transport mechanism from predominantly capacitive behavior to a coupled capacitive–diffusive response, which is essential for ionic actuation.

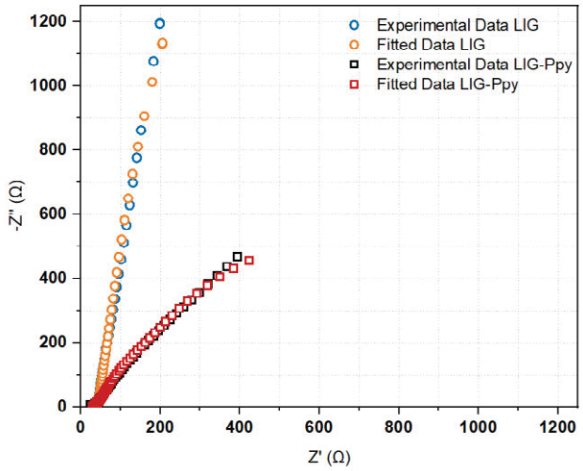


Figure 5. Comparison of Nyquist plots for bare LIG and LIG–PPy electrodes together with their fitted data.

4. Actuation performance LIG-Ppy.

In the Figure 7, the LIG–PPy actuator exhibited a reversible bending response under ±1 V, reaching angular deflections of approximately 30°. This behavior is attributed to ion insertion and extraction within the PPy matrix, enabled by the porous LIG structure. These results demonstrate the feasibility of LIG as a conductive platform for ionic actuators.

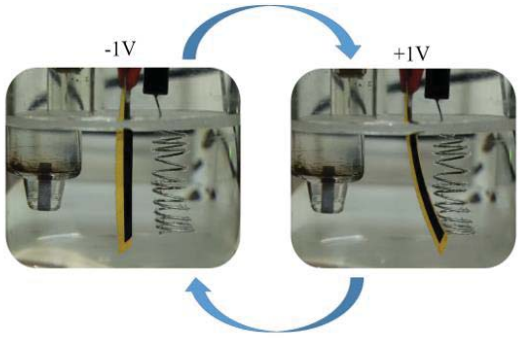


Figure 6. Reversible bending response of the LIG–PPy ionic actuator under applied potentials of −1 V and +1 V in $LiClO_4$ electrolyte.

4 Conclusion

Laser processing parameters strongly influence the structural and electrochemical properties of LIG. The optimized condition (LIG-12-100) provided the best balance between defect density and impedance, enabling efficient PPy integration and actuation performance. These findings highlight the importance of substrate engineering for improving ionic actuator systems.

5 Literature

[1] Liu, M., Wu, J. N., & Cheng, H. Y. (2022). Effects of laser processing parameters on properties of laser-induced graphene by irradiating CO_2 laser on polyimide.
[2] Wang, Y., et al. (2022). Laser-induced graphene based flexible electronic devices. Biosensors, 12(55).
[3] Li, X., et al. (2023). Actuation mechanisms and applications for soft robots: A comprehensive review. Applied Sciences.
[4] Murray, B. T., et al. (2021). Design of experiments and optimization of laser-induced graphene. ACS Omega.
[5] Fantinelli Franco, F., et al. (2024). Optimizing carbon structures in laser-induced graphene electrodes using design of experiments for enhanced electrochemical performance. ACS Applied Materials & Interfaces.
[6] Syugaev, A. V., et al (2023). Electrochemical impedance of laser-induced graphene: Frequency response of porous structure. Journal of Physics and Chemistry of Solids.
[7] Mei, B.-A., et al. (2018). Physical interpretations of Nyquist plots for EDLC electrodes and devices. The Journal of Physical Chemistry.
[8] Lasia, A. (2025). Impedance of porous electrodes. Current Opinion in Electrochemistry.
[9] Mikheev, K. G., et al (2023). Laser-induced graphene and its modification with polypyrrole for increasing microsupercapacitor capacitance. Physics of the Solid State.
[10] Etman, A. E.-S., et al. (2023). A 10 years-developmental study on conducting polymers composites for supercapacitors electrodes: A review. Journal of Industrial and Engineering Chemistry.

 DOI: 10.30420/456743054

Non-contact micro-mechanical stimulation of Arabidopsis root cap using ultrasonic standing waves for mechanotransduction analysis

Koki Ogawa, The University of Osaka, Suita, Japan, ogawak@live.mech.eng.osaka-u.ac.jp
Yingzhe Wang, The University of Osaka, Suita, Japan, ywang@live.mech.eng.osaka-u.ac.jp
Keisuke Morishima, The University of Osaka, Suita, Japan, morishima@mech.eng.osaka-u.ac.jp

Abstract

Plant roots function as sophisticated autonomous decentralized control systems, where the root cap integrates sensing, control, and actuation without a central nervous system. Understanding this mechanism provides critical insights for developing next-generation soft robots. However, using conventional contact-type methods such as microprobes, it is challenging to apply localized and quantitative mechanical 'inputs' to the tiny root cap (~250 μm). In this study, we developed an ultrasonic stimulation device employing an acoustic slit to focus ultrasound waves. By passing 2.2 MHz focused ultrasound through a 250 μm slit, we achieved a localized acoustic field in the near-field region. Verification experiments using a 3D-printed culture chip and tracer particles confirmed immediate particle aggregation, demonstrating successful local field formation. This method enables non-contact, non-invasive, and localized stimulation, facilitating the system identification of plant environmental responses.

1 Introduction

Plant roots function not only to absorb water and nutrients but also possess a highly sophisticated "autonomous decentralized control system." Despite lacking a central nervous system like a brain, they use the "root cap" at their tip as a sensor to autonomously alter their behavior. From an engineering perspective, the root cap can be viewed as a black box that returns a "response," such as a change in growth direction, to a physical "input"[1]. However, the details of its internal principles remain unclear. To identify this system, technology that can apply quantitative and localized mechanical inputs to the microscopic root cap, which is approximately 250 μm in size, is essential.

Therefore, in this study, we focused on the acoustic radiation force of ultrasound, which is characterized by being non-contact, high-output, and penetrative. By introducing spatial control using an acoustic slit to focus ultrasound waves, we propose a micro-mechanical stimulation device that can directly exert physical effects on internal cell components such as amyloplasts. Furthermore, this study aims to verify its usefulness from both physical and biological perspectives.

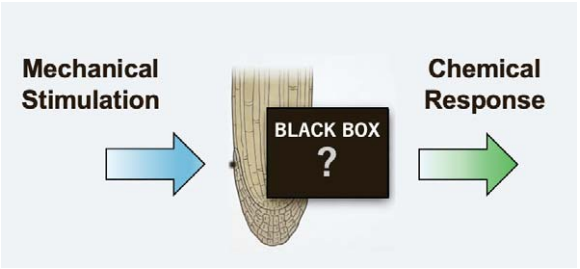


Figure 1 Conceptual diagram of system identification for the root cap environmental response system, modelled as a black box.

2 Principle

2.1 Structure of the Root Cap

Figure 2 shows the microscopic observation of the root cap of *Arabidopsis thaliana*, an actual model plant. Inside the columella cells at the center of the root cap, there are organelles called amyloplasts, which have a high specific gravity. Plants sense gravity as these amyloplasts sediment in the direction of gravity [2]. When a physical force is applied to the cell membrane, mechanosensitive channels open [3], causing an influx of calcium ions (Ca^{2+}), which triggers a series of signal transductions [4]. Since the root tip constantly translocate during growth, a motion-tracking confocal microscope has recently been developed to continuously observe root cap dynamics [5]. By utilizing this tracking technology combined with calcium imaging, dynamic changes in the intracellular calcium ion concentration distribution can be directly visualized even in a growing root.

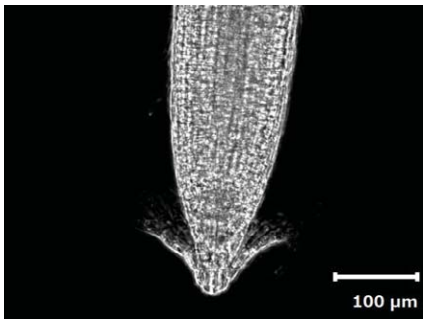


Figure 2 Microscopic observation of the *Arabidopsis thaliana* root cap.

 DOI: 10.30420/456743054

2.2 Feasibility of Stimulating Internal Tissue

Ultrasound can exert pressure on objects through the vibration of the medium, a phenomenon known as acoustic radiation force. Research on acoustic radiation force in liquid environments includes the micro-manipulation of particles by Kozuka et al. [6]. The radiation force F [N] acting on a sphere in a fluid is theoretically expressed by Equation (1) [7].

$$F = \pi r^2 E\, Y_{st} \quad (1)$$

Here, r is the radius of the sphere, E is the energy density of the sound wave, and Y_{st} is the acoustic radiation force function. The pressure exerted on an object depends on its shape and material properties, which are characterized by its acoustic impedance. Acoustic impedance Z is expressed as the product of density ρ and the speed of sound c, as shown in Equation (2).

$$Z = \rho c \quad (2)$$

The greater the difference in acoustic impedance between two media, the more difficult it is for sound waves to penetrate the interface. Because plant cells are primarily composed of water, if an appropriate sound field can be formed in a liquid environment, sound waves could potentially penetrate the cell wall and exert pressure on internal organelles. In particular, amyloplasts have a significantly different density compared to their surroundings, causing them to sediment downward and generate signals by sensing the direction of gravity. Therefore, there is a possibility that this mechanism can be artificially controlled using acoustic radiation force.

2.3 Acoustic Slit

To locally irradiate ultrasound only to the root cap, it is necessary to focus the sound waves to a similar scale. A common method to focus sound waves is to use a concave transducer to converge them at a geometric focal point (Figure 3). The beam width l_d in the focal region is expressed by Equation (3) using the wavelength λ, focal length l_f, and transducer radius a [4].

$$l_d = 1.2\frac{\lambda l_f}{a} \quad (3)$$

However, under the conditions of this study,

$$l_d \approx 1.08\, mm \quad (4)$$

Due to the diffraction limit, it can only be focused down to the millimeter order, which is excessively large for the target root cap. Other methods, such as using acoustic lenses or reflectors, exist but are accompanied by design constraints and limitations in the convergence range.

Furthermore, to construct a system that applies stimulation while growing the plant in a natural environment (vertical direction) and observing it in real-time from the lateral direction, a simple and space-saving design is essential to secure the working space for the observation system.

To address these challenges, we propose a method that utilizes the "near-field" of an "acoustic slit" consisting only of a simple setup with a transducer and a micro-hole placed at the focal position (Figure 4).

The acoustic slit physically blocks the sound waves, allowing them to pass through a hole smaller than the wavelength. While energy diffusion due to diffraction after transmission is a concern, in the near-field region immediately after passing through the slit, the aperture shape before diffraction spreading occurs is maintained. This enables localized stimulation with a spatial resolution not constrained by the wavelength. First, we aim to achieve selective ultrasonic exposure to the root cap using this simple setup.

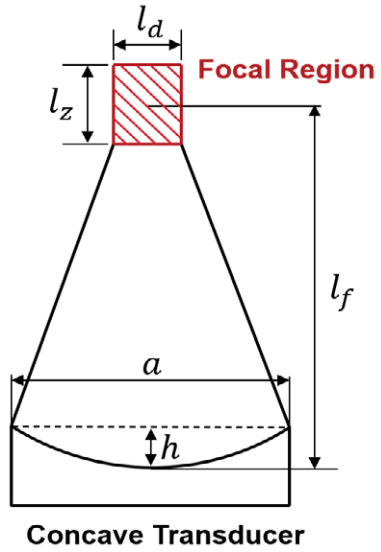


Figure 3 Focusing principle and the focal region of the concave ultrasonic transducer.

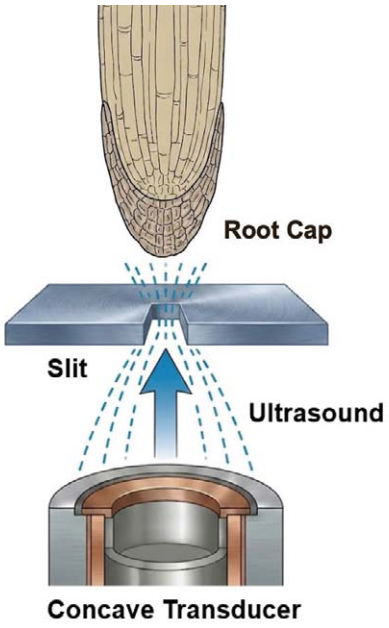


Figure 4 Concept of near-field stimulation using an acoustic slit and concave transducer.

 DOI: 10.30420/456743054

3 Design and Fabrication

In this study, to achieve precise local stimulation of the root cap, we designed and fabricated a unique "chamber" and "plant culture chip."

3.1 Experimental Setup

The overall experimental setup is shown in Figure 5.
The device used in this experiment is an integrated housing with a concave transducer (PZT: KAIJO Quava mini) fixed at the bottom of the chamber and a slit plate arranged at the top. It adopts a self-aligning structure where simply fitting the transducer into the chamber aligns the focal axis with the center of the slit. The slit part is 2 mm thick and has a 250 µm diameter through-hole in the center. The plant culture chip is a device for growing Arabidopsis thaliana, a model plant, from seeds. Inside, a tapered V-shaped guide groove with an exit width of 250 µm is provided, which serves to physically guide and maintain the root growth direction directly above the slit.

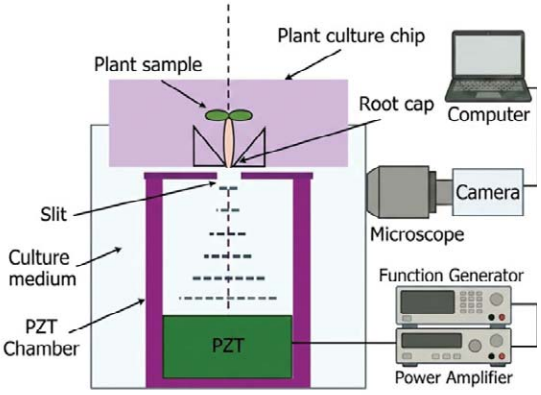


Figure 5 Schematic diagram of the experimental setup for ultrasonic stimulation.

3.2 Experimental Method

The stimulation experiment is performed according to the following procedure.

1. Grow the plant in the guide groove of the culture chip, controlling its elongation so that the root cap is located near the chip exit.
2. Insert the culture chip directly from the top of the chamber. At this time, a gap of 0.5 mm is always maintained between the slit surface and the bottom of the chip by a mechanical stopper.
3. Drive the transducer to emit 2.2 MHz ultrasound toward the acoustic slit in the chamber.
4. While monitoring the state of the root cap in real-time with a microscope on the side, manually move the culture chip in fine increments to align the root cap directly above the slit.

3.3 Fabrication

The chamber housing and culture chip were integrally molded using a stereolithography 3D printer (ELEGOO Mars 5 Ultra). The through-hole processing on the slit plate was performed using a 3-axis UV laser marker, achieving a slit with a diameter of 250 µm. The appearance of the actually fabricated culture chip and the assembled device is shown in Figure 6.

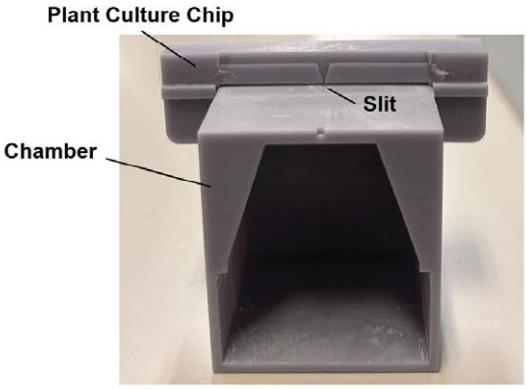


Figure 6 Fabricated acoustic chamber and 3D-printed plant culture chip.

4 Characterization and Discussion

To evaluate the performance and usefulness of the device created in this study, we verified it from the perspectives of physical characteristics and biological applicability.

4.1 Evaluation of Sound Wave Permeability through Plant Cell Walls

For ultrasonic stimulation to induce physiological responses inside the cell, the sound waves must penetrate the robust cell wall (cellulose layer) and exert physical effects on receptors and organelles in the cytoplasm. Therefore, using an onion epidermis as a macroscopic cell wall model (Figure 7), we conducted a permeability experiment. The configuration diagram of this experiment is shown in Figure 8. An onion epidermis, in which rectangular cells are regularly arranged, was placed 1 mm above the slit opening. A suspension of chalk powder for visualization was dropped onto the upper surface of the epidermis, and continuous sine waves with a frequency of 2.216 MHz and an output of 30 W were irradiated from below. The behavior of the particles behind the thin skin was observed from above using a microscope.

As a result of the experiment, particles that were randomly dispersed before irradiation formed a clear annular aggregation pattern immediately above the slit just 5 seconds after irradiation began (Figure 9). This pattern indicates the trapping of particles at the nodes of sound pressure due to the sound waves emitted from the slit reflecting off the liquid surface above the epidermis, forming a standing wave.s

 DOI: 10.30420/456743054

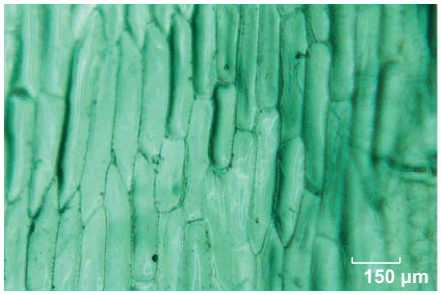


Figure 7 Microscopic observation of an onion epidermis cell wall.

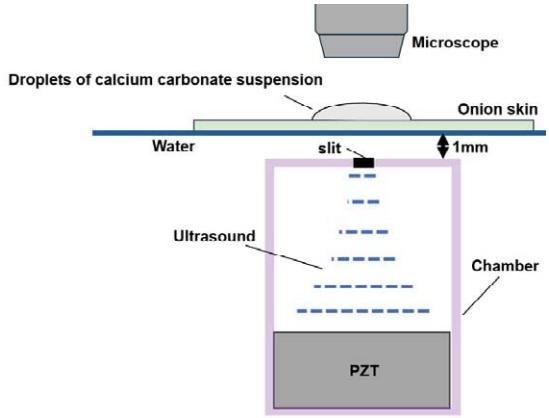


Figure 8 Schematic diagram of the ultrasound permeability experiment using an onion epidermis.

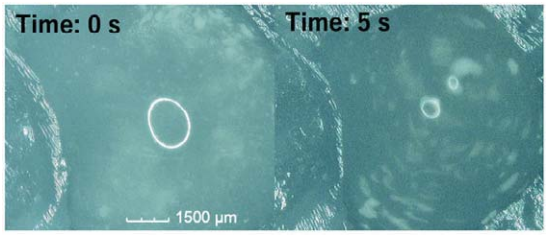


Figure 9 Aggregation of calcium carbonate particles above the onion epidermis layer 5 seconds after ultrasonic irradiation.

4.2 Visualization of the sound field inside the chip

Next, to confirm whether a localized sound field based on the slit shape is maintained inside the culture chip where the plant is set, we visualized the sound field using microparticles. Figure 10 shows the configuration diagram of this experiment.

A culture chip with a guide groove having an exit width of 250 µm, fabricated by a 3D printer, was used, and a chalk powder suspension was enclosed inside. The chip was manually fitted into a predetermined position on the chamber, and after confirming the alignment with a side microscope, ultrasound was irradiated. The results of this experiment are shown in Figure 11. In state (a) before ultrasound irradiation, the particle suspension is flowing downwards by its own weight due to gravity from the discharge port (width 250µm) of the culture chip. On the other hand, in (b) immediately after starting the 15 W ultrasound irradiation, the particles in the fluid started moving simultaneously, and a clear striped pattern corresponding to the wavelength was formed near the opening. Furthermore, in the steady state (c) where irradiation was continued, the contrast of the striped pattern became clearer, and it was observed that the particles were strongly constrained by the nodes of the standing wave's sound pressure and remained stable [8]. This particle arrangement was confirmed only in the limited area directly above the slit opening, and energy diffusion to the surrounding area was not observed.

This result physically proves that even in the closed space inside the chip, a localized sound field with suppressed diffraction effects can be constructed by using the "near-field" created by the acoustic slit. This method demonstrated the possibility of non-contact capture or precise guidance of the micro-target, the root cap.

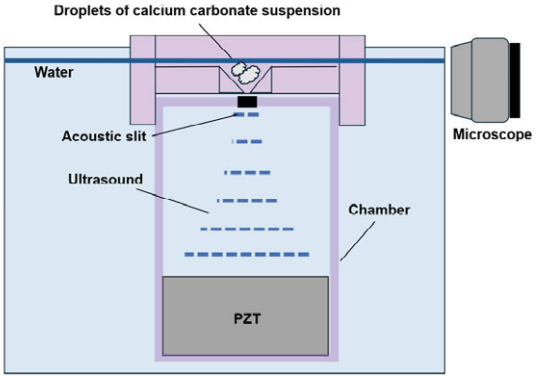


Figure 10 Schematic diagram of the sound field visualization inside the culture chip.

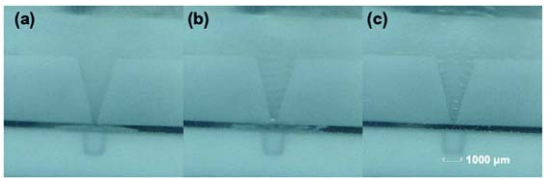


Figure 11 Visualization of the acoustic standing wave field inside the culture chip using a calcium carbonate suspension.

4.3 Stimulation experiment

Based on the physical evaluation of the acoustic field up to the previous section, we actually attempted ultrasonic stimulation of the Arabidopsis root cap. Figure 12 shows the state of the stimulation experiment in the actual setup inside the culture chip. In this verification, ultrasound was irradiated using a 15 W continuous sine wave, and the behavior of the root before the start of stimulation (0 s) and after the start (3 s) was observed under a microscope. From the comparison in Figure 12, it was confirmed that the tip

of the root was slightly displaced with the ultrasonic irradiation. However, it is inferred that this displacement is highly likely to have occurred due to being strongly influenced by the reflected waves at the liquid surface (water surface) and the accompanying macroscopic acoustic stream of the entire chip, rather than being a direct response by the localized acoustic radiation pressure in the near-field transmitted through the acoustic slit. The purpose of this method is to apply a quantitative mechanical input only to the root cap, which is a black box, and to perform system identification from its input-output relationship. Therefore, disturbances due to the macroscopic flow of the entire chip as observed this time must be eliminated.

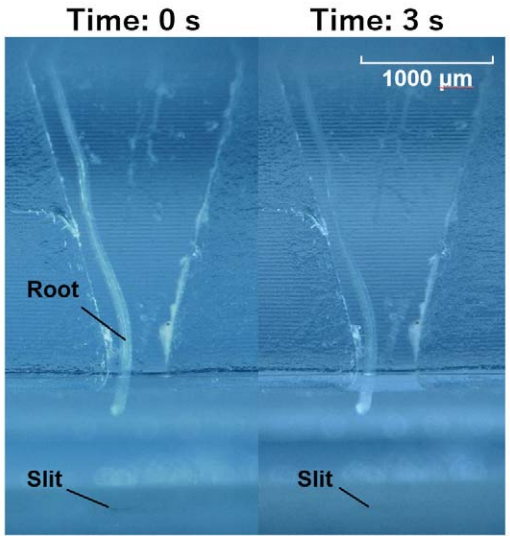


Figure 12 Microscopic observation of the Arabidopsis root cap before (0 s) and after (3 s) the onset of ultrasonic stimulation.

5 Conclusion

In this study, an ultrasonic stimulation device and a plant culture chip using microfabrication technology were developed to realize non-contact and quantitative mechanical stimulation locally applied to the plant root cap. As a result, it was demonstrated that acoustic energy can be concentrated in a micro-region equivalent to the root cap size by using an acoustic slit with a diameter of 250 µm. In addition, a permeability experiment using an onion epidermis confirmed that ultrasound can penetrate the plant-specific cell wall layer and exert physical effects on the internal tissue. Furthermore, it was clarified that a stable local sound field based on the slit shape is formed even in the closed space inside the 3D-printed culture chip, indicating the possibility of non-contact root cap capture and precise position control. However, to address the actual stimulation experimental challenges, we will focus on the technical improvements of our prototype system for the purpose of understanding the mechanotransduction mechanism of plants and the environmental response mechanism of plants as an autonomous decentralized control system.

6 Acknowledgments

Part of this research was supported by JSPS KAKENHI Grant-in-Aid for Transformative Research Areas (A) 26H00456. We would like to express our deep gratitude to Dr. Kozuka for his invaluable advice on ultrasound, and to KAIJO Corporation for providing the transducer as the experimental equipment in executing this research.

7 Literature

[1] G. D. Massa and S. Gilroy, "Touch modulates gravity sensing to regulate the growth of primary roots of Arabidopsis thaliana," The Plant Journal, 33(3), 435-445, 2003.

[2] Miyo T. Morita, "Directional gravity sensing in gravitropism," Annual Review of Plant Biology, 61, 705-720, 2010.

[3] E. S. Haswell, R. Phillips, and D. C. Rees, "Mechanosensitive channels: what can they do and how do they do it?" Structure, 19(10), 1356-1369, 2011.

[4] M. Toyota, et al., "Glutamate triggers long-distance, rapid calcium signaling in Arabidopsis wound response," Science, 361(6407), 1112-1115, 2018.

[5] K. Sakamoto, T. Goh, et al., "Autophagy regulates organelle rearrangement and cell shedding during root cap maturation," Development, vol. 149(11), dev200926, 2022.

[6] T. Kozuka, et al., "Non-contact Micromanipulation Using a Standing Wave of Ultrasound in Water," Journal of the Robotics Society of Japan, 18(1), 106-112, 2000.

[7] K. Yoshioka and Y. Kawashima, "Acoustic radiation pressure on a compressible sphere," Acustica, 5. 5, 167-173, 1955.

[8] T. Aikawa and N. Kudo, "Visualization of ultrasound fields inside a protuberance of water generated by an ultrasonic atomizer," Proceedings of Symposium on Ultrasonic Electronics, 40, 3P5-12, 2019.

 DOI: 10.30420/456743055

Thermal impact on the dynamic model of a magnetorheological elastomer: analysis and experiments

Paweł Orkisz[a], Janusz Gołdasz[b], and Bogdan Sapiński[c]
[a]Department of Process Control, AGH University of Krakow, Mickiewicza 30, 30-059 Krakow, Poland orkisz@agh.edu.pl
[b]Faculty of Electrical and Computer Engineering, Cracow University of Technology, Warszawska 24, 31-155 Krakow, Poland janusz.goldasz@pk.edu.pl
[c]Department of Process Control, AGH University of Krakow, Mickiewicza 30, 30-059 Krakow, Poland deep@agh.edu.pl

Abstract

The work focuses on the aspect of the ambient temperature on the behaviour of an isotropic MRE sample. The temperature change occurred either due to a change in the current flowing through the winding or was generated in a specially designed mini thermal chamber. The experiments were carried out on a designed experimental setup at selected temperature levels stabilised by the developed control subsystems. Based on the measured data, the authors estimated the parameters of the modified Kelvin–Voigt model and discussed the potential to predict its performance under the assumed test conditions.

1 Introduction

Magnetorheological elastomers (MREs) are a class of responsive materials that can alter their rheological properties in response to external magnetic fields [1], [2]. MREs are fabricated by embedding micron-sized magnetic particles in a non-magnetic matrix, either homogeneously or by curing with magnetic fields, and also by adding additives to affect their properties. In principle, these materials can be operated in one of the following fundamental modes: shear, squeeze, and active field [3]. MREs possess magnetic field-dependent characteristics that enable them to be utilised in control systems and robotics to develop advanced devices, such as actuators and sensors. The knowledge about the behaviour of MREs is extensive and widely reflected in the literature. The progress of MREs' models led to increasingly faithful mapping of their real behaviour (in particular via the stress-strain relationship), taking into account such real phenomena as hysteresis, viscoelasticity in larger deformations, amplitude and frequency characteristics, etc [4], [5]. In the available literature on the subject, one can find various models of MREs for mapping their field dependent behaviour, for example: Kelvin–Voigt, Bouc–Wen, Dahl, LuGre, etc. [6], [7].
The present work is focused on the aspect of thermal effect on the MRE sample model [8]. This issue seems to be given less attention in research studies. However, temperature is known to affect the MRE behaviour due to the changes in the properties of the silicon matrix. As a result, both the stiffness and damping moduli vary with temperature.
In the study the authors described the behavior of a selected material sample in a designed in-house measuring stand. They also presented the adopted measurement methodology and the results of processing and analysis. On this basis, the parameters of the modified Kelvin-Voigt model were estimated, and the suitability of its use under the adopted test conditions was summarized.

2 Materials and methods

For material testing, an MRE sample made by the authors was selected, consisting of a silicone matrix EcoFlex 00-10, in which 30% of the volume of carbon iron particles CIP was dissolved. A detailed description of the material, along with the methodology adopted for its preparation, was described in [9]. A cuboidal sample with dimensions of $32x32x16$ mm was cut out from the developed material (see **Figure 1a**). The base of the sample was fixed, while the upper wall was attached to a movable carriage with support, enabling the generation of displacement x_s and simultaneously measuring the force f_s. The influence of thermal impact on the sample was tested by applying a precompression force f_0 to the sample. To represent the sample behaviour, the modified Kelvin–Voigt model [10] was selected, which is shown in **Figure 1b** (t_s denotes the effect of temperature and b_s the effect of magnetic field density).

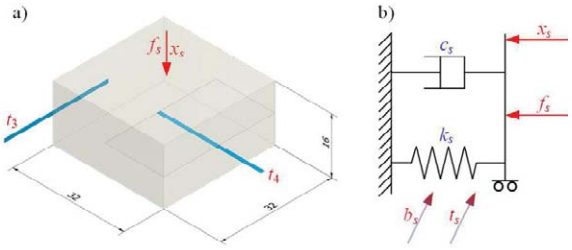


Figure 1 a) Sample shape and the position of temperature sensors t_3 and t_4, b) Sample model used in the calculations

The proposed model allows for the determination of equivalent stiffness k_s and damping c_s parameters as a function of displacement x_s, temperature t_s and magnetic field density b_s. A modified measuring stand was used for the tests. The root version of the stand was described in detail in [11]. It was used for two-axis horizontal positioning of the

 DOI: 10.30420/456743055

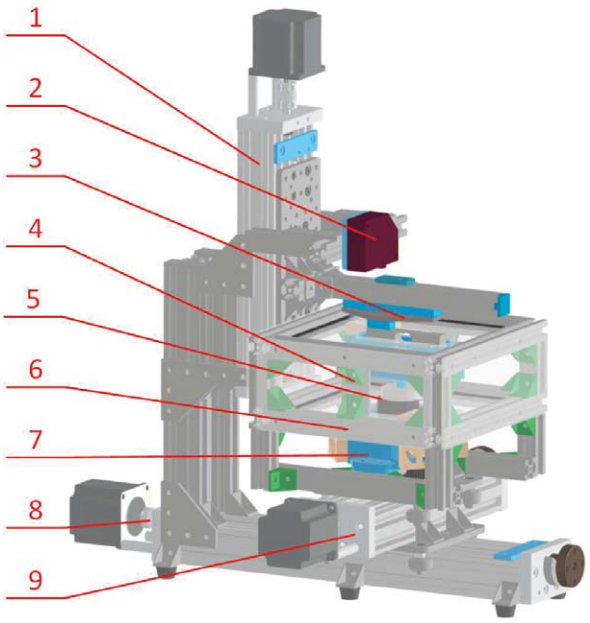


Figure 2 CAD model of the measuring stand

working platform relative to sensors placed on a vertically moving carriage. The mechanical part of the stand was modified as shown in the CAD model in **Figure 2**. The main modifications included:

- equipping the movable carriage (element 1) with a displacement sensor (element 2) and a force sensor (element 3),
- mounting a designed mini thermal chamber (element 6) equipped with heaters and integrated temperature sensors (element 4) on the working platform,
- modifying the electromagnet housing (element 7) to allow for mounting the sample and additional temperature and magnetic field sensors,
- fixing the horizontal movement of the working platform (deactivating mechanisms elements 8 and 9).

The tested material sample (element 5) was placed between an electromagnet and a piston connected to the lower end of the force sensor. The piston was made of paramagnetic stainless steel.

The electrical part of the stand consists of two independent systems: a control and a measurement system, as shown in **Figure 3**. The control system was divided into four subsystems based on their functions: displacement control (positioning), electromagnet field generation, electromagnet temperature stabilization, and thermal chamber control. Each subsystem was implemented on an independent microcontroller supporting dedicated peripherals. The positioning, magnetic field generation, and temperature stabilization subsystems were specified in [11]; therefore, their descriptions are omitted, and they are described in a simplified form in the block diagram.

The thermal chamber control subsystem was built using a Nucleo U545RE prototype system equipped with an IHM04A1 module. The module included a dual DC motor controller used to steer two 40-watt heating resistors. Both heaters were equipped with a heat sink, an AHT20 digital temperature sensor and an PWM controlled fans used to enhance thermal convection. Additionally, one AHT20 sensor was placed in the center of the chamber, close to the tested sample, and served as feedback to the control system. The subsystem was programmed in the STM32CubeIDE environment, implementing a cascaded PID controller. The first regulator stage used two independent PI controllers to stabilize the temperature of both heaters, while the second stage used a master PID controller to adjust the heater temperature setpoint based on temperature measurements from the central part of the chamber. An independent laboratory power supply powered all subsystem components.

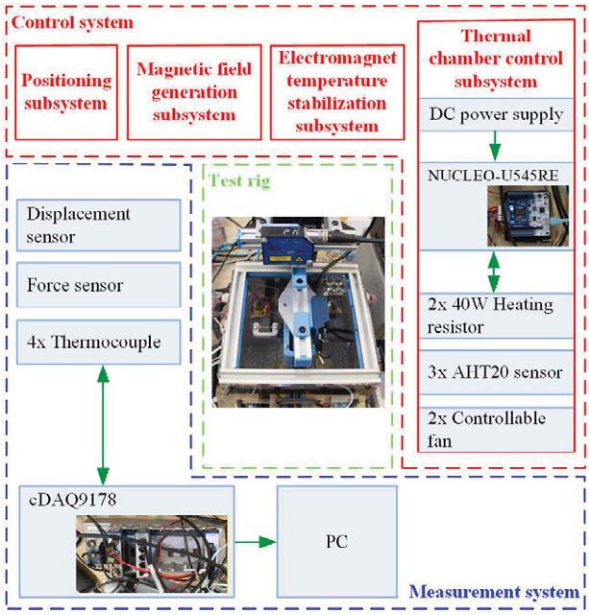


Figure 3 Block diagram of the control and measurement system

The measurement system was built using a personal computer connected to a universal cDA9178 chassis. The chassis was equipped with three data acquisition cards: NI 9211, NI 9215, and NI 9237, and programmed in the LabView environment. The measurement system configuration allows for data acquisition of:

- the pressure force f_s measured using a 5 kg Mavin strain gauge operating in a full bridge configuration,
- the carriage displacement x_s determined using an optoNCDT 1402 optical sensor,
- the ambient temperature t_1 calculated using a thermocouple attached to the side edge of the measuring stand (located away from the thermal chamber),
- the coil temperature t_2 measured using a thermocouple placed on the side edge of the electromagnet,
- the MRE sample temperature measured using two thermocouples: thermocouple t_3 placed at the center of the outer edge of the sample, and a thermocouple t_4 placed in the centre of the sample (the sample was cut out to allow the attachment of a thermocouple, see **Figure 1a**).

 DOI: 10.30420/456743055

3 Results and analysis

The material sample was tested at the measuring stand located in an enclosed room, where nonessential devices that affect thermal balance, such as additional computers, radiators, and the air conditioner, were turned off. Only the influence of natural environmental factors remained in the room, such as the diffusion of thermal energy through walls or covered windows (measurements were made remotely, from outside the room). According to the assumptions, the sample was placed in the chamber on the metal core of the electromagnet and compressed with an initial force 8.5 N . Direct connection of the sample to the core itself created a thermal bridge that dissipated thermal energy outside of the chamber when the electromagnet was turned off and, to some extent, provided heat when the electromagnet generated a magnetic field and the electromagnet temperature stabilization subsystem was turned on. In the described test cycle, the electromagnet was turned off. Tests began at noon, when the room was close to its maximum temperature of approximately 26.5°C, and ended at midnight when the room temperature had dropped by approximately 2°C. The indicated time interval was divided into four 3-hour stages: in the first and second stages, the chamber temperature t_c was raised first to 29.5°C and then set to 33°C; in the third and fourth stages, the chamber temperature was reduced first to 28.5°C and then set to 25°C.

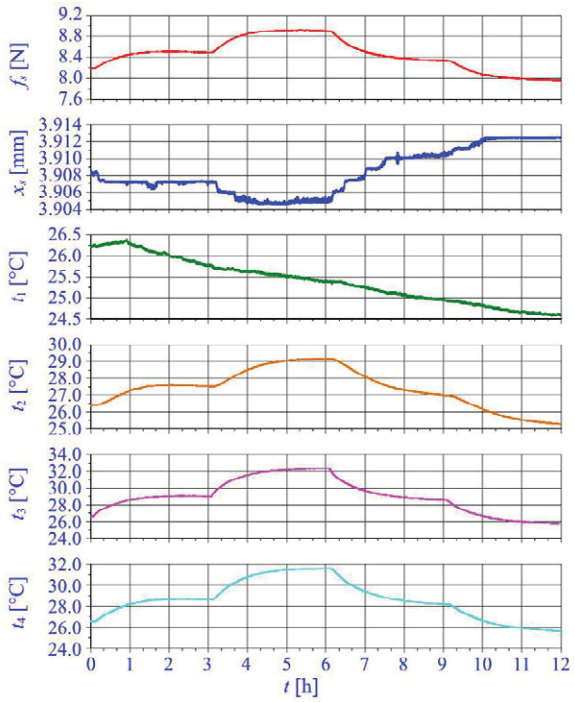


Figure 4 Time plots of recorded f_s, x_s, t_1, t_2, t_3, t_4 values.

The recorded time plots of force, displacement, and temperature sampled at 1000 Hz are shown in **Figure 4**. Additionally, **Table 1** compares the set chamber temperature t_c with the instantaneous values of force, displacement and temperatures recorded at the beginning of the test and at the end of each stage.

Table 1 Selected values of force, displacement and temperatures recorded at the start and at the end of each stage

Stage	t_c [°C]	f_s [N]	x_s [mm]	t_1 [°C]	t_2 [°C]	t_3 [°C]	t_4 [°C]
start	-	8.190	3.908	26.22	26.36	26.65	26.58
1	29.5	8.489	3.907	25.78	27.53	28.97	28.63
2	33.0	8.903	3.905	25.38	29.15	32.28	31.58
3	28.5	8.338	3.910	24.93	26.99	28.55	28.17
4	25.0	7.959	3.913	24.58	25.26	25.74	25.64

Analysis of the obtained results revealed a strong correlation between the values of the force signal f_s and the sample temperature measured both at the outer edge t_3 and inside t_4. During the test, changes in the sample's internal temperature were recorded at 7.96°C, within the range expected for typical indoor operating temperatures. This change introduces a force alteration of 0.95 N. Additionally, a very small change of $7.7 \cdot 10^{-3}$ mm in displacement was observed, resulting from the design of the movable carriage.

The considered model approximating the thermal behavior of the MRE sample was described by the equation:

$$f_m = c_s \cdot \dot{t_m} + k_s \cdot t_m + f_0 \quad (1)$$

where c_s, k_s were the previously mentioned parameters, f_0 is the initial force and f_m was the force resulting from temperature changes t_m. It was assumed that the temperature $t_m(t)$ is a triangular function defined in the time t interval changed from 0 to $2 \cdot t_{hf}$ according to the relationship:

$$t_m(t) = \begin{cases} 24 + p_m \cdot t & \text{for } t \le t_{hf} \\ \max(t_4) - p_m \cdot (t - t_{hf}) & \text{for } t > t_{hf} \end{cases} \quad (2)$$

where $t_{hf} = (\max(t_4) - 24)/p_m$ and $p_m = 0.005$ was the temperature sampling resolution.

Comparing the desired shape of the temperature signal t_m (red line in **Figure 5**), with the recorded signal t_4, it can be seen that the identification of model parameters required preliminary data preparation. The first step involved resampling t_4 signal to match the assumed p_m value and transformation values of $f_m(t_4)$.

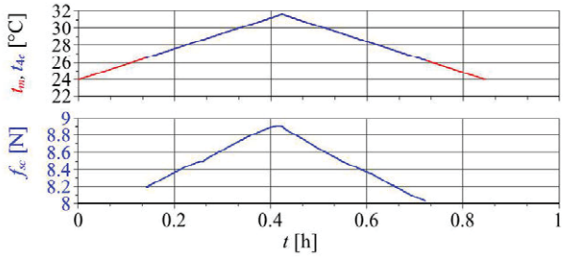


Figure 5 Preparation of measurement data, time histories of temperatures t_m, t_{4c} and forces f_{sc}

Because the temperature change is linear, developing the corrected signal t_{4c} required only determining the initial, maximum, and final values. For the force signal, developing the corrected signal f_{sc} required averaging the $f_s(t_{4c})$ values obtained at identical temperatures t_{4c} and interpolating missing values using data from adjacent samples.

ISBN: 978-3-8007-6743-4 @ VDE VERLAG GMBH · Berlin · Offenbach

The developed corrected signals f_{sc} and t_{4c} were shown in **Figure 5** in blue.

The model parameters were determined by minimizing the value of the mean square error of the difference in the force signals $f_{sc} - f_m$. For the considered measurement the equivalent stiffness $k_s = 0.1576\text{N/°C}$, the equivalent damping coefficient $c_s = 0.0543\ \text{N·s/°C}$ and the initial force $f_0 = 8.5099\ \text{N}$.

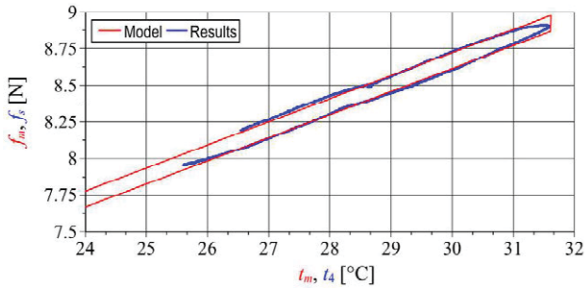


Figure 6 Comparison of the developed sample model $f_m(t_m)$ with the obtained results $f_s(t_4)$

Figure 6 compares the $f_s(t_4)$ characteristic of the model recorded during the test in blue with the $f_m(t_m)$ characteristic developed for the sample model in red. Given the similarity of the obtained characteristics, the developed model can be confirmed as correct.

4 Summary

Upon summarizing the carried out tests, the following conclusions were drawn:

- The described experiment was repeated three days later, obtaining similar results. The recorded changes concerned the temperature ranges resulting from changes in ambient temperature.
- The developed design of the mini thermal chamber allows only for the heating of material samples, so the recorded characteristics are limited by ambient conditions.
- An additional limitation is the dissipation of thermal energy through the electromagnet core during tests performed with the magnetic field generator turned off.

In the next stage of the research, the method for identifying sample parameters and their dependence on the initial pressure force exerted on the sample will be analyzed.

Acknowledgment

This work was supported by the AGH University of Krakow within the scope of the Excellence initiative–research university and the research program No. 501.00.10000.130000.

5 Literature

[1] M. F. Jaafar, F. Mustapha, and M. Mustapha, “Review of current research progress related to magnetorheological elastomer material,” J. Mater. Res. Technol., vol. 15, pp. 5010–5045, Nov. 2021, doi: 10.1016/j.jmrt.2021.10.058.

[2] S. Kang, K. Choi, J.-D. Nam, and H. Choi, “Magnetorheological Elastomers: Fabrication, Characteristics, and Applications,” Materials, vol. 13, no. 20, p. 4597, Oct. 2020, doi: 10.3390/ma13204597.

[3] H. Vatandoost, M. Hemmatian, R. Sedaghati, and S. Rakheja, “Dynamic characterization of isotropic and anisotropic magnetorheological elastomers in the oscillatory squeeze mode superimposed on large static prestrain,” Compos. Part B Eng., vol. 182, p. 107648, Feb. 2020, doi: 10.1016/j.compositesb.2019.107648.

[4] Y. Yu, J. Li, Y. Li, S. Li, H. Li, and W. Wang, “Comparative Investigation of Phenomenological Modeling for Hysteresis Responses of Magnetorheological Elastomer Devices,” Int. J. Mol. Sci., vol. 20, no. 13, p. 3216, Jun. 2019, doi: 10.3390/ijms20133216.

[5] A. K. Bastola and M. Hossain, “A review on magneto-mechanical characterizations of magnetorheological elastomers,” Compos. Part B Eng., vol. 200, p. 108348, Nov. 2020, doi: 10.1016/j.compositesb.2020.108348.

[6] A. Saber and R. Sedaghati, “The Modeling of Magnetorheological Elastomers: A State-of-the-Art Review,” Adv. Eng. Mater., vol. 25, no. 16, p. 2300182, Aug. 2023, doi: 10.1002/adem.202300182.

[7] R.-F. Fung, C.-F. Han, and J.-R. Chang, “Dynamic modeling of a high-precision self-moving stage with various frictional models,” Appl. Math. Model., vol. 32, no. 9, pp. 1769–1780, Sep. 2008, doi: 10.1016/j.apm.2007.06.012.

[8] W. Zhang, X. Gong, S. Xuan, and W. Jiang, “Temperature-Dependent Mechanical Properties and Model of Magnetorheological Elastomers,” Ind. Eng. Chem. Res., vol. 50, no. 11, pp. 6704–6712, Jun. 2011, doi: 10.1021/ie200386x.

[9] D. Gutenko, P. Orkisz, and B. Sapiński, “Laboratory Testing and Modelling of Magnetorheological Elastomers in Tension Mode,” Acta Mech. Autom., vol. 18, no. 2, pp. 291–299, Jun. 2024, doi: 10.2478/ama-2024-0032.

[10] M. Norouzi, S. M. Sajjadi Alehashem, H. Vatandoost, Y. Q. Ni, and M. M. Shahmardan, “A new approach for modeling of magnetorheological elastomers,” J. Intell. Mater. Syst. Struct., vol. 27, no. 8, pp. 1121–1135, May 2016, doi: 10.1177/1045389X15615966.

[11] P. Orkisz, B. Sapiński, S. Mondal, and F. Clemens, “Development of the experimental setup for testing magneto-deformation properties of magnetoactive materials,” IEEE Trans. Ind. Appl., pp. 1–13, 2025, doi: 10.1109/TIA.2025.3621574.

 DOI: 10.30420/456743056

Plasmid delivery to suspension cells through electromechanical poration induced by a microbubble generator

Nobutoshi Ota[1], Kei Tateishi[1], Shigeo S. Sugano[2], Niko Kimura[3], Shinya Sakuma[1], Yoko Yamanishi[1]
[1] Kyushu University, Fukuoka, Japan
[2] National Institute of Advanced Industrial Science and Technology, Ibaraki, Japan
[3] Tokyo University of Agriculture and Technology, Tokyo, Japan
yoko@mech.kyushu-u.ac.jp

Abstract

We have developed a method called electromechanical poration (EMP) for injecting plasmid into suspension cells by using a microbubble generator. This microbubble generator works as an actuator that provides both mechanical and electrical stimuli to induce perforation on cell membrane during EMP. Simultaneously, EMP induces temporal disruption of cytoskeletal component, F-actin, of the surrounding cells so that genetic materials can be introduced into the cells. Although this injection method has been applied to adherent cells, its capability has not been investigated with suspension cells. When a microbubble generator exerted appropriate power to cells, we have succeeded injection of genetic materials into suspension cells by controlling rates of transfection and cell death.

1 Introduction

Modification of cellular functions can be achieved by introducing desired materials into cells. Techniques of material introduction can be classified into three categories: biological [1], chemical [2], and physical methods [3]. Among these methods, physical methods can be applied to introduce materials into many cell types because the physical parameters can be precisely controlled. We have developed a core-shell structured microbubble generator as an actuator to physically deliver plasmid, a genetic material containing artificially designed DNA sequences, into cells. This method, called electromechanical poration (EMP), combines mechanical and electrical stimulation to perforate the membrane of cells. Although EMP has been applied to adherent cells [4], its capability has not been investigated for suspension cells which is more flexible than adherent cells due to less rigid structure of cytoskeleton.

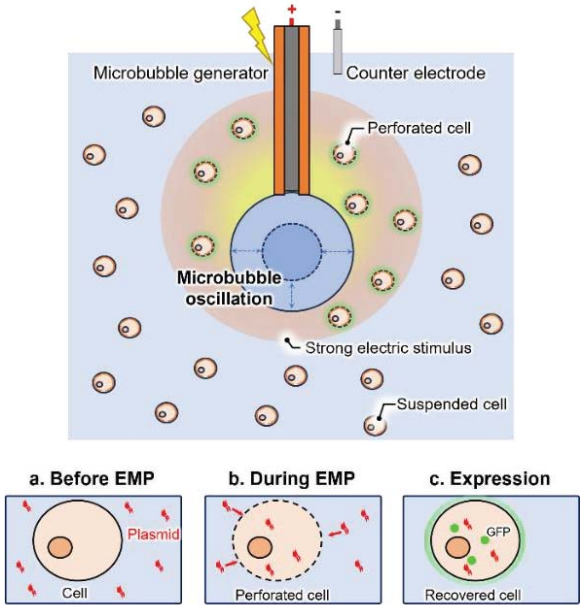


Figure 1 Schematic illustration of electromechanical poration (EMP) for transfection of cells. (a) Before EMP, cell membrane does not permit plasmid. (b) Cell membrane is perforated during EMP so that plasmids get into inside of cells. (c) After EMP and cell recovery, transfected cells encode plasmids, including a reporter gene such as green fluorescent protein (GFP).

2 Concept

Figure 1 illustrates plasmid introduction into cells via electromechanical poration which uses the combination of mechanical and electrical stimuli. When electric pulses are applied to a microbubble generator, microbubbles are formed at the tip of the generator. The microbubbles oscillate their

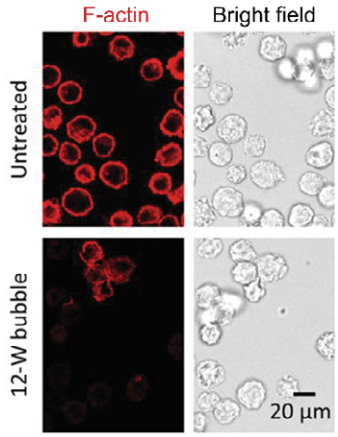


Figure 2 Temporal disruption of cytoskeletal component, F-actin by EMP. (Top row) Untreated cells with intact F-actin indicated by red fluorescence. (Bottom row) Cells treated by EMP with electrical input of 12 W. The appearance of the cells was similar under bright-field observation regardless of EMP treatment.

 DOI: 10.30420/456743056

volume based on applied electric pulses and provide mechanical stimulation to proximal cells. Simultaneously, electric pulses induce electric stimulation to suspended cells. Both mechanical and electrical stimuli contribute local perforation of cell membrane which results in introduction of plasmids into cells, called transfection. EMP is also expected to loosen the cytoskeleton of the cells [4] due to mechanical stimuli (Figure 2).

3 Experimental

The experimental setup is shown in Figure 3. A core-shell structured microbubble generator was consisted with a tungsten wire inserted to a glass capillary. A power source was connected to the microbubble generator to provide electric pulses for EMP. During EMP, cells and plasmids were suspended in culture medium supplemented with fetal bovine serum. After EMP, perforated cells were allowed to recover in an incubator of 37 ℃ with 5 % CO2 for 24 h. Recovered cells were evaluated by expression of a reporter gene such as green fluorescent protein (GFP), which indicates successful transfection.

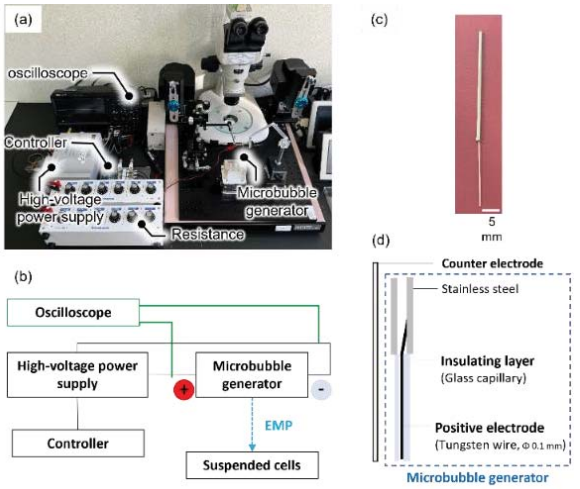


Figure 3 Setup for EMP. (a) Whole setup of EMP and (b) its diagram. (c) A microbubble generator and (d) illustrations of a microbubble generator and a counter electrode.

4 Results

Figure 4 shows bright field and fluorescence images of KHYG-1 cells under microscope observation. Green fluorescence given by GFP indicates successful introduction of plasmid into cells. Red fluorescence is given by propidium iodide (PI) to indicate dead cells. Changes in physical parameters, applied power and pulse number, resulted in various rates of transfection and cell death as shown in Figure 5. When cells are perforated appropriately, transfection rate was as high as 4% and cell death was kept as low as <10%. In this study, we investigate transfection of various suspension cells by controlling the physical parameters of the microbubble generator.

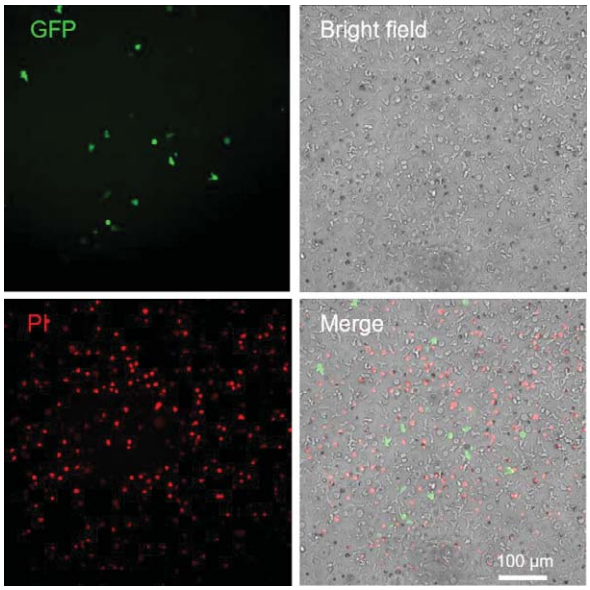


Figure 4 Transfection of a suspension cell line (KHYG-1) under microscope observation.

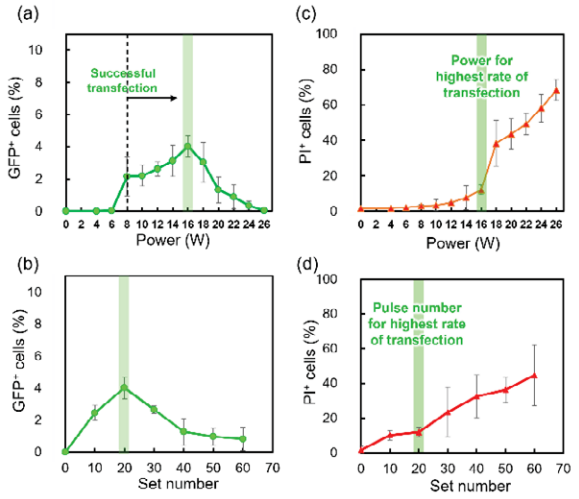


Figure 5 Transfection and cell death of KHYG-1 cells after EMP. Applied power for EMP influenced the rates of (a) transfection (GFP^+ cells) and (b) cell death (PI^+ cells). Number of electric pulses also influenced the rate of (c) transfection and (d) cell death. n = 9. 1 set = 1000 pulses.

5 Literature

[1] K.L. Douglas, “Toward development of artificial viruses for gene therapy: A comparative evaluation of viral and non‐viral transfection”, Biotechnology progress, Vol. 24, pp. 871, 2008.

[2] Y. Inoh, D. Kitamoto, N. Hirashima, and M. Nakanishi, “Biosurfactant MEL-A dramatically increases gene transfection via membrane fusion”, Journal of controlled release, Vol. 94, pp. 423, 2004.

[3] T.Y. Tsong, “Electroporation of cell membranes”, Biophysical journal, Vol. 60, pp. 297, 1991.

[4] W. Huang, S. Sakuma, N. Tottori, S.S. Sugano, and Y.

Yamanishi, “Viscosity-aided electromechanical poration of cells for transfecting molecules”, Lab on a Chip, Vol. 22, pp. 4276, 2022.

6 Acknowledgement

This work was supported by JSPS KAKENHI (JP22K18783, JP22H00198, and JP25H00410), JST CREST (JPMJCR19S6), and JST Moonshot R&D (JPMJMS2217-2-3, 3-1, 3-2, 4-1).

 DOI: 10.30420/456743057

Bistable Piezoelectric Energy harvester with embedded power management electronics for railway monitoring

Timotéo Payre[1], Boris Laluc[1], Guillaume Mansuy[1], Romane Anseaume[1], Nicolas Decroix[2], Quentin Deumouron[2], Célestin Métral[3], Menetrier Anaïs[3]
(1) Cedrat Technologies, 38240 Meylan, France, boris.laluc@cedrat-tec.com
(2) Université Savoie Mont Blanc, 74940 Annecy, quentin.demouron@univ-smb.fr
(3) Vossloh switch system SA, 69100 Villeurbanne, France anais.menetrier@vossloh.com

Abstract

Railway environments present a rich but challenging source of energy harvesting opportunities, thanks to the substantial vibrations, shocks and dynamic loads induced by passing trains and infrastructure deformations. To exploit this energy for powering low-power sensor systems in trackside or onboard applications, a nonlinear approach, namely a bistable energy harvester—offers a promising alternative to conventional linear resonant devices. A bistable harvester employs a mechanical system with two stable equilibrium positions separated by a potential barrier. Under sufficiently large external excitation, the system "jumps" between the two wells, achieving comparatively large amplitude motion and thereby generating more electrical energy over a broader frequency bandwidth. Compared to narrow-band linear harvesters, bistable designs are better suited to the broad, stochastic, and variable vibration spectra typical of railway conditions. The Bistable Piezoelectric Energy Harvester (BPEH) has been designed, tested in lab and installed in railways to monitor the harvested energy.

1 Introduction

Through this paper, we present the development of a buckling-based Bistable Piezoelectric Energy Harvester (BPEH) for railway applications, designed to withstand the large and variable vibrations encountered in railway environments. The proposed system exploits the elastic buckling of a slender beam to create two stable equilibrium positions, enabling large-amplitude oscillations and improved energy harvesting over a broad frequency range. To enhance the robustness of the device under severe dynamic loading, mechanical end stops are integrated to limit the displacement of the moving mass and prevent structural damage. The stiffness of these end stops was also optimized to reduce impact forces while maintaining acceptable loads on the supporting structure.

2 Railway vibrations analysis

This study began with an analysis of railway vibration signals. Twelve train passage signals were collected and post-processed to characterize the distribution of vibrational energy. Figure 1 presents the mean Power Spectral Density (PSD) computed from these signals.

The analysis reveals three dominant frequency peaks located approximately at 19 Hz, 39 Hz, and 61 Hz, with a mean RMS acceleration of 6.5 m/s².

A more detailed analysis indicates that these peaks are not systematically present in every signal, and that their frequencies exhibit slight variations between train passages.

In this context, bistable energy harvesters are particularly well suited due to their low effective stiffness and their ability to efficiently harvest energy over a wide frequency range.

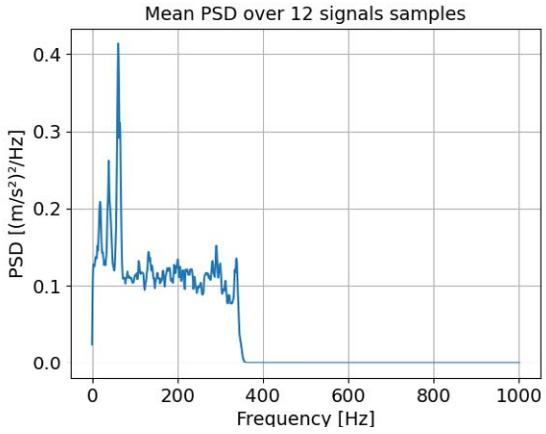


Figure 1 Mean PSD over 12 signals samples

3 Bistable and electronic extraction circuit design and modelling

The BPEH designed by Cedrat technologies is composed of three specific APA®150M (thermally equilibrated) with a moving mass at the centre of buckling which bring the bistability. In addition, endstops have been integrated into this prototype to withstand railway harsh environmental conditions. In addition, this piezoelectric energy harvester integrates an electronic extraction and energy management circuit developed by the Université Savoie Mont-Blanc (USMB). This circuit is composed of an SSHI extraction circuit and can manage the generated power to deliver a regulated output voltage and store the excess of instantaneous unused power.

 DOI: 10.30420/456743057

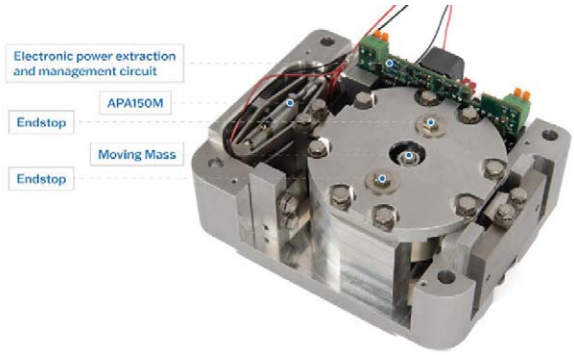


Figure 3 BPEH and electronic power management circuit

This prototype was developed to power a Vossloh device to monitor railway health. Thanks to the BPEH the sensor can be self-powered and do not need any external energy supply.



Figure 2 BPEH and electronic power management circuit integrated in the housing

The model used to estimate the energy harvested on each signal sample and the maximum reached displacement (to prevent the bistable from breakage) is presented in Figure 3. This model is enhanced compared to the previous version [1] with the integration of the endstop in the mathematical model with a nonlinear stiffness.

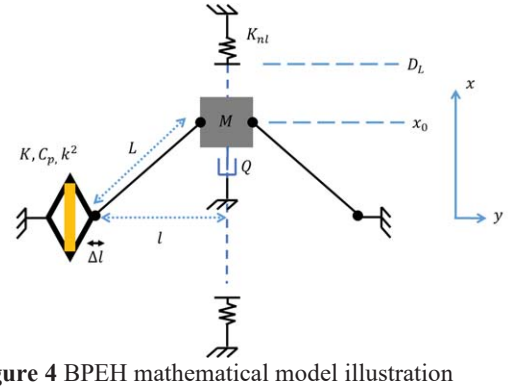


Figure 4 BPEH mathematical model illustration

The developed model allows to compute the time domain response of the bistable piezoelectric harvester under the representative samples to estimate the amount of harvested energy.
In addition, this simulation allows to estimate the maximum reached displacement to confirm there is no risk to break the harvester under this loading. The following table summarizes the main parameters used for the simulations.

Parameter	Symbol	Value	Unit
APA® stiffness	K	2.04	$N/\mu m$
Capacitance	C_p	4.95	μF
Moving mass	M	0.65	kg
Coupling coefficient	k^2	0.08	-
Q	$Q\ factor$	20 − 50 *	-

Table 1 BPEH parameters

4 Vibration testing

The vibration testing has been separated in two different tests sequence. The objective of the first test is to confirm the model prediction of the amount of harvested energy. Whereas the second test sequence aim to confirm the robustness of the BPEH to random and shocks loading. For every test an electrodynamic shaker is used to generate the vibrations. The BPEH is tested with its electronic circuit and in the Vossloh housing to be as representative as possible.

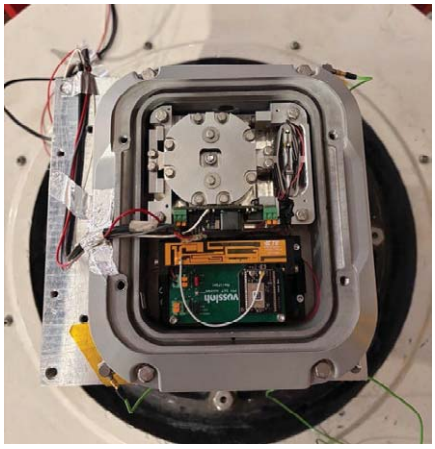


Figure 5 BPEH during shocks and vibrations testing

4.1 Train samples

The BPEH has been excited several times with each signal, and the value mean generated value is compared with the theoretical value obtained with the model of §2. The comparison for each train is given in the following table. The model prediction is satisfying has it as revealed to be conservative and accurate by almost 20%.

 DOI: 10.30420/456743057

Train n°	Energy (mJ) Simulation	Energy (mJ) Experimental
1	141	213
2	241	284
3	154	220
4	225	234
5	46	57
6	186	163
7	246	341
8	244	348
9	216	223
10	53	80
11	232	228
12	514	621
Mean	208	251

Table 2 Comparison of model and experimental results

4.2 Random and shock

The BPEH was submitted to shocks and vibrations to fulfil with the requirement from railway industry. The following tests has been performed with an electrodynamic shaker:
Half sine shocks:
300m/s² during 8 ms 3 times per axis and direction
800m/s² during 2 ms 3 times per axis and direction
Random vibrations:
PSD from 100Hz to 2000Hz at 13m/s²-rms, 9m/s² and 5m/s² during 1h30 (intensity depends on the axis).

After delta design iteration all tests were successfully passed and demonstrate the robustness to the railway environment of such device.

5 Field tests

Four protypes have been integrated at different locations on railway sleepers.



Figure 6 System integrated on railway sleepers

Thanks to the wireless communication device developed by Vossloh the generated energy can be sent and analysed. On the following figure each dot represents the measured energy during a train passage over one installed BPEH. The vertical axis represents the duration of the train passage whereas the horizontal axis gives the amount of harvested energy. For this prototype the mean energy per TGV has been measured around 130mJ which corresponds roughly to a mean power 10mW.

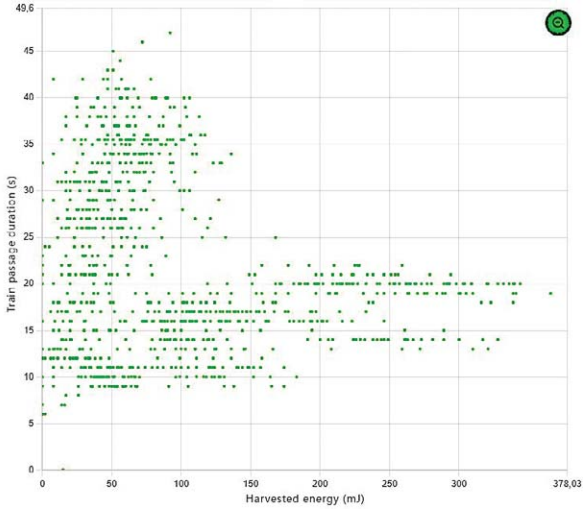


Figure 6 Harvested energy for each train passage

6 Conclusion

This work demonstrates a robust and efficient bistable piezoelectric energy harvester with embedded power management, specifically designed for the demanding railway environment. By leveraging nonlinear dynamics, the proposed system overcomes the limitations of conventional linear harvesters and efficiently exploits broadband vibrations.
Experimental results, supported by a predictive and conservative model, confirm energy generation up to 251 mJ per train passage in laboratory conditions and about 130 mJ in field operation, corresponding to ~10 mW—sufficient to enable autonomous railway monitoring systems.
Combined with validated mechanical robustness under severe shock and vibration loads, these results highlight the strong potential of bistable energy harvesting as a key enabler for reliable, maintenance-free sensing in harsh environments. Future work will focus on further optimization to align the result in laboratory conditions with field testing drawback.

7 Acknowledgment

We do thank you for VOSSLOH, Savoie Mont Blanc University for the cooperation during the project.
The RAILMON project has been funded by BPI.

8 Literature

[1] T. Payre, N. Bencheikh, C. Galteau, A. Pagès, G. Mansuy, B. Laluc, “A wideband vibration energy harvester with integrated energy management designed for harsh environment”, Actuator 2024

 DOI: 10.30420/456743058

Closed-loop cooperative control of dielectric elastomer actuator arrays

Alberto Priuli*[1], Saverio Addario[1], Benjamin Zemlin[2], John Heppe[2], Gianluca Rizzello[1]
[1.] Saarland University, Department of Systems Engineering, Saarbrücken, Germany.
[2.] University of Applied Sciences of Saarland, Department of Sensors and Thin Films, Saarbrücken, Germany.

Abstract

Dielectric elastomers are compliant capacitors composed of a soft, dielectric membrane coated on two sides with conductive electrodes that, when subjected to a voltage, cause the membrane to deform and vary its stiffness. A popular design solution consists of coupling the membrane with negative-stiffness bias mechanisms such as buckling beams to enhance the actuation stroke and the output force, realizing a dielectric elastomer actuator (DEA). To allow such systems to successfully achieve global tasks while ensuring a desired performance level, accurate and computationally efficient control-oriented models as well as appropriately designed control policies are needed. Several challenges, namely electromechanical coupling, large deformations, viscoelasticity, snap-through dynamics, and interactions among neighboring DEAs contribute to make the design of an appropriate control law a challenging task. This work proposes a tentative solution to the control problem by presenting the design and simulation-based validation of a cooperative control strategy tailored to a regulation scenario with rejection of constant disturbances. The controller design is based on an energy-based lumped-parameter model of the system that is suitable for distributed real-time implementation, and has previously been validated against experimental displacement data. Robust control actions are designed via a passivity-preserving integral control approach. The design of the controller is carried out by exploiting intrinsic properties of the system model and is validated through numerical simulations.

1 Introduction

Dielectric elastomer actuators (DEAs) are widely researched soft transducers exploited for their compliance, noiseless and fast actuation, and high efficiency [1]. The use of ultra-thin coated membranes with small-scale compliant mechanisms makes these systems particularly suitable for miniaturized applications that require highly precise positioning and a sufficiently wide range of exerted forces [2]. Further advances in manufacturing processes have enabled applications involving large numbers of DEAs to perform arbitrarily complex tasks [3]. Arranging these actuators in array or matrix configurations has been exploited to realize haptic devices [4] and loudspeakers [5]. Depending on the design choice, each single DEA might be an independent, isolated unit or can be electromechanically interconnected with the other actuators, such as by using the same dielectric membrane where each single actuator is characterized by a localized electrode pattern. The actuation performance of each DEA can thus be influenced by neighboring units at each actuation stage. This additionally implies the ability to sense and reconstruct the state of multiple DEAs by just using local information. DEAs also feature intrinsic nonidealities such as snap-through dynamics, large deformation, viscoelasticity and electromechanical actuation [6]. This makes it challenging to develop numerically-efficient and accurate models, as well as automatic control strategies to impose a desired level of performance. This work investigates the development of a closed-loop control policy able to tackle the presented challenges with the aim of regulating a DEA array to a desired configuration. The energy-based controllers explored in [7] represent the starting framework that is expanded with robustifying actions. Leveraging important physical properties of the system, such as passivity, the developed control law exploits energetic considerations to naturally provide stability guarantees to the resulting autonomous closed-loop system. The shaping of the system's potential energy is enforced through the control action to ensure stability of the desired regulation set-point. A port-Hamiltonian formulation of the system model is employed to facilitate the development of a controller as a separate dynamical system respecting interconnection properties. Design conditions where stability of the system is addressed by considering its total mechanical energy are presented in a convex linear matrix inequality framework, based on a quasi linear parameter-varying alternative formulation of the system model. Lastly, an integral controller that preserves the passivity properties of the closed-loop interconnection despite being linked to a non-passive output is used to provide robustness to constant perturbations.
The manuscript is organized as follows. In section 2 modeling insights of a 1-by-10 DEA actuator array are provided. Section 3 explores the layout of the design conditions for the stabilizing section of the controller as well as the robust integral controller applied to the system. Lastly, in Section 4 simulation results are presented.

2 Modeling

We start the analysis of the system model leveraging on an experimentally validated control-oriented model of a smaller 1-by-3 DEA array shown in **Figure 1** [8], which is subsequently expanded to a 1-by-10 line array.

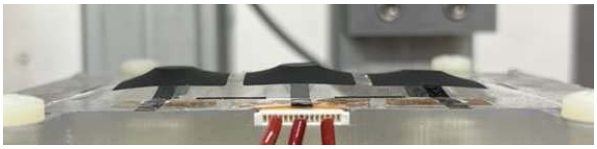


Figure 1 1-by-3 experimental DEA array platform employed in [8].

The dynamics equations of motion of a single DEA unit can be defined as

$$\begin{cases} \dot{p}_i = -\dfrac{\partial \mathcal{V}_{p,i}}{\partial q_i} - c_i p_i - \displaystyle\sum_{j \in \mathcal{N}_{c,i}} k_{c,i}(q_i - q_j) \\ \qquad -k_{v,i}(q_i - \xi_i) + b_i u_i, \\ \dot{q}_i = \dfrac{p_i}{m_i}, \\ \dot{\xi}_i = -\dfrac{k_{v,i}}{\eta_i}(\xi_i - q_i), \end{cases} \tag{1}$$

where p_i, q_i, ξ_i and u_i are, respectively, the momentum, the vertical displacement, the internal viscoelastic variable and the actuation input of the i-th DEA; $\mathcal{V}_{p,i}$ is the potential energy associated to the i-th DEA, here approximated as a 4-th order polynomial of the form $\mathcal{V}_{p,i}(q_i) = k_{0,i} + \frac{k_{1,i}}{2} q_i^2 + \frac{k_{2,i}}{3} q_i^3 + \frac{k_{3,i}}{4} q_i^4$; $m_i, c_i, k_{c,i}, k_{v,i}, \eta_i, b_i$ are, respectively, the mass, the linear damping coefficient, the coupling stiffness, the viscoelastic stiffness, the viscoelastic damping coefficient and the input coefficient of the i-th DEA; $\mathcal{N}_{c,i}$ is the set of all DEAs neighboring the i-th DEA. The stiffness coefficients are constrained so that $k_{4,i} \geq 0$ to preserve radial unboundedness of the potential energy. The formulation allows to write the overall interconnected system as a multi-input, multi-output port-Hamiltonian system where the total mechanical energy takes the form

$$\mathcal{H}(x) = \sum_{i=1}^{n} \left(\mathcal{H}_i(x) + \sum_{j \in \mathcal{N}_c} \mathcal{H}_{l,ij}(x) \right), \tag{2}$$

with $\mathcal{H}_i(x)$ being the Hamiltonian function of the i-th DEA and $\mathcal{H}_{l,ij}(x)$ the Hamiltonian function describing the potential energy stored in the interconnection between the i-th and j-th DEA. Given $W = W^T \in \mathbb{R}^{n \times n}$ as the adjacency matrix describing the interconnected system in a graph-oriented fashion

$$W_{ij} = \begin{cases} 1 & \text{if } i \text{ is adjacent to } j, \\ 0 & \text{otherwise,} \end{cases} \tag{3}$$

the two energy contribution can be defined as

$$\mathcal{H}(p_i, q_i, \xi_i) = \frac{p_i^2}{2m_i} + \mathcal{V}_{p,i}(q_i) + \frac{k_{v,i}}{2}(q_i - \xi_i)^2, \tag{4}$$

$$\mathcal{H}_{l,ij}(q_i, q_j) = W_{ij} \frac{k_{l,ij}}{2} (q_i - q_j)^2. \tag{5}$$

We now let $x = [p^T, q^T, \xi^T]^T$ with $p = [p_1, \dots, p_n]^T, q = [q_1, \dots, q_n]^T, \xi = [\xi_1, \dots, \xi_n]^T, u = [u_1, \dots, u_n]^T, d = [d_1, \dots, d_n]^T$ being the stacked vectors collecting the states, input and matched disturbances of each actuator, $M = \mathrm{diag}([m_1, \dots, m_n]^T), K_j = \mathrm{diag}([k_{j,1}, \dots, k_{j,n}]^T), j = 1,2,3, C = \mathrm{diag}([c_1, \dots, c_n]^T), B = \mathrm{diag}([b_1, \dots, b_n]^T), K_v = \mathrm{diag}\left([k_{v,1}, \dots, k_{v,n}]^T\right), R_v = \mathrm{diag}([\eta_1^{-1}, \dots, \eta_n^{-1}]^T)$ and the weighted Laplacian matrix $L = L^T \in \mathbb{R}^{n \times n}$

$$L_{ij} = \begin{cases} \displaystyle\sum_{k \in \mathcal{N}_{c,i}} k_{l,ik} & \text{if } i = j \\ -k_{l,ik} & \text{if } i \neq j \text{ and } j \in \mathcal{N}_{c,i} \\ 0 & \text{otherwise,} \end{cases} \tag{6}$$

and notice that the total mechanical energy of the system can be redefined as

$$\mathcal{H}(p, q, \xi) = \mathcal{V}(q, \xi) + \mathcal{T}(p), \tag{7}$$

$$\mathcal{V}(q, \xi) = \frac{1}{2} q^T (K_1 + L) q + \frac{1}{3} \sum_{i=1}^{n} k_{2,i} q_i^3 + \frac{1}{4} \sum_{i=1}^{n} k_{3,i} q_i^4 + \frac{1}{2} (q - \xi)^T K_v (q - \xi), \tag{8}$$

$$\mathcal{T}(p) = \frac{1}{2} p^T M^{-1} p, \tag{9}$$

Leading to a compact form of the equations of motion

$$\dot{x} = (J - R) \nabla \mathcal{H}(x) + G(u + d), \tag{10}$$

where $J = -J^T$; $R = R^T \geq 0$; $G = [B^T, 0, 0]^T$.

3 Control design

The control design problem relative to the stabilization of an arbitrary feasible configuration q^* while imposing a desired stiffness pattern to the DEA array is solved by means of IDA-PBC methods [9], in which the control action is used to modify the total Hamiltonian energy of the system so that it approximates a desired one.

In this work, we address the stabilization of a stationary point $x^* = \left[0, q^{*T}, q^{*T}\right]^T$ through the design of a linear controller that addresses and regularizes the snap-through behavior of the system. Moreover, to allow for controller implementation in large-scale scenarios where it would be computationally cumbersome for a single centralized unit to compute all control action, we impose a network-like structure to the feedback control gain. This allows for the computation of the control input of each DEA using only local information, such as the state of the DEA itself and of its neighbours. We assume this to be realized by means of simple communication protocols between the controllers of each DEA unit or by self-sensing techniques, which are a topic of interest in the recent literature.

By defining $w = B^{-1} q, w^* = B^{-1} q^*, K_c = K_c^T \in \mathbb{R}^{n \times n}, K_d = K_d^T \succcurlyeq 0, K_d \in \mathbb{R}^{n \times n}$, and

$$\mathcal{V}_c = \frac{1}{2}(w - w^*)^T K_c (w - w^*) + w^T \nabla_q \mathcal{V}(q^*) - \mathcal{V}(q^*), \tag{11}$$

$$u = -\nabla_w \mathcal{V}_c(w) - B^{-1} K_d M^{-1} p + u_{IC}. \tag{12}$$

u_{IC} represents the robustifying control action that will be developed separately.

 DOI: 10.30420/456743058

Lemma 1: with choice (12), if $\mathcal{V}_d = \mathcal{V} + \mathcal{V}_c$ is bounded from below and the following hold:

$$K_d \succcurlyeq 0 \tag{13}$$
$$\nabla_q \mathcal{V}_d(q^*) = 0 \tag{14}$$
$$\nabla_q^2 \mathcal{V}_d(q) \succ 0, \tag{15}$$

then $x^* = \left[0, q^{*T}, q^{*T}\right]^T$ is a globally asymptotically stable (GAS) equilibrium for system (10) and the port-Hamiltonian structure is preserved in closed-loop.

Proof: The proof directly follows from letting $\mathcal{H}_d = \mathcal{H} + \mathcal{V}_c$. The equivalent unperturbed closed-loop system takes the form

$$\dot{x} = (J - R_d)\nabla\mathcal{H}_d(x), \tag{16}$$

where

$$R_d = R + \begin{bmatrix} K_d & 0 & 0 \\ 0 & 0 & 0 \\ 0 & 0 & 0 \end{bmatrix}; \tag{17}$$
$$\nabla\mathcal{H}_d = \begin{bmatrix} M^{-1}p \\ \nabla_q \mathcal{V}_d \\ \nabla_\xi \mathcal{V}_d \end{bmatrix}. \tag{18}$$

(14) now implies that x^* is a minimum of the new potential energy of closed-loop system (16). In particular, this minimum is unique due to convexity of the potential energy as enforced by (15). ■

To minimize the norm of the proportional gain K_c, we define the following LMI

$$\begin{bmatrix} \gamma I & K_c^T \\ K_c & \gamma I \end{bmatrix} \succcurlyeq 0, \tag{19}$$

where $\gamma > 0$ is a parameter representing the upper bound for the Euclidean norm of K_c. For stability reasons, we additionally impose a lower bound on the overall minimum stiffness of the system as

$$\nabla_q^2 \mathcal{V}_d(q, K_c) \geq k_{min} I, \tag{20}$$

with $k_{min} > 0$ being an arbitrarily chosen scalar bounding the Hessian of the potential energy. To solve the stated problem in a convex fashion, we parametrize the gradient of the stiffness potential in the following way for the i-th DEA:

$$\nabla_q \mathcal{V}_{p,i}(q_i) = k_i(q_i) q_i, \tag{21}$$

where stiffness k_i can be bounded as $\underline{k_i} \leq k_i(q_i) \leq \overline{k}_i$ corresponding to the values $\left[\underline{q_i}, \overline{q}_i\right]$ assumed by the state variable. The 2^n resulting combinations of the stiffness vector $k(q)$ evaluated in these points correspond to the vertex of a polyhedron that bounds it, defined as $\mathcal{Q} = \{v \in \mathbb{R}^n | v_i \in \{\underline{k_i}, \overline{k}_i\}, \forall i = 1, \dots n\}$. Evaluation of the nonlinear stiffness in the vertex points in a quasi-LPV fashion provides a way to cast matrix inequalities (19), (20) as convex inequalities. The overall problem for the computation of the linear feedback gain K_c can thus be formulated as

$$\min_{K_c, \gamma} \gamma \tag{22}$$
$$\text{s.t.} \quad K_{tot}(q, K_c) \succcurlyeq k_{min} I \tag{23}$$
$$\begin{bmatrix} \gamma I & K_c^T \\ K_c & \gamma I \end{bmatrix} \succcurlyeq 0 \tag{24}$$
$$\forall q \in \mathcal{Q}.$$

We freely choose the damping matrix such that $K_d \succcurlyeq 0$. To additionally tackle steady state errors and constant disturbances, we follow the method in [10] to implement an integral controller that preserves passivity of the interconnection even in the case of non-passive outputs. It is immediate to see that the natural passive output of system (10) is defined as

$$y = G^T \nabla\mathcal{H}_d = B^T M^{-1} p, \tag{25}$$

which is related to the velocity of each DEA and does not include information on their positions q. Any kind of integral action that is wrapped around the passive output (25) to preserve the port-Hamiltonian structure would not be able to account for steady-state errors in the coordinates q. Following [10], we consider the following partition:

$$J = \begin{bmatrix} J_{aa} & J_{au} \\ -J_{au}^T & J_{uu} \end{bmatrix}, J_{aa} = 0,$$
$$J_{au} = [-I, 0], J_{uu} = \begin{bmatrix} 0 & 0 \\ 0 & 0 \end{bmatrix}, \tag{26}$$
$$R_d = \begin{bmatrix} R_{aa} & R_{au} \\ R_{au}^T & R_{uu} \end{bmatrix}, R_{aa} = C + K_d,$$
$$R_{au} = [0, 0], R_{uu} = \begin{bmatrix} 0 & 0 \\ 0 & R_v \end{bmatrix}, \tag{27}$$

and define the additional control action and integral state

$$u_{IC} = B^{-1}(C + K_d - R_{IC} - R_{IC2})M^{-1}p - R_{IC1}K_{IC}(p - x_{IC}), \tag{28}$$
$$\dot{x}_{IC} = -R_{IC2}\nabla_p \mathcal{H}_d + (J_{au} - R_{au})\left[\nabla_q \mathcal{H}_d^T, \nabla_\xi \mathcal{H}_d^T\right]^T. \tag{29}$$

By writing an extended set of coordinates, it is possible to write the overall closed-loop system in the form

$$z = \begin{bmatrix} p \\ q \\ \xi \\ p - x_{IC} \end{bmatrix}, \tag{30}$$
$$\dot{z} = (J_{cl} - R_{cl})\nabla\mathcal{H}_{cl}(z) + G_{cl} d, \tag{31}$$

where

$$G_{cl} = [B^T, 0, 0, B^T]^T, \tag{32}$$

 DOI: 10.30420/456743058

$$J_{cl} = \begin{bmatrix} J_{aa} & J_{au} & 0 \\ -J_{au}^T & J_{uu} & 0 \\ 0 & 0 & 0 \end{bmatrix}, \tag{33}$$

$$R_{cl} = \begin{bmatrix} R_{IC1} + R_{IC2} & R_{au} & R_{IC} \\ R_{au}^T & R_{uu} & 0 \\ R_{IC1} & 0 & R_{IC1} \end{bmatrix}, \tag{34}$$

$$\mathcal{H}_{cl}(z) = \mathcal{H}_d(x) + \frac{1}{2} K_{IC} z^2. \tag{35}$$

Implementation of control law (28) explicitly requires knowledge of the internal viscoelastic state vector ξ, which is not measurable in practice. For simplicity and conciseness, we assume in this work that the state ξ is known at each time instant. Despite the estimation of a similar quantity being a significant challenge in long-term operation, in short-term application scenarios like the presented one the problem can be circumvented by the application of observer techniques that preserve the port-Hamiltonian structure [11], which will not be explored in this paper.

4 Results

In this section, we present simulation results linked to the controllers previously proposed. The system is simulated by implementing the model and the dynamical controller on *Matlab2025b* and *Simulink*. A virtual, high-fidelity 1-by-10 DEA array simulated with finite element methods is taken as a reference for identification of model (10). As can be seen from **Figure 2**, the lumped-parameter model shows a pattern of snap-through dynamics, implying the presence of unstable actuation regions. In the case of simultaneous actuation of neighboring DEAs (cf. **Figure 3**), it is noticeable the variation in the time and amplitude of the snap-through thresholds, as well as a more general coupling in the relative displacements. The control action is always restricted to the rescaled range $u \in [0, 9]$ kV^2 to better represent realistic scenarios constrained by common commercially available high-voltage amplifiers.

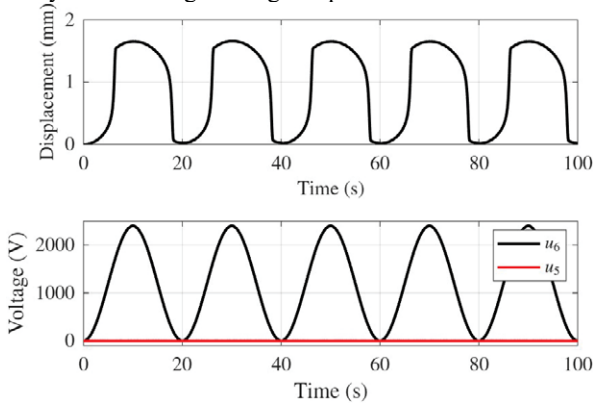


Figure 2 Relative displacement of DEA 6 in response to an open-loop actuation signal to DEA 6 only.

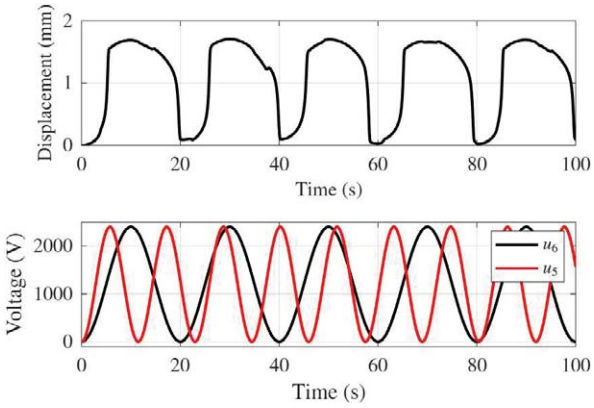


Figure 3 Relative displacement of DEA 6 in response to an open-loop actuation signal to DEA 6 and the neighboring DEA 5.

The reference setpoint q^* is randomly generated and tested as an admissible reference by imposing the normalized constraint

$$0 \leq B^{-1} \nabla_q \mathcal{V}(q^*) \leq 1, \tag{36}$$

to respect inherent actuation limits. We consider $q^* = [0.56, 0.21, 0.78, 0.47, 1.42, 1.24, 1.06, 0.37, 0.48, 0.62]$ mm. We impose a safety minimum stiffness bound of $k_{min} = 0.5$ N/mm. We furthermore impose a simple damping injection of $K_d = 0.01I$. We set the integral controller gains as $R_{c1} = 0.05I, R_{c2} = I, K_i = 20I$. After solving the optimization problem presented in the previous section, the system in closed loop is simulated with the designed control actions starting from an initial condition $x_0 = [0, 0, 0]^T$. As shown in **Figure 4**, the developed proportional controller with feedforward action can successfully bring each actuator to the desired configuration even in actuation ranges where the DEA units displayed unstable open-loop behavior (cf. **Figure 2** and **3**). Moreover, after the application of a constant disturbance at time $t = 30$s of -0.7N to DEA 4, 7, and 8, stability of the desired equilibrium q^* is respected.

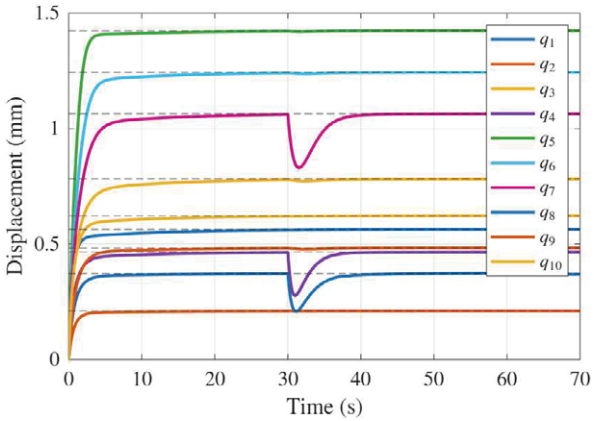


Figure 4 Relative displacement of each DEA unit in response to the application of the presented closed-loop control policy with constant disturbance $d = -0.7$N applied at $t = 30$s to DEAs n° 4, 7, 8.

5 Conclusions

In this work, we presented a control strategy aimed at robustly tackling set-point regulation problems for arrays of interconnected DEAs. Mutual cross-coupling actions, typical DEA nonlinearities such as snap-through dynamics and viscoelasticity were addressed with the design of an energy-shaping control action. Starting from a port-Hamiltonian, MIMO model of a 1-by-10 DEA array, a quasi linear parameter-varying approach was exploited along with convex conditions to synthesize the feedback gain matrix with stability guarantees. At the same time, a passivity-preserving integral action wrapped around a non-passive output was introduced to tackle steady-state errors in the position of the DEAs. Simulation results considering input saturation prove the feasibility of the presented technique in the presence of constant disturbances. Future works will envision validation of the proposed control strategy by means of experimental and/or high-fidelity frameworks.

6 Funding

Funded by the Deutsche Forschunggemeinschaft (DFG, German Research Foundation) under grant no. 424608471.

7 Literature

[1] Kofod, G. (2001). *Dielectric elastomer actuators*. Risø National Laboratory.

[2] He, T., Cui, L., Chen, C., & Suo, Z. (2010). Nonlinear deformation analysis of a dielectric elastomer membrane–spring system. *Smart Materials and Structures*, *19*(8), 085017.

[3] Akbari, S., & Shea, H. R. (2012). An array of 100 μm× 100 μm dielectric elastomer actuators with 80% strain for tissue engineering applications. *Sensors and Actuators A: Physical*, *186*, 236-241.

[4] Youn, J. H., Jang, S. Y., Hwang, I., Pei, Q., Yun, S., & Kyung, K. U. (2025). Skin-attached haptic patch for versatile and augmented tactile interaction. *Science Advances*, *11*(12), eadt4839.

[5] Gareis, M., & Maas, J. (2023). Wave field synthesis using buckling dielectric elastomer transducers. *Smart Materials and Structures*, *32*(12), 125024.

[6] Gu, G. Y., Gupta, U., Zhu, J., Zhu, L. M., & Zhu, X. (2017). Modeling of viscoelastic electromechanical behavior in a soft dielectric elastomer actuator. *IEEE Transactions on Robotics*, *33*(5), 1263-1271.

[7] Priuli, A., Addario, S., Zemlin, B., Heppe, J., Seelecke, S., & Rizzello, G. (in press). Energy-based cooperative control of dielectric elastomer actuator arrays. In *2026 IEEE International Symposium on Industrial Electronics (ISIE)*. IEEE.

[8] Priuli, A., Addario, S., Schultes, G., Seelecke, S., & Rizzello, G. (2025, July). Control-Oriented Energy-Based Modeling of Cooperative Dielectric Elastomer Actuator Arrays. In *2025 IEEE/ASME International Conference on Advanced Intelligent Mechatronics (AIM)* (pp. 1-6). IEEE.

[9] Ramírez, H., Sbarbaro, D., & Ortega, R. (2009). On the control of non-linear processes: An IDA–PBC approach. *Journal of Process Control*, *19*(3), 405-414.

[10] Ferguson, J., Donaire, A., Ortega, R., & Middleton, R. H. (2017). New results on disturbance rejection for energy-shaping controlled port-Hamiltonian systems. *arXiv preprint arXiv:1710.06070*.

[11] Venkatraman, A., & Van Der Schaft, A. J. (2010). Full-order observer design for a class of port-Hamiltonian systems. *Automatica*, *46*(3), 555-561.

 DOI: 10.30420/456743059

Engineering Liquid Crystal Elastomer Fibers for the Next Generation of Soft Robotics: A Comparative Analysis of Fabrication Techniques

Manuel Reis Carneiro 1,2, †*, Rafael Molter 2, Aníbal T. de Almeida 2, and Mahmoud Tavakoli 2,*

1 - Soft Machines Lab, Department of Mechanical Engineering, Carnegie Mellon University, Pittsburgh, PA 15213, USA
2 - Institute of Systems and Robotics, Department of Electrical and Computer Engineering, University of Coimbra, Coimbra 3030-290, Portugal
† - Current affiliation is: Biomedical and Mobile Health Technology Lab, Department of Health Sciences and Technology, ETH Zürich, Zürich 8008, Switzerland
* manuel.reiscarneiro@hest.ethz.ch ; mahmoud@isr.uc.pt

Abstract

Liquid Crystal Elastomers (LCEs) are an emerging class of polymer-based actuators valued for their simple operation and printability. However, bulk LCEs exhibit low efficiency because external stimuli such as heat or light struggle to penetrate the material. This has motivated the development of LCE fibers, which offer higher surface-to-volume ratio and a bioinspired architecture analogous to muscle fibers. LCE fibers can improve actuation efficiency, force output, and response time compared to bulk LCE. This paper presents the development and comparative analysis of four fabrication methods for LCE fibers—manual extrusion, 3D-printer-based extrusion, electrospinning, and mold injection—aimed at mimicking muscle-like functionality for soft robotics and assistive devices. Fibers produced by each method were fabricated and evaluated for actuation performance, with electrospinning yielding the highest stroke. Challenges in synthesis were addressed through an optimized rapid preparation route for LCE ink. Overall, the results highlight the potential of LCE fibers to enable more efficient, scalable, and adaptable soft-robotic actuators.

1 Introduction

The pursuit of biomimetic materials that replicate the dynamic behavior of human muscle remains a central challenge in soft robotics and materials science. Human muscle fascicles combine high strain (up to 40%), moderate stiffness (10–60 MPa), and substantial force generation (0.35 MPa) [1]. Liquid Crystal Elastomers (LCEs) have emerged as promising artificial-muscle candidates due to their reversible shape change and mechanical robustness [2], [3], [4], [5], [6], enabling applications in soft robotics [7], [8], prosthetics [9], [10], and wearable systems [11], [12]. Advances in soft materials have produced systems capable of electrical conduction [13], [14], [15], [16], sensing [17], [18], [19], [20], [21], [22], [23], [24], [25], [26], [27], [28], [29], [30], [31], and actuation [7], [32], [33], [34], [35], [36], [37], [38], [39], with LCEs attracting particular interest for their large, reversible deformations under external stimuli [4], [40], [41], [42], [43].

However, bulk LCE actuators suffer from low efficiency because their low surface-to-volume ratio limits heat or light penetration. LCE fibers address this limitation by increasing stimulus accessibility and improving heat dissipation, while also offering a bioinspired architecture analogous to muscle fascicles. Yet current fiber-fabrication methods face challenges in miniaturization, scalability, uniformity, and integration of sensing elements [11], [44], [45], [46], [47], [48], [49]. Actuation requires mesogen alignment in the nematic state, which is lost upon heating to the isotropic state [4][50]. Stronger initial alignment yields larger contractions, motivating the use of alignment techniques such as mechanical stretching [51], field-assisted alignment using electric or magnetic fields [52][53], surface alignment via microgrooves, and photoalignment for thin films [53] . Shear-induced alignment during extrusion-based methods such as DIW and 3D printing [2], [7], [8], [54], [55], [56], [57], [58], [59] also plays a key role, though nozzle diameter and rheology strongly influence alignment quality [4][60]. In this work, as shown in Figure 1,we refine the LCE synthesis method from [8] to obtain a more homogeneous ink and evaluate four fabrication routes for LCE fibers: manual extrusion, DIW extrusion, mold injection, and electrospinning. Mold injection additionally benefits from surface-guided alignment, and we

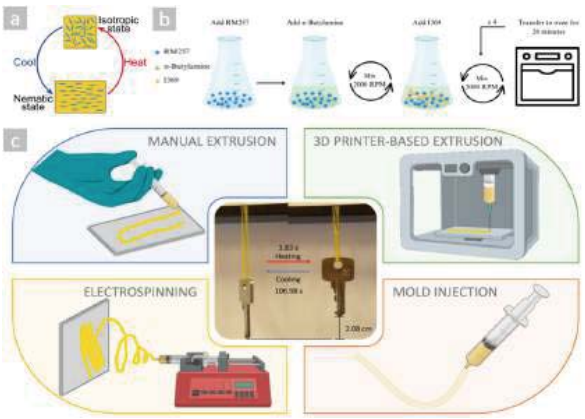


Figure 1 a) Liquid crystals transition between nematic and isotropic states under external stimuli, producing macroscopic deformation in the LCE. b) LCE synthesis workflow: the monomer and chain extender are mixed, the photoinitiator is added, and the mixture is placed in a 60 °C oven for 80 minutes with re-mixing every 20 minutes. c) The four LCE fiber-fabrication methods evaluated in this work: manual extrusion, direct-ink-writing extrusion, electrospinning, and mold injection into a silicone tube.

 DOI: 10.30420/456743059

explore field-assisted alignment using a current-carrying coil. Electrospinning is studied in both gap and magnetic-field-assisted configurations. Fibers produced by all methods are characterized in terms of mechanical behavior, actuation performance, repeatability, scalability, and fabrication simplicity.

2 Results

2.1 LCE Synthesis and ink preparation

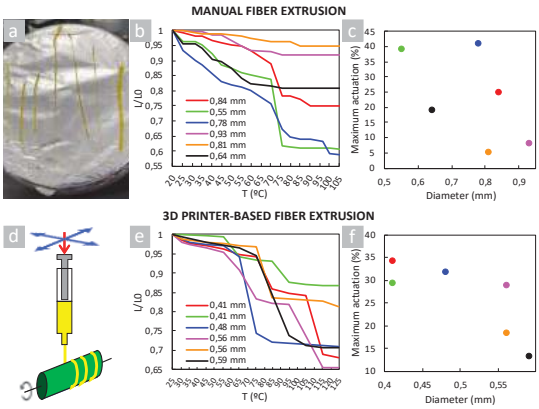
The LCE formulation was refined relative to our previous work[8] , yielding a more homogeneous ink (Figure S1) and a more repeatable synthesis. The monomer RM257 is first placed in a glass vial, followed by the dropwise addition of the chain extender (n-butylamine) at a 1.1:1 molar ratio. After mixing at 2000 RPM for 3 minutes, the photoinitiator I369 (4 wt%) is added and the mixture is stirred for an additional 3 minutes. The vial is then placed in a drying oven at 80 °C for 80 minutes to ensure uniform, controlled heating. Every 20 minutes, the solution is briefly re-mixed for 3 minutes and returned to the oven. This procedure, illustrated in Figure 1b, replaces the earlier hotplate-based approach used in [8] , which produced uneven heating, residual monomer, and viscosity inconsistencies. The temperature-controlled method eliminates these issues, producing a smooth, lump-free ink with fully incorporated RM257, as shown in Figure A1.

2.2 Fiber fabrication & characterization

Manual extrusion: Manual extrusion was used to produce LCE fibers by diluting the ink, extruding it through a syringe, and UV-curing the resulting filaments (Figure 2a). Most fibers stopped contracting near 90 °C, consistent with reaching the nematic–isotropic transition (Figure 2b). The average maximum contraction was 22.97%, with a best case of 40.99% (Table A1). A moderate negative correlation between diameter and actuation (r = –0.56) was observed, reflecting the competing effects of syringe speed and applied force on mesogen alignment. Because these parameters vary unpredictably during manual extrusion, fiber performance was highly inconsistent, with a large standard deviation of 15.08% (coefficient of variation 0.66). Despite its simplicity and speed, the method lacks reproducibility and is unsuitable for reliable fiber fabrication.

3D printer-based extrusion: For automated fabrication, the LCE ink was extruded through a heated reservoir and nozzle on a Hydra 21 3D printer, with a rotating collector drawing the filament and UV light initiating partial curing (Figure 2d). After printing, fibers were stretched by 30% to align the mesogens and fully UV-cured. The resulting fibers had an average diameter of 0.502 ± 0.080 mm. Actuation tests (Figure 2e) showed continued contraction at 90 °C, indicating a higher nematic–isotropic transition temperature than in manually extruded fibers, consistent with increased cross-link density. The fibers achieved an average maximum stroke of 26.05%, with the best reaching 34.38%, particularly in thinner samples where shear-induced alignment is stronger (Figure 2f). Variability was substantially lower than in manual extrusion (SD = 8.25%,

Figure 2 *a) Manually extruded LCE fibers on a hotplate. b) Normalized length–temperature response of manually extruded fibers. c) Correlation between fiber diameter and maximum actuation for manual extrusion. d) 3D-printer-based extrusion setup with roller-based fiber collection. e) Normalized length–temperature response of 3D-printed fibers. f) Relationship between 3D-printed fiber diameter and maximum actuation.*



CV = 0.32), demonstrating the benefit of controlled printing parameters. Mechanical testing yielded a Young's modulus of 14.75 ± 5.55 MPa, comparable to biological muscle. The best fiber supported a maximum stress of 22.70 MPa - far exceeding the ~1.3 MPa reported by Roach et al. [11] - and its maximum strain also surpassed the 130% previously reported.

Electrospinning and alignment strategies:

Electrospinning enables the fabrication of micro- and nanofibers by drawing a polymer jet toward a grounded collector under a high-voltage electric field while the solvent evaporates [61]. Using the setup in Figure 3a, diluted LCE ink was electrospun and UV-cured during deposition to preserve mesogen alignment. Initial tests showed that applied voltage influenced fiber diameter, consistent with prior reports [62], [63], [64], [65]: higher voltages produced thicker fibers, while shorter spinning durations yielded slightly smaller diameters [66]. Electrospinning produced fibers far thinner than human muscle fibers (20–200 µm [1]), improving surface-to-volume ratio and stimulus penetration [17], [67]. However, fibers collected on aluminum foil adhered strongly, and PVA-based substrates produced randomly oriented mats, motivating the exploration of alignment techniques.

Two strategies were investigated. **Gap electrospinning** (Figure 4a) used parallel electrodes to direct fibers across an insulating gap [68]. Although alignment was inconsistent across voltages, two retrieved fibers (≈0.20 mm diameter) exhibited strong mesogen alignment and the highest strokes in this study, reaching 44.2% and 26.63% at 100 °C. **Magnetic-field-assisted electrospinning** (Figure 4d) introduced a radial Lorentz force to guide fiber orientation. This method produced macroscopically aligned meshes, though microscopic alignment degraded in later layers, requiring short spinning durations. Bundled fibers showed average contractions of 18.79% at 120 °C. While isolating single, well-aligned fibers remains challenging,

DOI: 10.30420/456743059

Figure 3 a) Electrospinning setup with UV lamp pointing at the spined jet for immediate curing of the fibers. Optical microscopy images of electrospun fibers with different applied voltages and test durations: b) 10 kV, 10 minutes, c) 12 kV, 2 minutes, d) 15 kV, 10 minutes

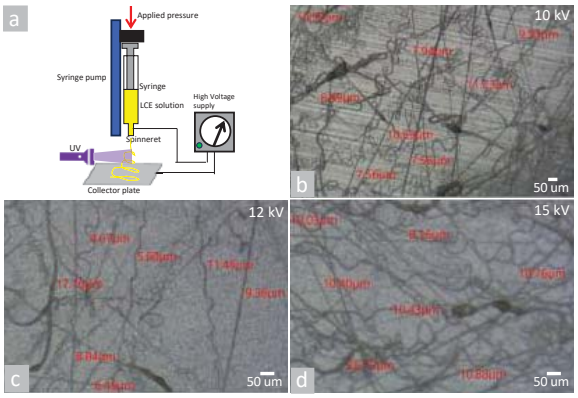
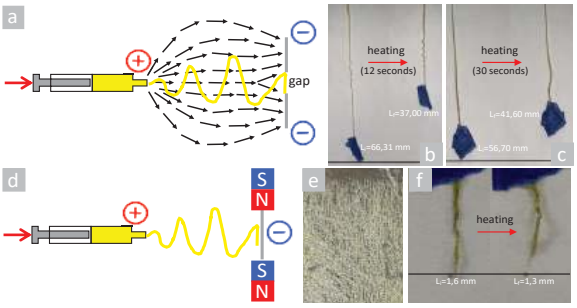


Figure 4 a) Gap-electrospinning setup. b–c) Actuating fibers produced via gap electrospinning. d) Magnetic-field-assisted electrospinning setup. e) Vertically aligned fibers obtained under magnetic-field assistance. f) Bundled MFAES fibers actuated after collection.



both approaches demonstrate the potential of electrospinning for producing high-performance, micrometer-scale LCE fibers suitable for compact wearable actuators.

Mold Injection: An unexpected observation during cleaning revealed that LCE cured inside tubing could be cleanly extracted after solvent-induced swelling, suggesting a simple route for producing highly uniform fibers (Figure 5a). This motivated a controlled mold-injection approach in which LCE ink was injected into silicone tubes and in situ (Figure 5c). The method produced long, highly uniform fibers, with the initial accidental sample showing a 1.07 mm diameter and a 13.50% contraction under 300 °C airflow (Figure 5b). Using 300 µm-diameter tubes and a precision dispenser, four fibers were fabricated and released after brief acetone swelling. Actuation tests at 120 °C yielded modest strokes (~5%), comparable to DIW-based fibers, but increasing the airflow temperature to 180 °C improved performance to an average of 14.66%, with a maximum of 17.14% (Table A4). These results indicate that added solvent raises the nematic–isotropic transition temperature and that injection pressure may influence alignment, though further experiments are needed to confirm this trend.

Figure 5 a) LCE fiber formed inside the tygon tube and removed after tube swelling in acetone. b) Actuation test of the extracted fiber under a 300 °C airflow. c) Setup for injecting LCE into a silicone tube using controlled pressure.

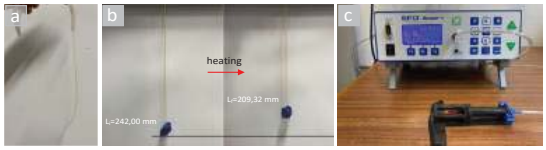
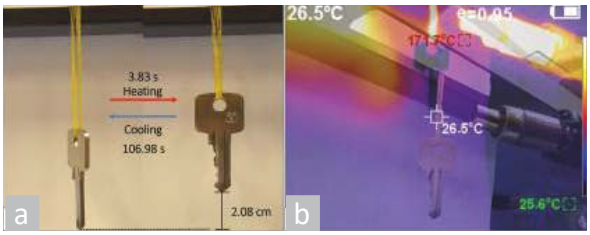


Figure 6 a) Bundle of extruded LCE fibers lifting a key, demonstrating a biomimetic muscle-like structure composed of multiple fiber fascicles; the bundle contracts up to 16.48%. b) Superimposed thermal images of the setup before and during actuation, showing heating by a heat gun.



2.3 Fiber Biomimetic Artificial Muscle through LCE fiber bundling

To show the biomimetism of the obtained LCE fibers, a long fiber extruded using the previously described 3D-printer-based extrusion was was folded in the middle 3 times to act as a bundle of 8 fibers, like human skeletal muscle, as shown in **Figure 6**. The artificial biomimetic muscle had a mass of 0.178 g and was attached to an 8g key, therefore each fiber was responsible for lifting a weight 5.62 times its own. The bundle was actuated by a heat gun at 172°C and was able to reversibly contract by 16.48%. From the recorded video, it was possible to calculate the actuation force at near-zero strain, by analyzing the video frames in Matlab. The acceleration was found to be 0.13 $m.s^{-2}$. The resultant force acting at the key is given by (1)

$$F_r = F_f - P_k , \qquad (1)$$

where F_f is the force exerted by the fibers and P_k is the weight of the key, which has a mass of 8g. The calculated F_f is 0.08 N. Considering an equal distribution of the force between the 8 fibers, each of them exerts 0.01 N at near zero strain. The actuation stress is then given by (2)

$$\sigma = F_f / A_f , \qquad (2)$$

where Af is the cross-section area of the fiber. A value of 50.52 kPa for the actuation stress is calculated, superior to previously reported LCE fiber also fabricated through 3D printer based extrusion[11], which demonstrated a maximum actuation stress of 38 kPa (0.5% strain, 80°C), and a force of 0.049 N in a bundle of 8 fibers. The total force result can be improved by adding more fibers. While this would increase the area necessary for the artificial muscle, this could be reduced by fabricating fibers with smaller diameters, as is the case for the fibers obtained from electrospinning or mold casting.

ISBN: 978-3-8007-6743-4

@ VDE VERLAG GMBH · Berlin · Offenbach

3 Discussion and Conclusion

Inspired by the fiber-based architecture of biological muscle, this work evaluated four fabrication strategies for liquid crystal elastomer (LCE) fibers—manual extrusion, 3D-printer-based extrusion, electrospinning, and mold injection—and demonstrated their potential for lightweight, compliant artificial muscles. A refined, temperature-controlled synthesis route produced a homogeneous LCE ink, overcoming the variability observed in earlier oligomerization attempts. Among the methods, manual extrusion offered simplicity and high contraction (~23%) but suffered from large variability and limited scalability. 3D-printing produced mechanically robust fibers with strains up to 240% and muscle-like modulus, making it suitable for wearable systems. Electrospinning achieved the smallest diameters and the highest actuation strokes, though isolating and aligning individual fibers remains a practical challenge. Mold injection proved the most scalable and consistent route, enabling long, uniform fibers with minimal parameter tuning, though solvent use increased the nematic–isotropic transition temperature. Overall, the four methods present complementary strengths: manual extrusion for rapid prototyping, 3D-printing for controlled geometries, electrospinning for high-performance microfibers, and mold injection for scalable production. The results show that LCE fibers can reach diameters far below those of human muscle, achieve contractions exceeding biological muscle, and generate forces several times their own weight. Future work should focus on scaling the mold-injection process and assembling multi-fiber bundles to realize fully functional biomimetic artificial muscles.

4 Appendix

Table S1 Actuation for the manually extruded fibers

Fiber diameter (mm)	Initial length (mm)	Final length (mm)	Max. actuation (%)
0.55	100.54	61.09	39.24
0.64	169.89	137.28	19.19
0.78	93.26	55.03	40.99
0.81	53	50.18	5.32
0.84	93.83	70.46	24.91
0.98	50.76	46.6	8.2

Table S2 Actuation for fibers extruded in 3D printer

Fiber diameter (mm)	Initial length (mm)	Final length (mm)	Max. actuation (%)
0.41	121.74	79.88	34.38
0.41	79.16	55.92	29.36
0.48	101.82	69.46	31.78
0.56	119.72	85.08	28.93
0.56	96.88	78.88	18.58
0.59	96.37	83.57	13.28

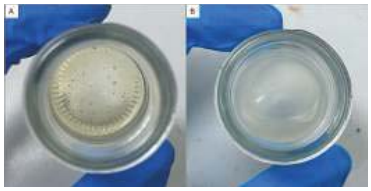
Table S3 Actuation for fibers obtained from magnetic field-assisted electrospinning

Initial length (mm)	Final length (mm)	Max. actuation (%)
1.5	1.25	16.66
1.3	1	23.08
1.6	1.3	18.75
1.2	1	16.66

Table S4 Actuation for mold-extruded fibers

Air pressure (bar)	Max. actuation (%)
5.0	17.14
6.0	17.07
6.5	13.33
6.5	11.11

Figure S1 Comparison between LCE inks produced using the previous synthesis method (a) and the improved method developed in this work (b), showing the enhanced homogeneity achieved with the updated process.



5 Acknowledgements

This work was supported by the Fundação para a Ciência e a Tecnologia through the Carnegie Mellon Portugal Program (SFRH/BD/150691/2020), by the CMU Portugal Exoskin project (CMU/TIC/0045/2021), and by the European Research Council under the Liquid3D grant (ERC 101045072).

6 Literature

[1] S. M. Mirvakili and I. W. Hunter, “Artificial Muscles: Mechanisms, Applications, and Challenges,” 2018. doi: 10.1002/adma.201704407.

[2] A. Kotikian, R. L. Truby, J. W. Boley, T. J. White, and J. A. Lewis, “3D Printing of Liquid Crystal Elastomeric Actuators with Spatially Programed Nematic Order,” *Advanced Materials*, vol. 30, no. 10, 2018, doi: 10.1002/adma.201706164.

[3] T. Guin *et al.*, “Layered liquid crystal elastomer actuators,” *Nat. Commun.*, vol. 9, no. 1, 2018, doi: 10.1038/s41467-018-04911-4.

[4] K. M. Herbert, H. E. Fowler, J. M. McCracken, K. R. Schlafmann, J. A. Koch, and T. J. White, “Synthesis and alignment of liquid crystalline elastomers,” 2022. doi: 10.1038/s41578-021-00359-z.

[5] A. J. J. Kragt, D. J. Broer, and A. P. H. J. Schenning, “Easily Processable and Programmable Responsive Semi-Interpenetrating Liquid Crystalline Polymer Network Coatings with Changing Reflectivities and Surface Topographies,” *Adv. Funct. Mater.*, vol. 28, no. 6, 2018, doi: 10.1002/adfm.201704756.

[6] G. Babakhanova *et al.*, “Liquid crystal elastomer coatings with programmed response of surface profile,” *Nat. Commun.*, vol. 9, no. 1, 2018, doi: 10.1038/s41467-018-02895-9.

[7] M. R. Vinciguerra, D. K. Patel, W. Zu, M. Tavakoli, C. Majidi, and L. Yao, "Multimaterial Printing of Liquid Crystal Elastomers with Integrated Stretchable Electronics," *ACS Appl. Mater. Interfaces*, vol. 15, no. 20, pp. 24777–24787, May 2023, doi: 10.1021/acsami.2c23028.

[8] J. Sgotti Veiga *et al.*, "Toward Fully Printed Soft Actuators: UV-Assisted Printing of Liquid Crystal Elastomers and Biphasic Liquid Metal Conductors," *Adv. Mater. Technol.*, no. 2300144, 2023, doi: https://doi.org/10.1002/admt.202300144.

[9] H. Lu, Z. Zou, X. Wu, C. Shi, Y. Liu, and J. Xiao, "Biomimetic prosthetic hand enabled by liquid crystal elastomer tendons," *Micromachines*, vol. 12, no. 7, 2021, doi: 10.3390/mi12070736.

[10] A. V. Maksimkin, T. Dayyoub, D. V. Telyshev, and A. Y. Gerasimenko, "Electroactive Polymer-Based Composites for Artificial Muscle-like Actuators: A Review," 2022. doi: 10.3390/nano12132272.

[11] D. J. Roach *et al.*, "Long Liquid Crystal Elastomer Fibers with Large Reversible Actuation Strains for Smart Textiles and Artificial Muscles," *ACS Applied Materials and Interfaces*, vol. 11, no. 21, 2019, doi: 10.1021/acsami.9b04401.

[12] M. Zhang, H. Shahsavan, Y. Guo, A. Pena-Francesch, Y. Zhang, and M. Sitti, "Liquid-Crystal-Elastomer-Actuated Reconfigurable Microscale Kirigami Metastructures," *Advanced Materials*, vol. 33, no. 25, 2021, doi: 10.1002/adma.202008605.

[13] Y. Zhao *et al.*, "A self-healing electrically conductive organogel composite," *Nat. Electron.*, 2023, doi: 10.1038/s41928-023-00932-0.

[14] F. M. Carvalho *et al.*, "Nondrying, sticky hydrogels for the next generation of high-resolution conformable bioelectronics," *ACS Appl. Electron. Mater.*, vol. 2, no. 10, 2020, doi: 10.1021/acsaelm.0c00653.

[15] W. Zu, Y. Ohm, M. Reis Carneiro, M. Vinciguerra, M. Tavakoli, and C. Majidi, "A Comparative Study of Silver Microflakes in Digitally Printable Liquid Metal Embedded Elastomer Inks for Stretchable Electronics," 2022, doi: 10.1002/admt.202200534.

[16] M. Reis Carneiro, C. Majidi, and M. Tavakoli, "Gallium-Based Liquid–Solid Biphasic Conductors for Soft Electronics," 2023. doi: 10.1002/adfm.202306453.

[17] M. Reis Carneiro, C. Majidi, and M. Tavakoli, "Multi-Electrode Printed Bioelectronic Patches for Long-Term Electrophysiological Monitoring," *Adv. Funct. Mater.*, 2022, doi: 10.1002/adfm.202205956.

[18] M. Tavakoli *et al.*, "3R Electronics: Scalable Fabrication of Resilient, Repairable, and Recyclable Soft-Matter Electronics," 2022, doi: 10.1002/adma.202203266.

[19] M. R. Carneiro and M. Tavakoli, "Wearable Pressure Mapping through Piezoresistive C-PU Foam and Tailor-Made Stretchable e-Textile," *IEEE Sens. J.*, vol. 21, no. 24, 2021, doi: 10.1109/JSEN.2021.3126159.

[20] M. R. Carneiro, L. P. Rosa, A. T. De Almeida, and M. Tavakoli, "Tailor-made smart glove for robot teleoperation, using printed stretchable sensors," *2022 IEEE 5th International Conference on Soft Robotics, RoboSoft 2022*, pp. 722–728, 2022, doi: 10.1109/ROBOSOFT54090.2022.9762214.

[21] M. Reis Carneiro, A. T. de Almeida, M. Tavakoli, and C. Majidi, "Recyclable Thin-Film Soft Electronics for Smart Packaging and E-Skins," *Advanced Science*, vol. n/a, no. n/a, p. 2301673, doi: https://doi.org/10.1002/advs.202301673.

[22] M. R. Carneiro, A. T. De Almeida, and M. Tavakoli, "Wearable and comfortable e-textile headband for long-term acquisition of forehead EEG signals," *IEEE Sens. J.*, pp. 1–1, 2020, doi: 10.1109/JSEN.2020.3009629.

[23] W. Wu, "Stretchable electronics: functional materials, fabrication strategies and applications," Jan. 01, 2019, *Taylor and Francis Ltd.* doi: 10.1080/14686996.2018.1549460.

[24] C. Pan, K. Kumar, J. Li, E. J. Markvicka, P. R. Herman, and C. Majidi, "Visually Imperceptible Liquid-Metal Circuits for Transparent, Stretchable Electronics with Direct Laser Writing," *Advanced Materials*, vol. 30, no. 12, 2018, doi: 10.1002/adma.201706937.

[25] R. Rocha, P. Lopes, A. T. De Almeida, M. Tavakoli, and C. Majidi, "Soft-matter sensor for proximity, tactile and pressure detection," in *IEEE International Conference on Intelligent Robots and Systems*, 2017. doi: 10.1109/IROS.2017.8206222.

[26] M. R. Carneiro, L. Rosa, and M. Tavakoli, "From Conventional Non-Conductive Foams to Soft Piezoresistive Pressure Sensors: A Low-Cost Approach to Large-Area Pressure-Mapping," in *2023 IEEE SENSORS*, 2023, pp. 1–4. doi: 10.1109/SENSORS56945.2023.10325315.

[27] M. Reis Carneiro, C. Majidi, and M. Tavakoli, "Gallium-Based Liquid–Solid Biphasic Conductors for Soft Electronics," *Adv. Funct. Mater.*, vol. 33, no. 41, p. 2306453, Oct. 2023, doi: 10.1002/ADFM.202306453.

[28] M. Reis Carneiro, M. Tavakoli, and C. Majidi, "Soft skin-interfacing electrodes for wearable bioelectronics," Oct. 01, 2025, *Cell Press*. doi: 10.1016/j.matt.2025.102409.

[29] M. R. Carneiro, L. Rosa, and M. Tavakoli, "From Conventional Non-Conductive Foams to Soft Piezoresistive Pressure Sensors: A Low-Cost Approach to Large-Area Pressure-Mapping," in *2023 IEEE SENSORS*, 2023, pp. 1–4. doi: 10.1109/SENSORS56945.2023.10325315.

[30] M. Reis Carneiro, T. Lopes, A. Silva, C. Majidi, and M. Tavakoli, "Micropatterned biphasic printed electrodes for high-fidelity on-skin bioelectronics," Oct. 2025. doi: 10.1002/adfm.202505419.

[31] N. Zavanelli *et al.*, "Intrinsically Soft Printed Electronics for Digitally Augmented Human Sensing and Vision," *Adv. Funct. Mater.*, 2025, doi: 10.1002/adfm.202519702.

[32] G. Peng, X. Fan, X. Liu, and L. Wang, "Design and Control of a Soft and Wearable Robotic Glove for Hand Rehabilitation," *Yiyong Shengwu Lixue/Journal of Medical Biomechanics*, vol. 34, no. 6, pp. 637–643, Dec. 2019, doi: 10.16156/j.1004-7220.2019.06.011.

[33] M. Duduta, E. Hajiesmaili, H. Zhao, R. J. Wood, and D. R. Clarke, "Realizing the potential of dielectric elastomer artificial muscles," *Proc. Natl. Acad. Sci. U. S. A.*, vol. 116, no. 7, pp. 2476–2481, Feb. 2019, doi: 10.1073/PNAS.1815053116.

[34] M. D. Bartlett *et al.*, "High thermal conductivity in soft elastomers with elongated liquid metal inclusions," *Proc. Natl. Acad. Sci. U. S. A.*, vol. 114, no. 9, pp. 2143–2148, Feb. 2017, doi: 10.1073/PNAS.1616377114.

[35] C. Pan *et al.*, "A Liquid-Metal–Elastomer Nanocomposite for Stretchable Dielectric Materials," *Advanced Materials*, vol. 31, no. 23, 2019, doi: 10.1002/adma.201900663.

[36] M. Reis Carneiro, C. Majidi, and M. Tavakoli, "Dielectric Elastomer Actuators with Biphasic Ag-EGaIn Electrodes," 2021, doi: 10.1002/adem.202100953.

[37] P. Won *et al.*, "3D Printing of Liquid Metal Embedded Elastomers for Soft Thermal and Electrical Materials," *ACS Appl. Mater. Interfaces*, vol. 14, no. 49, pp. 55028–55038, Dec. 2022, doi: 10.1021/ACSAMI.2C14815/SUPPL_FILE/AM2C14815_SI_004.MP4.

[38] E. Hajiesmaili and D. R. Clarke, “Dielectric elastomer actuators,” *J. Appl. Phys.*, vol. 129, no. 15, 2021, doi: 10.1063/5.0043959.

[39] H. Lu, Z. Zou, X. Wu, C. Shi, and J. Xiao, “Fabrication and Characterization of Highly Deformable Artificial Muscle Fibers Based on Liquid Crystal Elastomers,” *Journal of Applied Mechanics, Transactions ASME*, vol. 88, no. 4, 2021, doi: 10.1115/1.4049165.

[40] Y. Xiao, J. Wu, and Y. Zhang, “Recent advances in the design, fabrication, actuation mechanisms and applications of liquid crystal elastomers,” 2023. doi: 10.20517/ss.2023.03.

[41] Y. Xia, T. Mu, Y. He, Y. Liu, and J. Leng, “Fiber-reinforced liquid crystalline elastomer composite actuators with multi-stimulus response properties and multi-directional morphing capabilities,” *Composites Part B: Engineering*, vol. 256, 2023, doi: 10.1016/j.compositesb.2023.110640.

[42] J. Zhao, L. Zhang, and J. Hu, “Varied Alignment Methods and Versatile Actuations for Liquid Crystal Elastomers: A Review,” *Advanced Intelligent Systems*, vol. 4, no. 3, 2022, doi: 10.1002/aisy.202100065.

[43] Z. Z. Nie, M. Wang, and H. Yang, “Structure-induced Intelligence of Liquid Crystal Elastomers,” 2023. doi: 10.1002/chem.202301027.

[44] A. Sharma and J. P. F. Lagerwall, “Electrospun composite liquid crystal elastomer fibers,” *Materials*, vol. 11, no. 3, 2018, doi: 10.3390/ma11030393.

[45] J. Sun, Y. Wang, W. Liao, and Z. Yang, “Ultrafast, High-Contractile Electrothermal-Driven Liquid Crystal Elastomer Fibers towards Artificial Muscles,” *Small*, vol. 17, no. 44, 2021, doi: 10.1002/smll.202103700.

[46] S. J. D. Lugger, T. A. P. Engels, R. Cardinaels, T. Bus, D. J. Mulder, and A. P. H. J. Schenning, “Melt-Extruded Thermoplastic Liquid Crystal Elastomer Rotating Fiber Actuators,” *Advanced Functional Materials*, 2023, doi: 10.1002/adfm.202306853.

[47] Y. Wang, J. Sun, W. Liao, and Z. Yang, “Liquid Crystal Elastomer Twist Fibers toward Rotating Microengines,” *Advanced Materials*, vol. 34, no. 9, 2022, doi: 10.1002/adma.202107840.

[48] Y. B. Kim and D. S. Kim, “Understanding and Research Trends in Liquid Crystal Elastomer Fibers,” 2023. doi: 10.14478/ace.2023.1045.

[49] Y. Geng and J. P. F. Lagerwall, “Multiresponsive Cylindrically Symmetric Cholesteric Liquid Crystal Elastomer Fibers Templated by Tubular Confinement,” *Advanced Science*, vol. 10, no. 19, 2023, doi: 10.1002/advs.202301414.

[50] P. G. De Gennes, “Possibilites offertes par la reticulation de polymeres en presence d’un cristal liquide,” *Phys. Lett. A*, vol. 28, no. 11, 1969, doi: 10.1016/0375-9601(69)90584-2.

[51] H. Finkelmann, H.-J. Kock, and G. Rehage, “Investigations on liquid crystalline polysiloxanes 3. Liquid crystalline elastomers — a new type of liquid crystalline material,” *Die Makromolekulare Chemie, Rapid Communications*, vol. 2, no. 4, pp. 317–322, 1981, doi: https://doi.org/10.1002/marc.1981.030020413.

[52] Y. Sasaki *et al.*, “Polymer-Stabilized Micropixelated Liquid Crystals with Tunable Optical Properties Fabricated by Double Templating,” *Advanced Materials*, vol. 29, no. 37, 2017, doi: 10.1002/adma.201703054.

[53] Y. Wang, J. Liu, and S. Yang, “Multi-functional liquid crystal elastomer composites,” 2022. doi: 10.1063/5.0075471.

[54] W. Liao and Z. Yang, “3D printing programmable liquid crystal elastomer soft pneumatic actuators,” *Materials Horizons*, vol. 10, no. 2, 2022, doi: 10.1039/d2mh01001a.

[55] C. Luo, C. Chung, N. A. Traugutt, C. M. Yakacki, K. N. Long, and K. Yu, “3D Printing of Liquid Crystal Elastomer Foams for Enhanced Energy Dissipation under Mechanical Insult,” 2021. doi: 10.1021/acsami.0c17538.

[56] X. Song, W. Zhang, H. Liu, L. Zhao, Q. Chen, and H. Tian, “3D printing of liquid crystal elastomers-based actuator for an inchworm-inspired crawling soft robot,” *Frontiers in Robotics and AI*, vol. 9, 2022, doi: 10.3389/frobt.2022.889848.

[57] N. A. Traugutt, D. Mistry, C. Luo, K. Yu, Q. Ge, and C. M. Yakacki, “Liquid-Crystal-Elastomer-Based Dissipative Structures by Digital Light Processing 3D Printing,” *Advanced Materials*, vol. 32, no. 28, 2020, doi: 10.1002/adma.202000797.

[58] M. E. Prévôt *et al.*, “Physical Models from Physical Templates Using Biocompatible Liquid Crystal Elastomers as Morphologically Programmable Inks For 3D Printing,” *Macromolecular Bioscience*, vol. 23, no. 3, 2023, doi: 10.1002/mabi.202200343.

[59] S. J. D. Lugger, R. M. C. Verbroekken, D. J. Mulder, and A. P. H. J. Schenning, “Direct Ink Writing of Recyclable Supramolecular Soft Actuators,” *ACS Macro Letters*, vol. 11, no. 7, 2022, doi: 10.1021/acsmacrolett.2c00359.

[60] M. Charara, “Additive Manufacturing of Polydimethylsiloxane (PDMS)/Carbon Nanotube (CNT) Nanocomposite Sensors,” Gallogly College of Engineering, 2019.

[61] G. R. Williams, B. T. Raimi-Abraham, and C. J. Luo, “Electrospinning fundamentals,” in *Nanofibres in Drug Delivery*, UCL Press, 2018, pp. 24–59. doi: 10.2307/j.ctv550dd1.6.

[62] F. C. Chang, K. K. Chan, and C. Y. Chang, “The effect of processing parameters on formation of lignosulfonate fibers produced using electrospinning technology,” *BioResources*, vol. 11, no. 2, 2016, doi: 10.15376/biores.11.2.4705-4717.

[63] C. Zhang, X. Yuan, L. Wu, Y. Han, and J. Sheng, “Study on morphology of electrospun poly(vinyl alcohol) mats,” *European Polymer Journal*, vol. 41, no. 3, 2005, doi: 10.1016/j.eurpolymj.2004.10.027.

[64] S. S. Ray, S. S. Chen, N. C. Nguyen, and H. T. Nguyen, “Electrospinning: A Versatile Fabrication Technique for Nanofibrous Membranes for Use in Desalination,” in *Nanoscale Materials in Water Purification*, 2019. doi: 10.1016/B978-0-12-813926-4.00014-8.

[65] O. S. Yördem, M. Papila, and Y. Z. Menceloğlu, “Effects of electrospinning parameters on polyacrylonitrile nanofiber diameter: An investigation by response surface methodology,” *Materials and Design*, vol. 29, no. 1, 2008, doi: 10.1016/j.matdes.2006.12.013.

[66] Q. He *et al.*, “Electrospun liquid crystal elastomer microfiber actuator,” *Science Robotics*, vol. 6, no. 57, 2021, doi: 10.1126/scirobotics.abi9704.

[67] P. Lopes *et al.*, “Bi-Phasic Ag-In-Ga Embedded Elastomer inks for Digitally Printed, Ultra-Stretchable, Multi-Layer Electronics,” *ACS Appl. Mater. Interfaces*, vol. 13, no. 12, pp. 14552–14561, 2021, doi: 10.1021/acsami.0c22206. Epub 2021 Mar 10. PMID: 33689286.

[68] A. J. Robinson, A. Pérez-Nava, S. C. Ali, J. B. González-Campos, J. L. Holloway, and E. M. Cosgriff-Hernandez, “Comparative analysis of fiber alignment methods in electrospinning,” 2021. doi: 10.1016/j.matt.2020.12.022.

 DOI: 10.30420/456743060

Surface-dominated drying and crystallization effects in micropumps

Martin Richter, Mohammad Sheikhsarraf, Fraunhofer Institute for Electronic Microsystems and Solid State Technologies (EMFT), Munich, Germany, martin.richter@emft.fraunhofer.de

Abstract

Micropumps optimized for low dead volume and high compression ratio increasingly suffer from surface-dominated disturbance mechanisms that become critical at small scales. While classical disturbances such as trapped air bubbles, capillary menisci, or transported particles affect pump operation immediately and are comparatively well understood, slower physicochemical processes including crystallization, agglomeration, precipitation, and biofouling remain insufficiently investigated despite their major relevance for long-term reliability. In this work, drying- and storage-induced crystallization effects in liquid-filled micropumps are investigated as a representative example of such long-timescale surface-related disturbances. The drying behavior of highly miniaturized pump chambers was analyzed from the perspective of microscale wetting and diffusion-limited evaporation. It is shown that residual liquid remains trapped within wetted chamber corners even after prolonged gas flushing, because convective transport becomes ineffective at small dimensions. After evaporation of the solvent, non-volatile buffer components remain on the surfaces and gradually crystallize during storage. Experiments performed on thirteen micropumps filled with a pharmaceutical-like buffer solution resulted in complete valve sticking after several weeks of dry storage. A recovery method based on humidity-induced condensation cycles was developed to redissolve the crystallized residues and restore valve functionality without mechanical intervention. The results demonstrate that long-timescale surface-related processes can fundamentally limit micropump reliability and should be considered alongside classical operational disturbances during design, handling, and storage of highly miniaturized fluidic systems.

1 Introduction

Micropumps have become key components in numerous applications ranging from medical dosing systems and lab-on-chip platforms to analytical instrumentation and wearable devices. The increasing demand for miniaturization has led to pump architectures with extremely small chamber heights and minimized dead volumes in order to maximize compression ratio, improve bubble tolerance, and increase dosing precision [1]. However, these optimizations also shift the physical balance within the system. While technically usable forces such as displaced fluid volume or pressure generation scale approximately with the third power of the characteristic dimension, many disturbing effects scale predominantly with surface area. As dimensions decrease, surface-related mechanisms therefore become increasingly dominant.

Examples of such mechanisms include capillary forces, adhesion, air bubble retention, particle deposition, crystallization of dissolved components, and biofouling. In practical operation, these effects can strongly influence system reliability, particularly in pumps containing liquids with non-volatile components. Nevertheless, the interaction between drying processes, microscale wetting phenomena, and long-term storage behavior has received relatively little attention.

In conventional macroscopic systems, drying is often intuitively associated with convective flushing by air or nitrogen. However, this assumption becomes questionable at microscale dimensions. In narrow chambers with hydrophilic surfaces, liquid remains trapped in corners and near interfaces due to capillary wetting. In these regions, convective transport becomes ineffective and drying is governed mainly by evaporation and diffusion processes [2][3][5]. The present work investigates the drying and storage behavior of micropumps filled with buffer-containing liquids similar to those used in pharmaceutical formulations. Particular attention is given to the formation of salt residues after drying and their role in microvalve sticking. In addition, a recovery method based on controlled humidity and condensation cycles is presented. Beyond the specific application investigated here, the work aims to highlight a more general reliability mechanism associated with the increasing dominance of surface-related phenomena in miniaturized microfluidic systems.

2 Surface-Dominated Drying

2.1 Scaling of surface-related effects

Miniaturization fundamentally changes the relative importance of physical mechanisms within fluidic systems. Volumetric quantities such as displaced fluid volume or generated hydraulic energy scale approximately with the cube of the characteristic dimension, whereas surface-related interactions scale mainly with the square of the dimension. Consequently, the ratio between surface effects and volumetric effects increases significantly as dimensions decrease.

This scaling behavior has important implications for micropump operation. Many design strategies aim to minimize chamber height and dead volume in order to improve compression ratio and reduce sensitivity to compressible gas bubbles. However, the same geometric optimization simultaneously increases the influence of surface forces and surface-related disturbances. Residual wetting films, capillary retention, adhesion forces, and deposition processes can therefore become dominant factors determining long-term functionality.

ISBN: 978-3-8007-6743-4 @ VDE VERLAG GMBH · Berlin · Offenbach

 DOI: 10.30420/456743060

2.2 Wetting and liquid retention in microchambers

The micropumps investigated in this work contain hydrophilic chamber surfaces. When the pumps are filled with liquid, wetting occurs not only on planar surfaces but also within corners and narrow geometric features of the chamber and valve regions. Due to capillary forces, liquid remains trapped in these regions even after the main fluid volume has been removed.

After operation, the pumps were flushed with water and alcohol and subsequently dried using nitrogen flow. While gas flow efficiently removes liquid from larger open regions, essentially no convective replacement occurs inside narrow wetted corners. The capillary forces retaining the liquid exceed the forces generated by the gas flow by several orders of magnitude. As a result, the remaining liquid can only be removed by evaporation into the gas phase followed by diffusion of vapor toward the chamber center and outlet.

This situation resembles a microscale Stefan-type evaporation problem in which a moving liquid-vapor interface recedes slowly within confined geometries. The characteristic drying time therefore depends strongly on chamber dimensions, diffusion length, vapor concentration gradients, and ambient humidity.

2.3 Diffusion-limited drying

An analytical model combining evaporation and diffusion processes analogous to a confined Stefan-type moving boundary problem [6] was developed to estimate the characteristic drying time of the micropump chamber. The model predicts that complete drying requires several hours despite continuous gas flushing. Experimental measurements confirmed this prediction and demonstrated that the final drying phase is dominated by diffusion-controlled vapor transport rather than by convection.

The final drying phase was approximated by a one-dimensional diffusion-limited evaporation model. The vapor concentration at the liquid interface was assumed to correspond to saturation, whereas the vapor concentration at the outlet was determined by the ambient relative humidity. With $\Delta c = M(p_{\mathrm{sat}} - p_{\infty})/(RT)$, the characteristic evaporation time scales as

$$t_{\mathrm{dry}} \sim \frac{\rho L^2}{2D\Delta c} = \frac{L^2}{D}\frac{\rho RT}{2M(p_{\mathrm{sat}} - p_{\infty})}.$$

With the following parameters (see also figure 1):

- L(t): remaining liquid-filled length in the capillary at time t[m]
- L_0: Initial length of the liquid column [m]
- D: Diffusion coefficient of water vapor in air ($\sim 2.5 \times 10^{-5}\ \mathrm{m^2/s}$)
- M: Molecular mass of water (18×10^{-3} kg/mol)
- Δp: Partial pressure difference between the saturated water vapor concentration in the capillary and the surroundings [Pa]
- ρ: Density of water ($\sim 1000\ \mathrm{kg/m^3}$)
- R: Universal gas constant (8.314 J/(mol K))
- T: Temperature [K]
- t: Time [s]

This expression illustrates that the drying time is much longer than a simple molecular diffusion time L^2/D, because only a small vapor concentration gradient is available to remove the liquid mass. The results indicate that practical drying procedures based only on short gas flushing intervals are insufficient to completely remove residual liquid from highly miniaturized chambers. Even after apparently successful drying, non-volatile dissolved components remain on the surfaces after evaporation of the solvent. Figure 1 illustrates the calculated and experimentally verified drying behavior of the micropump chamber.

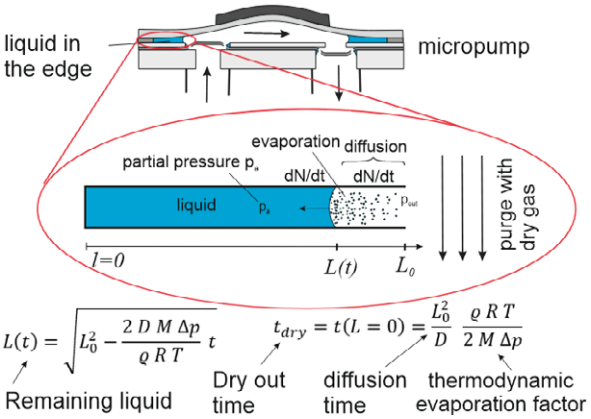


Figure 1 *The drying time for the micropump can be calculated using a model that combines evaporation and diffusion. This model was verified experimentally, it requires flushing times with dry air of several hours, depending on the dimensions of the pump chamber. However, non-volatile residues remain in the pump chamber.*

3 Residue Formation and Valve Sticking

The liquids used in the experiments contained dissolved buffer components comparable to those found in pharmaceutical formulations. After solvent evaporation, these dissolved substances remained on the chamber surfaces as solid residues. Particularly in the valve region, local accumulation of salts occurred during drying.

During storage, these initially amorphous residues gradually crystallized. The resulting crystalline structures generated strong sticking forces within the microvalves. After approximately six weeks of storage, all thirteen investigated micropumps exhibited severe sticking behavior and the valves could no longer be opened even by applying significant overpressure.

The observed mechanism differs from classical particle contamination or biofouling. Instead, the sticking originates from phase-transition-induced crystallization of previously dissolved non-volatile components. The phenomenon therefore represents a specific class of surface-related

 DOI: 10.30420/456743060

reliability problem associated with drying and storage processes in miniaturized fluidic systems. The observed sticking behavior is consistent with deposition and subsequent crystallization of non-volatile buffer residues near valve interfaces and wetted surfaces.

4 Experimental Methods

The investigated micropumps consisted of piezoelectrically actuated membrane pumps with integrated passive microvalves and highly miniaturized pump chambers. The pumps were filled with a buffer-containing liquid comparable to those used in insulin formulations.

Before the drying experiments, the pumps were flushed according to a defined cleaning protocol using deionized water followed by alcohol. Drying was subsequently performed using continuous nitrogen flow for approximately twelve hours. The dried pumps were then stored under ambient laboratory conditions.

To investigate recovery of stuck valves, a humidity-induced condensation setup was developed. The micropumps were placed inside a closed chamber partially filled with deionized water. The chamber was heated to approximately 50 °C to generate nearly 100 % relative humidity. Subsequent cooling caused condensation of water on the pump surfaces and within the valve regions. The condensation cycle was repeated multiple times.

Valve functionality was evaluated by applying defined overpressure and observing valve reopening behavior.

5 Results

5.1 Drying behaviour

The experimentally observed drying times were in good agreement with the analytical model. Although the bulk liquid was rapidly removed during gas flushing, residual liquid persisted within wetted chamber regions for extended periods. Complete evaporation required several hours, confirming that drying was limited primarily by diffusion-driven vapor transport. The experiments demonstrated that apparent macroscopic dryness does not imply complete removal of liquid from microstructured chambers.

5.2 Crystallization-induced sticking

After storage, all thirteen micropumps showed strong valve sticking. The valves could no longer be opened under normal operating conditions. The observed behavior is consistent with deposition and subsequent crystallization of non-volatile buffer residues near valve interfaces and wetted surfaces. Similar evaporation-driven deposition phenomena have been described in microfluidic systems and drying droplets in literature [4].

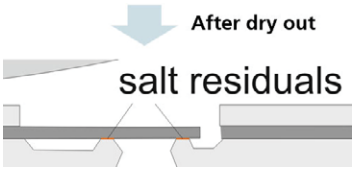


Figure 2 Schematic illustration: a*fter drying, salt residues from the buffer solution remain on the surfaces. After a storage time of several days, these residues crystallize and cause severe sticking.*

The results indicate that even very small amounts of residual dissolved substances can lead to severe functional impairment once crystallization occurs. Due to the small dimensions of the valve structures, relatively small crystalline forces are sufficient to immobilize the system.

5.3 Condensation based recovery

The humidity-induced condensation method successfully restored valve functionality in all investigated pumps. After a single condensation cycle, the valves could again be opened using small overpressure.

The recovery mechanism is attributed to diffusion of water vapor into the pump chamber followed by local condensation and redissolution of the salt crystals. In contrast to direct liquid injection, the vapor-based approach allows penetration into otherwise inaccessible dry regions.



Figure 3 *Setup for loosening the stuck valves: The valves are placed in a box partially filled with water and exposed to 100% humidity at an elevated temperature, then cooled, and the condensation is allowed to settle. This process is repeated a second time.*

The results demonstrate that the sticking phenomenon is reversible as long as the deposited material remains chemically stable and soluble.

6 Discussion

The present results also suggest a broader perspective on reliability mechanisms in highly miniaturized micropumps. Surface-related disturbances do not act on a single timescale but instead span a wide temporal range. Some disturbances occur immediately during operation, whereas others develop gradually over hours, days, or weeks.

ISBN: 978-3-8007-6743-4 @ VDE VERLAG GMBH · Berlin · Offenbach

 DOI: 10.30420/456743060

Classical disturbances such as trapped air bubbles, capillary menisci, or transported particles typically influence pump functionality instantaneously. Their effects appear directly during operation and are therefore relatively easy to identify experimentally. As a consequence, various engineering strategies have been developed over recent decades to maintain pump functionality in the presence of such disturbances. Examples include increasing the compression ratio to improve bubble tolerance, minimizing dead volume, implementing particle filters, or optimizing valve geometries.

In contrast, other surface-related mechanisms evolve much more slowly and remain less well understood. These include crystallization of dissolved substances, particle agglomeration, precipitation processes, adsorption layers, and biofouling. Such effects may initially be nearly invisible during normal operation but progressively alter the system state over extended storage or operating periods. In many cases, the disturbances become apparent only after a critical threshold has been reached, for example when deposits immobilize valves or modify flow resistance.

This difference in temporal behavior may explain why long-term surface-related degradation mechanisms have received comparatively limited scientific attention in micropump research. Many experimental studies focus primarily on immediate operational performance, while slower physicochemical evolution processes remain difficult to capture within standard test procedures.

The present work demonstrates that crystallization-induced sticking belongs to this second class of disturbances. The effect develops gradually after drying and storage, yet ultimately becomes sufficiently strong to completely suppress valve functionality. Similar long-timescale mechanisms may also contribute to other reliability limitations in miniaturized fluidic systems.

From a broader perspective, future micropump development may therefore require a transition from purely performance-oriented optimization toward reliability-aware system design. The challenge is no longer only to achieve stable operation under ideal conditions, but also to maintain functionality in the presence of evolving surface-related disturbances over extended time periods. This may require new handling concepts, adaptive operating strategies, material engineering approaches, or self-recovery mechanisms capable of mitigating long-term physicochemical degradation processes.

7 Conclusion

This work demonstrates that drying of micropumps containing liquids with dissolved non-volatile components can lead to severe surface-related disturbances caused by crystallization of residual substances. Due to microscale wetting and diffusion-limited evaporation, residual liquid remains trapped within chamber corners even after prolonged gas flushing. Subsequent crystallization of dissolved salts can immobilize microvalves during storage.

A recovery method based on humidity-induced condensation cycles was developed and successfully restored valve functionality without mechanical intervention. The results highlight the increasing importance of surface-dominated reliability mechanisms in highly miniaturized fluidic systems and emphasize the need to consider drying, handling, and storage conditions during micropump design and operation.

8 Acknowledgement

This work was partly funded by the Chips Joint Undertaking project UNLOOC (“Unlocking data content of Organ-on-Chips”, Grant Agreement No. 101140192) and by the EIC Pathfinder project MuSiC4Diabetes (“Unobtrusive Continuous Multi-Metabolite Monitoring for a Physiological Care of Insulin-treated Diabetes”, Grant Agreement No. 101115233).

9 Literature

[1] A. K. Au, H. Lai, B. R. Utela, and A. Folch, “Microvalves and Micropumps for BioMEMS,” Micromachines, vol. 2, no. 2, pp. 179–220, 2011. doi: 10.3390/mi2020179

[2] P. Chauvet, P. Duru, S. Geoffroy, and M. Prat, “Three periods of drying of a single square capillary tube,” Physical Review Letters, vol. 103, no. 12, 124502, 2009.

[3] M. Prat, “Recent advances in pore-scale models for drying of porous media,” Chemical Engineering Journal, vol. 86, no. 1–2, pp. 153–164, 2002.

[4] H. Hu and R. G. Larson, “Analysis of the microfluid flow in an evaporating sessile droplet,” Langmuir, vol. 21, no. 9, pp. 3963–3971, 2005.

[5] H. A. Stone, A. D. Stroock, and A. Ajdari, “Engineering flows in small devices: Microfluidics toward a lab-on-a-chip,” Annual Review of Fluid Mechanics, vol. 36, pp. 381–411, 2004.

[6] J. Crank, Free and Moving Boundary Problems, Oxford University Press, Oxford, UK, 1984.

 DOI: 10.30420/456743061

Conceptual Design of a Tunable Magnet-Based Reluctance Actuator

Endre P. Ronaes, Delft University of Technology, Delft, NL
e.p.ronaes@tudelft.nl
Andres Hunt, Delft University of Technology, Delft, NL
Ron van Ostayen, Delft University of Technology, Delft, NL
Hassan HosseinNia, Delft University of Technology, Delft, NL

Abstract

A method for providing a tunable sustained magnetic force bias in a reluctance actuator without continuous Joule heating has been developed through the project Beat the Heat, funded by the Dutch Research Council (NWO). An actuator was designed and manufactured to demonstrate the capability of exerting sustained reluctance forces within a reluctance actuator by tuning the magnetisation state of an AlNiCo magnet. This paper presents the conceptual design and models of the actuator, as well as some early measurement results.

1 Introduction

Electromagnetically actuated systems experience sustained Joule heating under constant actuation forces, leading to thermal expansion of machine components and a corresponding drift in positioning accuracy. To mitigate this, sustained electric currents and Joule heating are avoided in some recent designs through the integration of hysteretic elements, which provide an adjustable offset by being tuned to different stable remnant states. Such systems include the use of piezo stack actuators, magnetostrictive elements [1,2], which retain a remnant strain, and – as considered in this paper – magnets that are magnetised in-situ for sustained levels of magnetic flux [3,4,5]. In effect, input energy is applied only when changes in force are required.

Nevertheless, these forms of actuators are only suitable for applying constant forces. They are thus generally paired with other forms of actuators, such as reluctance or Lorentz actuators in [2] and [4]. This parallel stacking of actuators increases complexity and design space. The proposed design instead integrates a tunable magnetic bias directly into a hybrid reluctance actuator, allowing the same compact stator structure to provide both adjustable static force compensation and dynamic reluctance actuation.

This paper evaluates the concept (Section 2), through the development of a MEC model (Section 2.1) and FEM results (Section 2.2). Lastly the test setup is briefly described in Section 3, and some initial measurements of the magnetic flux are presented in Section 3.1.

2 Modelling and concept evaluation

The Tunable Magnet (TM) exploits the magnetic hysteresis of an AlNiCo 5 magnet that is magnetised in situ to different remanent states using a dedicated coil, allowing it to sustain a desired bias force (see: Figure 1). A second set of coils induces magnetic flux in adjacent C-shaped cores of laminated steel to generate a proportional actuation force.

The TM reaches magnetic saturation at currents above 8 A, and when the current is reduced back to zero within the saturation limits, some level of remanent magnetic flux is retained. In contrast, the laminated steel side cores exhibit an approximately linear field–flux relationship for excitation currents up to ±4 A.

As shown in Figure 1, the C-shaped cores are magnetically coupled to the central core via neodymium magnets that provide a permanent bias flux ϕ_{PM}. This flux is superimposed with contributions from the Tunable Magnet (ϕ_{TM}) and the steel cores (ϕ_C) to produce a proportional force on the mover.

The coils of the two steel cores are wound from 221 turns of wire and connected in series. While the central coil, for magnetisation state tuning is wound from 440 turns. With the cross-sectional area of the two outer cores equalling the half the area (A) of the central TM-core. The resulting force (F) on the mover are proportional to ϕ_{TM} and ϕ_C, assuming magnetic strictly follows the illustrated paths,

$$F = \frac{\phi_{PM}}{A\mu_0}(\phi_c + \phi_{TM}). \quad (1)$$

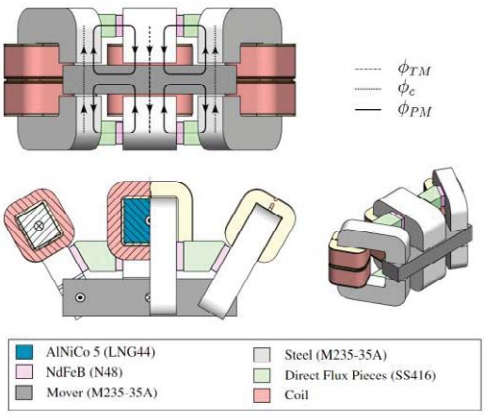


Figure 1 Actuator schematic / flux paths

 DOI: 10.30420/456743061

2.1 Lumped model

The concept is modelled using a coupled Magnetic Equivalent Circuit incorporating a Preisach hysteresis model to capture the variation in flux through the Tunable Magnet. Ohmic losses from continuous electric currents are essentially avoided at the expense of short pulses, resulting in high energy losses over brief periods. Power losses are especially high within the magnetic cores due to hysteresis, as shown in Figure 2, where a 250 V pulse is modelled to change the remnant magnetic flux *B* of the Tunable Magnet along the dashed load-line over a 6 ms duration. While reducing the tuning time would reduce the coil losses core losses cannot be reduced unless the material properties are changed.

This behaviour introduces a trade-off between using the excitation coils for magnetisation-state tuning (to adjust static bias) or for generating current-dependent reluctance forces during dynamic operation.

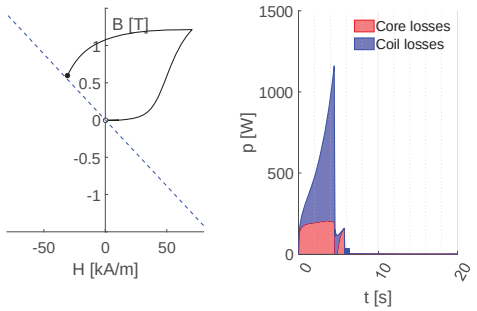


Figure 2 Energy losses during magnetisation state pulse

The remnant magnetisation states of the AlNiCo magnet are along the loadline illustrated by the black line in Figure 3. As the position of the mover is displaced in the operating region of -0.5 to 0.5 mm this line is expected to shift, but largely remain above the knee-point of the hysteresis loop. Application of 10 A through the TM coil results in a shift of the loadline that is sufficient to magnetise the TM close to saturation.

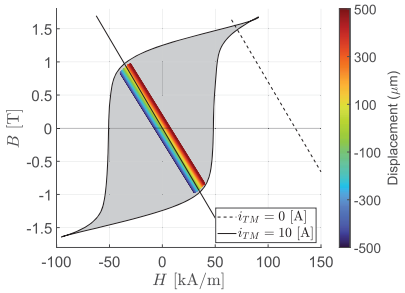


Figure 3 Shift in loadline from mover displacement and induced current in the TM coil

2.2 FEM validation

An experimental demonstrator, capable of compensating for a static force in excess of 200 N over a displacement range of -0.5 to 0.5 mm with zero steady-state power, was developed to validate the concept.

A static FEM model of the magnetic circuit provides a more accurate calculation of flux leakage, fringing, and actuation force. Figure 4 shows the resulting force on the mover as its position is displaced from -0.8 to -0.8 mm. The stiffness varies from 200 to 580 N/mm within the -0.5 to 0.5mm range.

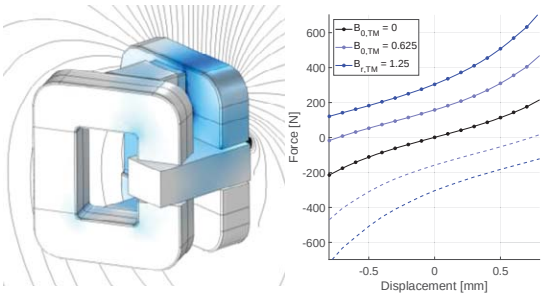


Figure 4 FEM Force displacement profile from TM

Applying a current through the coils of the side C-cores, results in a similar force displacement profile (Figure 5).

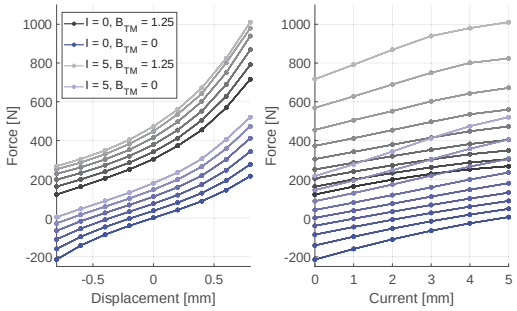


Figure 5 Change in actuation force with displacement and current applied to steel cores

3 Measurement

The mover is mounted on flexures to an aluminium base, while the stator is mounted to the same base on a set of rails, allowing it to be displaced (see: Figure 6). Capacitive probes are mounted to the base to measure the displacement of the mover.

 DOI: 10.30420/456743061

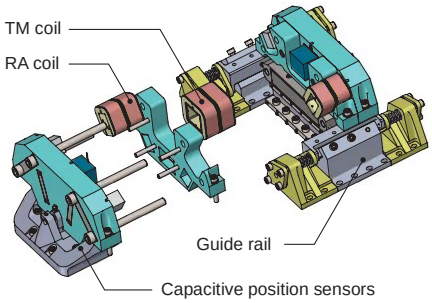


Figure 6 Assembly of the experimental setup.

A Hall sensor is placed in a groove in the AlNiCo magnet, and additional Hall sensors are temporarily placed on the stator poles. An accurate estimate of the static magnetic flux in the magnet is required for magnetisation-state control.
Sensing coils provide an estimate of the total magnetic flux through the core and are therefore placed within the coil packs and around the stator poles, as illustrated in Figure 7. Since the fraction of the magnetic flux passing through the Hall sensor changes during magnetisation, a sensing coil is required to estimate the flux during these short transient periods.

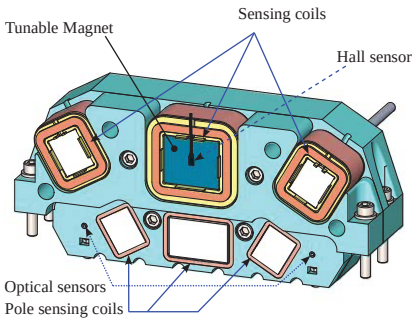


Figure 7 CAD model of on half of the stator

Optical sensors are embedded on either sides of the stator to measure the airgap.

3.1 Preliminary results

The coils were individually excited by a sinusoidal voltage. Figure 8 shows the magnetic flux derived from sensing-coil measurements in the Tunable Magnet and in one laminated steel core for decreasing current amplitudes.. The AlNiCo magnet is saturated by a current in excess of 8 A. The remanent points at zero current remain between the knee points of the hysteresis loop.

In contrast, the laminated steel side cores show a smaller hysteresis loop and an approximately linear current–flux below saturation, which occurs at approximately 5 A.

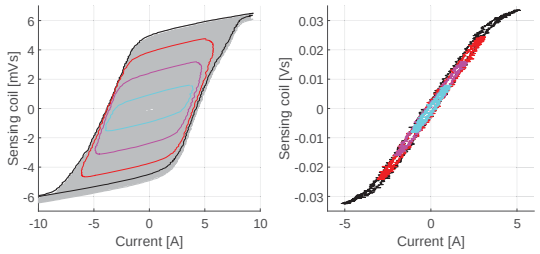


Figure 8 Measurements of magnetic flux in the Tunable Magnet the through one of the laminated C-cores

4 Conclusion

A compact hybrid reluctance actuator with an integrated tunable AlNiCo magnet was designed and manufactured for zero-power compensation of sustained forces. The design uses permanent magnet bias flux to linearise the force contribution of both the tunable magnet and the excitation coils. A coupled magnetic-equivalent-circuit model with hysteresis was used to evaluate remanent flux tuning, loss mechanisms, and displacement sensitivity. Preliminary measurements confirm remanent flux behaviour in the AlNiCo magnet and approximately linear flux generation in the laminated steel actuator cores. These results support the feasibility of using tunable magnetisation states to reduce steady-state Joule heating in precision electromagnetic actuators.
Future work will focus on force-displacement validation, improved sensor integration, and fusion of Hall sensor and sensing coil measurements to accurately control the remnant magnetisation of the TM. We would furthermore like to demonstrate active compensation of the variation in stiffness during operation.

5 Literature

[1] Reiser J., Marth H., PIRest Technology - How to Keep the Last Position of PZT Actuators without Electrical Power, Actuator 2018

[2] Raab, M.: Hutter M.: Kaxi, A.: Schinkoethe W., Gundelsweiler B., Magnetically Levitated Linear Drive Using an Active Gravity Compensation Based on Hybrid Shape Memory Actuators, IEEE/ASME Transactions on Mechatronics, 2021

[3] Hoekwater W., Ronaes E., HosseinNia H., Hybrid Tunable Magnet Actuator: Design of a Linearized Force–Flux Tunable Magnet Actuator, 2024

[4] Stadler G., Csencsics E., Ito S., Schitter G.: High Precision Hybrid Reluctance Actuator With Integrated Orientation Independent Zero Power Gravity Compensation, 2022

[5] Ronaes E., Hunt A., HosseinNia H.: Remnant Magnetisation State Control for Positioning of a Hybrid Tunable Magnet Actuator, Energies, 2023

 DOI: 10.30420/456743062

Design and Characterization of a Tactile Multi-Element Dielectric Elastomer Actuator

Lukas Roth[b], Sebastian Gratz-Kelly[b], Daniel Bruch[b], Sophie Nalbach[a], Paul Motzki[a,b]
[a] Smart Material Systems, Center for Mechatronics and Automation Technology – ZeMA gGmbH, Saarbrücken, Germany
[b] Saarland University, Department of Systems Engineering, Saarbrücken, Germany

Abstract

Smart wearable devices are becoming increasingly relevant in everyday applications, driven by advances in sensing technologies, soft materials, and miniaturized electronics. Their use spans medical monitoring, industrial assistance, and immersive digital environments such as virtual and augmented reality. Beyond technical performance, wearable systems must meet human-centred requirements, including comfort, flexibility, and intuitive operation. A key challenge is therefore the integration of compliant sensors and actuators into soft, lightweight structures while minimizing rigid components. [1], [2]
Dielectric elastomers (DEs) represent a promising solution to these challenges. They are soft, lightweight, and highly stretchable materials that can function as both actuators and sensors. Structurally, a DE consists of an elastic dielectric membrane with compliant electrodes on both sides, forming a deformable capacitor. When a voltage is applied, electrostatic forces compress the membrane, leading to in-plane expansion. Conversely, mechanical deformation can be detected via capacitance changes, enabling multifunctional use in soft robotic and wearable systems. [3], [4]
In this work, a novel DE-based wearable actuator is presented, capable of generating controlled tactile feedback directly on the user's skin. The system consists of three modular elements integrated into a flexible structure. Each element forms a sealed air chamber between an active DE membrane and a passive silicone membrane. The internal air pressure provides a fluidic preloading, while the DE membrane modulates the pressure through voltage-induced deformation. This results in a controllable normal force on the skin. By coordinating multiple elements, spatially distributed and dynamic tactile stimuli can be generated.
To optimize system performance, experimental studies are conducted focusing on excitation signals and frequency. The results provide insight into the actuator's dynamic behavior and form the basis for the development of a functional demonstrator.
The proposed approach enables compact actuation without external pumping systems and allows for tunable tactile feedback across a wide range of intensities and frequencies. In addition, the inherent sensing capability of DEs offers the potential for self-sensing and closed-loop control, enabling adaptive and responsive wearable haptic systems in future applications.

1 Introduction

Fluidically preloaded actuators represent a promising approach for wearable haptic devices. By replacing rigid mechanical components with compliant, fluid-based structures, they enable inherently flexible systems that can adapt to the human body. This is particularly relevant as the demand for wearable haptic technologies continues to grow across various fields, including medical applications, industrial human–machine interaction and immersive gaming. Such devices must be lightweight, adaptable to different body geometries, and intuitive to use, while still providing clearly perceivable feedback.[5], [6]
In this paper, a novel dielectric elastomer (DE)-based multi-element actuator is presented, capable of generating tactile feedback on the user's forearm. Dielectric elastomers belong to the class of electroactive polymers (EAPs) and consist of a soft elastomer layer, such as silicone, sandwiched between two compliant electrodes, for example carbon-based materials [7]. When a voltage is applied, an electric field is generated across the membrane, leading to electrostatic attraction between the electrodes. This so-called Maxwell stress compresses the elastomer in thickness and causes a lateral expansion due to its near incompressibility. This deformation can be utilized to generate mechanical motion. [8]
In addition to actuation, DEs can also function as sensors, as their capacitance changes with deformation. This enables the realization of systems in which sensing and actuation are combined within the same structure, reducing the need for additional external components. [9]
The actuator presented in this work consists of three active elements, each forming a sealed, pouch-like air chamber enclosed between an active DE membrane and a passive silicone membrane. The enclosed air volume introduces a fluidic pre-stretch to the membranes, enhancing the achievable deformation. The passive membrane is in direct contact with the user's skin and serves as the interface for haptic interaction. When a voltage is applied, the active membrane expands, effectively reducing the internal pressure of the chamber. As a result, the passive membrane changes its curvature, generating a tactile stimulus that can be perceived by the user.
To evaluate and optimize the haptic performance of the actuator, a comprehensive experimental characterization is

ISBN: 978-3-8007-6743-4 @ VDE VERLAG GMBH · Berlin · Offenbach

 DOI: 10.30420/456743062

conducted. The study focuses on identifying the key parameters influencing the perceived feedback and determining suitable operating conditions for wearable applications.

2 Actuator Design

This section shows an overview over the active elements, the multi-element actuator itself as well as the experimental setup for the characterization.

2.1 Single Active Element

The actuator consists of three identical active elements, each designed as a modular unit. The structure of a single active element is illustrated in **Figure 1**. Each element is composed of two membrane packs, one active and one passive, which are mechanically coupled via an intermediate silicone coupling element. Together, these components form a sealed air-filled chamber that enables pressure-based actuation.

Each membrane pack is realized as a multilayer stack, allowing multiple active layers to contribute to the overall force generation. The passive side consists of stacked silicone membranes, while the active side is formed by stacked dielectric elastomer membranes. Both membrane stacks are clamped within rigid frames to ensure defined boundary conditions and reproducible deformation behavior. The frames also provide mechanical stability and allow for straightforward assembly and disassembly.

The coupling element, made of silicone, serves multiple functions. It provides the mechanical interface between the two membrane packs, defines the enclosed air volume, and integrates an inlet for pressure adjustment. Through this inlet, the internal volume can be inflated, thereby introducing a controllable pre-strain to the membranes. When assembled, the components are compressed by external clamps, which ensures a reliable seal of the internal volume through the deformation of the silicone coupling structure.

The electrical connection of the DE membrane is realized via a flexible printed circuit board (PCB) that is bonded to the rigid frame. The connection to the DE electrodes is established using conductive adhesive, ensuring a reliable contact while maintaining the mechanical compliance of the system. Screw terminals integrated on the PCB serve as interfaces for the external wiring connected to the high-voltage control electronics, enabling a straightforward and detachable coupling.

During operation, the applied electric field reduces the effective stiffness of the active DE membrane due to the Maxwell stress. This results in an increase in its curvature and a corresponding expansion of the internal volume. Consequently, the internal pressure decreases, causing the passive membrane to deflect in the opposite direction. Since the passive membrane is in direct contact with the user's skin, this deformation is perceived as a tactile stimulus.

The generated haptic feedback is therefore directly governed by the electrical input signal, which modulates the pressure inside the sealed chamber. This pressure-based coupling enables a soft, compliant, and spatially distributed actuation mechanism that is well suited for wearable applications.

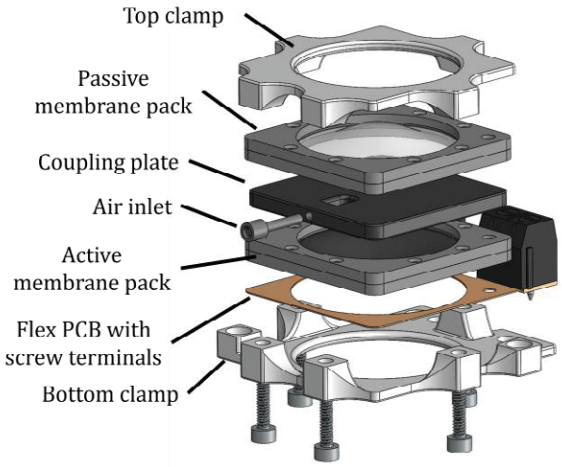


Figure 1: Exploded view (CAD) of a single active element, showing the membrane stacks, coupling structure and electrical interface

2.2 Multi-Element Actuator

The integration of the three active elements into a wearable system is shown in **Figure 2**. To enable a stable and reproducible coupling of the elements, each is mounted within a rigid rectangular casing. This housing ensures precise positioning and mechanical fixation, preventing relative movement between the elements during operation.

For electrical safety and mechanical protection, a thermoformed dome is integrated into each casing prior to assembly. This dome isolates the active dielectric elastomer from environmental influences such as dust and, at the same time, provides a protective barrier between the high-voltage components and the user.

The individual casings are subsequently mounted onto a flexible carrier structure made of thermoplastic polyurethane (TPU). This structure combines rigid and compliant regions: the central section, where the actuator elements are located, remains stiff to ensure efficient transmission of the generated forces to the user's skin. In contrast, the surrounding areas are designed to be flexible, allowing the system to conform to the curvature of the human arm.

To enable wearable use, the structure incorporates attachment points for hook-and-loop (Velcro) straps, allowing the actuator to be securely fastened around the arm with adjustable contact pressure. Additionally, integrated guide channels are provided for cable routing, as the driving electronics are implemented externally and connected via wired interfaces.

This hybrid design approach, combining rigid functional zones with flexible support structures, ensures both effective force transmission and high wearing comfort, making the actuator suitable for body-mounted applications.

ISBN: 978-3-8007-6743-4 @ VDE VERLAG GMBH · Berlin · Offenbach

 DOI: 10.30420/456743062

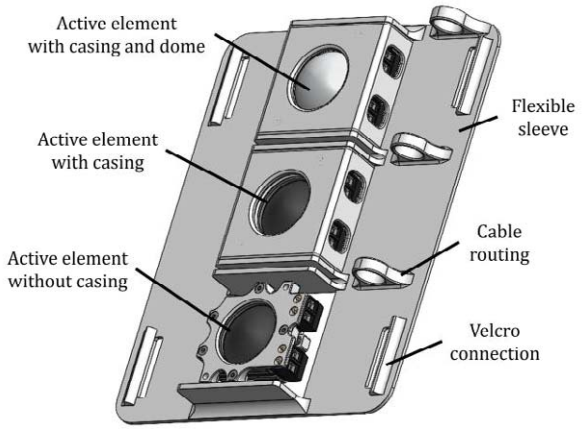


Figure 2: Top view (CAD) of the multi-element actuator, illustrating the integration of three active elements within a flexible wearable structure

2.3 Experimental Setup

The experimental setup is designed to characterize the actuator behavior in terms of force, displacement, and internal pressure under varying excitation conditions and is shown in **Figure 3**. A single active element is mounted via its fixation points on a rigid plate, allowing free access to the passive membrane, which represents the interface to the user.

The interaction with the arm is simulated using a rigid adapter, which defines the distance between the passive membrane and the contact surface. The resulting force is measured using a load cell (KD40s, ME-Meßsysteme) placed behind the contact adapter. Membrane deformation is recorded with a laser displacement sensor (LK-G157, Keyence), while a differential pressure sensor (ABPMRRN100MDAA5, Honeywell) measures the internal pressure relative to ambient conditions. A manual valve ensures a constant pressure during the measurements.

The experimental study includes variations of internal pressure and excitation frequency. First, the static operating limits are determined based on membrane deformation. Subsequently, the feasible operating range with respect to the contact distance is identified using force measurements.

For dynamic characterization, a linear frequency sweep from 1 Hz to 200 Hz is applied at constant voltage offset and amplitude at 50 mbar internal pressure. A programmable high-voltage amplifier (HA51U-3P5, hivolt.de) is used to generate the actuation signal. Based on these results, selected frequencies are further investigated using sinusoidal excitation to analyze steady-state behavior.

All measurements are repeated multiple times to ensure reproducibility and to capture effects such as leakage and material relaxation. In addition, leakage tests are conducted by monitoring the internal pressure over time.

To complement the experimental characterization, user studies are performed with the complete multi-element actuator. Test participants evaluate the perceived haptic feedback for different excitation signals, allowing assessment of the transferability of the measured system behavior to real-world conditions.

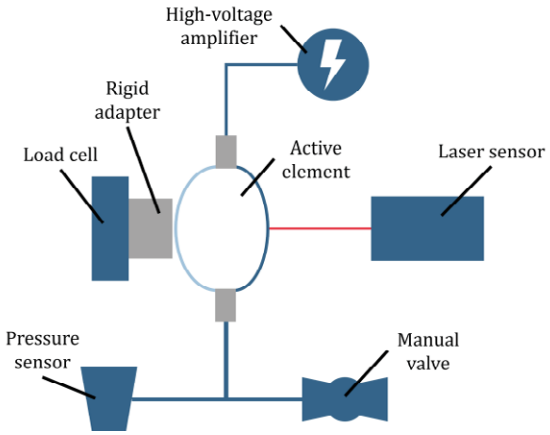


Figure 3: Schematic representation of the experimental setup for simultaneous measurement of pressure, displacement and force

3 Experimental Characterization

This section features the characterization of one active element, as well as the experiments with actual users for the whole actuator.

3.1 System Frequency Response

The dynamic behavior of the actuator is investigated using a linear frequency sweep from 1 Hz to 200 Hz in 60 seconds. The excitation signal is defined by a constant voltage offset of 2100 V and an amplitude of 200 V. The amplitude is limited by the current constraints of the high-voltage amplifier. However, as the actuator response scales proportionally with the applied voltage, the results can be transferred to higher amplitudes used in the final demonstrator. During the sweep, force, displacement and internal pressure are recorded simultaneously as shown in **Figure 4**. At low frequencies, the actuator exhibits a quasi-static behavior, where all measured quantities follow the excitation signal with gradually decreasing amplitudes.

With increasing frequency, a transition region is observed in which the dynamic response increases significantly. This region corresponds to a resonance of the coupled membrane–air system and defines the most effective operating range for generating haptic feedback, as force, displacement, and pressure reach their maximum response.

At higher frequencies, the displacement measured at the membrane center decreases, while the pressure variation continues to increase. This indicates a transition from uniform deformation to spatially distributed structural modes of the membrane. As a result, local displacement measurements are no longer sufficient to fully represent the global system behavior.

At elevated frequencies, deviations between the pressure signal and the mechanical measurements become apparent.

 DOI: 10.30420/456743062

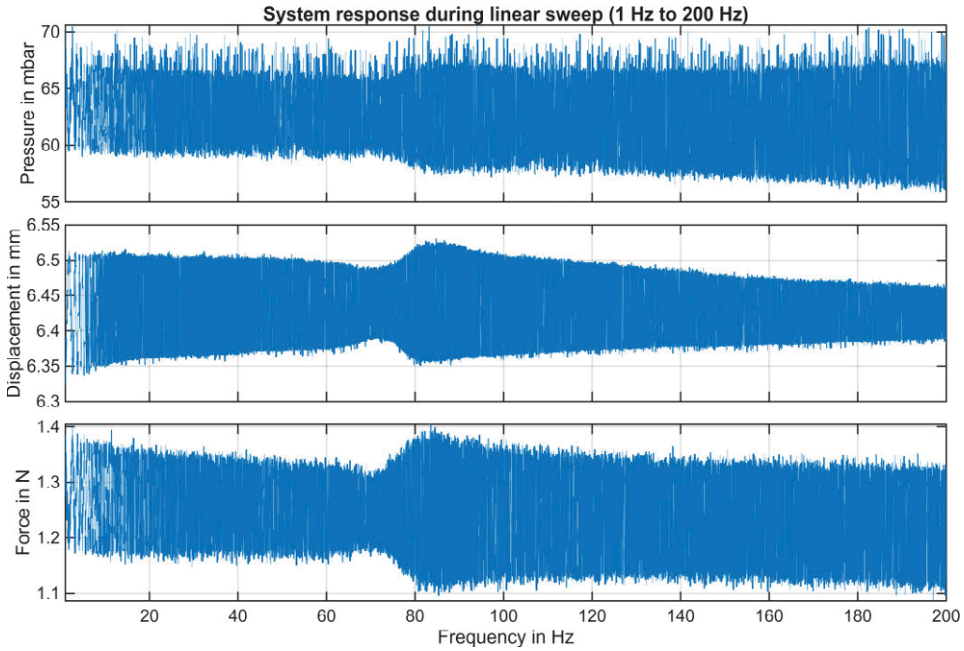


Figure 4: Frequency-resolved system response of internal pressure, displacement, and force during a linear frequency sweep from 1 Hz to 200 Hz

The pressure shows additional increases that are not reflected in the force or displacement signals. These effects are attributed to local pressure amplifications within the pneumatic measurement setup.

The connection between actuator and pressure sensor introduces an additional compliant volume with its own dynamic behavior. Consequently, the measured pressure does not purely represent the global actuator response in this frequency range. In contrast, the force signal remains consistent with the overall system behavior and therefore provides a more reliable representation of the actuator dynamics.

The observed discrepancies between displacement and pressure are further linked to higher-order deformation modes of the membrane. In these modes, the actuator exhibits spatially distributed oscillations, where local displacement can be reduced while the overall volume change remains significant.

3.2 Time-Dependent Behavior at Constant Frequencies

To separate dynamic effects from material behavior, the actuator is additionally investigated at constant excitation frequencies of 1 Hz, 83 Hz and 160 Hz. These frequencies represent the lower, intermediate and upper range of operation. The results are shown in **Figure 5**.

In all cases, a transient behavior is observed at the beginning of the measurement. The amplitudes of force and displacement increase during the first approximately 10 seconds before reaching a steady-state value. This behavior is independent of the excitation frequency and is attributed to the viscoelastic properties of the silicone membrane.

Under continuous loading, the material exhibits creep, resulting in a gradual stabilization of the deformation. This effect must be considered for applications requiring consistent and repeatable haptic signals. While clearly visible in force and displacement, it is less pronounced in the pressure signal due to measurement noise.

3.3 Leakage and Long-Term Stability

The long-term stability of the actuator is evaluated by monitoring the internal pressure over a period of 30 minutes at a constant initial pressure of 50 mbar. During this measurement, no mechanical contact is applied to the passive membrane.

The measured pressure decay corresponds to a total loss of 2.2 mbar. A stronger initial pressure drop occurs during the first minutes, followed by a nearly linear decrease over time. This initial phase is attributed to settling effects such as material relaxation and sealing adjustment.

In the subsequent linear regime, a leakage rate of approximately 0.073 mbar/min is observed. This behavior is mainly attributed to slow air diffusion through the silicone membranes and minor leakage paths at interfaces and sealing structures. The nearly linear decay indicates a stable and predictable leakage mechanism, confirming that the actuator exhibits sufficiently low leakage for practical operation.

3.4 User Study

To evaluate the actuator performance under real-world conditions, user studies are conducted using the final multi-element demonstrator. The goal is to assess the perceived haptic feedback and to relate the experimental findings to human perception.

Before each test, all actuator elements are pressurized to the same initial pressure. As no pressure sensor is integrated in the demonstrator, the pressure level is controlled

 DOI: 10.30420/456743062

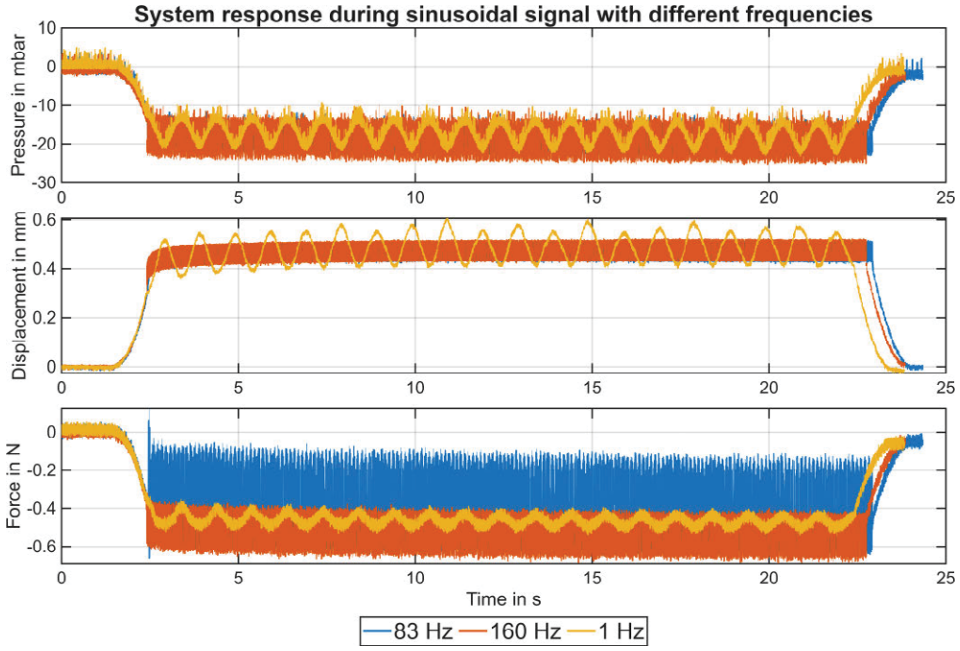


Figure 5: Time-resolved response of internal pressure, membrane displacement, and force under sinusoidal excitation at different frequencies

indirectly via membrane deformation. The device is mounted on the volar side of the forearm using a Velcro-based fixation, allowing each participant to adjust the contact pressure individually.

In the first test, the three actuator elements are activated sequentially using identical excitation parameters. All 15 participants are able to reliably distinguish the location of the active element, confirming the capability of the system to provide spatially localized feedback.

In the second test, one element is selected by each participant based on subjective perception. For this element, frequency (1 Hz to 160 Hz) and amplitude (0 kV to 2.3 kV) are varied systematically. The results shown in **Table 1** suggest that the strongest perception occurs within a frequency range of approximately 70 Hz to 100 Hz, which corresponds to the resonance region identified in the experimental characterization. This indicates that the actuator performance in practical use is primarily governed by its dynamic behavior and that the optimal operating range shifts slightly under real conditions.

Lower frequencies, particularly 1 Hz, are generally perceived as weak, especially after prior exposure to higher frequencies. Participants also report a decrease in sensitivity over time, indicating a habituation effect of the skin.

The perceived intensity increases with excitation amplitude, indicating that amplitude directly controls the strength of the feedback.

In a final test, multiple actuator elements are driven in a coordinated manner to generate a traveling wave across the arm. 14 out of 15 participants are able to perceive this motion as a continuous movement. However, variations in perceived intensity between users indicate that fixed actuation parameters are not sufficient to achieve uniform feedback, suggesting the need for adaptive control strategies.

Table 1: User frequency perception

User	Strongest f in Hz	Weakest f in Hz
1	85	67
2	85	1
3	85	1
4	75	1
5	97	1
6	93	160
7	103	1
8	100	160
9	100	1
10	90	1
11	88	1
12	80	1
13	100	1
14	95	1
15	70	160

4 Conclusion

This work presents a dielectric elastomer-based multi-element actuator with fluidic preloading for wearable haptic applications. The developed system demonstrates that the combination of soft membrane structures and an enclosed air volume enables a compact, lightweight, and flexible actuator capable of generating clearly perceivable tactile feedback.

The experimental characterization identifies a frequency-dependent operating range with a distinct resonance region that provides the most effective haptic response. The actu-

ator behavior is governed by the interaction between membrane mechanics and the enclosed air volume, while higher excitation frequencies lead to structural deformation modes that influence the global system response.
User studies confirm that these dynamic properties directly translate to human perception. The excitation frequency is identified as the dominant parameter for perceptual intensity, followed by the signal amplitude. In addition, the multi-element configuration enables spatially distributed and dynamic feedback patterns, such as the perception of continuous motion.
Future work will focus on the individual adaptation of actuation parameters to account for user-specific differences, as well as further miniaturization and integration of the system. In particular, the implementation of self-sensing capabilities of dielectric elastomers offers significant potential to enable closed-loop control, allowing the actuator to adapt its behavior in real time based on its deformation state. This approach is expected to improve the consistency, robustness, and overall quality of the perceived haptic feedback

5 Acknowledgement

Funded by the state of Saarland, provided through the European Regional Development Fund (ERDF) under the project “Multi immerse”.

6 Literature

[1] C. Gonçalves, A. Ferreira da Silva, J. Gomes, and R. Simoes, “Wearable E-Textile Technologies: A Review on Sensors, Actuators and Control Elements,” *Inventions*, vol. 3, no. 1, p. 14, Mar. 2018, doi: 10.3390/inventions3010014.

[2] J. Park *et al.*, “Soft Sensors and Actuators for Wearable Human–Machine Interfaces,” *Chem. Rev.*, vol. 124, no. 4, pp. 1464–1534, Feb. 2024, doi: 10.1021/acs.chemrev.3c00356.

[3] P. Loew, G. Rizzello, and S. Seelecke, “A novel biasing mechanism for circular out-of-plane dielectric actuators based on permanent magnets,” *Mechatronics*, vol. 56, pp. 48–57, Dec. 2018, doi: 10.1016/j.mechatronics.2018.10.005.

[4] Z. Li, J. Zhu, C. C. Foo, and C. H. Yap, “A robust dual-membrane dielectric elastomer actuator for large volume fluid pumping via snap-through,” *Appl. Phys. Lett.*, vol. 111, no. 21, Nov. 2017, doi: 10.1063/1.5005982.

[5] C. Pacchierotti, S. Sinclair, M. Solazzi, A. Frisoli, V. Hayward, and D. Prattichizzo, “Wearable Haptic Systems for the Fingertip and the Hand: Taxonomy, Review, and Perspectives,” *IEEE Trans. Haptics*, vol. 10, no. 4, pp. 580–600, Oct. 2017, doi: 10.1109/TOH.2017.2689006.

[6] P. Polygerinos, Z. Wang, K. C. Galloway, R. J. Wood, and C. J. Walsh, “Soft robotic glove for combined assistance and at-home rehabilitation,” *Rob. Auton. Syst.*, vol. 73, pp. 135–143, Nov. 2015, doi: 10.1016/j.robot.2014.08.014.

[7] B. Fasolt, M. Hodgins, and S. Seelecke, “Characterization of screen-printed electrodes for dielectric elastomer (DE) membranes: influence of screen dimensions and electrode thickness on actuator performance,” Y. Bar-Cohen and F. Vidal, Eds., Apr. 2016, p. 97983E. doi: 10.1117/12.2222095.

[8] P. Linnenbach, S. Hau, G. Rizzello, P. Motzki, and S. Seelecke, “Stroke Magnification in Dielectric Elastomer Actuators with Dynamic Excitation,” *ACTUATOR 2018; 16th International Conference on New Actuators*, Jun. 2018.

[9] G. Rizzello, D. Naso, A. York, and S. Seelecke, “Self-sensing in dielectric electro-active polymer actuator using linear-in-parametes online estimation,” in *2015 IEEE International Conference on Mechatronics (ICM)*, IEEE, Mar. 2015, pp. 300–306. doi: 10.1109/ICMECH.2015.7083992.

 DOI: 10.30420/456743063

Design and Control of Motion Stage Driven by Nonlinear Reluctance Actuator

Mohammad Al Saaideh[a], Natheer Alatawneh[b], and Mohammad Al Janaideh[b,c]
[a]Department of Electrical and Computer Engineering, Memorial University, St. John's, NL A1B 3X5, Canada.
[b]School of Engineering, University of Guelph, Guelph, ON N1G 2W1, Canada.
[c]Fraunhofer Institute for Applied Optics and Precision Engineering IOF, 07745 Jena, Germany.

Abstract

This paper presents the design and characterization of a motion stage driven by a reluctance actuator (RA). The study begins with system description and dynamic modeling. Next, the steady-state force characterization and open-loop responses are presented to highlight the nonlinear behavior and air-gap dependency. The magnetic hysteresis is then analyzed at different air gaps to capture its effect on system behavior. Finally, a feedforward controller is designed to partially linearize the RA dynamics, followed by a state feedback controller to achieve accurate displacement tracking and compensate for residual force errors. The system performance is evaluated using step and sinusoidal inputs.

1 Introduction

High-precision motion systems are essential for many micro/nano-positioning applications, including wafer scanners in lithography machines [1, 2] and microscopy motion stages for spectrometry imaging and nanostructure scanning [3]. Different actuators have been developed for these systems, such as piezoelectric actuators [4], shape-memory alloys [5], and electromagnetic actuators [6].

Recently, reluctance actuators (RAs) have attracted attention for short-stroke precision motion systems. These include C-core and E-core reluctance actuators [7, 8, 9], hybrid reluctance actuators [10, 11, 12], and plunger reluctance actuators [13, 14, 15]. Compared to other electromagnetic actuators, reluctance actuators provide higher force density and lower energy dissipation [16]. Therefore, they are promising for high-acceleration motion systems such as wafer scanners [7] and fast steering mirrors [17]. Despite these advantages, the strong nonlinear behavior of reluctance actuators limits their use in high-precision applications and complicates the modeling and control design [16]. These nonlinearities arise from the quadratic relationship between magnetic force and magnetic flux density, the air-gap dependency [8, 7], and the hysteresis effect of ferromagnetic materials [9, 12].

Several studies have investigated reluctance actuators for precision motion systems. The main goal has been to linearize their nonlinear dynamics using different control approaches [7, 9, 8]. However, most of these works consider a fixed air gap and do not include a full motion system. Limited attention has been given to cases where the reluctance actuator is integrated with a motion stage, where the mover forms part of the moving platform.

Compared to existing literature, the contribution of this work includes (i) an experimental characterization a custom-designed reluctance-actuated motion system (RAMS) and (ii) a feedback controller is designed to linearize the RA's dynamics, followed by a feedback state controller to achieve precise displacement control and compensate for residual force errors. The system's performance is evaluated for step and sinusoidal inputs.

2 Reluctance Actuated-motion System

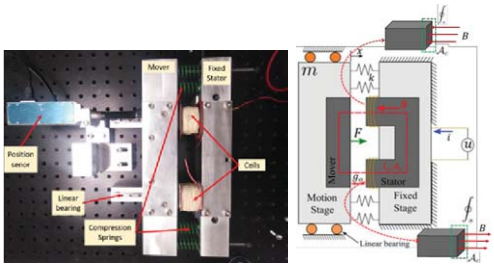
2.1 System Design and Experimental Setup

The RAMS consists of a fixed C-core stator and a movable I-core mover, as shown in Figure 1(a). Both cores are made of stacked 0.35 mm thick Non-Oriented Electrical Steel (M-19) laminations with a cross-sectional area of 25×25 mm ^{2}. The C-core laminations are enclosed in an aluminum frame for structural support. Two excitation coils, each with 120 turns, are wound around the C-core limbs to generate the magnetic flux. The I-core is attached to a motion stage guided by linear bearings and a preload mechanism. The stag mass is about 1.65 kg and the preload mechanism uses four compression springs with total stiffness $k = 100$ N/mm.

The experimental setup of the RAMS is shown in Figure 2. A linear voltage amplifier (AE Techron 7118) drives the two excitation coils of the reluctance actuator. The amplifier is a four-quadrant AC/DC amplifier with an output range of ± 150 V and adjustable

ISBN: 978-3-8007-6743-4 @ VDE VERLAG GMBH · Berlin · Offenbach

 DOI: 10.30420/456743063



(a) (b)

Figure 1 (a) The proposed prototype of the reluctance-actuated motion system (RAMS) and (b) the lumped model of the reluctance actuator with motion stage.

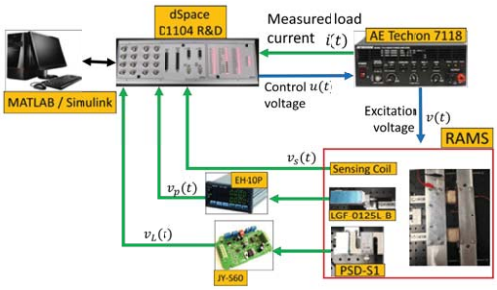


Figure 2 The block diagram representation of the experimental setup for the reluctance-actuated motion system (RAMS).

current from 1 A to 25 A, providing up to 425 VA of AC power. An S-type load cell (PSD-S1, Pushton) measures the attractive force between the stator and mover. The load cell has a maximum capacity of 490 N, a sensitivity of 2 mV/V, and a repeatability of ±0.02% F.S. The load cell is mounted between the mover and the support base while maintaining a fixed nominal air gap g_o. Its output signal is conditioned using a load cell amplifier (JY-S60), which converts the signal into a linear voltage output ranging from 0 V to 10 V with an accuracy of 0.2% F.S. A linear gauge (LGF-125L-B, Mitutoyo) is used to measure the position of the motion stage. The sensor has a measurement range of 25 mm and a resolution of 1 μm. A digital gauge counter (EH-10P, Mitutoyo) processes the measurements and provides an analog voltage output ranging from 1 V to 4 V with an accuracy of ±1%. A 15-turn sensing coil is mounted on one side of the C-core for flux measurement. The measured signals are acquired using a dSPACE data acquisition card (D1104 R&D) and system interfaced with MATLAB/Simulink for real-time control implementation and data processing. The dSPACE card receives the analog signals from the sensors, while the control signals generated in MATLAB/Simulink are sent to the power amplifier to drive the reluctance actuator.

2.2 Dynamics Model

Defining the states of the system as the displacement $x_1 = x$, the velocity $x_2 = \dot{x}$, and the magnetic flux density B allows to represent the dynamic model of the RAMS represented by the lumped model in Figure 1(b) as

$$\dot{x}_1 = x_2, \quad \dot{x}_2 = -\frac{k}{m}x_1 - \frac{b}{m}x_2 + \frac{1}{m}F + \Delta F, \qquad (1)$$

$$\dot{B} = -\alpha(g_o - x_1)B + \frac{Rl_c}{N^2 A_c}H_f + \frac{1}{NA_c}u, \qquad (2)$$

where $y = x_1$ is the output of the system, u is the applied voltage, g_o is the nominal air gap between the mover and the stator when $x = 0$, H_f is an unknown magnetic field intensity of the actuator, $\alpha \triangleq \frac{2R}{\mu_o N^2 A_c}$ is a positive constant related to the actuator's parameters, and ΔF presents the unmodeled forces in the system due to the uncertainties of the parameters or the friction.

3 Characterization of RAMS

This section presents experimental characterization of the RAMS under different operation conditions including fixed air gaps and variable air gaps due to the stage motion.

3.1 Steady-state force characterization at fixed air gap

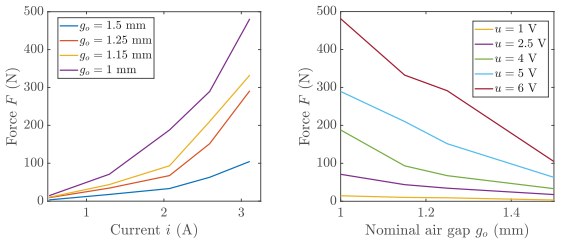
The experiment aims to measure the generated force F at different nominal air gaps g_o ($x = 0$) and constant applied voltages $u = U_s$. To maintain stable open-loop operation, the applied voltage is selected below the critical voltage $U_{cr} \approx 2\alpha g_o N\sqrt{\frac{k\mu_o A_c g_o}{27}}$ [18, 19]. The calculated critical voltages are $U_{cr} \approx [6.7,\ 8.25,\ 9.37,\ 12.32]$ V for $g_o = [1,\ 1.15,\ 1.25,\ 1.5]$ mm. A stair voltage signal with amplitudes $u = U_s = [4,\ 3,\ 0,\ 5,\ 6,\ 1,\ 0,\ 4]$ V is applied over $t = [0, 45]$ s.

Figure 3 shows the nonlinear force characteristics of the reluctance actuator. Figure 3(a) shows that the generated force is proportional to i^2 at a fixed air gap. Figure 3(b) shows that the force increases as the air gap decreases, following an approximate $\frac{1}{g_o^2}$ relationship. These results highlight the strong dependence of the generated force on both current and air gap.

3.2 Open-loop response with variable air gap

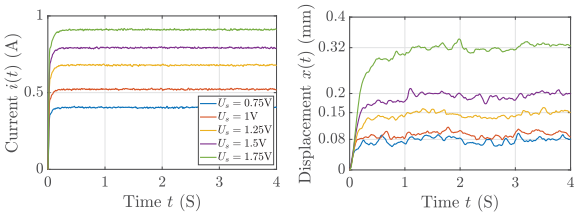
In this experiment, the RAMS is configured with four compression springs with a total stiffness of approximately $k = 100$ N/mm. This configuration allows to have variable air gap as $g(t) = g_o - x(t)$. For nominal air gaps of $g_o = [1,\ 2]$ mm, the corresponding critical voltages for stable open-loop operation are estimated as $U_{cr} \approx [2.12,\ 5.9]$ V. The associated maximum displacements are $x_{cr} = [0.333,\ 0.666]$ mm. Fig-

DOI: 10.30420/456743063



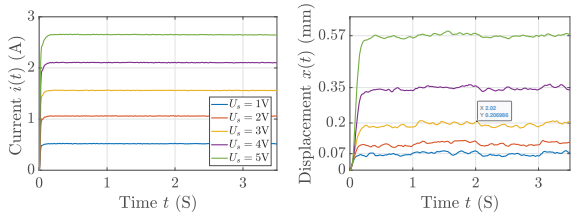
(a) (b)

Figure 3 (a) Force-current characteristic at different air gaps; and (b) force-gap characteristic under different applied voltages.



(a) (b)

Figure 4 The time response of the RAMS with stiffness $k = 100$ (N/mm) and nominal air gap of $g_o = 1$ (mm) (a) the measured current $i(t)$ (A); and (b) the measured displacement $x(t)$ (mm).



(a) (b)

Figure 5 The time response of the RAMS with stiffness $k = 100$ (N/mm) and nominal air gap of $g_o = 2$ (mm) (a) the measured current $i(t)$ (A); and (b) the measured displacement $x(t)$ (mm).

ure 4 shows the measured current and displacement responses at $g_o = 1$ mm under constant voltage inputs $u = U_s = [0.75,\ 1,\ 1.25,\ 1.5,\ 1.75]$ V. Figure 5 shows the responses at $g_o = 2$ mm for voltage inputs $u = U_s = [1,\ 2,\ 3,\ 4,\ 5]$ V. The step responses provide the steady-state current and displacement characteristics of the system. From Figures 4(b) and 5(b), the displacement settling time is approximately $t_s = 1$ s at $g_o = 1$ mm and $t_s = 0.2$ s at $g_o = 2$ mm. Using the rise-time approximation $f_{3dB} = 0.35/t_r$, the estimated bandwidth is about 1 Hz for $g_o = 1$ mm and 3 Hz for $g_o = 2$ mm.

The compression springs provide a total stiffness of approximately $k = 100$ N/mm, while the combined mass of the motion stage and mover is about $m = 1.655$ kg. Based on these values, the analytical natural frequency of the mechanical system is estimated as $f_n = 39$ Hz.

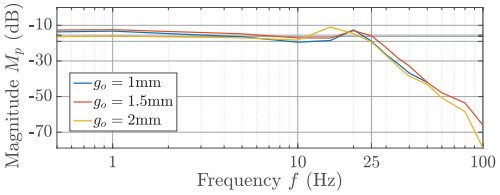


Figure 6 The frequency response of the RAMS with stiffness $k = 100$ (N/mm) where the magnitude $M_p = 20\log_{10}\left(\frac{|x|}{|i|}\right)$.

To measure the frequency response of the RAMS, the input voltage $u(t)$ is controlled to generate a sinusoidal coil current of the form $i(t) = \frac{I_m}{2}\sin(2\pi ft) + \frac{I_m}{2}$, where I_m is the current amplitude and f is the excitation frequency. To maintain stable open-loop operation, the current amplitudes are selected as $I_m = 0.8$ A for $g_o = 1$ mm, $I_m = 1.5$ A for $g_o = 1.5$ mm, and $I_m = 2$ A for $g_o = 2$ mm.

Figure 6 shows the measured frequency response, where the magnitude is defined as $M_p = 20\log_{10}\left(\frac{|x|}{|i|}\right)$. The RAMS maintains an approximately constant magnitude for frequencies below 25 Hz, while the magnitude decreases for frequencies above 25 Hz. Experimental results indicate that the natural frequency is approximately $f_n = 25$ Hz, which is lower than the analytical estimate of 39 Hz. A small oscillation near 25 Hz is also observed, indicating a damping ratio greater than $\zeta > 0.7$.

The variable air gap provides an important advantage for motion systems. At the of motion, a larger voltage is required to produce sufficient force. As the mover approaches the stator, the air gap decreases and the generated force increases. Therefore, the required voltage can be reduced during motion. This characteristic allows the reluctance actuator to achieve efficient and precise force control with lower operating voltage compared to actuators such as voice coils.

3.3 Magnetic Hysteresis Characterization

In this experiment, the flux-current and force-current characteristics are measured at fixed air gaps of $g_o = \{0, 0.5, 0.75, 1\}$ mm. The voltage source is controlled to generate a magnetic flux density $B(t) = B_{\max}\sin(\omega t + \phi_B)$ with a maximum amplitude of $B_{\max} = [0.2, 0.6, 0.8, 1]$ T, using a step size of 0.1 T and an excitation frequency of 3 Hz. During the experiment, the current $i(t)$ and sensing voltage $v_s(t)$ are measured. The magnetic flux density $B(t)$ and force $F(t)$ are then calculated using $B(t) = -\frac{1}{NA}\int v_s(t)dt$ and $F(t) = -\frac{A}{\mu_o}B^2(t)$, considering $N = 240$ turns and a core cross-sectional area of $A = 625$ mm^2.

Figure 7 compares the flux-current loops for a fixed maximum flux $B_{\max}$ across the tested air gaps. At small air gaps, the magnetic behavior is mainly dominated by the iron core since the air-gap reluctance is

ISBN: 978-3-8007-6743-4

@ VDE VERLAG GMBH · Berlin · Offenbach

DOI: 10.30420/456743063

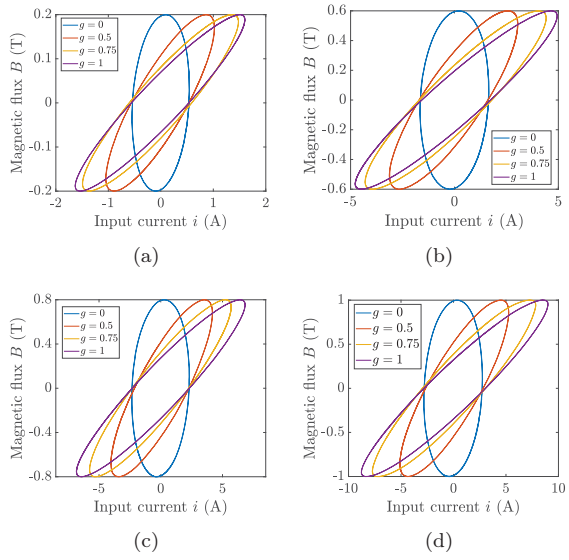


Figure 7 The comparison of the measured flux-current loops at air gaps $g = \{0,\ 0.5,\ 0.75, 1\}$ mm and a selected maximum flux of (a) $B_{\max} = 0.2$ T; (b) $B_{\max} = 0.6$ T; (c) $B_{\max} = 0.8$ T; and (d) $B_{\max} = 1$ T.

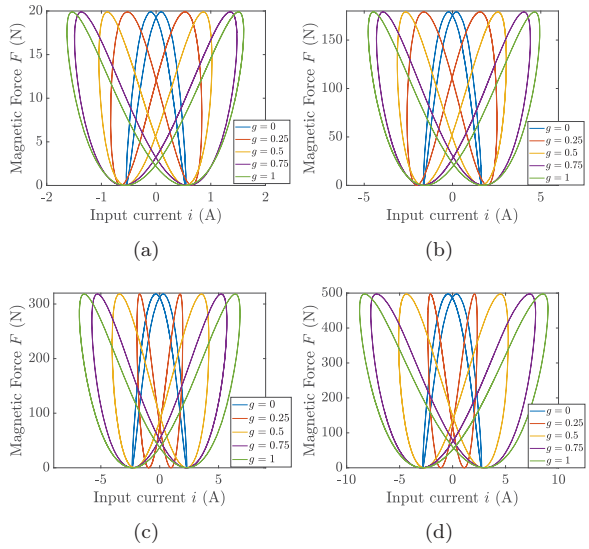


Figure 8 The comparison of the measured force-current loops at air gaps of $g = \{0,\ 0.5,\ 0.75, 1\}$ mm and a selected maximum flux of (a) $B_{\max} = 0.2$ T; (b) $B_{\max} = 0.6$ T; (c) $B_{\max} = 0.8$ T; and (d) $B_{\max} = 1$ T.

relatively low. Due to the nonlinear B-H characteristics of the iron, the system shows strong hysteresis and nonlinear response. As the air gap increases, the slope and loop width decrease with increasing air gap, indicating reduced magnetic nonlinearity and lower energy storage in the core. These trends are important for linearization and controller design of the reluctance actuator.

Fig. 8 compares the force-current loops for a fixed maximum flux $B_{\max}$ across different air gaps, showing the effect of air gap variation on force generation. As the air gap increases, the magnetic reluctance increases, which reduces force sensitivity and leads to narrower force-current loops. At small air gaps and higher flux levels, nonlinear magnetic effects and core saturation produce strong hysteresis, resulting in wider and more nonlinear loops. The observed decrease in slope and loop width with increasing air gap confirms weaker magnetic coupling between the C-core and I-core and reduced hysteresis effects. These results support force linearization through air-gap control and hysteresis modeling.

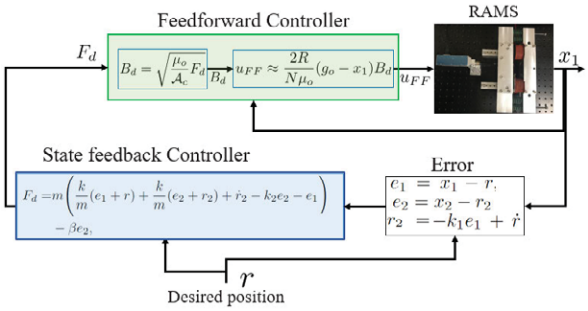


Figure 9 The feedforward and state feedback controller structure for the reluctance-actuated motion system (RAMS).

4 Control Design and Experimental Testing

The open-loop experimental results show that the reluctance-actuated system exhibits nonlinear force-voltage and force-gap characteristics. The system can operate stably only within a limited displacement range when the applied voltage remains below the critical voltage. To improve the system performance, a feedforward controller is first designed to linearize the actuator dynamics and generate the desired force with small error. Then, a state feedback controller is developed to regulate the system displacement x and track a desired reference. The remaining feedforward error is treated as an unknown system uncertainty in the controller design. The proposed controller structure for the RAMS combines a feedforward controller with a state feedback controller as illustrated in Figure 9.

4.1 Feedforward Controller

Defining a small parameter $\epsilon \triangleq \mu_0 A_c$, the model can be rewritten using a perturbation approach as

$$\epsilon \dot{B} = -\frac{2R}{N^2}(g_o - x_1)B + \epsilon\left(\frac{Rl_c}{N^2 A_c}H_f\right) + \frac{\mu_0}{N}u, \quad (3)$$

where $\mu_0 = 4\pi \times 10^{-7}$ H/m and A_c is the C-core cross-sectional area. Assuming $\epsilon \ll 1$, the system can be approximated as $B \approx \frac{N\mu_0}{2R(g_o - x_1)}u$. For a desired magnetic flux density B_d, determined from the desired

DOI: 10.30420/456743063

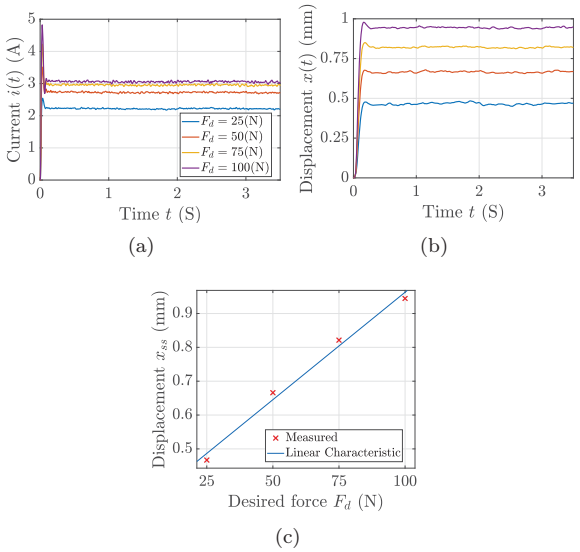


Figure 10 The time response under feedforward control law (4) for the RAMS with air gap of $g_o = 2$ (mm) for different desired constant force F_d (a) the measured current $i(t)$; (b) the measured displacement $x(t)$; and (c) the displacement-force characteristic.

force F_d as $B_d = \sqrt{\frac{\mu_0}{A_c} F_d}$, the corresponding feedforward control input is

$$u_{FF} \approx \frac{2R}{N\mu_0}(g_o - x_1)B_d. \tag{4}$$

Figure 10 shows the time response of the input current $i(t)$ and the measured displacement $x(t)$ at the nominal air gap $g_o = 2$ mm. The displacement–force behavior of the RAMS under the feedforward controller is shown in Figure 10(c). The results demonstrate that the proposed feedforward controller linearizes the RAMS dynamics, producing a near-linear relationship between the desired force F_d and the output displacement x, which can be approximated as a spring–mass–damper system.

4.2 Feedback Controller

The dynamic model of the RAMS under the feedforward controller is presented by

$$\dot{x}_1 = x_2, \quad \dot{x}_2 = -\frac{k}{m}x_1 - \frac{b}{m}x_2 + \frac{1}{m}F_d + \frac{1}{m}\sigma, \tag{5}$$

where F_d is the desired force to be obtained and $\sigma = e_F + m\Delta F$. Consider a tracking error defined as $e_1 = x_1 - r$, $e_2 = x_2 - r_2$, where r is the desired position with bounded derivatives, and r_2 is selected as $r_2 = -k_1 e_1 + \dot{r}$, for $k_1 > 0$. Then, the system (5) is rewritten as

$$\dot{e}_1 = -k_1 e_1 + e_2, \tag{6}$$

$$\dot{e}_2 = -\frac{k}{m}(e_1 + r) - \frac{b}{m}(e_2 + r_2) - \dot{r}_2 + \frac{1}{m}F_d + \sigma, \tag{7}$$

The task then is to design a state feedback control to make the origin of the transferred system exponentially stable, hence achieving the desired tracking goal by choosing F_d as

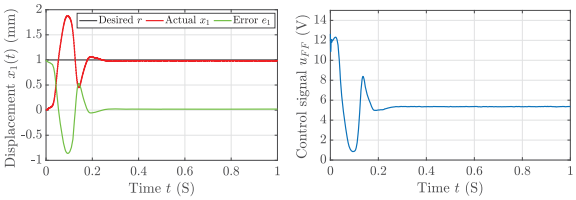


Figure 11 Step response of the RAMS using the proposed control approach (a) tracking performance of the displacement $x_1(t)$(mm); and (b) the control signal u_{FF} (V).

$$F_d = m\Big(\frac{k}{m}(e_1 + r) + \frac{k}{m}(e_2 + r_2) + \dot{r}_2 - k_2 e_2 - e_1\Big) - \beta e_2, \tag{8}$$

where $\dot{r}_2 = -k_1\dot{e}_1 + \ddot{r}$ and k_2 is a designed positive parameter. Figure 11 presents the tracking performance concerning a constant desired reference signal of $r = 1$ mm, and Figure12 depicts the tracking performance when subjected to a desired reference signal $r(t) = 0.5\sin(2\pi ft) + 0.7$ with frequency of $f = 0.5$ Hz and $f = 1$ Hz.

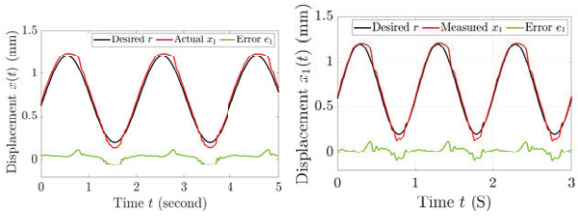


Figure 12 Tracking performance to a desired sinusoidal signal as $r(t) = 0.5\sin(2\pi ft) + 0.7$ with frequency (a) $f = 0.5$ Hz and (b) $f = 1$ Hz.

5 Conclusion

The paper presents the design, characterization, and control of a reluctance-actuated motion stage (RAMS) proposed for precision motion systems with a millimeter-scale range. Experimental results obtained without a controller demonstrate that the system exhibits nonlinear dynamics and gap-dependent behavior. A feedforward controller based on a perturbation approach is designed to linearize the actuator dynamics and establish a linear relationship between the output displacement and the desired force. Subsequently, a state-feedback controller is implemented to track the desired reference while accounting for unknown residual force errors arising from the feedforward controller and external disturbances. Experimental results demonstrate the effectiveness of the proposed control approach in achieving accurate

constant-position regulation and sinusoidal motion tracking.

6 Literature

[1] M. Steinbuch, T. Oomen, and H. Vermeulen, "Motion control, mechatronics design, and moore's law," *IEEJ Journal of Industry Applications*, vol. 11, no. 2, pp. 245–255, 2022.

[2] M. Heertjes, H. Butler, N. Dirkx, S. van der Meulen, R. Ahlawat, K. O'Brien, J. Simonelli, K. Teng, and Y. Zhao, "Control of wafer scanners: Methods and developments," in *2020 American Control Conference (ACC)*, pp. 3686–3703, IEEE, 2020.

[3] X. Wang, Y. Meng, W.-W. Huang, L. Li, Z. Zhu, and L. Zhu, "Design, modeling, and test of a normal-stressed electromagnetic actuated compliant nano-positioning stage," *Mechanical Systems and Signal Processing*, vol. 185, p. 109753, 2023.

[4] S. Mohith, A. R. Upadhya, K. P. Navin, S. Kulkarni, and M. Rao, "Recent trends in piezoelectric actuators for precision motion and their applications: A review," *Smart Materials and Structures*, vol. 30, p. 013002, 2020.

[5] A. AbuZaiter, M. Nafea, and M. S. M. Ali, "Development of a shape-memory-alloy micromanipulator based on integrated bimorph microactuators," *Mechatronics*, vol. 38, pp. 16–28, 2016.

[6] S. Xiao and Y. Li, "Optimal design, fabrication, and control of an *xy* micropositioning stage driven by electromagnetic actuators," *IEEE Transactions on Industrial Electronics*, vol. 60, no. 10, pp. 4613–4626, 2012.

[7] A. Katalenic, H. Butler, and P. Van Den Bosch, "High-precision force control of short-stroke reluctance actuators with an air gap observer," *IEEE/ASME Transactions on Mechatronics*, vol. 21, pp. 2431–2439, 2016.

[8] I. MacKenzie and D. Trumper, "Real-time hysteresis modeling of a reluctance actuator using a sheared-hysteresis-model observer," *IEEE/ASME Transactions on Mechatronics*, vol. 21, pp. 4–16, 2016.

[9] Y. Xu, X. Li, X. Yang, Z. Yang, L. Wu, and Q. Chen, "A two-stage model for rate-dependent inverse hysteresis in reluctance actuators," *Mechanical Systems and Signal Processing*, vol. 135, pp. 1–18, 2020.

[10] S. Ito, F. Cigarini, and G. Schitter, "Flux-controlled hybrid reluctance actuator for high-precision scanning motion," *IEEE Transactions on Industrial Electronics*, vol. 67, pp. 9593–9600, 2020.

[11] X. Zhang, L.-J. Lai, and L.-M. Zhu, "Data-driven fractional order phase-lead and proportional–integral feedback control strategy with application to a reluctance-actuated compliant micropositioning system," *Sensors and Actuators A: Physical*, vol. 348, pp. 1–11, 2022.

[12] X. Zhang, L. Lai, L. Zhang, and L. Zhu, "Hysteresis and magnetic flux leakage of long stroke micro/nanopositioning electromagnetic actuator based on maxwell normal stress," *Precision Engineering*, vol. 75, pp. 1–11, 2022.

[13] E. Serrano-Seco, E. Ramirez-Laboreo, E. Moya-Lasheras, and C. Sagues, "An audio-based iterative controller for soft landing of electromechanical relays," *IEEE Transactions on Industrial Electronics*, vol. 70, no. 12, pp. 12730–12738, 2023.

[14] E. Ramirez-Laboreo, E. Moya-Lasheras, and C. Sagues, "Real-time electromagnetic estimation for reluctance actuators," *IEEE Transactions on Industrial Electronics*, vol. 66, no. 3, pp. 1952–1961, 2018.

[15] E. Ramirez-Laboreo, C. Sagues, and S. Llorente, "A new run-to-run approach for reducing contact bounce in electromagnetic switches," *IEEE Transactions on Industrial Electronics*, vol. 64, no. 1, pp. 535–543, 2016.

[16] F. Cigarini, S. Ito, S. Troppmair, and G. Schitter, "Comparative finite element analysis of a voice coil actuator and a hybrid reluctance actuator," *IEEJ Journal of Industry Applications*, vol. 8, pp. 192–199, 2019.

[17] E. Csencsics, J. Schlarp, T. Schopf, and G. Schitter, "Compact high performance hybrid reluctance actuated fast steering mirror system," *Mechatronics*, vol. 62, p. 102251, 2019.

[18] M. Al Saaideh, N. Alatawneh, and M. Al Janaideh, "Design parameters of a reluctance actuation system for stable operation conditions with applications of high-precision motions in lithography machines," *IET Electric Power Applications*, vol. 16, pp. 68–85, 2022.

[19] M. Al Saaideh, M. Pumphrey, N. Alatawneh, K. Aljanaideh, and M. Al Janaideh, "A low-energy variable air gap-based reluctance-actuated motion system," *IEEE Transactions on Industrial Electronics*, vol. 72, no. 3, pp. 2882–2892, 2024.

 DOI: 10.30420/456743064

Displacement Control for Piezo-based Deformable Mirrors with Unmodelled Hysteresis and Actuator Coupling

Mohammad Al Saaideh[a], Matthias Goy[b], and Mohammad Al Janaideh[b,c]
[a]Department of Electrical and Computer Engineering, Memorial University, St. John's, NL A1B 3X5, Canada.
[b]Fraunhofer Institute for Applied Optics and Precision Engineering IOF, 07745 Jena, Germany.
[c]School of Engineering, University of Guelph, Guelph, ON N1G 2W1, Canada.

Abstract

Piezoelectric Deformable mirrors (PDMs) are essential components of adaptive optics (AO) systems, supporting a wide range of applications across various fields, such as enhancing the resolution of retinal imaging systems and enhancing laser control in advanced manufacturing process. However, the PDM performance can be affected by the nonlinearities of the piezoelectric actuator (PAs), particularly hysteresis effects and dynamic coupling between actuators. This paper presents a displacement control approach for the PA in the PDM, considering that the hysteresis nonlinearity and dynamic coupling are unknown. The proposed controller integrates state feedback control for tracking the desired displacement and an extended high-gain observer (EHGO) to estimate the unknown nonlinearities and dynamic coupling. A 41-PDM is used as a case study to assess the effectiveness of the proposed controller. Simulation results demonstrate that the controller achieves an average root mean square error (RMSE) of less than 4.7 nm and a tracking error convergence time of under 2 milliseconds.

1 Introduction

The deformable mirrors (DMs) play a pivotal role in adaptive optics (AO) systems, serving diverse applications across multiple fields. The DMs can be derived using different types of actuators [1], including piezoelectric actuators [2, 3, 4], MEMS actuator [5] and electromagnetic actuators [6]. For instance, in astronomy, piezoelectric deformable mirrors (PDMs) are integrated for wavefront correction in different fields, including atmospheric [7], and microscopy for biomedical imaging [8]. Recently, deformable mirrors (DMs) have been introduced in advanced manufacturing to improve the precision of laser welding, cutting, and additive manufacturing processes [9, 10]. By compensating for optical distortions and optimizing beam control, DMs enhance laser processing accuracy [11, 12]. Figure 1 illustrates a laser beam shaping system integrated with a DM for precision laser processing. In this system, a collimated laser beam is refined through a collimation lens and then corrected by the DM using feedback from a wavefront sensor and controller. The shaped beam is focused onto the workpiece through a focusing lens, while a dichroic mirror, optical filter, imaging lens, and coaxial camera enable real-time monitoring and wavefront analysis [9, 12].

The DM is a Multi-Input Multi-Output (MIMO) system, where actuator voltages serve as inputs and mirror displacements along the X and Y axes are the outputs. In adaptive optics (AO) systems, rapidly varying atmospheric turbulence introduces dynamic wavefront distortions, making DM control a highly coupled

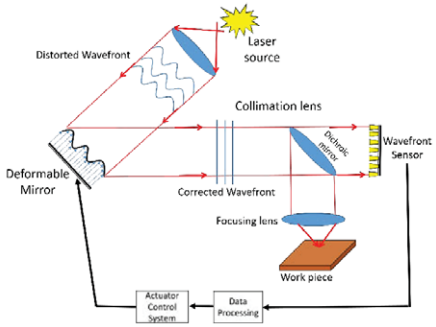


Figure 1 Schematic diagram of the basic components in the laser beam shaping system using a piezoelectric deformable mirror.

multi-variable problem with many degrees of freedom. As shown in Figure 2, the AO system typically employs a cascade control structure consisting of an inner displacement controller to compensate for actuator dynamics and hysteresis, and an outer wavefront controller that generates displacement references from the reconstructed wavefront. From a control perspective, the turbulent phase ϕ_t is treated as an external disturbance, while the residual phase ϕ_r represents the regulation error [1, 13].

Various wavefront control approaches have been proposed for adaptive optics systems, including minimum variance control [13] and linear quadratic Gaussian control [14]. However, these methods commonly assume linear piezoelectric actuator dynamics, neglecting hysteresis, position dependence, and actuator coupling effects. To address hysteresis nonlinearities, sev-

 DOI: 10.30420/456743064

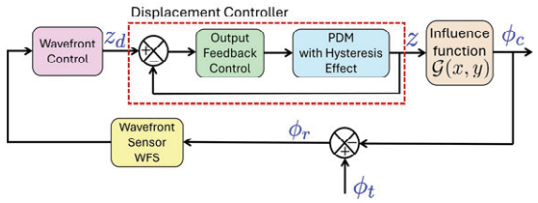


Figure 2 Block diagram of the control structure for the deformable mirror in an adaptive optics system.

eral studies incorporated the Bouc–Wen (BW) model into the control design, including optimal gain integrator control [15] and fixed-time observer-based tracking control [16]. Nevertheless, these approaches require prior knowledge of the BW hysteresis parameters. To overcome this limitation, a fixed-time disturbance observer was proposed in [2] to estimate hysteresis effects and identify generalized BW parameters. However, the method involves a large number of controller and observer parameters, increasing design complexity.
In this study, an output feedback control strategy based on an Extended High-Gain Observer (EHGO) is proposed for displacement control of piezoelectric deformable mirrors (PDMs). The EHGO estimates hysteresis nonlinearities and actuator coupling effects without explicit hysteresis model identification, unlike [2]. In addition, the proposed dynamic model accounts for unknown actuator coupling, providing a more realistic representation of PDM behavior. The main advantages of the proposed approach are:

- Independent controller design for each actuator while treating coupling effects as disturbances to be estimated and rejected.
- Reduced controller and observer tuning parameters compared to [2], simplifying implementation and improving suitability for real-time applications.

2 Dynamic Modeling

Figure 3 illustrates a PDM driven by N piezoelectric actuators (PAs). The PDM dynamics consist of a linear second-order model describing actuator vibrations and a nonlinear model representing hysteresis effects. In this work, the generalized Bouc–Wen (GBW) model from [2] is adopted to characterize actuator hysteresis. In practice, the DM also exhibits position-dependent dynamics due to actuator nonlinearities and mechanical coupling effects [17].

2.1 Deformable Mirror Model

The DM surface deforms according to the displacement of its actuators. Each actuator generates a local deformation described by an influence function [1].

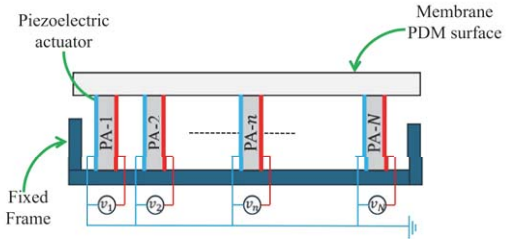


Figure 3 The cross-sectional area of the deformable mirror (DM) driven by piezoelectric actuators (PAs).

The correction wavefront is given by

$$\phi_c(t;x,y) = \sum_{n=1}^{N} \mathcal{G}_n(x,y) z_n(t), \tag{1}$$

where $\mathcal{G}_n(x,y)$ is the influence function and $z_n(t)$ is the displacement of the n^{th} actuator. Here, N denotes the total number of actuators. The influence function is commonly modeled using a Gaussian function [1].
The distorted wavefront caused by atmospheric turbulence is represented using Zernike polynomials [18] as

$$\phi_t(t;x,y) = \sum_{j=1}^{P} d_j(t) \mathcal{Z}_j(x,y), \tag{2}$$

where $d_j(t)$ is the coefficient of the j^{th} Zernike mode, $\mathcal{Z}_j(x,y)$ is the corresponding Zernike polynomial, and P is the total number of modes. Details of the first eighteen Zernike polynomials are provided in [16, 18].

2.2 Dynamic Model of Piezoelectric Actuator

The dynamics of each piezoelectric actuator (PA) in the PDM consist of a linear vibrational model and a nonlinear hysteresis model. The linear part is typically represented by a second-order differential equation. The nonlinear behavior is described using the GBW hysteresis model [2]. For the n^{th} PA, the system states are the displacement $z_{1n}(t)$, its velocity $z_{2n}(t)$, and the hysteresis term $h(t)$. The state-space model of the n^{th} actuator is given for $n = 1, 2, \ldots, N$, where N is the total number of actuators in the PDM as

$$\dot{z}_{1n} = z_{2n}, \tag{3}$$

$$\dot{z}_{2n} = -\frac{k_n(z)}{m} z_{1n} - \frac{b}{m} z_{2n} + \frac{k_n(z) d_p}{m} v_n - \frac{k_n(z)}{m} h_n - \sum_{\substack{j=1 \\ j \neq n}}^{N} \frac{k_{jn}(z)}{m} z_{1j} - \sum_{\substack{j=1 \\ j \neq n}}^{N} \frac{k_{jn}(z)}{m} h_j, \tag{4}$$

$$\dot{h}_n = a\dot{v}_n - \dot{v}_n.|h_n| \Big[b_1 \text{sgn}(\dot{v}_n) + b_2 \text{sgn}(v_n.\dot{v}_n) + b_3 \text{sgn}(v_n.h_n) + b_4 \text{sgn}(\dot{v}_n) + b_5 \text{sgn}(h_n) + b_6 \text{sgn}(v_n) \Big], \tag{5}$$

 DOI: 10.30420/456743064

where m is the mass, b is the damping ratio, k_n is the stiffness of n^{th} PA, k_{jn} is the coupling stiffness from the j^{th} PA to the n^{th} PA, and d_p is dielectric coefficient that presents the displacement-to-voltage ratio for the PA.

Compared to [2, 16], the proposed model (3)-(4) includes mechanical coupling between actuators. The displacement z_{1j} and hysteresis h_j of the j^{th} PA affect the n^{th} actuator. In addition, the stiffness is modeled as position-dependent, as reported in [17]. Experimental results in [17] show that this dependency can be well approximated by a polynomial in the actuator displacement.

Accordingly, the stiffness is expressed as

$$k(z) = k_0 + \sum_{n=1}^{N} p_n z_n + \sum_{n=1}^{N}\sum_{j=1}^{N} p_{nj} z_n z_j, \qquad (6)$$

where k_0 is the nominal stiffness, p_n and p_{nj} are polynomial coefficients. The first summation represents linear terms, while the second includes quadratic and coupling terms (z_n^2 and $z_n z_j$, $n \neq j$).

2.3 Problem Formulation

The model (3)-(4) describes the n^{th} PA dynamics, including hysteresis and mechanical coupling from other actuators. The nominal stiffness k_{n0} is known, while coupling effects and hysteresis are unknown. All unmodeled dynamics are grouped into the nonlinear term σ_n, defined as

$$\sigma_n = -\frac{k_n(z)-k_{n0}}{m} z_{1n}^2 - \frac{k_n(z)}{m} h_n - \sum_{\substack{j=1 \\ j\neq n}}^{N} \frac{k_{jn}(z)}{m} z_{1j} + \frac{(k_n(z)-k_{n0})d_p}{m} v_n - \sum_{\substack{j=1 \\ j\neq n}}^{N} \frac{k_{jn}(z)}{m} h_j, \qquad (7)$$

where σ_n is assumed to be bounded and Lipschitz, with $|\dot{\sigma}_n| \leq c_1$.

For control design, the system is rewritten as

$$\dot{z}_{1n} = z_{2n}, \qquad (8)$$

$$\dot{z}_{2n} = -\frac{kn0}{m} z_{1n} - \frac{b}{m} z_{2n} + \frac{k_{n0} d_p}{m} v_n + \sigma_n. \qquad (9)$$

The control objective is to design a displacement controller (Figure 2) so that z_{1n} tracks the reference z_n^d generated by the wavefront loop, despite unknown coupling and hysteresis captured by σ_n.

3 Proposed Control Design

This section presents the displacement control design for the PDM. The controller combines a backstepping-based state feedback law with an extended high-gain observer (EHGO). The state feedback is first derived assuming full state availability. The EHGO is then used to estimate the unmeasured state z_{2n} and the unknown nonlinear term σ_n from the measured output z_{1n}.

3.1 Reference Displacement Generation

As shown in Figure 2, the control architecture consists of two loops. The inner loop regulates actuator displacement while accounting for coupling and nonlinear dynamics. The outer loop minimizes the residual phase $\phi_r = \phi_t - \phi_c$ using wavefront sensor (WFS) measurements. A minimum variance control strategy [13] is used to generate the desired displacement by minimizing

$$J_c(z_{1n}) = \lim_{t\to\infty} \frac{1}{\tau} \int_0^{\tau} |\phi_t(t) - \phi_c(t)|^2 d\tau, \qquad (10)$$

which leads to

$$z^d = \mathcal{G}^T(x,y)\hat{\phi}t(t). \qquad (11)$$

Here, $z^d = [z1^d, z_2^d, \cdots, z_N^d]$ is the vector of desired actuator displacements. For control design, the desired trajectory z_n^d and its derivatives ($\dot{z}_n^d$, $\ddot{z}_n^d$) are assumed bounded and available from the outer wavefront loop.

3.2 Backstepping Control

A backstepping-based state feedback controller is designed assuming full state availability and known nonlinearities [19].

For the n^{th} actuator, define the tracking errors

$$e_{1n} = z_{1n} - z_n^d, \quad e_{2n} = z_{2n} - r_n, \qquad (12)$$

where z_n^d is the desired displacement and $r_n = -\alpha_{1n} e_{1n} + \dot{z}_n^d$. The error dynamics become

$$\dot{e}_{1n} = -\alpha_{1n} e_{1n} + e_{2n}, \qquad (13)$$

$$\dot{e}_{2n} = -\frac{k_{n0}}{m}(e_{1n} + z_n^d) - \frac{b}{m}(e_{2n} + r_n) + \frac{k_{n0} d_p}{m} v_n + \sigma_n - \dot{r}_n. \qquad (14)$$

A stabilizing control law is selected as

$$v_n = \triangleq \Phi(e_{1n}, e_{2n}, \sigma_n, r_n, z_n^d), \qquad (15)$$

$$\Phi = \frac{m}{k_{n0} d_p}\Big(-\alpha_{2n} e_{2n} + \frac{k_{n0}}{m}(e_{1n} + z_n^d) + \frac{b}{m}(e_{2n} + r_n) - \sigma_n + \dot{r}_n \Big), \qquad (16)$$

with $\alpha_{1n}, \alpha_{2n} > 0$.

3.3 EHGO-based Output Feedback

The extended high-gain observer (EHGO) is used to estimate unknown dynamics caused by modeling errors, parameter uncertainties, nonlinearities, and disturbances in nonlinear systems [20, 21, 22, 23].

The control law in (16) requires full state information and the nonlinear term σ_n. However, only the displacement z_{1n} of the n^{th} PA is measured. Therefore, an EHGO is designed to estimate the system states

DOI: 10.30420/456743064

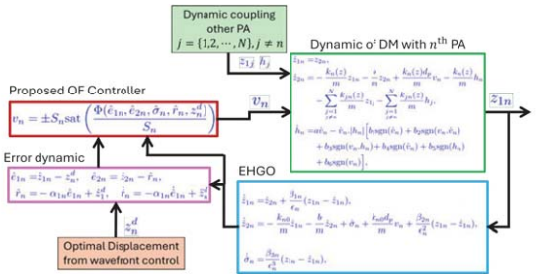
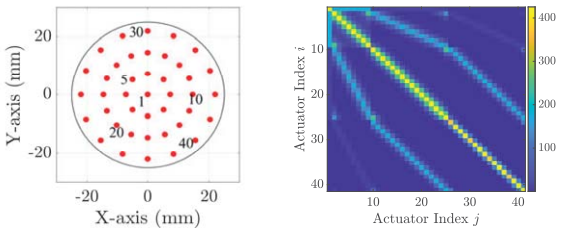


Figure 4 The structure of the proposed displacement control of the deformable mirror. The controller is presented for the n^{th} actuator.



(a) (b)

Figure 5 (a) Actuator pattern of a 41 piezoelectric actuator deformable mirror as a case study [25]; and (b) the cross-coupling of the Gaussian influence function $\mathcal{G}(x, y)$.

and σ_n as

$$\dot{\hat{z}}_{1n} = \hat{z}_{2n} + \frac{\beta_{1n}}{\epsilon_n}(z_{1n} - \hat{z}_{1n}), \tag{17}$$

$$\dot{\hat{z}}_{2n} = -\frac{k_{n0}}{m}\hat{z}_{1n} - \frac{b}{m}\hat{z}_{2n} + \hat{\sigma}n + \frac{k_{n0}d_p}{m}v_n + \frac{\beta_{2n}}{\epsilon_n^2}(z_{1n} - \hat{z}_{1n}), \tag{18}$$

$$\dot{\hat{\sigma}}_n = \frac{\beta_{3n}}{\epsilon_n^3}(z_{1n} - \hat{z}_{1n}), \tag{19}$$

where $\beta 1n$, β_{2n}, and β_{3n} are selected such that $s^3 + \beta_{1n}s^2 + \beta_{2n}s + \beta_{3n}$ is Hurwitz. The estimated tracking errors are defined as

$$\hat{e}_{1n} = \hat{z}_{1n} - z_n^d, \quad \hat{e}_{2n} = \hat{z}_{2n} - \hat{r}_n, \tag{20}$$

$$\hat{r}_n = -\alpha_{1n}\hat{e}_{1n} + \dot{z}_n^d, \quad \dot{\hat{r}}_n = -\alpha_{1n}\dot{\hat{e}}_{1n} + \ddot{z}_n^d. \tag{21}$$

The output-feedback controller is obtained by replacing the states in (16) with their estimates:

$$v_n = \pm S_n \text{sat}\left(\frac{\Phi(\hat{e}_{1n}, \hat{e}_{2n}, \hat{\sigma}_n, \hat{r}_n, z_n^d)}{S_n}\right), \tag{22}$$

where Φ is defined in (16), and sat$(\cdot)$ limits transient peaks during observer convergence [24]. The saturation bound S_n is selected according to the maximum allowable PA voltage.

Figure 4 shows the proposed control structure for the n^{th} actuator. The same controller is applied independently to all actuators, $n = 1, \ldots, N$. Compared to [16, 2], the proposed method has a simpler implementation and fewer tuning parameters.

4 Simulation Results

This section presents numerical simulations to evaluate the tracking performance of the proposed controller using the 41-piezoelectric actuator deformable mirror in [25]. The DM influence function $\mathcal{G}(x, y)$ is modeled as a Gaussian function [1]. Figure 5(a) shows the actuator layout, while Figure 5(b) illustrates the resulting cross-coupling between actuators. Unlike [16, 2], orthonormalization is not applied in order to preserve actuator coupling and evaluate the robustness of the proposed controller against unknown dynamic interactions.

The DM parameters are selected as $m = 0.02$ kg, $b = 99.26$ N.s/m, $k_{n0} = 2544$ N/m, and $d_p = 3.08 \times 10^{-7}$. The hysteresis model parameters are taken from [2]. The stiffness $k(z)$ is modeled using (6) with random coefficients. The controller and EHGO parameters are chosen as $\alpha_{1n} = 3000$, $\alpha_{2n} = 2500$, $\epsilon = 10^{-5}$, $\beta_{1n} = 25$, $\beta_{2n} = 20$, and $\beta_{3n} = 10$.

In this simulation, a rapidly varying random phase wavefront is used as the reference shape to be generated by the PDM. The desired optimal displacement z_n^d is obtained through wavefront control as defined in (11).

The tracking performance of the displacement z_{1n} to the desired displacement z_n^d for selected PAs $n = \{1, 7, 13, 38\}$ is illustrated in Figure 6. It can be observed that the proposed controller effectively tracks the desired displacement z_n^d with tracking error e_{1n} bounded within ± 10 nm. Figure 6(e) shows the control input v_n for the selected actuator within ± 20. It can be observed that the peak values occur in a very short time. The root mean square error (RMSE) is used as a performance index of the proposed controller, which is defined as $RMSE = \sqrt{\frac{\sum e_{1n}^2}{K}}$, where K is the number of data points. Figure 7 presents the RMSE values of 41-PAs with an average value of 4.7 nm. Additionally, the convergence of the tracking error e_{1n} occurs within a convergence time of less than 1 msec.

Finally, snapshots of the phase wavefront at $t = 0.15$ sec and $t = 0.48$ sec are shown in Figure 8. This figure demonstrates that the residual wavefront, defined as the difference between the desired and actual wavefronts, has a peak value of less than 0.03 μm.

The simulation results demonstrate the effectiveness of the proposed control approach in tracking the desired displacements, which are generated to reproduce the target wavefront. Compared to recent work [16, 2], the proposed control approach achieves a faster convergence time of less than 2 msec and an average RMSE of less than 4.7 nm, highlighting its efficiency. Additionally, a key advantage of the proposed controller is the reduced number of parameters that need to be tuned, compared to those required for the con-

ISBN: 978-3-8007-6743-4

@ VDE VERLAG GMBH · Berlin · Offenbach

DOI: 10.30420/456743064

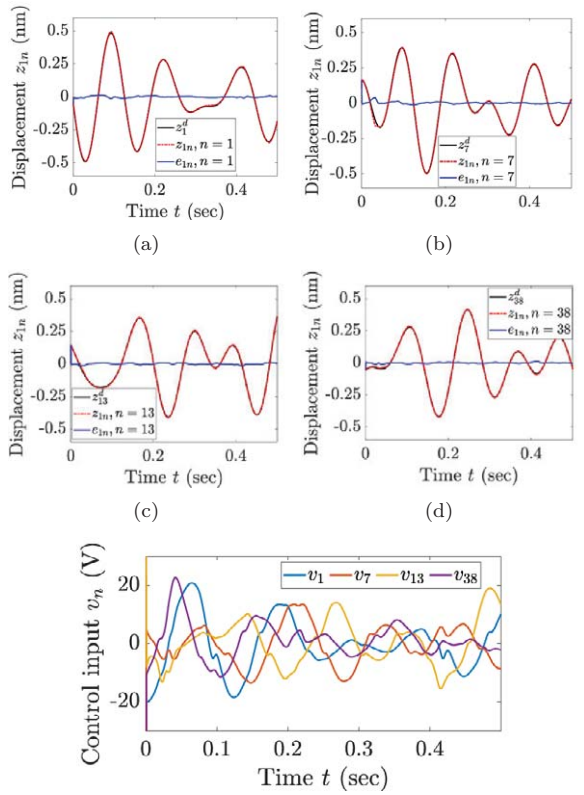


Figure 6 The tracking performance under the fastly changing wavefront of the displacement z_{1n} for the selected actuators (a) 1^{th} PA; (b) 7^{th} PA; (c) 13^{th} PA; and (d) 38^{th} PA; (b) the control input v_n.

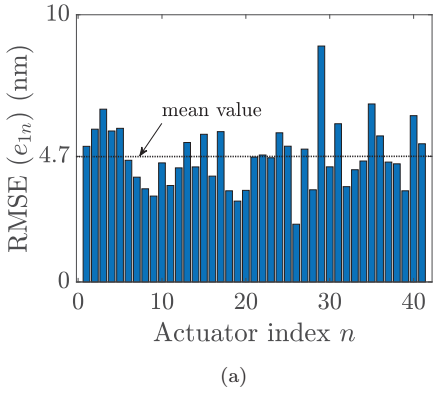


Figure 7 The root mean square error (RMSE) of the tracking error for the PA actuators (nm).

trollers in [16, 2].

5 Conclusion

In Piezoelectric deformable mirrors (PDMs), piezoelectric actuators (PAs) are employed for actuation; however, their performance is often compromised by nonlinearities such as hysteresis effects and dynamic coupling between actuators. This paper proposes a displacement control approach for the PAs in PDMs while accounting for unknown hysteresis nonlinearities and dynamic coupling. The proposed controller combines state feedback control for accurate displacement tracking with an extended high-gain observer (EHGO) to estimate and compensate for these unknown nonlinearities. A 41-PDM is used as a case study to evaluate the controller's performance. The controller's performance was validated through simulations using random phase wavefront, demonstrating its robustness across varying dynamic conditions. With an average RMSE of less than 4.7 nm and a convergence time of under 2 ms, the proposed approach enhances the precision and responsiveness of PDM actuation. These findings suggest that the controller is well-suited for adaptive optics applications, offering a reliable solution for improving wavefront correction accuracy in real-time systems.

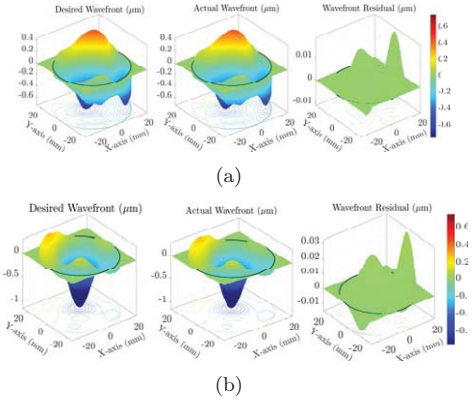


Figure 8 Tracking performance of the fast-changing random phase wavefront (μm) using the proposed controller at (a) $t = 0.15$ (sec) and (b) $t = 0.48$ (sec).

6 Literature

[1] X. Ke, "Deformable mirrors and their control algorithms," in *Handbook of Optical Wireless Communication*, pp. 987–1014, Springer, 2024.

[2] A. Mahzounieh, H. R. Koofigar, and H. Fallah, "Disturbance observer-based control with hysteresis identification in piezoelectric deformable mirrors," *International Journal of Systems Science*, pp. 1–16, 2024.

[3] X. Guo, H. Yin, M. Li, I. Kanno, D. Wang, S. Jiang, Y. Xia, and Z. Wang, "Deformable mirror driven by piezoelectric thin film based on multi-electrode array," *Sensors and Actuators A: Physical*, p. 115876, 2024.

[4] M. Al Saaideh, L. Zhang, and M. Al Janaideh, "Output feedback displacement control for piezoelectric deformable mirrors with unknown hysteresis and dynamics coupling," *IEEE Photonics Journal*, vol. 18, no. 3, pp. 1–10, 2026.

[5] A. Kamel, S. Kocer, L. Mukhangaliyeva, R. Saritas, A. Gulsaran, A. Elhady, M. Basha, P. Ha-

jireza, M. Yavuz, and E. Abdel-Rahman, "Resonant adaptive MEMS mirror," in *Actuators*, vol. 11, p. 224, 2022.

[6] L. Jiang, L. Hu, Q. Hu, X. Xu, J. Wu, L. Yu, and Y. Huang, "Sixty-nine-element voice coil deformable mirror for visible light communication," in *Photonics*, vol. 10, p. 322, 2023.

[7] Y. Guo, K. Chen, J. Zhou, Z. Li, W. Han, X. Rao, H. Bao, J. Yang, X. Fan, and C. Rao, "High-resolution visible imaging with piezoelectric deformable secondary mirror: experimental results at the 1.8-m adaptive telescope," *Opto-Electronic Advances*, vol. 6, no. 12, pp. 1–12, 2023.

[8] D. Williams, S. Burns, D. Miller, and A. Roorda, "Evolution of adaptive optics retinal imaging," *Biomedical Optics Express*, vol. 14, no. 3, pp. 1307–1338, 2023.

[9] Y. Mi, S. Mahade, F. Sikström, I. Choquet, S. Joshi, and A. Ancona, "Conduction mode laser welding with beam shaping using a deformable mirror," *Optics & Laser Technology*, vol. 148, p. 107718, 2022.

[10] S. Abadi, Y. Mi, F. Sikstrom, A. Ancona, I. Choquet, *et al.*, "Effect of shaped laser beam profiles on melt flow dynamics in conduction mode welding," *International Journal of Thermal Sciences*, vol. 166, 2021.

[11] P. Madec, "Overview of deformable mirror technologies for adaptive optics," in *Adaptive Optics: Analysis, Methods & Systems*, pp. AOTh2C–1, Optica Publishing Group, 2015.

[12] L. Mrňa, M. Sarbort, and M. Holá, "Deformable mirror for high power laser applications," in *Optics and Measurement Conference 2014*, vol. 9442, pp. 215–219, 2015.

[13] C. Kulcsár, H. Raynaud, C. Petit, and J. Conan, "Minimum variance prediction and control for adaptive optics," *automatica*, vol. 48, no. 9, pp. 1939–1954, 2012.

[14] L. Marquis, C. Kulcsár, I. Montilla, H. Raynaud, J. M. de la Rosa, Ó. T. Araújo, A. Basden, and M. García, "Linear quadratic gaussian predictive control for the gran telescopio canarias ao system: design issues and first bench results," in *Adaptive Optics Systems VIII*, vol. 12185, pp. 909–916, 2022.

[15] C. Kulcsár, H. Raynaud, C. Petit, J. Conan, and P. V. d. Lesegno, "Optimal control, observers and integrators in adaptive optics," *Optics express*, vol. 14, no. 17, pp. 7464–7476, 2006.

[16] A. Mahzounieh, H. r. Koofigar, and H. Fallah, "Fixed-time observer-based tracking controller for a hysteretic piezoelectric deformable mirror of an adaptive optic system," *Optics Express*, vol. 31, no. 11, pp. 17250–17267, 2023.

[17] M. Capat, *LPV modelling and predictive control of adjustable mirrors in an EUV lithography system.* Master thesis, Eindhoven University of Technology, Eindhoven,, NL, January 2024.

[18] K. Niu and C. Tian, "Zernike polynomials and their applications," *Journal of Optics*, vol. 24, no. 12, pp. 1–55, 2022.

[19] M. Krstic, P. Kokotovic, and I. Kanellakopoulos, *Nonlinear and Adaptive Control Design.* Hoboken, NJ: John Wiley & Sons, Inc., 1995.

[20] M. Al Saaideh, A. Boker, and M. Al Janaideh, "Output feedback with feedforward robust control for motion systems driven by nonlinear position-dependent actuators," *IEEE Transactions on Automation Science and Engineering*, vol. 22, pp. 5966–5981, 2025.

[21] M. Al Saaideh, Y. Al-Rawashdeh, K. Aljanaideh, L. Zhang, A. Boker, and M. Al Janaideh, "Output feedback control of variable-loaded four-joint manipulators with unknown saturated actuator dynamics," *International Journal of Control, Automation and Systems*, vol. 22, no. 12, pp. 3694–3707, 2024.

[22] M. Al Saaideh, A. Boker, and M. Al Janaideh, "Robust output feedback controller for a serial robotic manipulator with unknown nonlinearities and external disturbances," in *2023 IEEE International Conference on Robotics and Automation (ICRA)*, pp. 5298–5303, 2023.

[23] J. Sutton, M. Al Saaideh, M. Al Janaideh, and A. Boker, "Output feedback near-optimal control of atomic force microscope," *International Journal of Control*, pp. 1–20, 2025.

[24] F. Esfandiari and H. Khalil, "Output feedback stabilization of fully linearizable systems," *International Journal of control*, vol. 56, pp. 1007–1037, 1992.

[25] P. Rausch, S. Verpoort, and U. Wittrock, "Unimorph deformable mirror for space telescopes: environmental testing," *Optics express*, vol. 24, no. 2, pp. 1528–1542, 2016.

 DOI: 10.30420/456743065

Integration of sensors and trajectory control for the autonomous navigation of 3D-printed miniature robots driven by piezoelectric actuators

Byron Ricardo Zapata Chancusig*, Jaime Rolando Heredia Velastegui*,
Víctor Ruiz-Díez** and José Luis Sánchez-Rojas**.

*Mechatronic Department, Universidad Politécnica Salesiana, Quito 170701, Ecuador.
**Microsystems, Actuators and Sensors Group, INAMOL-Universidad de Castilla-La Mancha, 45004 Toledo, Spain; victor.ruiz@uclm.es (V.R.-D.)
Correspondence: bzapata@ups.edu.ec

Abstract

This work presents the fabrication and experimental validation of a miniature autonomous robot driven by piezoelectric standing-wave actuation. The platform combines 3D-printed resonant plates with bonded PZT patches, onboard electronics, an inertial measurement unit, a time-of-flight distance sensor, and a Total Volatile Organic Compounds (TVOC) sensor for environmental monitoring. Independent excitation of two resonant plates enables linear and rotational motion, while gyroscope feedback is used for closed-loop trajectory correction. Experiments show bidirectional locomotion with a linear speed of 7 mm/s and an angular speed of 30°/s. Compared with open-loop operation, closed-loop control reduced lateral drift from 58 mm to 4 mm over a 20 s trajectory, with a mean absolute angular error of 0.83° across ten trials. During navigation through a three-station track, the integrated sensor detected volatile organic compounds from an isopropyl alcohol source, with TVOC readings within 5–10% of reference equipment. These results demonstrate an integrated miniature platform for autonomous navigation and VOC inspection in confined environments.

1 Introduction

Robotics is evolving from large-scale industrial systems toward more compact, autonomous, and bio-inspired platforms. Within this trend, insect-scale miniature robots have attracted increasing interest due to their potential to operate in confined or hard-to-reach environments, with applications in inspection, micromanipulation, minimally invasive medicine, and infrastructure assessment [1–3].

One of the main challenges in this field is the selection of actuators capable of generating efficient motion at small scales. In this context, piezoelectric actuators represent a particularly attractive alternative due to their low power consumption, fast response, ease of miniaturization, high resolution, and robustness against electromagnetic interference [4–5]. Furthermore, the combination of piezoelectric patches with 3D-printed structures has simplified mechanical and electrical integration, enabling locomotion through standing waves in compact robotic systems [6–7].

Despite advances in speed and locomotion, many microrobots still face limitations in autonomy and precise trajectory control. Therefore, the integration of sensors and embedded systems—particularly inertial measurement units—has become a key strategy to improve autonomous navigation and closed-loop control. In this context, this work proposes the integration of an IMU into a miniature robot driven by piezoelectric standing waves, to achieve more precise trajectory control [8–10].

2 Materials and methods

The methodology used for generating controlled motion of the miniature robot and for acquiring air quality data is shown in **Figure 1.**

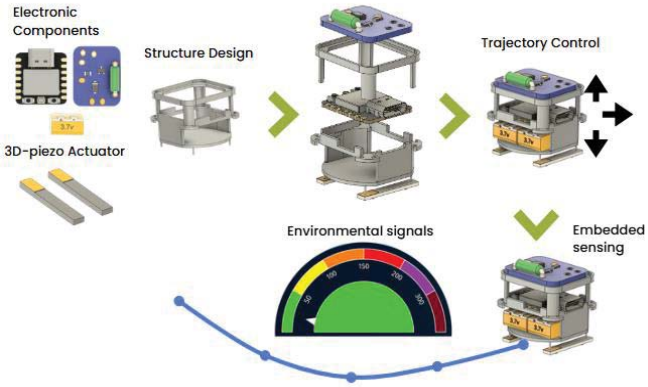


Figure 1 Methodology for the Trajectory Control of a Miniature Robot.

The system components are described below:

- **3D-piezo actuators:** These elements are responsible for generating the robot's motion. They are fabricated using 3D printing with Formlabs Rigid 10K resin and incorporate strategically placed PZT patches to generate standing waves (SW).
- **Electronic components:** The robot integrates onboard electronics consisting of batteries, a microcontroller, inertial sensors (IMU), an air quality sensor, a distance sensor, and a power board.

 DOI: 10.30420/456743065

- **Structure:** The structure is 3D-printed and includes mounting bases for the electronic components, as well as pillars positioned at the nodes of the standing waves, which serve as coupling elements with the 3D-printed plates and piezo actuators.
- **Trajectory control:** To ensure proper robot displacement, a control stage is implemented to maintain the robot along a predefined trajectory.
- **Environmental signals:** The integrated sensors acquire signals related to air quality and distance, which are transmitted and visualized on a computer through a telemetry stage.

2.1 3D-Printed plates with piezo actuators

For the robot's locomotion, unimorph piezoelectric patches made of lead zirconate titanate (PZT) PIC 255 from PI Ceramic [11] were used. These patches, with dimensions of $H_{pzt} = 100\mu m$, $L_{pzt} = 5.5mm$, and $W_{pzt} = 3.5mm$, were bonded onto plates (A and B) using cyanoacrylate-based adhesive. The plates were manufactured using a Form3 SLA 3D printer with Rigid 10K resin.

The plate design enables excitation of the (50) and (60) vibration modes to achieve resonance. This configuration allows for the strategic placement of small legs that convert vibration into an impact (tapping) motion against the surface, thereby generating the robot's linear displacement. The design of the plates and legs is based on a previous study [7].

2.2 Electronic components

The robot's onboard electronics are based on the Seeed Studio XIAO nRF52840 Sense microcontroller. This board integrates a 6-axis inertial measurement unit (IMU), consisting of a triaxial accelerometer and a gyroscope, which is used for trajectory control. It also features Bluetooth Low Energy (BLE) connectivity for telemetry, enabling data transmission from the robot to external software.

Additionally, the system incorporates a distance sensor (VL53L0X) and an air quality sensor (SGP30), both of which communicate with the microcontroller via the I2C protocol. Finally, the power stage consists of two 3.7 V Li-Po batteries (generic, China) connected in series, supplying the operating voltage to both the microcontroller and the control circuits. This integration is illustrated in the schematic diagram shown in **Figure 2.**

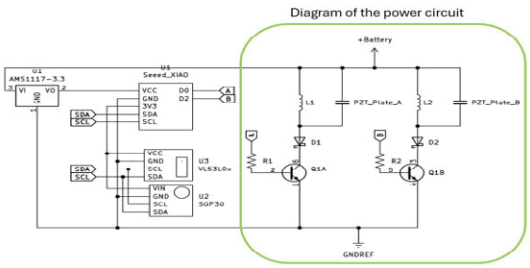


Figure 2. Electronic schematics of the miniature robot.

The power circuit is responsible for switching the 3.3 V control signals generated by the microcontroller with the 7.4 V supply obtained from the batteries. In conjunction with the two piezoelectric patches (PZT_Plate_A and PZT_Plate_B), this stage converts these signals into an $81.2Vpp$ waveform with a current of 30 mA. These excitation signals provide the necessary energy for the resonant plates to generate sufficient thrust for the robot's locomotion. To determine the appropriate inductor value for tuning the system to the (50) and (60) modes, Equation 1 was used, ensuring impedance matching and efficient resonance.

$$L_{Driver} = 1/((2\pi n f_{mode})^2 C_{PZT}) \quad (1)$$

Where n represents the ratio of the electrical resonance frequency of the LC circuit to the modal resonance frequency of the resonant plate f_{mode}. For the two vibration modes considered, the (50) mode at 60kHz and the (60) mode at 95kHz, the condition $n = 2$ would yield two different optimal inductance values.

However, when a single inductor is used, two scenarios arise:

• If L_{Driver} is adjusted to (60) mode, then $n_{60} = 2$ and $n_{50} = 2f_{60}/f_{50} \approx 3$.

• If L_{Driver} is chosen for (50) mode, then $n_{50} = 2$ and $n_{60} = 2f_{50}/f_{60} \approx 1.3$.

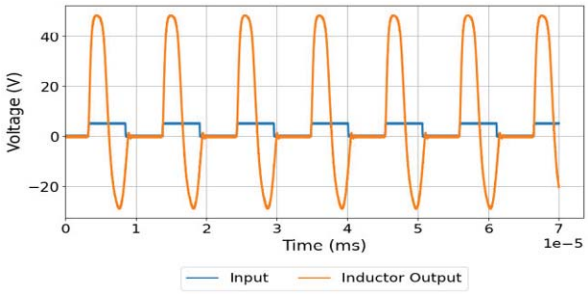


Figure 3. Piezoelectric voltage (voltage at the inductor terminals applied to the actuator) and control signal (PWM input from the microcontroller) at $f_{mode} = 95kHz$ with a 50% duty cycle.

2.3 Structure

The robot's structure consists of a compact and lightweight chassis fabricated through 3D printing using Clear resin [12]. This design is optimized to integrate the system modules: the control unit, power circuit, lithium polymer batteries, sensors, and piezoelectric actuators (**see Figure 1**). The chassis serves as the mechanical link between the control electronics and the resonant plates (Plates A and B). To maximize system efficiency, the connecting pillars are strategically positioned at the standing waves nodes, which are in close proximity for modes (50) and (60). This arrangement minimizes vibration damping and ensures effective resonant coupling between the actuators and the structure.

2.4 Trajectory control

For trajectory control, a Proportional-Derivative (PD) controller was implemented. This control strategy acquires the angular velocity around the Z-axis using an inertial measurement unit (IMU), whose signal is processed through a

 DOI: 10.30420/456743065

Kalman filter to mitigate intrinsic noise and mechanical disturbances caused by piezoelectric excitation. The filtered signal is then used to compute the error with respect to the reference trajectory.

Based on this error, the control algorithm compensates for deviations by modulating the excitation frequencies of (50) and (60) modes applied to the piezoelectric actuators, ensuring that the tracking error converges to zero during the robot's trajectory-following process. The system's control block diagram is presented in **Figure 4.**

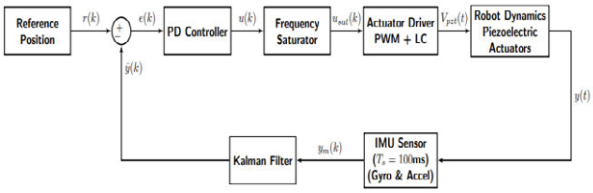


Figure 4. Block diagram for the trajectory control of the miniature robot.

The trajectory-tracking control law is based on a discrete PD controller, whose output, $PD_out|k$, is defined by the following experimentally tuned general equation:

$$PD_{out|k} = Kp.e_{k|k} + (Kd/Ts)\,(e_{k|k} - e_{k-1|k-1}) \quad (2)$$

Where the parameters $Kp = 700$ and $Kd = 80$ were selected to balance response speed and system stability, operating with a sampling time of $Ts = 100ms$.

To generate the robot's linear and rotational motions, a frequency-switching logic was implemented for actuators A and B. This logic enables clockwise (CW) or counterclockwise (CCW) rotations depending on the sign of the error, while maintaining a base frequency of $60kHz$ for linear displacement, as defined by the function $f(PD_{out})$:

$$\text{If } PD_{out} < 0, then\ (A = fr_{out}, B = 60000).$$
$$\text{If } PD_{out} = 0, then\ (A = 60000, B = 60000).$$
$$\text{If } PD_{out} > 0, then\ (A = 60000, B = fr_{out}).$$

Finally, to protect component integrity and avoid unnecessary saturation, the output frequency is limited by a saturator that constrains the maximum excitation value to 95 kHz:

$$fr_out_sat = min(fr_out, 95000) \quad (3)$$

2.5 Environmental and obstacle sensing

The VL53L0X and SGP30 sensors are strategically integrated at the front and bottom of the robot to expand its interaction capabilities with the environment. The VL53L0X sensor enables real-time obstacle detection that may interfere with the system's forward motion. Meanwhile, the SGP30 sensor is utilized for environmental monitoring to detect gas leaks and volatile organic compounds (VOCs) emitted by toxic substances encountered while navigating a predefined trajectory (**Figure 5**). This sensing configuration allows the robot not only to correct its path but also to function as an inspection platform in potentially hazardous environments.

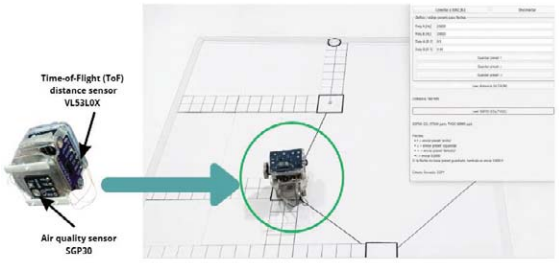


Figure 5. Placement of VL53L0X and SGP30 sensors for environmental data acquisition during trajectory execution.

To obtain parts-per-million (ppm) measurements, the SGP30 sensor leverages variations in the metal oxide film's electrical resistance triggered by the chemisorption of gas molecules. This relationship is expressed by Equation 4:

$$R_s = A \cdot C^{\alpha} \quad (4)$$

Where R_s is the sensor resistance, C is the gas concentration, A is a proportionality constant, and α is the material sensitivity factor. To process the signal, an internal dynamic baseline compensation algorithm is applied, which linearizes the logarithmic response. This allows the conversion of the ratio between the current resistance and a historical reference R_{base} into digital concentration values, as expressed in Equation 5:

$$TVOC\ (ppb) = f(R_s/R_{base}) \quad (5)$$

To ensure the accuracy of tested isopropyl alcohol and gas measurements during the robot's trajectory, a mathematical compensation based on absolute humidity H_a is applied, mitigating environmental disturbances as described by Equation 6:

$$R_{corr} = R_s \cdot e^{\beta}(H_a - H_{ref}) \quad (6)$$

3 Results

The experimental evaluation of the miniature robot was structured into two main tests:

1. Trajectory error tests, carried out under two conditions: (a) Without trajectory control; (b) With proportional–derivative (PD) control for path correction.
2. Air quality signal acquisition.

3.1. Trajectory error tests

The robot was evaluated in open loop using frequencies of $60kHz$ with a 65% duty cycle. When following a horizontal reference at $y_r(t) = 0$, monitored by a camera, the system exhibited progressive drift. After 19 seconds, the accumulated linear error, calculated as $e(t) = y_r(t) - y(t)$, reached 58 mm. The robot's trajectory without control is shown in **Figure 6**.

DOI: 10.30420/456743065

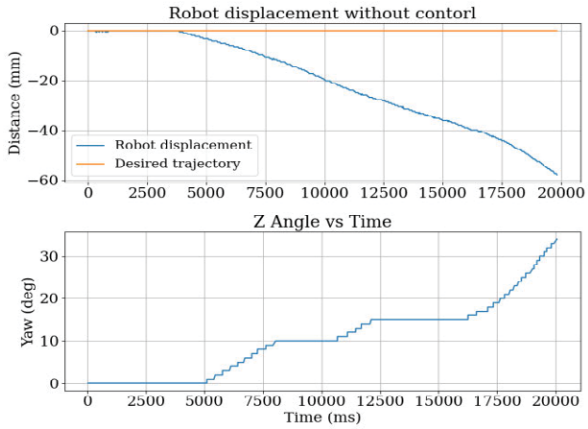


Figure 6. Open-loop motion of the miniature robot under excitation at 60 kHz (65% duty cycle), and angular deviation of the robot measured with the gyroscope during open-loop operation.

For closed-loop control, a PD controller was applied while following a reference of $y_r(t) = 0$ on a glass surface. By monitoring the motion with a camera over $20s$, the system successfully corrected its trajectory, reducing the deviation to an average error of just $4mm$.

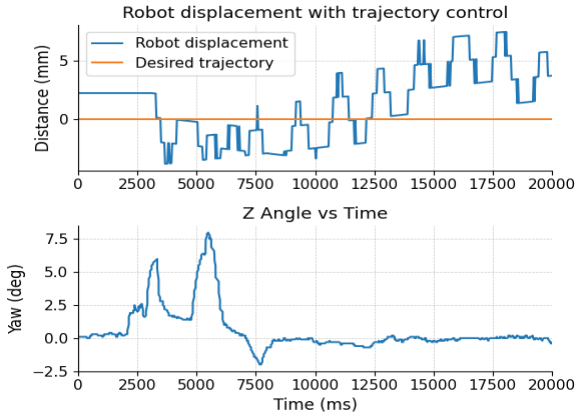


Figure 7. Closed-loop trajectory control performance using a PD controller and closed-loop angular response obtained from the gyroscope output.

Table 1 summarizes the mean of ten trials conducted under equivalent experimental conditions on the same surface.

Table 1. Trajectory deviation metrics in closed-loop condition.

MAE	RMSE	Max e
0.83°	1.73°	8°

3.2. Air quality signal acquisition

To evaluate the gas sensing capability, the robot navigated a predefined three-station track while the SGP30 sensor acquired TVOC measurements at 1 sample per second. Prior to testing, the sensor was powered for five hours to allow its internal baseline compensation algorithm to stabilize.

At station 1, the robot recorded near-baseline TVOC levels (approximately 400 ppb), confirming clean ambient conditions at the starting position. Upon reaching station 2, where 1 µL of isopropyl alcohol (C_3H_7OH) had been deposited, the sensor registered an abrupt increase peaking at approximately 7000 ppb, consistent with a high-concentration VOC exposure event. As the robot continued toward station 3, TVOC readings decreased progressively to approximately 3000 ppb, though they did not return to baseline due to residual alcohol vapor dispersed in the ambient environment (see **Figure 8**).

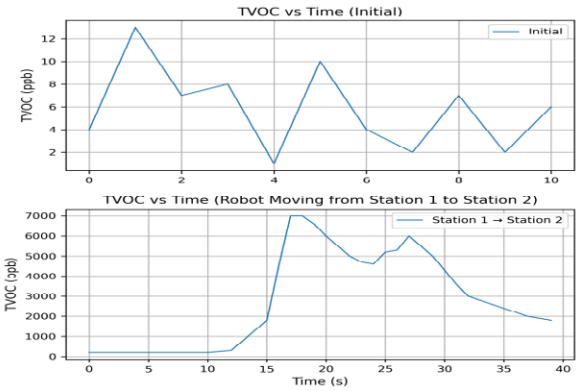


Figure 8. TVOC concentration recorded by the SGP30 sensor during robot navigation across the three-station navigation track. (a) Initial sensor baseline conditions. (b) TVOC profile during full navigation.

Table 2 presents the sensor data alongside a comparison with certified measurement equipment.

Table 2. TVOC readings from the SGP30 sensor at each navigation station.

Station	Condition	SGP30 TVOC (ppb)	Reference TVOC (ppb)	Absolute error (%)
1	Pre-source (baseline)	400	443	9.71
2	At alcohol source (peak)	7000	7600	7.89
3	Post-source (decreasing)	3000	2850	5.26

In addition, the VL53L0X time-of-flight sensor was used to measure the robot's distance to surrounding walls at each station, with the robot-oriented left, forward, and right. Table 3 compares the measured coordinates against the ground-truth reference values.

Table 3. Distance measurements from the VL53L0X sensor at each navigation station (cm).

Station	Reference (L × F × R)	Measured (L × F × R)	Err L	Err F	Err R
1	(6, 16, 21)	(6.3, 17.3, 21.3)	+0.3	+1.3	+0.3
2	(12, 9, 16)	(12.3, 10, 15.3)	+0.3	+1.0	−0.7
3	(21, 12, 7)	(20.6, 11.4, 8)	−0.4	−0.6	+1.0
MAE	—	—	**0.33**	**0.97**	**0.67**

The VL53L0X sensor achieved a mean multi-directional distance measurement error of 1.29 cm, corresponding to an overall percentage error of 5.23%, which is considered acceptable for this class of miniature robot.

4 Conclusions

This work demonstrated the successful integration of piezoelectric actuation, additive manufacturing, and embedded sensing into a compact insect-scale autonomous robot. Selective excitation of the (50) and (60) vibration modes enabled bidirectional locomotion at linear speeds of 7 mm/s and angular speeds of 30°/s.

Closed-loop trajectory control using a discrete PD controller with Kalman-filtered gyroscope feedback achieved a mean absolute error of 0.83° and an RMSE of 1.73° over ten trials, reducing lateral drift from 58 mm in open-loop to 4 mm under controlled operation.

Environmental sensing was validated across a three-station navigation track. The SGP30 sensor detected a peak TVOC concentration of approximately 7000 ppb at the isopropyl alcohol source, with readings decreasing to 3000 ppb downstream, showing comparable response to reference instrumentation. The VL53L0X sensor achieved a mean three-dimensional positioning error of 1.29 cm (5.23%).

These results confirm the platform's suitability for autonomous navigation and chemical inspection in confined environments. Future work will address two-dimensional path planning, extended battery autonomy, and validation across a broader range of volatile compounds.

5 Funding

This work was supported by the Universidad de Castilla-La Mancha, Spain, through MCIN/AEI and FEDER “ERDF A way of making Europe” under Grant PID2023-146163OB-I00 and Universidad Politécnica Salesiana, Quito-Ecuador.

6 Literature

[1] Pfeifer, R.; Lungarella, M.; Iida, F. The Challenges Ahead for Bio-Inspired ’Soft’ Robotics. Commun. ACM 2012, 55, 76–87.

[2] Zhang, Y.; Li, J.; Chen, X.; Wang, H. Bioinspired Sensors and Applications in Intelligent Robots: A Review. Robot. Artif. Intell. 2023, 10, 88–104.

[3] Li, Z.; Li, C.; Dong, L.; Zhao, J. A Review of Microrobot’s System: Towards System Integration for Autonomous Actuation In Vivo. Micromachines 2021, 12, 1249.

[4] Zou, W.; Ma, E.; Chen, H.; Lin, F.; Xiao, Z.; Zhang, Z.; Jiang, J.; Niu, Y.; Yu, P.; Wang, C. Locomotion for Insect-Scale Robots with Bionic Strategies: A Review. J. Field Robot. 2025, 42, 1586–1616.

[5] Ruiz-Díez, V.; Hernando-García, J.; Toledo, J.; Ababneh, A.; Seidel, H.; Sánchez-Rojas, J.L. Comparative Study of Traveling and Standing Wave-Based Locomotion of Legged Bidirectional Miniature Piezoelectric Robots. Actuators 2021, 10, 136.

[6] He, S.; Chen, W.; Tao, X.; Chen, Z. Standing Wave Bi-directional Linearly Moving Ultrasonic Motor. IEEE Trans. Ultrason. Ferroelectr. Freq. Control 1998, 45, 1133–1139.

[7] Ruiz-Díez, V.; García-Caraballo, J.L.; Hernando-García, J.; Sánchez-Rojas, J.L. 3D-Printed Miniature Robots with Piezoelectric Actuation for Locomotion and Steering Maneuverability Applications. Actuators 2021, 10, 335.

[8] Wang,W.; Li, J.; Zhang, S.; Deng, J.; Chen, W.; Liu, Y. A Snail-Inspired Traveling-Wave-Driven Miniature Piezoelectric Robot. Cell Rep. Phys. Sci. 2024, 5, 102201.

[9] Wu,Y.; Cao, L.; Lu, G.; Wang, P.; Ran, L.; Peng, B. Untethered Soft Microrobot Driven by a Single Actuator for Agile Navigations. Nat. Commun. 2025, 16, 61810.

[10] Goldberg, B.; Zufferey, R.; Doshi, N.; Helbling, E.F.; Whittredge, G.; Kovac, M.; Wood, R.J. Power and Control Autonomy for High-Speed Locomotion with an Insect-Scale Legged Robot. IEEE Robot. Autom. Lett. 2018, 3, 987–993.

[11] PI Ceramic GmbH. PI Ceramic Material Data. Datasheet. 2025. Available online: https://www.piceramic.com/fileadmin/user_upload/ physik_instrumente/files/datasheets/PI_Ceramic_Material_Data.pdf (accessed on 20 November 2025).

[12] Formlabs. Clear Resin—Safety Data Sheet (SDS).2022. Available online: https://formlabs-media.formlabs.com/datasheets/1801 037-SDS-ENUS-0.pdf (accessed on 11 November 2025).

 DOI: 10.30420/456743066

Investigation of the influence of dynamic magnetic excitation during drag finishing using abrasive magnetorheological fluids

Fabian Sordon[a] and Jürgen Maas[a]
[a]Mechatronic Systems Lab, Technische Universität Berlin, Hardenbergstraße 36, 10623 Berlin, Germany

Abstract

The demand for high-precision finished components with complex geometries in industrial applications is very high and diverse [1, 2]. Especially, finishing technologies involving abrasive magnetorheological fluids are becoming increasingly widespread, as they enable a controllable grinding effect, particularly for complex geometry components [3]. Previously, a novel finishing process involving magnetorheological fluids for drag finishing of milling tools has been investigated using static magnetic fields applied to the working area of the finishing process [4, 5]. In this work, the influence of dynamic magnetic fields on the overall finishing process will be investigated, promising enhanced particle blending and finishing performance. For that purpose, a magnetic excitation circuit made of laminated flux-conducting material is utilized, into which a container filled with magnetorheological fluids is inserted. Workpieces are moved through the container to achieve abrasive effects. Experimental testing involves variation of magnetic excitation frequency between 0 Hz and 50 Hz using workpieces of high-speed steel and micro-milling tools of tungsten carbide. The micro-geometry of the workpieces is analyzed before and after testing using optical microscopy. This work comprehensively investigates the potential of applying dynamic magnetic fields for drag finishing using abrasive magnetorheological fluids and enables the selection of desired excitation frequencies for enhanced finishing quality.

1 Introduction

Magnetorheological fluids (MRF) are suspensions of magnetizable carbonyl-iron particles, carrier fluid and additives. MRFs behave like Newtonian fluids without magnetic excitation, but under magnetic excitation form solid chains between magnetized particles that strongly influence the flow properties [6]. This behaviour qualifies MRF for application in finishing processes of complex geometries (e.g., milling tools), as process parameters such as material removal can be controlled by an applied magnetic field. Figure 1 shows a typical geometry of a milling tool and the general procedure of the cutting-edge preparation is illustrated, in which chipping of the edge is reduced and the overall surface is homogenized.

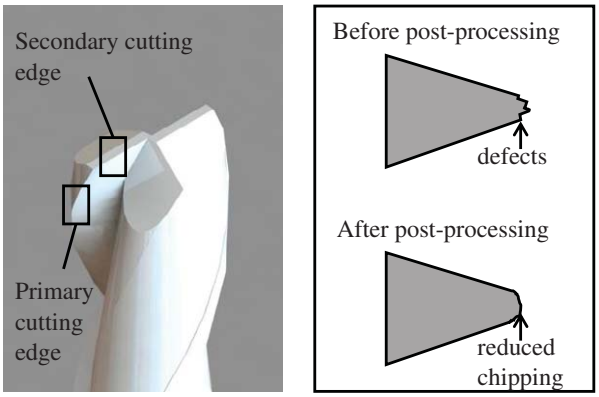


Figure 1 Typical micro-milling tool geometry and schematic diagram of cutting edge preparation, following [7].

In [4], the MRF drag finishing process was introduced, in which abrasive tests were conducted with specimens of high-speed steel (HSS) EW9Co10. The HSS specimens were moved and rotated through a container filled with abrasive MRF and excited with a static magnetic field. Figure 2 illustrates the procedure of the MRF drag finishing process using static magnetic fields. In (a), the abrasive MRF suspension is arbitrarily distributed within the container, in (b), solid-state chains form along the static magnetic flux and in (c), the specimen is moved within the container and grinding is achieved by interaction of abrasive particles and specimen surfaces.

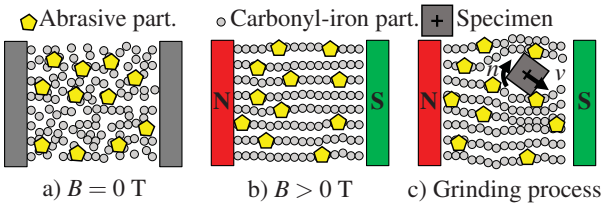


Figure 2 Schematic diagram of the MRF drag finishing process [5].

In this work, the influence of dynamic magnetic excitation frequency on the finishing performance of drag finishing using abrasive magnetorheological fluids is investigated, leading to the following key research questions:

- Can time-dependent magnetic excitations lead to improved surface quality results?

DOI: 10.30420/456743066

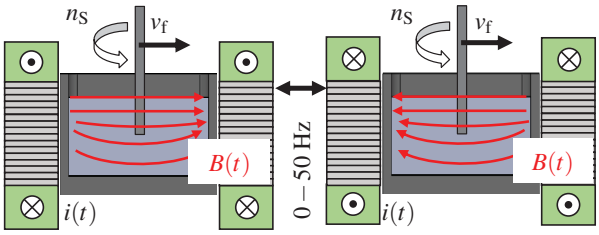


Figure 3 MRF drag finishing process with dynamic excitation.

Table 1 Parameters of the dynamic magnetic circuit.

Parameter name	Abbr.	Value
MRF-container height	h_{mrf}	12 mm
MRF-container diameter	d_{mrf}	36 mm
Wire diameter	d_w	0.65 mm
Max. mag. flux density	B_{air}	53 mT (@ $i_{max} = 2.5$ A)
Electrical resistance	R	1.4 Ω
Winding number	N	70
Coil-inductance	L_c	11.12 mH ($Q = 10.64$)

- Can time-dependent magnetic excitations also achieve enhanced finishing results with respect to removed material/ edge rounding?

For this purpose, a test bench consisting of a dynamic magnetic excitation circuit, an MRF container and a CNC portal system is implemented. In Figure 3, the functionality of the test bench is illustrated. The magnetic flux density is excited with two coil pairs on opposing laminated pole shoes connected to current-controlled power electronics. The alternating magnetic flux density $B(t)$ is excited with varying frequencies of $f_m = 0$ Hz up to higher frequencies of $f_m = 50$ Hz with a sinusoidal current signal $i(t)$. Within the abrasive MRF (between the pole-shoes), the specimens are rotated and moved translationally at a certain rotational speed n_S and feed rate v_f.

2 Materials and methods

2.1 MRF test bench

As a magnetic excitation circuit, suitable for time-dependent magnetic field variation of relatively high frequencies up to 50 Hz, we used the single-phase *stator field pole shoe 621708-9* of *Makita Werkzeug GmbH* with one pole-pair and magnetic flux-conducting casing built of laminated steel. Figure 4 illustrates the magnetic circuit including the MRF container with a diameter $d_{mrf} = 36$ mm, where the MRF is filled to at a height of $h_{mrf} = 12$ mm. In Table 1, all further parameters of the magnetic circuit are listed, including the wire diameter d_w, the magnetic field B_{air} within the air gap at a current of $i_{max} = 2.5$ A, the electrical resistance R, the winding number N and the coil-inductance L_c.

For mechanical movement of the specimens, the magnetic circuit is placed within the CNC milling machine *PFM 24*

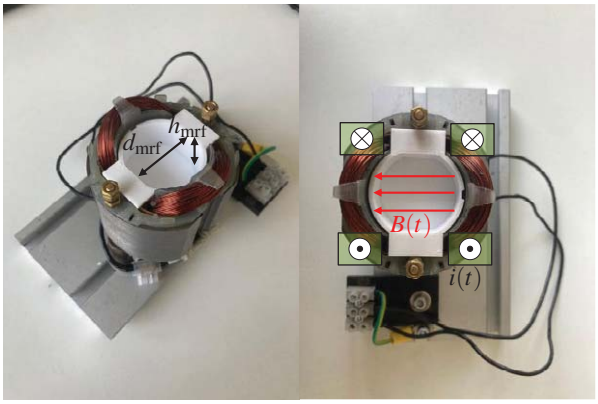


Figure 4 Dynamic magnetic excitation circuit made of laminated flux-conducting material.

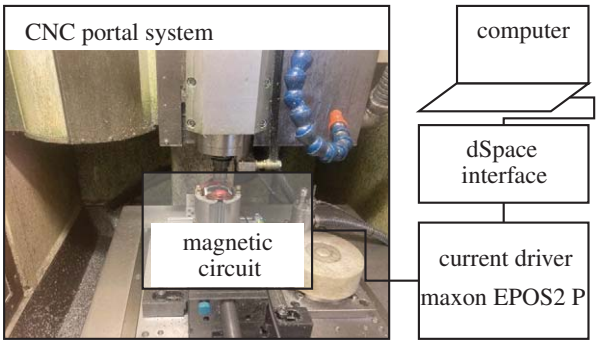


Figure 5 Overview of the test bench including the dynamic magnetic excitation circuit within the CNC portal system.

Medimill. To control the magnetic field during processing, the magnetic circuit is then connected to the current supply *maxon EPOS2 P*, which is controlled by a dSPACE interface. In Figure 5, a schematic overview of the test bench is illustrated, where the experiments are carried out.

2.2 Magnetic study

To investigate the magnetic behavior of the dynamic magnetic excitation circuit within the MRF container, a two-dimensional FE analysis was conducted within the magnetic fields framework of COMSOL Multiphysics. A stationary solver was utilized to compute a total of 17493 degrees of freedoms for 8646 triangular elements in a simulation time of $t_{sim} = 2$ s. Figure 6 shows the magnetic flux density B within the magnetic circuit for a coil current of $I_{max} = 2.5$ A. Qualitatively, the magnetic field remains relatively homogeneous within the MRF container. Within the air gap, the simulation results in a magnetic flux density of $B_{air,sim} = 0.45$ mT (compared to a measured magnetic field of $B_{air} = 0.53$ mT). Therefore, within the FE model, the magnetic flux density is slightly underestimated. One reason for this can be, that within the FE model, the third dimension is neglected. However, due to the larger relative permeability of MRF, the magnetic

 DOI: 10.30420/456743066

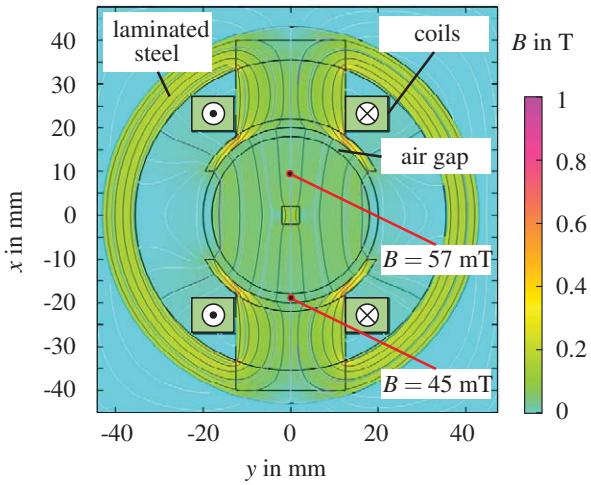


Figure 6 COMSOL Multiphysics simulation of the magnetic flux density B within dynamic magnetic excitation circuit at maximum coil current of $I_{\mathrm{max}} = 2.5$ A.

flux density within the MRF container is significantly larger at $B_{\mathrm{mrf,sim}} = 0.57$ mT. The ratio of magnetic field within the air gap and within the MRF is computed by $k_{\mathrm{m}} = B_{\mathrm{mrf,sim}}/B_{\mathrm{air,sim}} \approx 1.25$. We therefore determine the magnetic flux density of $B_{\mathrm{mrf}} = B_{\mathrm{air}} \cdot k_{\mathrm{m}} = 66$ mT within the MRF container in the experimental setup for a coil current of $I_{\mathrm{max}} = 2.5$ A.
In Figure 7, the measurement of the magnetic flux density within the air gap for varying static coil currents is shown. It is visible, that the magnetic flux density $|B|$ is nearly proportional to the coil current I under static conditions. Due to the low magnetic flux density, we can assume that the magnetic material exhibits linear behavior, as shown by the measurements in Figure 7. Furthermore, the influence of the magnetic excitation frequency f_{m} on the magnetic flux density was investigated. For that purpose, the magnetic flux density was measured for varying excitation frequencies $f_{\mathrm{m}} \in [0,5,25,50]$ Hz using a hall sensor of type AS active probe of *Mess - und Regelungstechnik GmbH*. In Figure 8, the corresponding measurements are illustrated. At static conditions in the first plot ($I = \mathrm{const.}$), a magnetic field of $B_{\mathrm{air}} = 53$ mT is reached as expected, according to Figure 7. For sinusoidal excitation, the current is chosen to $i(t) = \hat{i} \cdot \sin(2\pi \cdot f_{\mathrm{m}} \cdot t)$, with $\hat{i} = 2.5$ A $= \mathrm{const.}$ At an excitation frequency of 5 Hz, a maximum magnetic field of $B_{\mathrm{air,max}} = 51$ mT is measured, comparable to static results. At an excitation frequency of 25 Hz, the losses within the magnetic circuit slightly increase and a maximum magnetic field of $B_{\mathrm{air,max}} = 48$ mT is measured. At an excitation frequency of 50 Hz, however, the losses within the magnetic circuit significantly increase and a only maximum magnetic field of $B_{\mathrm{air,max}} = 37$ mT is measured. Subsequently, the dynamic magnetic circuit shows relatively low magnetic losses up to an excitation frequency of $f_{\mathrm{m}} = 25$ Hz, while at $f_{\mathrm{m}} = 50$ Hz, the losses significantly increase. But, the frequency response is still sufficient for the subesquent test

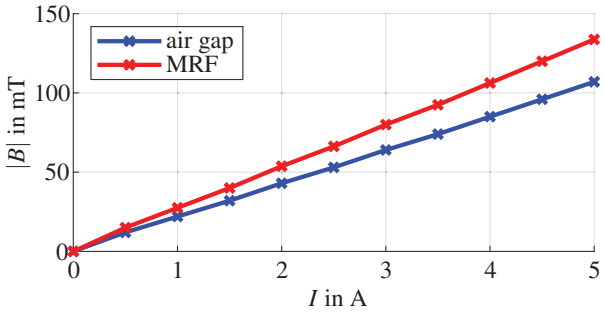


Figure 7 Static measurement of the magnetic flux density $|B|$ for variation of the coil current I.

up to a range of 50 Hz.

2.3 Preparation of MRF, samples and process parameters

Within this work, we investigate two different series of experiments:

1. Test-series with square-bar HSS specimens
2. Test-series with micro-milling tool specimens

For test-series 1, the HSS specimens have a geometry of $h_{\mathrm{hss}} \cdot b_{\mathrm{hss}} \cdot l_{\mathrm{hss}} = 4 \cdot 4 \cdot 65$ mm³ and are of EW9Co10 material. As abrasive particles, we use mono-crystalline diamond abrasive particles (AP) with a diameter of $d_{\mathrm{AP}} = 296.7$ µm. The abrasive particles are blended with the MRF with an AP volume fraction of $\varphi_{\mathrm{ap}} = 15$ %, while the carbonyl-iron particles (CIP) remained at a CIP volume fractino of $\varphi_{\mathrm{cip}} = 45$ %.
For test-series 2, the milling-tool specimens have a diameter of $d_{\mathrm{wc}} = 900$ µm and are of tungsten carbide WC-Co10. As abrasive particles, we use mono-crystalline diamond abrasive particles with a diameter of $d_{\mathrm{AP}} = 12.3$ µm. The abrasive particles are blended with the MRF with an AP volume fraction of $\varphi_{\mathrm{ap}} = 9$ %, while the carbonyl-iron particles remain at a CIP volume fraction of $\varphi_{\mathrm{cip}} = 45$ %.
In Figure 9, the different abrasive particle types for both test series are illustrated. Figure 10 shows the square-bar HSS specimens and the WC micro-milling tool specimens. In Table 2, the corresponding parameters are listed, including parameters, that remain constant for both test series, namely the immersion depth t_{E}, feed rate v_{f}, spindle speed n_{S} and test duration Δt. The micro-geometry of all specimens are monitored before and after the experiment using the *infiniteFocus G4* focus variation microscope, with which the edge radius and average mean roughness before ($r_{\beta 1}$, R_{z1}) and after testing ($r_{\beta 2}$, R_{z2}) can be deduced. For the material removal rate of the HSS samples, we calculate the material removal rate with $Q = 4 \cdot \Delta A \cdot t_{\mathrm{E}}/\Delta t$, where the change in the cross-sectional area of the edge is determined from $\Delta A = r_{\beta 2}^2(1-\pi/4) - r_{\beta 1}^2(1-\pi/4)$.

DOI: 10.30420/456743066

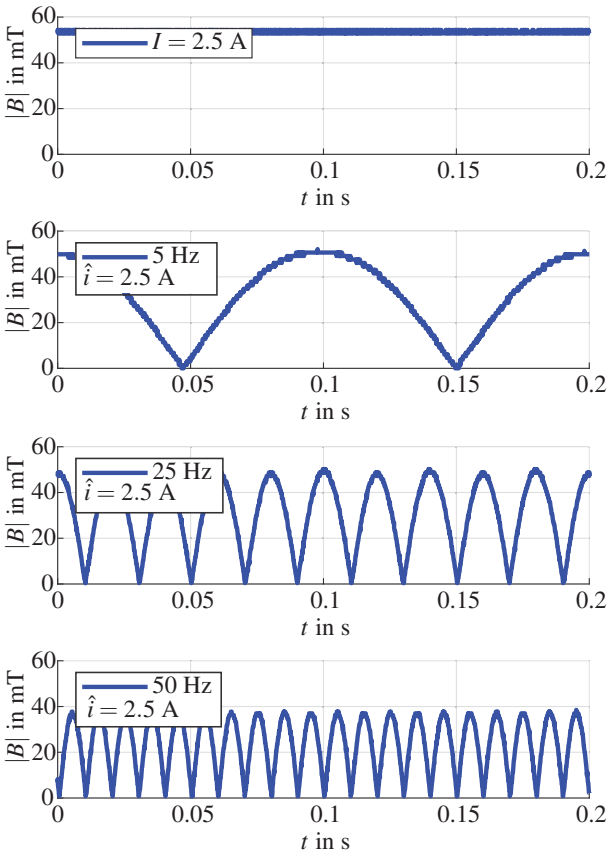


Figure 8 Dynamic measurement of the magnetic flux density $|B|$ for variation of the coil current $i \neq$ const. at excitation frequencies of $f_\mathrm{m} \in [0,5,25,50]$ Hz.

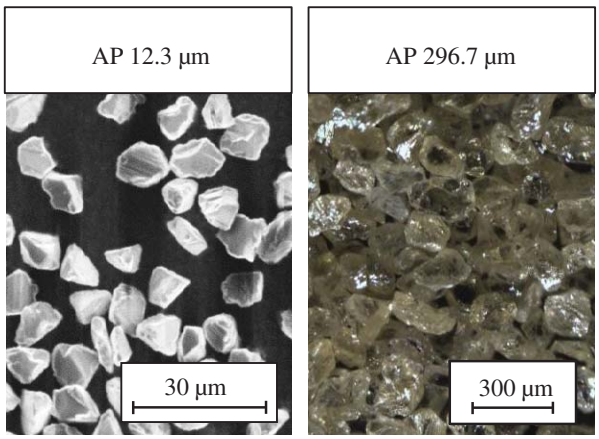


Figure 9 Abrasive particles consisting of monocrystalline diamond with a diameter of 12.3 µm and 296.7 µm.

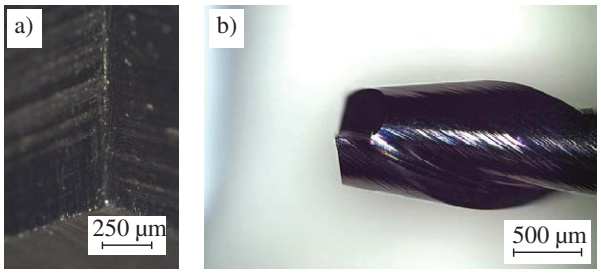


Figure 10 Abrasive samples for test series 1 and 2. a) HSS-specimen (4 mm · 4 mm · 65 mm) for test series 1 and b) micro-milling tool ($d = 900$ µm) of tungsten carbide for test series 2.

Table 2 Parameters of the MRF abrasive experiments.

Parameter name	Abbr.	Value
HSS specimen geom.	$h_\mathrm{hss} \cdot b_\mathrm{hss} \cdot l_\mathrm{hss}$	$4 \cdot 4 \cdot 65$ mm³
WC specimen diam.	d_wc	900 µm
Immersion depth	t_E	10 mm
Feed rate	v_f	10 mm/s
Spindle speed	n_S	10 000 rpm
Test duration	Δt	30 min

3 Results

For the test series with HSS square bar samples, five different testing configurations were used. Firstly, the magnetic flux density remained zero ("REF 0 T") as a reference. Secondly, a static magnetic field was excited ("0 Hz") at a coil current of $i_\mathrm{max} = 2.5$ A. Subsequently, the coil current was excited with a sinusoidal input signal at excitation frequencies ("5 Hz"), ("25 Hz") and ("50 Hz"). All tests were conducted twice, leading to a total of 10 abrasive tests. Figure 11 shows an exemplary image of one abrasive sample before and after processing at a magnetic excitation frequency of $f_\mathrm{m} = 5$ Hz. A homogeneous surface roughness reduction is qualitatively visible, as well as a material removal and rounding on the edges of the specimen. In Figure 12, a quantitative evaluation of the material removal rate Q and the change in average mean roughness $\mathrm{d}R_z = R_{z2} - R_{z1}$ is provided. It appears that material removal is increased and the average mean roughness is drastically decreased for an excitation frequency of $f_\mathrm{m} = 5$ Hz, while for the other experiments, there is no significant change compared to the reference experiment at 0 T and to the static case at 0 Hz. However, the standard deviation for this observation is relatively high.
Therefore, a test series with micro-milling tools was carried out for more reproducible results. For the milling tools, three different testing configurations were used, where, firstly, a static magnetic field was used ("0 Hz"), and secondly, the dynamic excitation frequencies ("5 Hz") and ("25 Hz") were utilized. The micro-geometry of each specimen was measured at six different positions to verify the reproducibility of the results. Figure 13 shows an examplary 3D-geometry of the cutting-edge of a specimen

ISBN: 978-3-8007-6743-4

@ VDE VERLAG GMBH · Berlin · Offenbach

DOI: 10.30420/456743066

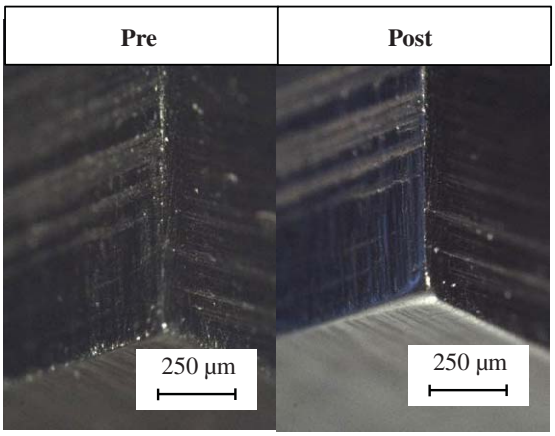


Figure 11 Exemplary characterization of the HSS specimen tool edges before and after finishing for $f_\mathrm{m} = 5$ Hz.

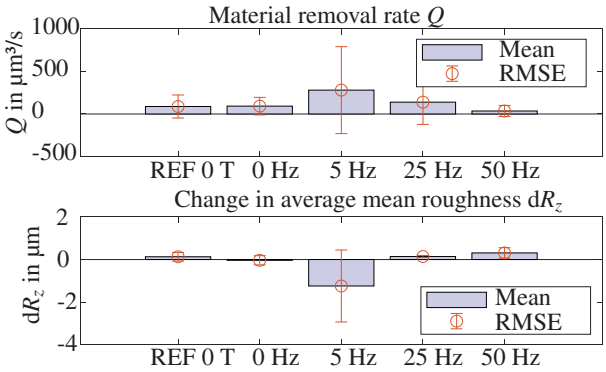


Figure 12 Quantitative micro-geometry analysis of the HSS specimens for varying f_m.

before and after testing. A slight rounding of the edges after testing (POST) can be seen in the colored contour lines. In Figure 14, the quantitative analysis is shown. Clearly, the RMSE was reduced for the experiments compared to the first test series. In the diagram above, the change in edge radius $\mathrm{d}r_\beta = r_{\beta 2} - r_{\beta 1}$ is visualized. It can be seen, that at $f_\mathrm{m} = 5$ Hz, the rounding of the cutting edge is significantly larger than for 0 Hz and 25 Hz, supporting the findings from the HSS experiments. However, all three experiments led to a decrease in surface roughness and no clearly advantageous excitation frequency could be determined.

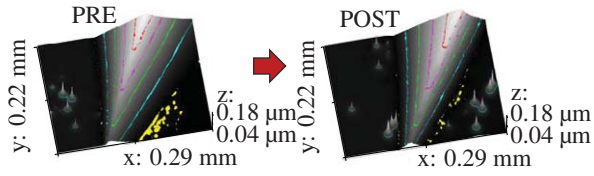


Figure 13 Exemplary characterization of the WC milling tool edges before and after finishing for $f_\mathrm{m} = 5$ Hz.

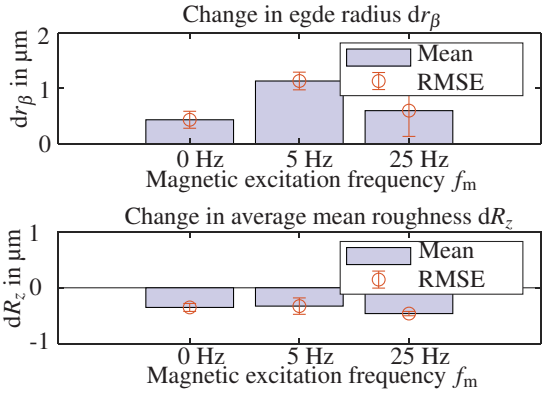


Figure 14 Quantitative micro-geometry analysis of the WC milling tools for varying f_m.

4 Conclusion and outlook

In this study, the effect of time-dependent magnetic excitations on the overall performance of MRF drag finishing was investigated. For this purpose, a test series with HSS square bar specimens was carried out followed by a test series using tungsten carbide milling tools. The following conclusions can be drawn:

- Both test series supported the initial hypothesis, that time-dependent magnetic excitations can improve the overall performance of MRF drag finishing.
- The HSS test series showed that both material removal rate and surface quality are improved at an excitation frequency of 5 Hz.
- The WC milling tool test series showed that edge rounding is increased at an excitation frequency of 5 Hz, while surface quality was improved at similar magnitudes for other excitation frequencies.

In future studies, we want to investigate a broader range of excitation frequencies to find the most desirable process parameters.

Acknowledgement

The authors thank the German research foundation DFG for funding this project (project number 503335130). Special thanks go to the Institute for Machine Tools and Factory Management (IWF), Technische Universität Berlin, Germany, for characterization of the abrasive samples.

Literature

[1] E Uhlmann et al. “Cutting edge preparation of micro milling tools”. In: *Procedia CIRP* 14 (2014), pp. 349–354.

[2] E Uhlmann et al. “Effects of different cutting edge preparation methods on micro milling performance”. In: *Procedia CIRP* 46 (2016), pp. 352–355.

 DOI: 10.30420/456743066

[3] Berend Denkena, Jens Köhler, and Andreas Schindler. “Behavior of the magnetic abrasive tool for cutting edge preparation of cemented carbide end mills”. In: *Production Engineering* 8.5 (2014), pp. 627–633.

[4] Fabian Sordon et al. “Abrasive properties of magnetorheological fluids for immersed tumbling processes”. In: *38th Annual Meeting of the American Society for Precision Engineering, ASPE 2023*. 2023.

[5] Fabian Sordon et al. “Rheological properties of abrasive magnetorheological fluids for immersed tumbling processes”. In: *ACTUATOR 2024; International Conference and Exhibition on New Actuator Systems and Applications*. VDE. 2024, pp. 64–67.

[6] Dirk Güth and Jürgen Maas. “Characterization and modeling of the behavior of magnetorheological fluids at high shear rates in rotational systems”. In: *Journal of Intelligent Material Systems and Structures* 27.5 (2016), pp. 689–704.

[7] Fabian Sordon et al. “Extended study on the composition of magnetorheological fluids for the post-processing of micro-milling tools”. In: *ASPE Annual Meeting 2024*. Vol. 83. American Society for Precision Engineering (ASPE), 2024, pp. 330–335.

ISBN: 978-3-8007-6743-4 @ VDE VERLAG GMBH · Berlin · Offenbach

 DOI: 10.30420/456743067

Amplified Piezo Actuators with embedded Eddy Current Sensor for cryo space De-SPIN mechanism

Olivia Stadler[1], Guillaume Mansuy[1], Jocelyn Rebufa[1], Alexis Gierczak[1], Clément Cote[1], David Ferris[1], François Barillot[1], Frank Claeyssen[1], Boris Laluc[1]
(1) Cedrat Technologies, 38240 Meylan, France, guillaume.mansuy@cedrat-tec.com

Abstract

Piezoelectric actuators are known as a compact and dynamic solution for space laser pointing applications. Yet, to avoid the use of an HDRM (Hold Down Release Mechanism), the usual maximum load force needs to be increased, which impacts directly on the stroke performances of the actuator. Additionally, the cryogenic environment has a significant impact on the piezoelectric components, mechanical part and integrated sensor performance, especially on strain gauges that present an advantage in compacity and precision but that cannot operate under low temperatures.
The ESA funded the De-SPIN Project to address those challenges by designing and testing an actuator based on Amplified Piezoelectric Actuator (APA®) technologies that integrate new features to ensure the cryogenic compatibility, low magnetism and vibration resistance once integrated in a complete Fast Steering Mirror. This actuator can reach a 105µm stroke at -150°C with redundancy and can withstand an 18.04 g-RMS random vibration launch with a 0.125kg payload.

1 Introduction

The APA® is a mechanical magnified preloaded stack of low voltage piezoelectric ceramics (MLA) [1]. It usually includes an external elliptical shell that magnifies the deformation of the active components and one to various MLA. It is used by Cedrat Technologies for various space mechanisms such as XY stages and Tip-tilt / FSM for many years [2-4] but with only few tests in cryogenics [5].
To assess the cryogenic and vibration constraints, some modifications are added onto the actuator. The developed product is the APA600MML-PP NM, which includes a parallel pre-stress option (-PP) and is composed of Titanium (NM) to reduce the impact of the temperature on performance.
In the context of De-SPIN Project, three actuators will be integrated in a Tip/tilt mechanism with a 600g mirror, the whole forming a Cryo Fast Steering Mirror (FSM).

1.1 Target specifications and challenges

Name	Value
Stroke [-150°C;80°C]	95 µm
Random Launch vibration (Erreur ! Source du renvoi introuvable.)	18.04g RMS
Resolution in close loop	>86dB

Table 1: Specifications

The actuator must provide the stroke in the operating temperature range and considering redundancy at the level of the ceramics, only half of the ceramics should be powered to obtain the stroke. The structure of the actuator (**Figure 1**) will include two active components – only one powered up at the same time, a thermal compensation in between the ceramics that also serves as a target for the Eddy Current Sensor (ECS), two springs in parallel of the ceramic stack, a shell that magnifies the displacement of the ceramics, and an ECS sensor.

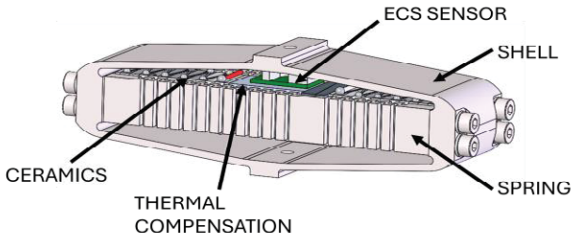


Figure 1: APA600MML-PP NM

2 Vibration performances

2.1 APA-PP design

To ensure the vibration performances, the actuator used includes a new feature compared to standard APA® by adding an overload of pre-stress on the piezo components to withstand up to twice the level of launch vibrations. It is based on the APA® Amplified Piezoelectric Actuator with Pre-Stressed option (APA-PP). This actuator combines the technologies of APA® and Parallel Pre-stressed Actuator (PPA) developed by Cedrat Technologies for various applications including space environment.
This feature was developed by Cedrat Technologies in the context of the APA120ML-PP (**Figure 2**) to increase the loading capabilities without impacting significantly the stroke and force performances.

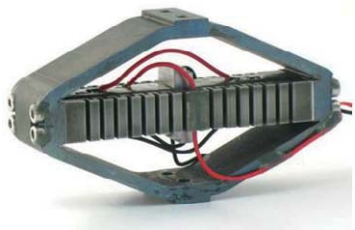


Figure 2: APA120ML-PP

 DOI: 10.30420/456743067

2.2 Applied force estimation

As first approach, the estimation of the force applied to the actuator during the launch is determined using Miles formula:

$$A_{RMS} = \sqrt{\frac{\pi}{2} * f * \left((1 + \left(\frac{1}{Q}\right)^2) * G_A * Q \right)}$$

Where

- A_{RMS} is acceleration in the axis of displacement of the actuator,
- f is the resonant frequency in displacement axis,
- Q is the quality factor of the piezoelectric component,
- G_A is the acceleration at the given resonant frequency depending on the vibration profile (**Figure 3**).

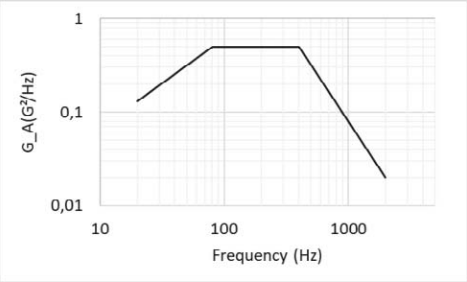


Figure 3: Vibration profile random

The force perceived by one actuator is computed using the formula:

$$F = A_{RMS} * m$$

where

- F is the force applied on the actuator in the displacement axis,
- m is the mobile mass from the mirror on one actuator (200g considered),

The Tip/Tilt mechanism in which the actuators are integrated can typically have three to four actuators integrated, dividing the maximum force perceived by each of them.
A 5-σ probability is added to reduce the probability of having a failure on the actuator.

Number of actuator integrated	Max. Force / actuator	Max. Force / actuator at 5-α probability
3	200 N	1015 N
4	150 N	760 N

Table 2: Applied Force per actuator

2.3 Force performances

The maximum force allowed on the APA600MML-PP NM is simulated using a three-dimensional finite element. The boundary conditions imposed are blocked-free configuration of the actuator.
A force is applied on top of the actuator in the displacement axis. The limit of the actuator is reached when the ceramics are left with no remaining preload.

The stroke specification for the actuator imposes a lowered stiffness of the actuator, inducing a better performance of the magnification for the ceramic stroke. Yet, it impacts directly on the limit for the dismounting force for the APA600MML-PP NM, the simulation shows a limit around 600N, which is not compatible with the Max. Force / actuator at 5-α probability showed in **Table 2** yet, it answers a 3-α probability (99.7%) for a three-actuator based mechanism. Four actuators integrated in a mechanism with a 0.5kg mirror could withstand the vibrations.
As a comparison, the APA200ML which provides an equivalent stroke when all ceramics are powered on, presents a maximum limit force of 470N. The additional prestress option allows to increase significantly the performances of the actuator under vibration for a lower ceramic ratio – the APA600MML-PP NM having 20% less of active components.

3 Cryogenic performances

Space environment can require an operating temperature in the cryogenic range which impacts directly the ceramic performances. Additionally, the use of standard strain gauges is not compatible with the use at -150°C, thus, an ECS sensor is integrated under the APA® head to measure the displacement of the actuator. Various tests are performed on another APA® actuator with similar ceramics and ECS sensor to validate the cryogenic performances.

3.1 Piezo ceramics

A prototype is used to validate the performance loss of the ceramics under cryogenic environment. The prototype actuator is placed in a cryogenic chamber with a Fabry-Perot interferometer sensor to measure the differential of displacement between the actuator and an inert target, limiting the coefficient of thermal expansion (CTE) effects of the test bench on the stroke performances results (**Figure 4**). The stroke is measured for different temperatures along the [-150°C;20°C] range.

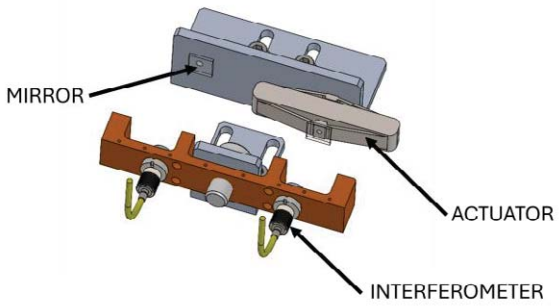


Figure 4: Test set-up for cryogenic chamber measurements

 DOI: 10.30420/456743067

3.2 Stroke loss of piezoelectric component in cryogenic environment

The displacement is measured in peak-to-peak mode, the initial value being subtracted.

Those measurements (**Figure 5**) show a loss of 50% of the ceramic performances under -150°C. Thus, in cryogenic environments, including redundancy, only one fourth of the active material performances are used.

The APA600MML-PP NM is dimensioned to have the 95 µm stroke at -150°C with only one ceramic due to the redundancy constraint.

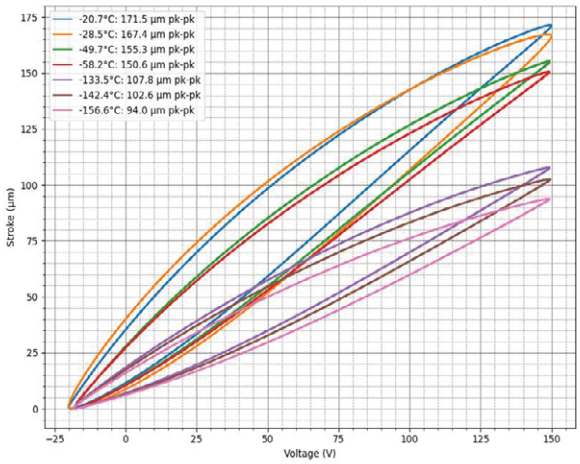


Figure 5: Evolution of stroke performances in cryogenic environment

3.3 CTE variation of APA® actuator in cryogenic environment

In parallel, the CTE of the actuator is measured during the temperature variation of the cryogenic chamber. The variation of CTE between the two Attocube heads is considered negligible compared to the CTE variation of the actuator.

This measurement shows a non-linear behavior of the CTE evolution for the APA prototype

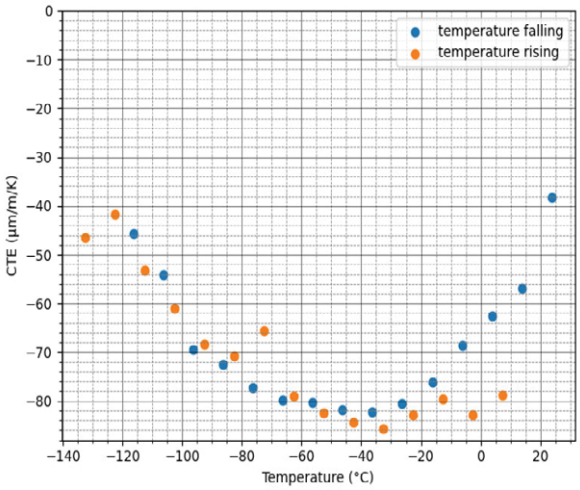


Figure 6: CTE Variation for prototype actuator

4 ECS Sensor integration

The ECS sensor developed by Cedrat Technologies is used as an alternative to the strain gauges which are often used to monitor piezoelectric component hysteresis and non-linearities. The ECS probe is based on coils in a PCB [6] leading to flat design, easily integrable below the APA head. The implementation of such technology presents other various advantages as compatibility with the cryogenic environment and the direct measurement of the actuator stroke - compared to the ceramic displacement in the case of the strain gauge. The tests were made using an equivalent prototype of ECS sensor and actuator.

4.1 ECS placement

The sensitivity of the ECS depends on the distance to the target due to the inductance variation.

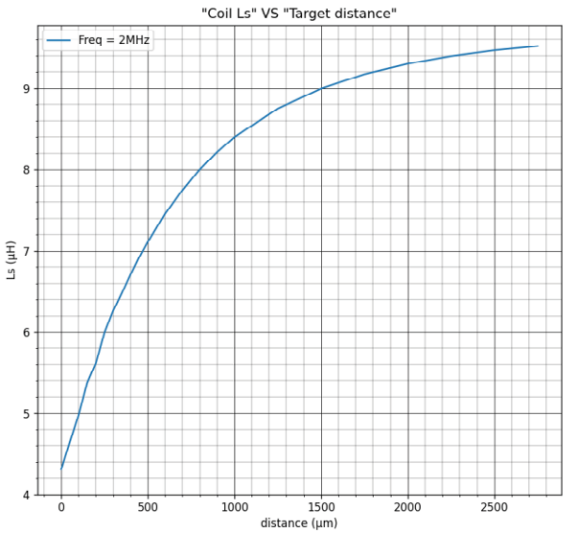


Figure 7: Sensitivity of ECS depending on target distance

The sensor presents an increased sensitivity below a target distance of 1000 µm (**Figure 7**), the variation of inductance is the greatest on this range of placement for the ECS – meaning that the resolution is increased. The **Figure 8** show the impact on the noise generated using an ECS sensor closer to the target. Two cases are compared, for the first one the target is placed at 1005 µm and for the second case the target is placed at 200 µm from the sensor.

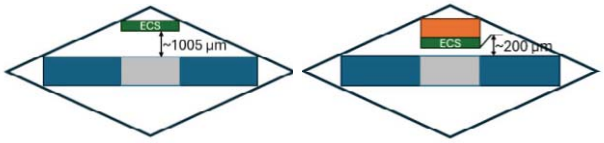


Figure 8: Distance to target for noise test

For the APA600MML-PP NM, the initial distance to target is 600 µm to maximize the sensor measurement on the operating temperature range.

 DOI: 10.30420/456743067

The noise level is measured in both cases, with the ECS at 1005 µm and the ECS at 200µm from its target. With a closer target, the noise level is reduced by a decade (**Figure 9).**

The test is made in open loop conditions using a CCBu20 driver, a Compact Controller Board developed by Cedrat Technologies. This driver is also an embedded all-in-one controller for piezo actuators.

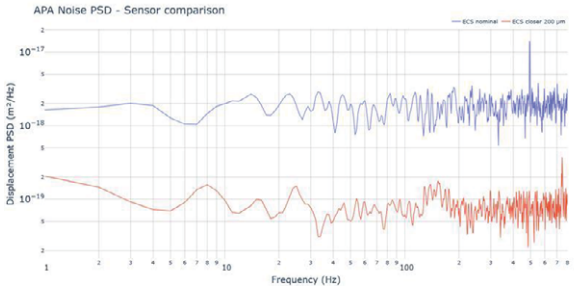


Figure 9: Noise from ECS sensor depending on target distance

	ECS nominal	ECS closer 200 µm
Noise RMS (bandwidth)	~17 nm	~3 nm
SNR with a full stroke	62 dB	77 dB

Table 3 : Noise comparison between the two positions of the ECP in the APA®

4.2 ECS results in cryogenic environment

The ECS sensor can measure the APA® stroke at -150°C temperature conditions (**Figure 10**). The voltage range measured by the ECS sensor and conditioner is -8 V to 4V, thus the linearization of the sensor can still be optimized to increase the resolution performances of the ECS.

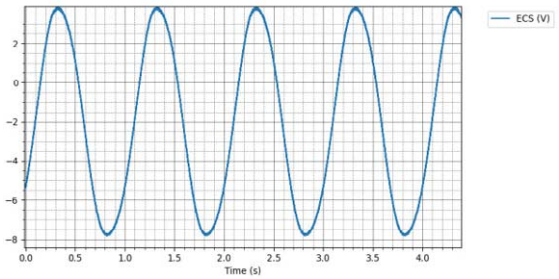


Figure 10: Temporal ECS signal (-150°C)

The behavior of the actuator in open loop is representative of the APA® expected displacement (**Figure 11**). Validating the ability of the ECS to measure the displacement under cryogenic conditions.

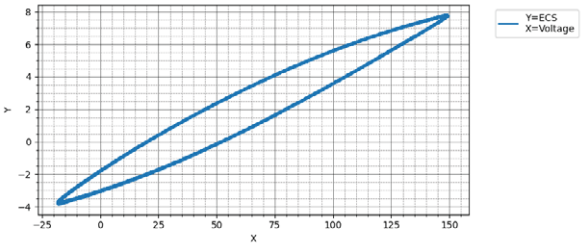


Figure 11: APA® hysteresis with ECS measurement at -150°C

5 Conclusion

The APA600MML-PP NM design is promising regarding the vibration withstanding aspects, it shows an increased force limit without impacting significantly on the static and dynamic performances of the actuator. There is still an uncertainty remaining about the probability of failure due to the mobile mass and number of actuators to integrate in the entire space mechanism. Test campaigns should enhance the capability of performing under 18.04 g-RMS with a 600g payload.

The tests performed in cryogenic conditions on the equivalent technology enhanced the loss of performances under such low temperatures. Introducing the fact that only one fourth of the ceramic performances will be used at -150°C - due to redundancy constraints. This aspect is a pivot in the APA600MML-PP NM design which require at least 95µm of stroke in those conditions. The current design shows a theoretical value of at least 105 µm of stroke, that leaves margins for the actuation.

The ECS implementation on the representative actuator is successful in cryogenic conditions, allowing to monitor the actuator movement and reducing the non-linearity effects of the piezoelectric elements. Yet, the test on the ECS noise enhances the dependence of the set-up on the results obtained. The distance from the target to the sensor must be controlled, considering the CTE mismatch of the actuator, the results of resolution in cryogenic environment might be impacted.

6 Acknowledgement

The authors are grateful to Borja Alvaro Provedo Presencio, SENER Aeroespacial, Paolo Zaltron, ESA for collaboration and funding of these works in DE-SPIN Project, and to Sebastian Netter, OHB for collaboration on the Project.

7 Bibliography

[1] R. Leletty, A New Amplified Piezoelectric Actuator for Precise Positioning and Active Damping, Proc SPIE, Smart Systems and Mat., San Diego Ca, March 1996.

[2] P. Guay, Piezo Qualification for Space Applications, Proc Actuator 2002, Ed. Messe Bremen, B3.2, pp.284-287

[3] R. Le Letty, Miniature Piezo Mechanisms for Optical and Space applications Proc ACTUATOR 2004 Conf, Ed. Messe Bremen (G), June 2004, pp 177-180

[4] C. Allegranza, Actuators for Space Applications: State of the Art and New Technologies, ACTUATOR Conf, Review paper, Bremen (DE), 2014

[5] C. Belly, Cryogenic piezo characterization and integration For Fine Steering Tip/Tilt Mechanism", Conference Actuator 2014

[6] O. Sosnicki, Eddy current sensors on Printed Circuit Board for compact mechatronic application, Proc SENSOR 2010, Ed ITG/GMA-Fachtagung Nürnberg, 18 May 2010

 DOI: 10.30420/456743068

Engineered Shape Memory Behavior in Nb-doped Lead Zirconate Titanate Piezoelectric Actuators.

Mireny Ugalde Reygadas, Discrete Technology and Production Automation, Engineering and Technology Institute Groningen, University of Groningen, 9747AG Groningen, The Netherlands.
m.ugalde.reygadas@rug.nl
Mónica Acuautla, Discrete Technology and Production Automation, Engineering and Technology Institute Groningen, University of Groningen, 9747AG Groningen, The Netherlands.
m.i.acuautla.meneses@rug.nl

Abstract

High-speed operation, compactness, high-efficiency conversion, and design versatility are key advantages of piezoelectric actuators for fast dynamic response and high-accuracy systems. However, in applications that require long-term displacement holding, such as in adaptive optics, the implementation of conventional piezoelectric actuators may result in significant power consumption. Shape memory piezoelectric actuators address this limitation by retaining strain after removal of the electric field. In this work, we develop a shape memory piezoelectric actuator based on Nb-doped PZT ceramics. The actuator exhibits asymmetric strain-electric field loops with a remnant strain of 0.124% and a maximum strain of 0.23% at 10 Hz. Ferroelectric fatigue tests over 10^4 bipolar cycles at 18 kV/cm show reductions of 17% and 22% in maximum and remnant strain, respectively, primarily due to a decrease in internal bias field. Compared with more chemically complex shape memory piezoelectric materials operated at higher cycling rates, the observed degradation indicates improved endurance of the proposed actuator.

1 Introduction

Piezoelectric actuators (PEAs) have shown diverse advantages, such as high-speed operation, compactness, high-efficiency conversion, precision, and design versatility, making them ideal for systems demanding high accuracy and fast dynamic response. Conventional PEAs are operated by applying either DC or AC driving voltage, which in turn actuates the device in accordance with the polarity of the electric field.

In 2007, a novel piezoelectric actuator was proposed by Morita and co-workers [1] known as Shape Memory Piezoelectric Actuator (SMPEA). The SMPEA exhibits an asymmetric strain-electric field (S-E) loop where there is a remnant strain S_r after the removal of an electric field, as illustrated in **Figure 1.** This asymmetry is associated with the imprint effect, mainly attributed to aligned dipole defects within the material [2]. As a result, for an SMPEA, there are two possible strain states at $E = 0$: a relaxed state ($S = 0$) and a deformed state ($S \neq 0$). This actuator is based on polarization reversal, so only piezo-ferroelectric ceramics might present this phenomenon.

SMPEAs represent a promising approach to reducing power consumption in devices based on PEAs, as they do not require a continuous electric field to maintain the displacement. Moreover, SMPEAs offer enhanced controllability owing to their electric-driven nature compared with thermal-activated actuators with shape memory. However, previous works on SMPEAs have primarily focused on inducing remnant strain through electrical poling of commercial unimorph $Pb(Zr_x,Ti_{1-x})O_3$ (PZT) actuators [1,3] or by chemical modification of complex PZT-based systems [4-8,11], which remain challenging to produce at a large scale.

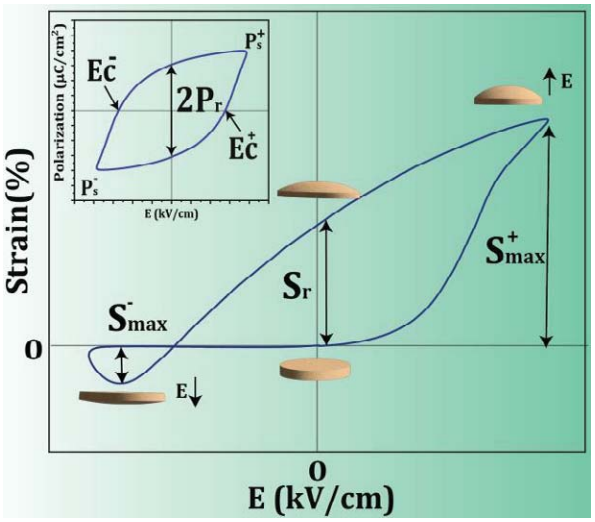


Figure 1 . P-E and S-E hysteresis loops of shape memory piezo-ferroelectric ceramics used in SMPEAs. Some of the most important parameters for shape and ferroelectric memory studies.

In this work, a simpler and more scalable material system for high-performance SMPEAs is presented. In our case, the asymmetric response is achieved by chemical modification, inducing an internal imprint as well as mechanical actuation asymmetry. Nb-doped PZT (PNZT) ceramics were synthesized by the solid-state route and characterized by ferroelectric and piezoelectric loops. In

 DOI: 10.30420/456743068

addition, the stability of the actuators was evaluated over 10^4 operational cycles via fatigue testing, during which polarization and strain were monitored after different electrical loading cycles.

2 Methodology

The SMPEAs were produced by solid-state synthesis. PbO (99.999 %) , ZrO_2 (99.978 %), TiO_2 (99.6 %), and Nb_2O_5 (99.9985 %) were used as reactant powders. An excess of 4 at.% of Pb was used to prevent further Pb volatilization during thermal treatment. The weighted powders were dry ball-milled for a total of 6 h, separating half of the powder after 3 h of milling, using zirconia grinding media. Coarse and fine powders were then mixed, and the resultant powder was calcined in air at 650 ˚C and 850 ˚C for 1 and 2 h, respectively. The calcined powder was uniaxially pressed at 3.2 tons into 10-mm diameter pellets of ∼0.40 g.

The resulting pellets were sintered at 600 ˚C and 1200 ˚C for 1 and 2 h, respectively. Silver paste was deposited on both sides of each pellet and dried at 120 ˚C for 5 minutes. The samples were then poled at 3.5 kV/mm and 120 ˚C for 30 min in a silicone oil bath. After poling, the samples were aged for 42 h. For comparison, a conventional PEA - consisting of a ferroelectric material with no shape memory- based on the same composition was synthesized following the same procedure described.

Ferroelectric (P-E) and S-E loops were obtained by a standard ferroelectric analyzer (TF Analyzer 2000F, aixACCT Systems GmbH) applying sinusoidal waveform electric fields at 10 Hz. From the ferroelectric hysteresis loops, the coercive field (E_c) was obtained. This value was considered for the performance test, where different electric fields were applied to a set of SMPEAs. The ferroelectric fatigue test consisted of the application of $0.5E_c$, $0.75E_c$ and E_c electric load for 10^4 cycles at 10Hz.

3 Results and Discussion

3.1 Ferroelectric and piezoelectric properties of PZT-based SMPEAs

Figure 2A and B show the respective P-E and S-E loops of the conventional PEA and SMPEA based on PZT developed in this work. The polarization response in conventional PEA is symmetric and does not shift along the electric field axis. In addition, the saturation polarization P_s^+ and P_s^- are symmetric. In contrast, the SMPEA ferroelectric loop is slightly asymmetric, showing saturation at positive electric fields but not at negative electric fields. The loop is shifted along negative electric fields, indicating internal electric bias, E_i, mainly attributed to defects within the ceramic. This was determined as the residue between the positive and negative coercive fields, i.e., $E_i = \left|E_C^+ - |E_C^-|\right|/2$.

The E_i of the actuators is ∼2.1 kV/mm under saturation conditions. On the other hand, compared with a conventional PEA, the SMPEA exhibits a significantly higher asymmetry in the S-E loop. Such behaviour has been reported in ferroelectric materials with stable non-180˚ domains and intrinsic defect dipoles aligned by poling [3], [4], [5], [6]. In our case, the defect dipoles $Nb_{Zr/Ti}^{\bullet} - V_{Pb}'' - Nb_{Zr/Ti}^{\bullet}$ are generated to maintain the material's electroneutrality. Moreover, the maximum strain obtained by the SMPEA, $S_{max,SMPEA}$ is larger than the conventional PEA $S_{max,PEA}$ being $S_{max,SMPEA} \geq 3\ S_{max,PEA}$, showing a superior electromechanical response of the SMPEA at the same driving conditions (i.e., $19\ kV/cm$), being $S_{max,SMPEA}^+ = 0.23\%$ and $S_{max,PEA}^+ = 0.06\%$. The linear fitting of both butterfly loops under saturation conditions revealed a d_{33} = 631 and 617 pm/V corresponding to the SMPEA and PEA, respectively. In **Figures 2C and 2D**, the electric field threshold where the remnant strain reaches its maximum is 18 kV/cm. This value is known as the operating electric field, E_O [7] . At this electric field, the remnant strain S_r is 0.124%. On the other hand, the coercive field is asymmetric due to the internal bias, with $E_C^- = -15.7\ kV/cm$ and $E_c^+ = 12.6\ kV/cm$ under saturation conditions. In this scenario, E_O facilitates most of the non-180˚ domain switching, leading to a maximum remnant strain. For larger electric fields, more 180° domains switch, leading to an increment of $S_{max,PEA}^-$.

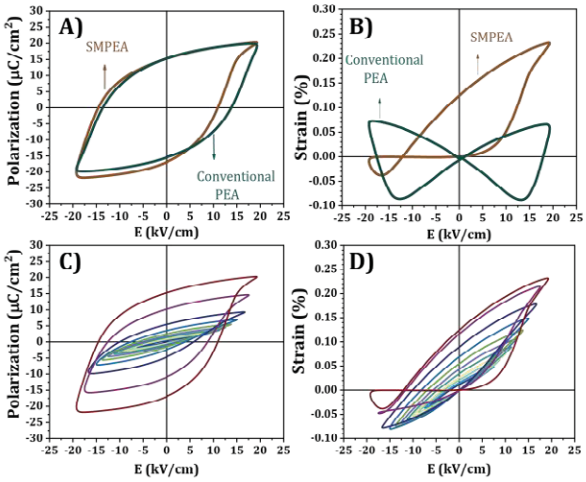


Figure 2. A) P-E and B) S-E hysteresis loops of conventional single PEA (blue) and SMPEA (brown), and C) SMPEA P-E and D) S-E loops evolution under different electric fields.

3.2 SMPEA performance

A previous study reported large shape-memory behaviour in more complex PZT-based ceramics, up to 1.75% [8].

 DOI: 10.30420/456743068

However, the operational stability of these devices has scarcely been studied [4], [9]. In this regard, the performance of the SMPEA was assessed using a ferroelectric fatigue test, in which the S-E and P-E loops were recorded at each decade of cyclic electrical loading.

Figure 3A shows the performance of the SMPEA along 10,000 cycles under application of a bipolar sinusoidal waveform at 10 Hz. At low electric cycling conditions, i.e., E < E_O, There are no noticeable changes in ferroelectricity and shape memory (see Figures **3**B and **3C**).

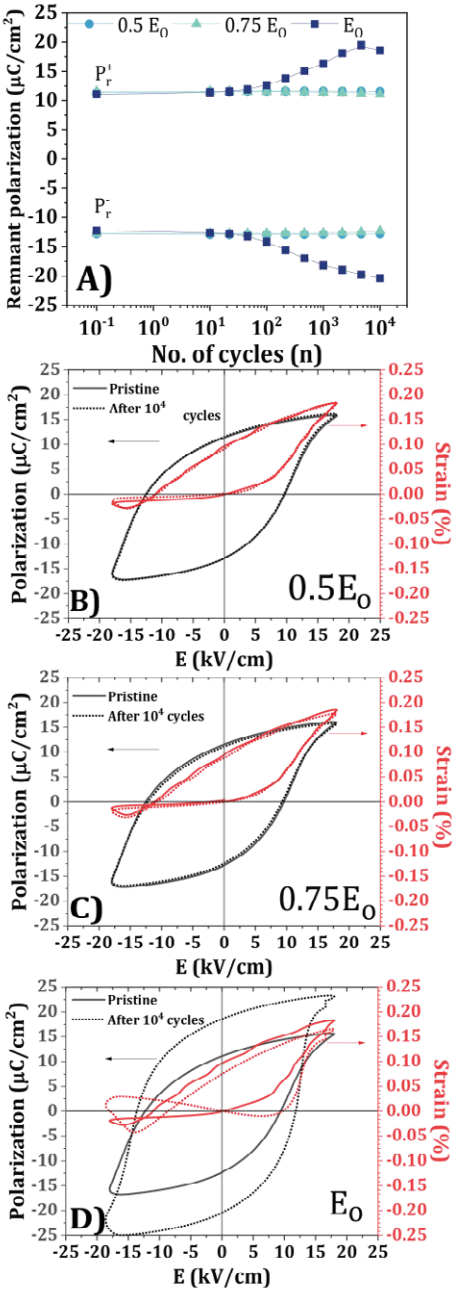


Figure 3. A) SMPEAs fatigue test at 10Hz at different cycling electric loads and the corresponding pristine, and fatigued (after 10^4 cycles) P-E and S-E hysteresis loops at B) $0.5E_O$, C) 0.75 E_O, and D) E_O fatigue electric fields.

Once the device is actuated at electric field $E = E_O$, where $E_O = 18\ kV/cm$, a larger $2P_r$ value is observed through the depinning of domains due to the redistribution of defects within the material[10]. **Figure 3D** shows the increment in the $2P_r$ value corresponding to the evolution of remnant polarization during cycling (**Figure 3A)**. However, the domain depinning is detrimental to the shape memory, as observed in **Figure 3D**, where the S-E pristine loop shows a larger S^+_{max} and S_r than the fatigued loop. This memory decrement is strongly related to internal bias reduction caused by the redistribution of defects within the bulk of the material and the lattice distortion reduction by 180˚ domain switching [3], [6], [11].

Figure 4 shows the evolution of the normalized S_r, S^+_{max}, $2P_r$, and E_i during the fatigue test at E_O. As previously discussed, the fatigue test increased the ferroelectric memory through remnant polarization ($2P_r$) up to 60% more than the pristine value. However, the repetitive large electric load on the actuator reduced the E_i and S_r. Under these conditions, the threshold cyclability is 110 cycles before remnant strain endurance (N) is 95%. The N at 110 cycles is further decreased up to 74% at 10^4 cycles, which is related to a decrease of 40% of the pristine E_i.

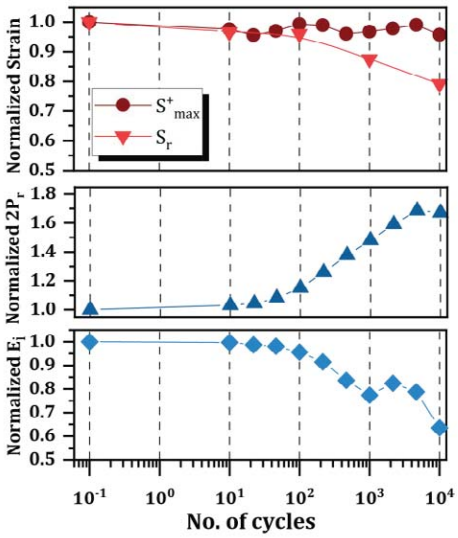


Figure 4. Normalized E_i, $2P_r$ and strain evolution of SMPEA during the fatigue test at $E = E_O$.

The performance stability of our actuators is comparable to the previous reports in chemically complex systems based on PZT [4], [9]. While N~84% at 20,000 cycles [9] and N~75% at 10,000 cycles [4] have been reported, our SMPEA retains the 78% of the initial S_r after 10,000 cycles. Since the conditions of the electric load were more severe in our test ($E = E_O$ at 10Hz), the latter result might be improved by effective design of asymmetrical actuation input signals to prevent the degradation of the shape memory through 180˚ domain switching [3], [5]. This actuator stability positions our SMPEA as a strong candidate for shape memory applications; however, studies of remnant strain retention over different periods are

 DOI: 10.30420/456743068

proposed for further characterization. Figure 5 shows a comparison between some recent literature on shape memory ceramics and this work. Notably, the current work demonstrates a superior piezoelectric coefficient among the ceramics and comparable endurance to heavily doped PSLZT. The addition of different doping agents to PZT lead to a larger remnant and maximum strains (PSLZT-0.15Mn) than the obtained in this work. However, the operability of the material as an actuator might be more challenging due to a larger operational field (E_O). The performance of this ceramic was comparable to some rather complex systems, however the improvement of the memory effect through processing optimization is still under research.

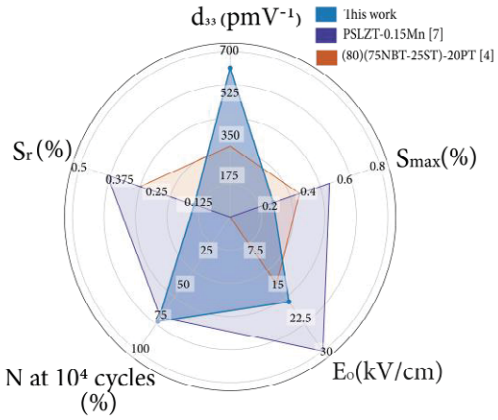


Figure 5. Comparative radar plot of the electromechanical performance of the current work against Pb-content ceramics for shape memory applications.

4 Conclusions

Shape memory piezoelectric actuators were developed by solid-state synthesis, and their ferroelectric and shape memory responses were studied by P-E and S-E hysteresis loops. In addition, the stability of responses was studied by a fatigue test under different electric load conditions. The asymmetric S-E loops show a larger S^{+}_{max} in our SMPEA than in conventional PEA based on the same material. An operating electric field $E_O = 18\,kV/cm$ and d_{33} = 631 pm/V was determined by S-E loops. The maximum and remnant strains achieved at the E_O were 0.23% and 0.12%, respectively. The stability under different electric loads based on this value revealed that actuation at $E < E_O$ was not detrimental for both memory types. However, at E_O, the ferroelectric memory was increased 60% of its original value, while the remnant strain decreased 22% after 10,000 cycles. This behaviour is attributed to 180˚ ferroelectric domains switching and the associated reduction of E_i due to domain depinning. These findings establish a viable pathway towards the development of scalable, chemically engineered piezoelectric materials for versatile shape memory piezoelectric actuators, valuable for nano-positioning systems and adaptive optics applications.

5 Literature

[1] T. Morita, Y. Kadota, and H. Hosaka, “Shape memory piezoelectric actuator,” *Appl. Phys. Lett.*, vol. 90, no. 8, Feb. 2007, doi: 10.1063/1.2709985.

[2] X. Ren, “Large electric-field-induced strain in ferroelectric crystals by point-defect-mediated reversible domain switching,” 2004, *Nature Publishing Group*. doi: 10.1038/nmat1051.

[3] Y. Kadota, H. Hosaka, and T. Morita, “Field-induced strain memory with non-180° domain-reorientation control,” *Journal of the Korean Physical Society*, vol. 57, no. 41, pp. 902–906, Oct. 2010, doi: 10.3938/jkps.57.902.

[4] Y. Yan and Y. Feng, “Large and Stable Shape Memory Effect Realized by Defect Dipoles in Acceptor-Doped Ferroelectric Ceramics,” *Journal of the American Ceramic Society*, vol. 99, no. 1, pp. 206–210, Jan. 2016, doi: 10.1111/jace.13942.

[5] H. Kungl and M. J. Hoffmann, “Temperature dependence of poling strain and strain under high electric fields in LaSr-doped morphotropic PZT and its relation to changes in structural characteristics,” *Acta Mater.*, vol. 55, no. 17, pp. 5780–5791, Oct. 2007, doi: 10.1016/j.actamat.2007.06.035.

[6] A. Pathak, R. Chatterjee, and C. Prakash, “Improvement in shape memory in magnesium niobate modified PZST,” *Ceram. Int.*, vol. 36, no. 8, pp. 2263–2267, Dec. 2010, doi: 10.1016/j.ceramint.2010.07.036.

[7] H. Gu *et al.*, “Oxygen vacancy engineering in Mn doped PZT-based ceramics enables superior strain memory and low overshoot,” *Ceram. Int.*, vol. 51, no. 24, pp. 41335–41344, Oct. 2025, doi: 10.1016/j.ceramint.2025.06.357.

[8] M. Li, W. Li, W. Cao, N. Xu, W. Li, and W. Fei, “Large Electromechanical Response and Field-Induced Shape Memory Effect in Ferroelectric Ceramics,” *Advanced Science*, vol. 12, no. 11, Mar. 2025, doi: 10.1002/advs.202410580.

[9] G. Du *et al.*, “Large stable strain memory effect in poled Mn-doped Pb(Mn 1/3Sb2/3)O3-Pb(Zr,Ti)O3 ceramics,” *Appl. Phys. Lett.*, vol. 102, no. 16, Apr. 2013, doi: 10.1063/1.4803098.

[10] K. Carl and K. H. Hardtl, “Electrical After-Effects In Pb(Ti, Zr)O3 Ceramics,” *Ferroelectrics*, vol. 17, no. 1, pp. 473–486, Jan. 1977, doi: 10.1080/00150197808236770.

[11] H. Gu *et al.*, “Maintainable displacement regulation of ferroelectric shape memory actuators by controlling stable non-180° domain switching,” *Sens. Actuators A Phys.*, vol. 376, Oct. 2024, doi: 10.1016/j.sna.2024.115636.

 DOI: 10.30420/456743069

SUPERPOSITION-BASED FORCE MODELING OF A MULTI-STABLE MAGNETIC LIFT ACTUATOR

Pascal M. Weber[1], Michael Olbrich[2], Yannik T. Rüde[1], Christoph Ament[2], Ulrike Wallrabe[1]*
[1] Laboratory for Microactuators, IMTEK – Department of Microsystems Engineering, University Freiburg, Germany
[2] Chair of Control Engineering, Faculty of Applied Computer Science, University of Augsburg, Germany

Abstract

Multi-stable magnetic actuators rely on nonlinear force–displacement characteristics generated by interactions between permanent magnets and soft magnetic materials. Predicting this behavior for systems with multiple interacting elements remains challenging. This work presents a phenomenological model for the force–displacement behavior of mu-metal ring structures. The interaction of a single ring is approximated by the difference of two weighted derivatives of Gaussian functions, providing an accurate and computationally efficient representation. The behavior of multi-ring configurations is then predicted using a superposition approach, where the total force is obtained as the sum of individual ring contributions. Experimental results show excellent agreement between model and measurements.

1 Introduction

Multi-stable actuators allow for energy-efficient operation by maintaining discrete positions without continuous power input. Such behavior can be achieved through nonlinear physical effects, for example in magnetic systems where interactions between permanent magnets and soft magnetic materials create position-dependent force profiles and corresponding energy landscapes [1, 2, 3]. The resulting force-displacement characteristics determine both the number and location of stable equilibrium positions. However, predicting these characteristics for magnetic systems remains challenging, especially when multiple interacting elements are involved. Established approaches such as finite element or boundary element methods [4] can reproduce the general shape of the characteristics, but are computationally expensive and therefore impractical for rapid evaluation of different configurations. Analytical models for magnetic fields [5] or magnet-to-magnet interactions [6] exist, yet they are often limited in accuracy or computational efficiency when applied to complex geometries. To overcome this limitation, a phenomenological model based on experimental data is introduced to describe the force-displacement behavior of multi-stable systems made of several mu-metal rings [7]. Combined with a superposition approach, this enables efficient and accurate prediction of multi-ring configurations.

2 Actuator Design

The investigated actuator is based on a cantilever-free magnetic lift design similar to [7] (Fig. 1). It consists of a movable plunger with a permanent magnet that slides freely within a linear bearing, without mechanical connection to the surrounding structure. The stable positions of the system are created by several mu-metal rings placed around the linear bearing and separated by FR2 spacers. These rings generate position-dependent reluctance forces acting on the magnet, resulting in multiple stable equilibrium positions. Actuation is achieved using four fixed coils located between the mu-metal rings, enabling controlled movement of the plunger between positions along the actuator axis.

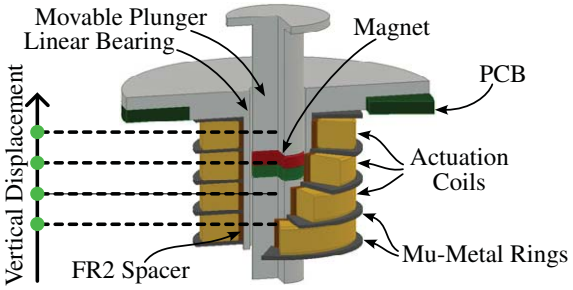


Figure 1 Cross-section of the actuator [7], showing the freely moving plunger within the linear bearing. Mu-metal rings are positioned at z_i using FR2 spacers, with four actuation coils placed in between.

3 Prediction via Superposition

In a first step, the force-displacement behavior of a single mu-metal ring has been measured for different inner diameters d_{in} (Fig. 2b). The force shows an antisymmetric shape with two stable equilibrium positions located symmetrically around the ring center Fig. 2a). To obtain a computationally efficient model, the measured behavior is approximated using the difference of two weighted derivatives of Gaussian functions:

$$F(z) = w_1 \overbrace{\frac{z}{\sigma_1^3\sqrt{2\pi}} \exp\left(-\frac{1}{2}\left(\frac{z}{\sigma_1}\right)^2\right)}^{\text{Derivative of Gaussian}_1} - w_2 \overbrace{\frac{z}{\sigma_2^3\sqrt{2\pi}} \exp\left(-\frac{1}{2}\left(\frac{z}{\sigma_2}\right)^2\right)}^{\text{Derivative of Gaussian}_2}$$

This phenomenological model is defined by four parameters (the weighting factors w_1, w_2 and the Gaussian widths

DOI: 10.30420/456743069

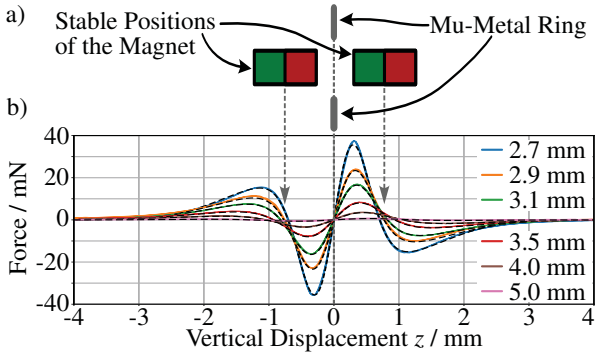


Figure 2 a) Stable positions of the magnet on either side of a mu-metal ring. b) Measured force–displacement curves for a single ring with $d_{out} = 6.5\,\text{mm}$ and varying d_{in}; dashed lines show fits of the model.

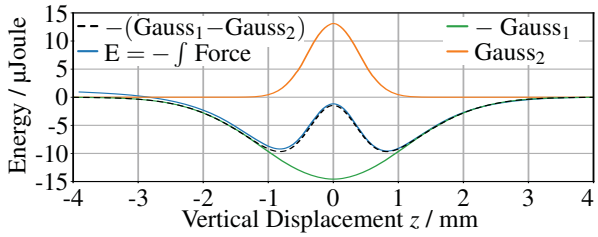


Figure 3 Energy profile (blue) obtained by integrating the measured force for a mu-metal ring ($d_{in} = 3.1\,\text{mm}$, $d_{out} = 6.5\,\text{mm}$). The dashed line shows the Gaussian model. Individual components are shown in green and orange.

σ_1, σ_2) and accurately reproduces the measured force with deviations of only a few millinewtons (dashed black lines). The choice of this formulation is supported by the system's energy landscape (Fig. 3), which can be approximated by the difference of two Gaussian functions, with stable positions corresponding to energy minima. Based on this single-ring model, the force-displacement behaviour of a multi-ring system is predicted using a superposition approach. This is shown in Fig. 4 where each of the five mu-metal rings is represented in gray. This is shown in Fig. 4 where each ring contributes an individual force (gray), shifted according to its position, and the total force is obtained by summation (red). Together with the measured force for this setup is shown in blue, demonstrating excellent agreement between prediction and measurement. Further validation for varying ring spacings (Fig. 5) confirms that the superposition model reliably captures the overall force–displacement behavior. For small ring distances, slight deviations are visible due to magnetic interaction effects not captured by the single-ring model. Nevertheless, the number and location of stable positions are predicted accurately, making the approach well-suited to describe our multi-stable actuator.

Acknowledgements
This research was funded by the German Research Foundation (DFG) within SPP2206 "KOMMMA", project "ADOPT - Adaptive Optics for THz", no. 424616052.

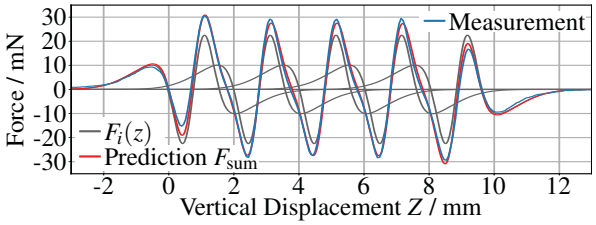


Figure 4 Graphical representation of the superposition, with each force contribution $F_i(z)$ shown in gray. The sum of the contributions forms the prediction (red) and can be compared to the measurement of an actual actuator.

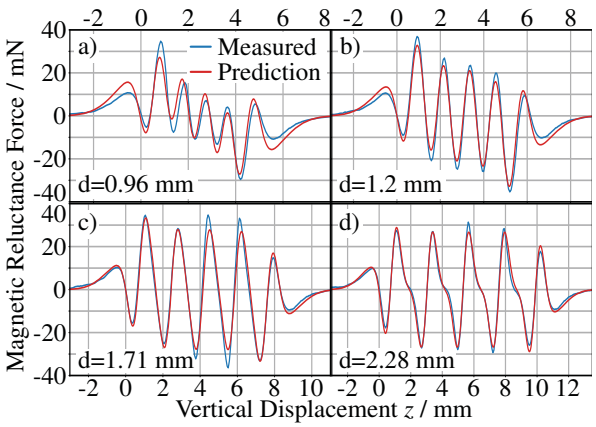


Figure 5 Predictions and measurements of four actuators with different distances d between the mu-metal rings.

4 Literature

[1] Y. Li et.al. A bi-stable vertical magnetic actuator with non-contact latching based on magnetic microlamination technology. *J. Micromech. Microeng.*, 28(10): 105010, jul 2018.

[2] X. Wang et.al. Design and analysis of micro inertial switch with magnetic latch and adjustable threshold. *Microsyst. Technol.*, 30(8):1039–1048, 2024.

[3] X.Q. Li et.al. Magnetic force induced tristability for dielectric elastomer actuators. *Smart Mater. Struct.*, 26(10), 2017.

[4] A. Vučković et.al. Quantitative analysis of magnetic force of axial symmetry permanent magnet structure using hybrid boundary element method. *Symmetry*, 16 (11), 2024.

[5] J.M. Camacho et.al. Alternative method to calculate the magnetic field of permanent magnets with azimuthal symmetry. *Rev. Mex. Fís. E*, 59(1):8–17, 2013.

[6] W. Robertson et.al. A simplified force equation for coaxial cylindrical magnets and thin coils. *IEEE Trans. Magn.*, 47(8):2045–2049, 2011.

[7] P.M. Weber et.al. Cantilever free multistable magnetic lift actuator for large out-of-plane displacements. *proc. TRANSDUCERS 2025*, pp.:600–603, 2025.

 DOI: 10.30420/456743070

Impact of Actuator Pretension and Heat Treatment on the Performance of Piezoelectric Micromembrane Pumps

Nora Weigel[1], Martin Wackerle[1], Daniel Anheuer[1], Gabriele Schrag[2], Martin Richter[1]
[1]Fraunhofer Research Institution for Microsystems and Solid-State Technologies EMFT, Munich, Germany
[2]Technical University of Munich, Germany
nora.weigel@emft.fraunhofer.de

Abstract

Piezoelectric silicon micromembrane pumps hold great potential for a wide range of biomedical applications in which reliability and accuracy are critical. Pump performance is largely determined by the compression ratio, which in turn depends on the membrane's pretension. The precise adjustment of the pretension is therefore essential for the design and operational reliability of the pump. However, the achieved pretension depends on various process parameters, and the influence of operating conditions, such as, elevated temperatures on the pretension remains to be determined. This study demonstrates that impedance analysis is fundamentally suitable as a method for monitoring pretension changes, with initial measurements showing promising results regarding sensitivity and the ability to detect changes at the interface of the piezo ceramic, adhesive, and membrane. Furthermore, it was found that thermal treatment of the pump has a positive effect on pump performance at ambient temperatures. However, this cannot be explained solely by changes in the membrane pretension since the pretensioning technique did not yield the intended convex shape of the actuator. This indicates that further insight into the influencing factors of pretension is required for more reliable operation of piezoelectric silicon micropumps.

1 Introduction

Piezoelectric driven micro diaphragm pumps offer great potential for biomedical devices due to their compact size and ability to transport small volumes of fluid with high efficiency [1]. However, biomedical applications impose multiple challenges and requirements on such systems. In particular, the pumps must be capable of generating sufficient pressure to overcome backpressure levels that may emerge for instance due to fluidic resistance in microchannels or in the form of hydraulic pressure resulting from height variations [1]. Additionally, to ensure reliable and safe usage the pumps must ensure dosing accuracy and precision which necessitates a high bubble tolerance. Bubble tolerance describes the ability to transport media without failure in the presence of bubbles.

Both backpressure capability and bubble tolerance are primarily determined by the compression ratio of the pump, which is defined as the ratio of the total volume to the dead volume [2]. An increased compression ratio enables higher bubble tolerance and greater backpressure capability for compressible fluids [3]. It can be achieved through either a reduction in dead volume or an increase in displacement volume [4]. Achieving both of these objectives is possible through a specific manufacturing technique, detailed in Section 2.2, which results in a pretensioned diaphragm of the micropump [4, 5]. However, the achieved pretension depends on many influencing factors and process parameters, and cannot be precisely adjusted during assembly according to the current state of the art. Furthermore, research is limited in terms of understanding if and how pretension changes during pump usage. Of particular interest is how operating the pump at elevated temperatures, or even briefly heating it, affects its performance.

This study examines the manufacturing process of pretensioning the micropump's membrane, with a focus on changes in impedance during this process. The objective is to gain a deeper understanding of the resonance behavior exhibited by the micromembrane pumps, and to assess the potential of impedance analysis as a monitoring tool for the manufacturing process. The pumps are characterized using both fluidic and optical methods. Fluidic characterization involves measuring backpressure capability, while optical measurements are conducted with a profilometer. The pumps are then exposed to an elevated temperature and re-characterized after the exposure. As part of the study, an electrical impedance measurement is taken after each step.

2 Material and Methods

Piezoelectric micromembrane pumps form the foundation of this study. Initially, piezo ceramics are mounted onto the pump chips. During this process, a specialized technique is employed to pretension the actuator and membrane. A white-light interferometer is used to monitor the changes after each process step is completed. Subsequently, the pump chips are mounted in housings and measured optically as well as fluidically. Multiple electrical impedance spectroscopic measurements are performed during and after the mounting process. Subsequently, the packaged pumps are subjected to heat. After the initial set of measurements, the fluidic, optical, and impedance measurements are repeated.

2.1 Micropumps

This study was conducted with 36 piezoelectrically actuated micro diaphragm pumps manufactured at Fraunhofer EMFT on the same wafer. They possess dimensions of 5 x 5 x 0.6 mm^3 with a pump chamber depth of 3 µm and a membrane thickness of 30 µm. The used piezo ceramics are made from PZT and have a thickness of 55 µm. The pumps are composed of a three-wafer stack made of silicon, as illustrated in Figure 1. The top wafer forms the diaphragm, while the other two wafers function as the upper and lower valve unit of the passive in- and outlet flap valves.

2.2 Pretensioning the Diaphragm – Piezo Ceramic Mounting Process

The aforementioned technique for pretensioning the micropump diaphragm is part of the mounting process for piezoelectric ceramics on pump chips at Fraunhofer EMFT. It is described in detail by Leistner et al. [5] and was used in this study with small adjustments. A pattern of a two-component, non-conductive epoxy adhesive (Epoxy Epo-Tek 353 ND, Epoxy Technology) is dispensed onto each pump chip by a pick-and-place machine. The adhesive has a glass transition temperature of over 90 °C. Subsequently, the piezo ceramic is placed on top of it by a vacuum

 DOI: 10.30420/456743070

nozzle with pressure to ensure electrical contact between the piezo ceramic and the aluminum electrode of the pump chip. The adhesive is then subjected to a curing process, which in this case is separated into two stages. Initially, the glue is left to cure overnight at room temperature. This enables the establishment of electrical contact of the ceramic and the ground electrode via wire bonding, without displacing the ceramic on the liquid adhesive with the force of the wire bonder during attachment of the wire in the next step. Secondly, a thermal curing takes place in an oven at 120 °C for one hour. During that time an electrical field is applied to the actuator (here: 100 V), bending it in downward direction. Once the curing is complete, the pump is cooled down. Below the glass transition temperature of the adhesive, the polymer chains lose their ability to move. The piezoelectric ceramic remains in its deflected shape. Its deformation and residual stress are both constrained. After the curing the voltage is removed, causing the piezo ceramic to return to its relaxed state, thereby bulging the now connecting membrane upwards as depicted in Figure 1. This increased the volume of the pump chamber and thus the compression ratio [1].

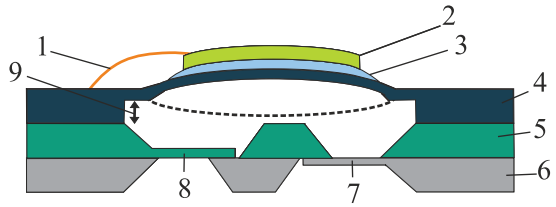


Figure 1 Schematic representation of a pretensioned micromembrane pump. The pump consists of a membrane (4), containing a pump chamber (9), a lower (6) and upper (5). The valve units form the passive flap valves of the inlet (8) and outlet valves (7). The piezo ceramic (2) is attached with an adhesive (3). Electrical connection is established via wire bonding (1). The upward bending of the actuator is caused by the pretension depicted by the convex shape of the membrane and piezo ceramic. The dashed line illustrates the downward deflection of the membrane.

2.3 Optical Characterization

Optical inspections utilizing a white light profilometer (FRT Microprof 300 from Camtek Ltd.) are employed for process control during piezo mounting as well as for analysis of the actuator behavior. The profilometer is equipped with a 2 mm range, 20 nm resolution optical sensor (CWL). A chromatic measuring head enables contactless assessment of two- or three-dimensional surface roughness and structural features.

During piezo mounting, the pump chips are placed in a tool marked with reference points. Using an assembly aid, the tool can be precisely positioned within the interferometer's working space. The reference points facilitate the calibration of the measurement, enabling accurate and easily comparable measurements. The mounting of the piezo ceramic is monitored by measuring a line across the middle axis of the actuator for each of the 36 pump chips after the following three process steps: after dosing the adhesive and the subsequent pick-and-place process, after gelation of the adhesive at room temperature overnight, and after final curing in the oven.

Following the mounting of the pump chips into housings, the behavior of the actuator is subjected to further optical analysis. Therefore, 31 samples are used. To again ensure comparability, measurements must be taken at the same point on the membrane. Another mount is fixed in the working space of the profilometer into which the pump housings are clamped and measured sequentially in the same position and orientation. The deflection of the piezo ceramic is measured at a fixed point, the center of the piezo ceramic, while the pump is actuated with a quasi-static voltage that is changing incrementally in steps of 5 V, reaching a maximum of 120 V and a minimum of -50 V. To ensure that the voltage is kept constant between two voltage steps, an analog amplifier SVR 500/3 (Piezomechanik GmbH) was included in the measurement setup. To achieve a more comprehensive understanding of the bulging of the membrane, an additional linescan is conducted across the middle axis of the actuator at the same voltage levels ranging from -50 V to 120 V. These measurements are repeated with each pump after reheating them in the oven, to determine whether the temperature increase influences the deflection of the actuator.

2.4 Impedance Measurement

In this study, electrical impedance analysis is performed on the piezoelectrically driven micropumps to determine whether the individual process steps lead to distinguishable variations in the recorded impedance curves, thereby validating its potential as a monitoring method and gaining insight into the electromechanical properties.

To ensure reproducibility, all measurements are carried out using a similar experimental setup using a Keysight E4990A Impedance Analyzer (Keysight Technologies). First a wide-range frequency sweep from 500 Hz to 1.5 MHz is conducted, to identify the first and second resonance modes. Then a second automatically positioned sweep is conducted with a span of ± 100 kHz around the identified resonances.

First, the electrical impedance characteristics of the 36 bare piezo ceramics are measured. Then, after mounting them onto the pump chips, the gelling of the adhesive is monitored overnight by taking a frequency sweep of a single pump chip every five minutes. Additionally, the curing of the adhesive at 120 °C with a DC voltage of 100 V applied is monitored of the same pump chip. Measurements are taken at intervals of five minutes. Next, the 36 pump chips are assembled into the housings, and another impedance analysis is conducted. Following a four-hour heating process at 80 °C in an oven, a final frequency sweep is conducted. In this case, the sample size is reduced to 29.

Except for the curing at 120 °C, and the reheating at 80 °C, all measurements are performed at room temperature (23 ± 3 °C).

2.5 Fluidic Characterization

A backpressure test is most suitable for characterizing the pump in terms of fluid dynamics and its capability to pump, as it displays multiple parameters of the pump at once. To accomplish this, the flow rate of the pump is measured while an increasing counterpressure is applied to the pump's outlet, until the pump is no longer able to operate against the pressure, causing the flow to cease. A flow sensor (mass flow meter EL-FLOW Prestige FG-110C from Bronkhorst High-Tech B.V., range: 0.014 ml/min to 0.7 ml/min, accuracy: ± 0.5 %) is installed upstream of the pump inlet. The pump is operated with a 400 Hz square wave signal with sine flanks between -40 V and 80 V, which is produced by a signal generator (33120A Function/Arbitrary Waveform Generator, Keysight Technologies, Inc.) and an amplifier (SVR 500/1, Piezomechanik GmbH). The applied backpressure is facilitated by a pressure controller (Mensor CPC4000) and ranges from 5 mbar to 200 mbar and was increased by steps of 25 mbar,

DOI: 10.30420/456743070

provided that the flow does not stagnate beforehand. The measurement is repeated twice to ensure reliable results. As there is a known linear relationship between applied backpressure and flow rate, as described by Bußmann [1], the measured values are extrapolated up to the maximum backpressure in order to reduce measurement time. All measurements were conducted at temperatures between 22 °C and 24 °C.

For this measurement, the sample size was reduced to 24, since pumps exhibiting valve sticking were excluded. Sticking describes the adhesion of the flap of a valve to the valve seat, which leads to a delay in the opening of the valves and thus a reduced flow since a substantial force is required to separate the components. This phenomenon is unrelated to the actuator and would therefore distort the results of this study.

3 Results

The performance of the assembled micropumps was evaluated through a combination of optical, fluidic and spectrocsopic measurements, during the piezo mounting process, before and after thermal treatment at 80 °C for four hours. The following section presents the recorded results for each pump.

3.1 Optical Characterization

Figure 2 illustrates the line measurements taken along a line through the center of the actuator during the mounting process of the piezo ceramic on two exemplary pumps (C1912, C1711), respectively. Where differences between measurements are given below, they are determined at the dashed line at the center of the piezo ceramic as well as within a range extending ±0.1 mm from it. The curves measured directly after placing the actuator on the adhesive and after drying the assembly overnight are almost equal and are therefore represented by the same light green line in Figure 2. The purple lines display the measurements taken after the adhesive has been cured by heat, thereby completing the mounting and pretensioning process of the piezo ceramic. At this stage, however, the pumps have not yet been assembled in the housing. As stated above, the objective of the pretensioning technique is intended to create an upward bulge in the membrane. This is illustrated in the top part of Figure 2 for C1912, where the purple line curves upwards slightly, reaching a difference of 5.42 µm above the light green line at the center of the ceramic. However, pump C1711 in the lower part of Figure 2 displays a concave form, even though the measurement taken after pretensioning (purple line) is still 2.56 µm higher than before (light green line). An analysis of the 35 pumps in which the piezo mounting was successful reveals that 19 actuators have exhibit a concave form. Otherwise, they show an upwards bulge, or the ceramic is found to be flat. Nevertheless, as illustrated in Figure 2, the concave-shaped membranes exhibit a less pronounced downward curvature, resulting in a significant difference of 4.01 ± 1.73 µm before and after pretensioning for all samples.

Figure 2 displays the measurements taken after the two pump chips were assembled into housings (turquoise line), as well as the measurements taken after reheating the pumps at 80 °C for four hours (dark blue line).

The considerable noise and asymmetry observed in the measurements taken with the profilometer can be attributed to the surface and material properties of the piezo ceramic. Due to the high roughness of the ceramic, it is important that measurements are taken as precisely as possible in the exact same location on the ceramic each time. For this purpose, a mount for the pumps has been attached within the profilometer's working area. Considering this, comparing the measurements after assembling the pumps into housings and after reheating reveals no significant difference.

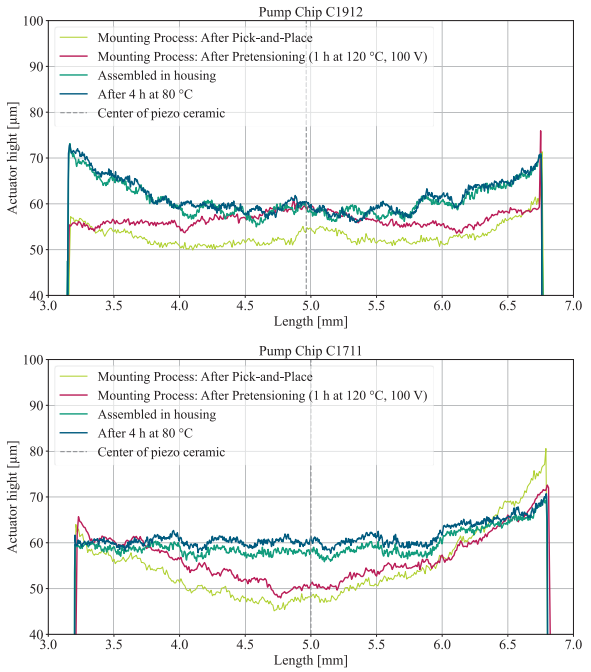


Figure 2 Linescans across the center of the piezo ceramic of pumps C1912 and C1711, showing the shape at zero voltage for different stages of the piezo mounting and pretensioning process, after housing assembly, and after thermal treatment.

The stroke movement of the membrane, which creates over- and underpressure in the pump chamber and thus constitutes the basic principle of the pump, is achieved by applying positive and negative voltages. Different voltage levels lead to different curvatures of the membrane. Negative voltage causes the actuator to bend upwards. When positive voltage is applied, the membrane is bent downwards toward the bottom of the pump chamber. At a certain voltage level, further bending is prevented by what is called the "touchdown", which occurs when the actuator membrane touches the bottom of the pump chamber.

Figure 3 illustrates the center-point deflection of the actuator of an exemplary pump C1906 as a function of the applied voltage levels. The shape of the curve can be attributed to the hysteresis

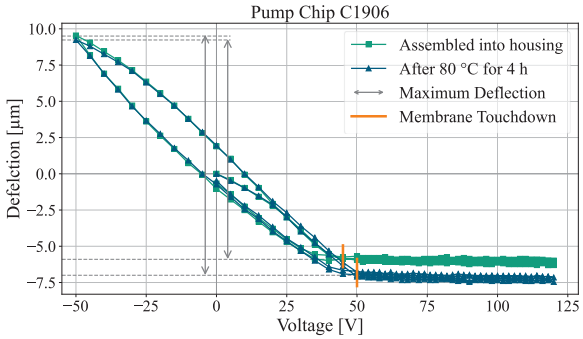


Figure 3 Center-point deflection of the actuator of pump C1906 at different voltage levels, showing the touchdown of the membrane at the bottom of the pump chamber and the maximum achieved stroke.

ISBN: 978-3-8007-6743-4

@ VDE VERLAG GMBH · Berlin · Offenbach

 DOI: 10.30420/456743070

behavior of the piezo ceramic. The voltage at which the touchdown occurs is represented by the orange lines in Figure 3. A comparison of the pre- and post-heating curves of the pumps clearly indicates that the touchdown has shifted to higher voltages. For the pump C1906, the membrane's touchdown at the base of the pump chamber occurred at 42 V following the pretensioning process and at 50 V after it was reheated to 80 °C. The maximum stroke can be determined from this figure, as displayed in the form of two arrows. After the mounting process the maximum achieved stroke is 14.7 µm (right arrow). The measurement taken following the reheating of the pump reveals a stroke of 16.2 µm, as illustrated by the left arrow.

These findings regarding the touchdown of the membrane and the higher stroke were observed in the majority of the 31 examined samples. Figure 4 illustrates the measurements taken after the mounting process of the piezo ceramic (green) and the subsequent reheating of the pumps to 80 °C for four hours (blue). The grey lines connecting two values represent a measurement pair belonging to the same pump. The analysis of the center-point deflection with the profilometer reveals a significant increase in the mean maximum achievable stroke of 1.16 ± 0.07 µm after reheating (Figure 4, left). The voltage at which the touchdown of the membrane occurs has also increased significantly by 5.33 ± 2.90 V, after the reheating of the pumps (Figure 4, right).

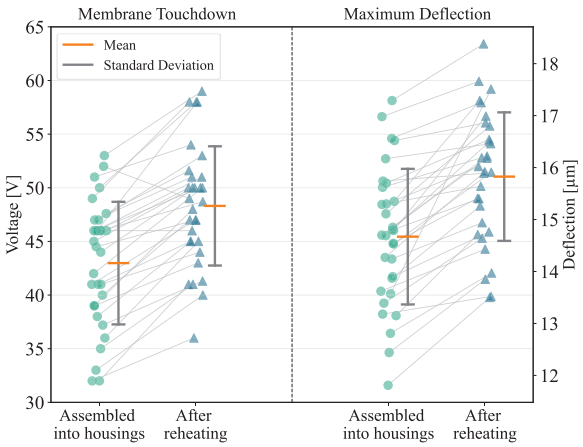


Figure 4 Membrane touchdown and maximum deflection values determined from center-point deflection measurements for each pump. Gray lines connect measurement pairs taken before (turquoise) and after (blue) thermal treatment of 80 °C for four hours.

3.2 Impedance Measurement

Impedance spectroscopy was used to evaluate the impact of thermal treatment on the actuator's electromechanical behavior and to gain deeper insight into the pretensioning process steps. First, impedance analysis was used to monitor an individual pump (C1906) during the piezo assembly process. The curing process of the adhesive is tracked by taking measurements every five minutes during its pre-curing at room temperature overnight and its final curing in the oven. The latter is displayed in Figure 5, with the magnitude of impedance as a function of the resonance frequency within the range of the first resonance. It represents the system's resonance behavior during the curing of the adhesive at 120 °C for 60 minutes with an applied DC voltage of 100 V. The color contours represent time, ranging from dark blue at the beginning to orange one hour later. As the adhesive cures, resonant

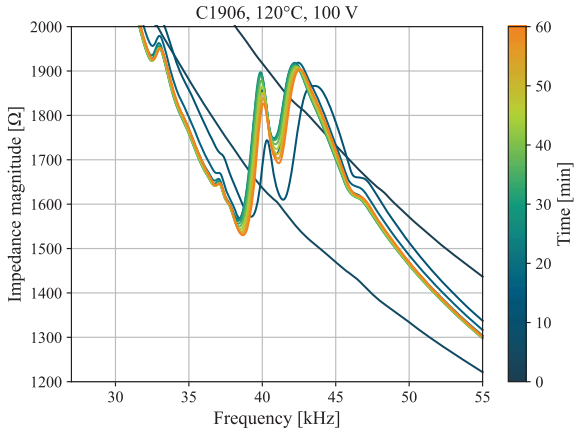


Figure 5 Impedance analysis during curing of the adhesive at 120 °C with 100 V applied during the mounting of the piezo ceramic of pump C1906, showing the impedance magnitude in the range of the first resonance frequency of the system.

peaks become apparent (blue/turquoise lines), which do not change further upon full curing of the adhesive (yellow and orange lines).

Once the pumps have cooled down after the curing in the oven, they are assembled into housings, and an impedance analysis is performed on each of the 35 pumps. The sample size was reduced to 29 for the four-hour thermal treatment at 80 °C. After the reheating process and subsequent cooling, the measurements are repeated. Figure 6 presents the magnitude of the impedance around the first resonance frequency for both measurements of the same exemplary pump (C1906). Resonance peaks are observed at 38.95 kHz with an impedance magnitude of 2237.5 Ω prior to reheating and at 35.20 kHz with 2357.2 Ω after reheating at 80 °C for 4 h.

The mean peak of the samples following the assembly has been recorded at 38.59 ± 2.22 kHz, with an average magnitude of impedance of 2124.1 ± 161.5 Ω. After the reheating process, the results of the impedance analysis show a mean peak at 34.62 ± 2.56 kHz, with an average magnitude of impedance of 2235.2 ± 165.6 Ω. It is evident that the resonance frequencies have significantly shifted towards lower frequencies, while the impedance magnitude has undergone a slight, but significant, increase. This is underlined by Figure 7, in which each data point

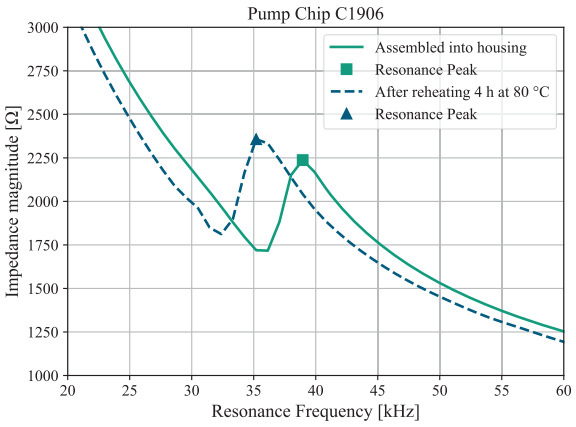


Figure 6 Impedance analysis of pump C1906 showing the frequencies in the range of the first resonance frequency of the system after assembly into the housing, and after reheating.

DOI: 10.30420/456743070

on the graph corresponds to the first resonance peak of a particular sample before and after the reheating process.

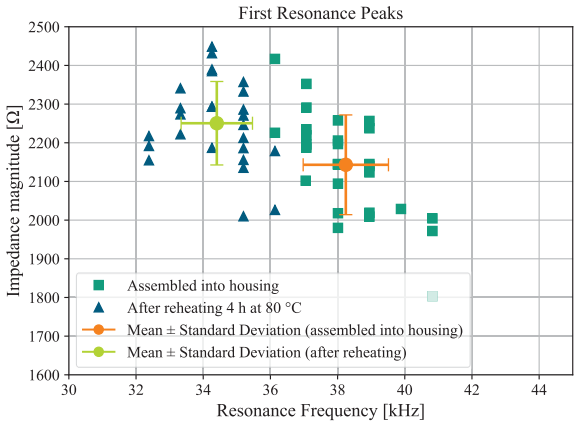


Figure 7 First resonance peaks of the whole sample size after assembly into housings (turquoise) and after reheating (dark blue). Each symbol represents the first resonance peak of a single pump. Mean and standard deviation of each group are also shown.

3.3 Fluidic Characterization

For fluidic characterization, the pump's ability to deliver fluids against an increasing back pressure at the outlet is measured. As described above and illustrated in Figure 8 for pump C1812, the flow rate decreases linearly with increasing pressure up to the maximum achievable backpressure, at which the fluid flow ceases. Figure 8 presents a comparison of the measurements taken after mounting the piezo ceramic and subsequently assembling the pump chips into housings, as well as after reheating the pumps at 80 °C for four hours. With 0 kPa backpressure flow rates of up to 0.51 ml/min after the mounting process and 0.71 ml/min after reheating the pump can be achieved, respectively. The maximum backpressure at which the pump is still able to transport fluid is 33.77 kPa after the assembly and 34.83 kPa after reheating, thereby indicating a shift to enhanced backpressure capabilities.
Figure 9 shows a comparison of the same measurements obtained for the sample size of 24 pumps, only displaying the values obtained for the maximum achievable backpressure and the zero

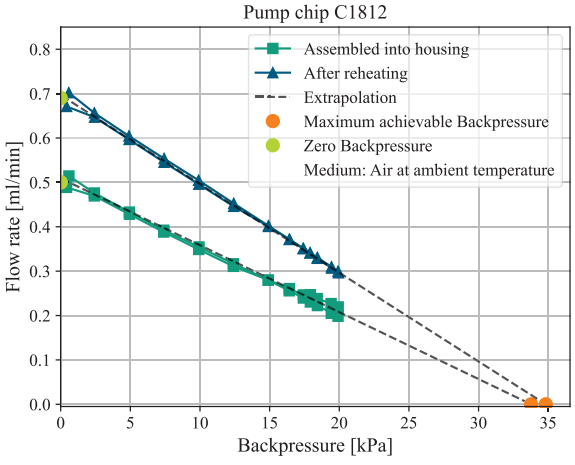


Figure 8 Backpressure measurement of pump C1812 after assembly into the housing (turquoise) and after thermal treatment (dark blue). Maximum achievable backpressure (orange) and maximum flow at zero backpressure (light green).

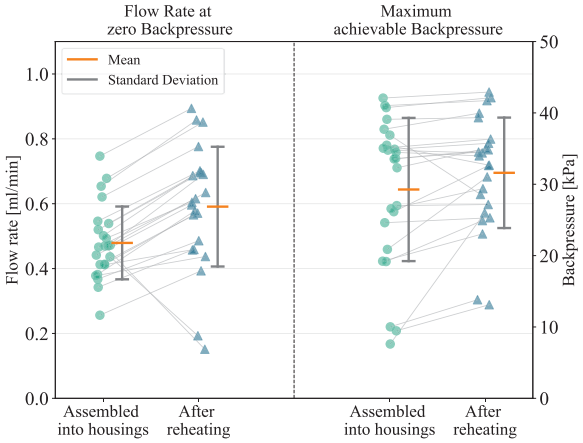


Figure 9 Flow at zero backpressure and maximum backpressure values determined from backpressure measurements for each pump. Gray lines connect measurement pairs taken before (turquoise) and after (blue) thermal treatment.

flow, when no backpressure is applied. The light grey lines connecting the two measurements, both prior to and following the reheating process, demonstrate that they are the same pump. Examining the individual data pairs reveals that the majority show an increase in flow rate and a higher maximum achievable backpressure after the thermal treatment. However, for two samples, it is noticeable that both values are deteriorating.
Considering the mean and standard deviations of the measurement groups, it becomes apparent that the flow rate at zero backpressure increases by 0.112 ± 0.13 ml/min after reheating (Figure 9, left side). The maximum achievable backpressure increases by 2.34 ± 4.82 kPa after thermal treatment. Both parameters show a significant increase following the thermal process, with backpressure exhibiting significantly higher interindividual variability.

4 Discussion and Conclusion

This study investigates the effect of heat on the actuator's pretension and the viability of impedance analysis as a technique for monitoring changes in the system consisting of silicon pump chip, piezoelectric ceramic and adhesive.
The mounting of the piezo ceramic did not achieve the anticipated outcome of curving the piezo ceramic and membrane upwards (Figure 2). According to Leistner et al. [5], the state of the membrane after the pretensioning process and with no voltage applied depends on the difference in the thermal expansion coefficients of the piezo ceramic and the silicon membrane, as well as the electrical pretension of the piezo ceramic. In the study by Leistner et al. [5], a mechanical downward force is applied to the ceramic through pins for electrical connection, which was minimized in the study leading to maximum pretension. However, in the present study, the electrical contact is established by bond wires, which do not apply any additional downward force to the ceramic, and still the pretension was minimal. An additional parameter that could influence pretensioning is the depth of the pump chamber. In this study, pumps with a shallow 3 µm chamber are used. A smaller chamber depth limits downward deflection until touchdown occurs, while a greater depth allows more membrane downward deflection and strain when voltage is applied, thus leading to a greater potential restoring force to push the membrane upward.

ISBN: 978-3-8007-6743-4

@ VDE VERLAG GMBH · Berlin · Offenbach

 DOI: 10.30420/456743070

Impedance spectroscopy reveals that reheating causes the first resonance peak to shift to lower frequencies with a higher magnitude of impedance (Figure 7). Based on the natural frequency equation, the higher magnitude indicates less mechanical dampening, and the shift to lower resonance frequencies indicates a reduced stiffness of the system. These observations suggest that a relaxation process is occurring. This is due to the epoxy adhesive exhibiting viscoelastic behavior at a temperature (80 °C) close to its glass transition temperature (90 °C). Through relaxation, residual stress in the system is reduced. Residual stresses could originate from multiple sources such as clamping forces introduced by the housing, different thermal contraction following cooling after the mounting of the piezo ceramic, or from an uneven adhesive distribution that is cured and introduced by the pressure applied during the pick-and-place process.

The impedance analysis, which was employed on a single pump to monitor different stages of piezo ceramic mounting such as curing of the adhesive, was able to detect the changes in the system's mechanical constraints. Initial changes in the resonant response during the curing are attributed to increased viscous damping, resulting from enhanced molecular mobility due to heating.

Backpressure measurements reveal that two pumps deviate significantly from the overall pattern of the other samples (Figure 9). Upon examination of the different fluidic, optical and spectroscopic measurements, it is evident that they all demonstrate a high standard deviation. This is due to the differences between the individual pump chips. Additionally, the packaging of the pump chips involves a number of manual steps, thereby causing additional variations.

To make changes in the actuator's deflection more visible, a shallow pump chamber was chosen in which touchdown occurs. This enables the change in deflection to be detected by the change in voltage required for touchdown. However, it should be noted that the precise voltage of some measurements cannot be determined with absolute certainty, as there is no discernible point after which deflection no longer changes, due to the measurement resolution. Despite the observed differences when comparing fluidic measurements and optical center-point deflection taken before and after the reheating process, no significant differences were detected in the line measurement across the center of the piezo ceramic of the pump chips assembled into housings. This demonstrates that the zero position of the membrane, with no voltage applied, did not change.

The piezo ceramic is manufactured by a sintering process and has pronounced surface roughness, which is significant at the microscopic level and clearly visible in the line scans in Figure 2. If the interferometer's sensor is not positioned exactly above the center of the piezo ceramic, the deflection of the membrane will result in a slight shift in the detected point. This could lead to a different measured deflection value. To reduce this effect, a mounting tool was used in the profilometer. Added to that, the line scans across the center of the ceramic are aligned to the chip surface. However, a discrepancy of ~10-15 µm is observed at the edges of the piezo ceramic when comparing measurements of the bare pump chip to those of the pump chip assembled into the housing. This occurs despite the thickness of the piezo ceramic remaining unchanged during assembly. We suspect the clamping force induced by the housing could influence the stresses in the membrane of the pump chip.

Following a heating period of four hours at 80 °C, a small but consistent enhancement in pump performance and electromechanical efficiency is observed. Optical measurements (Figure 4) obtained with a profilometer demonstrate that reheating leads to a 1.16 ± 0.07 µm increase in actuator deflection, indicating a modest pretension, while fluidic measurements (Figure 9) show an increase in flow of 0.112 ± 0.13 ml/min with zero backpressure applied and an increase in maximum achievable backpressure capability of 2.34 ± 4.82 kPa. However, it should be noted that this effect may differ when pretensioning leads to a different membrane shape, as in this study.

5 Summary and Outlook

To summarize, the pretension process did not yield the expected shape of the actuator. A modest pretensioning of the membrane still was achieved for all pumps, including those with a downwards curved membrane, which now show a less pronounced convex shape. The study demonstrated a need for additional research on the pretension technique and its determining factors. In this regard, impedance analysis represents a promising non-destructive monitoring tool for both the pretension process and pump characterization, as demonstrated by initial results. Moreover, the findings of this study suggest that the reheating process enhances the pump's performance and its electromechanical efficiency of the packaged pumps after a heating process of four hours at 80 °C. Further investigation is needed to determine the origin of the improved performance. Additionally, it would be interesting to determine whether these improvements are permanent or diminish over time.

Acknowledgements

The authors would like to express their gratitude to the european project MuSiC4Diabetes. MuSiC4Diabetes has received funding from the European Innovation Council (EIC) under grant agreement No. 101115233. The EIC receives support from the European Union's Horizon Europe research and innovation programme.

This project is supported by the Chips Joint Undertaking (Grant Agreement No. 101140192) and its members including the top-up funding of Belgium, Germany, Hungary, Ireland, Italy, the Netherlands, Portugal, Romania and Spain. This work has received funding from the Swiss State Secretariat for Education, Research and Innovation (SERI).

References

[1] A. Bußmann, "Biomedical Application of Piezoelectric Micro Diaphragm Pumps," Dissertation, Institut für Bio- und Lebensmitteltechnik (BLT), Karlsruher Institut für Technologie (KIT), Karlsruhe, 2022.

[2] A. Bußmann *et al.,* "Piezoelectric Silicon Micropump for Drug Delivery Applications," *Applied Sciences*, vol. 11, no. 17, p. 8008, 2021, doi: 10.3390/app11178008.

[3] M. Richter, R. Linnemann, and P. Woias, "Robust design of gas and liquid micropumps," *Sensors and Actuators A: Physical*, vol. 68, 1-3, pp. 480–486, 1998, doi: 10.1016/S0924-4247(98)00053-3.

[4] M. Herz, M. Richter, and M. Wackerle, "Method for manufacturing a bending transducer, a micro pump and a micro valve, micro pump and micro valve," US9410641B2, Mar 5, 2010. [Online]. Available: https://patents.google.com/patent/US9410641B2/en

[5] H. Leistner, M. Wackerle, Y. Congar, D. Anheuer, S. Roehl, and M. Richter, "Robust Silicon Micropump of Chip Size 5x5x0.6 mm3 with 4 ml/min Air and 0.5 ml/min Water Flow Rate for Medical and Consumer Applications," in *Actuator 2021: International Conference and Exhibition on New Actuator Systems and Applications : GMM conference, February 17-19, 2021, online event*, H. Schlaak, Ed., 2021, pp. 113–116.

 DOI: 10.30420/456743071

Prototype of a Camera Focusing Mechanism Driven by a Polyimide Bimorph Thin-film Actuator

Daisuke Yamaguchi, Saki Takamura, Shuichi Wakimoto, and Takefumi Kanda, Okayama University, Okayama, Japan
yamaguchi20@okayama-u.ac.jp

Abstract

A focusing mechanism for compact camera modules was developed using a polyimide bimorph thin-film actuator driven by the difference in thermal expansion between two polyimide layers. The proposed mechanism is ultrathin and lightweight, with a minimum thickness of 50 µm, and the actuator layout fits within a 20 × 20 mm footprint. The two 25-µm-thick polyimide films were welded without pretreatment or adhesive, and aluminium thin-film electrodes were formed for resistive heating. When electrical power was applied, the temperature-dependent expansion mismatch generated bending deformation and out-of-plane displacement of the lens stage. The feasibility of changing the focal position was demonstrated by obtaining focused images at object distances of 5 and 60 cm when electrical power was applied. Owing to its thin profile, non-magnetic operation, and compatibility with semiconductor fabrication processes, the proposed mechanism shows promise for miniaturized optical systems.

1 Background

In camera optical systems, higher pixel resolutions require longer focal lengths to achieve sufficient image quality. However, in compact devices such as smartphones, it is difficult to secure the physical space needed for long focal lengths. To address this limitation, multiple lens elements are often stacked to reproduce equivalent optical effects, which inevitably increases the overall thickness of the camera module. As a result, reducing the module height has become a crucial design challenge for mobile devices. In addition to lenses, mechanical units such as autofocus and optical image stabilization mechanisms further restrict miniaturization. Conventional voice-coil motor actuators face limitations in thickness reduction and can cause magnetic interference with image sensors. Therefore, new actuation mechanisms with thin profiles and non-magnetic operation are highly demanded [1-3].

In our study, a focusing mechanism for compact camera modules was developed using a thin-film actuator driven by the thermal expansion difference of two polyimide layers. It is ultrathin and lightweight, with a minimum thickness of 50 µm, fitting within a 20 × 20 mm footprint. The feasibility of changing the focal position was demonstrated by obtaining focused images at object distances of 5 and 60 cm when electrical power was applied.

2 Focusing Mechanism

A thin-film actuator composed of two 25-µm-thick polyimide (PI) films with different coefficients of thermal expansion has been previously fabricated [4]. In this study, a focusing mechanism was developed using this actuator, as shown in **Figure 1**.

The films were welded together using a proprietary pretreatment and adhesive-free welding process, followed by laser cutting to define the structure. A circular stage was designed at the centre of the mechanism. When a small lens is mounted in a subsequent experiment, an aperture is formed at the centre of the stage. The stage is supported by three thin-film actuators, each equipped with aluminium thin-film electrodes for resistive heating. When electrical power is applied, resistive heating occurs in the aluminium thin-film electrodes. The resulting temperature change causes a difference in thermal expansion between the two PI layers, which generates bending deformation and out-of-plane displacement of the lens stage.

The actuator layout fits within a 20 × 20 mm footprint, and this configuration is compatible with existing semiconductor fabrication processes.

3 Evaluation of Actuator Unit

Before evaluating the complete focusing mechanism, the basic actuation performance of a single thin-film actuator was characterized. The purpose of this evaluation was to confirm whether the actuator could generate mechanical force by resistive heating and thermal deformation. The actuator used for the evaluation is shown in **Figure 2**. The



Figure 1 Prototype of focusing mechanism



Figure 2 Fabricated actuator

ISBN: 978-3-8007-6743-4 @ VDE VERLAG GMBH · Berlin · Offenbach

 DOI: 10.30420/456743071

actuator deactuator dimensions were 8 mm in length, 3 mm in width, and 50 µm in thickness. The actuator was initially curved after fabrication and deformed toward a straight shape when heated by applying electrical power.

3.1 Evaluation of actuator deformation

The relationship between the applied electrical power and the deformation displacement is shown in **Figure 3**. The actuator motion was captured from the side using a camera, and the deformation displacement was measured by image analysis. At an applied electrical power of 2.1 W, the actuator generated a deformation displacement of 2.4 mm.

3.2 Evaluation of generated force

The relationship between the applied electrical power and the generated force was evaluated. The generated force was measured by pressing a load cell against the actuator in its initial configuration. The actuator generated a maximum output force of 2.60 mN when 15.74 W of electrical power was applied. This result indicates that the actuator can generate sufficient force to displace a plastic lens.

4 Feasibility demonstration of variable focusing

A plastic lens was mounted on the focusing mechanism, and a feasibility evaluation was conducted. An imaging sensor was placed under the stage. When electrical power was supplied to the three actuators, the focusing mechanism with the mounted lens moved in the out-of-plane direction. By applying an input power of 0.39 W, images with different focal positions were obtained at object distances of 5 and 60 cm (**Figure 4**). This result demonstrates the feasibility of changing the focal position using the proposed thin-film actuation mechanism, indicating its potential for compact optical systems requiring miniaturized actuation.

5 Conclusions

A focusing mechanism was fabricated using a thin-film actuator composed of two 25-µm-thick polyimide (PI) layers, and its actuation characteristics were evaluated. By applying electrical power, the focal position was successfully adjusted, demonstrating the effectiveness and applicability of the proposed mechanism.
Since PI films are widely used as one of the substrate materials in semiconductor fabrication, the proposed mechanism can be easily integrated around such sensors to realize an ultrathin focusing unit. In addition, the use of only two film layers enables further reduction of camera module thickness.

6 Acknowledgment

This study was partially supported by JSPS KAKENHI (Grant Nos. JP22K03884 and 25K00033).

7 Literature

[1] Nakshatharan, S. S.: Gil, J. G. M.: Punning, A.: Aabloo, A.: Jager, E.: Soft parallel manipulator fabricated by additive manufacturing. Sens. Actuators B Chem. 305 (2020)

[2] Lee, H.-K.: Choi, N.-J.: Jung, S.: Park, K.-H.: Jung, H.: Shim, J.-K.: Ryu, J.-W.: Kim, J.: Electroactive polymer actuator for lens-drive unit in auto-focus compact camera module. ETRI J. 31 (2009) H. 6, S. 695-702

[3] Gabdullin, N.: Ahmad, H.: Ro, J.: Next generation autofocus and optical image stabilization system for camera modules using magnetic shape memory actuators. IEEE Access 8 (2020)

[4] Yamaguchi, D.: Takahara, Y.: Wakimoto, S.: Kanda, T.: Texturing to dramatically increase thermal deformation of bilayer film and application to actuator. IEEJ Trans. Electr. Electron. Eng. 19 (2024) H. 4, S. 1-6

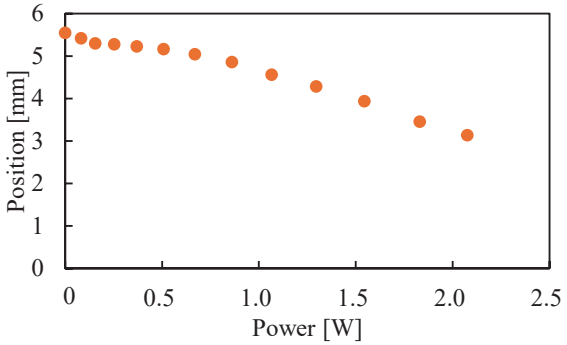


Figure 3 Relationship between the applied electrical power and position of actuator



(a) Focused at 5 cm

(b) Focused at 60 cm

Figure 4 Demonstration of variable focusing

 DOI: 10.30420/456743072

Interlocking-based multistable actuators as fluidic memristors

Ayberk Yüksek[a,b], Mohsen Jafarpour[a,b], and Edoardo Milana[a,b]
[a]FIT—Freiburg Center for Interactive Materials and Bioinspired Technologies, University of Freiburg, Freiburg, Germany
[b]Department of Microsystems Engineering (IMTEK), University of Freiburg, Freiburg, Germany

Abstract

This work introduces neurofluidic systems as a strategy to enable embodied intelligence in soft robots without reliance on conventional electronics. Central to this approach is a memristive fluidic actuator (MFA), a soft, pressure-driven component that integrates actuation, fluidic resistance and memory within a single structure. The MFA operates via a single pressure input–output port and exhibits multistate, nonvolatile resistance behavior, enabling its use as a tunable analog weight in fluidic networks. The MFA consists of a soft inflatable chamber driving the position of the internal pin valve. The multistable mechanism is introduced by attaching a jigsaw-inspired interlocking mechanism to the soft actuator. We also demonstrate control of three distinct behaviors of a dome-shaped snapping actuator that is enabled by a memristive fluidic actuator (MFA), switching between no motion, reciprocal motion and nonreciprocal motion.

1 Introduction

Soft robotics has made notable progress in achieving compliant, bio-inspired motion and sensing [1, 2, 3]. Despite these advances, the implementation of control and decision-making in such systems remains largely externalized, typically relying on rigid electronics or simplified fluidic logic elements [4, 5, 6] . This separation between body and control limits the ability of soft robots to fully exploit their inherent adaptability, particularly in complex or unpredictable environments.

A growing research direction seeks to address this gap by embedding functional intelligence directly into the physical substrate of the robot [7]. Rather than treating control as a separate layer, this approach leverages material properties and structural design to enable distributed, adaptive behavior. Fluidic systems, in particular, offer a promising platform for such integration, as they naturally couple mechanical response with signal transmission.

Physical controllers in soft robotics commonly include self-oscillators and sequencers, each enabling distinct forms of autonomous behavior [7]. Self-oscillators convert a constant input into periodic outputs, often through relaxation mechanisms that switch between discrete states based on output-dependent thresholds. For example, bistable soft valves leveraging the hysteretic response of snapping hyperelastic domes, combined with the kinking of flexible tubes, have been used to generate autonomous oscillations [8]. An entirely 3D-printed version of the valves has been used to implement a ring oscillator that controls the walking gait of turtle-like robot [9]. Other self-oscillators have been introduced in soft robotics, inspired by the ketchup valve design [10] or the "dancing" inflatable tube [11]. In a related study, the bistable memory and sensing elements with a ketchup valve design self-oscillator are implemented in a crawling soft robot and hence various crawling behaviors are achieved [12].

On the other hand, sequencers are designed to produce discrete, ordered patterns of actuation required for tasks such as locomotion or object manipulation [13]. However, implementing complex sequences typically demands multiple control signals and additional fluidic components, increasing system complexity, weight, and cost in soft robotic platforms. A study on nonlinear fluid flow networks also introduced the concept of the fluidic memristor, a soft fluidic element capable of exhibiting history-dependent resistance and hysteresis behavior [14]. Such systems have been explored for applications in soft robotics, where tunable fluidic resistance can enable adaptive control and memory-like functions in soft actuators and fluid-driven devices. These findings also provide insight into biological vascular networks and other soft material systems with nonlinear flow behavior. Furthermore, flexible memristors and systems have been explored for bio-inspired neuromorphic computing in soft robotics; however, this approach still relies on electronic components, whereas fully electronics-free soft robots remain an important goal [15] .

In this context, we introduce a memristive fluidic actuator (MFA) as a core element of neurofluidic systems. Unlike existing fluidic controllers that rely on discrete components, the MFA integrates actuation, fluidic resistance, and memory within a single soft, pressure-driven structure. Through its multistate resistance behavior, it enables modulation of pressure and flow, allowing it also to function as a tunable analog weight in a fluidic network. This provides a scalable approach toward adaptive, electronics-free control in soft robotic systems.

2 Design and Fabrication

2.1 Memristive fluidic actuator

The memristive fluidic actuator is made of a Smooth-Sil 936 silicone-based inflatable actuator that incorporates an

DOI: 10.30420/456743072

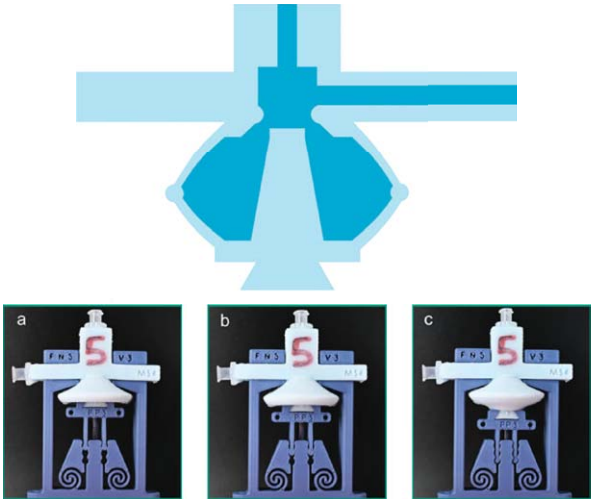


Figure 1 Cross-sectional view of the silicone actuator shows the internal pin valve that modulates the fluidic channel and hence fluidic resistance. Below: working principle of memory and resistance with (a) high, (b) medium, and (c) low resistance states.

internal pin valve and a progressively constricted fluidic channel. The silicone actuator is casted in a single step using 3D-printed molds (Fiberon PPS-CF10) and a 3D-printed sacrificial core (BVOH). The silicone actuator is then housed within a PLA frame (**Figure 1**). The internal pin is mechanically stabilized by a jigsaw-inspired interlocking structure integrated into the frame, enabling discrete and repeatable configurations that correspond to multiple fluidic resistance states [16].

State transitions are governed by a compliant double-spiral hinge mechanism, which constrains the motion of the pin and permits switching only when the applied pressure exceeds predefined thresholds [17]. This threshold-dependent behavior ensures stable retention of each resistance state under subcritical conditions. In addition, a spring element positioned between the pin and the frame facilitates reversible operation, allowing smooth transitions from low to high resistance states under vacuum actuation. The geometry of the interlocking features, the thickness of the double-spiral hinge, and the spring characteristics are carefully tuned to balance multi-stability, switching thresholds, and actuation performance. Together, these design elements enable controlled, repeatable state changes while maintaining reliable fluidic resistive memory within the fluidic system.

2.2 Asymmetric snapping actuator

To demonstrate the capabilities of the MFA, an asymmetric snapping actuator is used as a test platform (**Figure 2**). Fabricated from Smooth-Sil 950 silicone, the actuator features an eccentric dome geometry that induces controlled, directional deformation, as described in [18]. The offset design ensures that deformation initiates on one side and propagates across the structure during pressurization, with the sequence reversing upon depressurization. This results

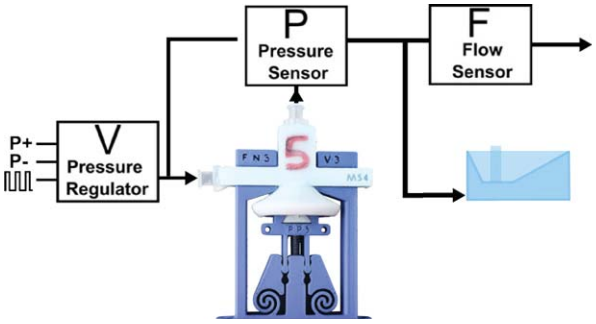


Figure 2 Experimental setup showing pressure regulator valve (V), pressure sensor (P), flow sensor (F), MFA, and asymmetric snapping actuator.

in a repeatable asymmetric motion cycle capable of producing diverse actuation behaviors. Varying the pressure amplitude or frequency of actuation results in dynamic behavior of the snapping cycle [18].

3 Experimental Setup

The control signal is generated using a Keysight 33600A Series Waveform Generator and applied to a pressure regulator valve connected to in-house positive and negative pressure supplies (**Figure 2**). The input signal consists of repeated sequences of five low-amplitude pulses alternating between 1 s at 0.049 bar and 1 s at a baseline level of 0 bar. The oscillatory pulse sequence is employed to drive the asymmetric snapping actuator mechanism within its subcritical regime and to characterize its dynamic response for each resistance state (**Figure 3**).

Between these pulse sequences, isolated higher-amplitude pressure spikes (e.g., 0.096 bar and 0.224 bar) are applied. These spikes, which exceed the respective switching thresholds of the resistance states, are used to induce transitions from the high to low resistance state. Between excitation segments, the signal returns to baseline to maintain the current state. The flow rate downstream of the MFA is measured using a Honeywell AWM5102VN flow sensor, while the pressure difference across the MFA is measured using a Honeywell 015PDAA5 differential pressure sensor, with all measurements recorded using a National Instruments DAQ system.

4 Results and Discussion

The results demonstrate that the MFA exhibits multistate resistance behavior governed by the applied pressure, with stable state retention. As the fluidic channel gap within the MFA progressively decreases, two key outcomes emerge.

First, a distinct pressure drop across the MFA is observed for each resistance state (**Figure 3**). In the high-resistance state (a), the pressure difference is close to the control pressure. In the medium-resistance state (b), the pressure difference is approximately half of the control pressure, while in the low-resistance state (c), it becomes nearly zero. Consequently, for a constant control pressure of 0.049 bar,

 DOI: 10.30420/456743072

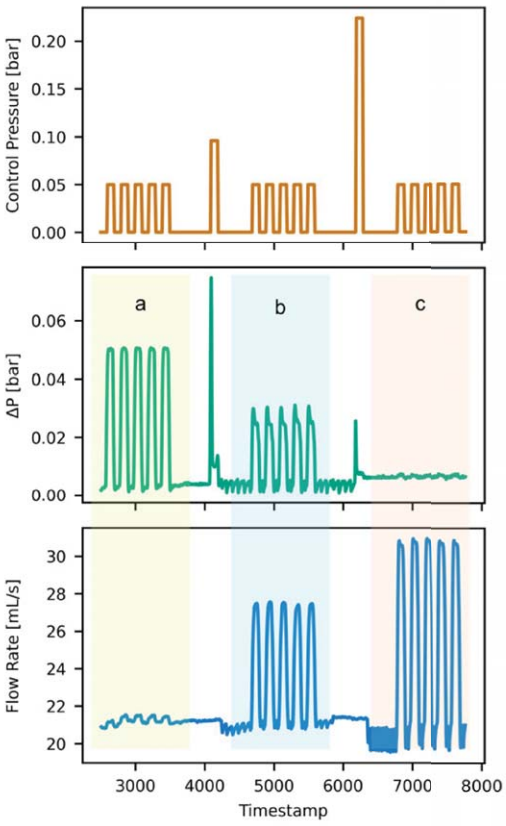


Figure 3 Control pressure input and corresponding MFA response: pressure difference and flow rate across resistance states (a) high, (b) medium, and (c) low.

three distinct output pressure levels can be achieved.

Second, analogous to an electrical circuit, variations in resistance lead to corresponding changes in flow rate. The measured flow rates clearly follow the defined resistance states, as shown in the plots (**Figure 3**). This behavior highlights the potential of these discrete resistance states to function as tunable weights within a neurofluidic circuit.

Building on this multistate behavior, the snapping actuator directly translates the discrete pressure outputs of the MFA into distinct responses (**Figure 4**). As the effective pressure delivered to the actuator varies across resistance states, a corresponding shift in deformation dynamics emerges. Considering that the actuator undergoes a snap-through transition at approximately 0.041 bar, these pressure levels determine whether the system remains below or crosses the instability threshold [18]. Accordingly, the asymmetric snapping actuator remains inactive in the high-resistance state (a). In the medium-resistance state (b), where the applied pressure is close to but below the snapping threshold, the deformation remains smooth and reversible, resulting in reciprocal trajectories under cyclic actuation. In contrast, in the low-resistance state (c), the higher effective pressure drives the actuator beyond the instability point, leading to nonreciprocal behavior characterized by asymmetric loading and unloading paths. Trajectory tracking implemented in Python further confirms this distinction, showing overlapping cycles in the mid-resistance regime and pronounced hysteresis in the low-resistance regime. Together, these results demonstrate how the MFA not only modulates pressure levels but also governs the transition between reciprocal and nonreciprocal actuation, which can be leveraged to emulate different locomotion strategies in soft robotic systems [18].

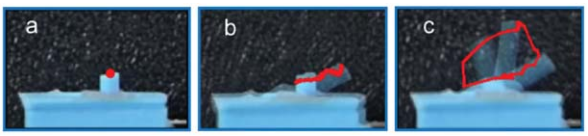


Figure 4 Asymmetric snapping actuator trajectories: (a) high resistance—no motion, (b) medium—reciprocal, (c) low—nonreciprocal

5 Conclusion

This work demonstrates that a memristive fluidic actuator can reliably encode and retain multiple resistance states, enabling direct modulation of pressure and flow within a soft system. These states produce three distinct pressure differences and corresponding flow rates, which in turn control the behavior of an asymmetric snapping actuator. As a result, the actuator exhibits three regimes: no actuation, reciprocal motion, and nonreciprocal dynamics. Future work will focus on combining multiple MFAs together to build a neuro-inspired fluidic network, which is capable to perform complex computation and adapt to dynamic inputs. Such integration provides a pathway toward adaptive and fully embodied control architectures, with potential applications in soft robotic locomotion.

Acknowledgment

This work was funded by the Volkswagen Foundation under the “Pioneering Research – Exploring the Unknown Unknown” program – 9D761.

6 Literature

[1] Rus, D.; Tolley, M. T.: Design, Fabrication and Control of Soft Robots. *Nature*, Vol. 521, No. 7553, 2015, pp. 467–475. doi: 10.1038/nature14543

[2] Laschi, C.; Mazzolai, B.; Cianchetti, M.: Soft Robotics: Technologies and Systems Pushing the Boundaries of Robot Abilities. *Sci. Robot.*, Vol. 1, No. 1, 2016, eaah3690. doi: 10.1126/scirobotics.aah3690

[3] Mazzolai, B.; Laschi, C.: A Vision for Future Bioinspired and Biohybrid Robots. *Sci. Robot.*, Vol. 5, No. 38, 2020, eaba6893. doi: 10.1126/scirobotics.aba6893

[4] Decker, C. J.; Jiang, H. J.; Nemitz, M. P.; Root, S. E.; Rajappan, A.; Alvarez, J. T.; Tracz, J.; Wille, L.; Preston, D. J.; Whitesides, G. M.: Programmable soft valves for digital and analog control. *Proc. Natl.*

Acad. Sci., Vol. 119, No. 40, 2022, e2205922119. doi: 10.1073/pnas.2205922119

[5] Jiao, Z.; Hu, Z.; Dong, Z.; Tang, W.; Yang, H.; Zou, J.: Reprogrammable Metamaterial Processors for Soft Machines. *Adv. Sci.*, Vol. 11, No. 11, 2024, 2305501. doi: 10.1002/advs.202305501

[6] Chen, Z.; Chen, J.; Jung, S.; Kim, H.-Y.; Lo Preti, M.; Laschi, C.; Ren, Z.; Sitti, M.; Full, R. J.; Yang, G.-Z.: Bioinspired and biohybrid soft robots: Principles and emerging technologies. *Matter*, Vol. 8, No. 4, 2025, 102045. doi: 10.1016/j.matt.2025.102045

[7] Milana, E.; Della Santina, C.; Gorissen, B.; Rothemund, P.: Physical control: A new avenue to achieve intelligence in soft robotics. *Sci. Robot.*, Vol. 10, No. 102, 2025, eadw7660. doi: 10.1126/scirobotics.adw7660

[8] Rothemund, P.; Ainla, A.; Belding, L.; Preston, D. J.; Kurihara, S.; Suo, Z.; Whitesides, G. M.: A soft, bistable valve for autonomous control of soft actuators. *Sci. Robot.*, Vol. 3, No. 16, 2018, eaar7986. doi: 10.1126/scirobotics.aar7986

[9] Conrad, S.; Teichmann, J.; Auth, P.; Knorr, N.; Ulrich, K.; Bellin, D.; Speck, T.; Tauber, F. J.: 3D-Printed Digital Pneumatic Logic for the Control of Soft Robotic Actuators. *Sci. Robot.*, Vol. 9, No. 86, 2024, eadh4060. doi: 10.1126/scirobotics.adh4060

[10] van Laake, L. C.; de Vries, J.; Malek Kani, S.; Overvelde, J. T. B.: A Fluidic Relaxation Oscillator for Reprogrammable Sequential Actuation in Soft Robots. *Matter*, Vol. 5, No. 9, 2022, pp. 2898–2917. doi: 10.1016/j.matt.2022.06.002

[11] Comoretto, A.; Schomaker, H. A. H.; Overvelde, J. T. B.: Physical Synchronization of Soft Self-Oscillating Limbs for Fast and Autonomous Locomotion. *Science*, Vol. 388, No. 6747, 2025, pp. 610–615. doi: 10.1126/science.adr3661

[12] Comoretto, A.; Koppen, S.; Mandke, T.; Overvelde, J. T. B.: Embodying Mechano-Fluidic Memory in Soft Machines to Program Behaviors upon Interactions. *Device*, Vol. 3, No. 10, 2025, 100863. doi: 10.1016/j.device.2025.100863

[13] Van Raemdonck, B.; Milana, E.; De Volder, M.; Reynaerts, D.; Gorissen, B.: Nonlinear inflatable actuators for distributed control in soft robots. *Adv. Mater.*, Vol. 35, No. 35, 2023, 2301487. doi: 10.1002/adma.202301487

[14] Martínez-Calvo, A.; Biviano, M. D.; Christensen, A. H.; et al.: The fluidic memristor as a collective phenomenon in elastohydrodynamic networks. *Nat. Commun.*, Vol. 15, 2024, 3121. doi: 10.1038/s41467-024-47110-0

[15] Xu, J.; Luo, Z.; Chen, L.; Zhou, X.; Zhang, H.; Zheng, Y.; Wei, L.: Recent advances in flexible memristors for advanced computing and sensing. *Mater. Horiz.*, Vol. 11, 2024, pp. 4015–4036. doi: 10.1039/d4mh00291a

[16] Malik, I. A.; Mirkhalaf, M.; Barthelat, F.: Bio-inspired "jigsaw"-like interlocking sutures: Modeling, optimization, 3D printing and testing. *J. Mech. Phys. Solids*, Vol. 102, 2017, pp. 224–238. doi: 10.1016/j.jmps.2017.03.003

[17] Jafarpour, M.; Gorb, S. N.: PLA Double-Spirals Offering Enhanced Spatial Extensibility. *Macromol. Mater. Eng.*, Vol. 310, No. 4, 2025, 2400208. doi: 10.1002/mame.202400208

[18] Li, X.; Jin, Y.; Jafarpour, M.; Oliveira, H. de S.; Milana, E.: Snapping Actuators with Asymmetric and Sequenced Motion. *2026 IEEE 9th International Conference on Soft Robotics (RoboSoft)*, 2026.

 DOI: 10.30420/456743073

Investigation of a pressure-driven dielectric elastomer multi-actuator system

Bingzhi Wang[a], Andreas Hubracht[a], Abdelkarim Masoud[a], Chen Jiao[b], Ashwani Sharan Tripathi[b], Uwe Marschner[b], Andreas Richter[b], E. F. Markus Vorrath[b], and Jürgen Maas[a]
[a]Mechatronic Systems Lab, Technische Universität Berlin, Hardenbergstraße 36, 10623 Berlin Germany
[b]Institute of Semiconductors and Microsystems, Technische Universität Dresden, Nöthnitzer Str. 64, 01062 Dresden, Germany

Abstract

Balloon-shaped dielectric elastomer actuator (BS-DEA) enables actuation in the out-of-plane direction and has found applications in various constructions and designs. One of them is a multi-actuator system, consisting of several BS-DEAs as base units. Through sequential activation of e.g. three base units with high voltage, a continuous movement can be transmitted in perpendicular direction. In order to achieve such movement, it is important to acquire a dynamic model of one BS-DEA and research the influence of the electrical activation of a BS-DEA on other BS-DEAs in the multi-actuator system. Therefore, an existing analytical model of single BS-DEA is dynamically extended and validated with experiments. Furthermore, the interaction of single actuators within the whole array is analyzed using the ideal gas equation and researched via simulation, through which several working modes of the multi-actuator system are defined. Finally, the overall interaction is also validated experimentally, with respect to different working modes.

1 Motivation

Among all the practical applications of dielectric elastomer transducers, multi-actuator systems are becoming more and more promising and attract increasing attention of the researchers, due to its ability to perform complex tasks autonomously [1–4]. A system of several DEAs as an array, taking only one input signal while utilizing their internal physical intelligence as 'internal control', can generate complex movement, for instance, wave signal generation. In early works [5, 6], a concept of a multi DEA-DES (dielectric elastomer switch) based multi-actuator system is suggested, after the physical properties of each were investigated and a combined DEA-DES base unit was constructed. In this paper, it is important to further research the interactions of the BS-DEAs during electrical activation, which provides valuable insights of the possible working conditions of the multi-actuator system and its control loop design.

2 Analytical modeling

The multi-actuator system analyzed in this part consists of three BS-DEAs, which share a common air chamber, as depicted in **Figure 1**. All BS-DEAs can be pneumatically pre-streched to a suitable deformation height before individual activation. By use of this fundamental setup, the BS-DEAs are activated sequentially and the system displays a wave-like movement. Since the BS-DEAs are intrinsically connected through the common air chamber, the activation of one actuator will influence the status of the others. In order to enable a general implementation of BS-DEAs into an array-like system, which utilizes the analogous individual movement to achieve a holistic movement control, it is important to research the dynamic behavior of one single BS-DEA and furthermore the overall interaction of the array.

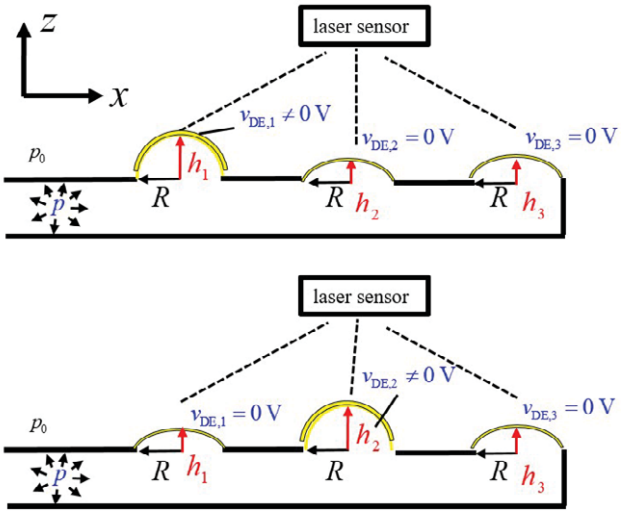


Figure 1: Scheme of the muti-actuator system of three BS-DEAs, through whose sequential activation, a wave movement is to be generated.

2.1 Dynamic modeling of a single DEA

Based on the previous works [5, 7], in which the electromechanical characteristics of BS-DEAs with different geometric scales are analytically modeled and experimentally

 DOI: 10.30420/456743073

validated, a dynamic model of the BS-DEA, using dynamic extension can be derived, by adding an inertia and a damping term:

$$m_{\mathrm{DE}}\ddot{h} + d\dot{h} + F_{\mathrm{m}}(h) = f_{\mathrm{DE}}(h)v_{\mathrm{DE}}^2 + f_{\mathrm{p}}(h)\Delta p, \quad (1)$$

where m_{DE} is the effective mass of the BS-DEA, d is empirically estimated damping as 1 Ns/m, f_{p}, f_{DE} are the pressure and voltage coefficient as functions of h, F_{m} the material force, Δp defined as the difference between the absolute pressure p and the atmospheric pressure p_0, and v_{DE} the voltage applied on the electrodes. The analytical model in the previous work [7], derived by energetic method and a material hyper-elastic model (Ogden or Gent model), can describe the quasi-static deformation process of the BS-DEA well.

2.2 Modeling of the actuator interaction

After activating one BS-DEA with high voltage, the others will be influenced by the pressure change in the common air chamber and their deformation will also change. This process can be modeled by ideal gas equation

$$pV = (p_0 + \Delta p)V = mR_{\mathrm{s}}T, \quad (2)$$

where p is the absolute pressure of the gas (to be differentiated from the gauge pressure Δp measured by the pressure sensor), V the total volume of the gas, m mass of the gas, R_{s} specific gas constant (depending on the particular gas), and T the absolute temperature (in Kelvin). Furthermore, the volume of the gas can be calculated from the measured deformation height h, using the volume formula of a spherical cap:

$$\begin{aligned} V &= V_1 + V_2 + V_3 + V_{\mathrm{chamber}}, \\ \text{with} \quad V_i &= \frac{1}{6}\pi h_i \left(3R^2 + h_i^2\right), \qquad i = 1,2,3, \end{aligned} \quad (3)$$

where h_i is the height of the corresponding BS-DEAs after deformation, V_{chamber} is the volume of the gas in the air chamber when all the BS-DEAs are flat, namely, in the beginning position $h_i = 0\,\mathrm{mm}$, and R is the radius of the BS-DEAs. Besides, the pressure in the air chamber is also influenced by the deformation of the BS-DEAs, which can be described with:

$$m_{\mathrm{DE}}\ddot{h_i} + d\dot{h_i} + F_{\mathrm{m}}(h_i) = f_{\mathrm{DE}}(h_i)v_{\mathrm{DE},i}^2 + f_{\mathrm{p}}(h_i)\Delta p, \quad (4)$$

where $v_{\mathrm{DE},i}$ is the voltage applied on the i^{th} BS-DEAs. Solving Eq. (2)-(4), the deformation heights of all the BS-DEAs after electrical activation, i.e. under a given voltage, e.g. $v_{\mathrm{DE},1} = 2000$ V, $v_{\mathrm{DE},2} = v_{\mathrm{DE},3} = 0$ V, can be determined. Those equations provide the mathematical basis to find suitable working modes and later to design the control loop.

3 Design of the test bench and configuration of the working modes

The test bench includes an air chamber, a pressure controller for the pressure-regulated air supply (ITV01003-BL, SMC, Japan), a gauge pressure sensor (OMSJD-XQYH-01), and three laser triangulation sensors (MICRO

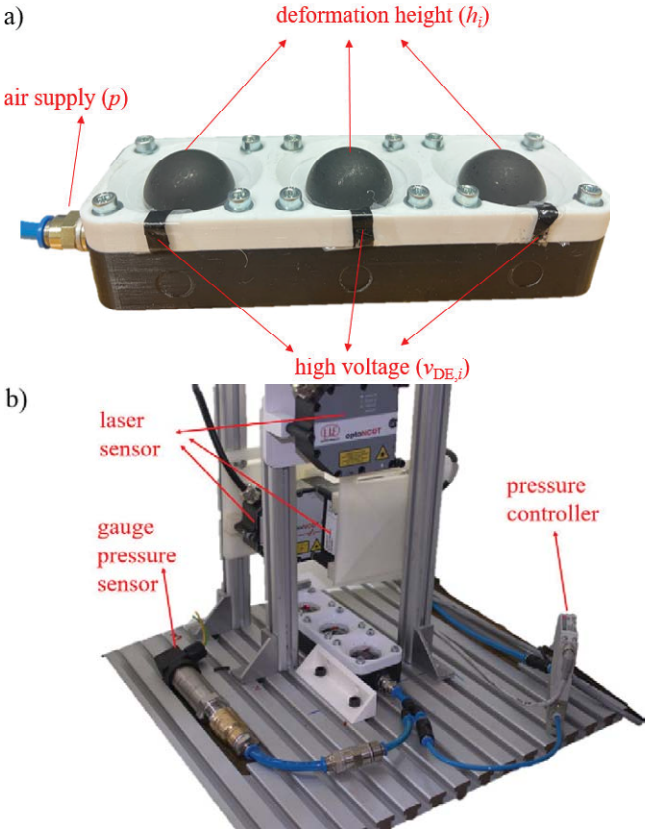


Figure 2: Photo of the common air chamber and the test bench : a) the air chamber embeds three BS-DEAs and the applied pressure is regulated by an air supply. High voltage is applied to the BS-DEAs by a HV-amplifier, while the deformation is measured at the apex of BS-DEAs by laser triangulation sensors. b) the test bench with the air chamber, implemented with three laser sensors, a pressure sensor, and a pressure controller.

EPSILON, optoNCDT 2220), which measure the height h_i (transversal displacement) of the BS-DEAs, as shown in **Figure 2**. The high voltage is applied using HV-amplifier TREK MODEL 10/10B. All the input and output signals are measured by a real-time system (MicroLabBox, dSPACE, Germany). The BS-DEAs tested have a circular form and are manufactured via laminating pre-fabricated thin silicon films as mentioned in [5, 8].

The air chamber is produced using 3D printing and its parts are coated with a thin epoxy resin layer. In order to eliminate the influence of the actuators on each other, each BS-DEA is placed in between its own pair of rings alongside two O-rings to ensure the ring pair with the film is airtight. A lid closed shut with screws is used to compress the O-rings, achieving airtight connections between the components.

The pneumatic coupling of the three BS-DEAs can be modeled using Eq. (2), which enables the definition of several working modes: 1. isobaric, 2. isovolumetric and 3. constant mass.

Those working modes enable diverse levels of actuator in-

 DOI: 10.30420/456743073

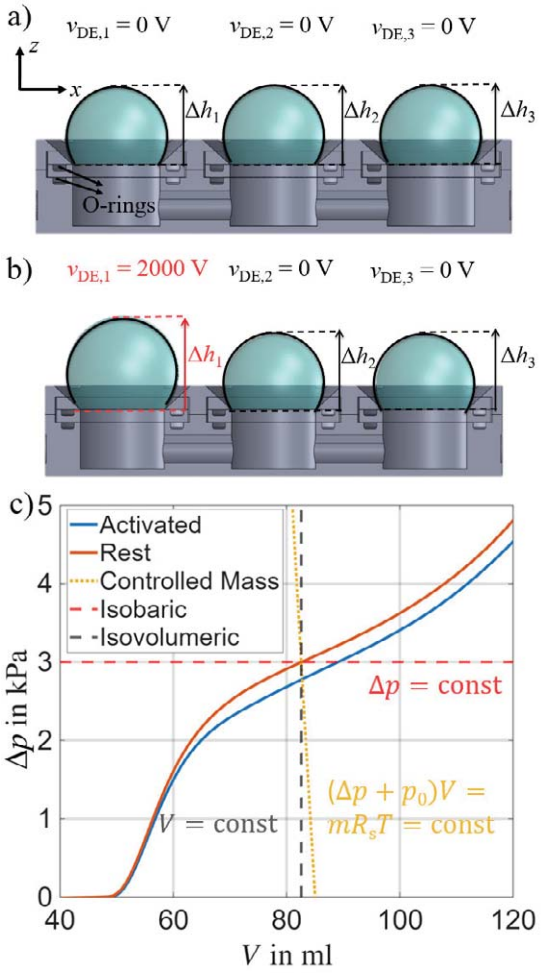


Figure 3: The working modes of the multi-actuator system: a) the rest position of the multi-actuator system; b) the activated position of the multi-actuator system, where high voltage is applied to one BS-DEA; c) the red curve depicts the rest position as shown in a; the blue depicts the activated position coresponding to b; three possible working modes are depicted as dashed lines according to ideal gas equation, where the red is the isobaric type, the grew describes isovolumeric behavior, and the yellow represents the constant mass control.

teraction and require different control loops. As depicted in **Figure 3**, where the blue and red curve describe the quasi-static pressure-volume relationship of the air for two situations: activated and rest, the three dash lines are representations of the three working modes. The isobaric mode, as the default working mode due to the pressure controller in the system, yields the largest volume change, since it theoretically isolates the influence of the activated BS-DEA on the others by stabilizing the pressure (in reality, due to the delay of the pressure controller, the stabilizing is not instant, as to be discussed later in **Section 4**). In contrast, isovolumetic mode guarantees no volume change in the system. It can, however, not be easily achieved due to the compressiblity of gas and requires alternative medium like fluid as coupling. Since it differs only slightly from the third mode, it is therefore not considered further in this paper. Finally, a constant mass mode can be defined as the third mode, which provides also relatively small volume change similar to the isovolumetic. This mode imitates the so called 'closed system', in which the air mass is completely separated from the outer environment.

Since the control element of the used pressure supply is primarily a two point controller, which measures the gauge pressure Δp in the system, compares it with the set value Δp^* and adjusts the air mass accordingly. By emitting air into the atmosphere, if the pressure is higher than the set value and vice versa, isobaric control is already available, while additional control loop is required for the constant mass control. Based on Eq. (2), a control loop is implemented, where the measured heights are transformed into volume using Eq. (3), further multiplied with the absolute pressure p, to calculate the mass m in the air chamber and are compared with the set value of mass m^* as shown in **Figure 4**. For the isobaric mode no extra controller is theoretically required. In reality, however, the two point pressure controller can only regulate the actual pressure Δp proportional to the set value Δp^*, i.e. the stationary deviation is greater when the set value Δp^* increased. In order to compensate the deviation, a PID controller is implemented for the isobaric mode.

In **Figure 5**, sequential activation of BS-DEAs is simulated for isobaric and constant mass mode. It shows that the actuation of one BS-DEA in the constant mass mode (case 3) causes indeed deformation on the other BS-DEAs while there is almost no interaction of BS-DEAs in isobaric mode (case 1).

4 Experimental validation

On the constructed test bench, several experiments are carried out, to validate the dynamic characteristics of BS-DEA and the workings modes of the multi-actuator platform. At first, the validity of the dynamic extension was tested. Therefore, high voltage sequential signals are applied on the electrodes of a single BS-DEA with random interval as shown in **Figure 6** and the deformation change is measured. It shows that the electrical activation can be modeled, especially its dynamic behavior, whereas the stationary deviation is due to the static simulation, to be specific, the fitting process, as discussed in [5]. This could be further improved through future development of a dedicated height-control loop.

Furthermore, the isobaric mode (case 1) of the system is tested. Before electrical activation, the BS-DEAs are pre-stretched pneumatically to a specified height: 8.5 mm under the pressure of 1.24 kPa. This position is used later as the reference point to define the deformation and pressure change. After that, a sequential voltage step signal with amplitude of 2.7 kV and period of 20 s is applied on the middle BS-DEA. The pressure change in the chamber and the deformation change of other BS-DEAs are measured, as shown in **Figure 7**. It can be concluded that the isobaric mode can generate a useful deformation change of approx-

 DOI: 10.30420/456743073

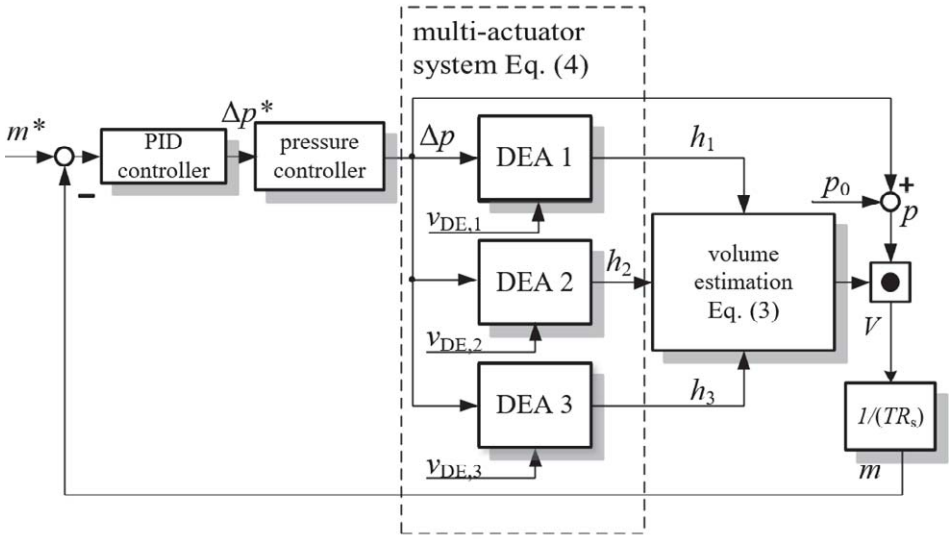


Figure 4: Implemented control loop for constant mass control, consisting of a PID controller, a pressure controller, the multi-actuator system of three BS-DEAs, a volume estimation block, and several components, to implement the ideal gas equation.

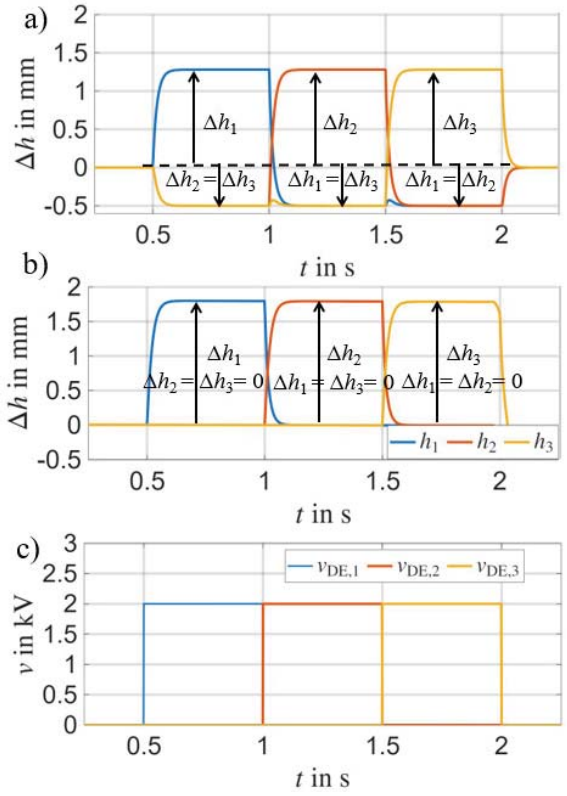


Figure 5: Simulation of sequential electrical activation in constant mass mode and isobaric mode: a) the deformation height change of the BS-DEAs in constant mass control mode; b) the deformation height change of the BS-DEAs in isobaric mode; c) the sequential voltage input applied on the BS-DEAs.

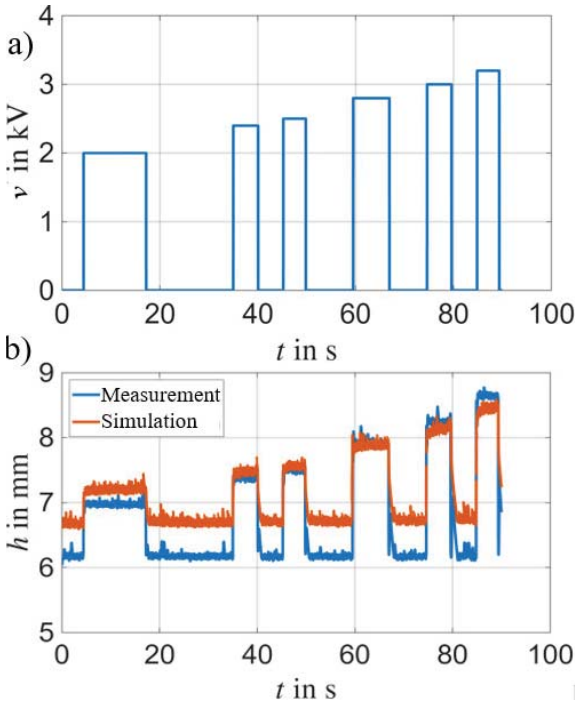


Figure 6: Experimental validation of the analytical model: a) the applied voltage signal and b) the measured deformation change compared with simulation.

imately 2.2 mm and indeed guarantees almost no deformation change on the not activated BS-DEAs. However, a transient peak of pressure and deformation change can still be observed, which is resulted from the delay of the pressure controller. It can also be observed that even with a PID controller, complete suppression of the transient response is not practical due to hardware limitations of the system,

 DOI: 10.30420/456743073

i.e., the response speed of the pressure controller in opening and closing the valves.

Finally, the same test with the sequential voltage is also carried out for the constant mass control. As it can be seen in **Figure 8**, the mass is kept constant at 69.3 mg and the pressure is adjusted by the controller according to Eq. (2). This leads to a reduced deformation height in the non-activated BS-DEAs, with a change of 0.5 mm, as well as a slightly lower deformation in the activated BS-DEA, measuring 1.2 mm. However, the relative difference between the activated and not-activated BS-DEA can still reach 1.7 mm. It is reasonable to indicate, if more BS-DEAs are activated, this relative difference can still increase, which is an appropriate method to improve the displacement of a single actuator.

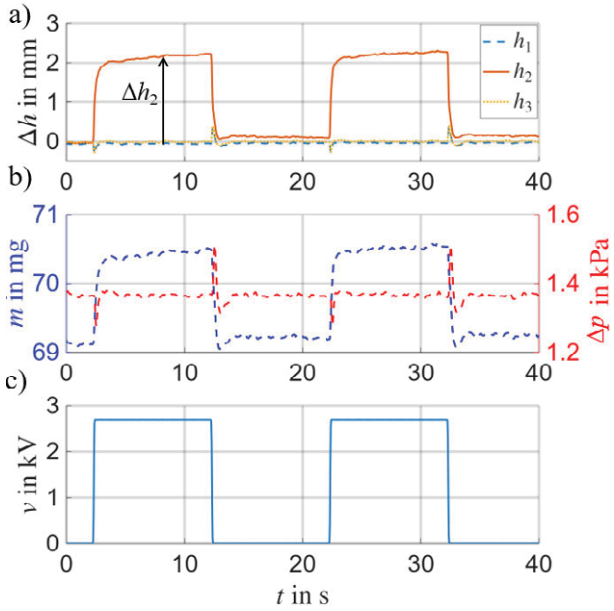


Figure 7: Experimental validation of isobaric mode: a) the deformation change of the BS-DEAs, where h_1 is the left, h_2 the middle, and h_3 the right one in the array; b) the measured gauge pressure change and the air mass in the air chamber; c) the applied voltage signal on the BS-DEA in the middle.

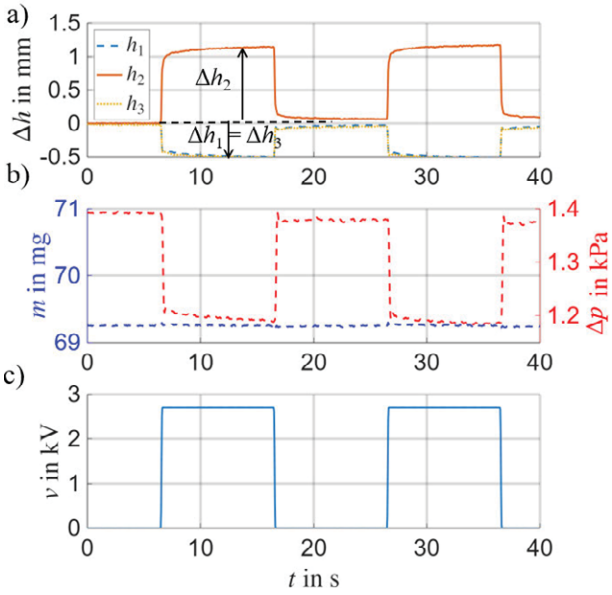


Figure 8: Experimental validation of the constant mass control: a) the deformation change of the BS-DEAs, where h_1 is the left, h_2 the middle, and h_3 the right one in the array; b) the measured gauge pressure change and the air mass in the air chamber; c) the applied voltage signal on the BS-DEA in the middle.

5 Conclusion

In this article a multi-actuator system of three BS-DEAs is investigated. Using the dynamically extended analytical model of the BS-DEA system together with the ideal gas law, two working modes—namely the isobaric mode (case 1) and the constant mass mode (case 3)—are developed, including their corresponding control loop structures. Their dynamic behavior is subsequently validated experimentally on the constructed test bench equipped with a real-time measurement system. Through sequential electrical activation of the individual actuators, both working modes demonstrate the expected mechanical interaction and coupling behavior of the system, confirming the consistency between the theoretical model and the observed experimental response under varying working conditions. The isobaric mode lays a solid foundation for future development of BS-DEA mult-actuator system, in which a minimal interaction of the actuators is expected. The constant mass control provides a possibility to enlarge the displacement of a single actuator by simultaneously activating more actuators in its surrounding. The results indicate that the isobaric mode achieves a deformation of approximately 2.2 mm while causing almost no deformation in the non-activated BS-DEAs. In contrast, the constant mass control results in a lower deformation of 1.2 mm in the activated BS-DEA and about 0.5 mm in the non-activated BS-DEAs, but still provides a relative displacement difference of up to 1.7 mm, which could further increase when additional BS-DEAs are activated.

6 Acknowledgement

This contribution was created as part of the joint project CALMAR in the priority program SPP2206 “KOMMMA” of the German Research Foundation (512586089).

7 Literature

[1] Kohl, M., et al: Cooperative Microactuator Devices and Systems, Actuators, 2024, doi: 10.3390/books978-3-7258-0901-1.

[2] Trivedi, D., et al: Soft robotics: biological inspira-

tion, state of the art, and future research, Appl Bionics Biomech 5:99–117,2008, https://doi.org/10.1080/11762320802557865.

[3] Jang, Y., et al: Analysis of the multi-balloon dielectric elastomer actuator for traveling wave motion, Sensors and Actuators A: Physical, 2022, https://doi.org/10.1016/j.sna.2021.113243.

[4] Seelecke, S., et al: Dielectric elastomer cooperative microactuator systems—DECMAS, Actuators 12(4), 2023.

[5] Hubracht, A., et al: Combination of dielectric elastomer membrane actuators with dielectric elastomer switches to create an autonomous elastomer-based platform, Proc. SPIE 13945, Electroactive Polymer Actuators, Sensors, and Devices (EAPAD), 2026, https://doi.org/10.1117/12.3091823.

[6] Jiao, C., et al: Modelling of Dielectric Elastomer Multiactuator Networks As Cooperative Systems, ASME 2024 Conference on Smart Materials, Adaptive Structures and Intelligent Systems, 2024, doi: 10.1115/SMASIS2024-140344.

[7] Theleman, A., et al: Control-oriented modeling and experimental investigation of a spherical cap dielectric elastomer actuator, MikroSystemTechnik Kongress, Duisburg, 2025.

[8] Krüger, T.S, et al: Manufacturing process for multilayer dielectric elastomer transducers based on sheet-to-sheet lamination and contactless electrode application, Actuators 12:95, 2023, https://doi.org/10.3390/act12030095.

 DOI: 10.30420/456743074

Investigation of bistable mechanisms for energy-free holding using shape memory alloys for 3D-printed valves

Andreas Erben[1], Kenny Pagel[1], Christoph Nitschke[1], Niklas Brömme[1], Welf-Guntram Drossel[1]
[1] Fraunhofer Institute for Machine Tools and Forming Technology IWU, Dresden, Germany
Andreas.Erben@iwu.fraunhofer.de

Abstract

Small, powerful actuators can be constructed using shape memory alloys (SMA). However, actuator designs with a shape memory actuator only have one stable state that can be maintained without energy. The combination of a shape memory actuator and bistable mechanics makes it possible to maintain two positions without energy and to use the actuator only to switch between the two states. This paper discusses the development of a 3D-printable valve powered by a SMA actuator using a bistable heart curve mechanism.

1 Introduction

The application options for SMA actuators are diverse and differ in terms of required stroke, switching force, switching duration and the available energy budget. Thanks to the high energy density and compact design of SMA wires, they can be switched with little energy by a battery. However, some use cases, such as irrigation valves, require that the actuator position can be maintained for a long time, both in a cooled and heated state. This requirement is often not achievable, because shape memory actuators cannot be permanently heated up, if they are powered by a battery. The following section discusses the development of an irrigation valve using a heart curve and a SMA actuator.

2 Experiments

A two-part approach was chosen for the development of the irrigation valve: the bistable mechanism was developed together with the SMA drive while simultaneously the fluidics were designed to switch the water flow. Finally, the complete system was examined to determine the actuating forces, actuating travel and flow rates.

3 Results and Discussion

3.1 Heart curve with SMA-Actuator

Bistable mechanisms are known to be found in ballpoint pens, using the heart curve mechanism. Figure 1 shows the sequence of a heart curve function. Position ① and ③ are stable positions, that can be held without energy. An SMA actuator can be used to switch between these two stable positions.

The switching behaviour of a 3D-printed heart curve was tested over 350 cycles and compared to the theoretically required movement (figure 2). After being heated up for 2 s at the 3.5 s mark, the SMA actuator cools down, maintaining stable position ③. After another 5 s, the actuator is heated again for 2 s, then cools down, reaching stable position ①. As the number of cycles increases, the switching behaviour changes due to the degradation of the SMA actuator and material abrasion from the 3D-printed material.

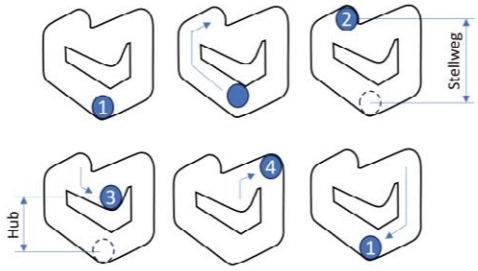


Figure 1: Heart curve bistable mechanism [1]

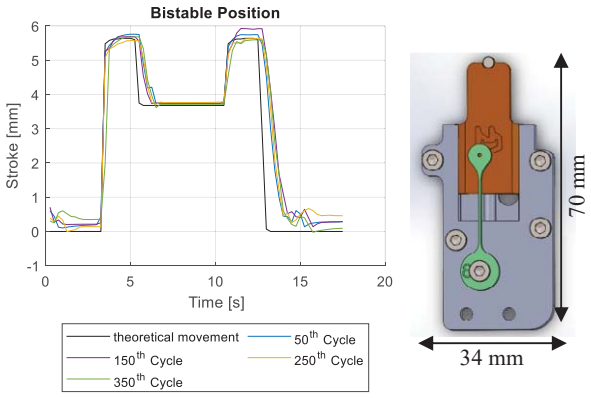


Figure 2: Switching path of the bistable heart curve

3.2 Valve for switching on the water supply

Both a pinch valve and a diaphragm valve were examined in detail and designed. In both versions, a chamfered slide transfers the movement by 90° to a metal ball, which then either presses a diaphragm into the diaphragm seat or, in the case of the pinch tube valve, presses a metal ball onto a silicone hose, reducing the cross-section and preventing any further flow (figure 3). The fluidics are only used to switch the water flow on and off and are not intended to function as a proportional valve.

ISBN: 978-3-8007-6743-4 @ VDE VERLAG GMBH · Berlin · Offenbach

DOI: 10.30420/456743074

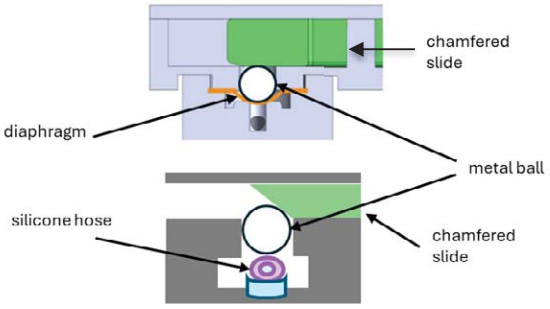


Figure 3: Schematic fluidics – top: diaphragm valve; bottom: pinch tube valve

3.3 Determination of actuating forces and actuating strokes

To identify the actuating force, required to open and close the valve, both valve designs were examined in a tensile-compression testing machine (figure 4), using flow sensors and compressed air for monitoring.

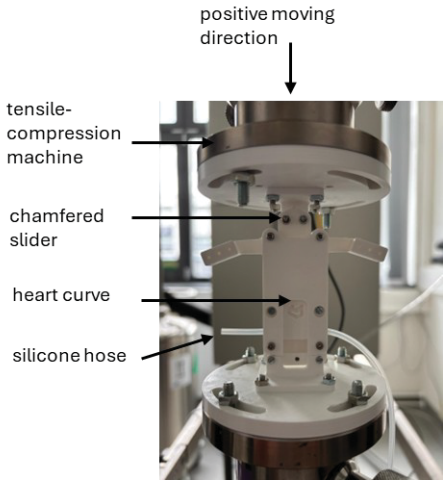


Figure 4: Test setup for measuring closing force and flow rate

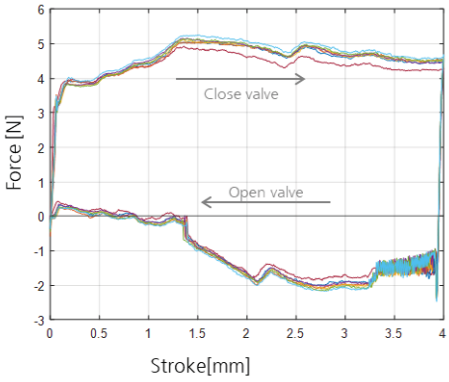


Figure 5: Measurement of the actuating force required to open and close the valve from 0.5-2.5 bar

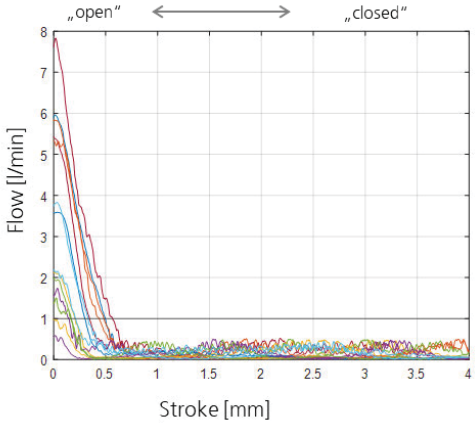


Figure 6: Measurement of flow via the stroke from 0.5-2.5 bar

The results show (figure 5-6) that the valve is already closed after 1 mm and the maximum force of 4-5 N is reached immediately. When the valve is opened, a negative force occurs, which corresponds to the friction in the overall system. Based on the measured values, the valve can be operated with a 150 µm wire, clamped in a V-arrangement with an actuator width of 114 mm and an angle of 27°.

4 Summary

The investigations have shown that it is possible to 3D-print a valve with a bistable mechanism using an SMA actuator. However, the components required a lot of post-processing to compensate for the tolerances of the manufacturing process.

Acknowledgement

We would like to thank the German Federal Ministry of Research, Technology, and Space, which funded this FLOW project as part of DatiPilot Sprint.

Literature

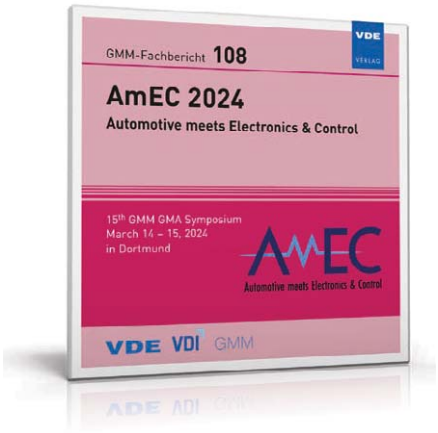
[1] Balck, A.: „Mikrofluidische Komponenten für die Medizintechnik und Biotechnologie“.
Diss. Shaker, 2012. DOI: 10.24355/dbbs.084-201901241300-0.

GMM-Fachberichte

Die Beiträge der GMM-Fachtagungen und -Workshops sind in den GMM-Fachberichten dokumentiert. Die von Programmausschüssen selektierten und zumeist reviewten Beiträge stellen aktuelle Entwicklungen aus der Mikroelektronik, Mikrosystem- und Feinwerktechnik vor.

VDE VERLAG

Technik. Wissen. Weiterwissen.



GMM-Fachbericht Band 108

AmEC 2024

Automotive meets Electronics & Control

15. GMM GMA Symposium, March 14 – 15, 2024 in Dortmund

- The first core field to mention is on applications of artificial intelligence/machine learning (AI/ML) to many different domains. The second core field is trajectory planning, where of course a strong interaction exists with AI/ML. Additional topics cover reliability, fuel cells, sensor technology and new computer architectures which become important for automotive.

2024, 94 Seiten, 140 x 124 mm, Slimlinebox, CD-ROM

54,– €

ISBN 978-3-8007-6284-2 (CD-ROM) ISBN 978-3-8007-6285-9 (E-Book)

Titel / Untertitel	Jahr	Seiten	Buch/CD/E-Book	ISBN-Nummer	Preis
GMM-Fachbericht Band 107 EBL 2024 – Elektronische Baugruppen und Leiterplatten 12. GMM/DVS-Tagung, 05. – 06. März 2024 in Fellbach	2024	316	- / + / +	978-3-8007-6265-1 (CD-ROM) 978-3-8007-6266-8 (E-Book)	148,-
GMM-Fachbericht Band 106 AmE 2023 – Automotive meets Electronics 14. GMM-Symposium, June 15 – 16, 2023 in Dortmund	2023	113	- / + / +	978-3-8007-5990-3 (CD-ROM) 978-3-8007-5991-0 (E-Book)	49,-
GMM-Fachbericht Band 105 Mikro-Nano-Integration Beiträge des 9. GMM-Workshops, 21. – 22.11.2022 in Aachen	2022	131	- / + / +	978-3-8007-5990-3 (CD-ROM) 978-3-8007-5991-0 (E-Book)	82,-
GMM-Fachbericht Band 104 AmE 2022 – Automotive meets Electronics 13. GMM-Symposium, September 29 – 30, 2022 in Dortmund	2022	104	- / + / +	978-3-8007-5955-2 (CD-ROM) 978-3-8007-5956-9 (E-Book)	67,-
GMM-Fachbericht Band 103 IKMT 2022 – Innovative Kleinantriebs- und Kleinmotorentechnik Innovative Small Drives and Motors, Beiträge der 13. GMM/ETG-Fachtagung, 14. – 15. September 2022, Johannes Kepler Universität Linz, Österreich	2022	310	- / + / +	978-3-8007-5938-5 (CD-ROM) 978-3-8007-5939-2 (E-Book)	161,-
GMM-Fachbericht Band 102 EASS 2022 – Energieautonome Sensorsysteme 2022 Beiträge der 11. GMM-Fachtagung, 5. – 6. Juli 2022 in Erfurt	2022	82	- / + / +	978-3-8007-5896-8 (CD-ROM) 978-3-8007-5897-5 (E-Book)	59,-
GMM-Fachbericht Band 101 ACTUATOR 2022 International Conference and Exhibtion on New Actuator Systems and Applications June 29 – 30, 2022 in Mannheim	2022	369	- / + / +	978-3-8007-5894-4 (CD-ROM) 978-3-8007-5895-1 (E-Book)	192,-
GMM-Fachbericht Band 100 Elektromagnetische Verträglichkeit in der Kfz-Technik Beiträge der 8. GMM-Fachtagung, 31. Mai – 1. Juni 2022, Schwieberdingen	2022	100	- / + / +	978-3-8007-5697-1 (CD-ROM) 978-3-8007-5698-8 (E-Book)	67,-
GMM-Fachbericht Band 99 AmE 2021 – Automotive meets Electronics 12. GMM-Symposium, March, 10 – 11, 2021, Online Event	2021	80	- / + / +	978-3-8007-5487-8 (CD-ROM) 978-3-8007-5488-5 (E-Book)	46,-

Sämtliche Veröffentlichungen der GMM-Fachberichte können auch im Abonnement bezogen werden. Preisänderungen und Irrtümer vorbehalten.

Bestellen Sie jetzt: (030) 34 80 01-222 oder
www.vde-verlag.de/gmm-fachberichte